A GENERIC, SEMI-EMPIRICAL APPROACH TO THE STOCHASTIC MODELLING OF BATH-TYPE PYROMETALLURGICAL REACTORS

by

JACOBUS JOHANNES EKSTEEN

Dissertation presented for the Degree

of

DOCTOR OF PHILOSOPHY IN ENGINEERING

Department of Process Engineering

University of Stellenbosch

Promoters:

PROF. M.A. REUTER (Delft University of Technology, The Netherlands)

PROF. S.M. BRADSHAW (University of Stellenbosch, South Africa)

Stellenbosch

April 2004

DECLARATION

I hereby certify that this dissertation is my own original work, except where specifically acknowledged in the text. Neither the present dissertation, nor any part thereof, has previously been submitted for a degree at any university.

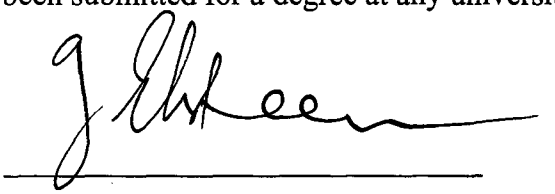

JJ EKSTEEN

FEBRUARY 2004

SUMMARY

Bath type furnaces have become an established technology for the intensive smelting, converting and refining of primary and secondary raw materials. Since these furnaces normally have large inventories, long time constants and complex metallurgies, a dynamic model-based prediction strategy is the only feasible approach to operator decision support and process control. This dissertation presents a semi-empirical approach to the stochastic modelling of bath-type pyrometallurgical reactors, which leads to a generic model type called the Equilib-ARMAX model. The modelling approach is applied to three case studies:

- A nickel-copper matte converting operation using a submerged lance injection reactor
- A chromite smelting operation to produce high carbon ferrochrome using a direct current (DC) plasma smelting furnace
- An ilmenite smelting operation to produce high titania slag and pig iron, using a direct current (DC) plasma smelting furnace

In each case, the industrial operations were analysed with regard to the practical and technological constraints which influence the type and quality of the process data. The fundamental process phenomena associated with each operation have been analysed to ascertain which fundamental variables should be included within the overall semi-empirical approach, without sacrificing model transparency, simplicity, accuracy and calculation time. It was considered that an overly complex model would be inappropriate given that data from industrial smelting operations show significant random variance.

The thermochemistry and phase equilibria associated with each operation are discussed in detail, as they become the fundamental backbone of the semi-empirical models. The equilibria have been modelled with software that uses non-ideal solutions models and Gibbs free energy minimisation to predict the phase and chemical equilibria that could be expected for a given feed recipe and operating temperature. As the thermodynamic modelling software is not stable within an industrial environment, an artificial intelligent mapping technique has been developed to map process inputs to equilibrium outputs. A multi-layer perceptron neural network has been used as the convenient mapping method to represent equilibrium. The neural networks were trained using tens of thousands of feed recipes, where the feed component ratios were varied based on a 3^N factorial design. The amounts and chemistries of all equilibrium phases could be calculated with high accuracies ($R^2 > 0.95$) in all cases.

Further stochastic analysis and modelling require additional information about the property distributions associated with each measurement. The homogeneities of the furnace products (slag, alloy and flue dust) critically influence the level of confidence that one can associate with plant measurements. The homogeneities were characterised for the DC plasma arc furnaces and they were benchmarked against a submerged arc furnace. It was found that the homogeneity varied per element, with silicon and sulphur tending to show highest variations in the alloy melts. The observation that the variation in these two elements are both high can partially be attributed to the fact that SiS evaporates from the bath surface, especially in regions close to the arc attachment zone. A significant negative correlation was found between the relative standard deviation per tap (using silicon) and the degree of superheat / subcooling of the alloy, indicating that the homogeneity can strongly influenced by the changes in rheology due to subcooling below the liquidus (which leads to the precipitation of solid phases and increases the observed melt viscosity). Mixedness or homogeneity and data uncertainty are therefore inseparably linked.

The relative standard deviations associated with the homogeneity characterisation, as well as known sampling and assaying variances were used to develop reconciled material balances based on measured plant data. Material balance closure was therefore obtained within the inherent uncertainties of the plant data. Biases in the plant data were identified simultaneously with data reconciliation. Moreover, it was shown using Fast Fourier Power Spectra and state-space analysis that the data reconciliation was a good low-pass filter, as it extracted the major process trends components in the noisy data and it also improved the overall dynamic behaviour characteristics of the data.

Finally systems identification techniques were used to develop dynamic transfer function models that were linear in the parameters to be estimated. These systems models were based on the reconciled plant data and equilibrium predictions. The final systems models are therefore equilibrium-autoregressive-moving-average models with exogenous variables (Equilib-ARMAX). The model parameters can be estimated recursively using a simple least squares method. The final models could dynamically predict the metallurgy of the subsequent tap 4-6 hours in advance, based on a given suite of set-points, within the inherent accuracy of the data. These models may be used to suggest the optimal operating conditions through an operator guidance system, or more simply, the models are simple enough to be used in a spreadsheet on a manager's desk.

OPSOMMING

Bad-tipe oonde is reeds 'n gevestigde tegnologie wat algemeen gebruik word vir die intensiewe smelting, omsetting en raffinering van primêre en sekondêre roumateriale. Aangesien hierdie oonde normaalweg groot inventarisse, lang tydkonstantes en komplekse metallurgieë het, is dinamiese, modelgebaseerde voorspelling die enigste uitvoerbare benadering tot operateur besluitnemingsteunstelsels en prosesbeheer. Hierdie proefskrif stel 'n nuwe generiese, semi-empiriese benadering voor om die bad-tipe oonde stogasties te modelleer en lei tot die sogenaamde Equilib-ARMAX model. Die modelleringsbenadering word geëvalueer deur drie gevallestudies:

- 'n Nikkel-koper swawelsteen omsettingsproses in 'n dompel-lans inspuit reaktor
- 'n Chromiet smeltingsproses om hoë-koolstof ferrochroom te produseer in 'n gelykstroom (GS) plasmaboogoond
- 'n Ilmeniet smeltingsproses om hoë titania slak en ruyster te produseer in 'n gelykstroom (GS) plasmaboogoond

In elke geval is die industriële prosesse ontleed met betrekking tot die praktiese en tegnologiese beperkings wat die tipe en die gehalte van die prosesdata beïnvloed. Die fundamentele prosesgedrag van elke proses is ontleed om te bepaal welke fundamentele veranderlikes ingesluit moet word in die semi-empiriese benadering, sonder om model deursigtigheid, eenvoud, akkuraatheid en berekeningstyd in te boet. Die ontwikkeling van oor-komplekse modelle is beskou as ongepas, gegewe dat die data van industriële smeltingsprosesse beduidende onsekerhede toon.

Die termochemiese en fase-ewewigte geassosieer met elke proses word breedvoerig bespreek, aangesien dit die fundamentele grondslag van die semi-empiriese modelle verskaf. Die ewewigte is gemodelleer met rekenaar simulasie-programmatuur wat nie-ideale oplossings-modelle en Gibbs vrye-energie minimering gebruik om die fase en chemiese ewewigte, wat verwag kan word vir 'n gegewe toevoerresep en bedryfstemperatuur, te voorspel. Aangesien termodinamiese modelleringsprogrammatuur normaalweg nie stabiele gedrag toon in 'n in-tydse industriële omgewing nie, word kunsmatig intelligente projeksietegnieke gebruik om prosesinsette te projekteer na die ekwavilente ewewigsvoorspellings. 'n Multilaag perseptron neurale netwerk is gebruik as 'n eenvoudige metode om hierdie ewewigsprojeksies voor te stel. Die neurale netwerke is afgerig deur van tienduisende toevoer resepte gebruik te maak. Die verhoudings van die komponente in die voer is gewissel gebaseer op 'n 3^N

faktoriaalontwerp. Die hoeveelhede en samestelling van al die ewewigsfases kon in alle gevalle bereken word met hoë akkuraatheid ($R^2 > 0.95$).

Verdere stogastiese analise en modellering is slegs moontlik met kennis oor die eienskapsverspreidings geassosieer met elke komponent. Die homogeniteite van die oondprodukte (slak, legering en vlieg-as) bepaal, tot 'n groot mate, die betroubaarheidsvlak van die aanlegmetings. Homogeniteite is gekarakteriseer vir die GS-plasmaboogoonde en is vergelyk met die homogeniteite wat in dompelboogoonde gevind word. Die homogeniteite het gevarieer per komponent. Silikon en swawel neig om die grootste ruimtelike variasies te toon in die legerings wat bestudeer is. 'n Beduidende negatiewe korrelasie is gevind tussen die relatiewe standaardafwyking per tap (gebaseer op silikon) en die graad van superverhitting / onderverkoeling van die legering. Dit dui aan dat die homogeniteit sterk beïnvloed word deur veranderinge in die smelt reologie. Vermenging, reologie, homogeniteit en data onsekerheid (integriteit) is daarom ten nouste gekoppel.

Die relatiewe standaardafwykings geassosieer met die homogeniteitsbepaling, asook die monsternemings- en ontledingsvariansies, is gebruik om die aanlegdata te rekonsilieer onderhewig aan die behoud van die komponent en totale stroom massabalanse. Die massabalanse is dus gesluit deur aanpassings aan die metings te maak binne die inherente onsekerhede in die data. Sistematiese foute in die data is gelyktydig met die rekonsiliasie geïdentifiseer. Verder is deur diskrete Fourier energiespektra en toestand-ruimte analises getoon dat massabalans-rekonsiliasie dien as 'n goeie seinfilter om hoë-frekwensie geraas te verminder en tergelykertyd die dinamiese gedragseienskappe van die data te verbeter.

Stelsel-identifikasietegnieke is gebruik om dinamiese oordragsfunksiemodelle te ontwikkel wat linieêr is met betrekking tot die modelparameters. Hierdie stelselmodelle is gebaseer op gerekonsilieerde data, eksogene prosesdata en ewewigsberekeninge, en word vervolgens ewewigs-autoregressiewe-lopende-gemiddelde modelle met eksogene veranderlikes (Equilib-ARMAX) genoem. Die modelparameters kan deur gewone kleinste-kwadrate metodes beraam word. Die finale modelle kan die metallurgie van toekomstige tappe 4-6 uur voortydig voorspel, gebaseer op beskikbare stelpunte en binne die inherente presisie van die data. Hierdie modelle kan gebruik word om optimale bedryfskondisies vir prosesbeheer te identifiseer, en is eenvoudig genoeg om in sigbladformaat op 'n aanlegbetuurder se rekenaar gebruik te kan word.

This dissertation is dedicated to my wife Louise

for her unconditional support, patience and love.

ACKNOWLEDGEMENTS

The completion of this dissertation would not have been possible without the support of many friends, colleagues and students, to whom I would like to express my sincere appreciation. In particular, I would like to thank the following people and organisations for their support:

- My wife Louise, for her faith in my abilities, her tolerance, love and patience;
- Professor Markus Reuter, who guided me and inspired me to take on this research. I would also like to thank him for his friendship and constructive criticism from the inception to the completion of this dissertation. It was his insights which led to expanding the suite of empirical modelling techniques with fundamental terms such as thermochemical equilibrium. This stemmed from his own research into the metallurgical behaviour of submerged arc furnaces and comparisons of furnace behaviour, modelled predictions and chemical equilibrium;
- Professor Steven Bradshaw, for his independent view and friendship;
- Greg Georgalli, my M.Sc student and friend, who was the first to quantitatively evaluate the Equilib-ARMAX model type for matte converters;
- Simon Frank, Wynand Wessels, Nicholas Beukes, Johan Bredell, Andrew MacClelland, Gavin Schreuder, all of whom have contributed in their undergraduate years to aid in capturing and collating industry data, and performing experiments with the laboratory plasma arc furnace;
- Crusader Systems (Pty) Ltd, who funded most of the research;
- the Department of Trade and Industry, who provided additional funding through the THRIP program;
- the government of the Netherlands, who contributed funds (through the NUFFIC program) towards my stay in Delft, Holland;
- Anglo Platinum, Samancor Chrome Division and Namakwa Sands for plant data;
- the workshop team, under the management of Jannie Barnard, for building the laboratory plasma arc furnace;
- Miranda Wildron at the University of Cape Town, for help with the SEM-EDS analyses;
- my parents, who always loved me and never doubted a moment;
- my other colleagues within the Department of Process Engineering, for their understanding and words of motivation.

Finally, I thank God for giving me the opportunities, friends and loved ones, who made everything possible.

TABLE OF CONTENTS

1 INTRODUCTION

> "In general, modelling is very much an art. The modeller must bring a significant level of creativity to the task, namely to make a set of simplifying assumptions that result in a realistic model. A realistic model incorporates all of the important dynamic effects, is no more complicated that is necessary, and keeps the number of variables and equations at a reasonable level." (Seborg *et al.*, 1989)

> "The society which scorns excellence in plumbing because plumbing is a humble activity and tolerates shoddiness in philosophy because it is an exalted activity will have neither good plumbing, nor good philosophy. Neither its pipes nor its theories will hold water." (Gardner's Rule, from Kelly and Spottiswood, 1982)

1.1 Furnace modelling and control in the context of sustainable resource processing and recovery

Pyrometallurgical reactors constitute a key processing component in the total primary and secondary resource cycle, as the furnaces perform both primary smelting, converting and extraction operations, as well as the reprocessing of scrap. To control the overall resource cycle effectively, one needs to take a systems modelling approach of the whole cycle, seeking to also understand the dynamic process behaviour of the individual components of the cycle, and then specifically the part that contributes most to the chemical conversion, namely the pyrometallurgical reactor or furnace.

Metals are produced through a long chain of processes. For primary resources, metal production proceeds via mining, mineral processing, ore smelting, conversion and refining steps or via hydrometallurgical processes, or a combination of pyro- and hydrometallurgy. For the secondary resources, metals are separated and recovered from metal scrap, which play an increasingly important role in the world. After metal extraction, either from primary or secondary resources, the crude metals have to be further refined or manufactured into various types of alloys and finally shaped into different products to the end-users. Since the end-user

eventually discards these products, the contained metals find their way back into the resource cycle as scrap. Therefore, good metallurgical reactor control implies improved control of the material quality in the complete metals cycle, from production to the end-use, up to the recycling phase. Therefore, the metallurgical processes in each unit operation in the metals production and processing chain have to be controlled, so as to achieve optimal performance of high product quality, low energy and materials consumption, and low environmental impact. Symbolically Figure 1.1, depicting the links between three interconnected cycles, best illustrates these interactions: the life cycle - the technology cycle - the resource cycle. The optimal control of all these cycles is affected substantially by good control of metal production and refining (Reuter *et al.*, 2003).

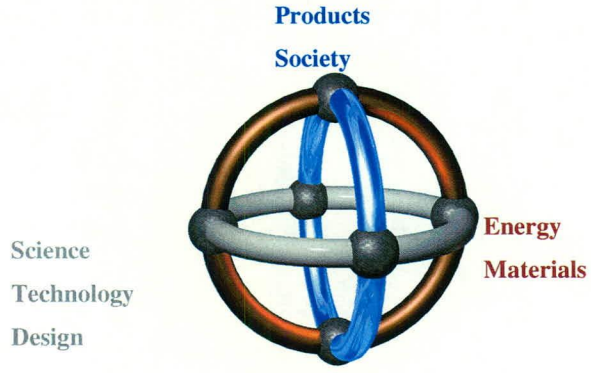

Figure 1.1: Achieving Sustainability (Reuter *et al.*, 2003)

Sustainable processing is not possible without proper reconciled material flow models and proper dynamic process models that can be used to manage or control processes. The objective of these control actions are very clear, i.e. they (i) optimize product quality, (ii) minimize energy consumption, and (iii) optimize metal flows. Therefore, control should not only maximize economical benefits, but at the same time also minimize associated ecological effects.

Despite the above-mentioned ideals for process modelling and control of pyrometallurgical reactors, actual model-based control of the process metallurgy in furnaces remains elusive. The nature of pyrometallurgical operations make the implementation of any form of modelling and control very difficult, as explained in the following section.

1.2 The nature of pyrometallurgical processes

Pyrometallurgical operations, such as those occurring in bath type furnaces, seldom lend themselves to accurate characterisation, unlike processes occurring at lower temperatures and less aggressive chemical conditions. Measurements of temperature, liquid level, pressure, and flow rates, which often are trivial at lower temperatures are either not possible or cannot be determined with acceptable level of reliability at higher temperatures. Moreover, where composition indicators such as reduction-oxidation potentials and pH are commonly measured at low temperatures, and on-line gas chromatography and a host of other on-line analytical techniques are available to the process modelling and control engineer, no reliable high temperature equivalent exists (for example molten samples are quenched, crushed, pulverised, mounted and sent for XRF, which only gives an analysis of the major elements – the whole cycle taking about 20 minutes when automated).

These practical limitations constrain furnace controllability, especially with conventional methods. Most furnaces are operated in a semi-batch way and operate with large inventories (very often over 500 tons of molten slag and metal at any given stage). Moreover, the residence times and process time constants are long (more than 3 hours). These controllability-issues imply that a good feedforward models becomes indispensable for proper control, as the cost of rectifying upset conditions are so significant. Traditionally furnace control is either experience based (with the expert device depending on the expert observer), or it is based on either a totally empirical approach, or on a thermochemical mass and energy balance model. The empirical approach very often provides short term accuracy, but only until some fundamental shift in operating conditions occurred. On the other hand, fundamental approaches are seldom of acceptable accuracy for the purpose of control; however, they do give some insight into the process phenomena.

As the profitable production of metals, metallurgical intermediates and alloys are under severe cost-cutting pressure due to ever-declining commodity prices, the experience-based method of furnace control is rapidly becoming an untenable option. As feedback-control for these furnaces is technically not feasible and unstable, one has to rely on dynamic model-based control which marries the qualities of fundamental predictive models with the empirical models.

1.3 Reasons to model

As a point of departure, it is worthwhile to define what a model is, and the reasons why modelling is done, as this influence the context within which we interpret the final model. In the field of pyrometallurgy, Thomas and Brimacombe (1997) defined a process model as "... a system of mathematical equations and constants that are usually solved on a computer to make quantitative predictions about some aspects of a real process. The specific variables required as inputs and the generated output predictions are important features of the model. The model also includes constants which represents material properties, empirical relationships, and other knowledge of the process." Considerable effort is required to obtain the data for the empirical relationships, be it in the form of industrial, experimental or literature data. To be relevant, they need to be validated with realistic measurements and finally implemented in practice.

Modelling of processes is done for a number of reasons, which include :

- Increasing the fundamental understanding of a process
- Assisting scale-up
- Design of experiments
- Evaluation of experimental results (and visa-versa)
- Quantifying property measurement
- On-line process control and optimization
- Technology transfer

All of the above are valid reasons for model development, and it is important that the complexity of the model should fit its final application, and that the modeller is honest about the simplifying assumptions. Very often, mathematically complex models are developed for processes where the large number of simplifying assumptions lead either to an irrelevant model or where irrelevance is caused by the inherent uncertainties in the measurements, as well as the ill-understood nature of many of the significant variables. Furthermore, issues such as development time, numerical stability (not freezing or hanging during operation), and solution time should also be taken into account. Thomas and Brimacombe (1997) mentions that of all the reasons why one models processes, the development of an on-line model and implementing it for process control, is the ultimate reason for process modelling. Pyrometallurgical model based control can be viewed as an umbrella covering very diverse skills and approaches as indicated in Figure 1.2 (Reuter, *et al.*, 2003).

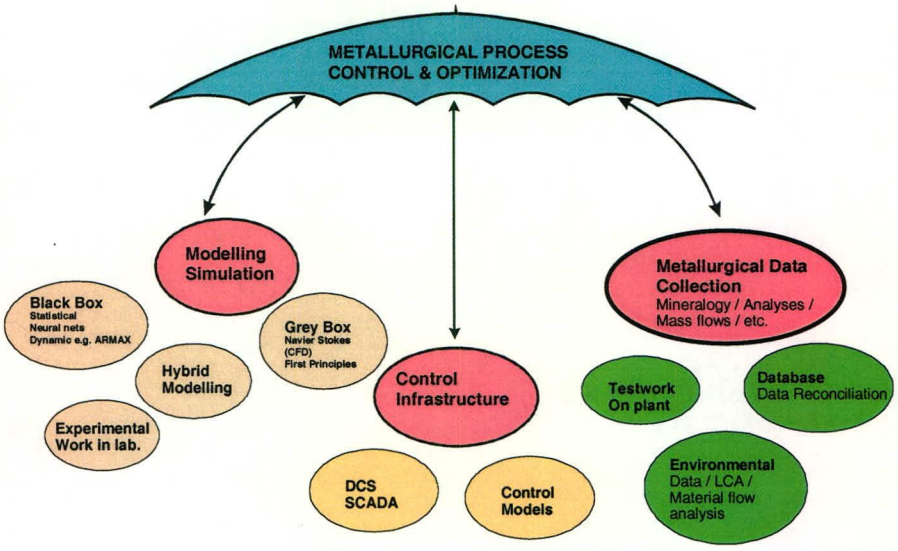

Figure 1.2: Umbrella of process control (Reuter *et al.*, 2003)

The various techniques discussed in this thesis will be placed in the context of modelling and controlling poorly defined industrial metallurgical reactor systems.

1.4 Data sources for model development

The basis for development, validation and evaluation of process models is data obtained from a number of sources, each having their own characteristics as to what can be achieved, with what integrity and with which relevance. Data can typically be obtained from the following sources:

- Industry experiments and production
- Pilot plant experiments
- Physical model experiments (or so-called "cold model" experiments)
- Laboratory experiments
- Literature
- Computer databases

Of these, the last two bulleted sources were also derived from laboratory experiments. In this thesis all these sources will be explored to a lesser or greater degree, where the limitations of each technique would be pointed out, for different bath type furnaces.

1.4.1 Industry experiments

Industrial measurements are obtained only with great difficulty, especially in the production environment where the pressures to meet production schedules are severe and dominant. Measurements made on industrial smelting processes are complicated by noise, heat, dust, electrical interference, as well as time and space (accessibility) constraints. However, the rewards are significant as much information regarding fluid interaction, heat transfer, and chemical reactions can be obtained which are difficult to study under well controlled, small scale laboratory conditions. The data tend to have a high level of redundancy allowing statistical analysis. The quality (integrity) of the data is highly variable and the quality and method of sampling have a significant impact on data reliability and integrity.

1.4.2 Pilot plant experiments

From the perspective of model development, the pilot plant offers the opportunity, away from the pressures of the production environment, to study the effects of changes in process parameters over a wider range than is typically allowable on the industrial plant. Despite being a model of the industrial plant, translation of pilot plant information still suffers from the following shortcomings:

- It is difficult to achieve complete similitude between pilot plant and plant.
- One is not completely certain that the fundamental process dynamics and fluid dynamics do not change in scale-up, for instance (Nelson, 2004):
    - The cathode spot changes to a diffuse plasma arc above arc currents of 10 kA.
    - The direction of bath stirring may change (upwards to downwards) due to increased Lorentz forces at higher arc currents.
    - Bubble sizes and size distributions may change as one scale up from smaller to larger submerged injection lances.

1.4.3 Physical model experiments

Very often, the very nature of industrial systems preclude direct observations, from which a physical picture may be deduced. In many cases one does not have the adequate physical basis for the construction of a rigorous or even approximate mathematical model. Furthermore, even though one may be able to represent the system rigorously in terms of appropriate differential equations, the ultimate set of equations would be too complex or too expensive to solve. Under such conditions it is useful to construct a physical model of the

system at more user-friendly conditions. Ideally one would want geometric (shape), kinematic (motion), dynamic (forces), thermal and chemical similarity. However, this is seldom achieved. The scaling and use of physical models should be made with considerable forethought.

Physical models may be classified into the following main groups (Szekely *et al.*, 1988a & b):

- Rigorous physical models can be constructed according to strict similarity criteria. Under these conditions, the quantitative measurements made in the course of the modelling experiments (e.g. Velocity fields), may be translated directly, through appropriate scaling, to describe the behaviour of real systems.
- One may study the relevant physical phenomena with the objective of providing information for the construction of a mathematical model.
- Furthermore one may conduct ad hoc experiments in order to acquire a feel for the system as a preliminary to mathematical modelling studies.

The main application of physical models is therefore in the study of fluid motion and mixing in metals. As such they are never used as models for control, but more so for process understanding. However, having an understanding of fluid motion provides a context within which we interpret measurement data for process control purposes. Furthermore, it may aid the process control engineer in determining optimal sampling strategies and aid in sensor positioning.

1.4.4 Laboratory experiments

Laboratory experiments offer the opportunity to vary the thermal and chemical conditions very widely. However, laboratory set-ups have the least number of continuous sensors and their completely discontinuous nature limits the number of measurements significantly. As is the case for pilot plants, the number of measurements that can be made and the high redundancy are sacrificed for higher quality data over which can be very well controlled. However, maintaining the same mixing, heat and mass transfer conditions become extremely difficult or even impossible. It is therefore ideal to obtain thermochemical and kinetic information, but it does not lend itself to predict the process dynamics of actual furnaces.

1.5 The chronology of dynamic process model development

While much of the contents addressed in this paragraph can be viewed as obvious, the author still feels that a proper understanding of the modelling process is crucial, as it provides the

context within which models will be created and evaluated in this thesis. In principle any process model development can generically be divided into a number of standard steps:

- Problem definition
- Identification of key phenomena
- Determination of approach and the complexity thereof
- Design the model architecture
- Estimation of the model parameters
- Validation of the model
- Testing of the model against real world data, data not used in the parameter estimation step.

Typical problem definitions for the metallurgical control problems can be:

- Control of the predicted assay of the bulk slag / alloy / dust, or minimize a specific (or suite) of contaminants;
- Control of the expected yields of bulk slag / alloy / dust.
- Control of the rheology of the product phases to ensure tappability, with minimum metal entrainment (For example alloy produced is normally seen as alloy tapped - not what is available in the furnace).
- Minimisation of the specific energy input while still maintaining yields and product specifications
- Control to minimise environmental impact.
- Control for cost minimisation or income maximisation

This must be done under the constraints of safety, maintenance of a fluid (tappable) melt, maintenance of furnace structural integrity, maintenance of a high furnace availability, or a prioritized combination of the above. It is of no use producing an alloy of an acceptable chemical specification, if the operating conditions is such that the melt is not tappable.

Identifying the key phenomena is crucial to the model development, even for the more empirical models. One should be aware of the fact that, when building completely empirical models, historic data (even from a long period) may not be truly representative, and that a good understanding of the key phenomena, even in a qualitative way, can be a useful guide when the furnace is operating in a region outside the traditional setpoint region. Moreover, if some type of fundamental sub-model can achieve some degree of quantitative estimation, it

makes the overall model more robust. Important phenomena which are ill understood, such as the mechanisms in most primary smelting operations, are often best treated empirically by calibrating the model to actual measurements (parameter estimation).

When deciding on the level of complexity, it should be done within total context of model accuracy, solution time, development time, inherent inaccuracies, numerical stability, and the degree to which the model can be validated (if a very complex model is developed, which seeks to model all the complexities of the actual system, but the phenomena themselves cannot be accurately measured, one has to ask if the level of complexity is truly relevant to the modelling problem at hand, irrespective of whether it was developed and solves within a reasonable time). Another guideline is to model phenomena based on the proportion that they contribute to the overall problem, and to how well they are understood. If important phenomena are well understood, it is worthwhile modelling them in more detail. On the other hand, when phenomena which are deemed important are not well understood, it is often better to use empirical models, for example power law models for heat and mass-transfer coefficients, polynomial models for heat capacity equations and solution thermodynamic interaction parameters, or even non-parametrical statistical models such as artificial neural networks.

Furthermore, it is important to keep the relative errors the same: if a more complex model gains a 1% improvement in accuracy, where the inherent uncertainties are of an order of magnitude larger, the additional effort becomes meaningless. This is especially relevant to melts with a stochastically distributed composition and / or temperature profile, as will be discussed later. The inherent assumptions made during the model formulation can place the mathematical model on track towards process or control system development, or could seriously derail it.

Parameter estimation, as to be done in the context of this thesis, automatically results in calibration of the model. If parameters are to be estimated on-line, one should take into account that the parameter calculation process should preferably be non-iterative and explicit (for instance using linear least squares). While this does not exclude non-linear parameter estimation, it should be the aim to constrain non-linear parameter estimation to off-line model development, keeping the non-linear parameters fixed, once the model is implemented on-line. Non-linear parameter estimation is essentially a non-linear optimisation process, prone to

convergence, stability and local minima problems. While these problems can be easily handled and detected in off-line mode, the occurrence of them during on-line prediction, will cause the on-line model to be permanently disabled.

1.6 Implementation of on-line predictive models

The final goal of on-line implementation of on-line models is to have either automatic control of the manipulated variables, or to have an operator guidance / decision support system, where the operator adjusts the setpoints and fulfils the control function. A model can be said to be implemented only when the modelling exercise leads to some tangible change in the process, that directly benefits the smelter and ultimately the industry.

The typical economic goal of a smelter would be to improve alloy recovery (or lower the standard deviation in grade, or increase furnace availability), of predefined alloy specification, by making achievable changes to certain control elements. The improvement should therefore be measurable, and the adjustments should be effective, practical and possible within the production constraints of the smelter. Furthermore, if the model is too complex for anyone else to rerun, then the potential implementation value has been lost.
Models can be implemented as (Thomas & Brimacombe, 1997):

- Fully on-line models
- Semi-on-line models
- Off-line models
- Literature models

Fully online models, which offer immediate production benefit, must be extremely fast in execution, robust (filtering noise and discounting bad sensor signals) and extremely simple, consisting of a few basic equations. The demand for reliable accuracy is the highest for fully on-line models. The model should be able to explain the major qualitative long term trends, while still being quantitatively accurate in the very short term. The largest effort is spent in generating and acquiring the information and knowledge needed and to refine it into a few simple equations. As the model is only required to produce accurate results for the limited set of process conditions, the equations may be based on curve fits of the results from the plant, pilot-plant, a physical model, laboratory scale measurements, or numerical simulations on

thermochemical, computational fluid dynamic (CFD) or process plant simulators (a concept that will be expanded upon in this thesis). Fully on-line models work with control variables, and have the ability to transform a standard operating procedure (SOP) variable into a control variable, thereby enabling significant improvement in overall process control.

Semi-on-line models are similar to fully on-line models, except that a plant operator and engineer interfaces between the model and the process. These models are best suited to help set optimum levels for SOP variables. Due to the human interaction, the frequency of adjustment should be less so than for fully on-line models, and would typically find its place in tap-to-tap predictions for smelters, as an example. Semi-online models which prove to be worthy may be eventually implemented as fully online models. Semi-empirical models, expert systems and fuzzy logic systems typically fall within this category.

Off-line models are aimed towards process understanding for the purpose of improving on either standard operating practise, or as a tool in the design of improved pyrometallurgical processes. The model implementation relies solely on the model user and consequently the user should have a thorough understanding of both the inner workings of the model as well as the process (typically a metallurgist at a smelter). It further aids in experimental design, interpreting the results from plant trials, quantifying phenomena that are difficult to measure, and it could be used for hypothesis testing. While very useful, and many process models fall into this category, their impact is more indirect and not suited towards process control. As such they will therefore not be dealt with in much detail in this thesis.

Literature models are off-line models used only by the person who developed the model. The modeller has no direct contact with the real process and normally would work for an academic institution. They are ideally suited for process analysis to test all the phenomena occurring in the process and may take very long times to develop and solve. CFD models typically fall within this category. The knowledge and the insights gained by the engineer are more important than the model itself. The implementation value of this model implementation type is little if it only echo's knowledge already known through plant experience. Its value is negative if it contradicts some of the plant knowledge and fails to explain why.

For the purpose of metallurgical control of furnaces, the first two implementation types are the only feasible options.

1.7 Thesis context and objectives

This thesis will focus on developing an approach for modelling the metallurgical dynamics of furnaces that are of special interest to the South African industry, namely the *bath type* smelting and converting furnaces. Bath-type furnaces have the common property that, both on a volume and a mass basis, the furnace inventory is predominantly liquid (the only solids being small quantities of unreacted high-melting point reactants or crystallised products). This can be contrasted with blast furnaces and submerged arc furnaces where the solid burden makes up the largest proportion of the total furnace volume and where solid-gas reactions contributes significantly to the overall reactor conversion. At first sight, bath-type furnace should then appear simpler to model, however, new complications arise that are particular to these type of furnaces and which will be discussed in more detail in subsequent chapters.

The main objective of this thesis is therefore to develop a generic dynamic modelling approach for bath type furnaces.

The foundation of this philosophy has already been laid by Reuter and Moolman (1999) and Reuter and Yang (2001), where the authors concluded that good process models will include both a proper thermodynamic basis, and also try to quantify the effects of process dynamics. Reuter and Moolmans' (1999) investigation of the dynamic behaviour of the %MnO in submerged arc furnace slags, led them to conclude that the dynamic prediction of actual plant data of a normal ARMAX model could be related to thermochemical equilibrium outcomes of the process, since the systems model clearly followed a similar trend to equilibrium trend, although a slightly variable bias were noted. Reuter and Moolman's (1999) equilibrium data, process data, and systems model predictions are presented (with permission) in Figure 1.3.

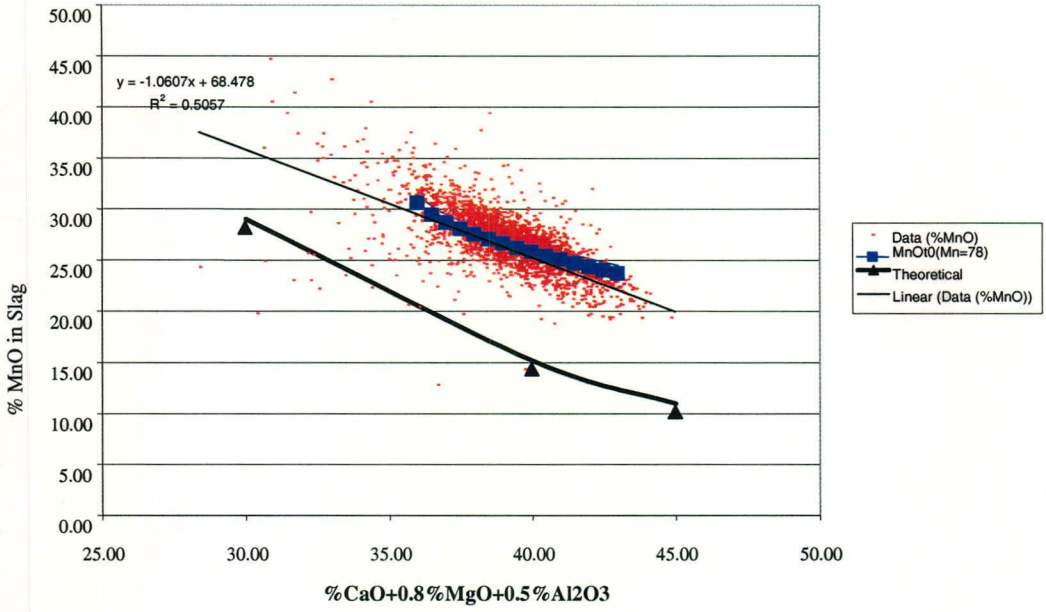

Figure 1.3: Comparison of plant data, systems model predictions and equilibrium predictions of the %MnO in high carbon ferromanganese slags (Reuter and Moolman, 1999)

Reuter (Reuter and Yang, 2001) therefore concluded that thermochemical equilibrium should be incorporated as a baseline for semi-empirical modelling, either explicitly as an "attractor" into a dynamic empirical model, or, at least, as a reference state to which the dynamic predictions should be compared and validated. This principle of a thermochemical baseline is best illustrated by an equilibrium surface from which the process deviates, depending on process conditions, distributions of temperatures, mineral properties, reaction paths and histories of each reactant in the reactor. Reuter and Yang (2000) demonstrated this concept by mapping the equilibrium surface and fictitious process data for any general pyrometallurgical reactor , as shown in Figure 1.4.

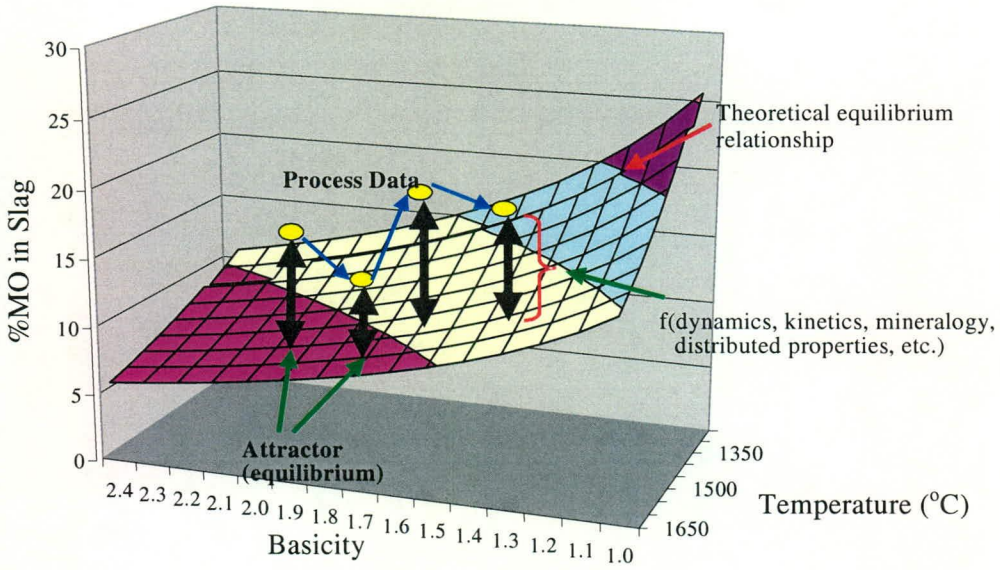

Figure 1.4: Loci of fictitious data points for a furnace positioned above their respective equilibrium data (the attractor) to illustrate the effect of process dynamics, kinetics, etc. (Reuter and Yang, 2001)

This thesis will further explore Reuter's (Reuter and Yang, 2001) concept of an equilibrium attractor through explicitly incorporating equilibrium into dynamic modelling of bath type furnaces.

This approach presented in this thesis will therefore culminate in a generic predictive model that will incorporate the thermochemical, dynamic and exogenous components that influence metallurgical dynamics. In principle, the modelling approach assumes that the bath chemistry dynamics of intensive smelting bath-type furnaces can be accurately modelled using a combination of:

- thermochemical equilibrium (a moving target, but also a good process reference state)
- ill-defined exogenous factors (for example electric arc resistance, lance-to-melt distance, coal reactivity, median particle size, etc.)
- dynamic autoregressive and moving average components (historic variable states and historic error states, respectively)

This model type will be called the *Equilib-ARMAX* model, which can be represented by the following generic equation:

$$\hat{y}(k) = \sum_{i=0}^{l} \alpha_i \cdot \tilde{y}_{\infty}(k-i) + \sum_{i=1}^{m} a_i \cdot y(k-i) + \sum_{i=1}^{n} \sum_{j=1}^{r} b_{ij} \cdot u_j(k-i-d) + \sum_{i=1}^{p} c_i \cdot e(k-i) \qquad (1.1)$$

Where $\hat{y}(k)$ is the predicted state (say a component concentration) of a subsequent tap. The $y(k-i)$ term refers to historic states of the variable to be predicted (also called the autoregressive variables), while the $u_j(k-i-d)$ term refers to the exogenous inputs of delay d, and the $e(k-i)$ term refers the error history (the moving average component). The variable $\tilde{y}_{\infty}(k\text{-}i)$ will be the predicted equilibrium component concentration of (y), based on a trained neural network prediction. The neural network approach to equilibrium prediction has been chosen in order to develop a non-iterative method of on-line prediction.

The variables used in the model will be based on filtered measurements, where the technique called variance-weighted material balance reconciliation will be used to separate the process signal from the process noise, and to determine if systematic errors, or biases exist in the data.

It is therefore an important objective of this thesis to show that the Equilib-ARMAX modelling approach is a valid, cost-effective, practical approach to model the dynamics of industrial bath type furnaces, within the inherent variance of the measurements. This thesis will elaborate on the reasons why this modelling approach has been chosen, and provide supporting diagnostic tools to ensure that significant model variables are identified and incorporated in the model using a combination of empirical system identification techniques and sound fundamental reasoning.

It is clear that material flows do not appear explicitly in the model, even though they may have a significant effect on the mixedness of the various phases in the system. Although fluid flow will not be incorporated in the model, the effect of fluid flow on mixedness will be implicitly included through characterisation of the spatial variance of furnace products. The variance associated with any component assay provides three useful pieces of information:

- The variance quantifies the inherent spread, and therefore the integrity and precision, of the data. It therefore establishes if the mean is representative of the sample population (in cases of small relative variances). Alternatively, the data can have a significantly distributed nature, in which case the mean becomes a poor representation of reality. However, if the actual data are random and non-deterministic, the mean may still be the best approximation of reality despite its lack of precision.
- The variance provides a weighting mechanism through which reconciled adjustments can be weighted when measured assays are adjusted to fulfil material balance constraints

- The natural variance gives the upper limit of model validation capability. Therefore, for a given uncertainty in the measured data, there is point beyond which further model improvement has little sense, as one model cannot be proven to be "better" than another, based on validation using measured data. It therefore sets a "cost-benefit" benchmark to establish when the effort spent on model development becomes excessive in relation to its prediction value.

The Equilib-ARMAX modelling approach will be evaluated using three industrial bath-type furnaces as case studies:

- An Ausmelt ® converter which converts smelter matte (of the Ni-Cu-Fe-S system) into an upgraded matte-alloy for the platinum industry using lance based injection technology (pilot plant scale) ;
- a DC-plasma arc furnace for the reductive smelting of chromite concentrate for ferrochrome production (industrial scale);
- a DC plasma arc furnace for the reductive smelting of ilmenite to obtain a high titania slag (industrial scale).

The complexities of all these furnaces and the reasons why they cannot be modelled well using fundamental models only, will be discussed in more detail in Chapter 2. The furnaces modelled in the case studies share a few common characteristics:

- The mineralogy of the raw materials changes significantly during the furnace operation. This is associated with wide variations in melting point, oxidation state (e.g. Fe, FeO, Fe_3O_4 and Fe_2O_3), and reactivity.
- Perfect mixing (melt homogeneity) is generally assumed for the melt phases. This perfect mixing assumption needs to be evaluated and the driving forces and deterrents to good mixing have to be identified and quantified. Should near-perfect mixing not be obtained, it automatically implies a distributed physico-chemical nature in the melt.
- The furnaces are all semi-batch in operation in that they are fed continuously but tapped intermittently (not always at regular intervals and the tap-to-tap duration varies).
- The furnaces contain large amounts of dangerously hot material with the large inventories associated with long process time constants.
- The energy input is either coupled to the combustion or reduction process which effects the overall oxidation/reduction balance in the furnace (converters with lance-

based injection), or to the melt and plasma-arc resistivity (and therefore melt and plasma chemistry), in the case of electric arc furnaces.

- The utilisation efficiencies of oxidising agents (for converters) or reductants (smelters) depends upon many ill-defined measurements. Such ill-defined measurements include particle size distribution, rank, ash composition and proximate analysis of coal (all of which vary significantly), in the case of reductive smelting, or upon the dispersion and intermixing in the case of converting operations with gas injection.
- Bath type furnaces are normally operated with a freeze-lining that protects the refractory brick lining, but varies dynamically with operating conditions, changing the available melt volume. Over and above the freeze lining, bank formation occurs which is much more stochastic in nature.

The above-mentioned list is not comprehensive and will be expanded upon when the case studies are presented. However, it reveals some of the challenges the process modeller have to face in the development of predictive dynamic models for furnaces. The features of bath types furnaces therefore establish the foundation of the modelling approach to be taken:

- The approach should take the technological and practical constraints into consideration. This relates to the way the furnace is operated, the procedures that are in place, and the practical constraints regarding data acquisition, the feasibility of implementing decision support or automatic control, and the determination of variables that are not measured on-line, but which may affect the process significantly.
- The modelling approach should quantify and take into account the distributed nature of the materials entering and being produced by the furnace.
- The approach should incorporate some form of noise-filtering capability.
- The model should incorporate a fundamental basis. The model itself, or some of its variables (via sub-models predicting them) should have a thermochemical basis that estimates the reaction equilibria, phase equilibria, and predict within material- and energy balance constraints.
- The model should be able to deal with the uncertain, probabilistic and ill-defined nature of the metallurgical outcomes, using statistical and data mining techniques, as well system identification and signal processing techniques.
- If the model is to be used on-line, it should not use iterative calculations or perform on-line optimisation when the algorithm is prone to hanging, or the solution becomes trapped in local minima.

- Finally, the model should remain as simple as possible, allowing rapid model development within a feasible timeframe.

It is felt that the Equilib-ARMAX approach suggested in this thesis will comply to the above-mentioned modelling requirements.

1.8 Thesis outline

The Equilib-ARMAX model reflects the convolution of many traditional schools of thought regarding furnace modelling. The thesis will develop the modelling philosophy from a qualitative phenomenological description of the production technologies, and will build towards the quantitative Equilib-ARMAX modelling approach in a series of 6 chapters:

Chapter 2 will discuss the technological, metallurgical and production aspects of the 3 bath type furnaces, in order to describe fully the current sampling, measurement, analysis and production environment within which the predictive model will have to be able to function. The chapter will show that the development of complete fundamental models are often impractical, due to the large number of ill-defined variables, and poorly characterised furnace states.

Chapter 3 will discuss the equilibrium thermochemistry and solution chemistry of the systems studied, based on an in-depth literature review. The information presented in this chapter is supported by a literature review and calculation algorithms presented in Appendix A. Moreover, Appendix A will present the phase equilibria associated with each system, which determine the fraction of solids in the melts. The fraction of solids in the melt becomes one of the determining factors of melt viscosity and homogeneity.

Chapter 4 will explore the spatial variance of temperature and composition of furnace products (such as slag, molten alloy and dust). Mixing theory will be reviewed within the context of bath type furnaces. The chapter will review results from literature, small scale experimental work, and industrial furnaces, and show how the results influence the way we measure, interpret and use the information derived from mixedness studies in process control. The effect of the phase equilibria and the chemistry on the physical properties of the melts in the furnaces will be discussed and quantified, especially where it relates to melt viscosity, which influences both entrainment/emulsification, foaming behaviour, mixedness and melt tappability.

Chapter 5 will cover the pre-processing of the raw data from the different plants using standard descriptive statistics and system identification tools (linear and non-linear). It will further elaborate on the crucial component of data reconciliation, using material balance constraints, and show how knowledge of the quantitative variances in composition and uncertainty in analyses may be used constructively in data reconciliation. Furthermore, it will be shown how reconciled data are then used to develop inventory models for the furnaces. Moreover, the chapter will show how biased measurements can be detected and dealt with. Finally, it will be shown how a representative thermochemical equilibrium database may be set up using the reconciled data, inventory models and factorial experimental design, in conjunction with artificial intelligent systems.

Chapter 6 will evaluate the final Equilib-ARMAX furnace models as derived from data and process fundamentals and discuss it with regard to accuracy, robustness and reliability. It will also be shown how the developed dynamic model may be used in a model predictive control architecture for either setpoint suggestion (for decision support) or automatic control.

Chapter 7 will present a summary of the generic modelling approach to bath type furnaces and give a diagrammatic representation of the "road-map" to develop these systems models.

Chapter 8 will present the overall conclusions of this dissertation and discuss how the objectives set out in this chapter have been addressed.

The nomenclature used in each chapter is discussed on a chapter-by-chapter basis, as the areas of furnace technology and transfer phenomena, thermodynamics, mixing theory, system identification and process control all have their own typical nomenclatures. However, the nomenclature is consistent within a chapter and is to be found at the end of each chapter.

2 PROCESS ANALYSIS AND CHARACTERISATION

> "I have yet to see any problem, however complicated, that when looked at the right way, did not become still more complicated" (Anderson's Law, from Kelly and Spottiswood, 1982)

> "Complex problems have simple, easy to find, wrong answers" (George Orwell)

2.1 Introduction

Real bath type furnaces are characterised by many ill-understood phenomena and non-idealities which influence the metallurgy and which pose significant modelling challenges. At first glance, the behaviour of these furnaces may very often seem to contradict thermodynamic equilibrium predictions (despite the supposedly good mixing conditions and fast reaction kinetics in bath smelting furnaces). Moreover, the relationships between variables show such scatter that it is very difficult to visually determine if relationships exist – more so because plant conditions are unlike laboratory situations where variables are not varied one at a time, but many simultaneously, most of the time. Moreover, the sampling period between metallurgical samples is very often not constant, as samples are only taken when the tap hole is opened for tapping. This chapter will investigate the technological aspects, practical and operational constraints of 3 bath smelting or converting operations. Table 2.1 gives an introductory comparison of the main metallurgical features of these operations. It is apparent from Table 2.1 that the furnaces studied cover a very broad spectrum of operations: from oxidative to reductive, exothermic to endothermic, low (in a pyrometallurgical sense) to high temperatures, various oxidation states, gas atmospheres, fluxing approaches and slag chemistries. The furnaces therefore have very diverse metallurgies, over and above the technological and operational features, which would differ from smelter to smelter, even for the same metallurgical system. The furnace operations will be discussed in the following order:

- Ausmelt Ni-Cu matte converter
- Electric arc chromite smelter
- Electric arc ilmenite smelter

Table 2.1: A summary of the main metallurgical features of the bath type furnaces to be studied

Furnace Type	Ausmelt Ni-Cu Matte Converter	DC Plasma Arc High Carbon Ferrochrome Smelter	DC Plasma Arc High Titania slag smelter
Main Product	A Ni-Cu-S-Fe matte containing Co, and Platinum Group Metals (PGM's)	High Carbon Ferro-chrome containing silicon (0.5 – 5%)	High Titania Slag
By-product	Recycled Slag	Slag for cement	Pig Iron
Typical chemistry of the product alloy / matte	22% S, 3% Fe, with Ni and Cu to a ratio of 1.88:1 (65%total)	55% Cr, 35% Fe, 8%C, 1-2% Si	97% Fe, 2.5% C, 0.2% Si
Typical Slag Chemistry (Main Components)	SiO_2, FeO, Fe_2O_3	Al_2O_3, MgO, SiO_2, CaO, CrO, Cr_2O_3	TiO_2, Ti_2O_3, FeO
Gas Atmosphere	SO_2, SO_3, N_2, O_2	CO, H_2, CO_2, N_2	CO, H_2, CO_2, N_2
Important Alloy / Matte contaminants	Fe, S, Sb, Bi, Te, CrS	Si, S, P	Si, Mn, S
Important slag minor components	NiO, CuO, CoO, Cr_xO	FeO, TiO_2	SiO_2, Al_2O_3, MgO, MnO
Scale	Pilot Plant	Industrial	Industrial
Reduction oxidation control reactant	Oxygen enriched air, $pO_2 = 10^{-3}$ to 10^{-5} atm	Anthracite Coal Mix $pO_2 = 10^{-13}$to 10^{-16}atm	Anthracite $pO_2 = 10^{-10}$to 10^{-12}atm
Main feed material	Granulated electric smelter matte	Chromite spinel fines	Ilmenite mineral sands
Main fluxing material(s)	SiO_2	$CaCO_3$, CaO, SiO_2	None
Normal Operating Temperature (°C)	1300	1600	1750
Exo / Endothermic	Exothermic	Endothermic	Endothermic
Energy Source	Combustion	Electric Arc	Electric Arc

2.2 Technological aspects of lance based gas injection converters

2.2.1 Background to injection based bath type furnaces

Many of the bath smelting reactors used today are pneumatic reactors where air or oxygen enriched air is injected into the bath to achieve oxidation reactions. These reactors may also be operated using a reducing or neutral gas mixture, or a fuel-air-oxygen combination, but where the overall oxygen potential may still lead to reducing conditions. Other types of bath smelting furnaces are, for example, the transferred arc furnaces (to be discussed later), and the tuyere-based converters. The development of the injection bath smelting techniques is reviewed by Floyd (1993), starting with Bessemer steelmaking in the 1850's to the Ausmelt /Sirosmelt / Isasmelt technologies as developed through 1970-1980. Of the different bath type furnaces, the Peirce-Smith type converter and the LD-converters made the most prominent impact of nonferrous and ferrous pyrometallurgical bath smelting processes respectively.

Intensive smelting through the exploitation of top lance entering a slag bath was developed by the Australian CSIRO in the 1970's, which led to a patent registration of the Sirosmelt Top Entry Submerged Lance (STL) melting system, championed by Floyd (1981). Subsequently licenses have been granted to two companies, Ausmelt Ltd., and Mount Isa Mines Ltd., to commercialise the innovation, which led to separate but parallel development of the technology. Figure 2.1 shows a cutaway diagram of a typical Ausmelt furnace. The degree to which the Ausmelt and similar furnaces compare to other technologies in smelting capacity (in Ton per day per m^2 hearth for chalcopyrite / chalcocite concentrate) has been shown (Vernon and Burks, 1997) to be :

- Reverberatory Furnace 4-8
- Flash Furnace 9-12
- Ausmelt Furnace 50-100

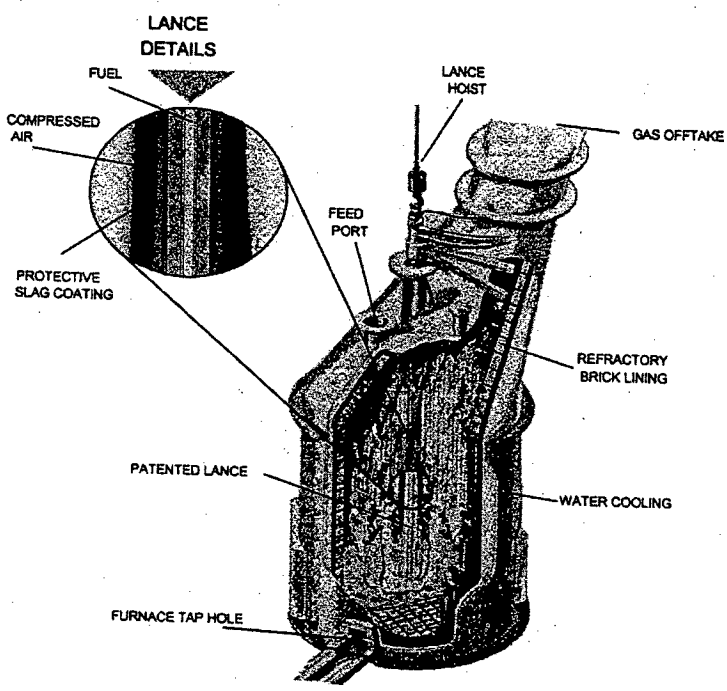

Figure 2.1: Cutaway diagram of an Ausmelt furnace (Vernon and Burks, 1997).

Floyd (1993) identify 3 methods of pneumatic injection into molten liquid baths, namely:

- Injection through tuyeres. The tuyeres may be in refractory lined furnaces or water jacketed furnaces.
- Top jet lancing injection onto the bath surface using water-cooled lances or consumable lances.
- Top submerged lancing.

Two methods are typically used to carry out reactions in bath smelting furnaces, one being direct feeding of the reactants into the bath (bath smelting). Alternatively the reactants may be fed into the gas space before separation of the molten products in a liquid bath (suspension smelting). Only bath smelting will be discussed in this thesis.

The bath smelting systems are characterised by relatively small temperature and concentration differences between the bath and the reactants, and the bath is claimed to be well stirred due to the injection of the high velocity gas jet (Floyd, 1993). Furthermore, splashed material provides the opportunity for reactions and heat transfer to occur in the gas space above the bath (freeboard region). The feed materials have long residence times in the bath so that even lumpy or wet materials may be used as feed. Furthermore , lance based injection bath smelting processes can accept fine or coarse, wet or dry materials as feed materials into the

furnace. Although control of the bath conditions are crucial for the efficient operation, they can be corrected relatively fast.

Bath smelting systems have a slag and matte / metal bath which acts as a thermal and chemical buffer, which controls the oxygen and sulphur potentials and the temperature at the reaction site. In FeO-containing slags under oxidising conditions, the magnetite formation can be controlled to be close to the equilibrium level for a particular operation. The good contacting of the bath via rising gas bubbles provides suitable conditions for removal of gaseous species from the bath. However, oxidised species will be rapidly dissolved in the slag where volatilisation occurs more slowly due to the lower activity of the slag components.

2.2.2 Reaction regions in pneumatic reactors (Floyd, 1993)

Injection methods in bath smelting operations can be mainly divided into operations applying a shrouded tuyere and applications using a top submerged lance, each having different reaction behaviour in the different zones of the reactor. The reactions regions typical of pneumatic reactors are shown in Figures 2.2 and 2.3.

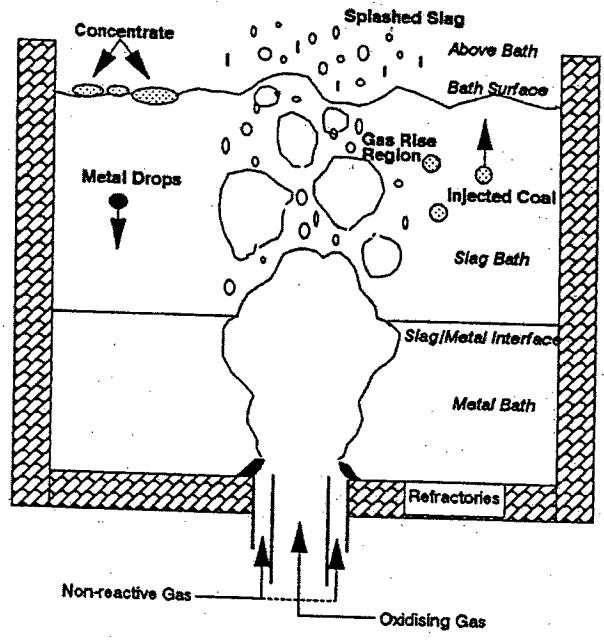

Figure 2.2: Reaction regions in shrouded bottom tuyere reactor types

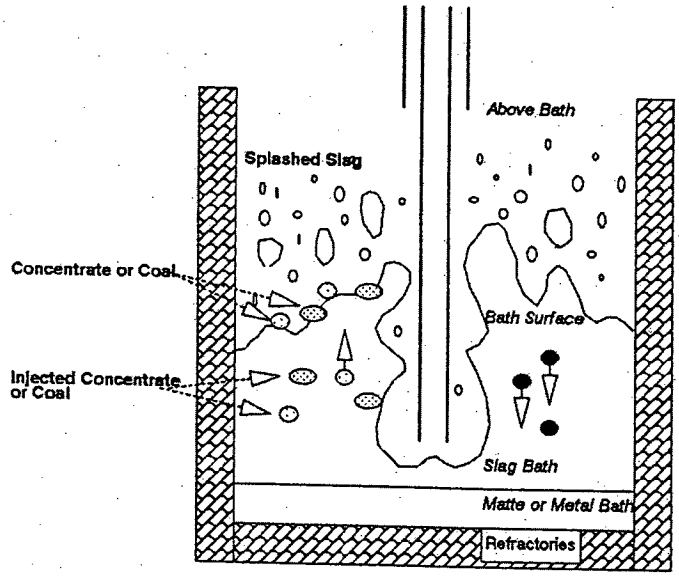

Figure 2.3: Reaction regions in top submerged lance reactor types

2.2.2.1 Injector Mouth

The first reaction region of the two reactor types is either the lance mouth or the tuyere region. For shrouded tuyeres, the reactive gas discharge takes place through non-reactive gas shroud injected into a metal or matte. No reactions takes place between the bath and the gas to prevent the refractories being subjected to the thermal cycling typically associated with non-shrouded injection of reactive gases. For top submerged lance applications, the oxidation or combustion reactions take place in the slag phase. The swirling gas stream does not penetrate the bath to any significant extent, and quiescent areas are formed at the bottom of the furnace.

2.2.2.2 Gas Rise

During oxidative converting operations, the rising gas will oxidise melts, with accompanied heat generation (exothermic reactions). In shrouded tuyere operation, the following reactions are expected to occur (M being any metallic component dissolved in the metal / matte, underline, "_" referring to metal/matte solution, "[ ]" referring to components dissolved in slag), and "< >" being solids, with all of the reactions taking place at the gas bubble – bath interface:

$$\underline{M} + \tfrac{1}{2}O_2\,(g) = [MO] \qquad (2.1)$$

$$\underline{FeS} + 1\tfrac{1}{2}O_2\,(g) = [FeO] + SO_2\,(g) \qquad (2.2)$$

$$\text{also: } [FeO] + \tfrac{1}{4}O_2\,(g) = [FeO_{1.5}] \qquad (2.3)$$

For the top submerged lance application, the gas rise region involves oxidation of the combustion gases or oxidising gas injection. Additional to the above reactions one therefore has the following reaction taking place to a limited extent:

$$[FeO] + \tfrac{1}{2}CO_2\,(g) = [FeO_{1.5}] + \tfrac{1}{2}CO\,(g) \qquad (2.4)$$

2.2.2.3 Bath Surface

The reactor is claimed to show high degree of turbulence at the bath surface. The wave motion or slopping of the surface is counteracted by the raining of ejected drops of slag, splashed into the gas space above the furnace by bursting gas envelopes. Material fed to the furnace from the top of the furnace drop onto the surface and react with the slag. The iron sulphide and metal sulphide component of the feed reacts with the ferric oxide and metal oxide in the slag according to the following reactions:

$$<FeS\ (feed)> + 6\,[FeO_{1.5}] = 7\,[FeO] + SO_2\,(g) \qquad (2.5)$$

$$<MS\ (feed)> + 6\,[FeO_{1.5}] = 6\,[FeO] + [MO] + SO_2\,(g) \qquad (2.6)$$

$$<MS\ (feed)> + 2\,[MO] = 3\underline{M} + SO_2\,(g) \qquad (2.7)$$

Magnetite (Fe_3O_4, or $FeO_{1.33}$) precipitation is possible at temperatures below its melting point (therefore at normal converting temperatures), depending on FeO and $FeO_{1.5}$ activities in the slag.

$$[FeO] + [Fe_2O_3] = <Fe_3O_4> \qquad (2.8)$$

However it may revert (very slowly, in the presence of enough flux) to FeO according to:

$$3<Fe_3O_4> + \underline{FeS} = 10[FeO] + SO_2\,(g) \qquad (2.9)$$

The multiphase-multimolecule nature of the reaction makes the kinetics quite slow. Magnetite is a very stable, slag wettable, inverse spinel particle with a high density (s.g. of 5.18 versus the slag density of the order 2.5 – 2.9: it therefore tends to settle in quiescent conditions). Reductant addition may control magnetite formation through reaction of the CO product with the magnetite (again a slow, heterogeneous reaction – the gas has to compete with slag and matte for surface coverage / adsorption on the magnetite):

$$<Fe_3O_4> + CO\,(g) = 3[FeO] + CO_2\,(g) \qquad (2.10)$$

Similar spinels (compounds with a stable isometric crystallography and a stoichiometry or solid solution of the form $\left(M_x^{2+}, 2M_y^{3+}\right)O_4$ when the feed contains Cr_2O_3, MgO and Al_2O_3. Concentrates and fluxes such as limestone and silica / quartz sand also dissolve in the slag at the top surface. Some fluxes such as limestone ($CaCO_3$) may decompose to generate CO_2, which has to be taken into account as it increases the gas load on the furnace. Reductant reactions also occur, such as :

$$<C(feed)> + 2\,[FeO_{1.5}] = 2\,[FeO] + CO\,(g) \quad (2.11)$$

and $$<C(feed)> + MO = \underline{M} + CO\,(g) \quad (2.12)$$

The generated carbon monoxide will also react with the slag according to the following reactions ($FeO_{1.5} = Fe_2O_3$):

$$[Fe_2O_3\,] + CO\,(g) = 2[FeO] + CO_2\,(g) \quad (2.13)$$

and $$[MO] + CO\,(g) = \underline{M} + CO_2\,(g) \quad (2.14)$$

In all cases M refers to metals more noble than iron, such as Cu, Co, Ni, Zn, Pb, Cd, Bi, Au, Ag and the PGM's. For typical sulphide matte converting conditions, metals such as Al, Cr, Mn, and Mg will not be reducible from their slag phase, due to the stability of their oxides.

Finally, the Boudouard reaction is always present as the regeneration reaction through which CO_2 reverts back to CO in the presence of solid (or dissolved) carbon:

$$CO_2\,(g) + <C\,(feed)> = 2CO\,(g) \quad (2.15)$$

2.2.2.4 Freeboard Region

Reactions in the freeboard region will take place with splashed slag reacting with the gas components rising from the bath. If the gas is oxidising, one would find reactions similar to the gas-rise reactions. On the other hand, should the gas be reducing, the presence of CO and H_2 from reduction reactions or the volatile components in the coal, will lead to reactions similar to those shown for the bath surface, with both gas species partaking. For the Ausmelt, shrouded top submerged lance system, the above-bath reactions include the afterburning of the CO, H_2 and coal volatile components in the gas rising from the bath.

2.2.2.5 Bath reactions

Metal / Matte drops produced by reactions at the slag surface will fall through the bath to join the metal or matte underneath the slag, while the surface reactions continue during the fall of the drops and at the slag/metal/matte interface between the bath layers. These reactions tend to be slow if the melt is not well stirred- which can occur with top submerged lancing with a high lance. Lowering of the lance would be required for improved inter-melt bath reactions. Carbon particles injected into the slag or entrained from the surface will react in the bath, generating a gas envelope and reducing the slag by the same reactions as shown for the surface above.

2.2.3 Mixing, phase separation and bath movement

The bath movement generated by gas injection has been studied by physical modelling, mathematical modelling and plant investigations. Floyd (1993) reports that initial studies on gas plumes from side injection through tuyeres have shown that substantial penetration of the bath occurred through the gas injection via the tuyeres (physical modelling using water as modelling medium). However, these findings were contradictory to later plant observations which showed that the gases rapidly lose their kinetic energy with much of the gas bypassing along the wall of the converter.

In-plant studies using tracers and instantaneous measuring devices (however, not for prolonged periods), such as oxygen potential probes, have been shown to be effective to evaluate industrial smelter performance. Urquhart *et al.* (1976) used tracer studies to determine the residence time distribution in a electrical smelter.

When solids as well as gases are injected into baths, the greater momentum of the solids is claimed to cause additional penetration into the bath (Floyd, 1993). The penetration of solids can be sufficient to cause changes in the normal liquid flow associated with pneumatic injection. The use of swirlers in top submerged lancing modifies the gas discharge conditions for solid capture by the bath (Floyd, 1993). Furthermore it helps lower lance consumption by improving lance cooling.

The phases present in more intense bath smelting operations tend to be well mixed. For Cu-Ni mattes and slag, large amounts of matte are emulsified in the slag due to the small density differences, and small matte-slag interfacial tension. The reactors used for matte smelting require some means to separate matte from slag, such as a quiescent settling zone. To create a quiescent zone, the Ausmelt type furnaces uses an underflow weir or siphon to remove slag from the furnace, which assists the prill-rich surface of the slag not to enter the settling region of the furnace. The need for a settler after the intense mixing in the smelting process means that the thermal efficiency of the process is slightly decreased. The operation should therefore be carried out with due consideration given to the problems of solid precipitates.

2.2.4 Heat and mass transfer

Due to the high degree of mixing and turbulence in a pneumatic bath smelting reactor, one finds that rapid mass and heat transfer occurs. In general it has been found (Floyd, 1993) that gases injected into the bath have reacted to completion by the time the gases leave the bath region. In the Ausmelt furnace, fuel and oxygen enriched air are introduced into the bath and the combustion and heat transfer processes have essentially gone to completion in a fraction of the time it takes for the gases to emerge from the bath. The heat and mass-transfer in top submerged lance injection are very fast indeed and do not limit the process efficiency, provided the bath is fluid (low viscosity) and the driving forces for the reactions are large. Slower heat and mass transfer inevitably occurs if the bath becomes viscous (either due to a highly polymerised slag, a subcooled slag or a slag with a significant amount of solid precipitates). The efficiency of heat transfer during combustion can also be decreased if the fuel is not finely dispersed and intimately mixed with the injected gas.

When solid reactants are injected into the bath, the maximum reaction rate achievable depends on submergence time of the solids in the bath. In the case of coal injection, the coal does not readily enter the slag phase (due to its low density and its poor wettability), as it is even more difficult to achieve proper melt penetration with fine coal. This could lead to severe losses of fine coal due to gas-entrainment to report as flue dust. The Ausmelt technology therefore makes use of coarser coal sizes than often found with injection bath smelting technologies. The shear and mixing conditions found at the tip of the submerged lance due to swirled gas flow, ensures that the solid coal enters the bath, with associated rapid reactions.

When injecting onto the top of the bath at high velocity (therefore not submerged operation), the heat and mass transfer occurs at a smaller interface between the gas and liquid phase over a shorter time interval than when injecting into the bath, which may lead to more significant concentration gradients in the gas and liquid phase. Where the process is oxidation of the matte or metal phase, the formation of a slag phase must be maintained at a minimum to avoid the formation of a physical barrier to gas penetration. It iron oxide is present in the slag at typical converting temperatures of between 1200 and 1350 °C, one needs to be careful to prevent excessive conversion of FeO to Fe_2O_3, and the eventual solidification of the bath due to magnetite formation (Once formed the reversion is slow). It is therefore preferred to operate with a submerged lance instead.

2.2.5 Design aspects of importance to furnace behaviour

One of the major claims made with regard to the Ausmelt technology is its low fugitive emissions compared to converters such as those of the Peirce-Smith type (Vernun and Burks, 1997; Mounsey *et al.*, 1999; Mounsey and Piret, 2000). To obtain this low level of emissions, the furnace is totally enclosed with up to 4 small openings in the roof to accommodate furnace feed, lance, standby burner and sample tool entry points. The furnace is typically operated under slightly negative pressure of –20 to –40 Pa to ensure that fugitive emissions are minimised when pressure fluctuations occur (Mounsey *et al.*, 1999). Additional sealing is ensured through the used of rotary powder feed valves and spinning disc feeders and water- and compressible bellow seals on the lance ports.

The conventional approach to cooling of the Ausmelt refractories to ensure the integrity of containment, is done by using a thermally conductive refractory lining with shower cooling on the outer shell. A freeze line of crystallised slag protects the furnace refractories from excessive slag corrosion. The theory behind the refractory cooling to maintain a stable freeze line is discussed in paragraph 2.4.8 together with the cooling of plasma arc furnaces, as the role of freeze line maintenance is important to both types of furnaces. Direct bonded MgO-Cr_2O_3 refractories are often used in the oxidising environments associated with base and precious metal smelting and converting.

The gas handling system is very dependent on the chemistry of the system, i.e., if it is operated under reducing or oxidising conditions, or if metal fuming (such as for zinc) occurs. Gas handling may include the use of evaporative gas coolers in conjunction with spray coolers and baghouse filters, or waste heat boilers in conjunctions with electrostatic precipitators, or venturi scrubbers and filters where the gas chemistry allows it. A typical design configuration, as proposed by Mounsey *et al.* (1999) is shown in Figure 2.4. This would be a typical design for a furnace with a waste heat boiler type off take, upper furnace and roof, enhanced copper cooling elements in the furnace bath and slag splash areas.

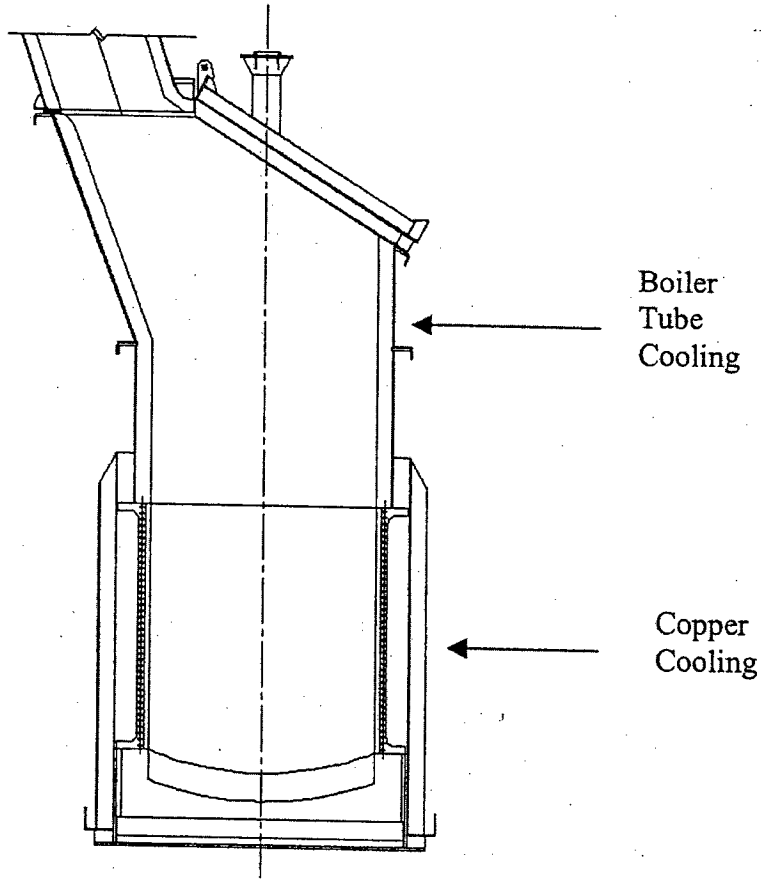

Figure 2.4: Ausmelt furnace with enhanced containment system (Mounsey and Piret, 1999)

Mounsey and Piret (2000) summarises much of the typical design features of industrial Ausmelt furnaces used in base metal smelting and converting. The conventional height to internal diameter ratio is of the order of 2.75:1. Lance heights are typically in the range from 15 to 17 m, with a lance diameter of 35 cm. The off take diameter is slightly more than 2 m, for a furnace with a inner diameter of 4.4. m. Tapping of metal/matte or slag occurs through underflow weir outlet and a normal tap hole drain (for emergency drainage). A diagrammatic representation of the Ausmelt patented lance is given for the upper and lower sections of the lance respectively in Figures 2.5 and 2.6.

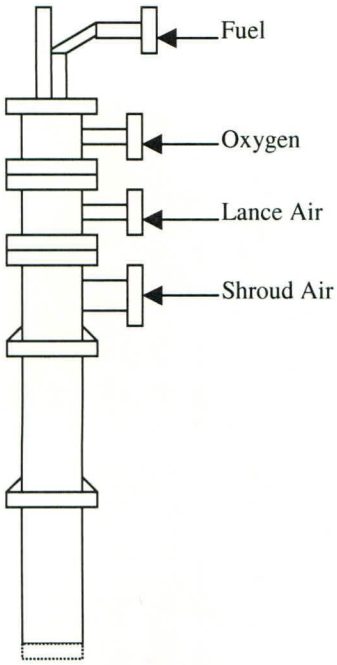

Figure 2.5: Upper section (outer view)

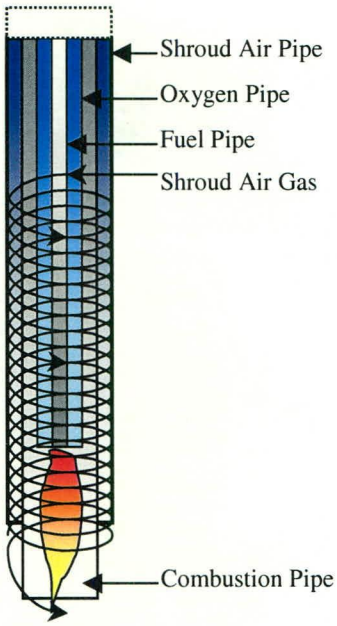

Figure 2.6: Lower section (cutaway)

The Ausmelt lance uses shroud air injected tangentially and typically can be designed for high turndown capability. Bath temperatures may be monitored using an optical pyrometer fitted to the furnace roof, with intermittent (not continuous, due to dust) monitoring and purging and cleaning of the pyrometer lens. Interlocking is normally provided to ensure that the fuel and air ratios remain within safe regions to prevent the formation of explosive mixtures.

It is viewed as critical to sound operation that an effective standby burner is always available when the Ausmelt lance is withdrawn (Mounsey *et al.*, 1999). The furnace has to be maintained at temperature and it crucial to use the standby burner with the right flame characteristics for down firing the Ausmelt furnace. As lance withdrawal can be routine operation, the whole operation of introducing the standby burners has been automated in more recent furnace installations. The burner incorporates ignition control, purging and flame detection. It is not only for temperature maintenance, but also start-up – to heat the refractories before the introduction of feed.

Accurate lance position control is achieved through a typical DCS system linked to a position measurement device and controlled to the required position though a hoist cradle linked to a mechanical clamp. Lance change times of less than 20 minutes have been reported for Ausmelt operating pants (Mounsey *et al.* 1999). Spare lances are typically stored in a rotary carousel with lance transfer being performed with a cross travel hoist. It is important to

realise that, while the position of the top part of the lance is relatively easy to determine, the greater difficulty lies therein that the exact position of the lance bottom end is extremely uncertain (relative to the bath surface).

It therefore appears that the Ausmelt reactor, while it could be perceived as a mature technology, still has many ill-characterised aspects which are particular to the technology. The Ausmelt application studied in this thesis has been developed for the conversion of a Ni-Cu-Fe-S matte – the objective being to blow an electric furnace matte product to the required Fe and S endpoint. This will be dealt with in the following section.

2.3 Ausmelt Ni-Cu Matte Converter

Anglo Platinum Ltd., the world's largest producer of platinum group metals (PGM's) identified the blowing of converter matte to within a fine metallurgical specification of iron and sulphur as a key process challenge. This arose due to the importance that these two elements have on the mineralization behaviour during the slow cooling of converter matte (Wicks, 2000). It was especially important as it was planned to change the converting technology from the traditional Peirce Smith converters to the modern top submerged shrouded lance technology marketed by Ausmelt Ltd. The main reasons for this was to reduce the fugitive SO_2 and SO_3 emissions typically associated with traditional converting operations, while intensifying the converting operation (larger capacity per unit processing volume) and to stabilise operation through advanced computer control. Anglo Platinum planned to increase its overall plant capacity (in terms of PGM production) with an 75% production increase. Much of this planned increase in production has arisen due to pending South African legislation regarding the use of mining rights ("use it or loose it principle"), as well as a bullish market for PGM's. Two 6-in line electrical smelters, one being the Mortimer Smelter, and the other being the Waterval smelter in Rustenburg, South Africa, produce the electric furnace matte. The matte from both furnaces are converted at the Waterval smelter. The ores processed include two main reef types, the chromite rich Upper Group 2 (or UG2) and the sulphide rich Merensky reef. Much work has been done, and is still in progress as how best to smelt the chrome rich UG2 in the traditional smelters. The reef type, while not directly fed to the Ausmelt converter, may influence converter operation through entrained slag from the smelter or dissolved chrome sulphides. The full chemistry of chrome containing mattes and impacts thereof, are still not well characterised.

2.3.1 Process Description

Wicks (2000) provides the conceptual overall process description of the current and future smelter plant at the Waterval site. This flowsheet is discussed to show how the units interrelate, and how the converting operation (be it in Ausmelt of Peirce-Smith converters) is dependant on its feed, and the converter products are recycled to the pant. The objective of Waterval smelter is to produce a sulphur deficient nickel-copper matte from wet concentrates containing PGM's, i.e. Platinum (Pt), Palladium (Pd), Rhodium (Rh), Iridium (Ir), Osmium (Os) and Ruthenium (Ru) as well as Gold (Au) together with Base Metals i.e. Nickel (Ni), Copper (Cu) and Cobalt (Co). The flowsheet indicating the main processing steps are presented in Figure 2.7, while Figure 2.8 shows the flowsheet of the expanded operation including the new converting operation.

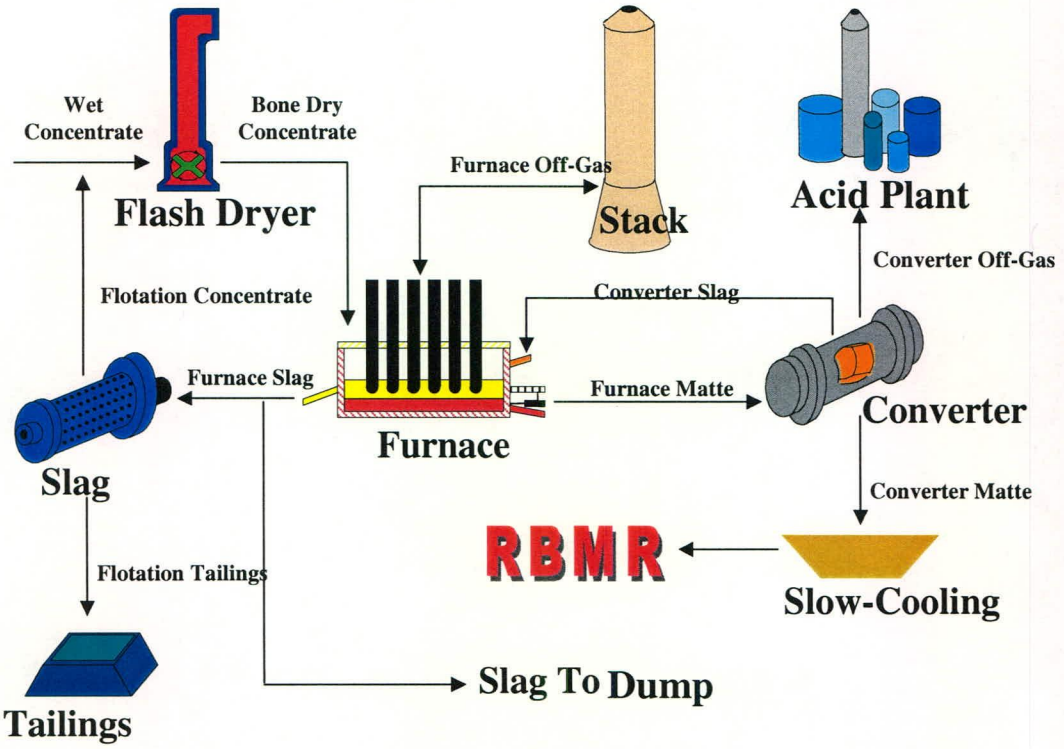

Figure 2.7: Flowsheet of the main processing steps at Waterval smelter by the year 2000 (after Wicks, 2000)

Concentrates are received from various concentrators, which are offloaded cranes into a 5,000 tonne storage shed. Due to the different filters in use, the moisture in the concentrate varies from 12% to above 25%. Concentrate is picked up from the stockpile by grab crane and fed onto conveyors leading to the flash dryers. Both streams are introduced into the drying column at the base and are accelerated by the disintegrator and air movement up the column. At the top of the column the bulk of the dry concentrate is separated from the gas by two cyclone sets in parallel. The exhaust gas from the cyclones is subsequently passed through a

multi-cyclone and bag house to remove any further particulate in the gas stream, before it is vented to atmosphere. The concentrate collected in the bag house and cyclones and is fed to the product bins at each flash dryer. The concentrate discharge from one of the cyclones can also be redirected to the back mixer to be mixed with the incoming wet concentrate in order to decrease the moisture of the feed to the disintegrator (from 18% to 10%). The final dried concentrate is then blended with a predetermined quantity of lime to aid the furnace slag chemistry. The material is then pneumatically conveyed to the electric furnaces. The two electric furnaces have six 1.25 m diameter Söderberg electrodes with an electrical capacity of 34MW. The two furnaces have internal dimensions of 8.0 m wide and 25.8 m long with 304 water-cooled copper coolers installed in the lower wall. The power flux is approximately 165kW/m^2. The furnaces have a combination of chrome magnesia and magnesite hearth refractories and a silica brick upper section. The incoming electrical power is 88kV that is then stepped down to 6.6kV. The maximum voltage supplied by the transformers is 350V and the maximum current is 27kA per phase. Smelting separates the gangue minerals from the sulphide minerals associated with the PGM's. As the concentrate melts, two liquid phases form; a lighter slag with a relative density around 3 and the heavier matte, with a relative density of about 5, containing the base metals and PGM's. Limestone flux is added to reduce the liquidus temperature and viscosity of the slag (for concentrate deriving from Merensky reef). The low concentration of the minerals in the concentrate means that the furnaces operate at a high slag to matte ratio. Thus the slag is tapped almost continuously and granulated using a high flow water stream. The dewatered slag is either sent to the slag milling section for recovery of metal values or is sold as blasting material. The intention is to operate the furnaces with a 'black top' which limits the amount of radiation to the walls, roof and to the gases. However, the periodic return of molten slag from the Peirce Smith converters frequently creates upset conditions in this regard. The return of slag from the converters containing magnetite and chrome spinels formed in the oxidising conditions, sometimes creates a 'mushy' layer between the matte and slag layers and can cause a reduction in operating volume and an increase in entrainment.

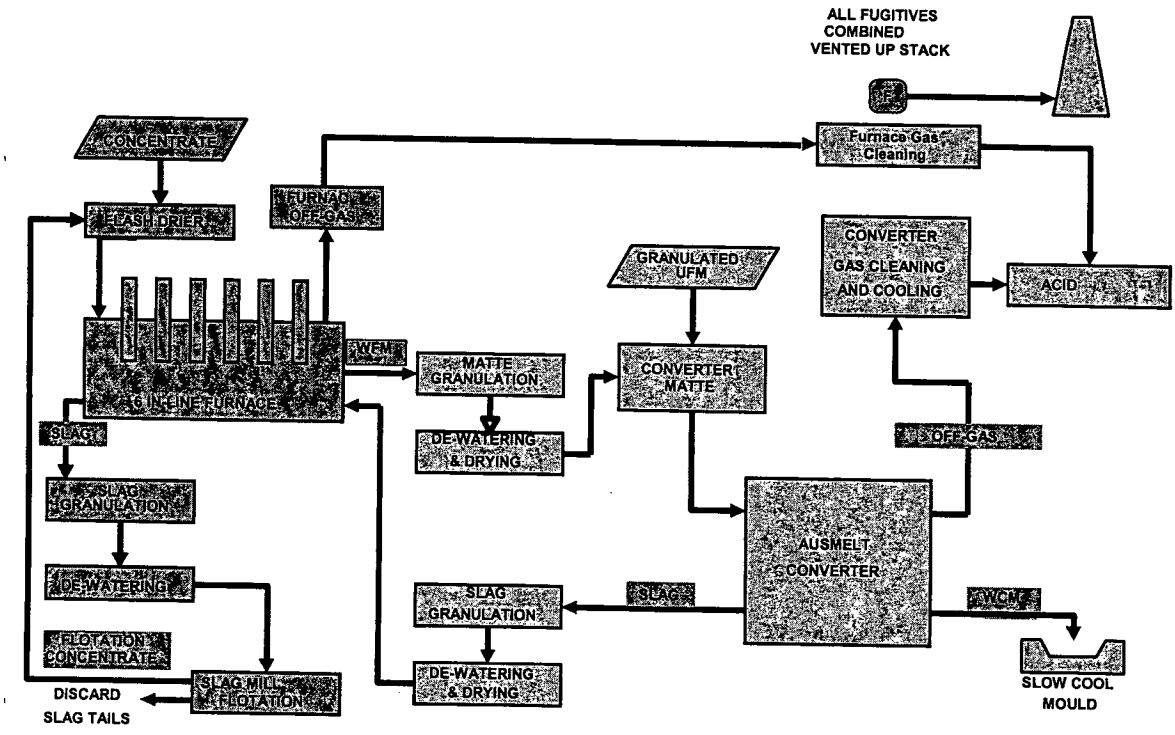

Figure 2.8: Proposed flowsheet of the main processing steps at Waterval smelter by the year 2006 (Wicks, 2000)

There are six Peirce Smith converters, each 2.9 m in diameter and 7.5 m long, lined with direct-bonded chrome-magnesite refractories. The tuyeres are inclined at an angle of 7°. Silica sand is added to the to blow to flux the iron oxide and to form an iron silicate slag, with the composition of fayalite, but also containing some dissolved magnetite. The required end point of the blow is 3% Fe and 22% S as dictated by the slow cooling process. In recent years there has been a deterioration in campaign lives but with the recent introduction of larger mouths an increase in lives has been noted. The sulphurous gas is then sent to the single absorption sulphuric acid plant with excess gas, that cannot be treated, vented to atmosphere. The slow cooling process ensures that the sulphur deficient matte forms magnetic plates enabling the PGM's to be separated from the base metals at the Base Metals Refinery. The matte from the converters is poured into refractory lined moulds aiding the slow, and controlled, removal of heat over a five-day period.

The characteristics of the slow-cooling process are:

>925 °C completely molten

920 °C Cu_2S precipitates

700 °C Primary alloy precipitation. This is composed of two components, the core containing most of the PGM's and the surrounding layer containing mostly Pd.

605 °C Ni_3S_2 separates

580 °C Eutectic alloy settles which contains all of the above phases

520 °C Phase transformation of Ni_3S_2 from β to β'

Once withdrawn from the mould the matte is then broken up and crushed before being sent to the Base Metals Refinery. Dust collection efficiency for the electric furnaces deteriorated so much with time that dust concentrations of up to 7,000+ mg/Nm^3, compared to the environmental guidelines of 120 mg/Nm^3, had been measured. This resulted in dust losses of ± 350 tonnes per month. In addition, high maintenance costs and low availability of the equipment had resulted. In 2000 SO_2 emissions from Waterval Smelter were in the order of 130 tpd which represents a S-fixation level of only 50-55% compared to the Department of Environmental Affairs and Tourism (DEAT) limit (year 2000) of 20 tpd of SO_2 and at a required S-fixation level of some 95%. Moreover, the international norm tended to 98% fixation. In addition, the DEAT guidelines for average SO_2 ground level concentrations are:

Annual	Monthly	Daily	Hourly
30pbb	50pbb	100pbb	300pbb

As the Waterval Smelter was exceeding these limits by a factor of 5, there was increasing legislative pressure form the authorities. An improvement in working conditions was also being demanded and environmental pressure groups were scrutinising Anglo Platinum's international image. Preliminary investigations commenced which soon established that high efficiency gas capture was impractical on the current operations and thus a detailed survey of world smelting practices was undertaken which had shown that:

- Importation of first world standards was required
- A gas stream with a high SO_2 concentration was required
- Oxygen flash smelting of concentrates was generally employed
- Fugitive gas treatment should be minimised
- Peirce Smith converters are environmentally incompatible
- Aisle/ladle operations are a major source of fugitive gas

Flash smelting of concentrate was not considered an option due to the following reasons:

- The deportment of the bulk of the S to the converters made Anglo Platinum very vulnerable to fugitive gas problems and the resultant costs

- The processing of furnace matte to product matte is within the experience envelope of established oxygen flash processes
- Replacement of the Peirce Smith converters with a continuous oxygen enriched process fed with granulated matte would meet the objectives.

The main conclusion was that the collection of SO_2 from the existing Peirce Smith converters would be complex and costly and that the existing system capacity was limited and could not meet future production levels. After a detailed evaluation of the alternatives, the Ausmelt converter furnace was chosen as the most suitable technology.

2.3.2 Operation of the Anglo Platinum Ausmelt Converter

The furnace design is based on the principles described in section 2.2 of this chapter. The furnace was at tested at pilot plant scale at first, which was the source of the data for part of this dissertation. The pilot plant was fully instrumented, and was, except for the capacity, an exact replica of the industrial furnace. The 3-dimensional layout diagram for the pilot plant furnace is provided in Figure 2.9.

The ACP Plant will process granulated furnace matte (both Waterval and Mortimer matte) to produce slow-cooled converter matte. The Ausmelt reactor will operate in staged mode, as follows (Georgalli, 2002):

- Stage 1: The objective of this stage is to melt the granulated matte and to remove some of the iron. Granulated matte is fed into the furnace via the Ausmelt lance. Lumpy reductant coal and silica flux, to control the slag chemistry, are fed into the furnace via a roof port. Granulated fuel coal is also fed into the bath via the Ausmelt lance. Process air enriched to 40% oxygen is blown into the slag. The slag produced during the first stage is tapped periodically until the matte level in the bath is at the correct height. The bath will run at a temperature ranging between 1250°C and 1350°C. During this stage the iron level in the matte is reduced from +/- 40% down to the desired 13% (+/- 2%).
- Stage 2: The objective of this stage is to blow the matte inventory in the furnace (built up during the first stage) to the required iron and sulphur endpoints. During this stage no matte is fed into the bath. The partially converted matte will be blown to the endpoint composition of 3% iron (+/- 0.5%) and 22% sulphur (+/- 0.2%). Silica flux, lumpy reductant coal as well as granulated fuel coal are all fed into the bath as in the

first stage. The process air is enriched to no more than 25% oxygen in order to maintain the bath temperature similar to that in the first stage. Once the matte product specification has been attained it will be tapped and allowed to slow cool. The remaining slag will be left as a heel in the furnace for the start of the next cycle.

Off-gas from the Ausmelt converter will be cooled in a water-cooled membrane wall uptake and an evaporative spray cooler. The off gas will be scrubbed before entering the wet gas cleaning section of the new acid plant.

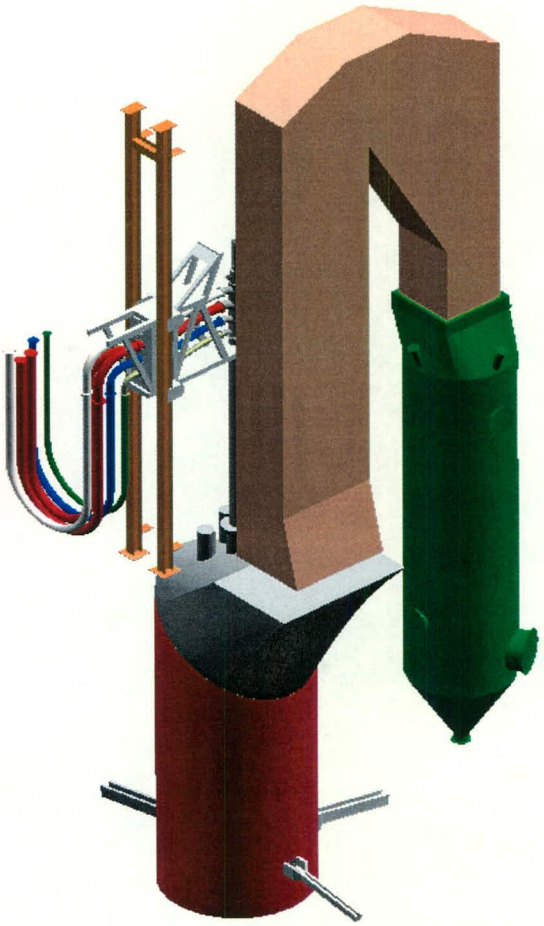

Figure 2.9: Three-dimensional Layout of the Ausmelt converter proposed to Anglo Platinum (after Wicks, 2000)

2.3.3 Production problems associated with matte converting

2.3.3.1 Foaming

Foaming may become a severe production constraint, if not controlled properly. Current practise in converting operations is to control slag foaming through the addition of lumpy coal. Although numerous publications exist in the field of slag foaming in steelmaking slags,

not much has been published regarding the foaming of slag associated with base metal smelting operations (generally high Fe_xO slags at low temperatures with high acidities) except recent for work done at the University of Stellenbosch, South Africa (Stadler *et al.*, 2003). For the FeO-CaO-SiO_2-Al_2O_3 systems studied, it was found that slag foaming, for base metal smelting and converting slags, is very dependent on:

- Solids precipitation – both in terms of amount and type / chemistry of the precipitate. In general, foaming increased significantly with increased solids precipitation, and more so for isometric surface active precipitates than for non-isometric particles.
- Slag basicity - the foaming generally decreased with increasing basicity, up to the point where solid precipitation occurred, when a marked increase in foaming is again observed.
- Fe_xO concentration – foaming normally decreased with increasing Fe_xO concentration, until a minimum is reached at about 25% FeO, after which it increases again. The cause of the foaming decrease could be attributed to lower viscosities, causing faster film drainage, while the subsequent increase, beyond the minimum, could be described by any of two factors, one being magnetite precipitation, the other being an overriding effect of the decrease in surface tension of the slag.
- The slag foaming index was always found to be proportional to the slag viscosity.

The studies were all for slags in the intermediate to high concentrations of FeO, and acidic, as typically found in base metal smelting and converting. Stadler *et al.* (2003) found that the behaviour of the slag foaming index could be related to slag properties according to the following power-law relationship:

$$\frac{\Sigma \cdot \Delta\sigma}{\eta_s d_b} = 7 \times 10^{13} \left(\frac{\Delta\sigma}{(\rho_s g) d_b^{\,2}} \right)^{7.57} \qquad (2.16)$$

Where :

Σ = Foaming index (sec) = foam height / superficial gas velocity (s^{-1})

$\Delta\sigma$ = Surface tension difference between the actual slag and pure SiO_2 melt ($N.m^{-1}$)

η_s = Slag viscosity (Pa.s)

d_b = Bubble diameter in slag (not froth region) (m)

ρ_s = Slag density ($kg.m^{-3}$)

g = Acceleration of gravity ($m.s^{-2}$)

The slag foam index, has been found to be the most common method of describing foaming behaviour. In the case of the Ausmelt reactor, the superficial velocity of the gas through the

slag is both dependant on gas injection though the lance, as well as the large number of gas-producing reactions. The slag viscosity always had a significant role to play in slag foaming – it is not a necessary condition for foaming (a surface tension gradient is more important in this regard), but, once foaming does occur, it very often is the overriding fluid property which determines foam stabilisation.

2.3.3.2 Entrainment and settling

As matte has a much lower interfacial tension with slags (compared to alloys) and due to the lower density of mattes relative to metals, the degree of entrainment for mattes is much higher in slags than for metal alloys. The lower interfacial tension leads to smaller droplet sizes and a larger emulsification driving force. This entrainment is exacerbated by high slag viscosities which slows down settling, as is obvious in the Stokes equation for laminar settling:

$$v_{\infty} = \frac{g \cdot d_d \cdot (\rho_m - \rho_s)}{18 \cdot \eta_s} \tag{2.17}$$

Where:

v_{∞} = terminal settling velocity ($m.s^{-1}$)

d_d = matte / metal droplet diameter (m)

ρ_m = matte / metal density ($kg.m^{-3}$)

ρ_s = slag density ($kg.m^{-3}$)

η_s = slag viscosity (Pa.s)

Unfortunately, not much has been published on the settling behaviour of Ni-mattes. However, entrainment is stochastic in behaviour – the droplets shows a distribution which may vary from one position to another in the furnace, and change as the chemistry and temperature of the melt changes. Entrainment prediction is therefore empirical at best.

2.3.3.3 Dust capture and blockages

The most common blockages that are found during the operation of bath type furnaces are due to the formations of accretions from pneumatically entrained melt droplets and dust. These tend to accumulate in the off-gas ducting, causing a loss of furnace availability. It was noted earlier, that due to the need to prevent fugitive emissions of SO_2 gas, the furnace has to be operated under slight negative pressure (overpressure resulting in emergency stops). It is therefore obvious that the gradual accumulation of flue-dust and semi-molten accretions in the off-gas ducting would cause an increased flow resistance, with insufficient suction occurring and subsequent loss of furnace availability until the situation is remedied. As yet, dust losses

cannot be prevented in bath type furnaces, and remains an operational problem. Any control system has to be able to the deal with the regular stoppages associated with these type of furnaces.

Dust capture occurs in a baghouse filters and cyclones. In the case of the pilot plant, from which the data were obtained, no accurate dust composition or dust quantity was measured on a regular basis. Dust estimates for the Ausmelt furnaces ranged from 1 to 3 % of the mass of material fed to the furnace. The problem, from a mass balancing perspective, remains to obtain proper closure of the mass balance without a proper knowledge of the dust composition.

2.3.3.4 Temperature measurement

Due to the chemically aggressive conditions found in the furnaces, temperature measurement is normally done though thermocouples embedded in the refractories of the furnace. Due to a varying freeze line of slag on the refractory surface, the amount of heat transferred to the thermocouple sheath is highly variable. The thermal lag is also considerable, compared to the inherent thermal dynamics of the furnace. Although the use of a dedicated infrared pyrometer has been suggested, no successful continuous application has been documented. Periodic and intermittent temperature measurement may be possible, assuming the pyrometer lens is not continuously exposed to the high temperature of the furnace and the dust and SO_2-laden gas. In the Ausmelt furnace, temperature maintenance is of utmost importance, not only from a metallurgical point of view, but also from a furnace integrity perspective.

2.3.4 Reaction kinetics

Most publications in the field of converter modelling, deal only with the thermodynamic modelling of the matte conversion process. Kyllo and Richards (1991, 1992, 1998a, 1998b) are of the few researchers who have published thermodynamic and kinetic models for nickel matte converting and copper matte converting in Peirce Smith converters. In their first publication, they have observed that the conversion process closely follows equilibrium up to the last few blows of a charge, when strong deviations started to occur from equilibrium, and which they ascribed to a switch from gas phase mass transfer control to liquid phase mass transfer control. Kyllo *et al.* (1998) identifies 3 mass transfer regimes:

- A slow increase in the mass transfer coefficient with increasing gas flow, at low gas flow rates

- Above a critical gas flow rate, a rapid increase in mass transfer rates were observed, due to the formation of droplets of slag (oxides) in the matte
- When the gas flow was increased even further, the increase in mass transfer rate reduced, as the slag has been totally emulsified.

As diffusivity information is required for estimation of the mass transfer coefficient, and very little information on the diffusivities of the species are available in the literature, they used the Nernst- Einstein relation for diffusivity:

$$D_i = \frac{k_B T}{6\eta_i \pi r_i} \tag{2.18}$$

where r_i is the atomic radius of a particle and k_B is the Boltzman constant, and η the dynamic viscosity. Using this equation, they found that the diffusivities were underestimated, when compared to known values for iron in mattes and slags. Reported values for the liquid-phase diffusivity of iron ranged from 5×10^{-11} to 5×10^{-8} m^2s^{-1} in the slag and between 2.9×10^{-8} and 1.4×10^{-8} m^2s^{-1} in the matte. The gas phase diffusivity is reported to be in the range of 3.75×10^{-7} m^2s^{-1} to 2.31×10^{-4} m^2s^{-1}.

Asaki (2002) have studied the kinetics of sulphides smelting and converting for the Mitshubishi process, which, like the Ausmelt reactor, also utilises a lance based reactor. He showed that, as the maximum bubble size is given by the critical Weber number:

$$We = \frac{\rho d_b v_b^2}{\sigma} = 10 \tag{2.19}$$

Where ρ and σ are the density and the surface tension of the molten matte, d_b and v_b are the diameter and rise velocity of the bubble. Furthermore, it is shown that (Asaki, 2002) the bubble rise velocity can, for Reynolds numbers above 5000, be approximated by:

$$v_b = \sqrt{0.5 g d_b} \tag{2.20}$$

Which, when equations 2.19 and 2.20 are solved simultaneously, for a matte with a density of 4900 kg/m^3 and a surface tension of 0.35 N/m, gives a bubble diameter of 1.2 cm and a rise velocity of 0.243 m/s, with an associated Reynolds number of 5950.

The liquid mass transfer coefficient can be estimated by:

$$k_l = 2\sqrt{\frac{D_i}{\pi\tau}}$$

$$\text{Where } \tau = \frac{d_b}{v_b} \qquad (2.21)$$

τ being the mean rise / residence time of the bubbles in the melt. Asaki (2002) used a diffusivity of 9×10^{-5} m^2s^{-1}, based on the reaction of matte with solid silica (in contrast to those noted by Kyllo and Richards of the order of 2×10^{-8} m^2s^{-1}, but more in line with their gas-phase diffusivity). If Asaki's diffusivity is used, in combination with the calculated rise velocity and bubble size, the bubble residence time is estimated at 4.9×10^{-2} s and consequently a mass transfer coefficient of 4.8×10^{-2} cm s^{-1}. It should however, be remembered, that the exact chemistries for the mattes were different.

Asaki (2002) subsequently showed that the oxygen consumption rate in the bubble, for the reaction (shown earlier):

$$\underline{FeS} + 1½O_2\,(g) = [FeO] + SO_2\,(g) \qquad (2.2)$$

can be represented by:

$$\frac{\pi}{6} d_b^3 \frac{dc_b}{dt} = -\frac{3}{2}\pi d_b^2 k_l (c_{int} - c_B) \qquad (2.22)$$

Where c_{int} and c_B are the concentrations of FeO at the interface and the bulk matte respectively, while c_b is the concentration of oxygen in the bubble, and therefore zeroth order with respect to oxygen concentration in the bubble. Integration of the differential equation between $c_b = c_{b0}$ at $t = 0$, gives:

$$\frac{d_b}{6}(c_{b0} - c_b) = \frac{3}{2} k_l (c_{int} - c_B)t \qquad (2.23)$$

The oxygen consumption time is therefore:

$$t = \frac{d_b}{9k_l} \cdot \frac{c_{b0}}{c_i - c_B} \tag{2.24}$$

Asaki (2002) consequently showed that the oxygen consumption time is of the order of 3 ms, which was much shorter than the time for the bubble to rise through the depth of the melt (0.12 s for a lance immersion depth of 1.2m), using lance injection technology, leading to the conclusion that oxygen utilisation was 100%. He further showed that the time for slag formation is of the order of one minute, and that slag formation occurs mainly in the well stirred bulk matte. Moreover, as the residence time in the reactors are so much longer, the overall conversion is not kinetically constrained, but depends mostly on the fluid flow and dynamic behaviour of the gas and the melt (such as the rise time of the gas, etc.). This has an important consequence, in that the overall process dynamics is not much influenced by the underlying kinetics. It can be conceived that when lance immersion is shallow and chemical conditions are different, kinetics/mass transfer may become predominant. However, it is not expected to be the case in a well-operated furnace with a fluid melt and a well-submerged lance.

2.3.5 Sampling, assaying, chemical analysis

Sampling for the pilot Ausmelt furnace was done using an immersion sampling tool, which could be immersed into the melt from the roof port at regular intervals. The turn-around time for matte samples were of the order of 5 minutes for Inductively Coupled Plasma (ICP) spectroscopic analysis of the main metallic elements in the matte, while a LECO® instrument was used for sulphur analysis (which uses infrared absorption to measure the S in the matte as SO_2). The fast turnaround times could be achieved through an automated robotic laboratory. The sampling is therefore discreet whereas, signals such as pressure, lance height, refractory temperature, and cooling water temperatures could be logged continuously on a data-historian. The flue dust analyses were not recorded during the pilot trials, and gas analyses were of little value due to ingress-air in the ducting before the analysis was made. It is foreseen that the industrial furnace would have a more reliable off-gas analyser. These factors would impact how the data is subsequently handled in this thesis (in comparison to data from the electric arc furnaces, where this information was available). Some estimates for submerged lance-based converters are available, such as quoted by Asaki (2002), who mentions an entrained dust figure of 2.5% of the total solid charge to the furnace.

2.3.6 Control objectives of the Ausmelt converter

The original objectives set out by Anglo Platinum were to develop a robust predictive model for sulphur and iron in the matte with a time horizon longer than the sample turn-around time. Temperature were to be measured intermittently using an infrared pyrometer, and this number would be fed into the model. However, at the time of the model development, no reliable temperature reading could be obtained. It was therefore decided that the predictive model would initially be based on a constant temperature for each blow, although the industrial scenario could be expected to be different, as a larger investment could be made into reliable temperature measurement instruments. It is apparent that, all other factors remaining constant, the total independent control of iron and sulphur is impossible. Minor changes in their ratio to each other may be achieved through kinetic or mixing effects, but their relationship is thermochemically coupled through equation 2.2. The sulphides associated with copper, nickel and cobalt also contribute sulphur, but to a much smaller degree, due to their thermodynamic stability. Therefore, due to stoichiometric and thermodynamic relationships, fully independent control of either S or Fe is possible, but not both simultaneously.

2.4 Technological aspects of DC plasma arc furnaces

Electric arc furnaces all apply the electric plasma arcs (either DC or AC current) to heat the furnace contents. The distribution of power dissipation through resistive heating of the molten or solid contents on the one hand, or plasma arc heating on the other hand, depends much on the electrical conductivity of the melts and solids, the particle size distribution of the feed and the electrical conductivity of the gas phase (for instance, the gas phase may contain much Zn, Mn or alkali metal or metal oxide vapours). Plasmas / electric arcs have peculiar properties which influence their application and interaction with the technologies in which their properties are exploited. Over and above the electric circuitry and anode and cathodes, the plasma and the melts are active (and variable) electronic components of the full electric circuit. The metallurgical energy balance, slag-alloy melt chemistry and the electric circuit are therefore linked and coupled. However, the dynamics of the electrical and metallurgical changes differ by order of magnitudes. As the DC plasma arc furnace is a relatively novel technology, as applied to large scale ore-smelting applications, the technology will be covered qualitatively in depth, in so far the literature covers the relevant aspects that influence the operation, modelling and control of these furnaces. When compared to submerged arc

furnaces, it is claimed that DC plasma arc furnaces have the following advantages (Curr *et al.*, 1982, Curr *et al.* 1983):

- The use of fine feed materials is possible
- Independent control of the feed rate and power can be achieved
- The electrical conductivity of the feed materials does not limit the input of power
- Cost savings on electrode consumption can be realised
- Higher power densities and smaller reaction vessels are probable.

This therefore proved a major incentive for the use for the processing of materials such as chromite fines and fine grained mineral sands.

2.4.1 Physical and thermal properties of thermal plasmas

A plasma is defined as the fourth state of matter, being an ionised gas consisting out of a combination of charged species, electrons, photons, and neutral species. The existence of a true 4^{th} state is sometimes questioned as the transition from gas to plasma is not sharp transition, but a gradual process as more of the gas becomes ionized until the point of complete ionisation. Overall, a plasma is electrical neutral, a property known as quasi neutrality (Fauchais *et al.* 1987). In a steady state situation, the rate of ionisation in the plasma is balanced by the rate of ion-electron recombination. Depending on the energy content of the plasma, the degree of ionisation may be so high that no neutral particles are left and the plasma is therefore fully ionised. Most of what follows regarding the physical properties of plasmas stem from the research reported as a review paper by the French researchers Fauchais, Boulos and Pfender (1987), unless noted otherwise. As most of the mathematical relationships of the physical properties and physics of plasmas are not required for the purpose of the subsequent discussions, the treatment will be qualitative, as to provide a context within which to evaluate arc furnace behaviour.

Two types of plasma can be identified, the equilibrium or thermal plasma, and the non-equilibrium or nonthermal plasma, where thermal plasma have equal electron (T_e) and heavy particle (T_h) temperatures, while non-thermal plasma do not show the equality, with $T_e > T_h$. The "sensible" temperature is characterised by the heavy particle temperatures (T_h), due to their mass contribution to the average kinetic energy of the ionised gas (the basis for the principle of temperature). Under moderate pressures (such as one would find in arc furnaces)

and high temperatures, plasmas behave as equilibrium plasmas. Such plasmas are typically in the range of 5000 to 50000 K (or 1.0 to 10.0 eV).

In plasma one may discriminate between photons, free electrons, atoms or molecules, and parent ions with collisions between these species being both elastic and inelastic (in comparison with neutral gases at ambient temperatures where the collisions are only elastic). All the species are characterised by their own separate velocity distributions. When these distributions do not change with time, the plasma is at steady state. In a uniform distribution, the distribution shape is independent of spatial dimension. Photons are emitted from particles in an excited state and may be reabsorbed during their travel through plasmas as they interact with heavy particles. The energy balance between the emitted and absorbed photons represents the dynamic equilibrium, where individual interactions are balanced by their own reverse processes – called the principle of micro-reversibility. Under such conditions, where all the emitted photons are coming from excited levels populated according to a Boltzman distribution are reabsorbed in the plasma, the photon emission follows Planck's law and the plasma therefore behaves like a blackbody. However, this situation is only found in large volumes of extremely dense plasmas (optically thick plasmas, such as lightning). As laboratory and industrial plasmas are usually small (a few cm in diameter) and not sufficiently dense, so that the emitted radiation intensity depends on the dimensions of the plasma, the most of the photons are not reabsorbed in the plasma (optically thin plasma) leading to deviations of micro reversibility in the plasma.

Optically thin plasmas, while not at complete internal thermodynamic equilibrium, may achieve Local Thermodynamic Equilibrium (LTE), where the collision processes within the plasma and not the radiative processes govern plasma ionisation-deionisation reactions, with micro reversibility among the collision processes. LTE requires that the local gradients of the plasma properties (Temperature, density, enthalpy, conductivity etc.) are sufficiently small so that a given particle which diffuses from one location to another in the plasma finds sufficient time to equilibrate, so that the diffusion time should be of the same order of magnitude or larger than the equilibration time. For the purposes of further discussion it is assumed that, in industry, we deal with plasma where LTE prevails.

The macroscopic transport of matter (diffusion), of charge (electrical conductivity), of momentum (viscosity) and of energy (thermal conductivity) are directly related to the

gradients that exists within the plasma. These properties are averaged over sufficiently large populations such that the discontinuity characters of the individual particles disappears, and are therefore quasi-fluid properties. While the density can be calculated according to the ideal gas law, the other physical properties deviate significantly from gases.

The viscosity of plasmas near 10000 K lies in the range $1 - 4 \times 10^{-3}$ Pa.s. These values are about 10 times higher than for the same gases at room temperature, which partly explains the difficulty of mixing gases or of introducing solid particles into thermal plasma streams. The viscosity of most of the plasmas yet studied tends to increase with temperature to a maximum (e.g. 10000 K for nitrogen, argon and hydrogen and 17000 for helium), after which it rapidly drop with further increase in temperature. As a plasma normally has the highest temperature (and highest viscosity) at its central axis, one very often finds that plasma may have a laminar flow pattern along its central axis with a turbulent perimeter at the outer edge of the plasma (and therefore opposite to fluid flow inside a pipe).

Under the action of thermal, pressure and concentration gradients and an electric field, transport of charges within the plasma constitutes and electric current. The influence of ionisation on electric conductivity is obvious – the plasma is an electric conductor when the gas is sufficiently ionised, the conductivity for Ar, N and H plasma being about 2000 $(\Omega.m)^{-1}$ and therefore similar to most metals (and also behave like metallic conductors).

The dissociation and ionisation phenomena in plasmas make a large contribution to energy transport. A diatomic gas is dissociated and ionised in the high temperature regions of the plasma and recombination occurs in the cooler regions of the plasma. Various mechanisms contribute to thermal conductivity, of which the discussion is outside the scope of this text. For most gases studied, the thermal conductivity lie within 1 to 5 W/m.K. It is normally found that the thermal conductivity for diatomic gases is much higher (at lower temperatures, e.g. around 5000 K) than for monatomic gases.

In the field of plasma research and plasma reactors there is a large distinction with regard to the way the plasma is constructed and operated. If the plasma is created using a high speed gas vortex that flows between a cylindrical cathode and a concentric annular anode, the arc is extended due to the gas flow, the fast rotating, extended arc creating the visual appearance of a tail flame exiting from the plasma torch. In these cases the plasma is referred to as a non-

transferred plasma, which is used mostly in the field of gas heating and tundish heating in metallurgy. However, the predominant mode of plasma utilisation in primary extraction pyrometallurgy is the application of a transferred plasma arc, where the arc is transferred from the cathode to the melt to be heated, provided the melt is sufficiently conductive. The melt, being into contact with a fixed anode at the bottom of the melt effectively transfers the position of the anode to the melt surface, in effect making the anode a dynamically moving component. This is also the mode of operation of arcs relevant to the furnaces studied in this research. Figure 2.10 shows diagrammatically the difference between non-transferred and transferred arcs. Transferred arcs are preferred for high throughput operations due to:

- The use of an open bath of liquid slag and metal (anode) permits greater control of the process metallurgy, than with a choke-fed furnace.
- The electrical supply characteristics and geometric arrangement of the transferred arc furnace are similar to the conventional submerged arc furnace and the change to DC is seen as straight forward.

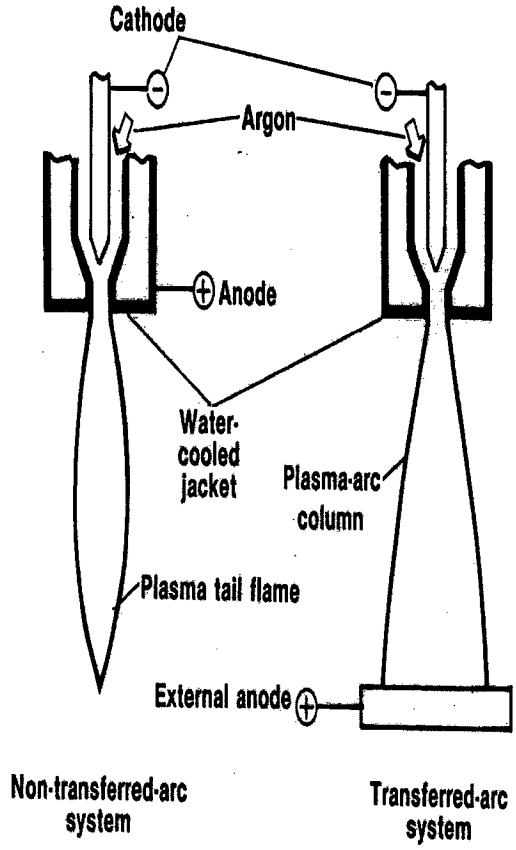

Figure 2.10: Non-transferred arc and transferred arc modes of plasma-arc operation.

2.4.2 Plasma generation

The research on plasma generation and behaviour has been reviewed by Pfender *et al.* (1987) and an extract of their relevant research will be briefly presented in this paragraph. Plasma arcs have a relatively high current density in the arc column of up to 10^6 A/m^2 being even more pronounced at the electrodes. Arcs may attach to the electrode, and in particular to the cathode , in the form of tiny spots in which the current densities may exceed 10^{10} A/m^2. The associated heat flux densities are of the order of 10^{10} to 10^{11} W/m^2, which requires precautions to ensure the integrity of the electrodes. To create a plasma arc a current of at least 1 A is required, although this is not a sufficient condition. A low cathode fall is furthermore required of an order of about 10 V (in comparison to glow discharges of 100 V). This is totally independent of the actual overall arc voltage, which may reach 15 000 V in vortex stabilised plasma gas heaters. Thermal arcs also have an extremely high luminosity, with an significant fraction of the light falling within the UV spectrum. Arc initiation in transferred arc plasma furnaces normally occurs due to a short circuit created after application of an electric potential to the electrodes (the anode connection may be covered with a start-up amount of iron or alloy). The short circuit current flowing through the contact bridge between the electrodes heats up the contact points sufficiently for thermionic emission from the cathode. At the same time electrode material is evaporated (sublimed carbon, or iron vapour) and ionised at the contact point, providing the required charge carriers for developing an arc as soon as the electrodes are separated – which is called the drawing of the arc.

Long arcs, where the arc length is larger than the arc diameter, can be broken down into three regions: the cathode region, the arc column and the anode region. As the cathode and anode regions may be considered as thin boundary layers overlying the electrodes, the column with its comparatively small potential gradient represents the main body of the arc. In contrast to the regions immediately in front of the electrodes, in which net space charges exist, the arc column represents a true plasma in which quasi neutrality exist. The pressure in the arc column is uniform and equal to the pressure in the surrounding fluid, with the exception of arcs operated at extremely high current levels. In such arcs, the interaction of the arc with the self magnetic field produces a pressure gradient in the radial direction - called a pinch effect - so that the pressure becomes elevated along the axis of the column. For a given arc current, the conditions of the column, such as the temperature distribution of thermodynamic and transport properties) adjust themselves in such a way that the field strength required for driving this current becomes a minimum. The relatively small field strength existing in the arc

column may be viewed as a result of the favourable energy balance which is mostly determined by the charge carrier balance. Phenomena at the electrode regions are still ill understood (Pfender *et al*, 1987), and also extremely difficult to measure due to extreme gradients in all the plasma characteristics in this region, and due to electro-fluid dynamic effects which causes plasma jetting. There is therefore yet no comprehensive theory describing all the phenomena in all the regions, and one still has to rely on a large degree of empiricism in the modelling of the arcs. Moreover, the effect of metal vapours and impurities, such as found in arc furnaces, strongly influences the plasma properties – the variability found in pyrometallurgical operations therefore causing significant uncertainty about the actual plasma chemistry and realised transport properties.

2.4.3 Arc electrical characteristics

The characteristics, referring to the voltage -current relationship, of low current arcs ($I < 50$A) are usually falling (i.e. $dV/dI < 0$) provided that the arc can freely expand with increasing current and that there is no severe influence of the arc by the evaporation of electrode material. This applies for free burning arc in air or other gases as long as the arc length is relatively short ($L \leq 20$ mm). Due to free convection effects, the shape of the column of long arcs changes continuously, accompanied by severe voltage fluctuations and severe instability. In contrast to low current arcs, high intensity arcs frequently show a rather flat of even rising characteristic (i.e. $dV/dI \geq 0$). The falling trend of a characteristic is a result of increasing arc conductance with increasing current, caused by an increase in electrical conductivity (temperature) or the arc diameter, or both. In high-intensity arcs this general trend may be overbalanced by disproportional large losses from the arc, to which the arc responds with an increase in field strength. It is therefore apparent that no general prediction about the characteristics of arc may be made due to the effects of stabilizing walls, magnetic or gas dynamic fields which may reverse the effects.

The typical voltage-current characteristics are shown in Figure 2.11 for plasmas in the low and medium current region. The actual shape of this arc characteristic depends on the plasma generator geometry, type, gas flow, pressure, etc. After ignition, the arc voltage decreases with increasing current. As discussed above, the arc resistance, $R_d = dV/dI$, is negative for low current arcs. For a plasma generator in the megawatt range, R_d might be of the order of -0.1 to -1 Ω. This has a significant impact on the arc dynamics and implies using large choke (inductor) in the rectification circuit so that the total circuit still has a positive dV/dI and

therefore have stable operation during arc ignition. V_b is the breakdown voltage for arcs. The asymptotic behaviour at high currents is also apparent from the figure.

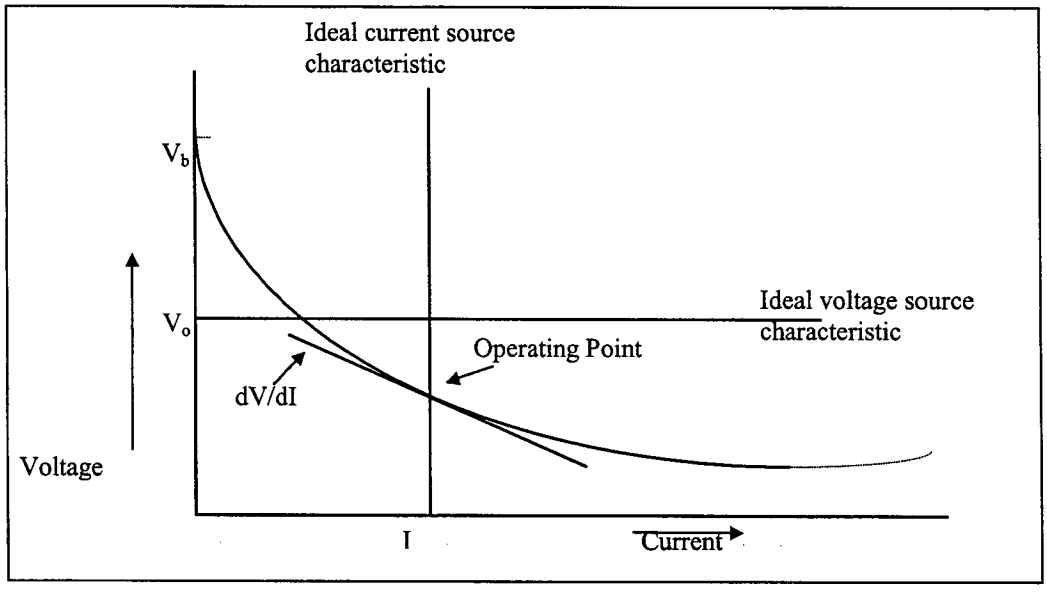

Figure 2.11: Static voltage-current characteristic for an arc, and for voltage and current sources, respectively (after Mogensen and Thörnblom, 1987)

Mogensen and Thörnblom (1987) reported that if the current excursion (refer to dI in Figure 2.11) is rapid, the corresponding voltage differential would be less negative, mainly due to the thermal inertia of the gas in the arc column.

The slope *dV/dI* can also be used to determine the slag resistance (Jones *et al.*, 1997). The slag resistance is a function of the molten bath depth and the slag chemistry. It should be noted that the same current passes through the arc column and the molten bath. Tests carried gave the results in Table 2.2 (Jones *et al.*, 1997) and showed that the recovery of cobalt and copper varied with change in the bath depth for cobalt containing copper dump slag cleaning operations in a 3.2 MW pilot plant DC plasma arc furnace. The bath geometry played a major role in optimising the efficiency of the process. As the bath size increased, it was observed that cobalt extraction improved but iron content was the highest. From the results it was speculated that the increased power fluxes could cause increased stirring thus resulting in increased recoveries with increasing depth. However, this was not proved scientifically.

Table 2.2: Bath resistance as a function of depth (Jones *et al.*, 1997)

Bath Depth, cm	9	18	19	20	29	40
Bath resistance, Ω	0.03	0.04	0.04	0.04	0.05	0.06

Voltages and currents were also measured at a number of arc lengths, and the arc voltage was calculated using the relationship:

$$V_{arc} = V_{total} - I \times R_{bath} \quad (2.25)$$

Averaged over all pilot plant campaigns, for different bath geometries and for the particular process of copper dump slag cleaning, Jones *et al.* (1997) found that the arc voltage could be estimated as:

$$V_{arc} = 74 + 4.1L \quad (2.26)$$

With the arc length, L, in cm.

Curr (1998) proposed the following equation to describe the static characteristic of open air arcs, and which applies to currents typically found in arc furnaces:

$$V_{arc} = 30 + 12L + 120L/I \quad (2.27)$$

With the same units as the preceding equations.

Browne (1955) have shown that the equation above simplifies to $V_{arc} = 30 + 12L$ (i.e. independent of arc current) when the current exceeds 100 amperes, where the constant voltage term may be explained due to electrode effects at the cathode and anode. However, the low-current behaviour is of interest in arcs approaching extinction and aids in understanding arc stability. However, the particular equation parameters are dependent of the bath and gas chemistry, as are apparent from values of the parameters in the different equations.

A more recent publications by Bowman (1994) reviews the behaviour of steady state arcs in the 1 to 10 kA range. The arc characteristics in terms of voltage as a function of arc length and current are reviewed for a given set of conditions in the furnace. If it is assumed that the arc is axi-symmetric, and experiences no interaction effects with the anode, Bowman have shown that the shape of the conducting volume of the arc as a function of distance, can be represented by:

$$\frac{r_a}{r_k} = 3.2 - 2.2\exp\left(-\frac{z}{5r_k}\right) \quad (2.28)$$

The arc radius, r_a, varies with arc distance, z, from the cathode surface. The radius of the cathode, r_k spot attachment is determined by the value of the cathode spot current density, estimated by Bowman to be around 3500 kA/cm^2. The arc shape function allows the arc

voltage to be estimated by integration. Several constants of Bowman's along with a single variable parameter, namely the arc resistivity (unique to every operation), appears in the arc voltage equation. These parameters can be estimated based on regression of plant data. The integration which is required to be done is:

$$V_{arc} = 2\rho_{arc}\sqrt{\frac{L \cdot j_k}{\pi}}\left[\int\left(\frac{r_k}{r_a}\right)^2 dZ\right] \quad , \qquad Z = \frac{z}{r_k} \tag{2.29}$$

Where:

ρ_{arc} = arc resistivity (Ω.cm)

j_k = cathode spot current density (kA/cm^2)

r_k = cathode spot radius (cm)

r_a = arc radius (cm)

L = arc length (cm)

V_{arc} =arc voltage (V)

If the equation is integrated with the shape function being substituted as integrand, one finds that the V_{arc} can be expressed, as a function of I and L, as shown in equation 2.30.

$$V_{arc} = \frac{I \cdot \rho_{arc}}{m \cdot \pi}\left\{-\frac{1}{a^2 + a \cdot b} + \frac{1}{a^2 + a \cdot b \cdot \exp(m \cdot L)} - \frac{\ln(a+b)}{a^2} + \frac{m \cdot L}{a^2} + \frac{\ln[a + b \cdot \exp(m \cdot L)]}{a^2}\right\}$$

$$a = 3.2 r_k$$

$$b = -2.2 r_k$$

$$m = \frac{-1}{r_k}$$

$$r_k = \sqrt{\frac{I}{\pi \cdot 3500 \quad (A/cm^2)}}$$

$$\therefore V_{arc} = f_{non-linear}(I, \rho_{arc}, L)$$

Where the nomenclature is the same as for equation 2.29. (2.30)

It is important to realise that the only regressible parameter in equation 2.30 is ρ_{arc} (a, b, m and r_k are all transformations of the current, I). It is therefore possible to regress the operating arc resistivity based on arc length, voltage and current measurements. The relationship is both non-linear in the variables but linear in the parameter. It is therefore a useful expression, when the variables (L, I and V_{arc}) can be determined through measurement. Once the resistivity has been determined, it may be used to determine the arc length at other voltages and currents, assuming the gas phase composition does not change significantly.

In pilot scale operations, the arc resistivity can be obtained experimentally by measuring the voltage while keeping the current constant and varying the arc length. The resistivity varies significantly depending on the prevalent gas atmosphere in the furnace. It is important to note that there is a potential difference (and resistance and power dissipation) associated with both the molten bath and the plasma, which effectively determines the mode of energy transfer to the bath and the overall voltage drop. The voltage due to bath resistance only should be determined before the arc-voltage can be determined.

2.4.4 Generating, stabilising and controlling industrial arcs

The metallurgy, the furnace design, and the electrical characteristics are coupled through the plasma properties, slag properties, plasma arc length, slag depth, as well as the operating voltage and current. The negative arc resistance prohibits direct operation from a voltage source with a low internal impedance (Mogensen and Thörnblom, 1987). The voltage would either be too low to sustain the arc or too high, giving runaway over-currents, depending on the position of the actual operating point. The ideal power supply for an arc would be a current source which has a vertical operating line. Stable operation can be achieved by connecting a resistor in series with the voltage source, provided that the resistor more than compensates for the negative arc resistance. The operating line of the power supply must have a more negative or steeper slope than the arc characteristic. Therefore only two points of intersection represent a stable operating point. If the current passes below the unstable operating point, the arc will extinguish, since the required potential is below the available potential. The ohmic losses due to the resistor would then always be large in comparison to the plasma power, so that this method is only feasible for low power operations, therefore not furnaces.

A very unstable operating situation may occur when the arc characteristic and the power supply characteristic have nearly the same slope, as a minor shift in arc characteristic (such a slight change in the gas composition due to more or less metals being vaporised at the arc attachment spot on melts, which changes the conductivity), would cause a major shift in the operating point. In practice it would therefore be very difficult to maintain steady operation for prolonged periods with such a set-up. In an AC circuit the resistor can be exchanged for an impedance, usually a reactor (electrical sense). The required current control may then be realised with small ohmic losses, but at the expense of a large reactive load on the grid. Due

to the fact that DC arcs are used in the applications in this research, no more will be discussed with regard to AC arc stabilisation in this review. If a plasma generator is to be fed by DC current, a rectifier bridge can be inserted before the plasma generator in the circuits mentioned above, and could also be generalised to three phase circuits. Alternatively, the plasma power supply could be fed with voltage regulation through current feedback, giving it source characteristics. Thyristor rectifiers are typically applied in modern applications, although newer DC chopper technologies are gaining acceptance in the industrial market (will not be discussed further). None of these devices on their own are capable of the short reaction times required for plasma arc control. As the plasma arc constant is of the order 0.1 –1 ms, it is necessary to add a choke to the circuit to provide short term stabilisation (choke typically in series with the arc).

The brief discussion relating to arc control, presented above, indicates that arc control is not trivial from an electrical point of view. Furthermore, one should always bear in mind that the melt itself is a resistor of variable resistance, due to chemical and thermal effects which influences the specific resistivity of the melt, as well as geometric or inventory factors, such as melt depth and, to much smaller degree, melt area. The combination of chemical and electrical interaction is therefore a complex and ill-understood phenomena. More information regarding power supplies for AC, DC transferred and non-transferred arc furnaces is provided by Mogensen and Thörnblom (1987) in their review paper.

2.4.5 Cathodes and anodes and the behaviour of industrial arcs

Physical and structural constraints limit the maximum current that can be used in industrial plasma arc furnaces. The current carrying ability of a graphite electrode, as used in typical plasma arc furnaces, is not determined by the saturation current density for thermionic transmission at the end of the electrode (as for other types of water-cooled metal cathodes), but rather by the temperature and stress profile generated in the bulk of the electrode column, largely by the resistive heating of the column itself (Eschenbach *et al.*, 1987). This heating depends on the electrical resistivity and thermal conductivity of the graphite electrode, which depends much on the electrode quality. Standard grade graphite for DC applications can typically handle an average current flux of up to 35 A/cm^2 (or 350 kA/m^2), which is 10-15 A/cm^2 more than for AC applications. However, AC operations allow larger flexibility with regard to the total current passed through electrodes, as it can also use self-baking Söderberg electrodes, which can be baked to electrodes of much larger diameters, in conjunction to the

fact that 3 or 6 electrodes enter the furnace at the same time (More recent DC arc applications have shifted to the use of more than one electrode). Chemical, electrical conductivity and particle size limitations may, however, constrain one to only using DC plasma arcs. Currently, commercially available graphite electrodes are limited to 700 mm in diameter, the amount of current that may be transferred using a single electrode to a maximum of about 135 kA.

The anodes of transferred DC plasma arc furnaces are normally covered with the melt inside the furnace. Either a pin anode system is applied where steel pins, connected to an anode base plate, pushes into the refractory materials of the hearth, or a conducting hearth is used (more often the case in ferroalloys). The hearth refractories are very often an electrically conductive mixture of MgO, some chromite and carbon, which may be either applied as bricks or a paste that is rammed into position (Pieters, 2001). The combination of the anode base plate, steel pins and electrically conductive refractory constitutes the anode. As the anode remains covered with metal during all times, except when the furnace is drained for maintenance, hearth refractory replacement or other infrequent interventions, the anode corrosion / erosion is very slow. Figure 2.12 shows a photograph of an old base plate and pin arrangement, as removed from a pilot plant plasma arc furnace.

Figure 2.12: Base plate and pin arrangement of an anode of an old pilot plant DC plasma arc furnace (Mintek, 2000)

The flow field of industrial plasma arcs, above 500 A, have been shown to be turbulent (Ramakrishnan *et al.* 1978). As a result of the turbulence, the transport properties increases markedly. Stenkvist and Bowman (1987) mentions that a noteworthy feature of the arcs volts per unit length variation, is the relatively low gradient for the 100 to 400 mm arc length range – at about 0.4 to 0.6 V/mm. In this part of the arc, radiation becomes the dominant loss

mechanism from the arc column, which would imply that as the arc is lengthened at constant current, the added power generated / dissipated goes into radiation rather than convection. Whereas the 100 mm long arc only radiates about 25% of is power (laboratory to small pilot scale arc furnace), this percentage may increase to 40-60 % for arc 200-300 mm in length (typical industrial scale arcs).

The stability of industrial free burning arcs is not well understood. The cathode spot is much smaller than the tip of the graphite electrode, with the current density at the tip exceeding 2500 A/cm^2 (2.5×10^7 A/m^2) which is typically two orders of magnitude greater than in the electrode itself. This cathode spot has been noted to move rapidly across the electrode surface, with an apparently random pattern. However, it was found that when the electrode tip was machined with a ridge the arc's tended to become positionally stable. However, the rapid erosion of the electrode tip makes any special machining of the tip unpractical.

According to Stenkvist and Bowman (1987), observation with high current DC arc furnaces have shown that the arc undergoes a transition from one with a defined and highly mobile core, to a diffuse arc, without a visible core, above a certain current level, depending on arc voltage and temperature. They believed it is caused by the lowering of the pressure at the cathode spot, due to the turbulent backflow in the convective gas movement above the arc waistline (region of transition of the main arc column to the cathode fall region). They found that the following current levels lead to a transition to a diffuse arc at various voltage levels and electrode diameters, with the furnace temperature remaining constant at 1600 °C:

15kA 200 mm electrode 150 V
25kA 400 mm electrode 250 V
40 kA 450 mm electrode 350 V

The importance of diffuse arc operation has not been evaluated, but the general thought at the time of writing (1987) was that it would be desirable as it lead to stable arcing and quiet operation.

Photographs taken at Mintek South Africa (Curr, 2000) shows the progression from visible core to diffuse plasma types in Figures 2.13 to 2.18. The dimple formation on the melt due to increased thrust from increased arc currents is also clearly visible. The arcs clearly become more diffuse as the arc current increases. The photos were taken using a high speed digital camera with an optical filter and high shutter speeds (50 Hz, 20 ms).

Figure 2.13: Low Current Arc, Visible core

Figure 2.14: Intermediate Current, Visible core

Figure 2.15: Transitory arc

Figure 2.16: Diffuse arc

Figure 2.17: High current, diffuse arc

Figure 2.18: High current, diffuse arc (dimple)

2.4.6 Mixing, fluid flow and heat transfer in plasma arc furnaces

Computational fluid dynamics (CFD) may prove very useful in analysing the mixing in systems. However, many simplifying assumptions have to be made when the furnace is a multiphase system with reactions, radiation, electro-hydrodynamic aspects and has ill-defined material properties. Yang (Reuter and Yang, 2001) reviewed the CFD applications in the field of arc furnace modelling. The only attempt been made yet to include both the arc and melt zones in arc furnaces was by Szekely *et al.* (1983). However, the melt flow and heat transfer were decoupled from the gas flow and heat transfer in the open arc region. As a simplifying assumption, the electromagnetic stirring and Joule (I^2R_{slag}) heating in the metal bath were neglected. The transport phenomena in an arc furnace can be classified in two different regions, which are distinctive from each other but interconnected, namely the gas phase in the top free space, where electric arcs may dominate the gas flow and energy transport, and the Maxwell equation's equations have to be solved together with Navier-Stokes equations; and the molten bath of slag and metal or matte, where the flow and heat transfer are governed by several possible factors such as :

- jet momentum transfer from the arcs above the bath,
- electromagnetic forces (Lorentz induced in the bath due to passage of electric current (DC arc furnaces) and Joule heating,
- natural convection due to the temperature gradient ,
- gas bubbling from oxygen lancing (EAF steelmaking), or from carbonaceous reductions (e.g. from smelting reduction of MnO in slag with C),
- free surfaces between gas/slag and slag/molten metal bath.

To the author's knowledge, no one has succeeded in incorporating the two regions with all above-mentioned factors. However, for different specific systems, the model have been further simplified without losing much of the realism. For example, in modelling the melt region, the electromagnetic force and Joule heating can be neglected for AC arc furnaces (open or submerged) or for DC arc and plasma furnaces (big simplification) (Szekely *et al.* 1983, Gunnewiek and Tullis, 1996). One of the melt layers (slag or alloy) and free surface behaviour are usually neglected due to the complexity of the multi-phase treatment.

The electromagnetic field or the Lorentz force plays important role in the gas flow, and the Joule heating and radiation heat losses from the plasma arc are of great importance in heat transfer. An example from Qian *et al.* (1995) illustrates the DC arc modelling concerning the

gas flow in the plasma (air) region, and interaction of thermal energy with the metal bath surface, which was treated as a rigid surface. The energy transfer efficiency from plasma jet to the metal bath was determined. Different operating conditions were simulated for arc current of 50 kA and 60 kA and for cathode – anode distance of 15 and 25 cm. In contrast to the work by Szekely *et al.* (1983) where the momentum transport from plasma jet to the metal bath was considered in their metal bath model, the metal bath was completely ignored, except the heat transfer. While Szekely *et al.* (1983) found that steep temperature gradients could exist close to the arc, the metal bath as a whole shows less than 2% relative variation in average temperature.

Gunnewiek and Tullis (1996) modelled heat and fluid flow in the slag phase of a 36 MW AC electric arc reduction furnace (six-in-line electrodes) using CFD. The computational domain is a symmetrical half, covering only one electrode. The slag – metal interface was treated as a no-slip wall, allowing heat exchange. For the slag – gas interface in the case of open arc operation, the momentum transfer from the arcs to the slag surface was treated in the same was as by Szekely *et al.* (1983). For immersed electrode operation, the slag surface was assumed to be free (flat without friction), and the driving force of flow is solely from buoyancy. Thermal energy transferred to (open arc case) and generated in (immersed electrode operation) was implemented in the model as heat source blocks with a correlation with total furnace power and slag volume in the model domain. Thermal energy consumption in the slag phase due to melting and reduction reactions was also modelled as heat sink, which is a linear function of slag depth. For both cases, the electromagnetic effect on the flow and Joule heating were neglected, which is fairly reasonable since the AC arcs are mainly among the electrode themselves, and the arc or electrode penetration in the slag is small. In general, they found that the flow in the bath is fully 3-dimensional and well mixed. For the open arc operation, the predicted fluid mixing is better than the case of immersed electrode operation, due to the arc momentum, which in turn favours less temperature gradient in the bath.

Caffery *et al.* (1997) modelled temperature homogenisation in an AC EAF steelmaking bath, using CFD. In the model, only the steel melt phase was considered (slag layer was excluded), and electromagnetic effect on the flow and heating was neglected. In their model, the momentum transfer from gas phase of the oxygen lance to the melt was modelled with a moving wall, and the momentum transferred is expressed proportional to the mass flow rate of the gas and the moving velocity. The heat transfer from three arcs to the steel bath was

considered. The exothermic oxidation reaction heat from oxygen with steel bath impurities (C etc.) was modelled at the oxygen impinging point as a heat source, which is proportional to the mass flow rate of oxygen blowing and reaction heat of $O_2 + 2\underline{C} = 2CO$. The molten steel surface behaves as a black body radiator at a fixed temperature. The heat loss from furnace shell was also taken into account with a fixed shell temperature.

2.4.7 Arc-melt interaction and arc submergence

Stenkvist and Bowman (1987) state that, due to the expansion of the current cross section from the cathode spot along the arc axis, there arises an axial component of the $\underline{\mathbf{J}} \times \underline{\mathbf{B}}$ Lorentz force which accelerates the plasma towards the anode (melt). The arc therefore acts as an electromagnetic pump, drawing gas near the cathode spot and ejecting it towards the anode. This axial jet contributes to stabilisation of the arc column, in the sense that it remains straight. Plasma flow fields of a 200 A arc were measured, and it was shown that the maximum axial velocities of approximately 330 m/s were obtained. In terms of industrial application, the strong plasma jet that results at high currents, represents a significant characteristic due to the magnitude of the thrust. The thrust (T_{arc}, thrust in N) can be accurately described by Maecker (1961) equation:

$$T_{arc} = 10^{-7} I^2 \ln\left(\frac{r_a}{r_c}\right) \tag{2.31}$$

The $\ln(r_a/r_c)$ term takes on a value of about 1.0. For 20 and 40 kA arcs, the values of T_{arc} given by the equation are 40 and 160 N respectively. Bowman (1982) has shown that the arc jet can be represented by a nozzle jet to describe the depression formed on the surface of the liquid metal, which is roughly parabolic if the jet is vertical. The magnitude of the depression, assuming a paraboloid shape for the depression can be related to the thrust (Bowman, 1990):

$$T_{arc} = \frac{\pi}{8} \rho_m \cdot g \cdot H \cdot d^2 \tag{2.32}$$

Where:

T_{arc} = thrust (N)

ρ_m = melt density (t/m^3)

g = 9.81 m.s^{-2}

d = diameter (m)

H = depression depth (m) (H < d)

The estimated depressions (for steel) are significant as shown below:

Current (kA)	Gap diameter (mm)	Depression depth (mm)
10	100	60
20	200	80
40	300	140

However, the tip diameter of the electrode also influences the thrust and consequently the depth of the depression. The fact that significant depressions do occur implies that it should be taken into account when interpreting arc voltage - electrode gap measurements. This is however, very difficult for industrial furnaces, and adds to the uncertainty in the arc length estimation.

Although it has not been empirically proved, it is speculated that the depression plays a role in the heat transfer to the melt, as the depression tends to shield the arc, but the scenario is complicated by the magnetically induced flows in the bath itself. As in the arc plasma, the current divergence in the bath causes a melt flow in the downwards direction, and that this mass flow may attain rates of 1.5 t/s at 60 kA, where the melt is molten steel.

Bowman (1990) have also shown that submergence of the arc in slag froths may be beneficial from an arc stability perspective for scrap melting furnaces, as it causes the voltage gradient to increase significantly due to the cooling effect of slag "walls" on the submerged arc volume. The voltage gradient in slag-froth submerged DC plasma arc was observed by Bowman to be even greater than for 3-phase AC plasma arcs (at 13 V/cm for DC vs. 9 V/cm for AC). This he explained to be due to a smaller arc volume and more effective cooling by the side "walls". When an arc is submerged into the slag melt, Bowman estimated the arc "diameter" (this is complex to define clearly for a diffuse arc) to be 10 cm and 15 cm for voltage gradients of 10 V/cm and 6 V/cm respectively, at an arc current of 60 kA. However, this calculated arc diameters depend on the net radiation loss from large diameter arcs (> 2cm) which are not optically thin, and self-absorption effects are therefore substantial.

The depression is normally associated with the concept of the arc attachment zone (AAZ), which is a metallurgically active zone within furnace due to the high fluid flow and heat transfer effects in combination with reaction that occur due to feeding into this zone. Barcza

et al. (1990) have shown that it is critical to balance the feed and power inputs particularly in this aforementioned AAZ to minimize unwanted side reactions. This sensitivity towards feed-power imbalances is viewed as an inherent problem associated with DC plasma arc furnaces.

2.4.8 Thermal distributions in arc furnaces and inertia in the thermal dynamics of melts

As the mass feed rate of materials and the power input of a DC plasma arc furnace can be varied independently, a very careful balance must be reached so that the most appropriate temperature distribution across the bath volume can be attained and maintained. Barcza *et al.* (1990) claims that optimal control of the process chemistry of the DC plasma arc furnace is extremely difficult during dynamic upsets such as feed recipe changes, furnace heating and cooling, setpoint changes in the power level, furnace start-up. Figure 2.19 shows the relationship between the selected power level and the feed rate, which is a function of the specific energy consumption, expressed as kWhr/kg of feed.

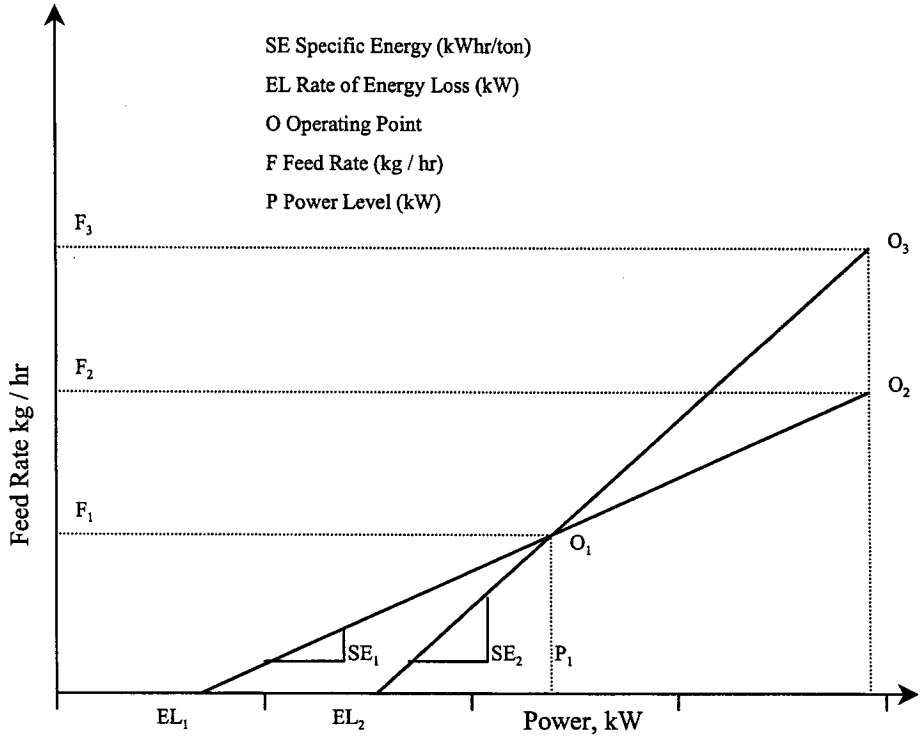

Figure 2.19: The relationship between feed rate and power at different rates of energy loss and specific energy consumption (redrawn after Barcza *et al.*, 1990).

An operating point O_1 with a feed rate F_1 for steady state conditions can be reached, given an apparent value of the energy loss, say EL_1, and a specific energy requirement SE_1 at a power

level of P_1 (kW). According to Barcza *et al.* (1990), if the power is to increase to P_2, based on the values of EL_1 and SE_1, then the operating point should be used for setting the feed rate F_2. However, if the values of EL_1 and SE_1 were incorrect (i.e. if they merely compensated for each other at point O1, as often occurs in practice), and the true value were EL_2, SE_2 and then operating point O_3, which is 25% higher in feed rate F_3, than is F_2, should have been selected. As result of the error, overheating of the bath would occur, starting with the AAZ, and moving progressively to the sidewall and hearth. If the thermocouples in the sidewall are used as the only monitors of the bath temperature, it could take a significant time to detect the imbalance between the feed and the power setting. On the other hand, the temperature in the AAZ would increase very fast, due to the much higher power flux associated with a much smaller volume. While some of the energy will be transferred away from the AAZ to the surrounding melt (depending on the slag viscosity and convection), some energy will be consumed in the AAZ itself to drive unwanted side reactions, while the balance would result in the establishment of a new, higher temperature level. Even under steady state conditions, the temperature distribution on the surface of the bath is expected to exhibit a steep gradient from the central arc attachment zone (at between 1800 to 3000 °C) to the sidewalls (1000 – 1500 °C) due to the extreme temperatures in the DC plasma column itself. The choice of recipe and the feed distribution has been identified as two aspects that may be manipulated to control the bath temperature and therefore the reactions (keeping the overall recipe chemistry the same, but the local chemistry different – it may imply significant changes to the feedpipe and hopper arrangement).

Conceptually, the contents of an open bath can be divided into 3 zones:

- The arc attachment zone (AAZ) – superheated melt
- The liquid bath zone – intermediate temperatures – from superheated to subcooled relative to the melt liquidus
- The freeze-line zone – at or below the melt solidus

These zones and their associated temperature profile are schematically illustrated in Figure 2.20.

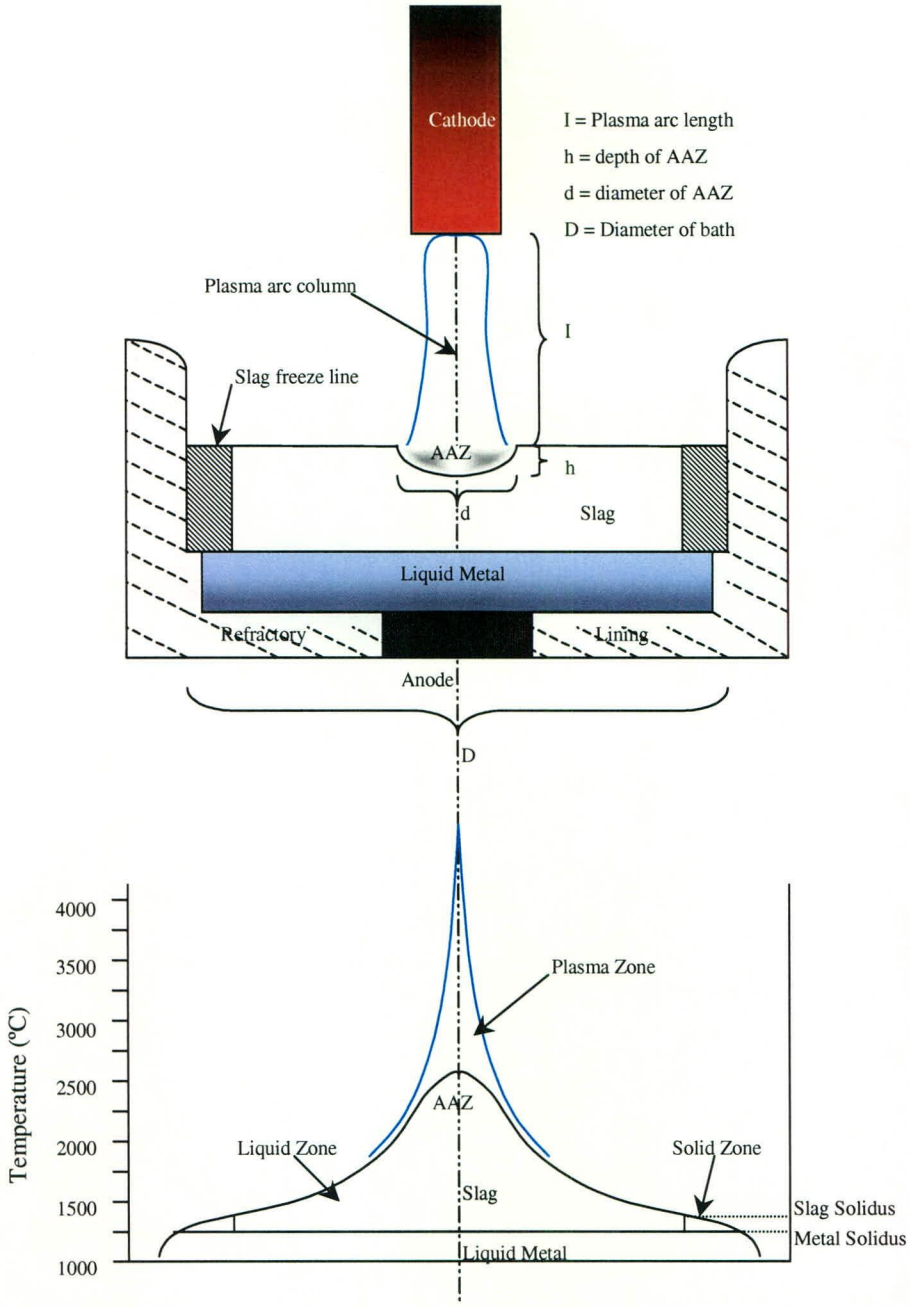

Figure 2.20: The three zones of an open bath transferred plasma arc furnace shown schematically in elevation

Due to the relevance to this research, some of the main results and conclusions from Barcza *et al.* (1990) will be highlighted. The simulations was performed using the Pyrosim software developed by Mintek (Jones, 1987) which is uses Gibbs Energy Minimisation and the ideal associated solution approach to simulate the non-ideal thermodynamics. A CaO-MgO-Al_2O_3-SiO_2 slag was investigated based on equal proportions of the oxides. Reducible oxides such as FeO and Cr_2O_3 was added up to 10 mass% of the feed, while the amount of reductant was varied between 2, 5, 10 and 15 % of the feed (relative to the 4-component slag, excluding the

reducible oxides – that is, the amount of carbon in excess of the stoichiometric amount required to completely reduce the oxide in the slag was varied from 60 to 500 %). It was shown that, at 1900 °C, the proportion of silicon reporting to the vapour phase (as SiO) for 15% addition is less that for 10% addition of carbon. This is explained as due to the formation of SiC, which formation is thermodynamically more favourable at these high carbon additions relative to SiO gas formation.

Energy consumption was found to be increase rapidly with increasing amounts of carbon in the feed and increasing process temperatures. Operations at 1600 °C requires about 60 kWhr per 110 kg feed (which includes the carbon), with only minor changes in energy requirement with changes in the amount of reductant added. However, as new reactions become thermodynamically feasible at temperatures above 2000 °C, the energy requirement changes from 75 to 240 kWhr/ 110 kg of feed, as the carbon addition is raised from 2 to 15 mass %. These temperatures are likely to exist in the AAZ of the melt. A quite surprising phenomenon was found in some cases in that the reduction of MgO to Mg(g) becomes more favourable that the reduction of FeO at temperatures above 2400 °C, as expected to be found in the AAZ. The iron distribution to the metal to below 40% and the proportion of Mg reporting to the vapour becoming as much as 80% at 2600°C.

Thermal inertia in furnaces can be viewed as the resistance to change in temperature of the melt in the furnace. Barcza *et al.* (1990) took the time taken for the temperature of the AAZ to rise by 100 °C as a measure of the thermal inertia. Although the overall average temperature of the bath as a whole is important in regard to attaining a steady state, it is the AAZ that is of primary concern when control of the process is borne in mind. It was found that when the temperature of the slag phase only was raised with 100 °C, very little thermal inertia was noticed. However, as soon as easily reducible oxides were added (such as FeO), the time (for the AAZ) to reach the 100°C high temperature increases with 300%.

The uncertainties in the above calculations are significant, as the actual size of the AAZ is difficult to determine with good accuracy – moreover, it does not represent the whole furnace contents, but only a small portion thereof – normally it would be very shallow and of a diameter of about 150% that of the electrode.

With scale-up the AAZ, as a proportion of the total furnace contents is expected to decrease rapidly, as well as the energy loss component as percentage of the power level – from 25% at the 200 kW level to 15% at 20 MW to less than 10% at 100 MW (Barcza *et al.*, 1990). The net result of the scale-up is therefore a greater sensitivity to the balance of feed rate vs. power input due to the decreasing thermal inertia.

Barcza *et al.* concluded that control of the feed rate and power level to within 0.5% accuracy appears necessary, especially for power levels exceeding 20 MW. The thermal inertia increases with increasing amounts of carbon addition and higher temperatures, but decreases with furnace capacity, especially above 20 MW. Direction of the feed materials directly into the AAZ therefore appears beneficial as it controls the temperature and chemical reactions taking place due to the cooling down effect associated with the energy requirement for melting and endothermic reactions.

The conclusions from the research on arc submergence, the arc attachment zone (AAZ) and arc stability should be seen in its totality – the coupled interactions showing the extreme complexity of the system. The fact that Mg, Mn, Zn and SiO are evolved as gases in the AAZ influences the arc conductivity and, consequently all the arc properties due to the variable amount of arc ionisation.

2.4.9 Furnace configuration, freeze lining maintenance and melt circulation

Electric arc furnaces take on a number of configurations depending if the furnace is operated as an open or submerged arc, transferred or non-transferred arc, with or without a solid burden, DC, AC (3 electrode circular furnace, or 6-in-line rectangular furnace), choked or non-choked feed, and so forth. Some typical electrical smelting furnace arrangements are shown diagrammatically in Figure 2.21 (Curr, 2000). The furnace type investigated in this research focuses on bottom left hand diagram of Figure 2.21. Specifically, the DC plasma arc furnace is presented schematically in more detail in Figure 2.22, with a 3-dimensional projection showing the stepped nature of the sidewall as well as the freeze-line (Figure 2.23).

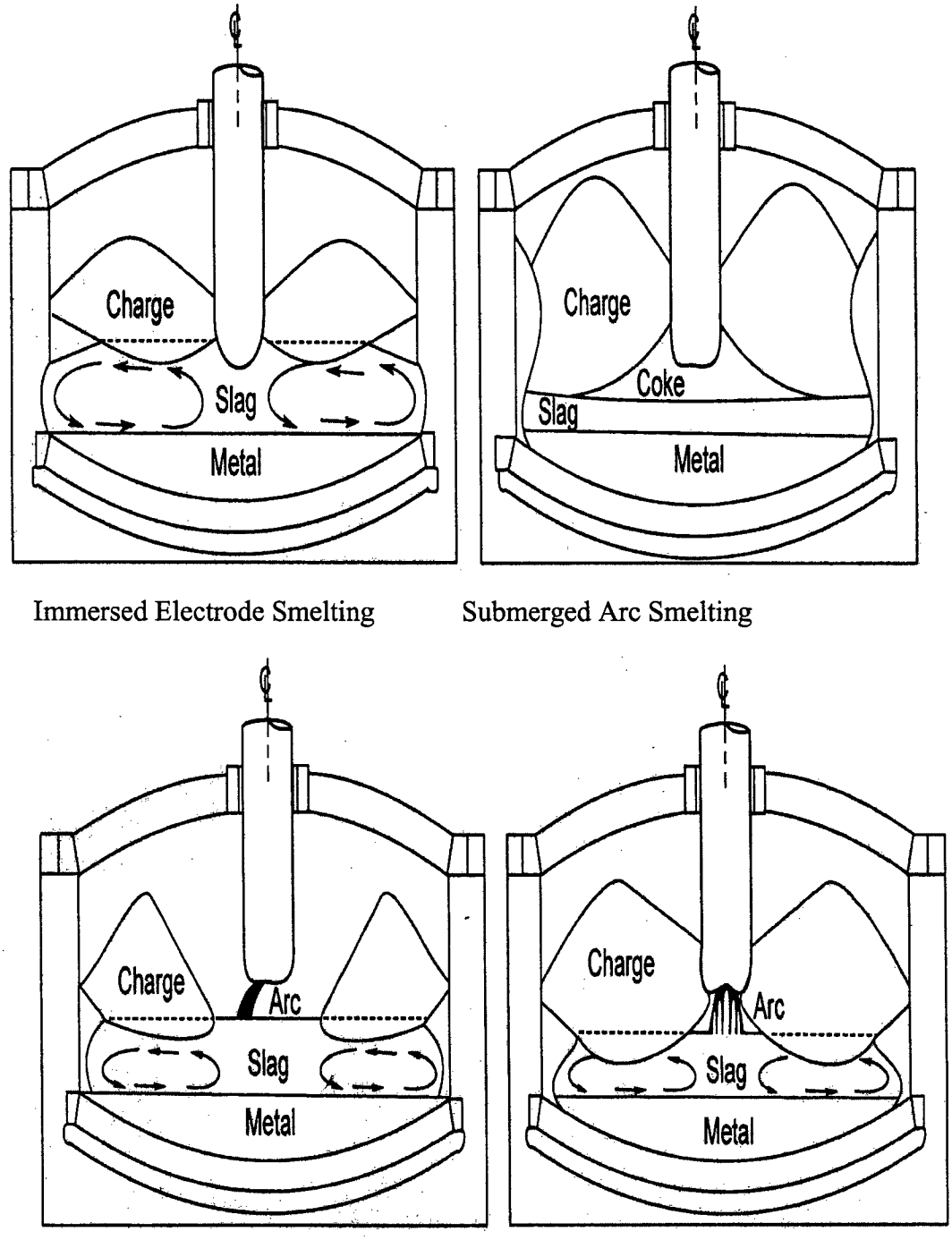

Immersed Electrode Smelting

Submerged Arc Smelting

Open Arc Smelting

Shielded Arc Smelting

Figure 2.21: Smelting furnace arrangements (after Curr, 2000)

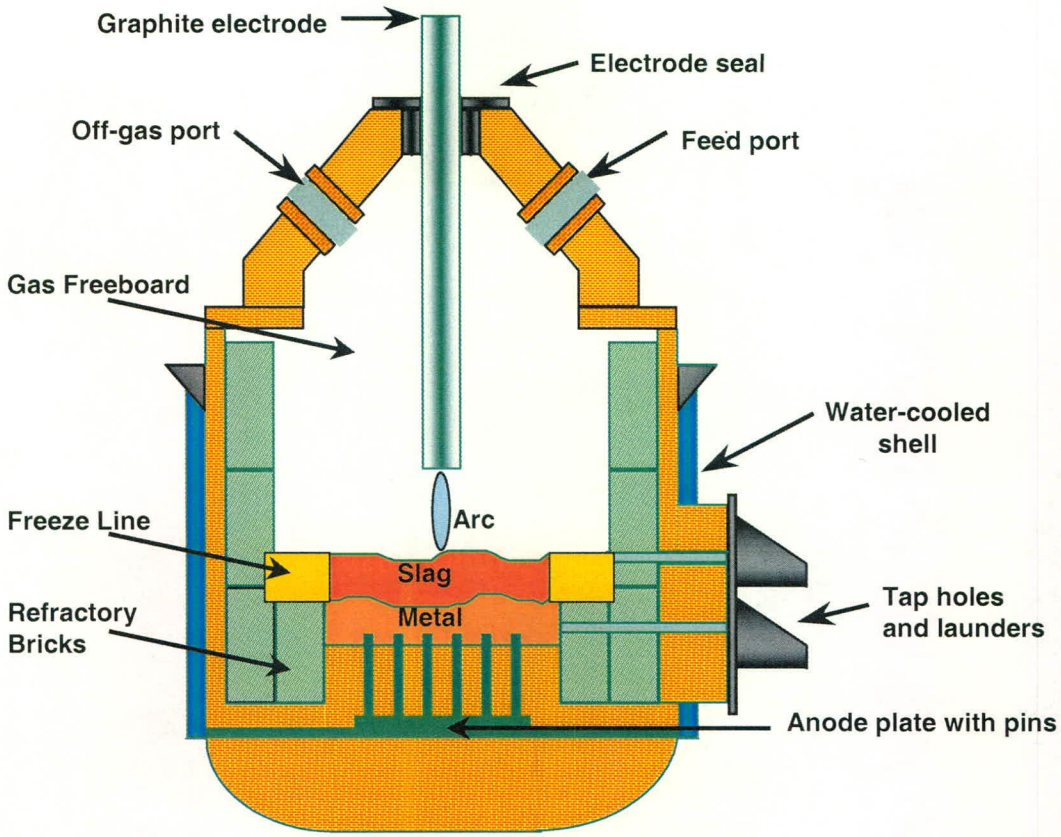

Figure 2.22: Schematic representation of a typical DC plasma transferred arc smelting furnace

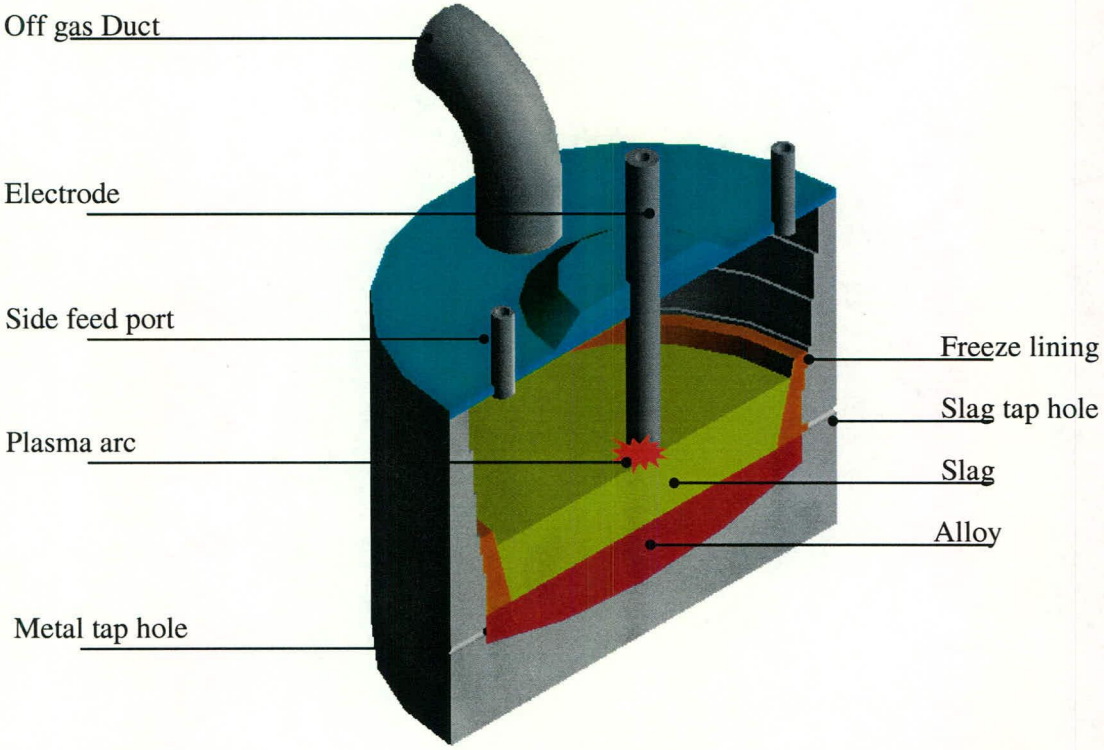

Figure 2.23: Schematic representation of a typical DC plasma transferred arc smelting furnace

The freeze linings of bath type furnaces show dynamic behaviour as they grow or shrink based on the thermal gradient and bath properties. They therefore also influence the active melt cross-sectional area, and the melt inventory / melt height dynamics in the furnaces, as well as the dead volumes and locked inventories in the furnace. For instance, any amount of slag frozen as part of the freeze lining at a given moment, may remelt at any future instant to form part of a slag melt somewhere in the future. The actual size of the freeze lining can vary quite significantly. This uncertainty is further worsened through the formation of thick banks against the sidewall. For example, for the plasma arc furnace used to produce ferrochrome, as studied in this thesis, the freeze lining (+ refractory bricks) may vary typically between 0.5 m and 1.7 m for a furnace with a shell radius of 5.5 m, therefore between 10% and 30% of the furnace radius). As the freeze-lining effectively forms an outer annulus around the slag melt, the % of the furnace cross-sectional area frozen as freeze lining may be estimated to be between 17% and 52% (for freeze linings of 0.5 m and 0.7 meters respectively).

The maintenance of a proper "freeze line", or a layer of crystallised melt which deposits on the hot face of the refractory bricks inside the furnace is very important. As the freeze line has a similar chemistry to the melt, it prevents melt contamination due to corroding refractory bricks. During start-up of a furnace the refractory bricks are normally of sacrificial nature, i.e. they corrode rapidly until a new freeze line has formed. For proper freezeline development a combination of a well-selected refractories and good cooling system design is required. The role of the refractories is not to retain the heat, but to conduct it away from the hotface as fast as possible so that a freeze line may crystallise on the hot face – the freeze line becoming the insulating and chemically resistant "container" for the melt. As the thermocouples used to infer process temperatures are embedded into the refractories, it is important to know heat flux versus thickness relationships for typical arc furnace refractories. The refractory and freeze line also leads to a significant dynamic lag with regard to the process temperature, and should also be seen in the context of the discussion presented in paragraph 2.4.7 regarding the arc attachment zone and thermal inhomogeneities in the furnace.

It should be noted that the alloy / matte phases do not normally form freeze linings as the conductivity of these melts are so much higher than for slags. It is therefore difficult to establish a steep thermal gradient required to produce the freeze lining. Metal / matte inventories are therefore not "locked up" in the same way as slags. On the other hand, a fully liquid slag with a thin freeze lining can be nearly completely drained from a furnace. This is

not possible for the metal melt below the furnace tap-line. This part becomes part of the molten alloy heel that is recycled from one tap to the next.

Very little research has been published regarding the slag flow velocities, heat flux density and the heat transfer coefficient in the molten slag phase for arc furnaces. Sheng (1998) have shown that most of the stirring in submerged arc slag cleaning furnaces is provided by the gas formed at the electrodes, from the reaction of the graphite with the slag. Gunnewiek and Tullis (1996) ignored gas driven flow and showed that the electro-hydrodynamics and buoyancy provided enough driving force to establish high enough velocities for good mixing. Choudhary and Szekely (1980) speculated that mixing in arc furnaces would be very bad and that the local velocities in the slag is determined by natural convection. On the other hand, Roberstson and Kang (1999) identified laboratory studies by A. Deneys that tend to support the view that plasma jet and electromagnetic forces combine to produce significant stirring.

To further investigate the fluid flow associated with heat transfer in arc furnaces, Robertson and Kang (1999) developed a physical model of the system, using waxes with similar Prandtl numbers than those found for slags, with centrally placed heating element and wall cooling. They found that the bath was horizontally stratified in temperature in all cases studied, in cases where no gas bubbling occurred. They found that, when gas bubbling did occur (as one would expect in an arc furnace running employing carbothermic reduction), the bath temperature became much more uniform, due to improved mixing with an associated increase in the heat transfer coefficient. However, even under bubbling conditions, they found the bath to be thermally stratified, although the freeze line formed was much thinner. The bulk slag did, however, show a significant improvement of thermal homogeneity. However, they claim that many of the assumptions they made in the work may be controversial, especially trying to simulate arc furnace conditions using a physical model with no actual arc.

It becomes apparent that the plasma arc, electro-hydrodynamic factors, melt mixing, reaction kinetics, bubbling and gas generation and heat transfer are all inseparably linked for arc furnaces, and that studying the phenomena one by one on a quantitative basis is extremely difficult – moreover it may divert one from the correct remedial action if the problem is not studied holistically. Due to the importance of the phenomena, and the way it constrains one's control actions to a furnace, the above mentioned phenomena were dealt with qualitatively in

a reasonable amount of depth. It forms the basis to perform an technological analysis of the smelting of chromite and ilmenite in arc furnaces.

2.5 Electric arc chromite smelter

Ferrochrome is typically produced in South Africa from chromite (a iron, chrome, aluminium, magnesium spinel mineral) in either a submerged arc or open arc furnaces (DC plasma). The raw material particle size requirement and reductant requirement are significantly different, as the submerged arc furnaces requires a porous burden with a narrow range of electrical conductivity and a reductant of high strength, while the open arc furnaces are not constrained in this way. Open arc furnaces can therefore treat chromite fines and operate with low-strength, high rank coals such as anthracite of reasonably small particle size (1 - 20 mm). In the South African context, this capability has special significance, as it makes the extraction of ferrochrome from finely milled chromite rich gangue (the main constituent of the PGM-rich UG2 reef) from the PGM industry. A number of ferrochrome producers are to be found in the central-southeast Bushveld complex, where a combination of high alloy steel producers (Highveld Steel and Vanadium and Columbus Stainless Steel), the availability of coal, inexpensive electrical power and chromite creates a area of industrial synergism.

2.5.1 Ferrochrome production with DC plasma arc furnaces

In 1982, Mintek (The Council for Mineral Technology of South Africa) and Middelburg Steel and Alloys (currently split between the operations of Middelburg Ferrochrome and Columbus Stainless Steel) lodged a patent for the production and treatment of ferrochrome (Barcza and Curr, 1982). The patent claims revolve around ferrochrome production from chromite fines and a carbonaceous reductant in an open bath furnace, applying DC-transferred arc technology. The patent further claims that high quality coke are not required and as the process is not very sensitive to reductant particle size, less expensive reductants may be used. An oxygen partial pressure of 10^{-12} atm is identified as the most desirable to attain the most favourable dissolution of chromite spinel in the feed materials and to attain the most favourable equilibrium in the process. The patent further notes that the partial pressure of oxygen had a direct bearing on the solubility of the chromite spinel in the slag and that while the solubility is essentially zero at atmospheric conditions, it increases to about 40% when the oxygen partial pressure is reduced to 10^{-8} atm. It is further noted that it is preferable to add fluxes to the chromite feed to create a slag with a liquidus temperature of about the same or slightly higher than the associated ferrochrome alloy liquidus temperature. However, the

liquidus may be higher provided that fully liquid conditions are maintained in the slag. Lime and silica addition are the preferred fluxes, as they are instrumental to control (in conjunction with temperature and reductant addition) the alloy silicon content and to control the sulphur capacity of the slag. Over and above the ability to handle chromite and reductant fines, the furnace can also reprocess ferrochrome alloy fines. The use of an plasma as major power dissipation mode also implies that lime additions can be made to control the slag chemistry, without the need to be concerned about the electrical resistivity, allowing a partial decoupling of the power input and the furnace chemistry.

As the bath is directly exposed to the gas atmosphere, as opposed to the burden-based shielding in submerged arc furnaces, the operation becomes sensitive to ingress air. It is therefore noted in the patent (Barcza and Curr, 1982) that if ingress air is excluded and nitrogen or argon is used as purge / shield gas, the chromium content of the slag (and therefore the chromium losses) reduced from around 20% to as low as 3%. It was found that where significant air ingress did occur, the chromium was present in the slag mostly as undissolved chromium spinel.

2.5.2 Process Description

The operation to be modelled is therefore an open bath DC plasma arc furnace, which is fed continuously with raw materials, and tapped intermittently, while energy is provided to drive the endothermic reactions through a direct current plasma arc from a single central graphite cathode and a melt covered anode. The furnace has a shell diameter of 11m (radius 5.5 m), a depth of 7 m, and a crucible diameter of 8.8 m. The furnace is rated at 40 Mwatt, to produce a plasma with a DC current of 65 kA, with a secondary operating voltage of 550V, an operating resistance of 8.5-12 milliohm and an electrode diameter of 0.615 m. Such a furnace can produce between 140 and 270 metric tons of HCFeCr alloy per day. The raw materials fed to the furnace can be divided into 4 main classes, being chrome ores, reductants, fluxes and "other" additions.

Chrome ores would typically be chromite spinel minerals $(Fe,Mg)^{2+}(Cr,Al,Fe)^{3+}{}_2O_4$ derived from the South African Bushveld complex (Howat 1986). The chromite spinel is therefore a solid solution, which may be intergrown with siliceous gangue components. Although chrome to iron ratios of close to 3 are found at some locations, the typical chrome to iron ratios in chrome spinels are of the order of 1.5 to 1.6. In the temperature range 1550 to 1700 °C

(melting point range of the alloy), the reducible components of the mineral are the Cr_2O_3 and FeO / Fe_2O_3 components. An unfluxed slag, where most of the Cr and Fe oxides have been reduced therefore leads to slag with a phase diagram corresponding to the MgO-SiO_2-Al_2O_3 system, which tend to be highly refractory in nature unless additional fluxing agents, such as lime, are added. The silica contents of an unfluxed, totally reduced, slag would typically lie within 25-45% and the ratio of MgO to Al_2O_3 would typically be in the range of 0.7 to 1.5. Howat (1986) shows that the liquidus rises from 1550 to 1900 °C as the silicon content of the slag decreases from 45 to 25%. Furthermore there is the incompatibility of increasing viscosity (due to slag polymerisation) with increasing silica, and therefore decreasing liquidus. Moreover, the electrical conductivity of the slag decreases with increasing amount of silica. Typical other components in an industrial slag would be CaO, FeO and Cr_2O_3. FeO and up to 6% CaO do not influence the liquidus significantly, but an increase in Cr_2O_3 causes a rapid rise in liquidus temperature. All three of the latter components reduces the viscosity of the slag, while CaO and FeO increases the electrical conductivity. A more detailed description of the thermochemistry will be presented in Chapter 3.

As DC plasma arc furnaces do not require a solid porous burden, they can be fed with low grade (high ash) coals, char, bituminous coal or anthracite. South African anthracite is normally used as it provides a good combination of a high fixed carbon content and a reasonable reactivity. The reductant typically has a small particle size with the mean particle size being smaller than 10 mm (Barcza *et al.*, 1981). However, fine coal has the problem of being more prone to partial oxidation during the feeding process (before it ends up in the molten slag bath), and it is more susceptible to entrainment in the off-gas. Additionally, the electrode is also consumed, albeit at a much slower rate than in submerged arc furnaces.

The effect of fluxes has already been mentioned in the discussion of the chromite minerals, as some chromite ores may be self-fluxing. Silica and lime, as limestone or calcined lime are added as required to obtain the slag with acceptable physical properties (liquidus, basicity, viscosity and electrical conductivity). Basicity (Index) in the Ferrochrome industry refers to the ratio:

$$BI = \frac{(\text{wt \% CaO} + \text{wt\% MgO})}{\text{wt\% SiO}_2} \qquad (2.33)$$

A minimum basicity of 1.0 is required to prevent chemical corrosion of the refractories, ensure a readily conductive slag, to improve slag fluidity, and increase the slag's sulphur capacity.

"Other additions" refers to any waste material that are recycled, be they ferrochrome alloy fines, spills of chromite from the conveyor belts, recycled slag or dust. In all cases for which historic data were available, the other additions refer to spilled chromite and ferrochrome fines.

All the additions, except for the "other additions" are fed from bunkers, feeding into silos, which in turn feed intermediate hopper bins above the furnace. These bins transfer feed material, using rotary valves and standpipes, into a centrally located hopper, where it is mixed, before transfer via a hollow electrode into the furnace. "Other additions" are sporadically made, with the chemistry and amount of these additions being known. Side feeding of quartz is sometimes done, directly above the tap holes, and shortly before tapping, partially to cool the melt in the area, while the same time lower the slag liquidus in the region of the tap hole.

The furnace shell and roof are cooled using water cooling panels of which the water inlet and outlet temperatures and flow rates are measured on a panel-by-panel basis. However, the hearth is air cooled at the bottom and heat losses from the hearth is much more difficult to estimate. The refractory temperatures are measured at various locations around the hearth as well as at different heights. The electrode depth is controlled by a hydraulic electrode arm. The electrode has to be lowered as it is gradually consumed, and new pieces of electrode are to be screwed onto the top electrode portion once the electrode arm drops below a specified datum line. Movement of the electrode tip away from the bath leads to increased arc lengths and increases in the arc voltage drop and resistance. The furnace feed system is purged with nitrogen or argon which enters via the feed chute through the electrode. The furnace off-gas is removed via a water-cooled duct which leads to a venturi scrubber. The scrubber effluent is subsequently thickened and filtered. The filtered flue dust is typically not analysed, nor weighed.

Tapping is typically on a 6 hour tap-to-tap basis for slag and alloy respectively, although it was found to be highly variable. Slag is normally tapped before alloy to reduce the hydrostatic

head on the alloy and to recover most of the slag above the slag tap hole. If alloy would have been tapped first, a significant portion of the slag would be below the slag tap hole, leading to the recycling of a very large slag heel, and also reducing the hydrostatic head of slag above the slag tap hole (and therefore the driving force for slag flow). If the slag is at a subliquidus temperature, the slag may behave rheologically (Chapter 4) like a Bingham plastic which requires a yield stress to flow, and the hydrostatic head too small, the slag may not flow at all. The tapping order (slag first-metal later) is applicable to all furnaces where the slag and alloy melts are tapped from separate slag and alloy tapholes.

The tapping procedure typically starts with a preparation of the tapping launder for tapping, after which taphole drill is swung into place and drilling commences. After a specified depth has been reached, the drilled hole is lanced with a oxygen torch which consumes the iron lance very rapidly in a metallothermic reaction. Lancing is continued for a while after the taphole was opened, until a fully developed flow of slag / alloy occurs. The taphole may be lanced repeatedly depending on the operators' perception that there may be large residual amount of slag left in the furnace, based on the number of ladles (in the case of slag) tapped and the amount of material fed. Ferrochrome alloy is not tapped into ladles, but flows down a launder into sand moulds, specially made for every tap on the tapping floor. The tap holes are closed with clay (castable refractory) using a "mud gun" which very often is on the same rig as the drill. The clay is subsequently baked *in situ*. The mass of slag tapped is gauged by eye (e.g. 2¾ ladles) with an accuracy of no better than 30% per ladle (although the error is diluted due to more than one ladle being produced and therefore being spread over all ladles. The alloy mass tapped is typically estimated on a tap by tap basis by the number of moulds filled. However, all the alloy of one production day (from 05:00 until the next day 04:59) is accumulated and weighed accurately. It is apparent from the way the furnace is operated (at the time of the study) that significant uncertainty exists with regard to the actual amounts of material produced.

2.5.3 Aspects of mass transfer and kinetics of chromite smelting

Demir and Eric (1994) studied the reduction of chromite in liquid Fe-Cr-C-Si alloys. They found that an increase of chromium in the alloy melt led to faster reaction kinetics. The effect of increasing Si was even more marked, as it caused a drastic increase in the reduction rate of spinels. Moreover, they found that a dense metal carbide layer (M_7C_3) formed when no silicon was present, but that the addition of silica led to the carbide not forming at all. They

concluded that reduction rate of chromite was controlled by the liquid state mass transfer of oxygen. Using a rotating cylinder (chromite cylinder in alloy melt) method, they found that the mass transfer coefficients for oxygen and silicon, for the reaction:

$$2\underline{O} + \underline{Si} = [SiO_2] \qquad (2.34)$$

and the mass transfer coefficients of oxygen and carbon for the reaction:

$$\underline{O} + \underline{C} = CO\ (g) \qquad (2.35)$$

To follow the general power law relationship :

$$\left(\frac{k_l}{v}\right) = c \cdot Sc^{-0.644}\, Re^{-m} \qquad (2.36)$$

with c and m being constant parameters, k_l is the mass transfer coefficient (cm/s), v is the relative velocity of the chromite to the alloy melt, and Re and Sc are the Reynolds and Schmidt numbers respectively. Table 2.3 shows the values of the exponent, m, and the system under consideration:

Table 2.3: Mass transfer correlation parameters for equation 2.36

Diffusing atom	Mass transfer coefficient range (cm/s)	m
O in relationship to Si	7.6×10^{-4} to 5.9×10^{-3}	0.18
Si	4.7×10^{-2} to 3.2×10^{-1}	0.15
O in relationship to C	5.8×10^{-4} to 3.8×10^{-3}	0.41
C	7.2×10^{-4} to 3.7×10^{-3}	0.43

The constant, c, was of the order of 0.1. Demir and Eric (1994) proposed that the reduction of chromite by carbon and silicon dissolved in ferrochrome alloy occurs as follows:. The reduction of iron oxide in the spinel, by carbon and silicon starts at the surface, and at surface defects such as microcracks and grain boundaries to form SiO_2 (s) and CO gas. As the reduction proceeds by the reduction of iron oxides to iron, the SiO_2 (s) starts to dissolve the surface of the spinel to form a slag phase. Chromium oxide also dissolves in this slag. The spinel structure therefore progressively disintegrates and new microcracks and defects are formed as the Fe and Cr are reduced. All reactions were found to tend to completeness after 2 to 2½ hours.

It is important to note that Demir and Eric's (1994) mechanism does not investigate the effect of liquid phase reduction, the main mechanism proposed by Barcza *et al.* (1981). The presence of lime and quarts as fluxing agents would therefore contribute to the fluxing of the chromite. However, both groups of researchers agree that chrome reduction rate increases significantly as the conditions become more reducing, as this improves chromite solid state reduction and dissolution and liquid state reduction.

While this mechanistic discussion does give some insight into the actual reduction process, it does not offer much with regard to a practical model. However it shows that the reactions are:

- mass transfer controlled (therefore the rate is proportional to the difference of the bulk concentration and the equilibrium interfacial concentration to the exponent of one);
- dissolved carbon and dissolved silicon are the main driving forces in the reduction, with silicon being surface active by limiting carbide formation;
- the liquid-phase mass transfer of oxygen across the metal-oxide (slag) boundary is rate limiting;
- increased interfacial flow (due to improved mixing and surface renewal) will improve the overall rate of reduction.

These qualitative aspects may serve as guide in subsequent analysis of industrial data.

2.5.4 Measurement and procedural control

Production challenges may arise due to off-gas dust blockages, uneven refractory corrosion, not being able to tap, and not being able to obtain good online measurements of either the chemistry or the actual process temperature, or the mass of materials produced. Feed pipe blockages occur sporadically due to moisture in the feed materials, or the electrode may drop to the point of submergence (causing slag to freeze in the feed cavity). Furthermore, water leakages into the furnace bath sometimes occur. These are detected when the bath surface is inspected, where dark spots are viewed as indicative of a water leak. Downtimes due to remedial action may be significant. No measurement of slag or alloy inventory in the furnace is available and there is no indication of the actual level of the melt in the furnace.

The electrical control seeks to control around a power setpoint, while the electrode height is set according to the overall resistance. Temperature measurements of the slag or alloy are seldom made. Gas temperature measurements are unreliable due to encrustation of the dust particles on the thermocouple sheath in the off-gas ducting.

Good control is therefore hampered by the lack of reliable, accurate and timely data, sampled at the correct position and with a constant sampling time. At the same time much is expected of advanced control as a possible solution to the control dilemma. One of the key problems in the present control approach is the single cause – single effect way of thinking among production staff, while the system is inherently a dynamically coupled non-linear multi-input-multi-output system. Typical procedural "control" actions are based mostly on if the furnace is, according to operator perception, "over or underfed" (relative to the power input) or "over- or undercarbon". These scenarios are evaluated as follows by the operating staff:

2.5.4.1 Effects of Underfeeding

Underfeeding was viewed to have occurred when the specific energy input was too high, leading to melt superheating, and subsequent corrosion of the side wall feed banks / freeze line. It is judged to have occurred when there is an excursion in the temperature as logged by the thermocouples embedded in the refractories. Underfeeding is also associated with a phenomena described by production staff as "stewing"- which is a high temperature bath which is associated with high silicon transfer to the alloy if enough carbon is present.

2.5.4.2 Effects of Overfeeding

Overfeeding was viewed to have occurred when the specific energy input was too low, leading to melt cooling, and "closing up of the bath" due to growing a side wall feed bank or freeze lining, causing tapping difficulties as the taphole has to be cut much deeper to access the molten slag or alloy. It is judged to have occurred when one investigates the top of the bath melt and significant banks occur on top and sides of the melt surface. Formation of banks or false banks may lead to redirection of the melt during tapping which, in the worst case, may lead to tapping the wrong melt from a taphole, for example tapping slag from an alloy taphole or visa-versa.

2.5.4.3 Over/under carbon conditions in the furnace

Over carbon conditions are also associated with bank formation in the furnace, and tapping problems may occur due to a "cold" alloy, while under carbon conditions are viewed similar to the "Underfed" scenario, therefore leading to the corrosion of the side walls. The effect of

over/under carbon result from the endothermicity of the reaction – therefore cooling the slag if too much carbon is added, given that all other variables are maintained constant.

The problem with the above line of reasoning is immediately apparent: different causes may have the same effect, and the effects are then evaluated to determine the cause. Unfortunately, an "under carbon" situation cannot be remedied by feeding more feed (because it could have been misjudged as an underfed situation). Moreover, taking the wrong corrective action would worsen the situation even further. Furthermore, the whole approach is reactive, and due to the slow registration of the effects (large thermal lag due to embedded and isolated thermocouples as well as the need to wait until the plasma is switched of before the bath surface can be evaluated), the process metallurgy may have moved into the wrong direction for a significant period of time before remedial action is taken.

2.5.5 Sampling, assaying, chemical analysis

Receipt analysis are used for the assays of the raw materials. These receipt analysis are often spot-checked by the on-site laboratories. The different types of chromite are analysed by X-ray fluorescence (XRF), based on fused discs. Proximate analysis of the coal / anthracite are based on receipt analysis (but also sporadically spot-checked). The slag is analysed using XRF, but the distribution of Cr and Fe between its various oxidation states (Cr_{metal}, Cr^{2+}, Cr^{3+}, Fe_{metal}, Fe^{2+}) is not known, unless a special request is made for this kind of analysis (which is then done using quantitative wet chemistry). No carbon, sulphur or phosphorous analysis is made of the slag. The alloy is analysed using a spark optical emission spectrometer (OES), which provides the analysis of Cr, Si, S, and P in the alloy, while Carbon was usually determined by a LECO-infrared cell. The practice of carbon analysis of the alloy has been stopped since December 2000. The dust is neither analysed nor weighed on a regular basis. The off-gas is analysed for H_2, CO and O_2- more for the aim of explosion prevention than as a control mechanism.

For the purposes of this research, grab samples of the flue dust were analysed using XRF and a SEM-EDS. Furthermore, LECO analysis of all feed and product materials were made to determine the carbon and sulphur contents. Temperature measurements of a number of slag and alloy taps were made using an infrared pyrometer. Sometimes repetitive samples were taken of taps to gauge the composition variation during a tap.

2.6 High titania slag production in open arc furnaces

A patent for the production of high titania slags in DC plasma arc furnaces from ilmenite (derived from mineral sands), have been registered by Mintek (Denton and Schoukens, 1993) relatively recently. Subsequently Anglo American Corporation Plc and Iscor Ltd (Now Kumba Resources Ltd) in South Africa commercialized the technology for industrial scale operation. Rio Tinto Plc has been in the field of mineral sands processing in South Africa for a substantial period, but uses a six-in-line AC open arc furnace. The Mintek patent shows that ilmenite sands of 48% TiO_2 can be upgraded to a slag containing 80-90% equivalent "TiO_2". While titanium occurs nearly totally in its Ti^{4+} form in ilmenite, the slag contains titanium in the forms of TiO_2, Ti_2O_3, TiC and TiO, all of which are together reported as "TiO_2", based on XRF analysis. The FeO content reduced from over 50% to below 10%. Fe can exist in both the Fe^{2+} and Fe^{3+} forms in natural ilmenite, but only as Fe^{2+} under the highly reducing conditions found with high titania slags.

Denton and Schoukens (1993) identifies the key problems with the traditional AC six-in-line open arc furnace production. They identify the feeding as problematic, as the smelter is typically fed through more than 20 feedports, most of which are situated near the sidewalls to protect the sidewalls from refractory erosion. It renders process control extremely difficult where, despite sophisticated computerised control, localised regions of over-reduced slag are often produced leading to foaming. Corrective measures which are taken are noted to lower the efficiency and availability of the furnace. However, from a furnace design perspective it is much easier to design for a freeze lining and taphole protection in a six-in-line configuration (Nelson, 2004).

The process Denton and Schoukens (1993) therefore propose is the reduction of ilmenite to high titania slag and pig iron by feeding ilmenite and a carbonaceous reductant simultaneously (in the absence of fluxes, to the central region of a molten bath (in the arc attachment zone) in a circular DC plasma arc furnace, using a freeze line to protect the refractory lining in side the furnace. Freeze lining maintenance and maintenance of a proper operating or tapping temperature is said to occur through adjustment of the feed rate to power ratio, optionally in combination with water cooling. The feed may or may not be preheated by the furnace off-gas. Air should be excluded from the furnace to maintain highly reducing conditions.

Preferably the carbonaceous reductant should be added in quantities in excess of the stoichiometric amount required to reduce all the iron oxides present in the ilmenite concentrate to metallic iron and to ensure that oxygen in the off-gas is in the form of carbon monoxide. The furnace has to be operated at a temperature between 1650 and 1750 °C.

2.6.1 High titania slag production with DC arc furnaces

As is apparent from the description above, the operation and smelting technology are in many ways similar to chromite smelting. However, some significant differences exist. Firstly, one does not have the degree of freedom in ilmenite smelting, as one has with chromite smelting, to add other fluxes and slag modifiers, and therefore one is limited in one's capability to change the reaction chemistry. The only two variables that could be changed to affect the chemistry of the system are the ilmenite-to-power ratio and the reductant-to-ilmenite ratio.

A second significant difference stems from the melt conductivity. While the resistance could be varied at the same power level, it is not normally a variable that is used in control. In contrast to ferroalloys smelting with a silica-containing slag, high titania slags have very high electrical conductivities; their conductivities tend towards the conductivities of metals. Consequently, as the conductivity increases with temperature, the contribution of I^2R heating within the bath is much less than for chromite smelting. In principle, there is a need to draw out the arc as long as is possible, while still maintaining arc stability and preventing stray arcing to the furnace inner roof and side-walls. As noted earlier, the current flux capacity of graphite electrodes is limited, and the largest diameter electrode that is commercially available (0.7 m at the time of writing) determines the maximum current that could be conducted through the electrode. The largest voltage that could be safely operated at depends on the voltage required to arc to furnace components other than the slag bath. Therefore, if arcing to the inner roof section allows the arc to close the electrical circuit at lower voltage drop than that associated with the arc to the bath, the plasma will preferentially arc to the roof or sidewalls, doing significant structural damage in the process.

The furnace construction is similar to the ferrochrome producing furnace. However, the off-gas handling and materials handling during tapping is slightly different. Both metal and slag are tapped into ladles and weighed subsequent, as both are valuable saleable products (although this would be an advisable practice at any smelter). In contrast to the ferrochrome production, the temperatures of both the melts are measured for every tap (using a pyrometer).

However, the tapping is logistically constrained due to the availability of ladles and access to the furnaces. It is therefore seldom that the melt reaches to the tapline – most of the time significant heels of both slag and metal remain in the furnace. The chronology of tapping follows the same reasoning as for ferrochrome (section 2.5.2). Drilling and closing the taphole are also similar to the procedure used at the ferrochrome smelter.

In contrast to the ferrochrome smelter, the dust is not captured in a venturi scrubber, but instead in a baghouse filter. It is normally not analysed unless an analysis is required for a specific purpose. The mass of dust produced between two taps is not measured.
The off-gas is analysed for hydrogen and carbon monoxide.

2.6.2 Kinetics of plasma arc ilmenite smelting

Very little has been published regarding the kinetics of ilmenite melt reduction (although much more has been published regarding the solid state reduction). Only Ma and Warner (1999) published quantitative data directly applicable to carbothermic reduction of molten ilmenite. However, much more has been published regarding FeO reduction in slags, which will be briefly reviewed here.

Pistorius (1999) have shown that reaction 2.37 deviates from equilibrium tending to the left of the reaction coordinate, therefore favouring Fe and TiO_2 over FeO and Ti_2O_3. It follows that Fe is first reduced from its oxide in melt, and subsequently reduces TiO_2 electrochemically (reaction 2.37), although a substantial amount of TiO_2 is also reduced to Ti_2O_3 through reduction with <C> and CO gas. The reduction of FeO melts by carbon and CO have been studied by many researchers (Hayes *et al.*, 1995; Utigard *et al.*, 1997, Sarma *et al.*, 1996; Hong *et al.*, 1996; Sun and Jahanshahi, 2000).

As the general metal oxide carbon reaction: [MO] + <C> = CO (g) + $\underline{M}$ requires four phases to make contact simultaneously, it is unlikely that in practice they will proceed in a single step. It is therefore generally accepted that all the metal oxides are reduced through the following two-step gas ferrying mechanism involving carbon monoxide and carbon dioxide:

$$[MO] + CO\ (g) = \underline{M} + CO_2\ (g) \qquad (2.37)$$

$$CO_2\ (g) + <C> = 2CO\ (g) \qquad (2.38)$$

The reaction cycle is completed when the carbon dioxide returns to reacts once more with the solid carbon. If the gasification (Boudouard) reaction is fast compared to the gas-slag reaction, the resultant product gas should approach gas/carbon equilibrium (Hayes, 1995). On the other hand, when the carbon gasification reaction is slow compared with the reaction of gas with slag, the composition of the resultant gas phase should approach gas/slag equilibrium. If species exist in more than one oxidation state, electrochemical reactions may also play important roles. Hayes (1995) subsequently found through X-ray studies that there are significant differences in the wetting behaviour of carbon by molten oxides; these wetting characteristics appear to depend principally on the oxide composition. Furthermore, it was found that when wetting does occur, reduction can take place very rapidly, even under conditions where the rate of carbon gasification is very low. Fe^{2+} in silicate slags is typically reduced through the gas ferrying mechanism.

The ferrying mechanism was found to be a dominant reaction mechanism under conditions where:

- the contact angle is high $90° < \Theta < 180°$
- the reactivity of the carbon surface with CO_2 is high
- electron transfer in the carbon or slag phase is limited.

However, the gas ferrying mechanism was found to be insufficient for other metal oxides. The carbon slag reactions may also be presented in its electrochemical form, i.e.:

$$<C> + [O^{2-}] = CO\ (g) + 2e^- \qquad (2.39)$$

and

$$[M^{2+}] + 2e^- = M^0 \qquad (2.40)$$

For systems to which the gas-ferrying mechanism do not apply, an electrochemical mechanism may be favoured under conditions where:

- the contact angle is low $\Theta \rightarrow 0°$
- the reactivity of the carbon surface with CO_2 gas is low, and
- electron transfer can occur readily in the carbon and in the slag.

The low contact angle favours high slag-carbon contact, and restricts the size and coverage of the gas bubbles at the interface. Low Boudouard-reactivity carbons are normally associated with highly graphitised materials such as anthracites. Coals with higher volatiles to fixed carbon ratio's are typically more gaseous reactive (where the Boudouard reaction is the main mechanism of reduction). Mróz (1994) found that the reduction rate of iron with solid carbon

could be described with first order behaviour relative to the FeO activity in the slag. Min *et al.* (1999) found that the rate determining step would change from mass transfer control at FeO concentrations < 5 weight % to chemical reaction at the gas/carbon interface at high FeO concentrations (>30 weight %), while the total reduction rate would increase with increasing FeO content in the slag. Mixed (mass transfer / chemical reaction) control was suggested for the intermediate region. Sarma *et al.* (1996) also show that the liquid phase mass transfer of FeO is a major factor in the reduction of iron oxide from slags by carbonaceous materials. They agree with Min *et al.* (1999) regarding the observation of mixed control for FeO reduction. Utigard *et al.* (1997) also agree that the rate controlling mechanism for FeO reduction is through mass transfer, that is the transport of FeO to the reacting interface in the slag melt.

Ma and Warner (1999) studied the smelting reduction of ilmenite by carbon in molten pig iron. Although there is no proof that this is the main reaction contributing to ilmenite reduction, it is a contributing reaction. These researchers also found that mass-transfer is rate controlling. Unfortunately, no rate model parameters were published.

2.6.3 Measurement and procedural control

Measurement and procedural control are quite similar to chromite smelting, although measurements of more streams are made more frequently. As for chromite smelting, production challenges may arise due to off-gas dust blockages, uneven refractory corrosion, or not being able to tap. However, as the composition, temperature and weight of the molten products produced are known, and the feed chemistry remains relatively fixed, the system overall lends itself to better monitoring. Water leakages into the furnace bath occur sporadically with devastating affects to the furnace structure with pressure bursts being possible. Downtimes due to remedial action are significant (specifically due to MgO hydration, refractory expansion and splitting of the shell are significant risks). As with the chromite smelting furnace, no measurement of slag or alloy inventory in the furnace is available and there is no indication of the actual level of the melts in the furnace.

Foaming in high titania slags is a much larger problem than for any of the other systems mentioned. Although ilmenite slags are highly ionic and depolymerised, high viscosities may still occur due to either operating subliquidus with regard to the FeO-Ti_2O_3-TiO_2 system, or precipitating slag-wettable high-melting solids such as oxycarbides, with a similar density as

the slag. Moreover, foaming may also arise in colder high FeO slags where the slag is highly reactive due to the high FeO activity, and surface tension effect may be overriding. Normally high titania slags are highly fluid, but they are extremely sensitive to subliquidus operation, with the % solids increasing significantly with only a small drop in operating temperature (Handfield and Charette, 1971). Severely stable foams may arise leading to foam overflow through the roof and erratic behaviour of the electrode, seeking to maintain a constant resistance.

As with chromite smelting, the key problems in the present control approach are the single cause – single effect way of thinking among production staff. Typical procedural "control" actions are based mostly on if the furnace is, according to operator perception, "over or underfed" (relative to the power input) or "over- or undercarbon". These scenarios are evaluated similarly to the chromite smelting case.

2.6.4 Sampling, assaying, chemical analysis

The reductant coal is analysed (Proximate Analysis) on a 4-hourly basis, while the ilmenite raw material is analysed daily based on a composite sample from a ilmenite powder conveyor. The analysis is based on XRF analysis of the ilmenite and the ratio of Fe^{3+} to Fe^{2+} is not analysed for as a rule.

The slag is analysed using XRF, but the distribution of Ti between its various oxidation states (Ti_{metal}, Ti^{2+}, Ti^{3+}, Ti^{4+}) is not known on a tap-to tap basis, unless a special request is made for this kind of analysis (which is then done using quantitative wet chemistry). No carbon, sulphur or phosphorous analysis is made of the slag. The alloy is analysed using a spark optical emission spectrometer (OES), while Carbon was usually determined by a LECO-infrared cell. The dust is neither analysed nor weighed on a regular basis. The off-gas is analysed for H_2 and CO.

For the purposes of this research, grab samples of the flue dust were analysed using XRF and a SEM-EDS. Although the smelter measures the temperature of both the metal and slag taps, additional temperature measurements of a number of slag and alloy taps were made using an infrared pyrometer. As for chromite smelting, repetitive samples were sometimes taken of taps to gauge the composition variation during a tap.

2.7 Final comments regarding furnace technology and operation

It should clear throughout Chapter 2 that a total fundamental modelling approach to bath type furnaces is, for the purpose of model-based control or on-line prediction, an impractical objective. Although quantitative relationships exist for some of the phenomena in the furnaces, the same cannot be said for all of the phenomena that dynamically influence the furnace metallurgy. It is the objective of the remainder of this thesis to develop a practical and feasible approach to bath type furnace modelling, taking into account the fundamental phenomena, in cases where they make a significant contribution to metallurgical outcomes.

2.8 Nomenclature of Chapter 2

A = Cross-sectional area (m^2)

BI = Basicity Index (dimensionless)

d_b = diameter of bubble in melt (m)

d_d = matte / metal droplet diameter (m)

D_i = Mass diffusivity of species i

E = arc column field strength ($V.\ m^{-1}$)

g= Acceleration of gravity ($m.s^{-2}$)

H = depression depth (m)

I = Current (A)

j_k = cathode spot current density ($kA\ m^{-2}$)

k_B = Boltzman constant

k_l = liquid phase mass transfer coeffcient

L = arc length (cm)

R = arc column resistance per unit length ($\Omega.cm^{-1}$)

r_a = electric arc radius (m)

r_k = radius of cathode spot attachment (m)

r_p = radius at electric arc periphery (m)

Re = Reynolds number (dimensionless)

Sc = Schmidt number (dimensionless)

T = temperature (K)

T_{arc} = arc thrust (N)

T_L = Liquidus temperature (K)

t_P = freeze lining thickness (m)

T_S = Slag temperature (K)

v_∞ = terminal settling velocity ($m.s^{-1}$)

v_b = rise velocity of bubble in melt ($m.s^{-1}$)

V = Voltage (V)

V_{arc} =arc voltage (V)

We = Weber number (dimensionless)

z = axial coordinate (m)

Greek Symbols

η_s= Slag viscosity ($kg.m^{-1}s^{-1}$)

ρ_m = matte / metal density ($kg.m^{-3}$)

ρ_s= Slag density ($kg.m^{-3}$)

ρ_{arc}= arc resistivity ($\Omega.m$)

σ_m =surface tension of the molten matte

$\Delta\sigma$ = Surface tension difference between the actual slag and pure SiO_2 melt

Σ= Foaming index (sec)

τ = residence time (s)

This page is intentionally blank.

3 PREDICTING EQUILIBRIUM

> "Thermodynamic concepts are very important since they show the final states of any kind of physical and chemical changes, including the driving force of the change and its direction" (Sano, 1997)

3.1 Introduction

This Chapter investigates how the equilibrium term of the Equilib-ARMAX modelling approach, as proposed in the Chapter 1, may be predicted. The main reaction equilibria will be identified, as these consitute the fundamental basis of the modelling approach. The Chapter will outline the important aspects to consider when performing the thermodynamic modelling, since the relevance of the equilibrium term is influenced by the quality of the equilibrium model. To achieve this goal, this chapter will identify the solid and melt solutions used in the thermochemical simulations and how they are incorporated into the thermochemical submodel. The mathematical structures of the solutions models, and some of the phase diagram results obtained through their use, are provided in Appendix A. Moreover, Appendix A provides the literature references to support the selection of stoichiometric compounds, as well as the solid and melt solutions used for the modelling. This chapter will therefore provide a summary of the compounds and solutions used in the final modelling. The phase equilibria and liquidus surface projection are also given in Appendix A. The liquidus temperatures are important because they determine which melt chemistries cause phase-discontinuities that may lead to significant increases in observed viscosity due to solids precipitation. The proper modelling of the chemical and phase equilibria requires a good knowledge of all the phases present in the system (all the gases, melt solutions, solid solutions, and all the pure compounds in all the phases)

Despite chemical equilibrium not always being achieved, the tendency of a system towards equilibrium remains the driving force behind chemical reactions and phase transitions. In high temperature systems much more attention is paid to chemical and phase equilibria, as the systems studied often approach equilibrium much closer than lower temperature reactions. The study of high temperature equilibria has become so entrenched in general pyrometallurgical research that it is the first research area that springs to mind when something is mentioned in the field of pyrometallurgy.

However, does equilibrium thermodynamics play such a significant role in the control of the furnace metallurgy? Many practicing production metallurgists have become sceptical about the use of equilibrium thermodynamics as a prediction tool and have reverted to a totally empirical approach towards metallurgy prediction, and then very often in a reactive, post-mortem way. It will be shown that the field of equilibrium thermodynamics definitely has a major part to play as the anchor point in dynamic prediction, if used in conjunction with a proper dynamic modelling approach.

This chapter will establish the thermochemical basis of the matte converting, ilmenite smelting and chromite smelting processes. The following aspects will be reviewed in this chapter:

- the main chemical equilibria
- the possible stable phases at the operating conditions (solid and melt solutions and mineral precipitates with a fixed stoichiometry);
- thermochemical equilibrium modelling of the three bath types furnace case studies.

The equilibrium thermochemistry will be discussed for each of the bath type furnaces in turn.

3.2 Gibbs Free Energy Minimisation and Equilibrium

In a complex melt with a number of possible phase and chemical equilibria, the Gibbs Free Energy (GFE) of the system will typically not be zero, as with equilibria of single reactions. Instead, equilibrium is established at that set of compositions and activities which minimise the overall GFE of the system.

The GFE minimisation used in this research, has been performed using software (FactSage®) which implements the Solgasmix® GFE minimisation algorithm developed by Eriksson (1975). Fitting of the solution models to experimental data is done using a number of non-linear optimisation techniques such as Bayesian parameter estimation (Königsberger and Eriksson, 1995). Therefore, the Solgasmix® algorithm finds the relative amounts of the different phase assemblages that minimises the total system Gibbs Free Energy:

$$G_{system} = \sum_{i=1}^{N} n_i G_i^o + RT \sum_{gas}^{N} n_i \ln f_i + RT \sum_{Solution1}^{N} n_i \ln a_i + RT \sum_{Solution2}^{N} n_i \ln a_i + \ldots \qquad (3.1)$$

where a_i are the component activities for components $i = 1$ to N as calculated by the solution models, n_i are the moles of the various components, G_i° are the pure component GFE's of formation, G_{system} is the overall system GFE, and f_i are the fugacities of the gaseous components (equal to the partial pressures where the gas can be assumed to behave ideally, as in most pyrometallurgical cases).

FactSage®, the thermochemical modelling and simulation software as developed by the Centre for Research in Computational Thermochemistry and GTT Technologies (Bale *et al.*, 2002), has been used as the standard software for the implementation of the non-ideal solution models and the Solgasmix® minimisation algorithm.

The software uses the modified quasichemical model for short-range ordering (Pelton and Blander, 1984, 1986, 1987) to molten model slags and mattes, while sublattice models (Pelton, 1997a) have been used for the solid solutions, and polynomial expansions (Pelton, 1997b) or the unified interaction parameters formalism were used to model alloy melts. The most recent version of FactSage® systematically varies the moles of each species in a way that makes G_{system} most negative at a particular combination of temperature and pressure. If the existence of a particular solution phase does not assist in minimizing G, it will be dropped in the course of successive iterations. The maximum number of equilibrium phases cannot exceed the number of different elements in the reactants in order to conform to the Gibbs Phase Rule.

The quasichemical formalism, on which all the simulations are based, is discussed in detail in Appendix A. It is discussed as it is the basis of the solution models used in FactSage ® and will be referred to in subsequent sections. The modified quasichemical formalism is discussed in relative detail as only a few academic papers discuss it and its derivation is not generally available in metallurgy textbooks.

3.3 The limitations of thermodynamic modelling and simulation software

The FactSage® software used for thermodynamic modelling in this dissertation is currently viewed as the state-of-the-art software for modelling of high temperature multicomponent chemical and phase equilibria. However, it should be remembered that, although the models were developed and validated on critically assessed experimental data, the pure component heat capacity correlations are empirical polynomials which are valid only when the modelling

is performed within the range over which the parameters were regressed. In none of the simulations in this work were heat capacity correlations used outside their validated range.

The modified quasi-chemical model structure used to model the solution chemistries has a fundamental structure (See Appendix A), but the solute interactions are again stored as polynomials. The *only relevant* case where the solute interactions have not yet been fully optimised, are the interactions in the MgO-Cr_xO subsystem (which is relevant to chromite smelting) and may lead to less accurate equilibrium estimates.

The FactSage® databases are frequently updated as new experimental data becomes available to allow further modelling of the solute interactions. The FactSage® software warns the user when simulations are performed outside the range that a correlation has been validated (No such cases were observed during the modelling). Appendix A provides some examples where the FactSage® predictions are validated against experimental data.

The effect of Cr_xO was further excluded during the modelling of the Ausmelt matte converting process as the mattes studied in the pilot plant studies had insignificant amounts of chrome present due to being derived from Merensky matte smelting furnaces (compared to UG2 smelting, which results in high chrome mattes). However, chrome cannot be ignored in the industrial matte converting operation as the converter has to treat smelter mattes from both Merensky and UG2 concentrates.

3.4 The basic thermochemistry of Ni-Cu matte converting

As mentioned in section 2.3.2, the conversion of Ni-Cu matte occurs in a 2-step process, of which the second stage is the most important with regard to achieving the required endpoint. Only the second stage blow will be evaluated thermodynamically, as this is the most critical stage to control the iron and sulphur endpoints in the matte phase. The nickel-copper matte derived from the first blow consists of 34%Ni, 20%Cu, 16%Fe, 25%S, 0.5%Co, the rest being minor components such as As, Bi, Te, and Se. The matte at the end of the second blow consists of 47%Ni, 26%Cu, 3%Fe, and 22%S, the remainder consisting of minor components. The distributions of only the major elements will be reviewed here. It is important to note that the distribution and solubility graphs show only the effect of chemically dissolved species and not mechanically entrained species. The industrially reported amounts of metals in the slag

would be more than predicted through thermodynamics only due to the industrial laboratories measuring the total (dissolved + entrained) amounts.

3.4.1 Matte-slag-gas reaction chemistry

The reaction chemistry pertaining to nickel-copper matte converting, in an Ausmelt converter and in the presence of PGM's, is discussed by Vernon and Burks (1997). The principle converting reactions for Fe and S are similar to those provided in paragraph 2.2.2. As the slag tapped from the first stage and second stage blow contains much cobalt, a valuable commodity, these slags are normally recycled to the electric smelters, which are operated under less oxidizing conditions. The PGM's associate mostly with a second, molten alloy phase that forms during the second stage when the iron concentration in the matte becomes relatively depleted. The low sulphur-low iron conditions which lead to the formation of this Ni-Cu alloy phase are presented in Appendix A. The following reactions are based on the generic reactions identified by Vernon and Burks:

$$\underline{FeS} + 3/2O_2(g) \rightarrow [FeO] + SO_2(g) \quad (3.2)$$

$$\underline{Ni_3S_2} + 7/2O_2(g) \rightarrow 3[NiO] + 2SO_2(g) \quad (3.3)$$

$$\underline{Cu_2S} + 3/2O_2(g) \rightarrow [Cu_2O] + SO_2(g) \quad (3.4)$$

Iron sulphide is preferentially oxidised before cobalt, nickel and copper (in that order). Some oxidation of these nobler elements will occur according to their relative thermodynamic stabilities. The silica complexes the metal oxides to form a slag with a low liquidus temperature and a high fluidity. The addition of reductant coal leads to the following reactions:

$$[NiO] + <C> \rightarrow \underline{Ni} + CO(g) \quad (3.5)$$

$$[Cu_2O] + <C> \rightarrow 2\underline{Cu} + CO(g) \quad (3.6)$$

Furthermore the main slag forming reaction occurs:

$$2[FeO] + [SiO_2] \rightarrow [Fe_2SiO_4] \quad (3.7)$$

The slag has a capacity for ferric iron (Fe^{3+}) which is dependent on temperature and silica concentration. Ultimately magnetite crystallises as the predominant solid phase when the slag is saturated with ferric iron.

As the mattes that were processed in the Ausmelt furnace contained very little Cr, the effect of Cr was not modelled. This may require some revision in the industrial scenario where chrome may be transferred with the smelting furnace mattes to converter.

3.4.2 Thermochemical modelling of Ni-Cu matte converting

Various researchers have attempted the thermodynamic modelling of matte smelting and converting operations. (Degterov and Pelton, 1999; Björkman and Eriksson, 1982; Tan and Neuschütz, 2001; Kongoli and Pelton; Tan and Zhang, 1998 a and b). It is not the aim of this thesis to review all the solution models used by the different authors. Instead, the extended quasichemical formalism (Pelton, 1997a) developed for commercial use as FactSage® by Bale *et al.* (2002) will be used to simulate the thermochemical equilibria for the operating conditions associated with matte converting. Optimised values for the interaction parameters ω_{ij} and η_{ij} (Appendix A) were used derived from critically assessed experimental data.

The solution model "SOLN-MATT" was used for the matte phase. It contains recent fully optimised data (for binary and ternary and some quaternary subsystems) for the molten matte phase with 30 to 60 mol % S in the system Cu-Fe-Pb-Zn-As-S-Ni-Co. Of these components, the matte system Cu-Fe-Ni-S-Co is the one applicable to the data being produced. All these components appear in SOLN-MATT hence it is suitable.

The solution model "SOLN-SLAGA" was used to model the solution thermochemistry of the slag. In this solution model there are data for molten/glass oxide solutions of the components Al_2O_3-As_2O_3-B_2O_3-CaO-CrO-Cr_2O_3-Cu_2O-FeO-Fe_2O_3-K_2O-MgO-Na_2O-NiO-PbO-SiO_2-TiO_2-Ti_2O_3-ZnO-ZrO_2, with S, SO_4, PO_4, H_2O/OH, CO_3, F, Cl, I in dilute solution, with a miscibility gap at high SiO_2 contents. Of these oxides, the slag system FeO-Fe_2O_3-NiO-SiO_2-Cu_2O is applicable to the data being produced.

Due to the slight mutual solubility of a few sulphides the following sulphides also appear in the slag and are also incorporated in the solution model: NiS-FeS-Cu_2S. The model is particularly well suited to systems with short-range ordering such as molten silicates. A

shortcoming in this solution model is that it does not contain any thermodynamic data on cobalt oxide, hence cobalt will never report to the slag phase as is expected.

To cover the occasional formation of a spinel solid solution the solution model "SOLN-FZSP" was used. This solid solution model covers the formation of various non-stoichiometric magnetites (Fe_3O_4), namely: $Fe_3O_4^{2-}$, $Fe_3O_4^{-}$, Fe_3O_4, $Fe_3O_4^{+}$, FeO_4^{6-}, and FeO_4^{5}. This model uses the sublattice formalism as solution model.

The formation of a copper/nickel liquid alloy phase was modelled using "SOLN-CuLQ". This solution model covers the formation of metal liquid phases containing Cu (presence not essential), Ni, S (<15 mol %) and O (<10 mol %).

Although not expected to be present in significant quantities, the presence of an olivine solution was modelled using the "FACT-Oli2". For the system this solution model covers the formation of $(Fe, Ni)_2SiO_4$. The list of solutions and predominant stoichiometric compounds is given in Table 3.1.

The outcomes of the model prediction were validated against published equilibrium data, where available. Examples of the validation are provided in Appendix A.

Table 3.1: Predominant solid and melt solutions and stoichiometric compounds associated with matte conversion.

Phase	Solution Type	Components
Gas	Ideal Gas	N_2, O_2, SO_2, CO_2, CO, SO_3
Matte	Melt Solution	Fe-Ni-Cu-S
Slag	Melt Solution	Al_2O_3-As_2O_3-B_2O_3-CaO-CrO-Cr_2O_3-Cu_2O-FeO-Fe_2O_3-K_2O-MgO-Na_2O-NiO-PbO-SiO_2-TiO_2-Ti_2O_3-ZnO-ZrO_2, with S, SO_4, PO_4, H_2O/OH, CO_3, F, Cl, I in dilute solution, with a miscibility gap at high SiO_2 contents.
Alloy liquid	Melt Solution	Cu, Ni, S
Fe-Spinel	Solid Solution	$Fe_3O_4^{2-}$, $Fe_3O_4^{-}$, Fe_3O_4, $Fe_3O_4^{+}$, FeO_4^{6-}, and FeO_4^{5}
Olivine	Solid Solution	$(Ca, Mg, Fe, Ni)_2SiO_4$
Fcc Alloy	Solid Solution	Ni, Cu, Fe, S
Tridimyte	Stoichiometric, Pure	SiO_2
Cristobalite	Stoichiometric, Pure	SiO_2
Fayalite	Stoichiometric, Pure	Fe_2SiO_4
Wustite	Stoichiometric, Pure	FeO
Hematite	Stoichiometric, Pure	Fe_2O_3

It is apparent from the discussion in section 2.3, that control of the iron and sulphur in the matte at the end of the second stage blow is most important to ensure good slow cooling characteristics for the separation of the alloy (see phase diagrams in Figures 3.11 and 3.12). The discussion will therefore focus on the equilibrium behaviour of these two elements. The results of the simulations on FactSage were presented by Georgalli (2002), Eksteen *et al.* (2002), Georgalli *et al.* (2001a), Georgalli *et al.* (2001b) and Georgalli *et al.* (2002b). The simulations on FactSage were performed to develop a thermodynamic equilibrium database,

which is to be implemented in the final modelling algorithm via a neural network architecture, as will be described in detail in Chapter 5. A number of assumptions were made during the thermochemical modelling of the second stage blow for matte converting:

- The initial temperature of the feeds to the bath was assumed constant at 25°C, while the initial temperature of the matte inventory was assumed constant at 1300°C. This was done to minimise the number of simulations. This was done as the model outcomes are insensitive to these initial temperatures (Except for the energy balance).
- The pressure was assumed constant at 0.85 atm. This is the atmospheric pressure of the proposed industrial location.
- The ash, volatile and moisture content of the coal added to the bath (both reductant and fuel coal), were assumed to be negligible with respect to the overall bath chemistry. Only the fixed carbon contribution of the coal was used as an input. An improved model should include the effect of ash, when the ash composition is known.
- The minimal slag heel remaining after stage one (if any) was not expected to have any drastic effect on the second stage endpoint. This assumption will have to be revisited during the modelling of the industrial furnace, where the maintenance of a heel is critical for slag taphole protection against the matte.
- The silica addition to the bath was assumed to be constant and always in excess. This was done as the silica was found to have a negligible effect on the matte composition during the pilot plant campaign, due to the slag always being saturated with it.
- Dissolved sulphides present in the slag phase were not solved for during the simulations. Some simulations were evaluated, but the effect of dissolved sulphur in the fayalitic slags was found to be insignificant. Simeonov *et al.* (1995) found that sulphur makes up less than 0.25% (mass) of the slag composition at concentrations of iron in the matte less than 10% (mass), which is the case for the majority of the 2^{nd} stage blow.
- The cobalt content of the matte was assumed to be negligible and therefore not used as an input. This was due to the low concentrations of cobalt in the matte as well as the fact that the software has not yet been optimised for cobalt oxides.

Once these assumptions had been made the system was simplified to a total of eight input variables. When doing the thermochemical simulations the following inputs were used:

- Carbon addition
- Oxygen addition
- Nitrogen addition
- Silica addition - constant
- Initial temperature - constant
- Equilibrium temperature
- Pressure - constant
- Matte composition, which includes:
- Copper, Iron, Sulphur, and Nickel

In total the generated database was made up of more than 32 000 simulations. A range was then needed for the non-constant variables in order to create an evenly spread data structure over the entire operating range of the converter. This range was obtained from the pilot plant data. The matte component masses were normalised to a total of 100 mass units (grams in this case). The oxygen, nitrogen and carbon additions were then also scaled to be per 100 grams matte. This was done to ensure that the database generated would be applicable to a converter of any size, as long as the operating conditions were similar.

In order to attain a better understanding of the dynamic deviation from equilibrium of the system, the predicted equilibrium concentrations of iron and sulphur were compared to the actual concentrations. The results of this comparison are shown in Figures 3.1 and 3.2.

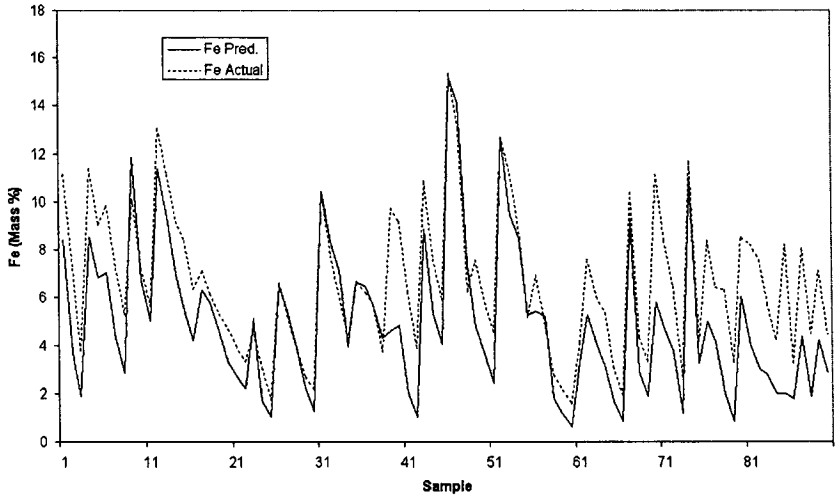

Figure 3.1: Equilibrium vs. actual iron concentration in the matte

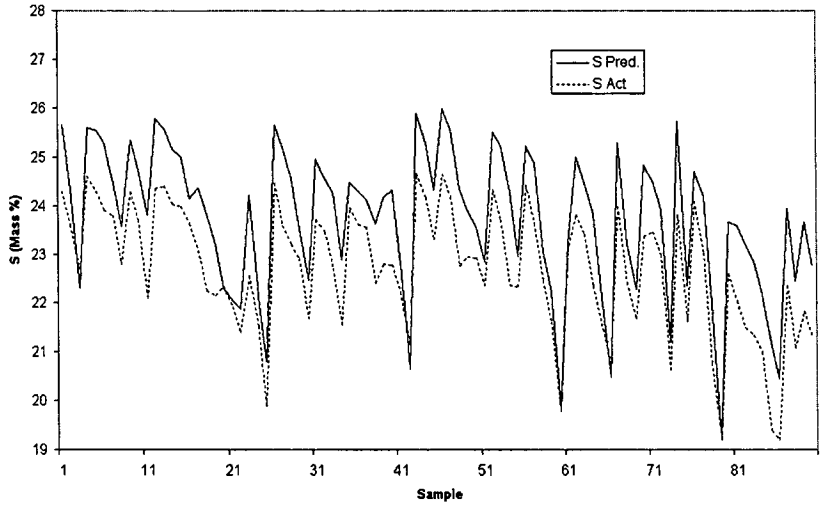

Figure 3.2: Equilibrium vs. actual sulphur concentration in the matte

It is apparent from Figures 3.1 and 3.2 that the predicted equilibrium concentrations of the iron and sulphur in the matte exhibit a similar trend to that of the actual concentrations. The equilibrium concentration of the iron is generally (but not always) lower than the actual measured concentration while that of the equilibrium sulphur is generally (but not always) above that of the actual measured values. Although it is theoretically improbable for the equilibrium concentration to be higher than the actual, it is felt that this difference can be explained by the fact that the dissolved sulphides in the slag were not solved for during the simulations. This would result in a higher predicted matte sulphur equilibrium composition. The results do, however, indicate that the system is generally running very close to equilibrium, which indicates that the mixing and mass transfer dynamics are relatively similar throughout the different blows. It also implies that the mixing in the bath is very close to ideal, which is not a surprising observation due to the high velocities at which the gasses are injected into the slag via the Ausmelt lance. Good mixing will also result in minimal temperature gradients within the bath, resulting in a closer approximation to thermochemical equilibrium.

Plotting the predicted equilibrium concentrations of iron and sulphur against the actual bath concentrations of these species resulted in R^2 values of 0.69 and 0.60 respectively, which shows that using thermochemical models only would not suffice for accurate prediction, as required for control. Surface plots of the iron and sulphur equilibrium concentrations in the matte versus the oxygen and carbon additions are shown in Figures 3.3 and 3.4 respectively.

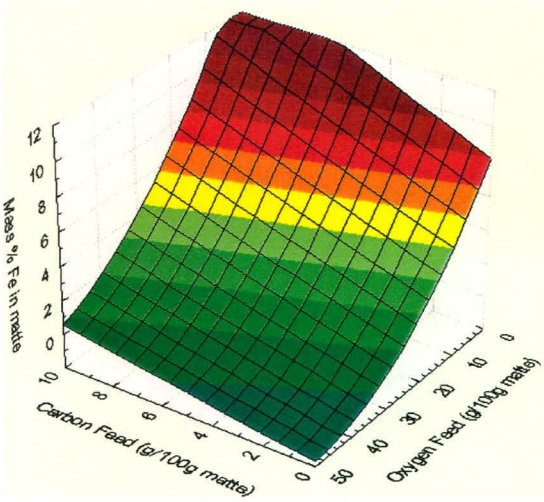

Figure 3.3: Predicted equilibrium iron concentration as a function of carbon and oxygen addition

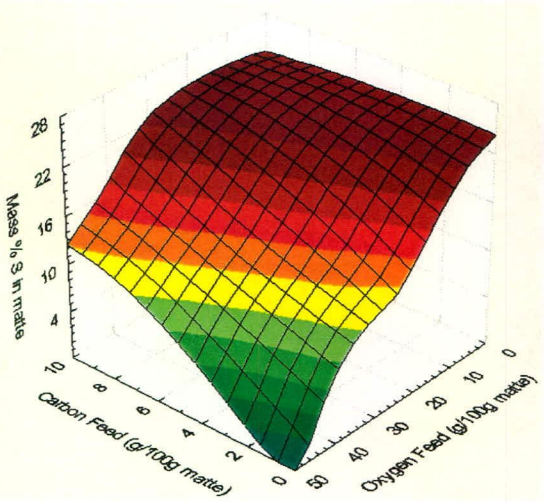

Figure 3.4: Predicted equilibrium iron concentration as a function of carbon and oxygen addition

As anticipated, Figure 3.3 illustrates that an increase in oxygen fed causes a decrease in iron content in the matte. This is clearly due to the iron being preferentially oxidised to the slag phase. An increase in the amount of carbon fed, however, increases the equilibrium iron content in the matte. This is probably due to the carbon combusting to form carbon monoxide and carbon dioxide gas, thereby depleting the oxygen available to oxidise the iron to the slag phase. The carbon can also act as a reducing agent, but it is felt that though the carbon may reduce the higher iron oxides in the slag to lower oxides, it will not reduce the iron oxides to the matte phase, its role being more significant in the gas free board region, which controls the overall O_2 and SO_2 partial pressures.

From Figure 3.4 we can see that the sulphur content in the matte displays a trend similar to that of iron. The trend with oxygen is due to the sulphur being preferentially oxidised to sulphur dioxide gas. The trend with the carbon addition is felt to be due to the same reasoning as already discussed for Figure 3.3, as it is impossible for any sulphur to be reduced back into the slag phase, under the relatively oxidising conditions found in the converter at any given moment. The effect of temperature on sulphur and iron in the matte has been simulated by Georgalli *et al.* (2001a), but was found to have a very small effect on the iron and sulphur partitioning, relative to the effect of oxygen and carbon.

It is apparent from these graphs that both the equilibrium iron and sulphur behaves non-linearly with respect to the two most important manipulated variables (oxygen and coal/carbon). Any model that is to predict the iron and sulphur levels therefore needs to non-

linearly transform the manipulated variables to predict the equilibrium outcomes of iron and sulphur. Chapter 6 will show how the non-linearly predicted equilibrium results are incorporated in adaptive predictive process models.

3.5 Thermochemistry and metal distributions in reductive chromite smelting

During the reductive smelting of chromite in a bath type DC plasma arc furnace, chromite fines are reduced, in the presence of flux (quartz and limestone) to a low Cr_xO slag and high carbon ferrochrome (HCFeCr) alloy. A typical (major component) composition of the chromite, slag and alloy are as follows:

Chromite: 13.7% Al_2O_3, 1% CaO, 37% Cr_2O_3, 23%Fe_2O_3, 12%MgO, 10% SiO_2.

Slag: 27%Al_2O_3, 17% CaO, 6% Cr, 5.5%Fe, 20%MgO, 22% SiO_2 and up to 1%TiO_2.

Alloy: 53.5% Cr, 36.5% Fe, 1% Si, 8.5% C, 0.3% Mn, 0.02% P, 0.01% S.

The analysis given above is as-reported, meaning that it does not necessarily reflect the true oxidation states of the metals, especially with regard to the metals Fe and Cr, which exist in a number of oxidation states. Moreover, the slag analysis includes entrained alloy droplets which cannot be thermodynamically predicted – their mechanical entrainment is determined more through the rheological properties of the slag than through thermochemical behaviour. If it assumed that the chrome and iron exists primarily as entrained droplets, then the dissolved Cr and Fe becomes relatively insignificant relative to the other major slag components. This assumption will be shown to be true in the subsequent paragraphs. This would imply that, for the purpose of investigating the equivalent phase diagrams, only Al_2O_3, CaO, MgO, and SiO_2 should used for phase diagram evaluation. If the entrained Cr and Fe are therefore subtracted and the compositions renormalized, the slag take on the following composition with respect to the major components : 30% Al_2O_3, 20% CaO, 24%MgO, 26% SiO_2. However, this remains an oversimplification as undissolved partially altered chromites (PACs) remain in the slag (Cr^{3+}). The amount of PACs becomes the main form of Fe an Cr losses in submerged arc furnaces as the slow dissolution of the lumpy ore types used limits complete dissolution. The fact that the chromite dissolves so much faster in a plasma arc furnace slag is one of the major advantages of plasma arc furnace production. The liquidus surface projections of the alloy and the slag, as well as the primary phase fields of compounds within the liquidus map, are presented in Appendix A.

3.5.1 Alloy-slag-gas reaction chemistry and mechanisms

Barcza *et al.* (1981) proposed a possible smelting reaction mechanism of chromium ore fines and fluxes at 1600 °C, and classified the reaction in various reaction groups :

Group I: Control of the p_{O_2} in the gaseous phase:

$$<C> + \tfrac{1}{2}O_2\,(g) = CO\,(g) \quad (3.8)$$

$$<C> + O_2\,(g) = CO_2\,(g) \quad (3.9)$$

$$<C> + CO_2\,(g) = 2CO\,(g) \text{ (Boudouard Reaction)} \quad (3.10)$$

$$CO\,(g) + \tfrac{1}{2}O_2\,(g) = CO_2\,(g) \quad (3.11)$$

Group II: Solid state reductions on the surface of the bath. Iron oxide reduction becomes feasible at p_{O_2} of less than 10^{-5} atm:

$$<(Fe,Mg)(Cr, Al)_2O_4> + CO\,(g) = \underline{Fe} + <Mg(Cr, Al)_2O_4> + CO_2\,(g) \quad (3.12)$$

or

$$<(Fe,Mg)(Cr, Al)_2O_4> + <C> = \underline{Fe} + <Mg(Cr, Al)_2O_4> + CO\,(g) \quad (3.13)$$

The reduction of chromium oxide becomes feasible at a p_{O_2} of less than 10^{-7} atm:

$$<(Fe,Mg)(Cr, Al)_2O_4> + {}^{40}\!/_{7}CO\,(g) = \underline{Fe} + {}^{2}\!/_{7} <Cr_7C_3> + <MgAl_2O_4> + {}^{34}\!/_{7}CO_2\,(g) \quad (3.14)$$

or

$$<(Fe,Mg)(Cr, Al)_2O_4> + {}^{34}\!/_{7}<C> = \underline{Fe} + {}^{2}\!/_{7} <Cr_7C_3> + <MgAl_2O_4> + 4CO\,(g) \quad (3.15)$$

Group III: Dissolution of the chrome spinel in the slag phase at p_{O_2} of less than 10^{-8} atm:

$$<(Fe,Mg)(Cr, Al)_2O_4> + CO\,(g) = [FeO] + 2[CrO] + [MgO] + [Al_2O_3] + CO_2\,(g) \quad (3.16)$$

or

$$<(Fe,Mg)(Cr, Al)_2O_4> + <C> = [FeO] + 2[CrO] + [MgO] + [Al_2O_3] + CO\,(g) \quad (3.17)$$

Furthermore:

$$<CaO> = [CaO] \quad (3.18)$$

$$<SiO_2> = [SiO_2] \quad (3.19)$$

$$<C> = \underline{C} \quad (3.20)$$

$$\text{Slag} = [FeO] + [CrO] + [Cr_2O_3] + [MgO] + [Al_2O_3] + [CaO] + SiO_2 \quad (3.21)$$

$$[Cr_2O_3] + <C> = 2[CrO] + CO\ (g) \quad (3.22)$$

Group IV: Reduction reactions

$$[FeO] + <C> = \underline{Fe} + CO\ (g) \quad (3.23)$$

$$7[CrO] + 10<C> = \underline{Cr_7C_3} + 7CO\ (g) \quad (3.24)$$

$$[SiO_2] + 2<C> = \underline{Si} + 2CO\ (g) \quad (3.25)$$

Acid-base reaction in the slag (simplified):

Metal oxide ionisation reactions, for example:

$$[CaO] = [Ca^{2+}] + [O^{2-}] \quad (3.26)$$

Polymerisation / depolymerization reactions

$$\left[Si_nO_{3n+1}^{2(n+1)-}\right] + \left[SiO_4^{4-}\right] = \left[Si_{n+1}O_{3n+4}^{2(n+2)-}\right] + O^{2-} \quad (3.27)$$

and

$$\left[SiO_4^{4-}\right] = \left[SiO_2\right] + O^{2-} \quad (3.28)$$

Alloy formation

$$\underline{Cr_7C_3} + 7\underline{Fe} = \underline{(Fe, Cr)_7C_3} \quad (3.29)$$

As before, "< >" refer to the solid phases, "_" refers to the alloy phase and "[ ]" refers to the slag phase. Barcza *et al.* (1981) noted that the reactions in a pilot scale furnace proceeded extremely fast and that well reduced slags (Cr_2O_3 below 5%) were tapped from the furnace 5 minutes after the feed has been shut off. Two major reaction mechanisms were proposed, one in which the (solid state reduction) the spinel retains its form (Mechanism A), whereas in the other, the entire spinel dissolves (Mechanism B). Mechanism A, while contributing slightly to the overall reduction of chromite was observed to be too slow to account for the actual conversion. Mechanism B becomes favourable under very low oxygen partial pressures (as stated earlier, the solubility of chromite in the slag is very dependent on the oxygen partial pressure, its solubility increasing with reducing pO_2. As the approach of equilibrium via gas-liquid reactions is relatively slow, it is unlikely that the gas phase will control the oxygen activity in the slag system under consideration. Barcza *et al.* (1981) therefore show that the metal phases present, especially chromium and silicon, have a far greater controlling influence on the oxygen activity in the slag. They also show that there is a strong relationship between Si in the metal and the Cr_2O_3 content of the slag. As silicon is reduced from silica in the slag with carbon (also carbon dissolved in the alloy), the solubility of Cr_2O_3 in the slag is

therefore inherently dependent of the carbon addition: The lower the oxygen activity (due to carbon addition), the larger is the Cr^{2+}-to-Cr^{3+} ratio and therefore the greater the solubility of chromium oxide in slag. On the other hand, they have shown that the dissolution and reduction of iron is possible at higher oxygen partial pressures, leading to residual, altered, but virtually undissolved spinel particles, with almost no iron oxide remaining.

3.5.2 Thermochemical modelling of chromite smelting

The approach to the thermochemical modelling has been similar to the modelling of the Ni-Cu matte converting presented above. The predominant phases which were use to model the system are presented in Table 3.2. It is clear that both the alloy and the slag melts show complex solution behaviour, and multiple solution types exist in both the solid and liquid states. It is therefore very important that the full complex on-ideal reaction and phase equilibria are to be modelled, if relevant equilibrium predictions are to be made.

Table 3.2: Predominant solutions and stoichiometric compounds associated with chromite smelting.

Phase	Solution Type	Components
Gas	Ideal Gas	N_2, O_2, CO_2, CO, H_2, H_2O
Slag	Melt Solution	Al_2O_3-CaO-CrO-Cr_2O_3-FeO-Fe_2O_3-MgO-SiO_2 with S, SO_4, PO_4, H_2O/OH, CO_3, F, Cl, I in dilute solution, with a miscibility gap at high SiO_2 contents.
Alloy liquid	Melt Solution	Fe, Cr, C, Si
$(Cr, Fe)_7C_3$	Solid Solution	Fe, Cr, C
$(Cr,Fe)_{23}C_6$	Solid Solution	Fe, Cr, C
BCC Alloy	Solid Solution	Fe, Cr, C, Si in body-centred cubic lattice configuration
Spinel	Solid Solution	$(Mg^{2+}, Fe^{2+})(Cr^{3+}, Al^{3+}, Fe^{3+})_2O_4$
Corundum	Solid Solution	$(Al, Cr, Fe^{3+})_2O_3$
Melilite	Solid Solution	$Ca_2(Mg, Fe^{2+})Si_2O_7$
Pyroxenes (Ortho-, Clino-, Proto-)	Solid Solution	(Ca, Mg, Fe^{2+}) $(Mg, Fe)Si_2O_6$
Wollastonite	Solid Solution	$(Ca,Mg)SiO_3$
Monoxide	Solid Solution	$(Mg, Ca, Fe^{2+})O$

(Periclase, Wustite, Lime)		
Cr_4C*	Stoichiometric, Pure	Cr_4C, *There is some controversy about the presence of this phase, which can also be $Cr_{23}C_6$
Cr_3C_2	Stoichiometric, Pure	Cr_3C_2

The modelling was further complicated as the heel remaining in the furnace had to be taken into account as feed for the subsequent tap. The estimation of the heel is presented in Chapter 5. The temperatures were varied at 50 °C intervals from 1500 to 1750 and the feed to the furnace was broken down to its elemental composition and varied in their operating range. The feed elements chosen were therefore: Cr, Fe, C, O, Si, Ca, Mg, and Al. The graphs showing equilibrium versus plant data are presented in Chapter 6, together with the prediction of the Equilib-ARMAX model. In general, it was found that the equilibrium plays a significant role in determining the tap-to-tap outcome, but the deviation from equilibrium remains significant, so that equilibrium prediction on its own would be insufficient.

A comparison of the accuracies of equilibrium prediction of the plant data is presented in Figure 3.5. A similar figure has been presented by the author and co-authors (Reuter *et al.*, 2003), with the difference that the previous equilibrium estimation excluded the effect of the heel, which led to poorer estimations of the iron in the HCFeCr alloy (R^2 of 0.22 noted for the Fe in the alloy, vs. 0.32 in this case). It is quite apparent that the ferrochrome production in a plasma arc furnace deviates much further from equilibrium than matte converting presented above, despite both being smelting operations. However, the mixing and fluid flow in the two systems are quite different – an aspect that will be dealt with in more detail in the following chapter. Furthermore, the kinetics of the reactions are very different.

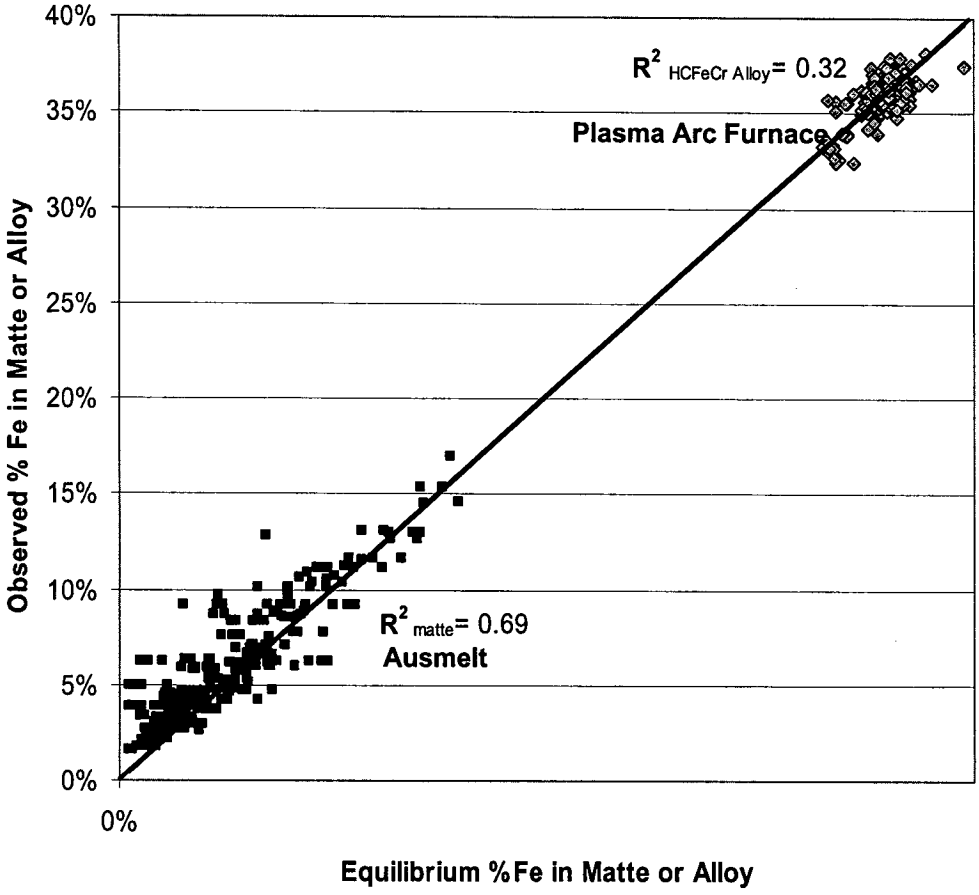

Figure 3.5: A comparison of the degree to which equilibrium outcomes explain reconciled data in a matte converter and a ferrochrome smelting furnace (both bath smelting furnaces)

3.6 Thermochemistry and metal distributions in reductive ilmenite smelting

During the reductive smelting of ilmenite in a bath type DC plasma arc furnace, ilmenite mineral sands are reduced without any fluxes to a low TiO_2-Ti_2O_3-FeO slag and pig iron. The typical (major component) compositions of the ilmenite, slag and alloy are as follows:

Ilmenite: 45.5% TiO_2, 25.9% Fe_2O_3, 24.7% FeO, 1.0% MnO; 0.4% MgO, 1.0% SiO_2, 0.55%Al_2O_3, 0.5% CaO (total "FeO" = 48%, "FeO" = Fe^{2+} + Fe^{3+});

Slag: 50% TiO_2, 29% Ti_2O_3, 3.5% $TiO_xC_{(1-x)}$, 11% FeO, 2% MnO; 0.6% MgO, 2% SiO_2, 1%Al_2O_3 (total "TiO_2" = 84%, "TiO_2" = Ti^{4+} + Ti^{3+});

Pig Iron: 97% Fe, 2.55% C, 0.05% Mn, 0.03% P, 0.07% S, 0.14% Si, 0.05, 0.03% Cr.

The oxidation states of Fe and Ti are not measured on a routine basis (i.e. for process control purposes for ilmenite and slag respectively). Only the thermochemistry of the major components is discussed in this chapter. A good review of the interactions of the minor components with the Fe and Ti oxides are given by Pesl (1997a & b) and will not be discussed here. Appendix A will present a detailed literature review to support the choice of stable phases used in the modelling. Moreover, the most important phase diagrams associated with ilmenite smelting are also presented in Appendix A. As mentioned throughout this chapter, the determination of the liquidus temperatures and predominant phases are critically important to estimate the amount of solids that could precipitate upon cooling, or due to changes in melt chemistry. In all cases the amounts of solids have a large impact on rheology and flow of the melts in the system.

3.6.1 Alloy-slag-gas reaction chemistry and mechanisms

The Fe-Ti minerals tend to have a complex mineralogy due to the number of oxidation states that exist for both Fe and Ti. Moreover, Ti can form a number of sub-oxides of TiO_2, called the Magnelli phases. The mineralogy of weathered ilmenite can normally be described by the FeO-Fe_2O_3-TiO_2 system which includes the minerals: Rutile (TiO_2) and its polymorphs Anatase and Brookite, Pseudobrookite (Fe_2TiO_5), Pseudorutile ($Fe_2Ti_3O_9$),Hematite (Fe_2O_3), Magnetite (Fe_3O_4), Wustite (FeO), Ulvospinel (Fe_2TiO_4), Ilmenite ($FeTiO_3$), Ferropseudobrookite ($FeTiO_5$) as well as Leucoxene (weathered ilmenite in a transitory state between $FeTiO_3$ and TiO_2). Grey *et al.* (1974) identifies a number of M_3O_5 solid solutions ranging from Fe_2TiO_5 to $Fe_{0.75}Ti_{2.25}O_5$. Initial reduction at $pO_2 < 10^{-12}$ atm may lead to a number of spinel phases of the structure $(FeTiO_3)_x(Ti_2O_3)_{1-x}$. It is therefore nearly impossible (without continuous X-Ray Diffraction (XRD) or wet chemistry), to discern or correctly match the reductant with the oxygen availability associated with the "ilmenite", although statistically the mean composition may closely correspond to a Fe:Ti molar ratio of 1.00, as in stoichiometric ilmenite. As XRF analysis of the feed material are normally done, and not XRD or wet chemistry analysis, only the Fe:Ti ratio is known with accuracy. The reduction sequence of ilmenite will be discussed here. Where the reactions are similar to the chromite smelting, the equation numbers associated with chromite smelting will be used.

Group I: Control of the p_{O_2} in the gaseous phase:

$$<C> + \tfrac{1}{2}O_2\,(g) = CO\,(g) \qquad (3.8)$$

$$<C> + O_2\,(g) = CO_2\,(g) \qquad (3.9)$$

$$<C> + CO_2\,(g) = 2CO\,(g)\ \text{(Boudouard Reaction)} \quad (3.10)$$

$$CO\,(g) + \tfrac{1}{2}O_2\,(g) = CO_2\,(g) \quad (3.11)$$

Group II: Solid state reductions on the bath surface: As the bath temperature is far above the melting point of the ilmenite particles, the melting of the ilmenite particles is expected to occur extremely fast to give an oxide slag of Fe, Fe^{2+}, Ti^{4+}, Ti^{3+} and contaminants.

Group III: Fluid-phase reduction reaction reactions:

$$[Fe_2O_3] + \underline{Fe} = 3[FeO] \quad (3.30)$$

$$[Fe_2O_3] + [Ti_2O_3] = 2[FeO] + 2[TiO_2] \quad (3.31)$$

$$[FeO] + CO\,(g) = \underline{Fe} + CO_2\,(g) \quad (3.32)$$

$$[FeO] + [Ti_2O_3] = \underline{Fe} + 2[TiO_2] \quad (3.33)$$

$$2[TiO_2] + CO\,(g) = [Ti_2O_3] + CO_2\,(g) \quad (3.34)$$

The Fe_2O_3 refers to the relatively minor amounts entering with other Fe-Ti minerals.

Group IV: Solid-liquid reduction reactions

$$<C> + [FeO] = \underline{Fe} + CO\,(g) \quad (3.35)$$

$$<C> + 2[TiO_2] = [Ti_2O_3] + CO\,(g) \quad (3.36)$$

$$(7-6x)<C> + [Ti_2O_3] = 2<TiO_xC_{(1-x)}> + (5-4x)CO\,(g) \quad (3.37)$$

The titanium oxycarbide (a TiO-TiC solid solution) is a high melting point compound which will precipitate at the operating temperature if the conditions are sufficiently reducing, or may dissolve in the metallic phase up to its saturation point. Very little titanium is reduced to the metallic phase.

Contrary to chromite smelting, the slag basicity cannot be independently controlled, without compromising the final slag product chemistry.

Bessinger *et al.* (1997) found that the $[Ti_2O_3]$ content of industrial / pilot scale slags could be linearly related to the [FeO] content. Their data are presented in Figure 3.6, and are based on spoon samples taken from a pilot plant plasma arc furnace. However, the relationship does not follow the equilibrium relationship presented in reaction 3.33.

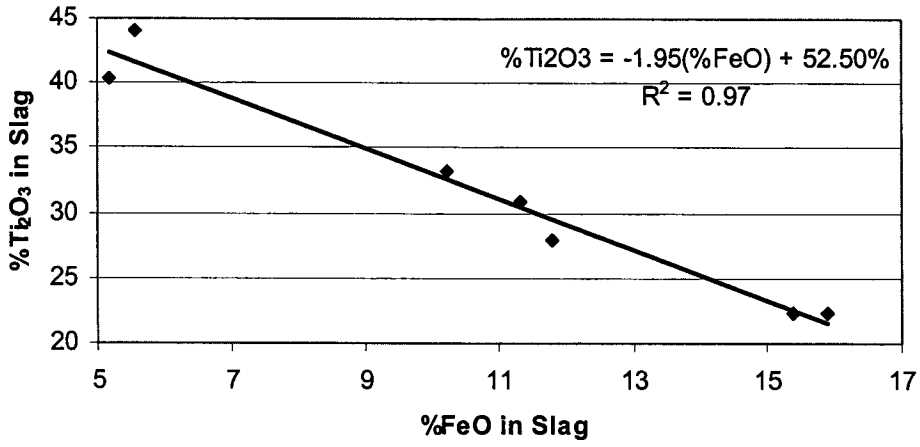

Figure 3.6: The relationship between the Ti_2O_3 and the FeO content of high titania slags based on pilot plant spoon samples (based on data from Bessinger *et al.* (1997)).

The linear relationship would imply that one should be able to gauge the $\%Ti_2O_3$ in industrial slags and determine the ratio of Ti^{3+} and Ti^{4+}, which influences the phase behaviour significantly, as shown in the phase diagram in Appendix A. The data in Figure 3.6 were not normalised for the TiO_2-Ti_2O_3-FeO system and therefore the slag assay include minor contaminants. However, normalisation does not change the form significantly: the linear relationship changes to $\%Ti_2O_3 = -1.97(\%FeO) + 56.5\%$ with a similar fit.

3.6.2 Thermochemical modelling of ilmenite smelting through carbothermic reduction

The approach to the thermochemical modelling has been similar to the modelling of the chromite smelting presented above. The predominant phases which were use to model the system are presented in Table 3.3. Again, both the alloy and the slag melts show complex solution behaviour, with numerous solid phases that may precipitate, depending on the operating partial pressure of O_2 and the Ti:Fe ratio in the feed.

Table 3.3: Predominant solutions and stoichiometric compounds associated with ilmenite smelting.

Phase	Solution Type	Components
Gas	Ideal Gas	N_2, O_2, CO_2, CO, H_2, H_2O
Slag	Melt Solution	TiO_2-Ti_2O_3-FeO-Fe_2O_3-MgO, MnO, Al_2O_3, SiO_2
Alloy liquid	Melt Solution	Fe, C, Ti, Mn, Si
FCC Alloy	Solid Solution	Fe, C in face-centred cubic lattice configuration
BCC Alloy	Solid Solution	Fe, C in body-centred cubic lattice configuration
Ti-Spinel / Ulvospinel	Solid Solution	$(Fe^{2+})(Ti^{3+}, Fe^{3+})_2O_4 - (FeTiO_3)_x(Ti_2O_3)_{1-x}$
Corundum	Solid Solution	$(Ti^{3+}, Fe^{3+})_2O_3$
Ferrous Pseudobrookite	Solid Solution	$(Fe^{2+})(Ti^{4+})_2O_5$ to $(Ti^{3+})_2(Ti^{4+})O_5$
Ferric Pseudobrookite	Solid Solution	$(Fe^{3+})_2(Ti^{4+})O_5$
Ilmenite	Solid Solution	$(Fe,Mg)TiO_3$
Leucoxene	Solid Solution	$Fe_{1-x}TiO_{3-x}$
Ti-Oxycarbide	Solid Solution	TiO_xC_{1-x}
Anatase, Brookite, Rutile	Stoichiometric, Pure	TiO_2
Cementite	Stoichiometric, Pure	Fe_3C
Magnelli Phases	Stoichiometric, Pure	Ti_xO_{2x-1}

The fully liquid slag and alloy regions are therefore bordered by a complex range of possible precipitates that may form. FactSage® was used not only to predict the bulk slag chemistry, but also the type and quantity of the precipitates.

As for chromite smelting, the remaining heel in the furnace had to be taken into account in the equilibrium model as "feed" for the subsequent tap. The estimation of the heel associated with ilmenite smelting is also presented in Chapter 5. The temperatures were varied at 50 °C

intervals from 1550°C to 1900°C. The feed to the furnace was broken down to its elemental composition and varied in their operating range, as for chromite smelting. The feed elements chosen were therefore: Ti, Fe, C, O, Si, Mn, Mg, and Al. The graphs showing equilibrium data versus plant data are presented in Chapter 6, together with the prediction of the Equilib-ARMAX model. Of all three furnace types, the ilmenite reduction equilibria showed the largest deviation from equilibrium predictions. As there are much larger uncertainties associated with the experimental determination of high temperature equilibria of high-titania slags (due to the extreme temperature of above 1800°C to achieve fully liquid slags) the uncertainty in the thermodynamic (quasichemical) model parameters are much larger. Much experimental research is still required to obtain a higher degree of certainty of the phases in the Fe-Ti-O-C system. Kinetic and fluid dynamic influences will also cause a deviation from equilibrium, but it is not known why these influences would play a more prominent role than, for instance, chromite smelting, especially as the slag is highly ionic (therefore not as polymerized as silicate slags) and extremely fluid (as long as it is operated above the liquidus).

3.7 Conclusions based on the thermochemical equilibria

It is clear that not one of the systems can be characterised by simple reactions or simple phase equilibria. The equilibrium approach provides two valuable tools for further modelling:

- Chemical equilibrium compositions of the bulk slag, matte and alloy phases
- The amounts of phases, and specifically, the amounts of solids precipitated from each melt phase.
- The liquidus temperatures from measured melt chemistries

This information above will be used to:

- predict the equilibrium term of the Equilib-ARMAX model,
- predict melt viscosities (refer to chapter 4), which impacts directly on production, as well as mixedness, and subsequently on the variances used to filter the plant data.

Proper thermodynamic modelling therefore provide a wealth of information which is not immediately apparent if one performs data mining on plant data only. This information should therefore be used to augment, but not replace, dynamic empirical models. Neither should only dynamic empirical models be used, as they are critically constrained to the data ranges for

which they were developed. This chapter, in combination with Appendix A, should therefore show that simulation of the chemical thermodynamics still has its place in the development of reliable predictive metallurgical models.

3.8 Nomenclature of Chapter 3

a_i = component activities for components $i = 1$ to N

n_i = moles of the various components (mole)

G° = pure component Gibbs Free Energy (GFE) of formation (J.mole^{-1})

G_{system} = overall system GFE (J)

f_i = fugacities of the gaseous components (atm)

T = system temperature (K)

R = ideal gas constant (J.mole^{-1}K^{-1})

This page is intentionally blank.

4 RELATIONSHIPS BETWEEN HETEROGENEITY, VARIANCE, ASSAY DATA INTEGRITY AND RHEOLOGY

> "Viscosities of molten metals and slags play vital roles in many high temperature phenomena that are important for advancing process control and product quality in molten-metal processing and casting."
> (Sridhar, 2002)

4.1 Introduction

It was noted in the Introduction that the proposed Equilib-ARMAX model structure does not explicitly take into account the flow of materials in the furnace. Instead, the effect of flow in bath type furnaces is to homogenise the separate fluid phases. The degree of homogeneity is reflected in spatial variance, a quantifiable measure that would be used subsequently to filter the data used in the Equilib-ARMAX model. In plant practice it is normally assumed that satisfactory homogeneity is achieved and that one sample from a fluid stream would be sufficient. However, no publications could be found to indicate that this assumption was valid.

It became clear through the process evaluations in Chapter 2 that open bath type processes are inherently ill-defined. It was also shown that, although one would expect a submerged lance based converter to be well mixed, the same cannot necessarily be said about open arc furnaces. In principle one would therefore expect the spatial variation of composition of the melt to be greater than the inherent statistical uncertainty associated with the sample assay. Moreover, all the streams fed into, or being produced by a bath type furnace may show significant variations in time (temporal variations) and sequence, which will be dealt with in more detail in Chapter 5. It will also be made clear in Chapter 5 how spatial and temporal variation are both implicit to the Equilib-ARMAX approach.

Spatial variation in the product materials (condensed phases) from bath type furnaces is directly related to the mixing achieved in the furnace. Mixing of melts, the methods of quantifying mixedness and the relationship of mixedness to melt viscosity are to be discussed in this chapter. The effect of particles on melt viscosity and published viscosity-chemistry

relationships will be reviewed, where they are relevant to the systems being discussed. One may rightly ask whether a discussion on mixing is relevant to the topic of furnace control. It is thought to be relevant, as the reduction of variance around a required setpoint is one of the major objectives of process control. It is therefore important to understand the main driving forces and mechanisms of mixing and how inherent uncertainty in process data can be dealt with in a scientifically acceptable manner.

As industrial mixedness data are only available for the open arc industrial furnaces and not for the Ausmelt pilot plant furnace, the latter will not be evaluated in this chapter. However, the approach as applied to the open arc furnaces can just as easily be applied to an industrial Ausmelt furnace, should industrial online date become available for an extended period.

While laboratory studies on mixing in arc furnaces were performed by the author, these will only be discussed superficially as it was found that practical difficulties with the quenching rates of the melts induced heterogeneity which may not have been present at high temperatures. A more detailed discussion of the laboratory studies (arc furnace research) is presented in Appendix B.

Finally, it is apparent that mixing, being a fluid-dynamic activity, is inseparable from melt rheology. The melt rheology is directly dependent on the observed melt viscosity, which, in turn is very much influenced by the presence of solids. This mixedness-rheology-viscosity relationship is further explored in this chapter for arc furnaces. For the purposes of comparison, the heterogeneity of ferrochrome slags and alloys produced in a DC plasma arc furnace is benchmarked against comparable melts derived from submerged arc smelting.

Actual predictions of fluidity of melts will be presented in Chapter 6, but the basis for the viscosity estimations will be presented in this Chapter.

4.2 Mixing in liquids

4.2.1 Mixing mechanisms

To achieve an acceptable level of homogeneity in smelting furnaces, two elements are required. Firstly, there must be overall bulk or convective flow so that no stagnant regions exist within the reactor. Secondly, there should be an intensive or high-shear mixing region which is capable of providing the reduction in inhomogeneities. Both these elements require energy to sustain them. Laminar and turbulent flow conditions, as well as a transitory region may all exist within one pyrometallurgical reactor. Laminar flow is typically associated with high viscosity melts such as polymerised melts (e.g. acid slags) and melts containing a significant amount of solid particles. In the process industry, fluids with viscosities greater than 10 Pa.s (100 Poise) are required for the flow to be truly laminar (Harnby *et al.*, 1985) at typical energy inputs. However, in pyrometallurgical furnaces the driving forces for mixing are limited, gas jets or gas bubbles from reactions are the main methods of inducing mixing, although magneto-hydrodynamics, natural convection and plasma jet impingement may also contribute to mixing.

In regions of high shear (e.g. a high gas flux bubbling through the melt), fluid elements become elongated, deformed, stretched and thinned. Due to this deformation process the surface area between the different fluid elements becomes enlarged so that inter-element diffusion is enhanced. However, until the fluid elements are sufficiently small, their specific area is not great enough for the rate of molecular diffusion to be significant. On the other hand, for ultimate homogenisation, molecular diffusion is required. With highly viscous fluids, it becomes a slow process, as molecular diffusivity is itself inherently slow. In most process applications outside the pyrometallurgical industry, the bulk fluid flow inside a reactor may be viewed as turbulent if the liquid has a viscosity below 0.01 Pa.s (0.1 Poise). Unfortunately most silica-containing slag melts lie in the region with viscosities greater than 1 Poise, so that the precise fluid flow regime is not always clear. Turbulent flow is characterised by eddy diffusion which is much more rapid than diffusion caused by laminar flow. Turbulent flow can be viewed as a superposition of a spectrum of velocity fluctuations and eddy sizes on the overall mean flow (Nienow *et al.*, 1985). The large primary eddies have large velocity fluctuations of low frequency and are of the size comparable with the physical dimension of overall flow field. Interaction of the large eddies with slow moving streams produce smaller eddies of higher frequency which further disintegrate until they are finally dissipated into heat

by viscous forces. There is a transfer of kinetic energy down the scale from larger eddies to the smaller eddies, with the directional element of the main flow being lost in the process. In principle one may therefore use the techniques from signal processing or system identification, such as Fourier spectra to analyse the velocity signal time series from local flow measurements (Kovács, Trägårdh & Fuchs, 2001). Turbulent flow therefore has both a deterministic component, resulting from the main flow field, and a stochastic component resulting from the higher frequency random eddies. Although the Fourier power spectrum will not be applied for this purpose in the current dissertation (due to the difficulty of measuring local velocities at high temperature), it is interesting to note how the same technique is used down from molecular / eddy level up to the characterisation of the overall process. Significant stochastic uncertainty is therefore implicit to all the measurements.

As all the solids fed into the furnace (those close to the AAZ or the lance gas impingement zone) are melted quite rapidly to obtain the furnace melt, the effect of solid mixedness of the feed of open bath type furnaces on melt homogeneity is expected to be insignificant. This feed flow behaviour is therefore much different from submerged arc furnace, where flow pattern in the burden is expected to have a far more significant influence.

4.2.2 Assessment of mixture quality

When is a mixture well mixed? There is much disagreement as to how to precisely define this point of well mixedness. Danckwerts (1958) defined a few useful terms. The "scale of segregation" is a measure of the size of the regions of segregation within the mixture. The smaller the scale of segregation, the better the mixture. To explain the scale of segregation in mixing in reactors, Levenspiel (1999) discerns between microfluids and macrofluids. A microfluid he describes as a normal multi-species fluid where molecules are free to collide and intermix on a molecular level. On the other hand, a macrofluid is viewed as a large number of sealed packets, each containing a large number, say between 10^{12} to 10^{18} molecules. A typical fluid would lie within these extremes and would be a partially segregated fluid. Alternatively one may speak of the intensity of segregation, which refers to the amount of dilution that occurred in segregated regions. The lower the intensity of segregation, the better the mixture. Both the scale and intensity of segregation influence mixture quality. The most common method to assess mixture quality is through a range of indices which are all based on the principle of composition variance.

4.2.3 Mixing time and compositional variance

When a tracer is introduced as a pulse into a homogenous liquid in which it is soluble in all proportions, the "mixing time" is the time measured from the instant of addition, until the vessel contents have reached a specific degree of uniformity, when the system is said to be mixed. The equilibrium concentration, C_∞ of a tracer of known volume can be calculated from a simple mass balance if is to be introduced into a melt / liquid of known volume. The mixing time may be defined as the time from the instant of tracer addition for the concentration of the tracer to reach a equilibrium value, as illustrated in Figure 4.1. However, the mixing time depends on the way of tracer addition and the location of the concentration detector. Moreover, the asymptotic approach of the equilibrium concentration make it difficult to detect with precision.

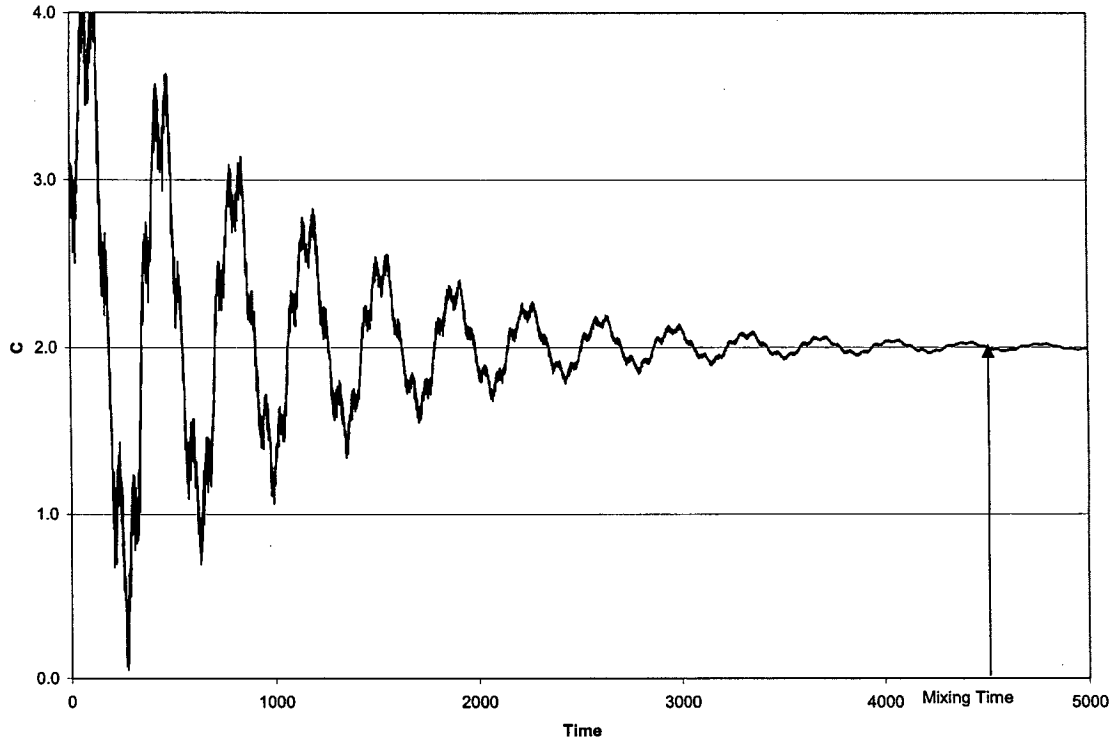

Figure 4.1: Mixing time determination

In order to eliminate the influence of detector position, the concentration variance (or standard deviation) could be determined by taking a number of samples from different positions in the melt, at say n different locations. The population variance could be calculated as (Harby, 1985):

$$\sigma^2 = \frac{1}{n-1}\sum_{i=1}^{n}(C_i - C_\infty)^2 \qquad (4.1)$$

In the case where tracers or the ratio of tracer to liquid volume is unknown, one first need to calculate the arithmetic average concentration (sample average), as an estimate of the equilibrium concentration (population average).

$$\overline{C} = \sum_{i=1}^{n} \frac{C_i}{n} \tag{4.2}$$

In such a case, the sample variance estimate is:

$$s^2 = \frac{1}{n-1} \sum_{i=1}^{n} \left(C_i - \overline{C}\right)^2 \tag{4.3}$$

If mixing time is now to be estimated, it can be done based on the point where the sample variances approaches zero. Although the effect of the location of the detector / sensor has been eliminated, the asymptotic nature of the approach is still present. Consequently, the time to achieve 5% relative variation is taken as the mixing time.

Levenspiel (1999) shows how to estimate the break-up time of macrofluids according to Einstein's random walk equation:

$$t = \frac{\left(Size\ of\ element\right)^2}{\left(Diff.\ Coeff.\right)} = \frac{d^2_{element}}{D_{mass}} \tag{4.4}$$

It is shown that for a dilute aqueous solution, a water element of 1 micron in size and a diffusion coefficient of 10^{-5} cm^2/s would loose its identity in one millisecond, but that a viscous polymer of 100 micron in size 1000 times as viscous as water would retain its identity for up to 3 hours. If it is taken into account that discrete mineral particles have to melt, intermix with other fluxes, be reduced, and that silicate polymers also exist within slag melts, it becomes apparent that fluid elements of slags may take a significant time to break down.
The interaction between mixing with reactions becomes important when the time to become homogenous is not short with respect to the time for reaction to take place. This is typically the case with very fast reactions and viscous reactant fluids (Levenspiel, 1999). In the case of molten bath systems, both very fast reactions occur, and the fluids could be viscous, especially when any of the melt temperatures are below the melt liquidus temperatures. This makes the fundamental predictability of reaction yields so much more difficult.

Mixing time as such is not of so much importance for furnaces already in operation (it is much more important during the furnace design stage). However, there is much sense in determining the variance in the composition at a given stage (say during the tapping of a melt) and investigating the statistical properties of the variances for several taps. It would also be sensible to relate variance to the operating and metallurgical conditions of the furnace. However, taking many samples per tap for many taps is not only laborious, it is an expensive and inherently unsafe task, considering the practical aspect of drawing spoon samples from fast flowing melts above 1500 °C. Furthermore, it makes little sense to base mixedness variance on species in the melt with a concentration of higher than say 5%, as one would then be analysing the solvent, and not the minor components, which inherently have smaller sample variances. However, the determination of sampling variances of all species do have some importance as it gives an estimate of the relative certainty one can associate with a sample.

Harnby *et al.* (1985) mentions that the most relevant description of mixing process in the process industry is the variation coefficient, or relative coefficient of variation, s_{rel}:

$$s_{rel} = \sqrt{\frac{s^2}{\overline{C}^2}} \tag{4.5}$$

As a rule-of-thumb, a system may be considered fully mixed when the relative coefficient of variation s_{rel} is below 5%.

As the relative standard deviation (absolute standard deviation divided by the average) of assaying and chemical analysis is seldom more than 2%, one may compare the relative standard deviation associated with sampling to the inherent analytical instrument variance to determine if sampling variance is associated with the analyses instrument only, or if the variance was already present in the melt due to poor mixing.

Normally a Students-t estimate could be made of the upper and lower confidence limits of the standard deviation, based on a specified significance, say $\alpha = 0.05$. However, as only a few samples are taken per tap (typically 6 per tap), the χ^2- estimate of the upper and lower confidence limits would be more correct. For n samples at a significance of α, the sample population deviation is between the limits:

$$\sqrt{\frac{(n-1)\cdot s^2}{\chi^2_{\left(\frac{\alpha}{2},n-1\right)}}} \leq \sigma \leq \sqrt{\frac{(n-1)\cdot s^2}{\chi^2_{\left(1-\frac{\alpha}{2},n-1\right)}}} \tag{4.6}$$

χ^2 is evaluated at (α/2) for the lower confidence limit and (1-α/2) for the upper confidence limit. For the two-tailed 95% confidence limits (α/2=0.025, or 1-α/2=0.975), with 5 (ν=6-1) degrees of freedom, χ^2 takes on a value of 0.831 and 12.8 respectively (Bayer, 1968), so that the upper and lower limits can be determined with 95% (i.e. significant) confidence.

4.2.4 Thermal versus compositional mixedness of melts

While temperature variation with position can be used to quantify mixedness (Harnby, 1985), for the purpose of estimating mixing times, it is of less value to determine mixedness on a meso- and micro scale (as would applicable to solute components in a melt) and thermal mixedness cannot be extrapolated to compositional mixedness. One of the main reasons is the difference one finds between thermal diffusivity:

$$D_{\text{thermal}} = \frac{k_{\text{thermal}}}{\rho \cdot C_P} \tag{4.7}$$

and mass the diffusivities D_{ij}, which could be estimated from viscosity data or obtained from literature or experiment. Both the diffusivities could be stated in the SI units of m^2s^{-1}. Thermal energy is transferred up to an order of magnitude faster than molecules could move from one location to another, showing that a system could tend to thermal homogeneity, but still be far from compositional homogeneity. For a typical slag system found in reductive chromite smelting, consisting of MgO, CaO, Al_2O_3, SiO_2 and smaller amounts of FeO and CrO, one may investigate the relationship between thermal and mass diffusivity through lumping MgO, FeO and CrO with CaO as "CaO", and investigating the ternary system CaO, SiO_2, Al_2O_3. This system approaches the system 40CaO: $20Al_2O_3$: $40SiO_2$ investigated by Turkdogan (1983). Various radioactive tracers have been used, such as the isotopes of ^{45}Ca, ^{31}Si and ^{26}Al. As Si is the only component reduced from CaO-Al_2O_3-SiO_2 slag to alloy, it would be worthwhile to look at Si behaviour in particular. Using the values given by Turkdogan (1983), and as diffusivity follows an Arrhenius relationship, the pre-exponential factor was estimated at 70.0 cm^2s^{-1} and the diffusion activation energy as –288.5 kJ/mole, the diffusivity was estimated at 1550 °C as about 4.00×10^{-7} cm^2s^{-1}. Based on the information by Turkdogan (1983), the effective thermal conductivity of these type of slags was noted to be 0.01 to 0.02

$W.cm^{-1}K^{-1}$, while the density was noted to be 2.58 $g.cm^{-3}$ and the specific heat was of the order 0.8-1.0 $J.g^{-1}K^{-1}$. (while not required here, the silica activity in the slag is recorded as about 0.5 at a mass fraction of 0.4). Using the values above (average values in the case of ranges), the thermal diffusivity can be estimated as: 7.3×10^{-3} cm^2s^{-1} (compare with the mass diffusivity of 4.00×10^{-7} cm^2s^{-1}) The thermal diffusivity is therefore 1.8×10^5 times (5 orders of magnitude) as much as the mass diffusivity. This quick calculation demonstrates the significant difference between the rate of heat transfer in a melt and the rate of mass transfer. The viscosity of the melt at this temperature (1550 °C) was noted to be about 0.6 Pa.s (600 cp. in the *cgs* unit system, and therefore 600 times as viscous as water, and comparable to the viscosity of glycerine at room temperature).

4.2.5 Viscosity and rheology: Driving Heterogeneity

As viscosity is a measure of the resistance of a fluid to flow, it is clear that high viscosities may cause poorly mixed systems, which influence subsequent data integrity. However, the study of viscosity is part of the larger field of rheology, which is a study of the shear stress versus shear rate behaviour of materials (Harnby, 1985). From the above discussion it is apparent that viscosity, mixedness and rheology are inseparably linked.

The rheological properties of melts will be briefly revisited to show the effect thereof on mixing and tappability. If a fluid shows a linear shear stress versus shear rate relationship with a zero yield stress, the fluid behaves as a well characterised Newtonian fluid. However, if this relationship is either non-linear or has a non-zero yield stress, the behaviour becomes non-Newtonian, which has significant impacts on mixing. In slag melts non-Newtonian behaviour derives mainly due to the presence of solids which are formed when operating below the melt liquidus, or due to the precipitation of stable, high melting point, solid reaction products. While one would expect polymerisation of silicate chains to lead to non-Newtonian behaviour, Turkdogan (1983) claims that, based on a review of the results of many researchers, fully fluid silicate slag melts behave as Newtonian fluids even at a large degree of silicate polymerisation. While time-dependent rheological behaviour such as thixotropic and rheopectic melts may exist at pyrometallurgical conditions, the behaviour of these dynamic rheologies has not been well researched for high temperature melts. The main rheology types are depicted in Figure 4.2.

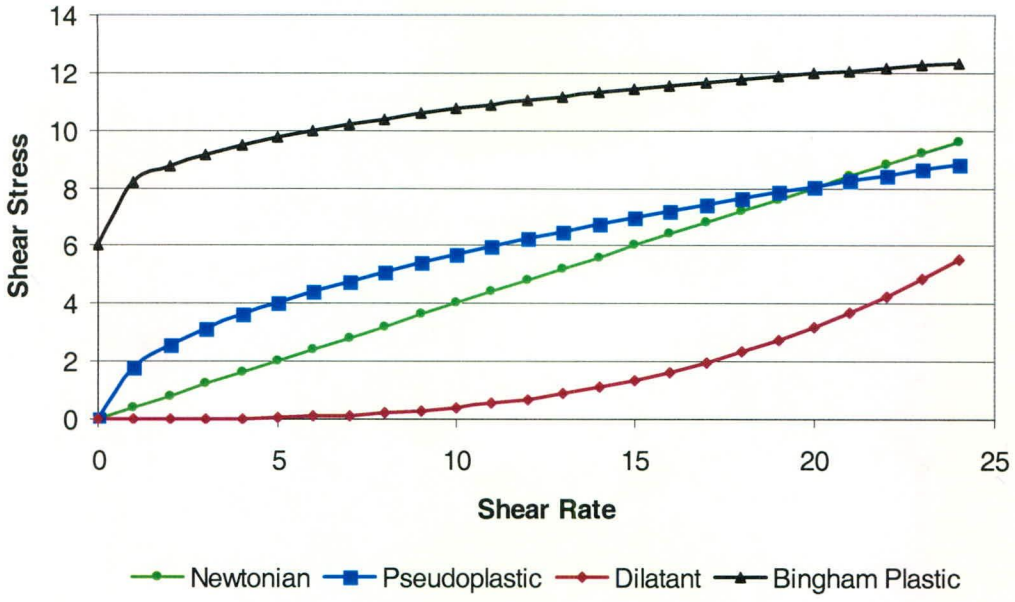

Figure 4.2: Different kinds of rheological behaviour

Wright *et al.* (2000) has shown that CaO-MgO-Al_2O_3-SiO_2 slags containing more than 8 mass% spinel-type particles (such as the chromite smelting slags) show Bingham plastic behaviour and therefore have a finite, non-zero yield stress. For a given solids loading, once the yield stress has been exceeded, the same authors also found that significant shear thinning occurs at increasing shear rates. Shear in furnace melts is caused by:

- Gas injection, or gas generation within the melts
- Hydraulic pressure gradient across the tap hole during tapping
- Plasma impingement on a molten bath
- Buoyancy driven convective flow
- Electro-hydrodynamic effects due to interaction of electrical and magnetic fields in electrical furnaces.

A non-zero yield stress therefore implies that a significant shear stress has to present in the furnace to induce melt flow and movement. The prediction of melt behaviour becomes even more difficult due to the presence of gas bubbles. The yield stress has been found to depend on the relative densities of solid and liquid phases, particle size, volume fractions of solids, and the shapes of solids (Dabak and Yucel, 1987; Sigworth, 1996; Jinescu, 1974; and Shi and Napier-Munn, 1996). Sigworth (1996) also showed that for molten alloy systems containing dendritic crystals, the size and shape of the dendrites can be modified at high shear rates. In oxide systems (such as slags and glasses), dendritic, equiaxed, and platelike crystals are commonly observed (Kondratiev *et al.* 2001) and the crystal shapes have been found to

depend critically on the compositions of the crystals and the liquid phase. However, under the low shear rate found in pyrometallurgical applications, shear stress modification of the solids is not likely to be a significant factor.

Kondratiev *et al.* (2001) show that the most important factors in estimating the viscosities of 2-phase melts are the volume % solids and the composition of the liquid phase present. In the case of a solid-liquid mixture formed from the partial crystallisation of a slag of fixed bulk composition, the volume % of each solid, the volume % of liquid, and the composition of the remaining liquid will all vary with process temperature; the liquid composition in the partially crystallised melt is not the same as the bulk composition of the material. Significant effects may be observed due to the change in liquid composition due to crystallisation: For example, the precipitation of a M_3O_4 spinel phase (which contains no silica) from siliceous slags, would lead to an increase in the silica concentration of the remaining liquid. The resulting increase in viscosity stems from an increase of the viscosity of the liquid phase (due to increased silicate polymerisation and / or lower temperature) and due to presence of solid particles. Moreover, for melts containing large particle sizes with densities between the solid and liquid phases, the buoyancy forces become significant relative to the viscous forces in the melt, resulting in the settling or flotation of solid phases. Segregation of the phases within the melt can therefore occur, and the slag viscosity characteristics would therefore vary with position in the reactor. The extent of segregation would depend on the bulk flow and mixing characteristics within the reactor. In order to predict the viscosity of partially crystallised melts, one needs to define the phase assemblages and effective oxygen potential and the process temperature. For systems more complex than binary systems, the use of Gibbs free energy minimisation software, together with the use of proper thermodynamic solution models and viscosity models becomes necessary. The application of the thermodynamic tools to the systems studied has been described in Chapter 3. Several models have been developed to predict the viscosities of slag and alloy melts as a function of temperature and composition. These models will be discussed briefly in the following paragraphs.

4.2.5.1 Slag systems

Although slag viscosities tend to show an Arrhenius type of dependence on temperature over limited temperature ranges, the more recent models are based on the Weymann-Frenkel (WF) kinetic theory of liquids, which Urbain used as the basis to develop a semi-empirical model to predict slag viscosities (Urbain, 1987; Urbain and Boiret, 1990) based on temperature and

composition. The semi-empirical form of the WF-model for fully fluid liquids takes on the general form:

$$\eta = A_\eta \cdot T \cdot \exp\left(1000\frac{E_\eta}{T}\right) \tag{4.8}$$

Where A_η and E_η are compositionally dependent pre-exponential and activation energy parameters for viscous flow, and the calculated viscosity is in Poise. Urbain's empirical model for slag viscosities is presented in Appendix C, and will also be contrasted with a model by Riboud *et al.* (1981).

4.2.5.2 Alloy melts

The structure of metallic melts of different compositions are fairly similar as the co-ordination number of the nearest neighbour atoms are more or less the same (Shridhar, 2002). The viscosities of metal alloy system furthermore tend to follow the liquidus temperatures of the system (systems with their liquidus temperatures going through a maximum also show a maximum in viscosity at the same composition, and eutectic systems show viscosity minima at the eutectic composition. Hirai (1993) developed the following set of equations to compute the viscosity of alloys:

$$\eta = A_{\eta,Alloy} \cdot \exp\left(\frac{E_{\eta,Alloy}}{RT}\right) \tag{4.9}$$

$$A_{\eta,Alloy} = \frac{1.7 \cdot 10^{-7} \rho^{2/3} \cdot T_M^{1/2} \cdot M_R^{-1/6}}{\exp\left(\frac{E_{\eta,Alloy}}{RT_M}\right)} \tag{4.10}$$

$$E_{\eta,Alloy} = 2.65 \cdot T_M^{1.27} \tag{4.11}$$

T_M is the melting (liquidus temperature) of the alloy, while M_R is the mean atomic mass of the alloy. More rigorous fundamental models exist for the prediction of metal viscosities, such as the Adjustable Hard Sphere Radial Distribution Curve as discussed by Hines and Chung (1996), but these models have only been validated for some pure metals, and are not very useful as estimators for alloy viscosities. In the absence of experimental data, equations 4.9 to 4.11 will be used to estimate alloy viscosities. It is apparent that the alloy phase equilibria (liquidus mapping) is required to estimate the alloy viscosity.

4.2.5.3 Effect of solids on viscosity

A number of empirical and semi-empirical viscosity models of suspensions have been reviewed by Jinescu (1974). The most well known equation, which has served as the basis for the further development of two-phase viscosity models, has been proposed by Einstein (1956):

$$\eta_R = \frac{\eta_S}{\eta_L} = 1 + 2.5\Phi_S \tag{4.12}$$

where η_R is the relative viscosity of the slurry with viscosity η_S and the remaining liquid η_L, while Φ_S refer to the volume fraction of solids (assuming that the solids do not segregate and float or settle from the fluid). This equation was valid for suspensions of low concentrations of solids (Φ_S <5 vol%, or 0.05). Roscoe (1952) also developed an equation for more concentrated suspensions of the general form:

$$\eta_R = \frac{\eta_S}{\eta_L} = \left(1 - R \cdot \Phi_S\right)^{-n} \tag{4.13}$$

Where R and n are empirical parameters which equals 1.35 and 2.5 respectively for spheres of equal size and 1 and 2.5 respectively for rigid spheres of diverse sizes and was found to provide a good fit to experimental data on viscosity of 2-phase crystallised melts (Lejeune and Richet, 1995). Many other viscosity equations can be expressed in the form of the following power series (Jinescu, 1974):

$$\eta_R = \frac{\eta_S}{\eta_L} = 1 + k_1\Phi_S + k_2\Phi_S^2 + k_3\Phi_S^3 + \ldots \tag{4.14}$$

Kondratiev and Jak (2001b) found that the Roscoe equation (4.13) provides a very good fit of the model to experimental data for the Al_2O_3-CaO-Fe_xO-SiO_2 partially crystallised slag system. They also have shown that the software F*A*C*T (Facility for Advanced Computational Thermodynamics, a predecessor the more recent FactSage® software, used in this thesis) predicts the proportion, type and compositions of the solid and liquid phases of this slag system very well and can therefore be used to calculate the fraction of solids as required by the Roscoe equation. Wright *et al.* (2000) also studied the rheological behaviour of CaO-MgO-Al_2O_3-SiO_2 melts containing $MgAl_2O_4$ spinel particles and, as in the case of Kondratiev and Jak (2001), found that the Roscoe equation provided a good fit of the model to the observations. Although they found that R and n varied slightly with particle size they

concluded that if the value of n is held constant at n = 2.5 and R is allowed to vary with particles size, that R takes on values of 2.6, 3.2 and 3.4 for fine (particle size< 100 μm), medium sized (100 μm < particle size < 440 μm)and coarse particles (440 μm < particle size < 1000 μm) respectively. In general the slags studied which contained more than 8 mass % solids tend to show Bingham plastic behaviour.

4.2.6 Viscosity of melts encountered in the smelting of chromite

While some of the more general models for viscosity were discussed in the paragraphs above, it is worthwhile to consider if any models or data exist for the specific systems considered in this thesis.

4.2.6.1 Chromite Smelting Slag

A chromite smelting slag for the production of high carbon ferrochrome (HCFeCr) typically has bulk compositions in the following range:

SiO_2 15-30%, typically 22%

Al_2O_3 19-33%, typically 28%

MgO 13-25%, typically 20%

CaO 10-27%, typically 17%

Fe 1-14% (may be as FeO or as entrained HCFeCr), typically 5%

Cr 1-24% (may be as CrO, Cr_2O_3 or as entrained HCFeCr), typically 6%

As the % carbon in the slag was found to follow the chemistry of the HCFeCr, it was estimated that most of the reported Fe and Cr are in the form of entrained HCFeCr and not as dissolved oxides. The remaining Fe, and Cr in the slag (as oxides) were found to be too little to contribute significantly to the phase diagram or viscosity relationships. The slag could therefore be approximated as a CaO-MgO-SiO_2-Al_2O_3 slag with spinel particles as the main precipitating phase. The viscosity of this system was studied, as shown in section 4.2.5.3 by Wright *et al.* (2000).

4.2.6.2 High Carbon Ferrochrome Alloy

Viscosity data on the HCFeCr alloy system were found to be extremely scarce. However, some Russian researchers reported their findings for the system (Vostryakov *et al.*, 1963). They found that for a system containing 5% C, the kinematic viscosity remains nearly constant (at about 0.020 stokes at 1500 °C and 0.017 stokes at 1600 °C) for alloys containing more than 30% chromium. The same authors found a very drastic rise in the kinematic

viscosity when the alloy was cooled below the alloy liquidus. The kinematic viscosity rose from about 0.020 Stokes (14 cp.) just above the alloy liquidus (about 1550 °C for an alloy containing 7% C, 31%Cr, remainder Fe) to about 0.400 Stokes (282 cp.) for a temperature drop of about 50°C (therefore an increase of 40 times), based on an alloy density of 7055 kg/m^3. This indicates that the amount of solids precipitated is extremely sensitive to subcooling relative to the liquidus. Vostryakov *et al.* (1963) also determined that the viscosity and activation energy isotherms of Fe-Cr systems comprise minimums approximately corresponding to the minimums in the liquidus line (There is therefore reason to believe that Hirai's (1993) estimation formula of the alloy liquid viscosity would be applicable to this system). The phase equilibrium of the Cr-Fe-C-Si system, as pertaining to HCFeCr production, was experimentally determined and critically reviewed by Wethmar *et al.* (1975) as is discussed in detail in Appendix A. As is the case for slags, a whole range of carbides of different compositions to the bulk alloy chemistry may precipitate below the liquidus, thereby changing the chemistry of remaining liquid. Therefore, while the Einstein-Roscoe type equations are still applicable, the alloy-slurry viscosity should be estimated relative to the viscosity based on the chemistry of the remaining liquid, and not the bulk slag composition.

4.2.7 Viscosity of melts encountered in the smelting of ilmenite

In contrast to chromite smelting, ilmenite smelting (high titania) slags contain very little silica. The slag composition is comprised mainly of the FeO-TiO_2-Ti_2O_3 system, with silica, lime, MnO and magnesia typically making up less than 5% of the slag mass. This slag system is in contact with nearly pure iron containing carbon (up to 2.5%) and some small amounts of S, Mn, Ti and Si. As for the chromite smelting, the phase equilibria applicable to ilmenite smelting was be discussed in Chapter 3.

4.2.7.1 High Titania Slag

The viscosities of high titania slags have been measured by Handfield and Charette (1971) and Handfield *et al.* (1972). At temperatures above the liquidus, the viscosity was found to remain relatively constant at a value of 30 cp., even at other slag chemistries. A typical Sorel-slag (about 72% "TiO_2") showed an increase in viscosity of 30 cp. at 1579 °C to over 400 cp. at 1571°C (therefore more than a 10-fold increase in viscosity for a temperature drop of a mere 8 °C). A similar sensitivity to crystallisation was observed for Titania slags with 80% TiO_2, except that the temperature of incipient crystallisation increased to around 1700 °C. Handfield and Charette (1971) observed that Sorelslags crystallised in long needle-like

crystals upon slow cooling of the melt. This may lead to a significant degree of crystal interlocking, even at low solids concentrations. As no additional publications were found on high titania slags the base value of 30 cp. for the liquid phase will be used, while the Einstein-Roscoe equation will be used to estimate viscosities below the slag liquidus.

4.2.7.2 Pig Iron

Even though pure iron melts at 1536 °C, the presence of small amounts carbon causes a significant decrease in the melting point (Refer to Appendix A for the Fe-C phase diagram, as simulated by FactSage ®). For the % carbon in the range 0f 2.0 - 3.5%, a constant solidus of 1130 °C (including the other major impurities) is observed, while the liquidus gradually drops from 1380 °C at 2% C to 1292 at 3% C. A eutectic is observed at 4.3% C, where the liquids temperature equals the solidus temperature of 1130 °C. The dynamic viscosity of pure iron at its melting point is 0.0055 Pa.s (5.5 cp.). The viscosity of impure iron will be calculated by the estimation formula of Hirai (1993).

4.2.8 Spatial variance of composition, in materials associated with HCFeCr production

During normal operating practice, the slag and alloy are sampled once each, at any ad-hoc time, once the flow of the melt flow through the tapping launder is fully developed. To determine if significant spatial variance exists with regard to the composition and temperature, two designated sampling campaigns were scheduled, where the temperature and compositions of the slag, alloy, and flue dust were monitored. For a number of slag and alloy taps, 6 equispaced samples were taken per tap, once the melt flow through the launder to the ladle was fully developed. These samples were all handled identically, with regard to quenching and assaying of the samples. All the sample sizes were similar and of the order of about 50-60 cm^3. A number of alloy and slag taps were also monitored using a Mikron M90 H pyrometer, mounted on a tripod and focused on the molten alloy at the tap hole during the tapping. The pyrometer, with a range from 600 °C to 3000 °C and a precision of 0.4% was calibrated using disposable dip thermocouples.

The slag samples were analysed using X-ray fluorescence spectrometry (XRF), while the alloy samples were analysed using a spark optical emission spectrometry (spark OES). Carbon and sulphur in all feed and product phases were analysed using a LECO CS200 analyser. It was found that the slag also contained carbon, even though no visible free carbon

was present. It was assumed that the carbon in the slag derives from entrained alloy droplets which contain in the order of 8-9% carbon.

The dust was analysed based on grab samples from the fresh filter cake as it was discharged from an automatic plate-and-frame pressure filter. The filter cake was dried at slightly above 100 °C to drive off the moisture. The particles were analysed using a SEM EDS. The dust was also analysed using XRF for the metal oxides and the LECO CS200 analyser for carbon and sulphur. The dust is not analysed on a routine basis on the plant. The flue gas composition was fairly consistent although the quantities varied significantly, depending on the reductant to mineral feed ratio and the reactivity of the reductant, which in turns is dependent on the ratio of volatiles to fixed carbon.

It was also possible to perform a similar sampling campaign on submerged arc furnaces at the same smelter site. Although the submerged arc furnaces are not bath type furnaces, they do provide a comparative baseline, as the chromite raw materials for both furnace types (DC open arc, and AC submerged arc) derive from the same supplier. It should be noted that the operation and the particle sizes fed to the furnaces differ very widely.

4.2.8.1 Alloy

Over and above the need to obtain an idea of the variation of tap composition for the purpose of furnace control and mixedness analysis, accurate assays of the contaminants in the ferrochrome alloy are especially important in the modern age where ferrochrome and stainless steel plants are operated in close proximity, as there is currently a drive for "just-in-time" molten alloy transfer from the ferrochrome plants to the stainless steel plants. Analysis of the alloy samples of high carbon ferrochrome showed that the HCFeCr alloy derived from a direct current plasma arc furnace (PAF) is not necessarily well mixed with respect to the solutes (assuming a solvent of Cr-Fe-C). The significance of the relative deviation with respect to the average assay per tap is shown in Figure 4.3 for Si and Figure 4.4 for S, two of the metallurgical important solutes (typical average values for silicon and sulphur in a PAF are 2% and 0.01% respectively). The variation is extreme in the case for silicon (-90% to over 100% relative to the tap average) and slightly less so for S. No clear pattern was visible as to the order in which positive and negative, large and small variations occurred. That is to say that large positive and negative variations may occur at the start of tapping, or at any time during tapping – sampling after half of the material has been tapped does not ensure a representative sample of the specific tap. Sampling based on one sample per tap is therefore

not representative. The Si assays shown in Figure 4.3 stem from taps from two sampling campaigns spaced 18 months from another.

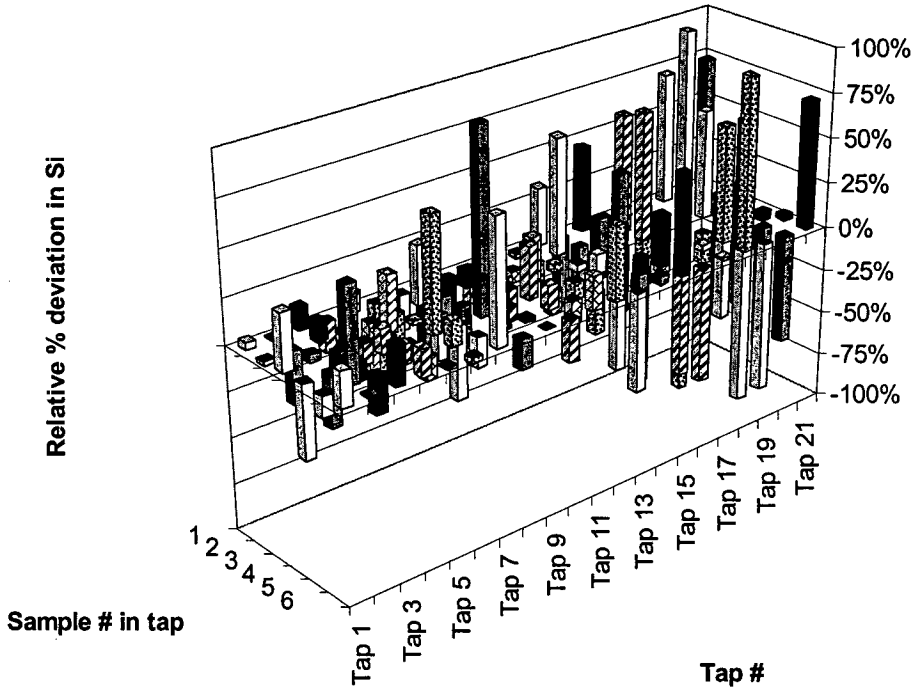

Figure 4.3: Sample by sample variation of Si for a number of alloy taps (both campaigns).

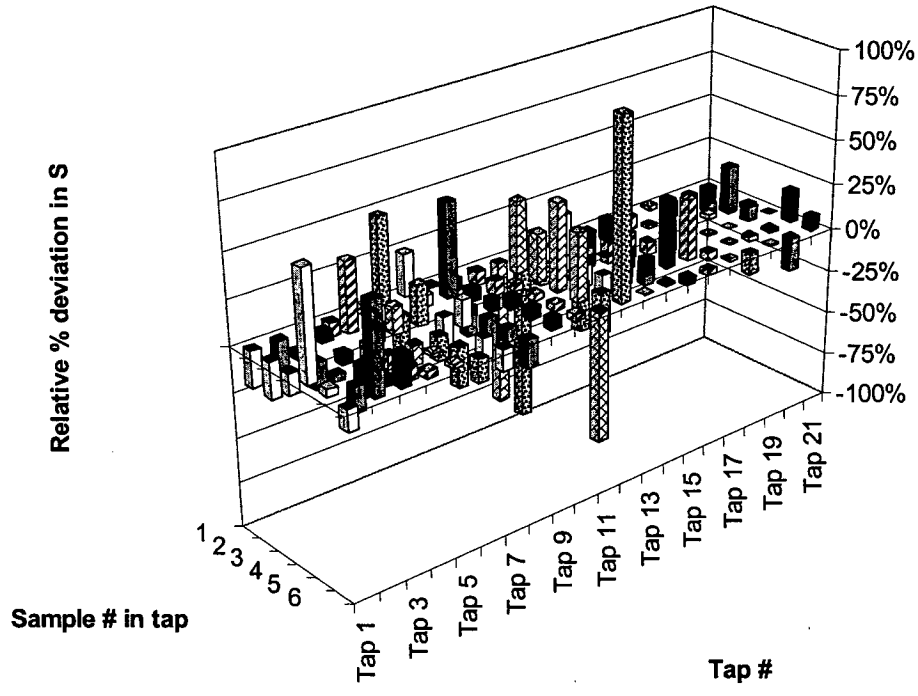

Figure 4.4: Sample by sample variation of S for a number of alloy taps (both campaigns).

To establish the distribution of % relative deviation for the different solution components, the relative deviations per tap were collated for all taps, and a histogram was constructed for each component. The histogram of relative variation aids one to determine:

- If the distribution appears to be normal (Gaussian) and centred around a zero mean;
- The range of variation (maximum and minimum variation)
- The spread and the degree of central tendency

Moreover, it is insightful to develop the histograms for both the plasma arc furnace (PAF) and the submerged arc furnaces (SAF), as the mixing driving forces are different, even though similar alloys and slags are produced from chemically similar raw materials. Histograms for the main alloy components and contaminants are shown in Figures 4.5 - 4.16. The distributions tend to show Gaussian characteristics, except for the distributions of Cr, Mn and P in the SAF. The ranges of relative variation for the different components are, without exception, larger for the PAF than for the SAF. As the frequent occurrence of larger relative variations in the melt constituents indicates poorer mixing, one may conclude that the HCFeCr alloy produced by the PAF is not as well mixed as in the SAF.

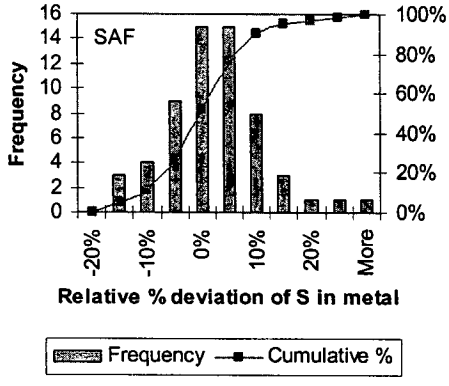

Figure 4.5: Distribution of S in SAF-alloy

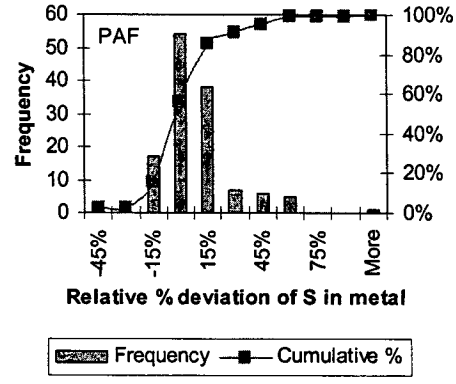

Figure 4.6: Distribution of S in PAF-alloy

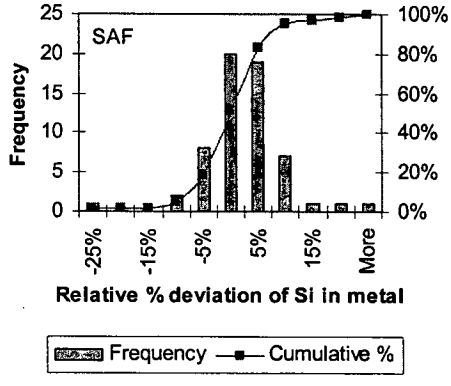

Figure 4.7: Distribution of Si in SAF-alloy

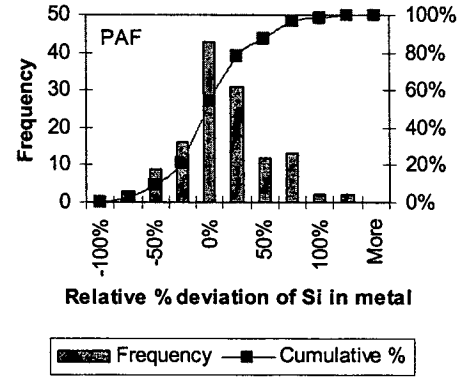

Figure 4.8: Distribution of Si in PAF-alloy

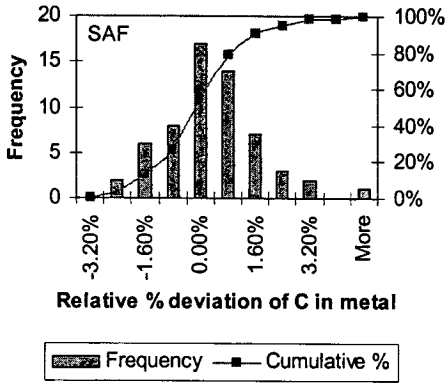

Figure 4.9: Distribution of C in SAF-alloy

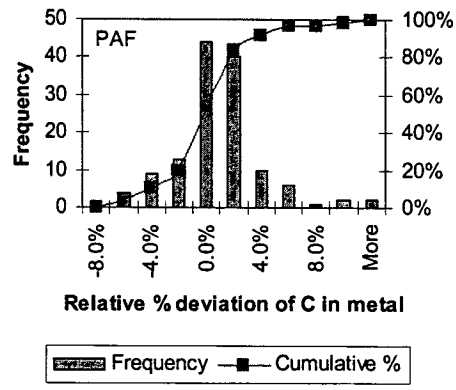

Figure 4.10: Distribution of C in PAF-alloy

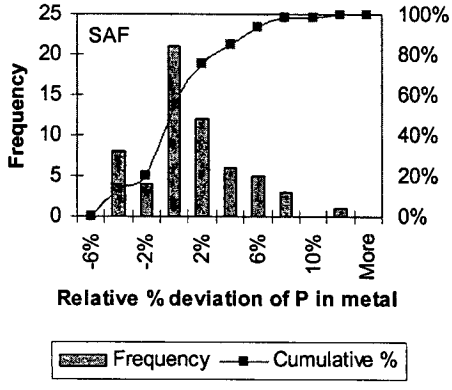

Figure 4.11: Distribution of P in SAF-alloy

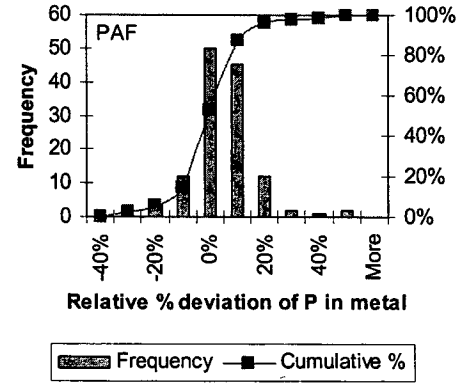

Figure 4.12: Distribution of P in PAF-alloy

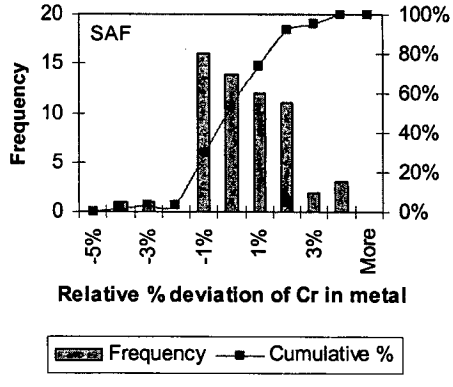

Figure 4.13: Distribution of Cr in SAF-alloy

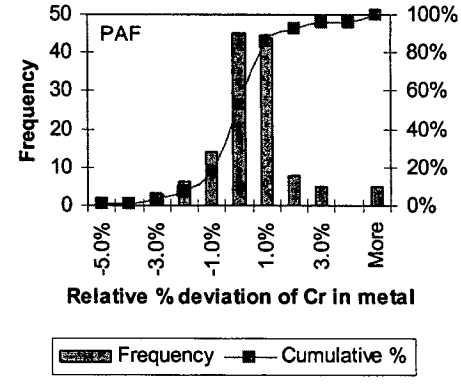

Figure 4.14: Distribution of Cr in PAF-alloy

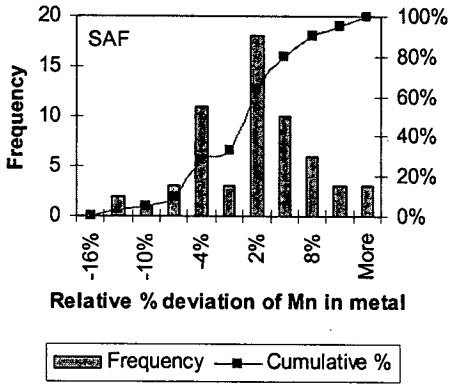

Figure 4.15: Distribution of Mn in SAF-alloy

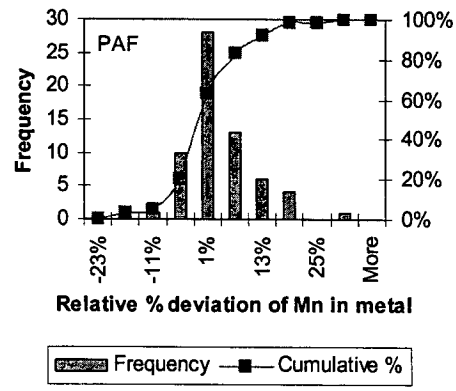

Figure 4.16: Distribution of Mn in PAF-alloy

The poor alloy mixing in the PAF relative to the SAF is shown very clearly in Figure 4.17. Of all HCFeCr alloy elements Si and S are least homogeneously distributed (It is important that Si and S are pyrometallurgically connected through the volatile component SiS). As expected, the solvent components (Cr and C, Fe is not shown but is similar) are homogeneously distributed with associated low standard deviations. The standard deviations of all minor components are much larger than one can ascribe to analytical instrument error (< 2% relative error). Although one might think that, due to the PAF being an open bath with in-bath reduction and gas generation, and plasma impingement on the bath, the PAF should be better stirred than the SAF, these measurements point towards the contrary. The better mixedness of the SAF system can be explained by the difference in electro-hydrodynamic forces acting between the two melt systems. In the case of the PAF, the single cathode electrical direct current flows in one direction only, with very little variation in the electrical and magnetic field strength. In the case of the alternating current 3 phase - 3 electrode SAF, an electrical star configuration (in comparison to the delta configuration) is formed. The dynamic resistance-inductance circuit (due to the dynamic nature of the AC circuit) has the anchor point of the star in the melt phase. This anchor point changes in position as the electrical phases change and the resistances vary. The creation of a variable and rotating induced magnetic field would therefore be able to serve as driving force to electromagnetically "pump" the conductive melt around the electrodes. This is considered to contribute to the overall mixing, although a sequence is noted in the magnitude of driving forces: Gas bubble-driven circulation (upwards), thermal buoyancy (downwards), electromagnetic (Lorentz) stirring (downwards) and finally Marangoni surface tension driven forces.

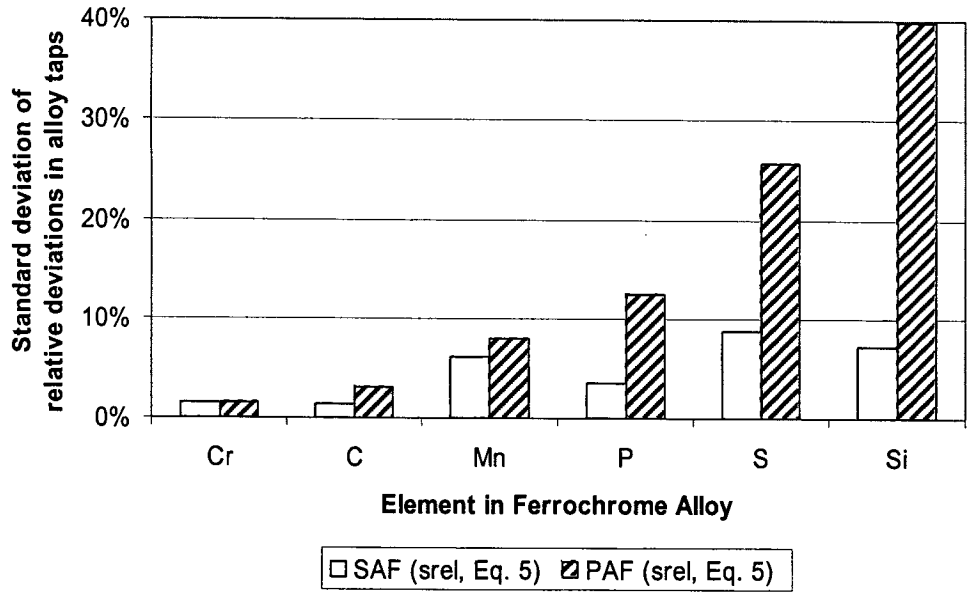

Figure 4.17: A comparison of the standard deviations of the relative deviations for alloy elements for submerged (SAF) and plasma (PAF) arc furnaces.

Even though silicon appears in appreciable quantities in HCFeCr melts (1 – 5%) it is the element that shows the largest degree of inhomogeneity. It was consequently decided to use silicon as identifier of mixedness. It was found that when the alloy melt was subcooled relative to the melt liquidus (as dictated by the average melt chemistry), the degree inhomogeneity increased (as measured by the standard deviation per tap in the relative Si deviation from the tap average). For the PAF, there appears to be a decreasing relationship between the % relative standard deviation in %Si per tap and increasing degrees of superheat associated with the tap, as shown in Figure 4.18. An R^2 of 40% (correlation coefficient of 0.63), based on the best straight line fit, indicates that there is a significant relationship, but that other factors may also play a role (e.g. the electro-hydrodynamic effects).

Figure 4.18 makes much sense when one consider that subcooling below the liquidus dramatically increases the viscosity due to partial melt crystallisation (the liquidus surface of the alloy system is provided in Appendix A). This effect was demonstrated by Vostryakov *et al.* (1963) as discussed in section 4.2.6.2 and it is as one would expect based on the predictions by the Einstein-Roscoe equation (Eq. 4.21). As the alloy melt does not experience the effect of the plasma impingement on the melt surface (except for a situation of low slag depth), nor of gas bubbling due to oxide reduction reactions, as is the case for the slag, one would also expect that rheology becomes the overriding factor in determining alloy melt homogeneity.

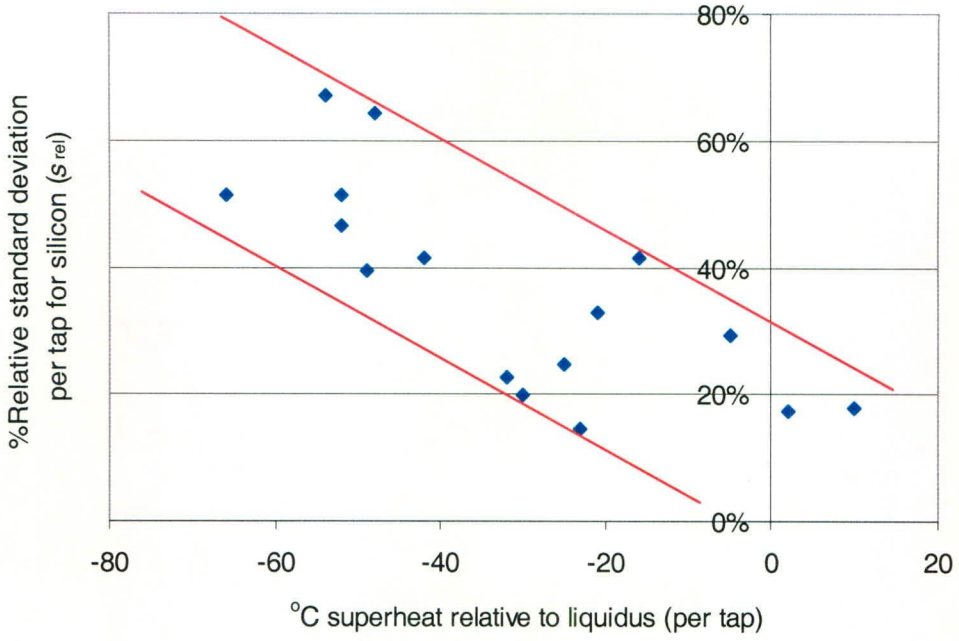

Figure 4.18: Relationship of heterogeneity of the alloy, measured in terms of the relative standard deviation per tap in Si, to the degrees superheat of the alloy melt relative to the alloy liquidus.

4.2.8.2 Slag

The slag chemistry associated with ferrochrome production lies within the domain of the $CaO\text{-}MgO\text{-}SiO_2\text{-}Al_2O_3$ system, containing Fe and Cr in the M^0 (entrained), M^{+2} and M^{+3} (very little) oxidation states. Sulphur is normally dissolved as sulphide. None of the SEM-photos of slags investigated, show the presence of free carbon. In all cases it was associated with entrained alloy droplets.

Figure 4.19 shows how significant the Cr variation in the slag truly is, relative to the average per tap. The samples from the first twelve tap numbers derive from the second campaign, while samples from tap numbers 13-21 derives from the first campaign, performed 18 months earlier, on the same furnace. Significant positive deviations (up to 80%) from the specific tap-average occurred. The six samples per tap were ordered per tap according to their order of sampling, that is, the first sample per tap was taken the first moment fully developed flow through the launder was observed. The subsequent samples were then taken based on a equal time interval. The time intervals were determined based on the total duration of typical slag taps divided by 8 (6+2) to allow for the start and end periods during which no samples were taken. The sample position per tap where the maximum Cr-assay was observed varied from tap to tap. Neither did minimum deviations necessarily occur close to the middle of the tap.

One can therefore not claim that sampling at any given time is more representative than at another instant. There is therefore no common pattern in the assays from different taps.

A similar level of stochastic behaviour is apparent for FeO, as shown in Figure 4.20, the other reducible component in the slag. As for Cr in the slag, the sampling and assaying of Fe occurred during two separate sampling campaigns. It is unknown which proportion of these two metals is entrained, and which proportion is dissolved.

The variation in the other slags components are less marked, as is apparent in the histograms for the slag components in Figures 4.21 to 4.36.

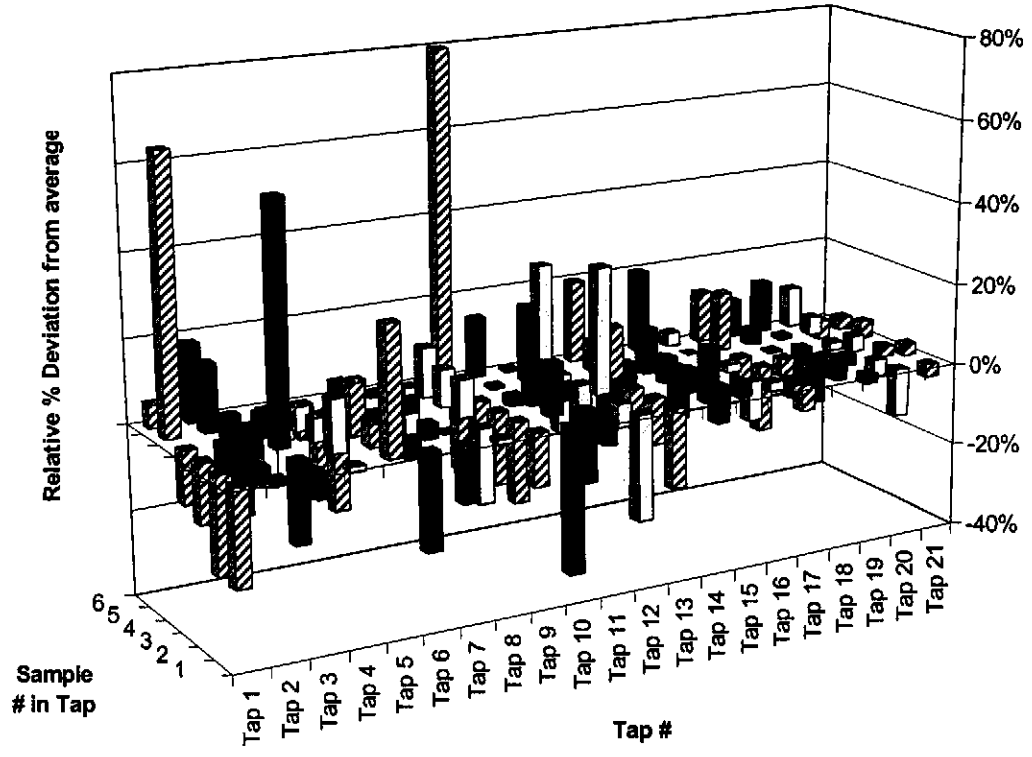

Figure 4.19: Sample by sample variation in Cr (as Cr_2O_3) within slags (both campaigns).

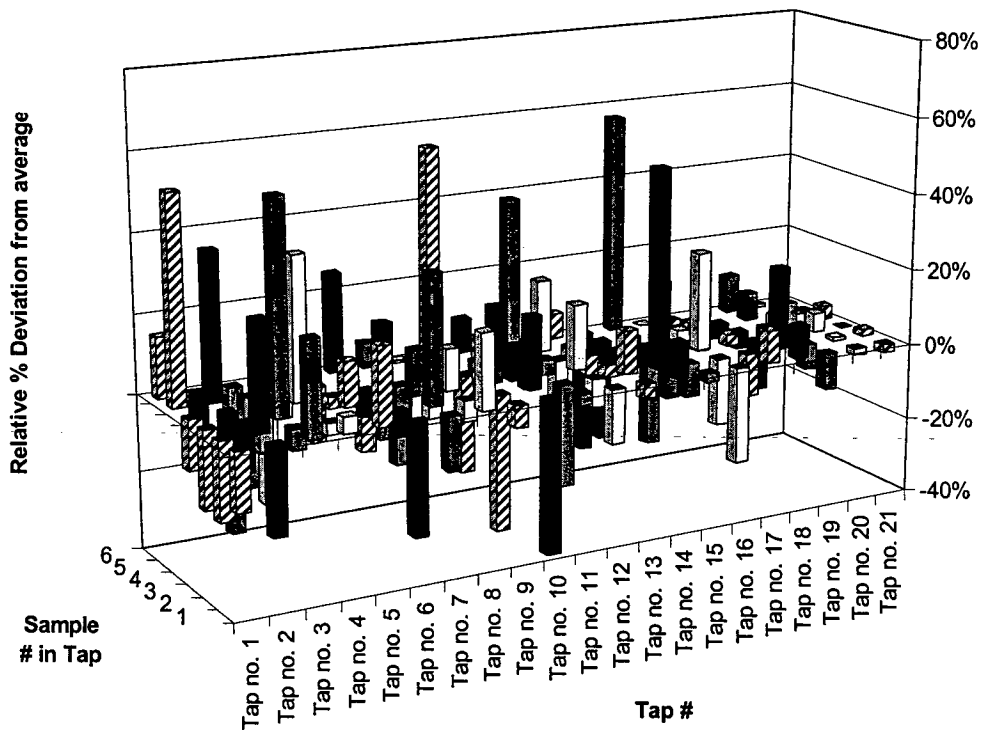

Figure 4.20: Sample by sample variation in Fe (as FeO) within slags (both campaigns).

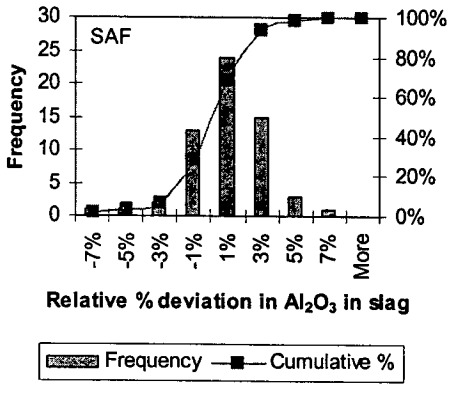

Figure 4.21: Distribution of Al_2O_3 in SAF-slag

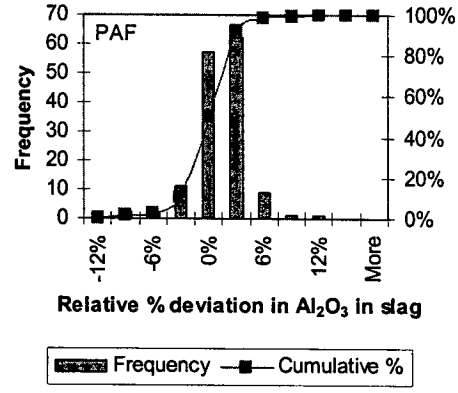

Figure 4.22: Distribution of Al_2O_3 in PAF-slag

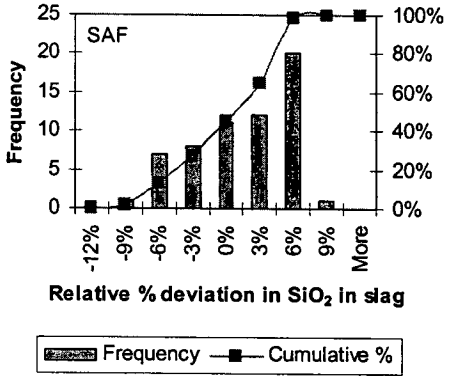

Figure 4.23: Distribution of SiO_2 in SAF-slag

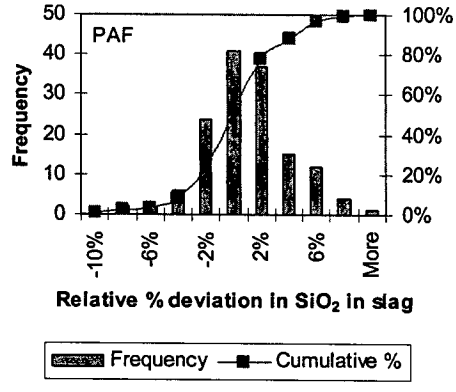

Figure 4.24: Distribution of SiO_2 in PAF-slag

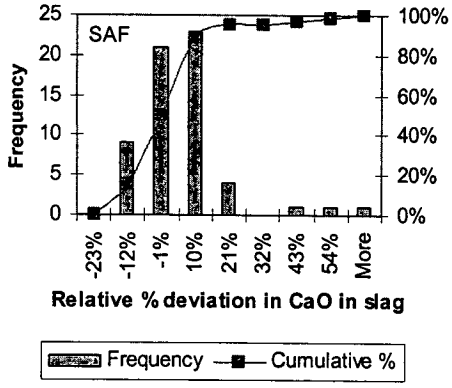

Figure 4.25: Distribution of CaO in SAF-slag

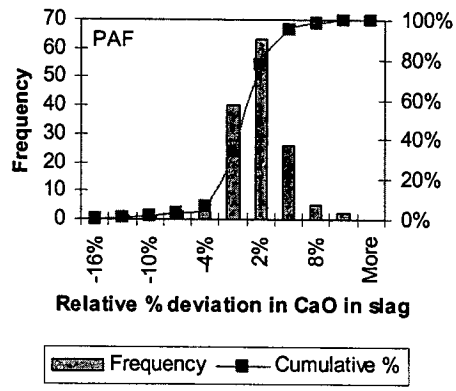

Figure 4.26: Distribution of CaO in PAF-slag

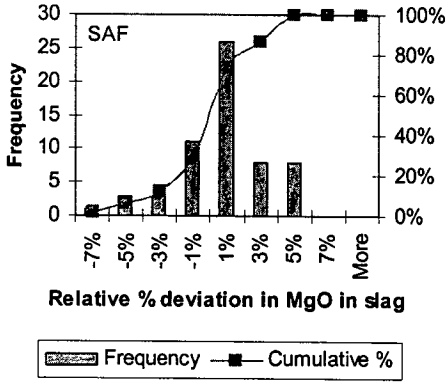

Figure 4.27: Distribution of MgO in SAF-slag

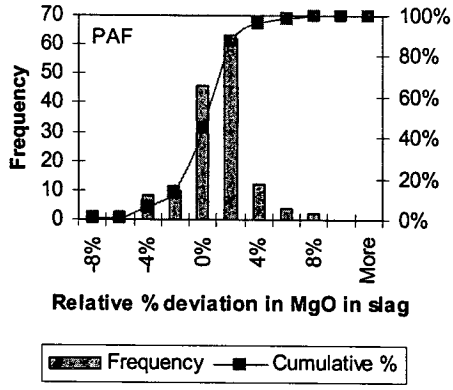

Figure 4.28: Distribution of MgO in PAF-slag

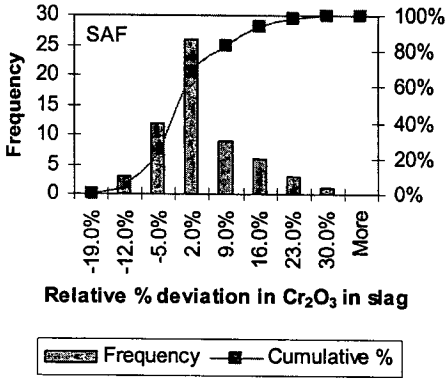

Figure 4.29: Distribution of Cr_2O_3 in SAF-slag

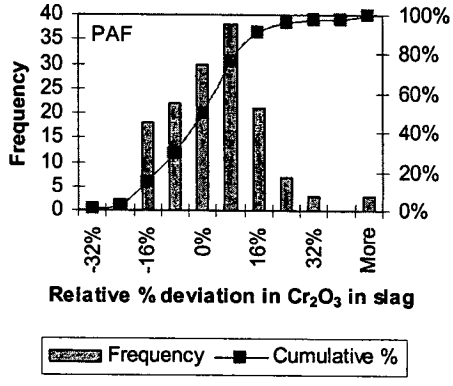

Figure 4.30: Distribution of Cr_2O_3 in PAF-slag

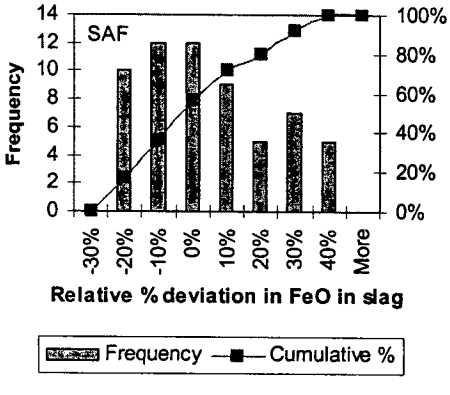

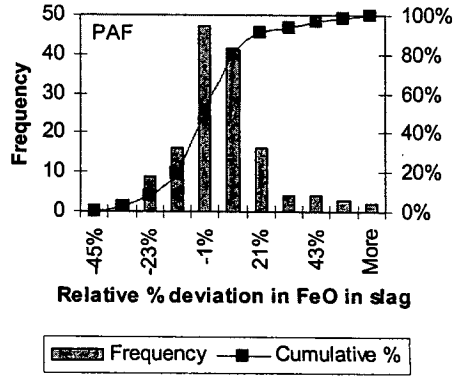

Figure 4.31: Distribution of FeO in SAF-slag

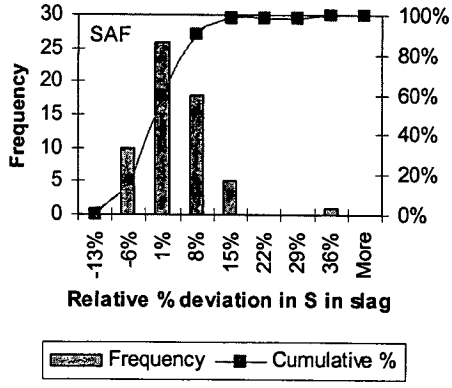

Figure 4.32: Distribution of FeO in PAF-slag

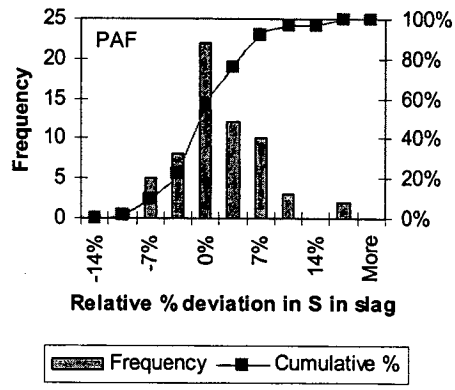

Figure 4.33: Distribution of S in SAF-slag

Figure 4.34: Distribution of S in PAF-slag

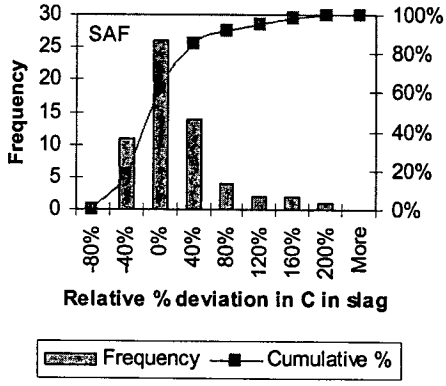

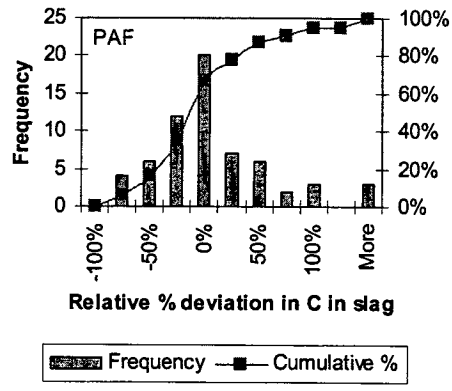

Figure 4.35: Distribution of S in SAF-slag

Figure 4.36: Distribution of S in PAF-slag

Figures 4.21 to 4.36 show that the distributions of the PAF tend to be close to normal, while the distributions of the SAF system are significantly skewed for C, FeO, CaO and SiO_2. Most slag components show a comparative range and central tendency with the exception of CaO and Cr_2O_3, where large difference in composition deviation is apparent for the PAF and SAF and systems. The large variation in CaO could be ascribed due to improper mixing in the burden of the SAF of the flux with the chromite and carbonaceous reductant. The variation in carbon is the most significant for both furnace types. As no noticeable free carbon was present in the slags, the carbon is expected to be associated with the entrained HCFeCr alloy droplets. It appears that the presence of a second phase (entrained alloy or undissolved particles) in bulk melts lead to an decrease in melt homogeneity.

Table 4.1 presents a summary of the standard deviations of the relative compositional variations of the different melts associated with HCFeCr production in SAF and PAF furnaces. It is apparent that the slag from the PAF is well mixed with respect to the dissolved

non-reduced oxides, but shows a very large degree of inhomogeneity with respect to components that are present (either totally or in part) as entrained phases.

Table 4.1 : A comparison of the standard deviation of the relative deviations of melt compositions for the submerged arc and plasma arc furnaces.

Slag	**Al_2O_3**	**CaO**	**Cr_2O_3**	**FeO**	**MgO**	**SiO_2**	**S**	**C**
SAF s_{rel}	2.3%	13.8%	9.0%	19.3%	2.6%	4.4%	7.3%	52.7%
PAF s_{rel}	2.8%	3.3%	15.7%	17.7%	2.4%	3.2%	5.3%	69.1%
Alloy	**Cr**	**C**	**Mn**	**P**	**S**	**Si**		
SAF s_{rel}	1.5%	1.4%	6.1%	3.5%	8.8%	7.3%		
PAF s_{rel}	1.6%	3.0%	8.0%	12.5%	25.6%	39.9%		

4.2.8.3 Melt spatial temperature distributions

Melt temperatures were logged based on continuous monitoring of the melt using the Mikron pyrometer. As expected, the temperature variation is much less than the composition variation of the solute components. In fact, the relative standard deviations of the melt temperatures are comparable in magnitude to the relative standard deviation of the solvent components, as is shown in Table 4.2. The low relative standard deviations supports the hypothesis that the thermal diffusivity is much larger than the mass diffusivity of the solute components in viscous melts. The larger thermal variation found in the PAF slag compared to the PAF alloy can be explained by the fact that the slag experiences extreme thermal gradients close to the arc attachment zone (AAZ), and close to the slag freeze line. The metal also conducts heat far better than the slag, and establishes thermal homogeneity much quicker.

Table 4.2: Maximum and average relative standard deviations in temperature for PAF and SAF melts.

Description	Average	Maximum
PAF, Alloy: Relative standard deviation (thermal)	1.6%	2.3%
PAF, Slag: Relative standard deviation (thermal)	1.8%	3.2%
SAF, Alloy: Relative standard deviation (thermal)	1.2%	2.8%
SAF, Slag: Relative standard deviation (thermal)	1.2%	2.8%

As the metal and slag of the SAF are tapped simultaneously through the same taphole (as opposed to the slag and alloy which are tapped consecutively through separate tap holes for the PAF under investigation) the metal and slag of the SAF shows the same thermal variance as well as overall temperatures. Based on the average standard deviation for all taps

monitored (more than 10 taps in each case), one may conclude that, as was observed for composition, the SAF is also thermally better mixed than the PAF.

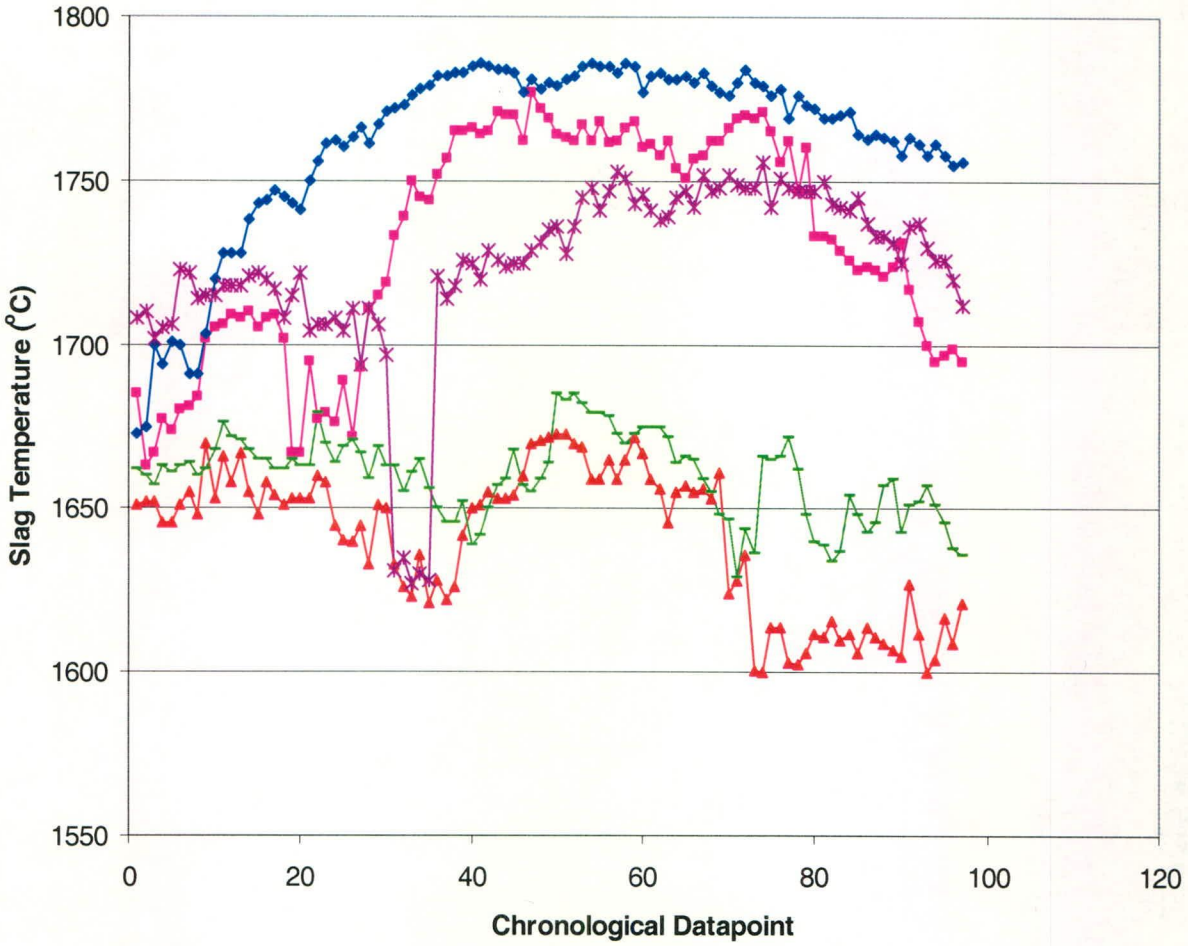

Figure 4.37: Examples of temperature profiles of slags tapped from a HCFeCr PAF

Figure 4.37 shows a few typical examples of temperature profiles of slag melts during tapping. In general a temperature maximum is normally observed about at, or shortly after, half the tapping duration. Although this "head-and-shoulders" pattern in the tapped melt temperature was the one most commonly observed, inverted "bucket" patterns, or monotonic increasing, or monotonic decreasing patterns were also noted.

In the case of the alloy melt, no clear patterns emerged. The temperature profiles are highly erratic, as can be seen from a number of examples shown in Figure 4.38.

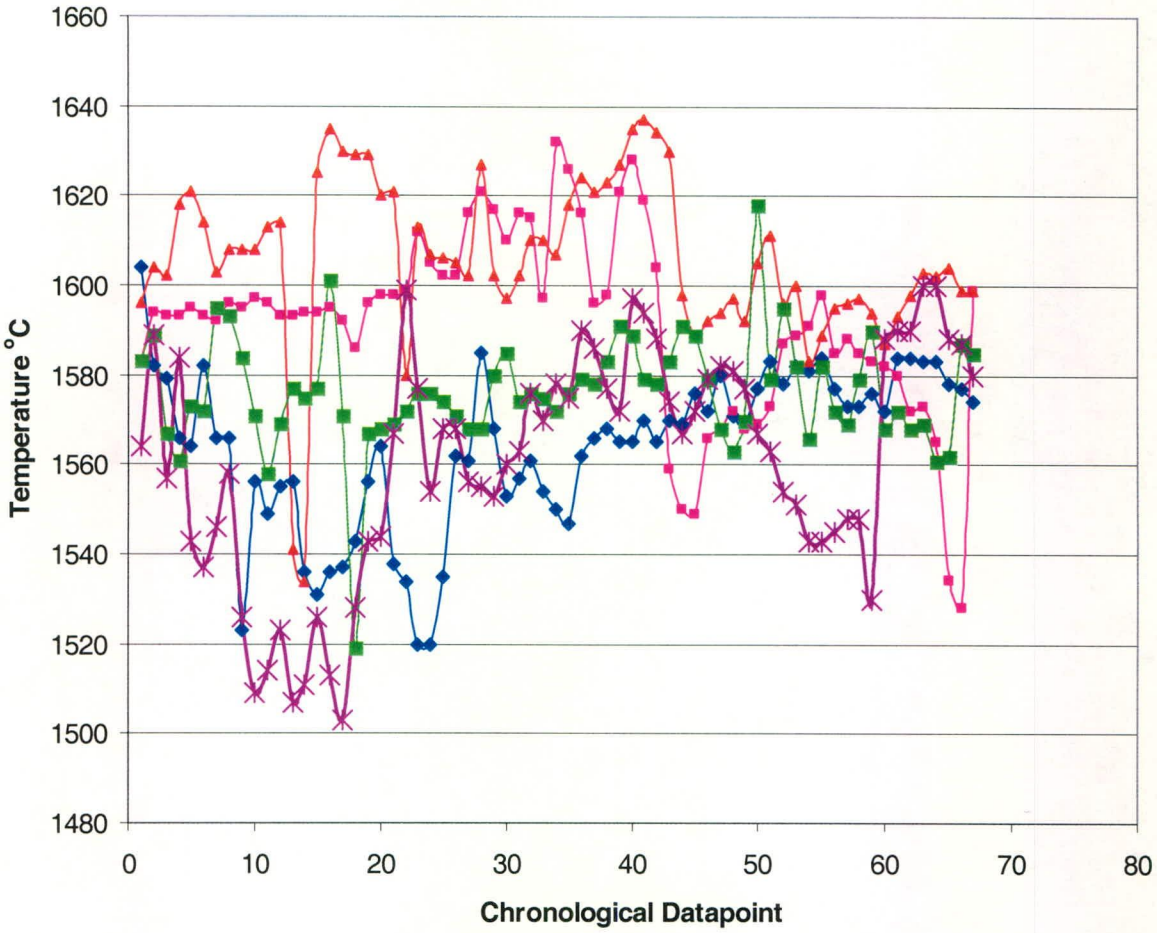

Figure 4.38: Examples of temperature profiles of alloys tapped from a HCFeCr PAF

It is interesting to note that the relative thermal deviation for the PAF is of similar magnitude to the relative thermal deviation predicted by Szekely *et al.* (1983) for electric arc furnace steelmaking, using CFD modelling techniques (see paragraph 2.4.7.1 and Figure 2.28) if the thermal zones in the figure are graphically integrated according to their proportional contribution to the bulk temperature.

To compare the deviation patterns (from the tap averages) of silicon in the alloy and the associated temperatures, the average temperature associated with the time the sample was taken from the tap, was determined. These "sample average temperatures" were calculated based on the average temperature of the alloy between two alloy samples. This was done to have a similar number of temperature and composition measurements. The percentage deviations were then calculated relative to the tap average. The results for typical (not worst case) PAF and SAF taps are presented in Figures 4.39 and 4.40. In each case, the temperature deviation pattern is given to the right of the corresponding silicon deviation for the same tap.

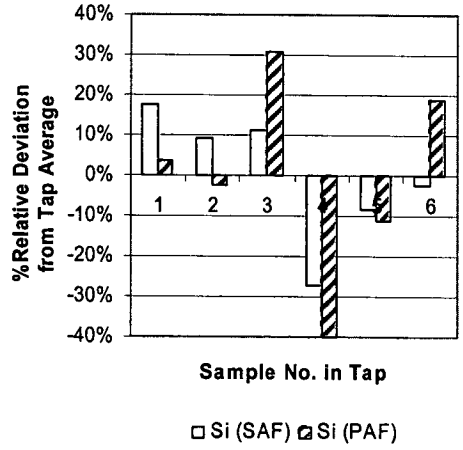

Figure 4.39: Deviation pattern of the silicon in the alloy for a selected PAF and a SAF tap

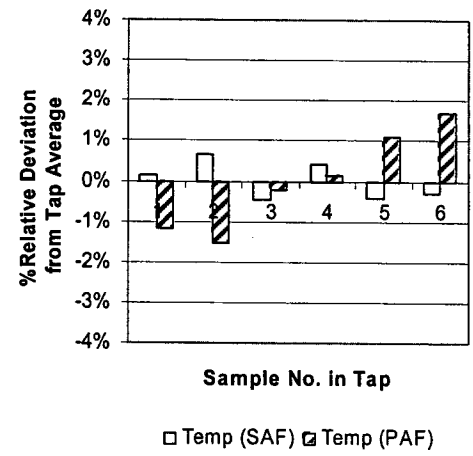

Figure 4.40: Deviation pattern of the alloy temperature for the same PAF and SAF taps shown in Figure 4.39

From Figures 4.39 and 4.40, it should be noted that the scales of the axes differ by an order of magnitude. Moreover, there is no correlation between the chronology of the temperature deviation pattern and the silicon deviation pattern. For silicon in this particular case in the PAF, the major deviations occurred close to the middle of the tap, while the temperature deviated much more from the tap average initially and then again to the end of the corresponding tap. For both alloy temperature and alloy composition the SAF showed lower variation in comparison to the PAF.

It may therefore be concluded that, for HCFeCr production, both the PAF and SAF furnaces are, from a thermal perspective, well mixed.

4.2.8.4 Dust

The dust from the HCFeCr PAF is captured through a venturi scrubber. The effluent from the scrubber is thickened and filtered using an automated plate & frame filter press. The wet filter cake is dumped on a heap, from where it transported as waste. To obtain an idea of phases and chemistry of the dust, which is not analysed as a rule, the dust was analysed using, XRF, SEM-EDS and a LECO CS200 for carbon and sulphur. Figure 4.41 shows a SEM photograph of the dust with a corresponding EDS analysis. The amounts of dust were estimated from the known weight of filter cake released, the known moisture level and the frequency of filter discharges.

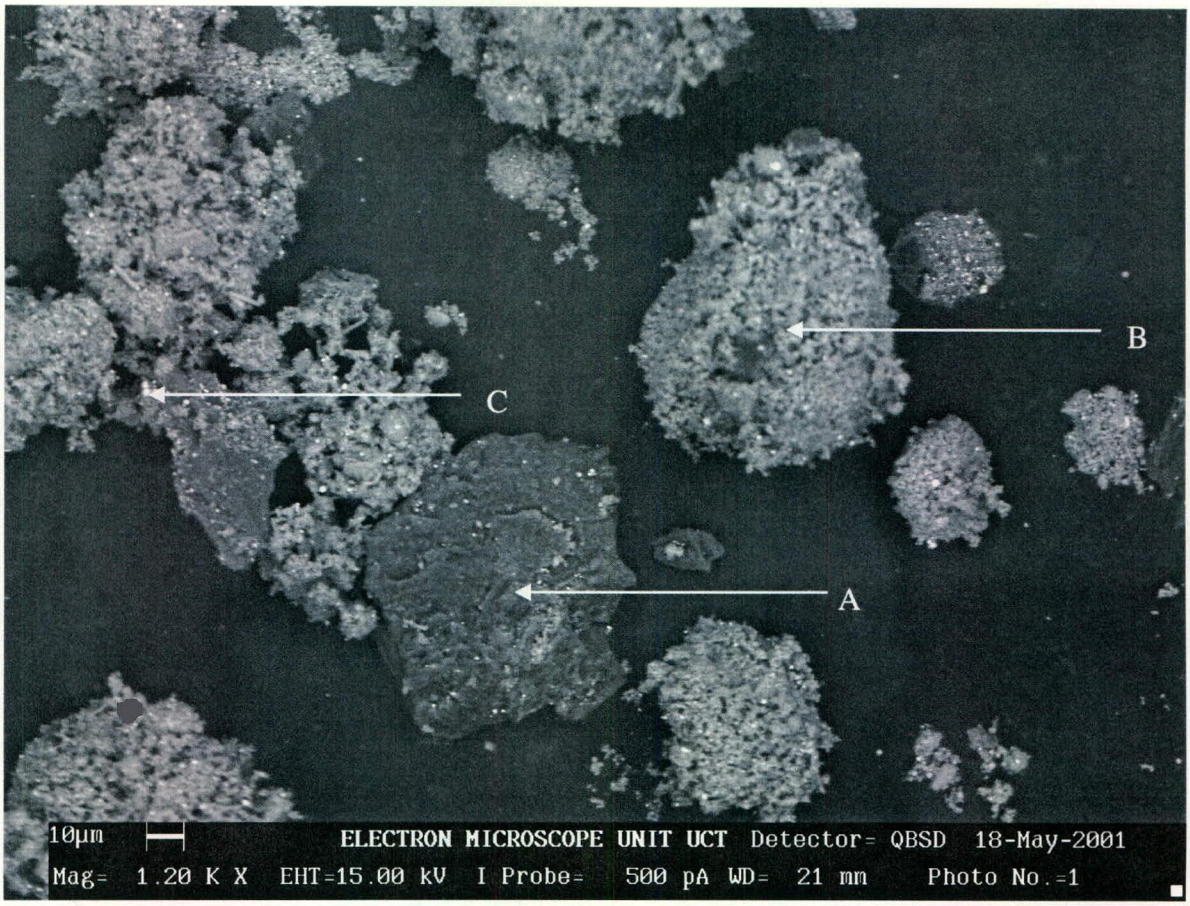

Figure 4.41: Scanning Electron Microscope Photo of the HCFeCr PAF dust (1)

A description and analysis of the three main particle types as identified in Figure 4.41 is presented in Table 4.3. A brief discussion of how a char particle type arrived in the dust is also presented in Table 4.3.

Table 4.3 : EDS analyses of the phases identified in Figure 4.41

Particle	Element	Mass %	Comment
A	C O Si S K	95.8 2.7 0.3 0.7 0.5	This particle is a piece of de-volatilised reductant. It is distinguishable by its darker colour which is due to the high carbon content. As the flue dust is in-homogenous the quantity thereof will differ from sample to sample. Dust with a high proportion of carbon may be indicative of poor reductant utilisation in the furnace. The texture of this particle is more crystalline than the rest implying that this particle was entrained in the dust.
B	O Na Mg Al Si S K Ca Cr Fe Zn	30.1 2.0 22.4 2.7 21.5 3.3 2.0 2.1 5.4 3.7 4.8	Particles of this nature make up the majority of the sample. This specific particle is a dust particle, however partially reduced feed material has also been identified, but to a lesser degree than the dust particles – partially reduced feed has a more crystalline texture than the dust. Typical dust particles have high proportions of Mg and Si present. Analyses of other similar particles also yielded high proportions of Mn, Zn while Cr appeared only in small amounts. This is primarily due to the high volatility of these elements when reduced to metal from the slag. The high oxygen percentage is due to the fact that the elements are present in their oxidised state – the elements are re-oxidised in the venturi scrubber
C	S Fe	1.0 98.0	These bright particles are tiny specks of metal entrained in the dust. From the image it is clear that the size is very small in comparison to the other particles. Particles with a high percent of Cr are also observed in the dust.

The presence of entrained char particles is very common as is apparent by the number of dark carbonaceous particles visible in Figure 4.42. It is also apparent that, as one would expect,

there is a concentrating effect (relative to the feed) of volatile elements (Zn, Mn, and S) volatile oxides (Na_2O, K_2O) and compounds that appear in the dust via a volatile or gaseous intermediate such as SiO_2 and MgO which appear due the volatile SiO and Mg in the gas when SiO_2 and MgO are reduced in the slag, especially at the arc attachment zone (AAZ) – refer to paragraph 2.4.8.

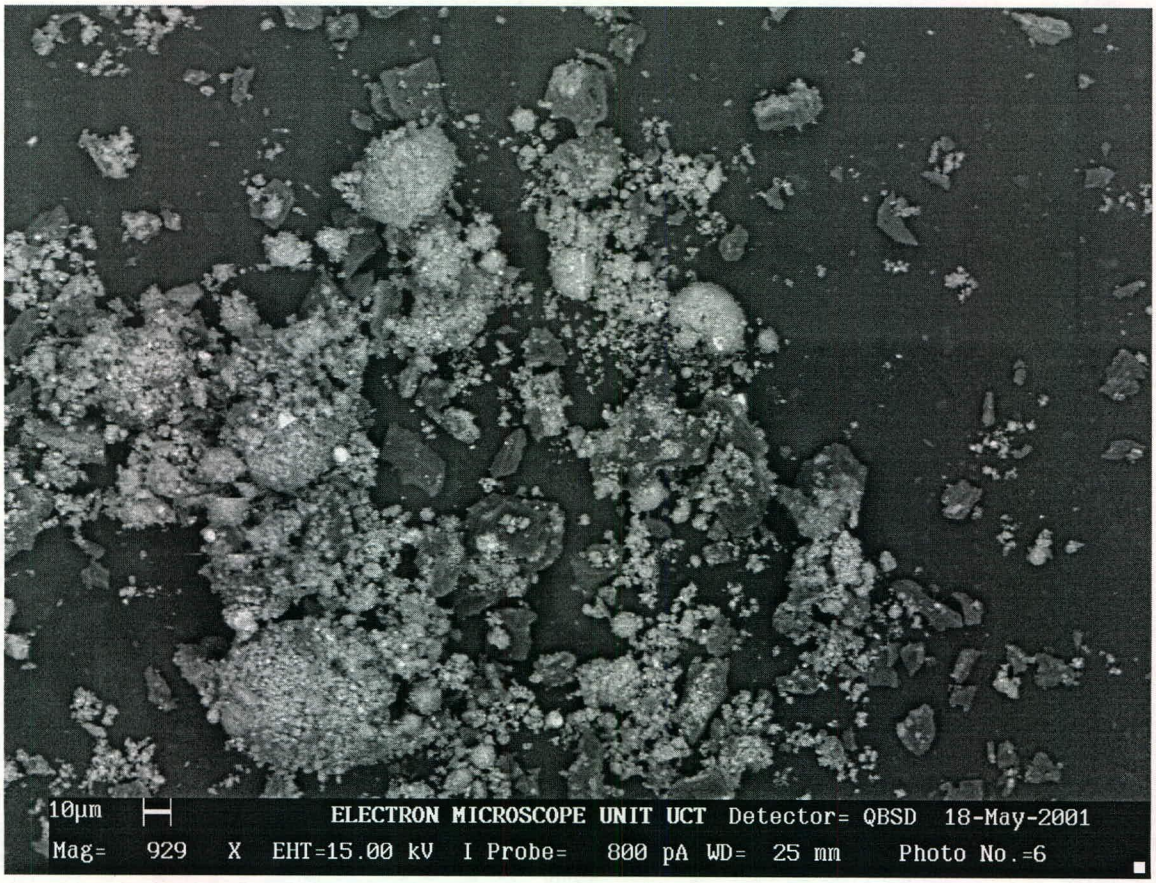

Figure 4.42: Scanning Electron Microscope Photo of the HCFeCr PAF dust (2)

18 Dust samples were taken spread over a number of days. After drying the samples had the following (normalised) analysis and corresponding relative standard deviations:

Table 4.4: Dust analysis and assay variation

Component	SiO_2	Al_2O_3	MnO	FeO	TiO_2	CaO	K	MgO	Zn	S	Cr_2O_3	C
Mass %	26.9	3.85	6.01	9.54	0.66	3.04	4.17	26.75	2.35	3.85	9.01	3.79
s_{rel}(%mean)	8.2	17.2	10.5	27.9	8.8	20.7	24.2	17.2	24.8	20.4	32.1	92.5

The significant variance found for C can be attributed to the highly variable amount of coal fines found in the feed, which are entrained in the off-gas. The relative standard deviation of all dust components are quite high and should be taken into account when one seeks to close the material balance for the smelter.

4.2.9 Spatial variance in ilmenite smelting

The sampling of the products from ilmenite smelter took place in exactly the same way as for the chromite smelting furnaces. Two major differences are however notable:

- The slag is not polymerised and has an extremely low viscosity when it is fully fluid or the % solids is low.
- The metal phase is nearly pure iron with 2-3% C contamination and very small amounts of other impurities.

4.2.9.1 Pig Iron

It is interesting to note that the pig iron from ilmenite smelting also showed the highest variances in dissolved sulphur and silicon throughout the bulk of the metal. Moreover, these variances, although slightly smaller, are comparable to the variances found for Si and S in HCFeCr produced in the plasma arc furnace. The relative deviations per tap for silicon and sulphur are shown in Figures 4.43 and 4.44 respectively.

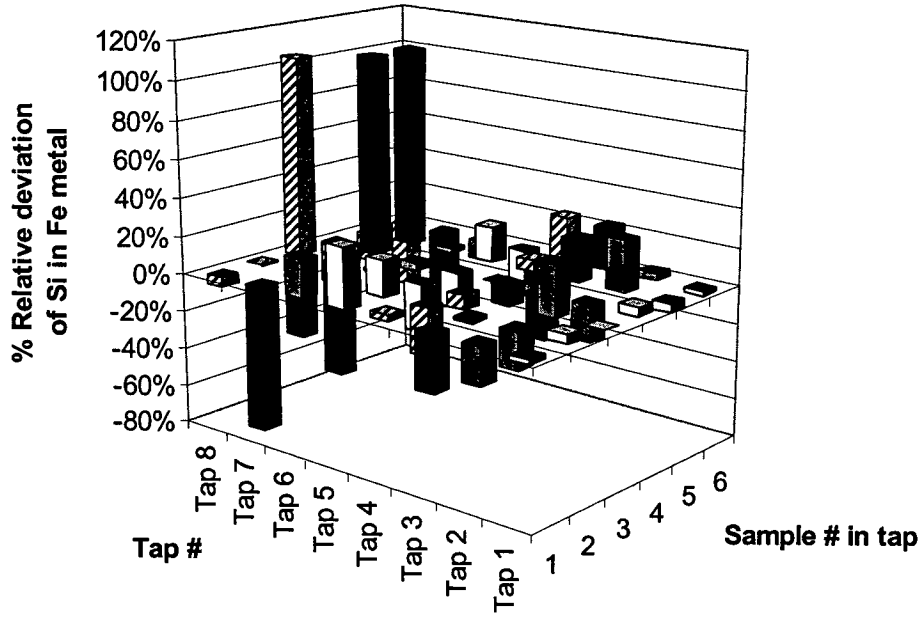

Figure 4.43: Relative variation (to tap average) of silicon in iron from ilmenite smelting.

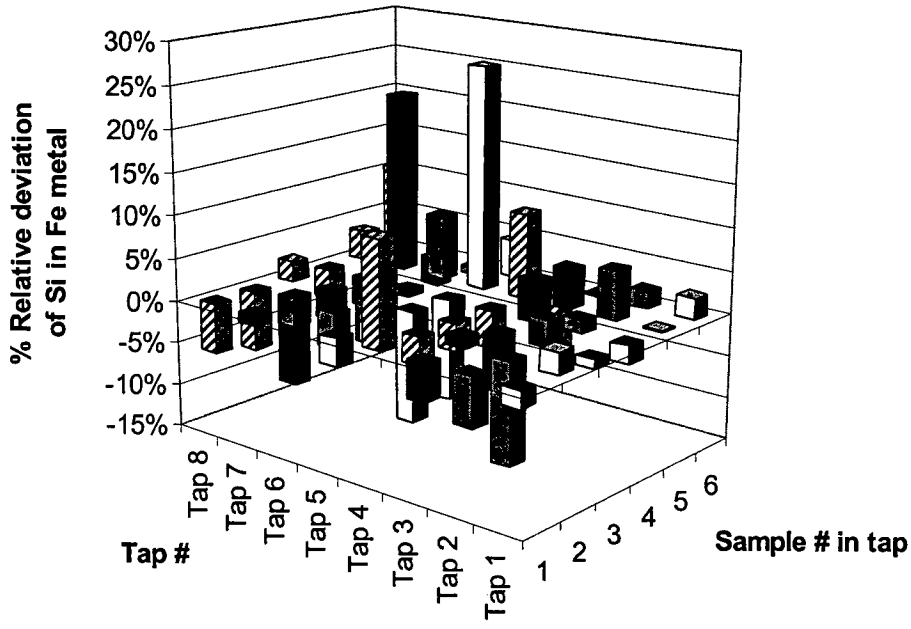

Figure 4.44: Relative variation (to tap average) of sulphur in iron from ilmenite smelting.

Histogram evaluations of the pig iron have shown that the minor component deviations are clustered around the mean assay (relative deviation of zero) and that the deviation distributions show normal behaviour. As for the HCFeCr alloy, the histograms for the non-metallic solutes, excluding carbon, in the pig iron metal shows the highest variance. The histograms for Si, S, P ,C , Mn and Ti are shown in Figures 4.45 to 4.50.

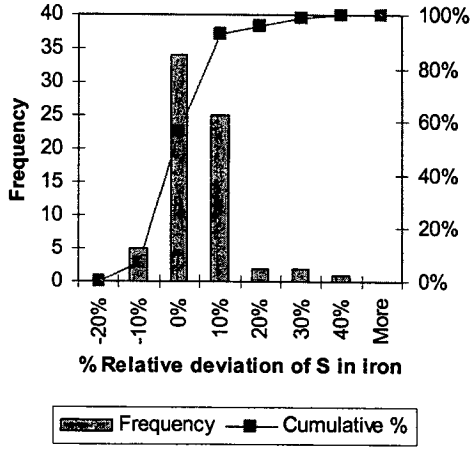

Figure 4.45: Distribution of sulphur in pig iron.

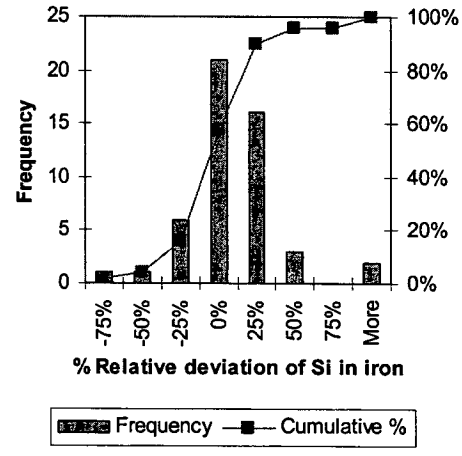

Figure 4.46: Distribution of silicon in pig iron.

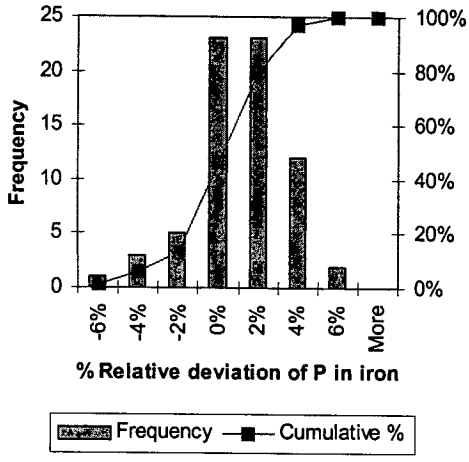

Figure 4.47: Distribution of P in pig iron

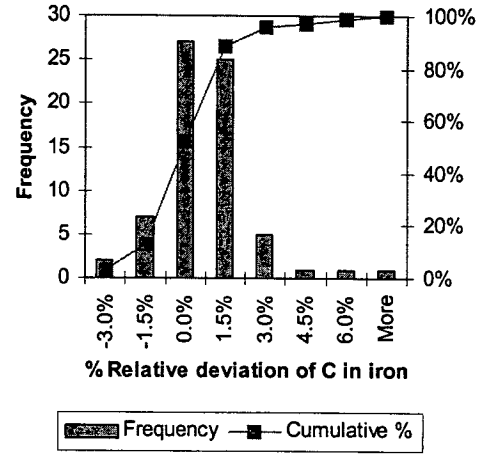

Figure 4.48: Distribution of C in pig iron

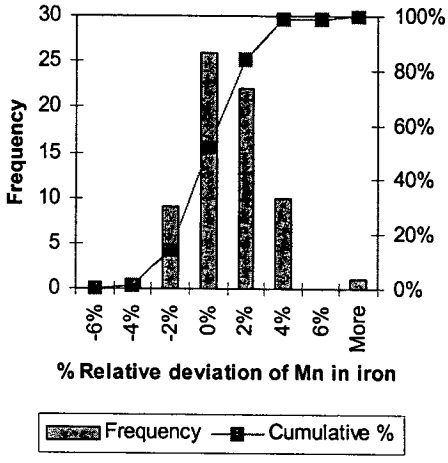

Figure 4.49: Distribution of Mn in pig iron

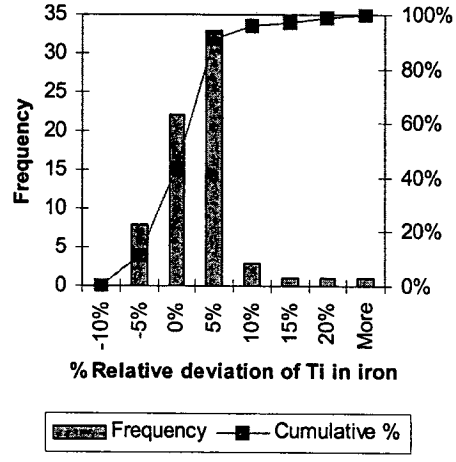

Figure 4.50: Distribution of Ti in pig iron

Due to the large amounts of dust generation during tapping, the temperatures of only a few metal taps could measured. Consequently, not enough data points exist to draw a similar graph to Figure 4.18 which relates metal mixedness to the degree of subcooling. Only two metal taps were available where both the relative standard deviation in silicon and the temperature profiles were available simultaneously. It is interesting that for these two taps, the mixedness as a function of the degrees of subcooling also supports the conclusion made for ferrochrome alloy melts – that the degree of mixedness decreases (relative standard deviation increases) with increased degree of subcooling. Again the rheology of the pig-iron seem to play a significant role in the segregation, especially of silicon. Table 4.5 gives a comparison of the degree of subcooling versus the relative % deviation in silicon for the two taps. The liquidus of Fe-C alloys is presented by Smithells (1976) was used to calculate the degree of subcooling.

Table 4.5: Variation of heterogeneity (relative deviation) with degree of superheat for pig iron

Superheat (°C) relative to liquidus	12	-17
% Relative standard deviation in Si (relative to tap average)	4%	45%

The average assays and relative standard deviations of the metal contaminants are given in Table 4.6.

Table 4.6: Assays and relative standard deviation associated with spatial composition variance in pig iron

Component	C	P	S	Fe	Mn	Ti	Si	Cr	Ni	V
Mean Assay	2.59	0.03	0.09	97.05	0.05	0.08	0.01	0.03	0.02	0.04
s_{rel} (%mean)	1.2	1.9	5.4	0.1	1.7	4.2	16	1.2	1.9	1.6

Of the elemental contaminants listed, only Si, S, and Ti have significant relative standard deviations that is, more than one could attribute to analysis error only. Moreover, the relative standard deviations for Si and S are less than half of those found for ferrochrome alloy as produced by a plasma arc furnace (and therefore a similar production technology).

4.2.9.2 High Titania Slag

High titania slag has the FeO-TiO_2-Ti_2O_3 components as solvent species, while SiO_2, MnO, MgO and Al_2O_3 are the main solute components with concentrations below 5 mass%. As is the case for chromite smelting, ilmenite smelting is associated with plasma stirring and gas bubbling, but without a polymerised slag structure, and therefore has similar driving forces with regard to mixing, but less resistance to fluid flow. As one would expect from the discussion of ferrochrome, the homogeneity of the melt should be at least as good or better than for chromite smelting slags. One would also anticipate, based on the results found for chromite smelting, that the species showing the highest variance would be those species which constitute entrained phases such as iron metal droplets or titanium oxycarbide particles (for chromite Fe, Cr, and C making up HCFeCr, was found to vary most in the slag).

This behaviour was also found typical for high titania slags, as is apparent from Figure 4.51, which shows the variation in the amount of metallic iron entrainment per tap relative to the average amount of metallic iron per tap. The variation is quite significant and is comparable to Cr and Fe deviations in chromite smelting slags. Similarly, the variation in titanium oxycarbide entrainment is also within the same magnitude range. The relative composition variation in titanium oxycarbide per tap is shown in Figure 4.52.

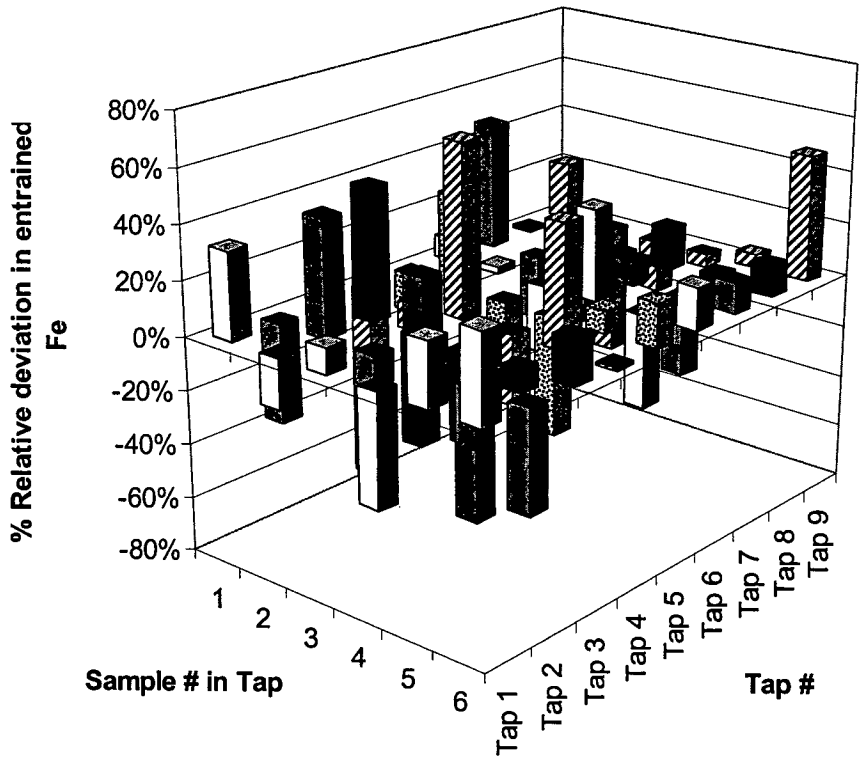

Figure 4.51: Relative variation (to tap average) of entrained iron in high titania slag.

As for the metal, it was found that the soluble components of the slag showed minimal variation. Figure 4.52 shows that the relative deviation in "insoluble" Titanium oxycarbide is similar in magnitude to entrained iron. However, a larger proportion of the reported "TiO_2" is as entrained oxycarbide (4% of the total reported Ti), compared to Fe as a proportion of reported "FeO" (1% of total Fe).

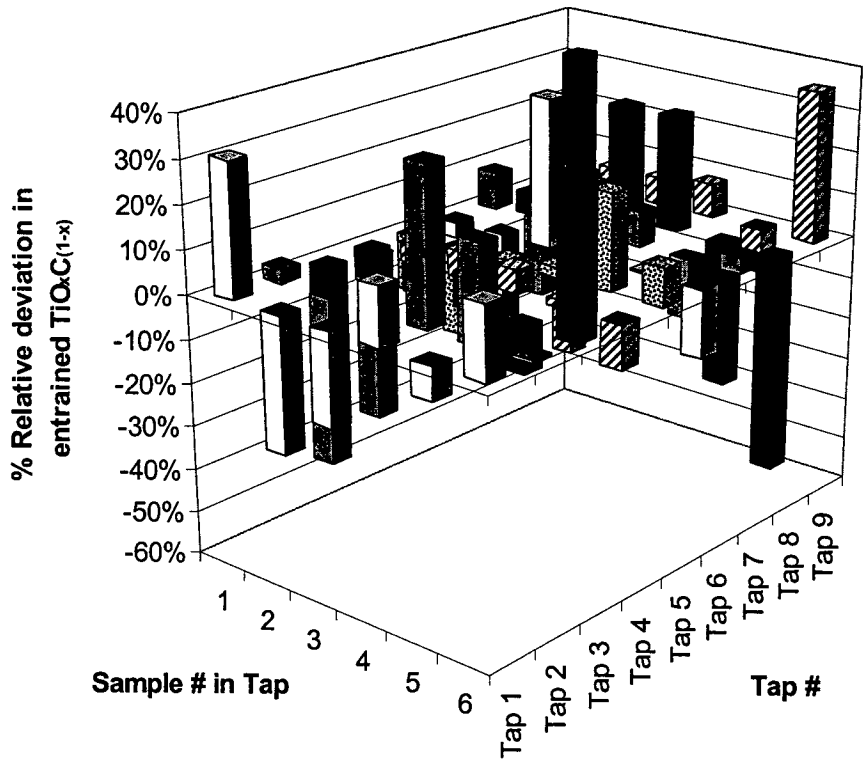

Figure 4.52: Relative variation (to tap average) of entrained titanium oxycarbide in high titania slag.

A histogram study of the all the slag components show that for the period of the sampling campaign, only the entrained melt or precipitated phases show a large variance, while the bulk of the slag can be considered well mixed. The histograms for the main slag components are presented in Figures 4.53 to 4.50.

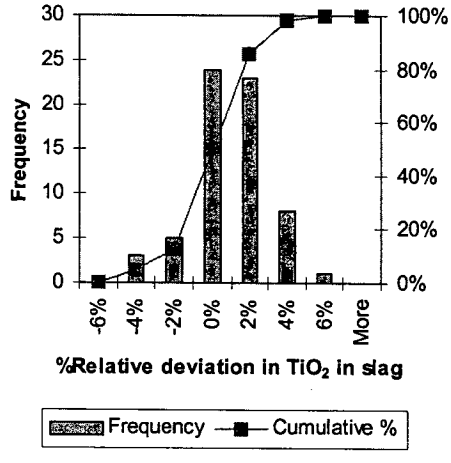

Figure 4.53: Distribution of actual TiO_2 in slag

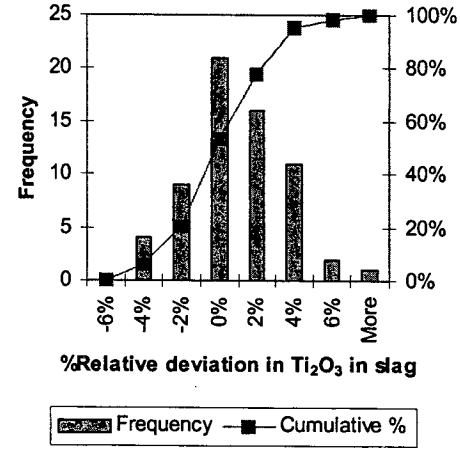

Figure 4.54: Distribution of Ti_2O_3 in slag

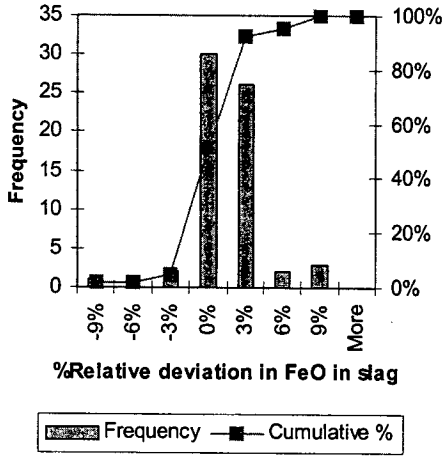

Figure 4.55: Distribution of actual FeO in slag

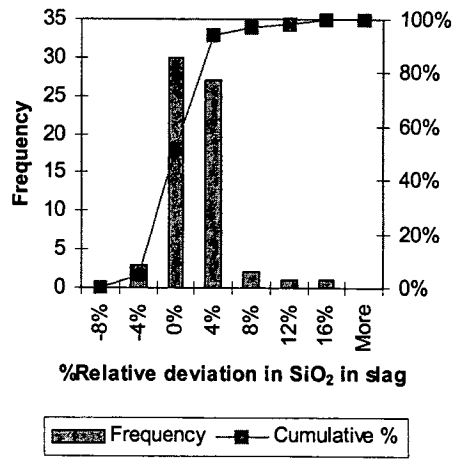

Figure 4.56: Distribution of SiO_2 in slag

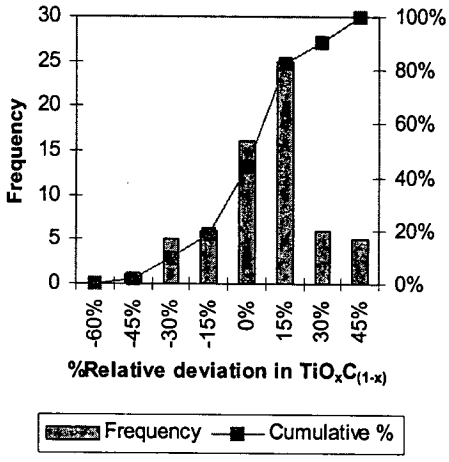

Figure 4.57: Distribution of Ti-oxycarbide in slag

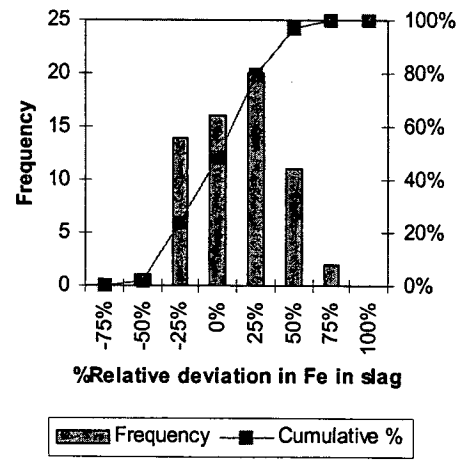

Figure 4.58: Distribution of metallic Fe in slag

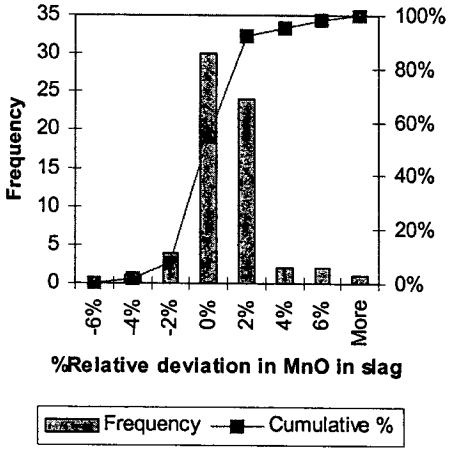

Figure 4.59: Distribution of MnO in slag

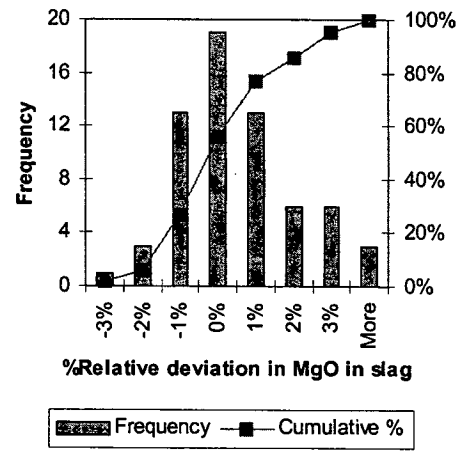

Figure 4.60: Distribution of MgO in slag

The good mixedness of the solute components of the slag is in line with expectation as the slag consists of small, non-polymerised, ionic components. Moreover, the viscosity of the slag has been noted in section 4.2.7.1 to be very low indeed, explaining the low variances observed, over and above other mixing driving forces. The mean slag assay for all the taps

analysed for spatial variance, and the mean relative deviation per tap for all the taps analysed is presented in Table 4.7.

Table 4.7: Assays and relative standard deviation associated with spatial composition variance in slag

Components	Total Ti as "TiO_2"	TiO_2	Ti_2O_3	FeO	TiO_x $C_{(1-x)}$	Fe (metal)	MnO	SiO_2	MgO	Al_2O_3
Mean Assay	85.68	50.26	28.62	10.91	3.62	0.11	1.90	1.97	0.65	1.10
s_{rel} (%mean)	1.6	1.4	2.0	1.7	15.0	25.4	1.1	1.9	1.0	1.2

The mean relative standard deviations of the different slag components other than entrained metallic iron and entrained titanium oxycarbide are too small to be significant. The slag is therefore well mixed with regard to the soluble components. It should be noted that, during the normal operating practise, all titanium is lumped together by the XRF instrument and reported as "TiO_2" and all iron is totalled and reported as "Fe_2O_3". The analysis above is therefore based on the results from the dedicated and detailed sampling campaign.

4.2.9.3 Dust

The dust generated by the DC plasma arc furnace for ilmenite smelting is accumulated in a baghouse filter which is seldom discharged. Any carbon that could have been entrained would therefore have had ample opportunity to be oxidised to CO gas. Consequently it was decided to take samples of encrusted dust from within the off-gas duct directly above the furnace and to analyse it using XRF and LECO analysis. It should be noted that it remains a grab sample, and it is assumed that the encrustation is representative of the dust leaving the furnace, which it may not be at all.

Six dust samples were taken from the furnace duct. After drying the samples had the following (normalised) analysis and corresponding relative standard deviations:

Table 4.8: Dust analysis and assay variation

Component	SiO_2	Al_2O_3	MnO	FeO	TiO_2	Na_2O	MgO	S	C
Assay (m %)	6.76	0.93	4.34	42.4	40.5	1.1	0.98	0.42	1.22
s_{rel}(%mean)	16	9	21	11	5	40	13	31	27

The FeO to TiO_2 ratio, and their absolute values are in a range similar to that of the ilmenite feedstock. One may therefore conclude that the largest portion of the dust is entrained ilmenite particles. As is the case for chromite, some concentrating effect is observed for the oxides of volatile components such as SiO_2 and MnO. The % carbon assay is highly suspect, not so much due to the accuracy of analysis, but more due to unrepresentative sampling (a larger carbon is expected due to entrainement mechanisms similar to ferrochrome production in a PAF).

4.3 Laboratory mixing studies

At the inception of the research it was considered sensible to perform a number of mixing tests in a laboratory plasma arc furnace to identify which operating conditions led to improved mixing in the furnace. The aim was to characterise the plasma and relate it to the spatial variance observed in the crucible upon quenching. The characterisation, operation and experiments performed are discussed in Appendix B and only a summary of the major findings are presented here.

Nine trials were performed on ilmenite smelting, using the same raw materials and ratios as found industrially. Figures 4.61 and 4.62 show the histograms for Fe (as a combination of FeO and entrained Fe) and SiO_2 in the slag phase respectively.

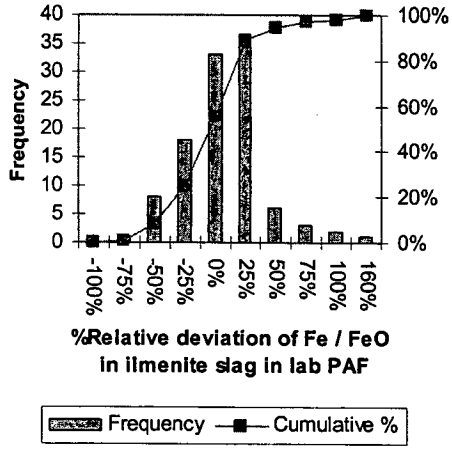

Figure 4.61: Distribution of iron in slag.

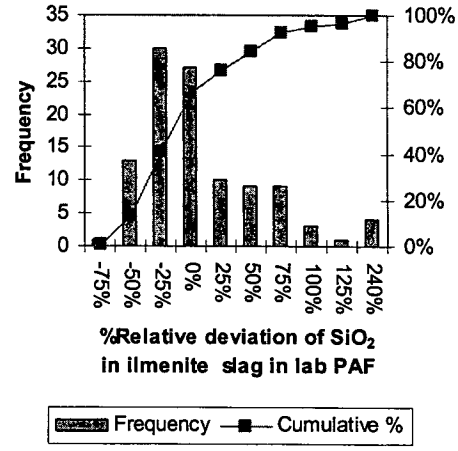

Figure 4.62: Distribution of silica in slag.

Figures 4.62 and 4.63 both show a very large spread in composition relative to the average composition of the melt in the crucible. This increased variance was expected for the laboratory furnace for reasons as discussed above. The non-normal distributions may be

attributed to the few (9) runs performed. Normally 8 samples were drilled at random positions across the cross section of the solidified melt. The pig iron metal was analysed similarly and the distributions of the relative deviations of S and Si from the average bulk chemistry is depicted in the histograms in Figures 4.63 and 4.64 respectively.

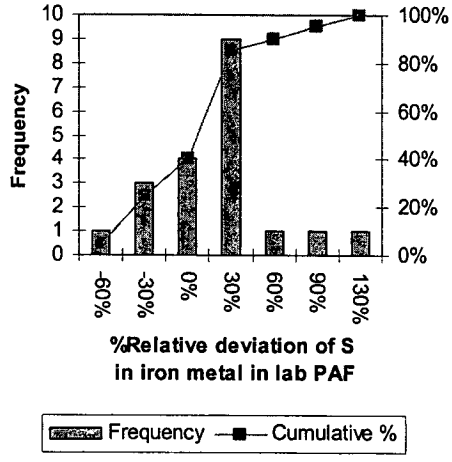

Figure 4.63: Distribution of iron in the slag.

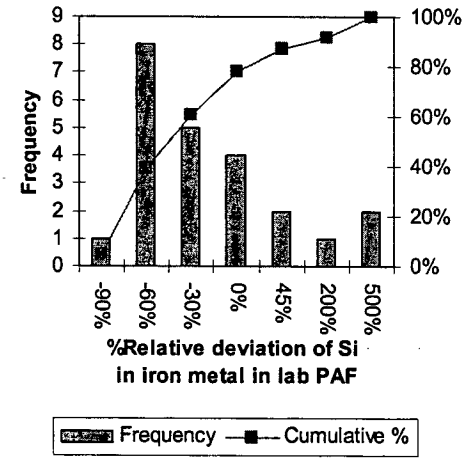

Figure 4.64: Distribution of silica in slag.

These two contaminants show the highest variance, as found in the industrial furnaces. However, the spreads for both elements are larger than found in industry. A summary of the relative standard deviations is given in Table 4.9.

Table 4.9: Mean relative deviations from bulk chemistry for ilmenite smelting in a laboratory PAF.

Component	Fe	Ti	Mn	Si	S
%σ (metal)	4%	75%	28%	86%	32%
%σ (slag)	24%	16%	15%	42%	49%

4.4 Summary of the observations made in the Chapter 4

It was shown that the alloy from plasma arc furnaces can be poorly mixed with regard to the dilute components, of which Si and S always showed the largest deviations. Although the slags showed less deviation in mixedness, they were also not perfectly mixed. The heterogeneity of the Si in the alloy melt could be correlated to the degree of alloy subcooling relative to the alloy liquidus, and therefore melt viscosity. However, it is noted that viscosity is not the only factor to consider during mixing, but also gas generation, Marangoni flow, and

electromagnetic flow. Laboratory studies also showed large spatial variations in the melt, although the results cannot be extrapolated to industrial situations.

The variances associated with the observed melt heterogeneity will subsequently be used in processing and interpretation of the data from the industrial operations.

4.5 Nomenclature of Chapter 4

C = concentration (%)

$\overline{C}$ = sample average concentration (%)

C_∞ = population average concentration (%)

D_{mass} = mass diffusivity ($m^2.s^{-1}$)

$D_{thermal}$ = thermal diffusivity ($m^2.s^{-1}$)

n = number of samples

s = sample standard deviation (%)

s_{rel} = relative sample standard deviation

Cp = specific heat capacity (kg. J^{-1} K^{-1})

x = mole fraction

ρ = density (kg. m^{-3})

t = time for a liquid to break up and become fully homogenized (s)

$d_{element}$ = liquid element diameter before breakup due to mixing (m)

$k_{thermal}$ = (W. m^{-1} K^{-1})

σ = population standard deviation

χ^2 = Chi-squared function

η , η_S , η_L = dynamic viscosity in general, of slurry and of liquid-only melts ($kg.m^{-1}s^{-1}$)

η_R = dynamic viscosity ratio

R = Einstein-Roscoe equation parameter

Φ_S = volume fraction of solids in solid-liquid mixture

A_η , E_η = pre-exponential and activation energy parameters of the viscosity model

5 SYSTEM IDENTIFICATION, DATA RECONCILIATION AND ARTIFICIAL INTELLIGENCE

"When you are working towards the solution of a problem it always helps if you know the answer"
"Provided of course, you know there is a problem"
(Rule of accuracy and its corollary, Kelly and Spottiswood, 1982)

"Artificial Intelligence is no match for natural stupidity"
(Anonymous, 2002)

"If the brain was so simple we could understand it, we would be so simple that we couldn't"
(Lyall Watson, 2002)

5.1 Introduction

A significant degree of uncertainty can be associated with industrial data, be it due to poor mixedness of the material sampled (as shown in Chapter 4), poor sampling practice, inaccurate measurements, inaccuracy in the assaying method and, in the cases where certain data are still captured manually, typing errors. A stated in Chapter 1, it makes no sense to develop a model which supposedly predicts process behaviour to a higher accuracy than the inherent total variance associated with a variable.

Therefore, a first step towards the development of empirical or semi-empirical predictive models is to reconcile the data within their inherent variance. A degree of dynamic prediction could be incorporated if consecutive measurements show dynamic structure. It is the aim of this chapter is to indicate how this may be achieved for bath type smelting furnaces.

Transient variations become apparent when one observes a time series of the feed and product materials. One can therefore not discuss the transient variations in the metallurgical data without referring to the tools one requires to interpret time series. As the techniques to analyse time series fall within the domain of systems identification, the basic principles of systems identification need to be discussed. These would include a discussion of the descriptive

statistics, the power spectrum analysis of raw data time series and the exploration of coincidental linear relationships in the data, through correlation analysis and inspection. Furthermore, the basic definitions and concepts for subsequent systems modelling will be discussed. It should also be clear that the spatial variations discussed in Chapter 4 are implicitly incorporated in transient behaviour – each data point on a time series is associated with an uncertainty which could be related to the state of mixedness of the material from which the sample was drawn.

5.2 Mathematical foundation of dynamic behaviour and time series analysis

The textbook by Kanjilal (1995) will be the main literature source which will be used as background to systems identification and predictive control, unless otherwise stated.

5.2.1 The stochastic nature on industrial processes

The word stochastic is of Greek origin and relates to the word guess. A stochastic process is therefore a random process evolving in time whose behaviour can be analysed statistically, but cannot be predicted precisely (Kanjilal, 1995). If the uncertainty or unknown disturbance in an observed process is described by a stochastic process and, due to the presence of the uncertainty, the overall process is also called a stochastic process. As the statistical representation of the uncertainty becomes more accurate, the probability increases of the model response to be close to the actual response of the process. It is important to note that by a stochastic process it is not meant that the process is purely random, but that some underlying trends exist, with varying degrees of randomness superimposed onto them. Some of the basic concepts and basic types of processes need to be discussed.

5.2.1.1 Autocovariance

If a measurement is characterised by a time series $\{x(k) = x(1), x(2), \ldots, x(N)\}$, then only for a purely random series will neighbouring values be independent. In general the neighbouring values will be correlated. In addition to specifying the mean (Eq. 4.2), and the variance (Eq. 4.3), as defined in the previous chapter, it is also required to specify the autocovariance. Note that Chapter 4 dealt with spatial variance (not a time series as discussed here). The autocovariance function is specified as:

$$R(k, k+\tau) = E\{x(k)x(k+\tau)\} \qquad \forall \quad k \in T \tag{5.1}$$

In practice, R can be estimated by:

$$R(\tau)=\frac{1}{N}\sum_{k=1}^{N-\tau}[x(k)-\bar{x}][x(k+\tau)-\bar{x}] \tag{5.2}$$

A plot of $R(\tau)$ versus τ is called the sample autocovariance function of a time series. It is sometimes convenient when comparing series of different scales to normalize $R(\tau)$ by dividing by the variance $\sigma^2 \cong s^2 = R(0)$ The sample autocorrelation function is therefore:

$$r(\tau)=\frac{R(\tau)}{R(0)} \tag{5.3}$$

The autocorrelation function is useful in some situations because it gives a visual picture of the way in which the interdependence in the series dampens out with lag or separation of τ between points in the series. On the other hand, the autocorrelation function is sometimes difficult to interpret because neighbouring values can be highly correlated.

5.2.1.2 Discrete time stochastic processes

A stochastic process $X(t)$ belongs to a family of random variables $\{x(t),\ t \in T\}$, where the random variables are indexed with the parameter t, all of whose values lie in an index set T. The random variables may be scalars or vectors. If T is a set of discrete time instants, that is $T = \{k+1 : \ldots, -1, 0, 1, \ldots\}$, the process k is called a discrete time stochastic process. The sampling period is chosen as time units which are distinct, but not necessarily equispaced. A stochastic process is called a Gaussian or Normal process if for any n points: $k_1, k_2, \ldots, k_n$ in T, the random variables $x(k_1), \ldots, x(k_n)$ are jointly of Gaussian or Normal probability density distribution, being:

$$P(x)=\frac{1}{\sqrt{2\pi\sigma}}\exp\left(-\frac{(x-\bar{x})^2}{2\sigma^2}\right) \tag{5.4}$$

The probability law for the joint density function a Gaussian stochastic process is completely specified by two positive numbers, being the mean value $\bar{x}$ and the autocorrelation function R.

$$\bar{x}(k)=E\{x(k)\} \qquad \forall \quad k \in T \tag{5.5}$$

$$R(k_1,k_2)=E\{x(k_1)x(k_2)\} \quad \forall \quad k \in T \tag{5.6}$$

where $E \equiv$ expected value of a probability density function. A subset of a Gaussian vector is also Gaussian. Gaussian variables retain their Gaussian character under linear transformation.

5.2.1.3 Stationary processes

A stochastic process, $x(k)$, is said to be strict sense stationary when its probability density functions are independent of the shift in the time origin, and therefore two processes $x(k)$ and $x(k+\tau)$ have the same probability density function for any τ. Two processes, say an input $x(k)$ and an output $x(k)$, are jointly stationary if their joint statistics are time invariant. Therefore the joint statistics are the same as that of $x(k+\tau)$ and $y(k+\tau)$ for any τ. Moreover, the process $x(k)$ is said to be wide sense (or weak sense) stationary if its mean is constant and its autocorrelation depends only on the time difference, expressed as:

$$\bar{x}(k) = E\{x(k)\} = const. \qquad \forall \quad k \in T \tag{5.7}$$

$$R(k, k+\tau) = E\{x(k)x(k+\tau)\} = R(\tau) \qquad \forall \quad k \in T \tag{5.8}$$

Therefore, the wide sense stationarity does not require the probability density function to be invariant, unlike the strict sense stationary process. Moreover, stationary processes for which the time averages equal probabilistic averages, are called ergodic. If the discrete time process $\{x(k),\ k = 1, 2, \ldots, N\}$ is ergodic, it can be completely described by its expectation:

$$\bar{x} = E\{x(k)\} = \lim_{N\to\infty} \frac{1}{N} \sum_{k=1}^{N} x(k) \tag{5.9}$$

and by its autocorrelation function

$$R = E\{x(k), x(k+\tau)\} = \lim_{N\to\infty} \frac{1}{N} \sum_{k=1}^{N} x(k) \cdot x(k+\tau) \tag{5.10}$$

Furthermore, if a process is covariance stationary process $\{x(k)\}$, it may be decomposed as:

$$x(k) = x_d(k) + x_n(k) \tag{5.11}$$

where x_d is the purely deterministic component and x_n, the purely stochastic component, which is known as Wold's decomposition (Kanjilal, 1995).

5.2.1.4 Markov Processes

According to the Markov theory, the future only depends on knowledge of the present and not on the knowledge of the past. A stochastic process $\{x(k),\ k \in T\}$ is called a Markov process, if:

$$P\{x(k+1) \mid x(k), x(k-1), \ldots, x(k_0)\} = P\{x(k+1) \mid x(k)\} \tag{5.12}$$

Therefore, the conditional probability density function for a future value $x(k+1)$ only depends on its present value $x(k)$ and not any value further into the past. The joint probability density function of the Markov sequence $\{x(k+1), x(k), x(k-1), \ldots, x(k_0)\}$ is completely specified in term of the initial probability density function $P\{x(k_0)\}$ and the transition density function $P\{x(k+1) \mid x(k)\}$. Therefore: $P\{x(k+1), x(k), x(k-1), \ldots, x(k_0)\} =$

$$P\{x(k+1) \mid x(k)\} \cdot P\{x(k) \mid x(k-1)\} \cdot \ldots \cdot P\{x(k_0+1) \mid x(k_0)\} \tag{5.13}$$

This Markov process is also sometimes called a first order Markov sequence. The underlying principle may be extended and a second order Markov sequence may be defined as one requiring the two most recent information elements to describe the future, and so forth for higher order Markov sequences. A Markov sequence has the properties that a subset of a Markov sequence remains a Markov sequence, and if a Markov sequence is reversed in time, it still retains Markov property. A stochastic process is called a Gauss-Markov sequence if it has a Gaussian distribution and, at the same time, is a Markov sequence.

5.2.1.5 White noise process

A stochastic sequence $\{x(k+1), x(k), x(k-1), \ldots, x(k_0)\}$ is a purely random or white noise sequence if $x(k_i)$ and $x(k_j)$ are totally independent for any $i \neq j$. For such processes, the conditional density equals the marginal density, therefore:

$$P\{x(k_n) \mid x(k_{n-1})\} = P\{x(k_n)\} \tag{5.14}$$

Therefore white noise processes do not possess memory, as say Markov processes, and the present is independent of the past as the future is independent of the present. The autocorrelation is given by :

$$E\{x(k_i)x(k_j)\} = R\delta_{ij} \tag{5.15}$$

Where δ_{ij} is the Kronecker delta function:

$$\delta_{ij} = \begin{cases} 1 & \forall \quad i = j \\ 0 & \forall \quad i \neq j \end{cases} \tag{5.16}$$

Moreover, when white noise has a Gaussian distribution, it is named a white Gaussian process, which is completely specified by the mean and covariance matrix.

5.2.1.6 Some system definitions

A system or process with input u and output y is said to be causal if the output is dependent on the inputs up to that time. A system is said to be time invariant if the response of the system, therefore the relationship between the output and the input, does not vary with time (it is important to notice that the relationship does not change with time, it does not imply that the variables themselves do not change with time). A system is said to be linear if its inputs and outputs satisfy the principle of superposition. If the process characteristics / relationships do not vary with time, the process is called a deterministic process. Most actual processes are not deterministic and hence not exactly known. There is therefore a factor of uncertainty in the process. Stochastic control concerns control of processes in the presence of uncertainty.

With the background of the types of stochastic processes, one can proceed to dynamic modelling of the data. Three approaches exist, namely transfer function models, models based on frequency domain analysis and structural models.

5.2.2 Transfer function models

Transfer function models normally relates a measured output $y(k)$, (or $\Delta y(k)$, is the case of integrated models) with the model variables types shown in Table 5.1:

Table 5.1: Model variable types

Variable	Variable type	Model type
$y(k\text{-}1),\ldots, y(k\text{-}n)$	Its own history	Autoregressive (AR)
$e(k\text{-}1), \ldots, e(k\text{-}n)$	Past model errors, $e(k\text{-}1)= y(k\text{-}1)- \hat{y}(k\text{-}1)$, where $\hat{y}(k\text{-}1)$ is the model estimate of $y(k\text{-}1)$.	Moving average (MA)
$u(k\text{-}d\text{-}1),\ldots, u(k\text{-}d\text{-}n)$	External forcing function, or exogenous variables with delay d.	Exogenous (X)
$\Delta y(k\text{-}1),\ldots, \Delta y(k\text{-}n)$	Integrated noise structure where $\Delta y(k\text{-}1) = y(k\text{-}1) - y(k\text{-}2)$	Integrated (I)

These elements can be combined to form ARMA, ARIMA, ARX, ARMAX, ARIMAX, MAX type models. If the relationship between the variables are non-linear, the model types are prefixed with a capital N, for example NARMAX would imply non-linear autoregressive moving average model with exogenous variable inputs. The model order refers to the number

of historic variables used for the AR, MA, and X components. A mixed order results when all the model components do not have the same order.

A typical autoregressive moving average model with exogenous inputs takes on the general form:

$$y(k)+a_1y(k-1)+\ldots+a_ny(k-n)=b_0+b_1u(k-d)+\ldots+b_mu(k-d-m)+e(k)+c_1e(k-1)+\ldots c_r(k-r) \tag{5.17}$$

Which could be expressed in digital control (z-transform) notation as :

$$A(z^{-1})y(k)=B(z^{-1})u(k-d)+C(z^{-1})e(k) \tag{5.18}$$

Where, for the autoregressive part:

$$A(z^{-1})=1+a_1z^{-1}+\ldots+a_nz^{-n} \tag{5.19}$$

and, for the exogenous part:

$$B(z^{-1})=b_0+b_1z^{-1}+\ldots+b_mz^{-m} \tag{5.20}$$

and, for the moving average part:

$$C(z^{-1})=1+c_1z^{-1}+\ldots+c_rz^{-r} \tag{5.21}$$

where z^{-1} is the discrete time backward shift operator.

If the model has an integrated noise structure, the structure changes to:

$$\Delta y(k)+a_1\Delta y(k-1)+\ldots+a_n\Delta y(k-n)=b_0+b_1u(k-d)+\ldots+b_mu(k-d-m)+e(k)+c_1e(k-1)+\ldots c_r(k-r) \tag{5.22}$$

or, in z-transform notation:

$$A(z^{-1})y(k)=B(z^{-1})u(k-d)+\frac{C(z^{-1})e(k)}{1-z^{-1}} \tag{5.23}$$

5.2.3 Relationship between the transfer function models and fundamental process models

The relationship between time domain continuous process models and discrete time transfer function models is described in most modern process control literature, for example the textbook by Seborg *et al.*(1989). It is not within the scope of this thesis to review the z-transforms or to design digital controllers. However, it is important to show that digital

feedforward control can be related to the transfer-function models presented above, and to continuous-time process models, which are normally used to model process on a fundamental basis. This will be done by example rather than rigid mathematical proof. Say a species *i* is consumed in a first order reaction limited by equilibrium, in a CSTR reactor. Say furthermore that the residence time distribution for non-ideal mixing could be represented by two CSTR's in series and that the deviation of the setpoint concentration is controlled through a PID controller. The dynamic behaviour of this system could be modelled by a second order differential equation of the form (Seborg *et al.*, 1989).:

$$\frac{d^2y(t)}{dt^2}+\alpha_1\frac{dy(t)}{dt}+\alpha_2[y(t)-y_\infty]-\beta_1\frac{du(t)}{dt}-\beta_2u(t)=\bar{p}+K\left[e(t)+\frac{1}{\tau_I}\int_0^t e(t)dt-\tau_D\frac{de(t)}{dt}\right] \tag{5.24}$$

Where $y(t)$ is the reactor output, y_∞ is the equilibrium limit, $u(t)$ is the forcing function (say for instance an inlet concentration of a compound), and $e(t)$ is the deviation from setpoint, while K, τ_I and τ_D are the controller settings.

Discretisation, using finite difference approximations, and in the PID in the velocity form gives:

$$\frac{1}{(\Delta t)^2}[y(k)-2y(k-1)+y(k-2)]+\frac{\alpha_1}{\Delta t}[y(k)-y(k-1)]+\alpha_2[y(k)-y_\infty]-\frac{\beta_1}{\Delta t}[u(k)-u(k-1)]-\beta_2u(k)$$
$$=K\left[(e(k)-e(k-1))+\frac{\Delta t}{\tau_I}e(k)++\frac{\tau_D}{\Delta t}(e(k)-2e(k-1)+e(k-2))\right] \tag{5.25}$$

The relationship to the ARMAX form is immediately apparent.

Grouping the discrete variables and simplifying, one obtains:

$$y(k)+a_0y_\infty+a_1y(k-1)+a_2y(k-2)=b_0+b_1u(k)+b_2u(k-1)+c_1e(k)+c_2e(k-1)+c_3e(k-2) \tag{5.26}$$

Similar solutions could be found using the *z*-transformation.

This thesis will make much use of the discrete transfer function form to dynamically model data. The discussion above shows that an equivalent differential equation exists for each finite difference equation. Although the transition from continuous differential equations to the discrete transfer function form is clear, the opposite transition from the finite difference equation to the equivalent differential equation is not trivial, mainly due to the fact that the estimated parameters of the finite difference equation are non-linear convolutions of the

parameters of the original differential equation. This would imply that fundamental parameters such as rate constants, mass transfer coefficients, volumes, inter-sample times, flows and so forth are not directly determinable for a system with complex dynamics.

Even for very simple first order systems with negligible error dynamics, the coefficients are convoluted as was shown by Eksteen *et al.* (2002a) for iron behaviour during matte converting:

$$\frac{d(M_{Fe})}{dt} = -k_L a_{\text{interface}}\left(C_{Fe} - C_{Fe,\text{Equilibrium}}\right) = -ka\left(C_{Fe} - C_{Fe}^{\infty}\right) + e \tag{5.27}$$

$$\therefore \frac{d(M_{Tot}C_{Fe})}{dt} = -ka\left(C_{Fe} - C_{Fe}^{\infty}\right) + e \tag{5.28}$$

$$\therefore C_{Fe}\frac{dM_{Tot}}{dt} + M_{Tot}\frac{dC_{Fe}}{dt} = -ka\left(C_{Fe} - C_{Fe}^{\infty}\right) + e \tag{5.29}$$

$$\therefore C_{Fe}(t)\left[M_{Tot}(t) - M_{Tot}(t-1)\right] + M_{Tot}(t)\left[C_{Fe}(t) - C_{Fe}(t-1)\right] = \Delta t \cdot ka\left[C_{Fe}^{\infty}(t) - C_{Fe}(t)\right] + \Delta t \cdot e \tag{5.30}$$

If, for the sake of illustrative purposes only, the matte mass is assumed at quasi steady state, then:

$$\frac{dM_{Tot}}{dt} = 0, M_{Tot} \approx \text{constant} \tag{5.31}$$

$$\therefore C_{Fe}(t) = \left[\frac{\frac{\Delta t \cdot k \cdot a}{M_{Tot}}}{1 + \frac{\Delta t \cdot k \cdot a}{M_{Tot}}}\right] \cdot C_{Fe}^{\infty}(t) + \left[\frac{1}{1 + \frac{\Delta t \cdot k \cdot a}{M_{Tot}}}\right] \cdot C_{Fe}(t-1) + \left[\frac{\Delta t}{1 + \frac{\Delta t \cdot k \cdot a}{M_{Tot}}}\right] \cdot e \tag{5.32}$$

$$\therefore C_{Fe}(t) = \alpha \cdot C_{Fe}^{\infty}(t) + \beta \cdot C_{Fe}(t-1) + \delta \cdot e \tag{5.34}$$

Again the convoluted nature of the parameters of the discrete transform function model is apparent. The fact that the coefficients themselves cannot be constant over an extended period of time due to the embedding of flow rates, variable mass transfer rates etc., implies that, should a linear transform model be chosen to represent the process, the parameters should be estimated recursively and continuously, say through recursive least squares. This therefore implies that adaptive prediction with recursive estimation is required.

5.2.4 Parameter estimation and the noise process

The proper characterisation of noise is important from a parameter estimation perspective. The assumed noise structure has to conform to the requirements of the estimation method,

otherwise the estimates may not be valid. A convenient assumption is that the noise process is white. In such cases the least square estimate is one of the simplest methods of estimation. Unfortunately, industrial data rarely have a Gaussian distribution. Models are then very often configured so that the noise has a convenient structure. The integrated noise structure model such as the ARI, ARIMA and ARIMAX models are produced with such an objective. The differencing of the data implicit in these models tends to result in the noise being uncorrelated with the data.

On the other hand, one should consider the characteristics of the data from a frequency content perspective. For every process, the frequency components are expected to be within a certain bounded range. Very low frequency components are responsible for the mean or zero frequency component and represents the trend component in the data. As the variations in the trend component are small, estimation of the corresponding parameters is difficult and hence should be avoided. (Kanjilal, 1995). As shall be seen in later in this chapter, the trend is estimated though fundamental nonlinear modelling, and it is not estimated from the data. It is therefore often desirable to configure the model so that the low frequency components are absent. This could be done through high-pass filtering before estimation. Simple time differencing, as is done for the integrated (I) models, is a basic form of high-pass filtering. However, two important issues have to be considered:

- The noise associated with the data often contain high frequency components;
- High pass filtering tends to accentuate high frequency noise. The effect of such noise can be eliminated by low pass filtering, of which data reconciliation as presented later in this chapter is one advanced method.

Therefore empirical modelling has to satisfy three main requirements:

- The noise component of uncertainty should be uncorrelated with the data;
- it should not be required to estimate the parameters associated with the low frequency components in the data;
- the estimator should be protected from the effects of noise associated with the data.

5.2.5 Discrete-time signals and their Fourier Transform

5.2.5.1 Sampling theorem for discrete time signals:

The sampling rate is of fundamental significance for any discrete time representation. The sampling theorem states that the sampling frequency, f_s in the number of cycles per second,

has to be at least twice the highest frequency component, f_m, in the signal ($f_s \geq 2f_m$). Therefore, if a continuous time signal is sampled at f_s, the sampled signal will contain all the frequency components of the original signal which are less or equal to $f_c = f_s/2$, where f_c is called the Nyquist critical frequency and f_s is called the Nyquist sampling rate. The theorem has two important implications:

- Only frequency components lower than f_c can be used to form the original signal.
- If the signal is not band limited to less than the f_c, all the power spectral density outside the frequency range, $-f_c < f < f_c$, spuriously moves into the frequency range ($-f_c, f_c$). This phenomenon is called aliasing or frequency folding.

5.2.5.2 The Discrete and Fast Fourier Transform (FFT)

The Fourier Transform decomposes a signal into constituent components having different frequencies. The Fourier Transform of an aperiodic signal is a linear combination of the exponential functions of frequencies occurring at the continuum of frequencies. The underlying sinusoidal signals that constitute a finite discrete data sequence could be specified using the so-called discrete Fourier Transform. For a N-long data sequence $\{x(j) = x(0), x(1), x(2), \ldots, x(N\text{-}1)$, the discrete Fourier Transform (DFT) is defined as:

$$x_\omega(\tau) = \frac{1}{N}\sum_{k=0}^{N-1} x(k)\exp\left[-i\left(\frac{2\pi\tau}{N}\right)\cdot k\right] \tag{5.35}$$

If the data are very complex, the DFT will be the complex values density functions of the N sinusoidal components having frequencies 0, $1/N$, $2/N$, …, $(N\text{-}1)/N$, where the frequencies are normalised frequencies. The Fast Fourier Transform (FFT) algorithms refer to the various efficient computer algorithms to compute the DFT.

5.2.5.3 The power spectrum

If a time series $x(k)$ could be represented by a cosine / sinusoidal function with a fundamental frequency f_0, which are multiples of the fundamental frequency $1/N$, it may be verified, using Eq. 5.2 that the variance $R(0)$ is $a^2/2$, where a is the amplitude of the cosine function. In general , if $x(t)$ consists of a mixture of cosine waves with frequencies f_i and amplitudes a_i, then the variance is:

$$R(0)=\sum_i \frac{a_i^2}{2} \tag{5.36}$$

Eq. 5.36 shows that if $x(k)$ can be regarded as a mixture of cosine waves, its variance can be decomposed into components of average power (or variances) $a^2/2$ at various frequencies f_i. If $x(k)$ is a stationary time series , the variance of the corresponding stochastic process can be decomposed into contributions at a continuous range of frequencies according to:

$$\sigma^2 = R(0) = \int_{-\infty}^{\infty} \Gamma(f) df \tag{5.37}$$

Where $\Gamma(f)$ is called the power spectrum of the stochastic process. Thus $\Gamma(f)\delta f$ is a approximate measure of the average power or variance in the frequency band f to $f + \delta f$. A spectrum with high power at low frequencies and low power at high frequencies can normally be matched with high autocorrelation function values at small lags (τ).

The spectrum and the autocovariance functions are related according to the Fourier Transform relation (after discretising the integral):

$$\Gamma\left(\frac{1}{N}\right) = \sum_{\tau} R(\tau) \exp\left(-i \cdot \frac{2\pi\tau}{N}\right) \tag{5.38}$$

and hence knowledge of the autocovariance function of the process is equivalent to knowledge of the spectrum of the process. However, in the analysis of a finite length record, such as industrial data, the spectrum is often preferable to the autocovariance function as the estimates of the spectrum at neighbouring frequencies are approximately independent, and hence the interpretation of the sample spectrum is usually easier than that of a sample autocovariance function. The FFT power spectrum becomes a useful tool to identify where the frequencies with high powers occur, how many high power frequency components are present, and if there is a clear distinction between signal and noise.

To illustrate the typical time series behaviour, non-stationarity, the effect of differencing and the use of FFT power spectra, the dynamic behaviour of silicon and carbon in PAF HCFeCr are presented as typical examples.

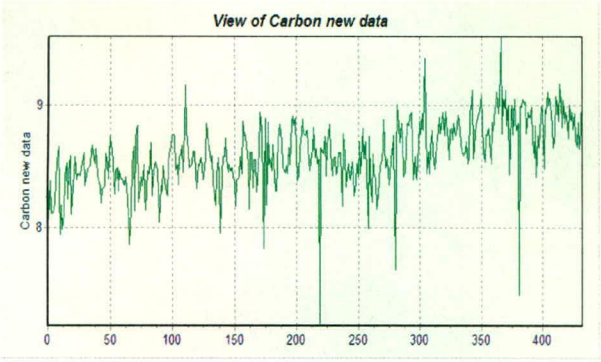

Figure 5.1: Measured carbon in HCFeCr (1st Campaign)

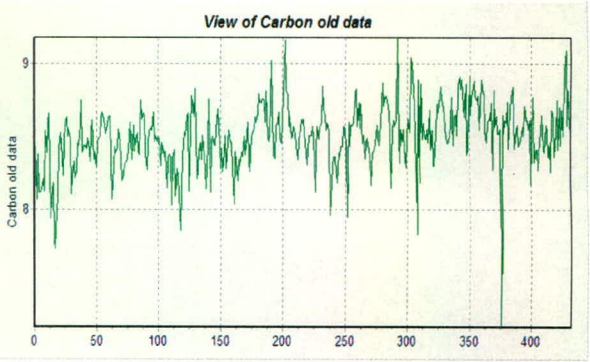

Figure 5.2: Measured carbon in HCFeCr (2nd Campaign)

There is a clear difference between the periodicity of the carbon measurements in HCFeCr for the 1st (old data) and 2nd (new data) sampling campaigns. The 1st campaign is characterised by a slowly rising tendency, with a weak periodic wave superimposed on it. The 2nd campaign appears to have stronger sinusoidal waveform around the mean. Both campaigns were done on the same DC plasma arc furnace, with the campaigns being 18 months from another. However, little could be gauged from viewing the actual data time series only and other techniques need to be exploited. The effect of differencing the data becomes apparent if one views the histograms of the data as presented in Figures 5.3 and 5.4:

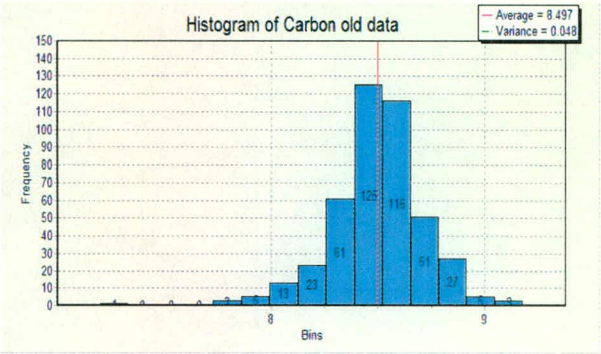

Figure 5.3 Histogram of carbon in HCFeCr times series (1st Campaign)

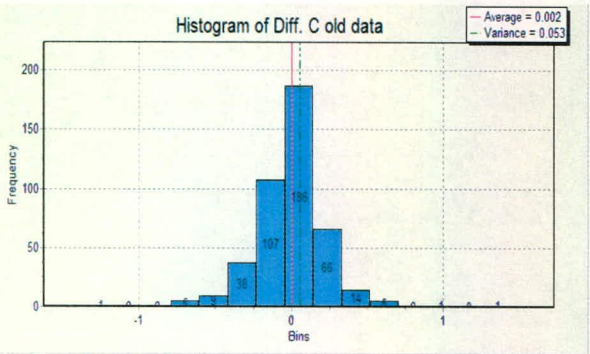

Figure 5.4 Histogram of carbon in HCFeCr times series (2nd Campaign)

Differencing of the data, i.e. giving it an integrated noise structure, results in centring the data around a zero mean, and reducing the overall variance. It is therefore a method of high pass filtering. If the data are visualised in the frequency domain through a FFT Power spectrum, the difference in frequency behaviour in the dynamics become more apparent for the two campaigns. As expected, high pass filtering results in removing the low frequency components, while amplifying the power of the high frequency components, visually demonstrating the effect of high pass filtering.

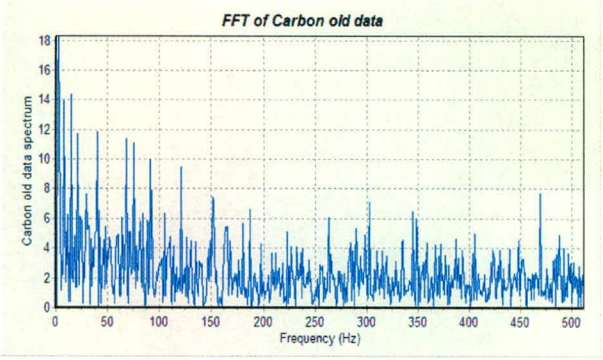

Figure 5.5: FFT Power spectrum of carbon in HCFeCr times series (1st Campaign)

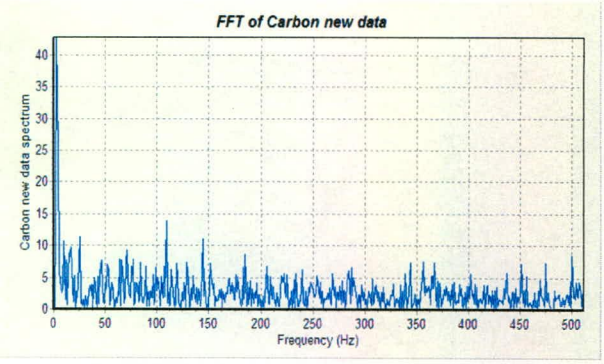

Figure 5.6: FFT Power spectrum of carbon in HCFeCr times series (2nd Campaign)

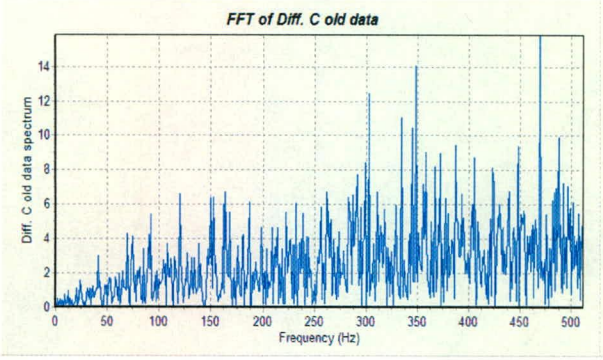

Figure 5.7: FFT Power spectrum of the dynamic difference in the carbon times series (1st Campaign)

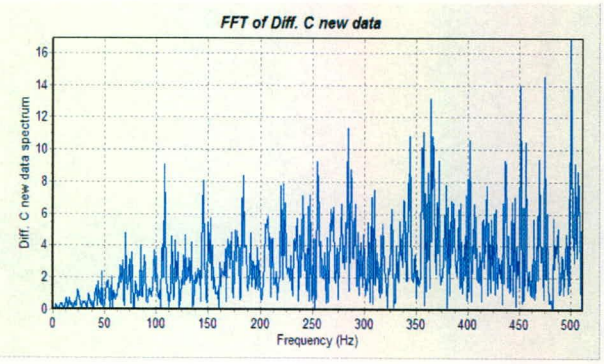

Figure 5.8: FFT Power spectrum of the dynamic difference in the carbon times series (2nd Campaign)

Comparing Figures 5.7 and 5.8 leads one to believe that the strength of the higher frequency components relative to the underlying trend component is smaller for the 2nd campaign than for the first (± 5/16 vs. 5/40). The FFT spectra of the differenced time series clearly show that the low frequency components (0-50) have nearly been removed through the differencing process. The higher order dynamics have comparatively the same power at similar frequencies. It appears therefore that during the first campaign, much of the trend (signal) component has been overshadowed by the effects of higher order effects or noise. However, the noise may have some structure and may not be totally random.

A similar study may be performed for Si which is of greater importance, from a metallurgical perspective in the production of HCFeCr. Figures 5.9 and 5.10 shows the time series behaviour of Si during the two sampling campaigns. Some periodicity is apparent, for example with a major peak above %Si =2 about every 30-40 taps (for instance at tap numbers 150, 185, 215, 240, 270 in Figure 5.9, and tap numbers 240, 275, 315, 370)

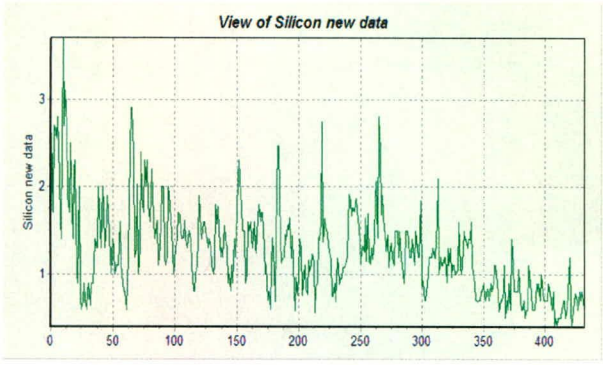

Figure 5.9: Measured %Si in HCFeCr (1st Campaign)

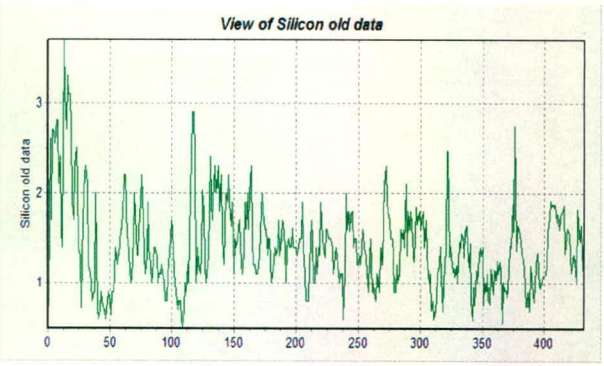

Figure 5.10: Measured %Si in HCFeCr (2nd Campaign)

The effect of differencing is much more pronounced for Si than for C, as shown in Figures 5.11 and 5.12. Differencing the time series not only centralises the histogram, but gives it a much more normal (Gaussian) appearance, while also reducing the overall variance.

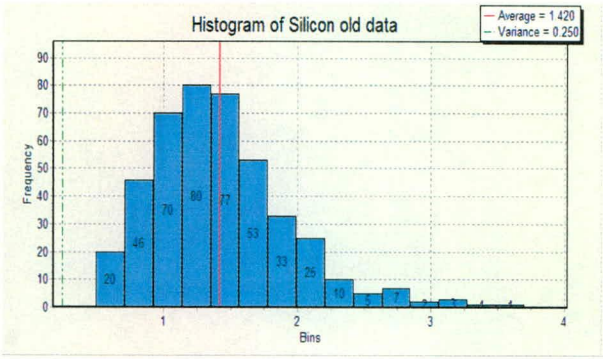

Figure 5.11: Histogram of %Si in HCFeCr times series (1st Campaign)

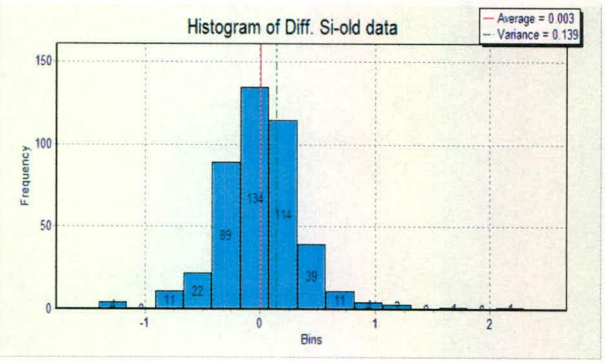

Figure 5.12: Histogram of %Si in HCFeCr times series (2nd Campaign)

Similar to the periodic behaviour of carbon, the FFT spectrum of silicon shows that the noise-to-signal ratio for the 1st campaign is significantly more than for the 2nd campaign, as shown in Figures 5.13 and 5.14. The trend component would therefore be extracted more accurately using, for instance, low pass filtering.

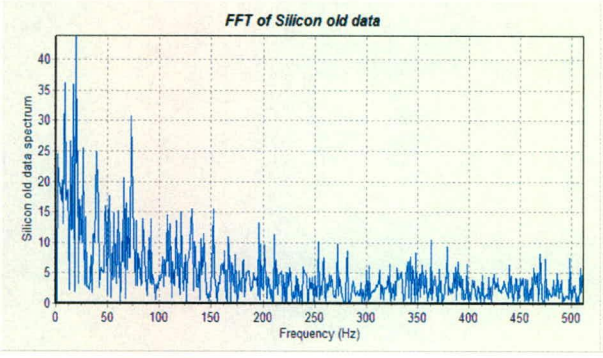

Figure 5.13: FFT Power spectrum of silicon in HCFeCr times series (1st Campaign)

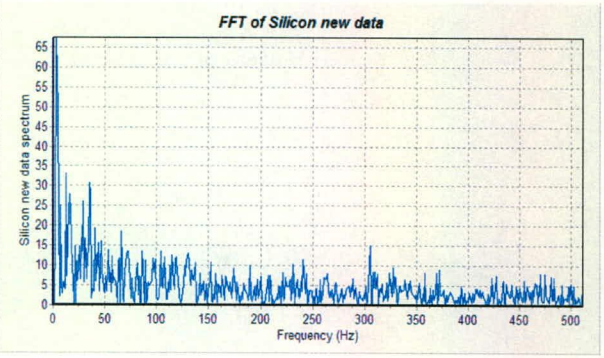

Figure 5.14: FFT Power spectrum of silicon in HCFeCr times series (2nd Campaign)

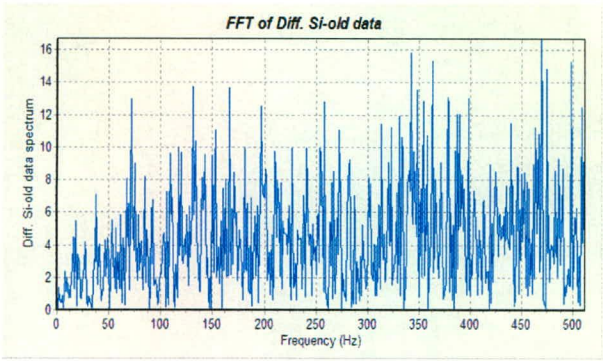

Figure 5.15: FFT Power spectrum of the dynamic difference in the silicon times series (1st Campaign)

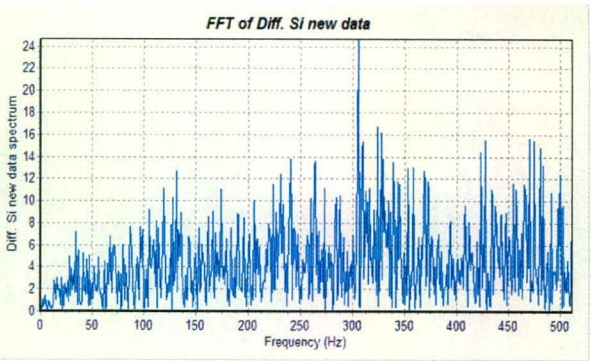

Figure 5.16: FFT Power spectrum of the dynamic difference in the silicon times series (2nd Campaign)

The effect of differencing reveals that, except for the strong peak observed at about 305 cycles for the 2nd campaign, the structures are comparable with all peaks lying below a spectrum power of 16. Just as for C, the trend component has been filtered out.

When the data from the 1st campaigns of both carbon and silicon are scaled between their respective observed minimum and maximum (new time series expressed as percentage of the range maximum-minimum) their FFT power spectra reveals additional information (Figures 5.17 and 5.18). It is clear from the FFT spectrum for carbon that the ratio of the power of high frequency components to the underlying signal is significantly less than for silicon. Carbon appears to maintain a complex frequency structure throughout the frequency range, while the power of the spectrum for silicon rapidly reduces relative to the power of the trend component. The location of significant peaks are also quite different. It should also be remembered that the certainty of each assayed element is different, due to different degrees of mixedness.

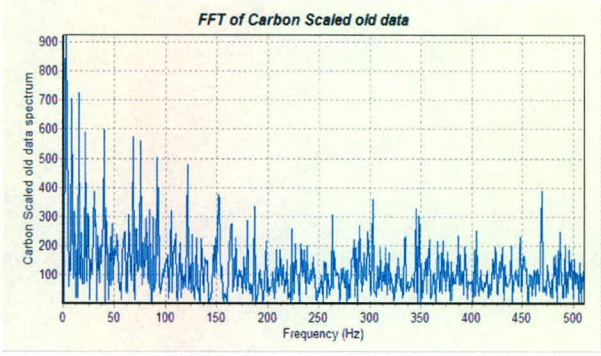

Figure 5.17: FFT Power spectrum of the carbon (scaled) times series (1st Campaign)

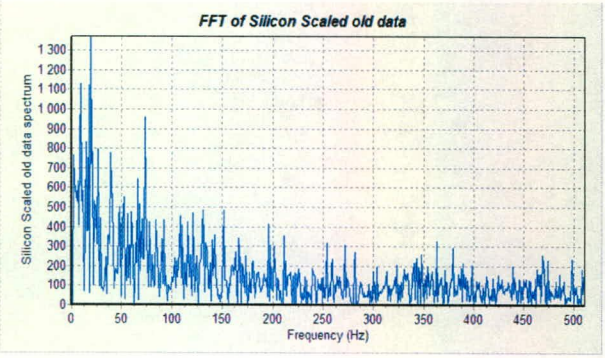

Figure 5.18: FFT Power spectrum of the silicon (scaled) times series (1st Campaign)

Similar results can be demonstrated and conclusions can be drawn for the other melt components and for the other (ilmenite smelting) furnaces.

5.3 Data reconciliation

Data reconciliation, also referred to as measurement error reconciliation, is the adjustment of a set of data in order that the quantities derived from the data obey natural laws, such as material and energy balances (Adul-el-zeet *et al.*, 2002). It is, in essence, also a low-pass filtering technique. The application of data reconciliation techniques to process data from the pyrometallurgical industry is quite recent. Bazin *et al.* (1999) applied data reconciliation techniques to the induration of iron oxide pellets. It has also been applied (Grund *et al.*, 1999) to flash smelter data in order to derive a smoothed mass and heat balance for the processing of tin concentrates. In both cases the generalised reduced gradient method (which implicitly uses Newton's method) were used to find the vector of reconciled values that minimised the sum of the squared errors of the adjustments. Measurements made on the process are adjusted in proportion to the standard error of the measurement. The adjustments are based on the availability of high degrees of freedom associated with redundant data. After adjustment one finds that the material balances and, if considered, the energy balances, are exactly satisfied within the standard deviations of the data (Boddington, 1995). The reconciled values may now be used for more advanced furnace modelling and may serve as a point of departure for the development of model predictive control.

The application of data reconciliation techniques using various error minimisation gross error detection techniques has become established in the minerals processing field and has been expanded to handle complex circuits (Cutting,1976; Lynch, 1977; Hodouin and Everell, 1980; Hodouin *et al.*, 1981; Wills, 1986; Ragot *et al.*, 1999; Hodouin and Berton, 2000).

Measurement bias is one aspect that may impact significantly on data reconciliation results. It is a type of gross error that could be caused by many sources, such as poorly calibrated or malfunctioning instruments. Process leaks can also be represented by a number of biased measurements. If data corrupted with gross errors are reconciled, the error is spread across all variables, degrading the quality of the estimates. For this reason much research has been done to detect the presence of such systematic errors and reduce their impact on the rest of the data or to remove them completely. Soderstrom *et al.* (2001) investigated a mixed integer approach for simultaneous data reconciliation and identification of measurement bias. They confirm that the problem of data reconciliation and the detection and identification of gross errors, such as measurement bias, are closely related. They subsequently developed a techniques to simultaneously perform both gross error detection and data reconciliation using mixed integer

linear programming. The basic idea was to place the gross error detection problem within the framework of data reconciliation and then change the objective function and add constraints to incorporate gross error detection in the overall strategy. Jiang and Bagajewicz (1999) investigated a strategy for the serial identification with collective compensation for multiple gross error estimation in linear steady state reconciliation. A serial identification strategy implies that the gross errors are estimated and the measurements compensated for one by one, rather than eliminated. Collective (vs. serial) compensation is viewed (Jiang and Bagajewicz 1999) as computationally too intensive and impractical, but is seen to be more accurate. In the case of the furnace system to be evaluated the system is however simple enough (compared to a complex chemical plant with multiple interacting streams and inventories) to apply collective error compensation. Outlier detection and elimination has been studied by numerous authors (Crowe 1988 and 1992, Chen and Romagnoli, 1998, Chen *et al.* 1998, Singh *et al.*, 2001) and will not be dealt with in further detail here.

Amand *et al.* (2001) pointed out the synergy between principle component analysis (PCA) and data reconciliation and combined the two analysis tools into a single method for the purpose of fault detection and process monitoring. Principle components of the covariance matrix refers to the eigenvectors associated with the largest eigenvalues and corresponds to the major trends of normal and accepted variations. Most of the variability in the process can normally be represented by the first few principle components, which spans a subspace of lower dimension corresponding to the normal process states. It is a technique often used for process diagnosis and fault detection (more so than for model based control). They suggest that data reconciliation is a recommended filtering step before the determination of the principle component (PC) projection matrix and the principle component correlation matrix between the principle components and the original variables. They found that if (unreconciled) raw data were to be used for the determination of the PC matrices, a larger number of PC's would be needed to represent the data variability at the same confidence level. Unfortunately, their research was based on simulated and not industrial data.

The two methods for data reconciliation that appear to find favour among the researchers in minerals processing are either the Lagrange Multiplier technique or a direct minimisation technique of the variance weighted sum of square error which work on the independent variables (Hodouin and Everell, 1980). The direct minimisation techniques may employ a number of non-linear programming (NLP) algorithms such as any of quadratic programming

(QP), sequential quadratic programming (SQP), the generalised reduced gradient method (GRG) which implicitly uses Newton's method, or random search methods, each algorithm having each own set of advantages and disadvantages. An exhaustive evaluation of the algorithms, based on efficiency, reliability, global convergence, performance in solving degenerate problems, performance in solving ill-conditioned problems, performance in solving indefinite problems, sensitivity to variations in the problem and ease of use, has shown that the GRG and SQP methods significantly outperformed the other algorithms (Edgar and Himmelblau, 1989).

As stated above, two general approaches are followed to determine the required adjustments to process data, being the direct minimisation of the sum square of the variance-weighted adjustments and the application of the Lagrange Multiplier method which in this case is applied to the minimisation of the weighted closure residuals. Each method will be briefly discussed in turn. Both are essentially weighted least squares techniques which inherently assume that the errors (adjustments) are normally distributed and unbiased. Since it is not known a priori that the errors are of the normal type and unbiased, and since the variances can, at best, only be estimated, the least squares approach is still expected to give a reasonable solution (Wiegel, 1972). The bias and normality of the adjustments will be evaluated post-reconciliation.

Abu-el-zeet *et al.* (2002) also showed how model predictive control could be enhanced by using dynamic data reconciliation. Their research investigates the control of a theoretical CSTR system with random noise imposed on it. Much development would be required to make this approach applicable to furnace data, especially due to the low frequency that data becomes available, in comparison to a theoretical system. This method was therefore not applied.

In an attempt to find if dynamic relationships exist between data reconciliation adjustments, one may investigate the time series behaviour of the adjustments. Should there by any dynamic structure in the error / adjustment on a day-by-day, or tap-to-tap basis, it would imply that an estimate of future adjustments may be made before the future data is available to be reconciled. Dynamic structure in the error would imply that the error does not follow a random or white noise sequence, that is where any event in the sequence is completely

independent of any preceding event (Kanjilal, 1995; Bonekamp *et al.*, 1999; Reuter and Grund, 2001).

5.4 Direct minimisation of the sum of squares of weighted adjustments

In its most general form, the GRG approach seeks to the minimise a non-linear function $J(\mathbf{x})$, subject to linear (or linearised) constraints. In general, the measurement vector (x_m) may be written as:

$$x_m = x_{adjusted} + \varepsilon \tag{5.39}$$

where $x_{adjusted}$ is the vector of the adjusted (true) values of the variables, ε, the vector of unbiased random measurement errors normally distributed with a zero mean and covariance matrix V.

The reconciliation problem can therefore be formulated as a constrained least squares estimation problem where the weighted sum of adjustments is to be minimised:

$$\min_{x_{adjusted}} \left(x_m - x_{adjusted}\right)^T V^{-1} \left(x_m - x_{adjusted}\right) \tag{5.40}$$

subject to

$$f\left(x_{adjusted}\right) = 0 \tag{5.41}$$

where $V \in \Re^{n_x \times n_x}$ is the covariance matrix of the measured variables x_m. In our case the linear constraints arise from the linear mass balance equations for the different elements of the system, and the overall material balance. When the data may be biased, the systematic bias may be estimated as a parameter, where the objective function is reformulated as follows:

$$\min J(x) = \min \sum_{i=1}^{k} \frac{\left(\bar{x}_i - \left(x_m - \hat{b}_i\right)\right)^2}{V_i} \tag{5.42}$$

subject to

$$\begin{aligned} & f\left(\bar{x}_i\right) = 0 \\ & \bar{x}_{l,i} \le \bar{x}_i \le \bar{x}_{u,i} \qquad \forall i \\ & \hat{b}_{l,i} \le \hat{b}_i \le \hat{b}_{u,i} \qquad \forall i \end{aligned} \tag{5.43}$$

In the case where both total flows as well as compositions are to be adjusted, equation (5.42) becomes:

$$\min J(x,Q) = \min\left\{\sum_{j=1}^{n}\frac{\left(\overline{Q}_j - \left(Q_m - \hat{b}_j\right)\right)^2}{V_j} + \sum_{j=1}^{n}\sum_{i=1}^{k}\frac{\left(\overline{x}_{ij} - \left(x_{m,j} - \hat{b}_{ij}\right)\right)^2}{V_{ij}}\right\} \quad (5.44)$$

subject to the same constraints as (5.43) with the additional total mass balance constraint:

$$\sum_{j=1}^{n}\overline{Q}_j = 0 \quad (5.45)$$

Soderstrom *et al.* (2001) shows that the optimisation may lead to non-zero bias values $\hat{b}_i$ even though no actual bias may be present. They therefore expand their algorithm to make the inclusion of the bias variable a discrete event. For each variable they associate a binary variable (0, 1) to indicate the existence of a bias. A nonzero value for the binary variable would signify that the corresponding variable is biased. Constraints could then be added to ensure the magnitude of the estimated bias is zero if the binary variable is turned off. A threshold parameter could then be added to eliminate those cases considered which have a very small bias.

The GRG algorithm, as well as the SQP algorithms for minimisation is described by Edgar and Himmelblau (1989) and is incorporated into most general optimisation software, including the Premium Solver Platform ™ for Microsoft Excel, which is the software used for the optimisation in this thesis.

5.5 Minimisation of weighted closure residuals through the application of the Lagrange Multiplier Method

This method determines the minimum of the variance weighted closure residuals of the mass balance equations through direct analytical differentiation of the Lagrangian, to be defined later. The basis for this method can be found in many textbooks, and the approach of Wills (1997) is used and expanded upon. For the purposes of the derivation in this thesis, the furnace system is defined as:

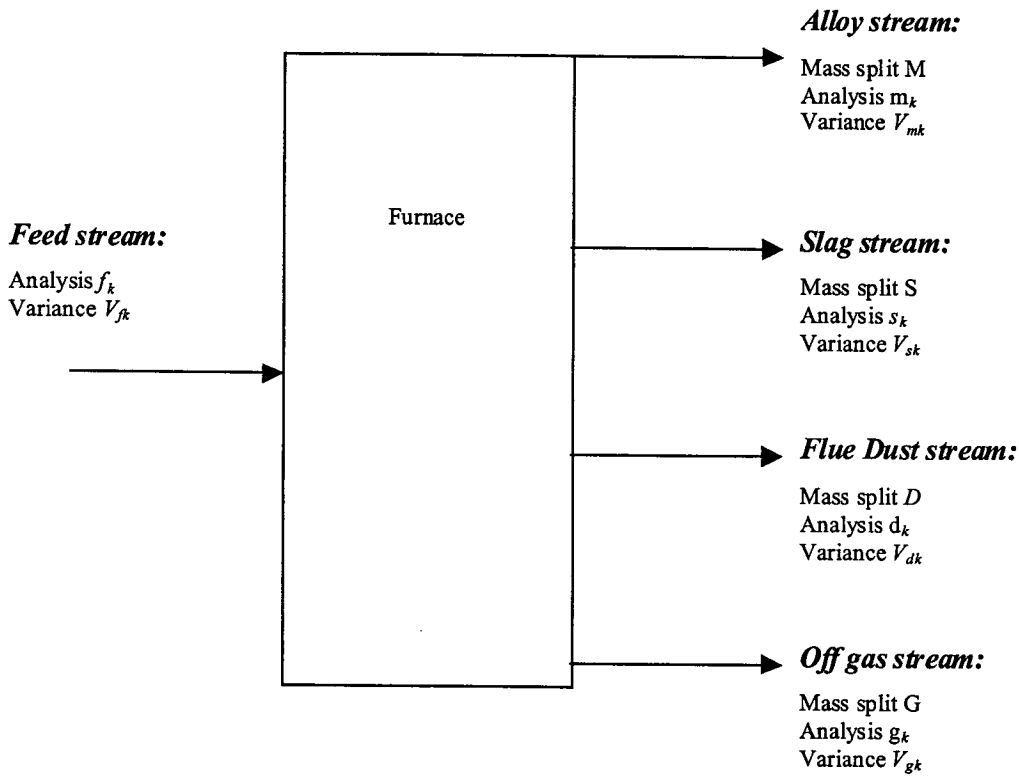

Figure 5.19: Combined feed stream and product streams from the furnace (daily basis)

Where the element mass balances can be represented by the following equation:

$$F.f_k - M \cdot m_k - S \cdot s_k - D \cdot d_k - G \cdot g_k = r_k \qquad (5.46)$$

Where: k: Chemical Element

r_k: Difference from the balance for element k

For the purpose of mass balance reconciliation, the mass split ratios will be expressed as a fraction of the total product or feed mass, and the elemental values will be expressed as mass. Eq. 5.46 may be further manipulated to give us the result:

$$(f_k - g_k) - M \cdot (m_k - g_k) - S \cdot (s_k - g_k) - D \cdot (d_k - g_k) = r_k \qquad (5.47)$$

Following the concept of the least squares approach, we want to minimize the sum of the difference from the balance (r_k) for each element. This enables us to obtain adjusted values for M, S, D, and G, and for the stream compositions, thus satisfying the following equation:

$$\hat{f}_k - \hat{M} \cdot \hat{m}_k - \hat{S} \cdot \hat{s}_k - \hat{D}\hat{d}_k - \left(1 - \hat{M} - \hat{S} - \hat{D}\right)g_k = 0 \qquad (5.48)$$

On a mathematical basis, the concept of the least squares approach can be followed by the minimization of the following equation, with taking into account the data variance:

$$\min_{SSQ} = \sum_{k=1}^{n} \frac{(r_k)^2}{V_{rk}} \tag{5.49}$$

where:

$$V_{rk} = \left(\frac{\partial r_k}{\partial f_k}\right)^2 V_{fk} + \left(\frac{\partial r_k}{\partial m_k}\right)^2 V_{mk} + \left(\frac{\partial r_k}{\partial s_k}\right)^2 V_{sk} + \left(\frac{\partial r_k}{\partial d_k}\right)^2 V_{dk} + \left(\frac{\partial r_k}{\partial g_k}\right)^2 V_{gk} \tag{5.50}$$

which equates to:

$$V_{rk} = V_{fk} + V_{mk}\hat{M}^2 + V_{sk}\hat{S}^2 + V_{dk}\hat{D}^2 + V_{gk}\left(1 - \hat{M} - \hat{S} - \hat{D}\right)^2 \tag{5.51}$$

and

$$\begin{aligned}(r_k)^2 =& (f_k - g_k)^2 - 2\cdot M(m_k - g_k)(f_k - g_k) - 2\cdot S(s_k - g_k)(f_k - g_k) - 2\cdot D(d_k - g_k)(f_k - g_k) \\ &+ C^2(m_k - g_k)^2 + 2\cdot M\cdot S(s_k - g_k)(m_k - g_k) + 2\cdot M\cdot D(d_k - g_k)(m_k - g_k) \\ &+ S^2(s_k - g_k)^2 + 2\cdot S\cdot D(d_k - g_k)(s_k - g_k) + D^2(d_k - g_k)^2\end{aligned} \tag{5.52}$$

By the minimization of equation (5.52), we are able to obtain the adjusted values for M, S and D by finding the respective partial derivatives for the variables and equalling them to zero.

$$\frac{\partial SSQ}{\partial M} = \hat{M}\sum\frac{(m_k - g_k)^2}{V_{rk}} + \hat{S}\sum\frac{(s_k - g_k)(m_k - g_k)}{V_{rk}} + \hat{D}\sum\frac{(d_k - g_k)(m_k - g_k)}{V_{rk}} - \sum\frac{(m_k - g_k)(f_k - g_k)}{V_{rk}} = 0 \tag{5.53}$$

$$\frac{\partial SSQ}{\partial S} = \hat{M}\sum\frac{(s_k - g_k)(m_k - g_k)}{V_{rk}} + \hat{S}\sum\frac{(s_k - g_k)^2}{V_{rk}} + \hat{D}\sum\frac{(d_k - g_k)(s_k - g_k)}{V_{rk}} - \sum\frac{(s_k - g_k)(f_k - g_k)}{V_{rk}} = 0 \tag{5.54}$$

$$\frac{\partial SSQ}{\partial D} = \hat{M}\sum\frac{(d_k - g_k)(c_k - g_k)}{V_{rk}} + \hat{S}\sum\frac{(d_k - g_k)(s_k - g_k)}{V_{rk}} + \hat{D}\sum\frac{(d_k - g_k)^2}{V_{rk}} - \sum\frac{(d_k - g_k)(f_k - g_k)}{V_{rk}} = 0 \tag{5.55}$$

It is possible to solve for the above variables by expressing the terms in the form of a matrix.

$$\begin{bmatrix} \sum\frac{(m_k - g_k)^2}{V_{rk}} & \sum\frac{(s_k - g_k)(m_k - g_k)}{V_{rk}} & \sum\frac{(d_k - g_k)(m_k - g_k)}{V_{rk}} \\ \sum\frac{(s_k - g_k)(m_k - g_k)}{V_{rk}} & \sum\frac{(s_k - g_k)^2}{V_{rk}} & \sum\frac{(d_k - g_k)(s_k - g_k)}{V_{rk}} \\ \sum\frac{(d_k - g_k)(m_k - g_k)}{V_{rk}} & \sum\frac{(d_k - g_k)(s_k - g_k)}{V_{rk}} & \sum\frac{(d_k - g_k)^2}{V_{rk}} \end{bmatrix} \times \begin{bmatrix} \hat{M} \\ \hat{S} \\ \hat{D} \end{bmatrix} = \begin{bmatrix} \sum\frac{(m_k - g_k)(f_k - g_k)}{V_{rk}} \\ \sum\frac{(s_k - g_k)(f_k - g_k)}{V_{rk}} \\ \sum\frac{(d_k - g_k)(f_k - g_k)}{V_{rk}} \end{bmatrix} \tag{5.56}$$

In matrix notation the above matrix can be written as:

$$\mathbf{A}\times\mathbf{B}=\mathbf{C} \tag{5.57}$$

The stream vector **B** can be calculated my multiplying vector **C** with the inverse of matrix **A**:

$$\mathbf{B}=\mathbf{C}\times\mathbf{A}^{-1} \tag{5.58}$$

Solving by obtaining the matrix inverse and multiplying, one therefore obtain the "best fit" values for the split fractions *M, S, D* and *G*. To find the final reconciled values we have to make incremental changes to the elemental compositions of the streams. By making these changes the goal is to further minimise the difference of the sum of the balance for each element, for example for a component in the feed (and similarly for the other phases):

$$\hat{f}_k = f_k - f_{ka} \tag{5.59}$$

$$\hat{m}_k = m_k - m_{ka} \tag{5.60}$$

$$\hat{s}_k = s_k - s_{ka} \tag{5.61}$$

$$\hat{d}_k = d_k - d_{ka} \tag{5.62}$$

$$\hat{g}_k = g_k - g_{ka} \tag{5.63}$$

The adjustments (subscript *ka*) can be calculated by minimising the following Langrangian multiplier:

$$L = SS_a + 2\sum_{k=1}^{n}\lambda_k\left(r_k - f_{ka} + \hat{M}\cdot\hat{m}_{ka} + \hat{S}\cdot\hat{s}_{ka} + \hat{D}\cdot\hat{d}_{ka} + \left(1-\hat{M}-\hat{S}-\hat{D}\right)\cdot\hat{g}_{ka}\right) \tag{5.64}$$

where:

$$SS_a = \sum_{k=1}^{n}\left(\frac{f_{ka}^2}{V_{fk}} + \frac{m_{ka}^2}{V_{mk}} + \frac{s_{ka}^2}{V_{sk}} + \frac{d_{ka}^2}{V_{dk}} + \frac{g_{ka}^2}{V_{gk}}\right) \tag{5.65}$$

Minimisation can be done by taking the partial derivatives with respect to each variable, making it equal zero and simplifying, for example with respect to the feed components (and similarly for the other phases):

$$\frac{\partial L}{\partial f_{ka}} = 2\frac{f_{ka}}{V_{fk}} - 2\lambda_k = 0 \Rightarrow f_{ka} = \lambda_k V_{fk} \tag{5.66}$$

$$\frac{\partial L}{\partial m_{ka}} = 2\frac{m_{ka}}{V_{mk}} + 2\lambda_k\hat{M} = 0 \Rightarrow m_{ka} = -V_{mk}\lambda_k\hat{M} \tag{5.67}$$

$$\frac{\partial L}{\partial s_{ka}} = 2\frac{s_{ka}}{V_{sk}} + 2\lambda_k \hat{S} = 0 \Rightarrow s_{ka} = -V_{sk}\lambda_k \hat{S} \tag{5.68}$$

$$\frac{\partial L}{\partial d_{ka}} = 2\frac{d_{ka}}{V_{tk}} + 2\lambda_k \hat{D} = 0 \Rightarrow d_{ka} = -V_{dk}\lambda_k \hat{D} \tag{5.69}$$

$$\frac{\partial L}{\partial g_{ka}} = 2\frac{g_{ka}}{V_{gk}} + 2\lambda_k \left(1 - \hat{M} - \hat{S} - \hat{D}\right) = 0 \Rightarrow g_{ka} = -V_{gk}\lambda_k \left(1 - \hat{M} - \hat{S} - \hat{D}\right) \tag{5.70}$$

Through back substitution the above results into the following equation,

$$r_k = f_{ka} - \hat{M}m_{ka} - \hat{S}s_{ka} - \hat{D}d_{ka} - \left(1 - \hat{M} - \hat{S} - \hat{D}\right)g_{ka} \tag{5.71}$$

we obtain

$$r_k = \lambda_k h_k \tag{5.72}$$

where

$$h_k = V_{fk} + V_{mk}\hat{M}^2 + V_{sk}\hat{S}^2 + V_{dk}\hat{D}^2 + V_{gk}\left(1 - \hat{M} - \hat{S} - \hat{D}\right)^2 \tag{5.73}$$

By manipulating Eq. (5.73) and substituting it into Eq. (5.71) (similarly for all the other phases), we obtain expressions for the amount by which each variable must be adjusted:

$$f_{ka} = \frac{r_k V_{fk}}{h_k} \tag{5.74}$$

$$m_{ka} = \frac{-\hat{M} r_k V_{mk}}{h_k} \tag{5.75}$$

$$s_{ka} = \frac{-\hat{S} r_k V_{sk}}{h_k} \tag{5.76}$$

$$d_{ka} = \frac{-\hat{D} r_k V_{dk}}{h_k} \tag{5.77}$$

$$g_{ka} = \frac{-\left(1 - \hat{M} - \hat{S} - \hat{D}\right) \cdot r_k V_{gk}}{h_k} \tag{5.78}$$

Subtracting the adjustments from the original values can thus represent the reconciled values. This method therefore results in explicit forms for the adjustments. The Lagrange method therefore gives an explicit method to determine the adjustments.

Despite the apparent differences between the above-mentioned approaches, it has been shown by Edgar and Himmelblau (1989) that the Lagrange Multiplier method and the GRG method can be related to each other.

5.6 Important practical aspects regarding data availability and integrity

Due to the relative shortage of data points for the Ni-Cu matte converter, the unavailability of dust and gas data, and the operation being a pilot batch operation, the data reconciliation could not be done for the matte converting. However, it will be shown how data reconciliation was performed for the ilmenite and chromite smelting operations. To aid the reconciliation process, especially for periods when all the detail information was not available, trends in samples taken from the dedicated sampling campaigns to determine material homogeneity were identified to aid and deconvolute the data during the data reconciliation process. For instance, in the case of ilmenite smelting, all the iron is reported as FeO, while the actual iron is distributed over metallic Fe and FeO. This is also the case for titanium in the high titania slags which exists as TiO_2, Ti_2O_3, and Ti oxycarbides. In chromite smelting, carbon and iron are not measured as a rule for the alloy phase. It would therefore be useful if relationships exist through which to accurately estimate the amount of a specific melt component through knowledge of the concentrations of other measured components.

It is therefore apparent that some prior knowledge of the system is required before any reconciliation can be done. Reconciliation without a good metallurgical understanding will therefore lead to erroneous results. Metallurgical understanding is required to set-up the sampling campaign and to know which components to analyse for, in what way and what information is provided with each analysis technique. For example X-ray fluorescence spectroscopy only provides the relative total amounts of each element analysed for, and reports everything as oxides, or elements. X-ray diffraction may provide a identification of the species associations in the systems, but tends to have a low accuracy when used in quantitative mode. Spark optical emission spectrometry is accurate to determine alloy constituents, except for the elements C, S, O and N and other non-metals. Combustion techniques in conjunction with infrared and optical absorption spectrometry or thermal conductivity detection are used for C, S, N and O (principle of the LECO analysers). The determination of the oxidation states of iron requires Mösbauer spectrometry or wet chemical analyses. Similarly the determination of the oxidation states of other metal oxides require wet chemical analysis. Although all these analyses could be performed on a dedicated research

campaign for a short period, the number of techniques required and costs associated with all the analyses therefore preclude their use on a frequent basis as required for typical process control. Normal process control analyses are limited to XRF and Spark OES tests (sometimes ICP-MS analyses in the case of base metal mattes). The fact that all the materials (except for the off-gas) are solid being either crystallised melts, minerals or dusts, complicates the analytic effort and increases the analysis duration significantly.

5.7 Component associations found in the feeds and products from furnaces

5.7.1 Chromite Smelting

At some stage during production, the ferrochrome producer decided not to analyse the HCFeCr for carbon and iron anymore on a routine basis, while the alloys are routinely sampled for chromium, silicon, sulphur and phosphorous. If an accurate relationship could be found between the carbon and iron and the elements that are analyzed for, it may be used to accurately estimate carbon and iron percentages in other samples.

From the dedicated sampling campaigns on both plasma arc and submerged arc furnaces, it was found that both carbon and iron could indeed be accurately estimated (taking into account that these are industrial data), as shown in Figures 5.20 and 5.21. For the HCFeCr alloys, iron and chromium shows a negative linear relationship, while carbon is parabolically related to the silicon. It is important to realise that the raw data stem from two different technologies to produce HCFeCr. The left-hand-side cluster in Figure 5.21 derives from the DC plasma arc furnace, while the remainder of the data derives from the submerged arc furnace. Figure 5.21 corresponds to the half-parabolic shape of the equilibrium relationship studied by Akyüzlü and Eric (1992) and presented in Figure 3.29.

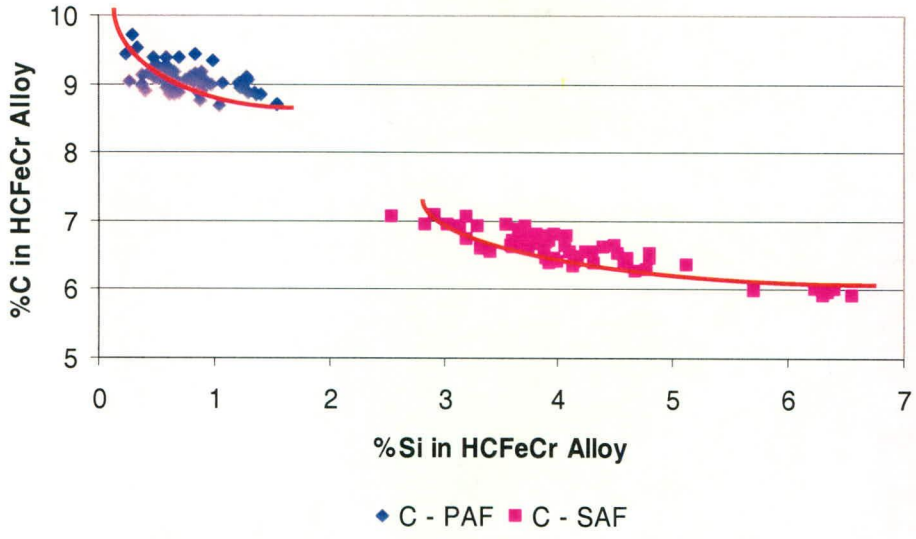

Figure 5.20: Relationship between the weight %carbon and %silicon in HCFeCr alloy samples (SAF and PAF)

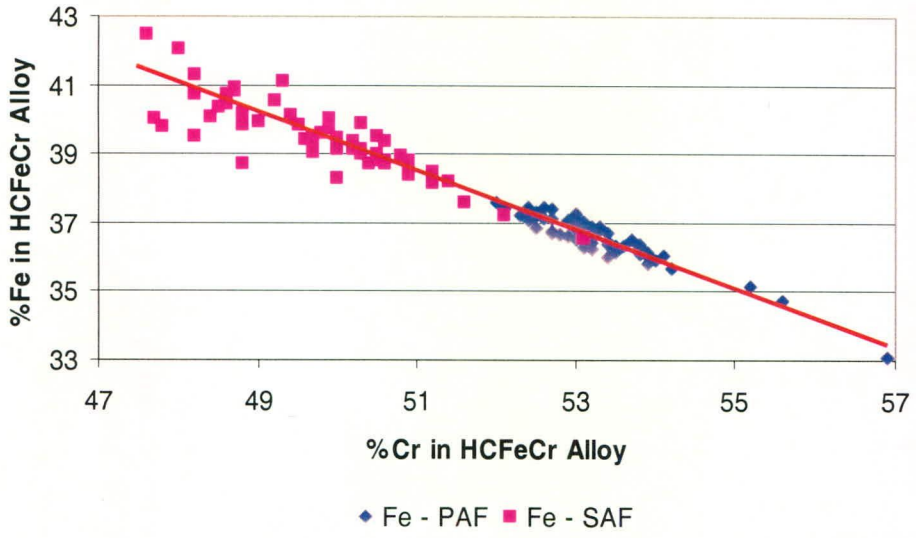

Figure 5.21: Relationship between the weight %iron and %chromium in HCFeCr alloy samples

The data presented above have also not been reconciled yet. The greater spread in data for the plasma arc furnace cluster derives from the poorer mixing found in this furnace, compared to the submerged arc furnace, as shown in the Chapter 4. It can for instance be noted that at a carbon concentration of 9.0%, the silicon assays vary from 0.3% to 1.5%. On the other hand it should be realised that the data stems from various industrial operating conditions and not a well controlled laboratory experiment. All the main components of the slag associated with HCFeCr production are analysed for and no special relationships need to be derived.

5.7.2 Ilmenite Smelting

For ilmenite smelting, both the slag and the pig-iron are analysed for the main components, but the oxidation states of the components are not known for the metal oxides in the slag. As the slag consists nearly completely of FeO-TiO_2-Ti_2O_3, with up to 40% Ti_2O_3 which significantly influences the phase equilibria, some method is required to estimate the Ti_2O_3 concentration from the bulk slag analyses. During the dedicated sampling campaign performed to gauge the melt mixedness, as described in Chapter 4, wet analyses were done to determine the amounts of Ti_2O_3 and the amounts of entrained "insoluble" titanium oxycarbides. It was fortunate that a very strong linear relationship exists between mass % Ti_2O_3 and the mass % FeO in the slag, as shown in Figure 5.22.

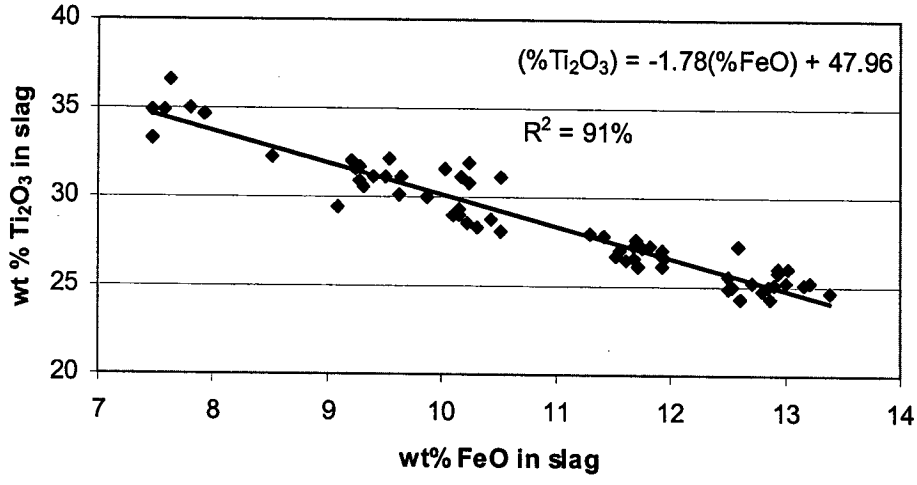

Figure 5.22: Relationship between the weight %Ti_2O_3 and %FeO in high titania slag samples

The relationship presented in Figure 5.22 also correspond with the pilot plant results by Bessinger *et al.* (1997), presented in Chapter 3 as Figure 3.35.

The relationships between undissolved, or entrained phases, and the bulk slag chemistry are not so well defined, as shown for the association of the precipitated oxycarbide (a solid solution of TiO and TiC) in Figure 5.23. Although some linear correlation exists (with correlation coefficient of 0.45) the precise quantitative relationship is less certain. As the range does not vary that much beyond 2.5 to 4.5 % (2% span), the average value of about 3.5% is of more importance than the trend in relation to other slag compounds.

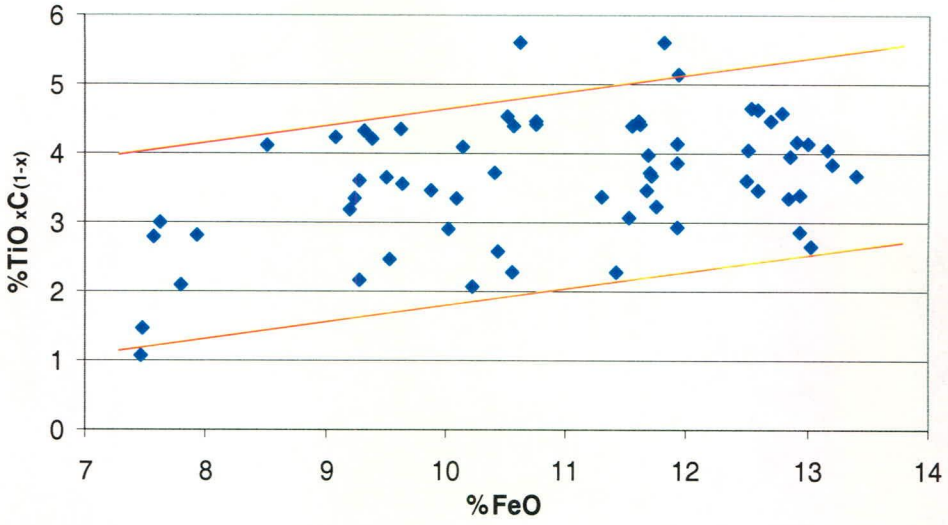

Figure 5.23: Relationship between the weight $\%TiO_xC_{(1-x)}$ and %FeO in high titania slag samples

5.8 Metallurgical process chemistry and data reconciliation

The data were reconciled for all elements flowing into and out of the furnaces on a daily basis. Data reconciliation was performed on a daily basis versus a tap-to-tap basis so as to eliminate the effect of variations in the furnace freeze lining, smoothing of the error associated with electrode consumption estimation and minimising the effect of residual inventories after tapping which constitutes a feed stream from the perspective of the subsequent tap. In so doing, the major dynamic fluctuations were smoothed out. It was assumed that the reconciliation adjustments as determined for a day would be applicable on a tap to tap basis once the variation in inventory is allowed for. The calculated adjustments are therefore on a basis of per ton of a specific element (base-element) in the feed or per ton of total feed.

Data reconciliation is done on the basis of the material balance closure of each element separately. The trends that were identified in paragraph 5.7 were used to match the oxygen to the various oxidation states of the different components in the furnace feeds and products, where the assays were not available. For the highly reducing conditions found in ilmenite smelting and chromite smelting, the oxygen in the off-gas can only be associated with carbon monoxide (mostly) or carbon dioxide (little). Insignificant amounts of free oxygen (oxygen partial pressure lower than 10^{-9} atm) can exist. Adjustments are calculated and distributed according to their variance-weights. Bias exists when a significant non-zero mode (maximum likelihood) is apparent in the adjustments. Oxygen associations (maximum and minimum)

with slag and mineral components are constrained by stoichiometric relationships - for example, there cannot be more oxygen in a specific material stream than the oxygen associated with the elements when they are all in their highest oxidation states. The dust is a significant problematic material to reconcile for, especially as some metal occurs partially in their metallic state, as well as in higher oxidation states, therefore greatly complicating the process of estimating the associated oxygen. Fortunately the quantity of dust is small compared to the other material streams. There are therefore additional hard constraints to the optimisation problem over and above the material balance constraints. Obtaining a good estimate for the oxygen entering and leaving the system is critical as it influences the total reduction-oxidation behaviour. In principle the following constraints exist:

- The linear element mass balances (equality constraints)
- All stream quantities and compositions are non-negative (variable ≥ 0 constraints)
- Stoichiometric constraints (minimum $\geq$ ratio of an element to another $\geq$ maximum)
- Additional constraints (for example no oxygen in the metal, or typical maximum and minimum bounds on the compositions).

Taking these constraints into account, an evaluation is required to determine the performance of the Lagrange method and Generalised Reduced Gradient (GRG) method with regard to reconciliation. For the comparative purposes, only the chromite smelting furnace will be used as an example for the comparison of the two methods.

5.9 Comparing data reconciliation methods

For the purpose of comparison and due to the way the Lagrange approach was structured, the variables were reconciled based on the fractional recovery of an element to a specific stream based on the fraction of the element in the total feed (where the total feed is the sum of all the fluxes, ores, reductants, recycled wastes and electrode material). The total feed was normalised to 1 ton and the measured and reconciled split ratios of the different streams are shown in Figures 5.24 to 5.28. On the other hand, the element fractions (shown for Si in Figures 5.29 to 5.30) are defined as the product of the mass fraction of an element, say for Si in the slag, s_{Si}, and the split fraction of slag, S (refer to Figure 5.1).

Figures 5.24 to 5.28 gives the output graphs for 68 consecutive days of the measured amounts, and the reconciled amounts using the GRG and Lagrangian methods. In all the

reconciled cases, mass balance closures were obtained within the inherent measurement variance. However, systematic biases did occur (such as the proportion silicon of the total feed fed to the furnace). It is apparent that the two methods very often gave significantly different reconciled values, but similar trends. The alloy (*A*), slag (*S*), flue dust (*D*) and gas (*G*) splits are based on a unit total feed. This approach is required for the Lagrange method as expressed above, but not for the GRG direct method, where adjusted values for all the feed streams may be calculated directly.

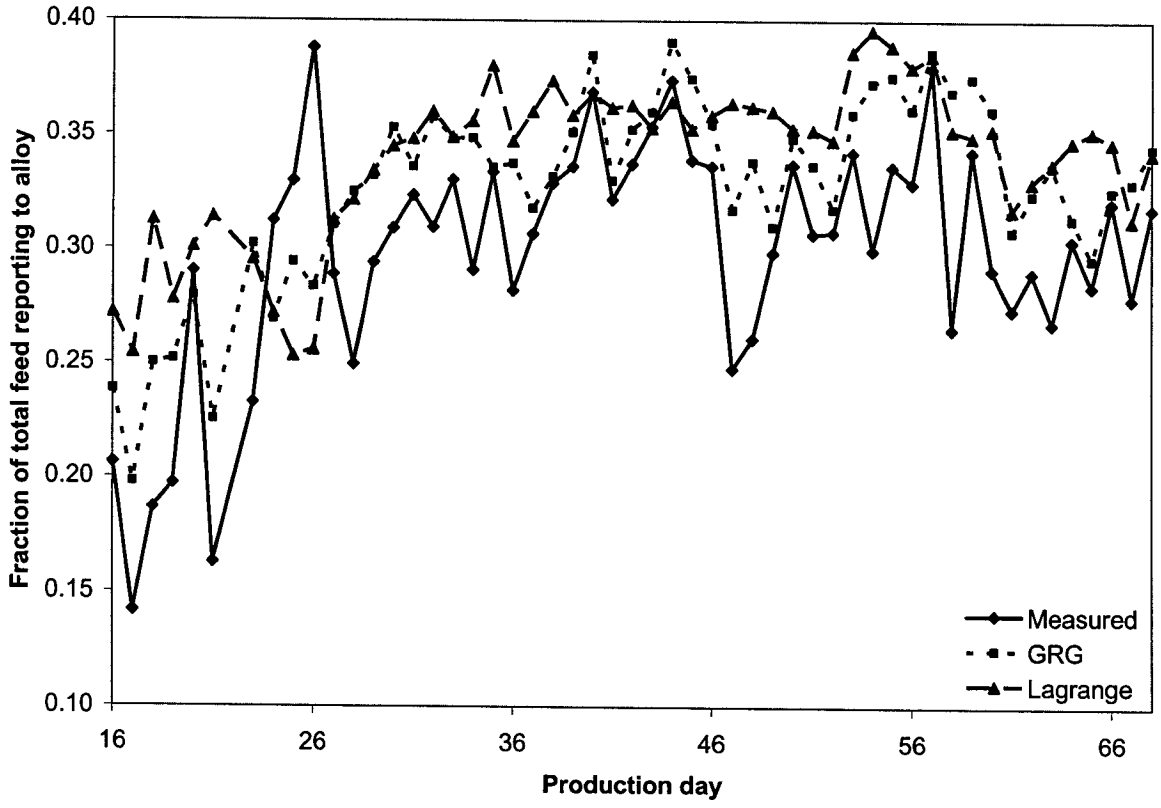

Figure 5.24: Timeseries of actual and reconciled alloy as a mass fraction of total feed

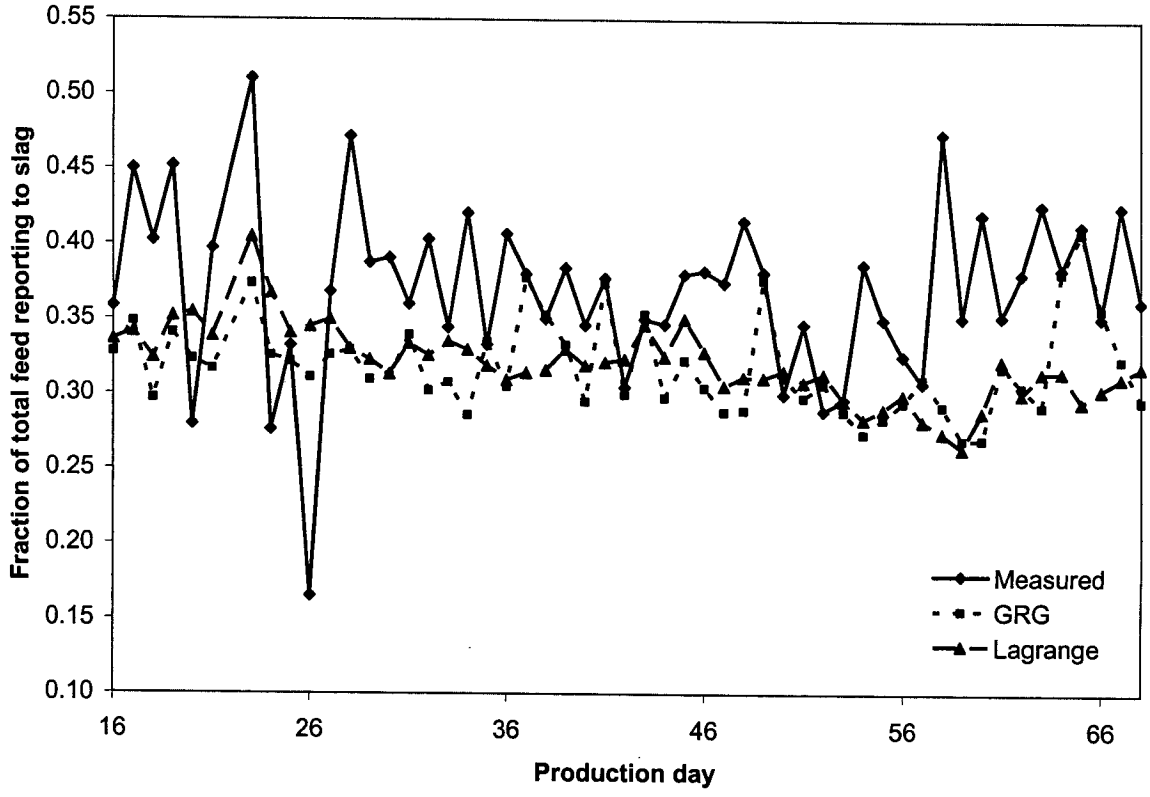

Figure 5.25: Timeseries of actual and reconciled slag as a mass fraction of total feed

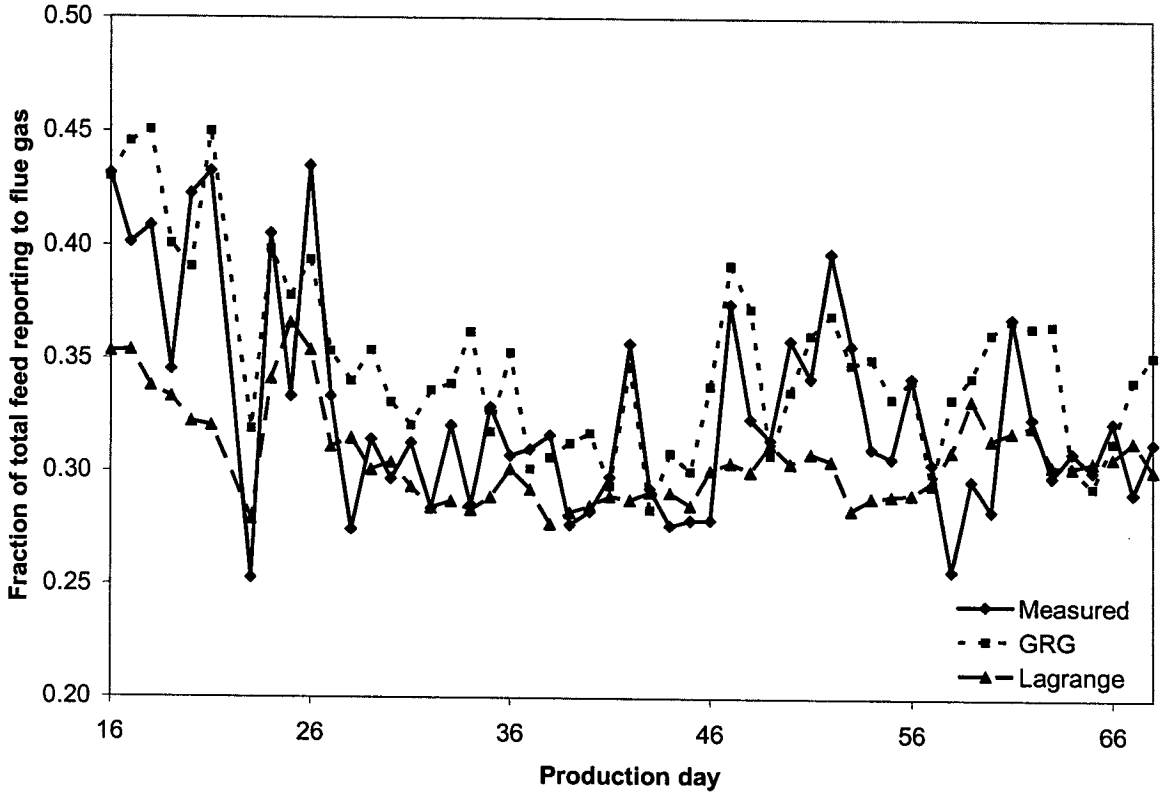

Figure 5.26: Timeseries of actual and reconciled flue gas as a mass fraction of total feed

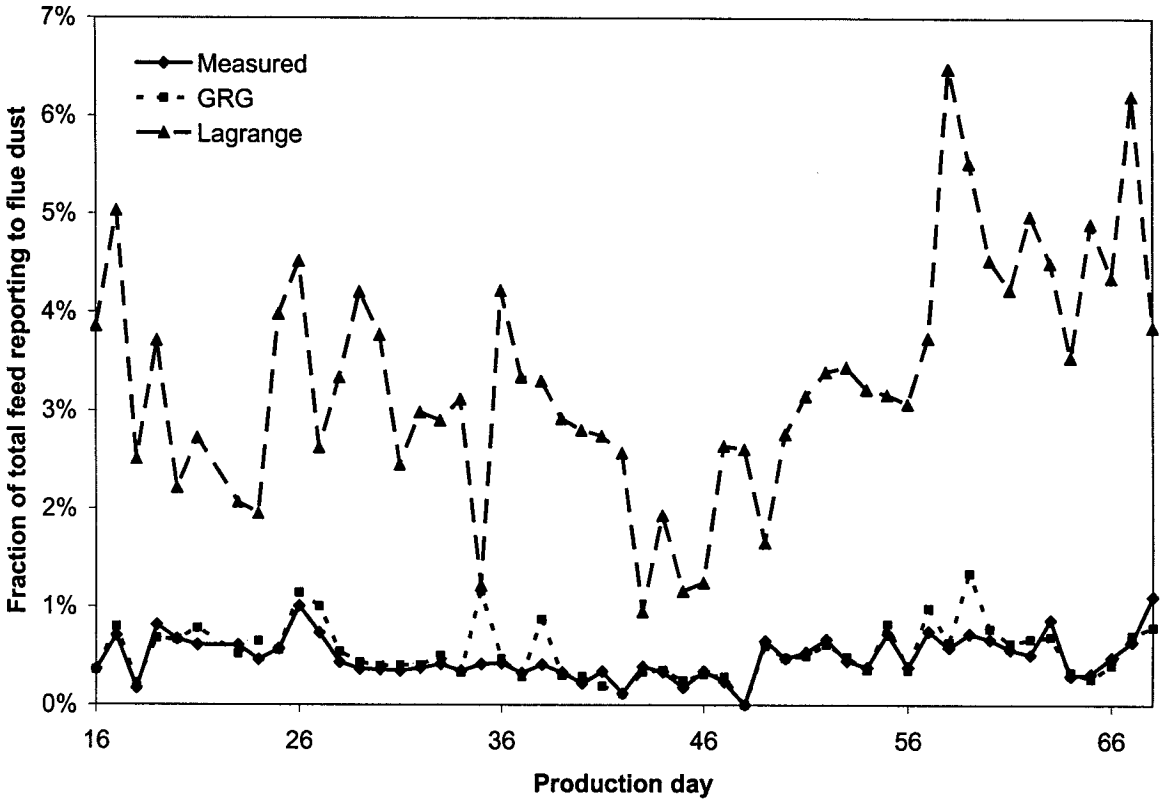

Figure 5.27: Timeseries of actual and reconciled flue dust as a mass fraction of total feed

It is apparent from the time series in Figures 5.24 - 5.27 that, in general the reconciled data sequence is significantly smoothed relative to the original measurements. Significant systematic biases were observed for nearly all the cases where the Lagrange multiplier method was used. These biases became particularly evident in the calculated dust splits – due to it being calculated as 1-(alloy split + slag split + gas split): a small change in any of the other spilt ratios resulted in a significant change in the dust split ratio. The silicon fractions (split fraction times assay) are discussed by way of example.

Both reconciliation methods adjusted the silicon in the feed within the same band, but with a large bias relative to the measurement. Smelter operating staff later confirmed the probability of occurrence of a systematic error in the feed assays pertaining to silicon (in the form of SiO_2). The reconciliation aids operating staff to gauge if any measurement bias exist and to develop a reliable feed recipe that could be accurately balanced with all product from the furnace. A reconciled estimate of the dust production, and especially the carbon component in the dust is useful to gauge the reductant utilisation efficiency. Determination of the slag split ratio as fraction of the feed allows determination of the slag production and chrome losses with the slag.

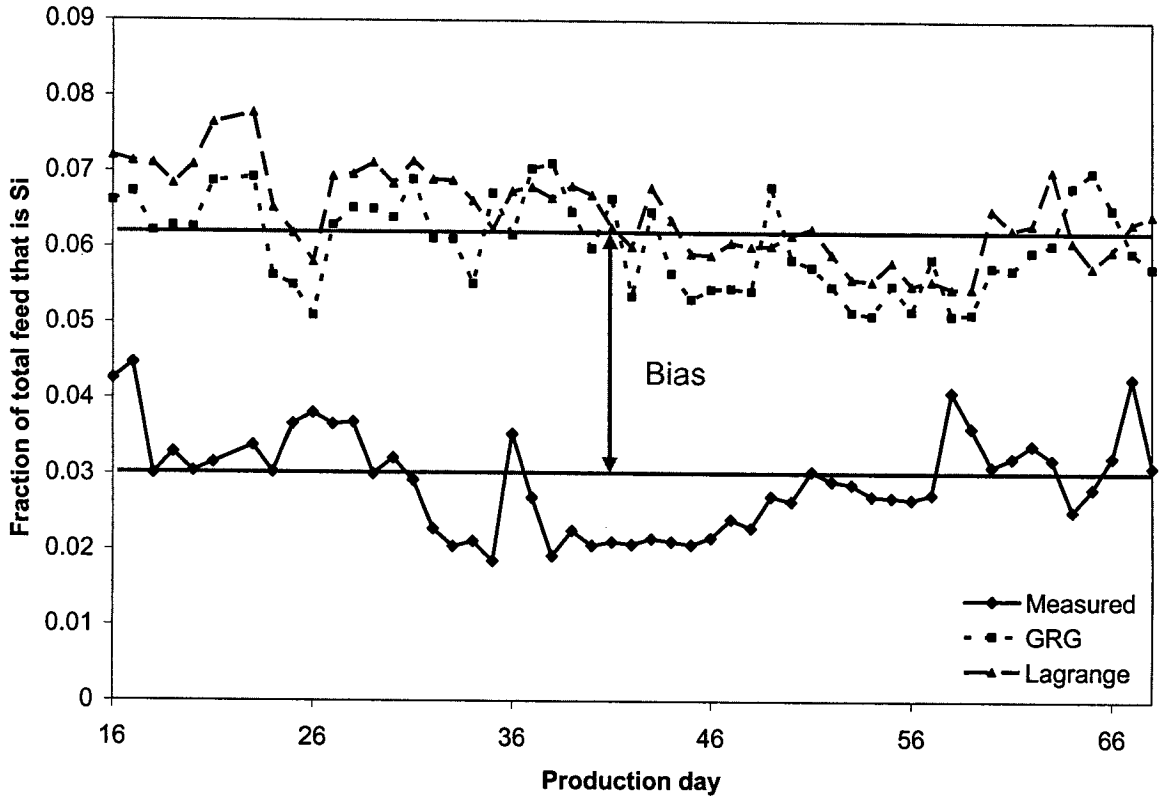

Figure 5.28: Timeseries of actual and reconciled Si fraction in the feed (bias indicated).

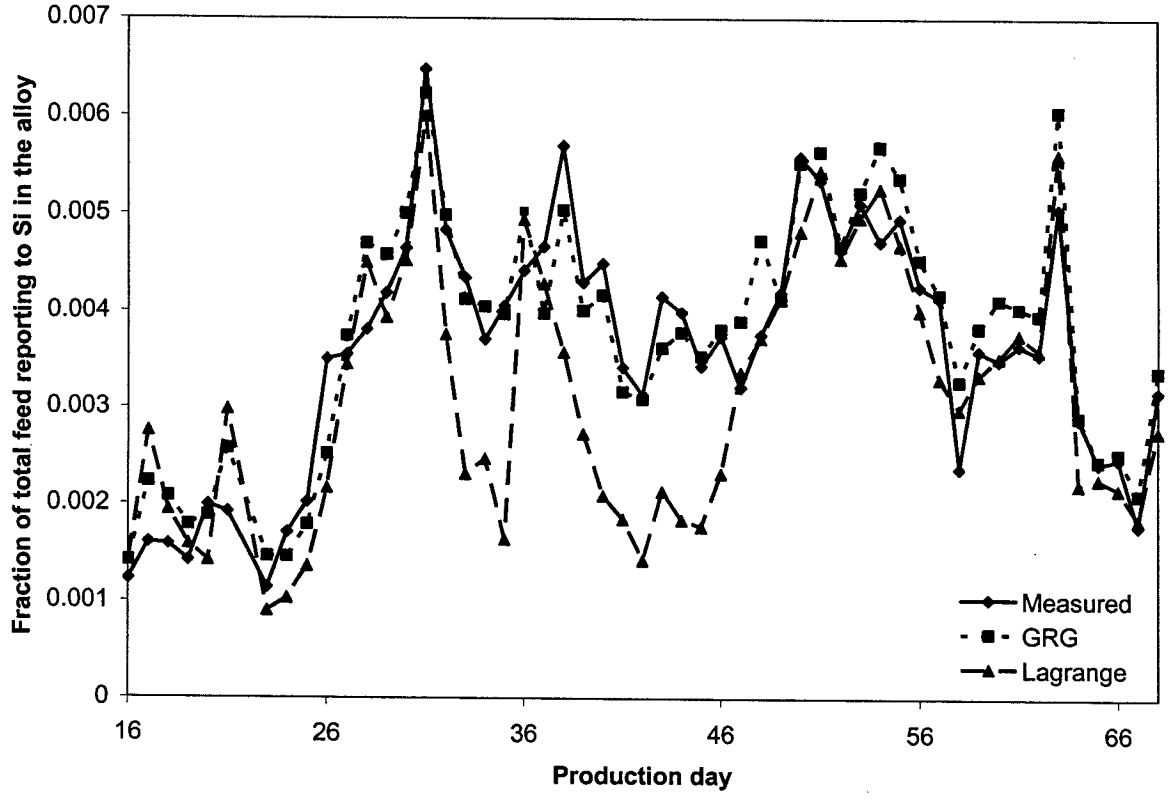

Figure 5.29: Timeseries of actual and reconciled Si in the alloy as a fraction of total feed

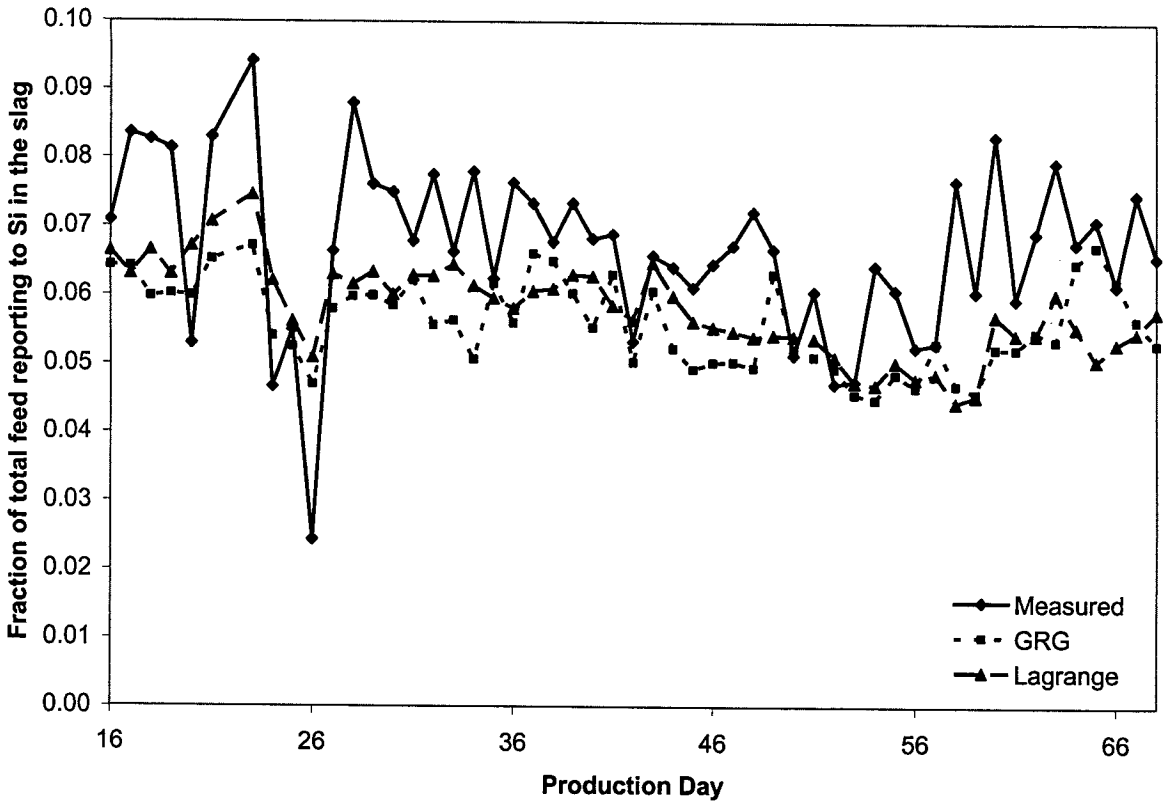

Figure 5.30: Timeseries of actual and reconciled Si in the slag as a fraction of total feed

The series of graphs presented in the figures above emphasises that the Lagrange method led to larger adjustments and a larger observed bias. The detection of bias is always important as it indicates either that some material is added or removed to the furnace, which is not logged on the data acquisition system, or significant error in the analysis instrumentation, or a very poor sampling methodology. Bias is therefore a measure of the inaccuracy of the measurement, while random errors (positive and negative) are within the natural variance of a measurement, and relates to the precision of the measurement. Once the mass balance is reconciled an energy balance may be developed based on the reconciled mass balance. Finally, data reconciliation is a tool to reconcile masses over a certain period. If this period is longer than the inherent time constant of the furnace melt, one would expect a loss in dynamic predictability. This may be the case in the reconciliation done as above, as the period of reconciliation was 24 hours, much longer than the tap-to-tap time for open arc furnaces. Consequently, the dynamics have to be characterised to determine if some degree of dynamic predictability is present (versus steady state predictions made by the reconciled mass balances).

5.10 Dynamic patterns in the reconciliation adjustments

The measurement errors (adjustments) were analysed to determine if they are truly random, normally distributed and independent. The adjustments calculated for any given day were analysed to determine if they were dynamically related, albeit not with a high accuracy, to the calculated adjustments (measurements errors) of previous days. A Fast Fourier Transform (FFT) power spectrum was used to determine if any such autocorrelation exists. A strong periodic component (and therefore a high degree of autocorrelation) exists, as demonstrated by the amplitude occurring typically within the first five frequency components of the FFT power spectrum of the adjustments time series. This is demonstrated for silicon in the alloy and slag in Figures 5.31 and 5.32 respectively. The FFT for chrome adjustments in alloy and slag, shown in Figures 5.33 and 5.34 respectively, indicate that very little periodicity occur for the chrome adjustments and that there is a very low signal to noise ratio. For the silicon adjustments, the 1st 5 frequency components are particularly prominent. The FFT spectra shown are all based on the adjustments time series as determined by the Lagrange multiplier method.

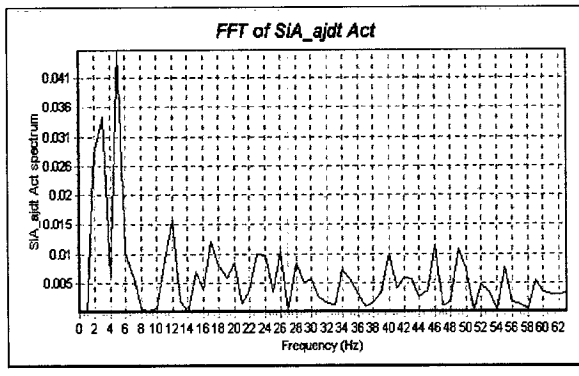

Figure 5.31: FFT spectrum of Si (alloy) errors

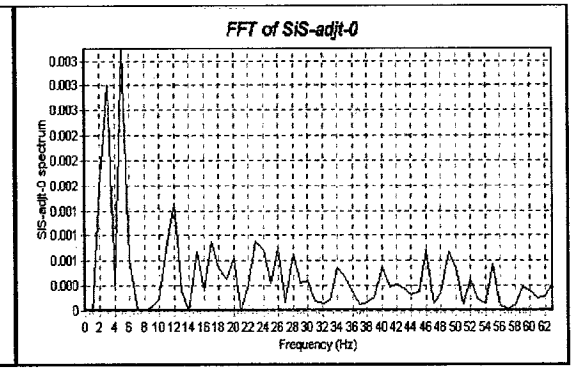

Figure 5.32: FFT of Si (slag) errors

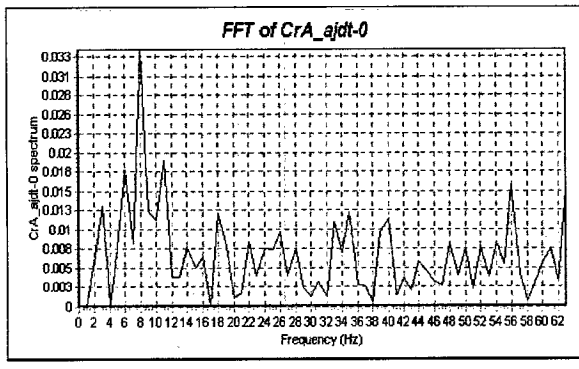

Figure 5.33: FFT spectrum of Cr (alloy) errors

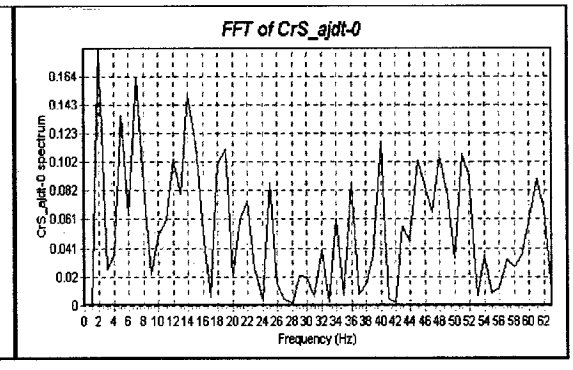

Figure 5.34: FFT of Cr (slag) errors

To demonstrate this more clearly, 5th order linear time series models of the adjustments were evaluated. The objective was not to prove that the adjustments definitely follows a 5th order and not higher order dynamics, but only to identify if the adjustment history is related to

future adjustments. Should this be the case, one may use time series models to estimate future adjustments. A n^{th} order time series model of the adjustment, ε, would have the following general structure.

$$\hat{\varepsilon}(t) = \alpha_0 + \alpha_1\varepsilon(t-1) + \alpha_2\varepsilon(t-2) + \alpha_3\varepsilon(t-3) + \alpha_4\varepsilon(t-4) + \alpha_5\varepsilon(t-5) + \ldots + \alpha_n\varepsilon(t-n) \tag{5.79}$$

The R^2, which determines which portion of the variance in the error can be explained by the model, and model coefficients are listed in Table 5.2, which gives the best least squares fit based on the simple time series model where the first six terms of Eq. (5.79) were used.

Table 5.2: Coefficients of 5th order time series models (of the reconciliation adjustments).

Error Minimisation method			Coefficients				
GRG-based SSE* minimisation	R^2	α_0	α_1	α_2	α_3	α_4	α_5
Silicon Adjustments (Alloy Phase):	0.46	0.0001	0.615	-0.129	0.146	-0.005	0.159
Chromium Adjustments (Alloy Phase):	0.25	-0.0126	0.375	0.181	0.048	-0.236	0.009
Silicon Adjustments (Slag Phase):	0.40	0.0012	0.382	0.132	0.017	0.386	-0.171
Chromium Adjustments (Slag Phase):	0.04	-0.0050	-0.051	-0.002	-0.060	0.173	0.028
Lagrange multiplier SSE* minimisation							
Silicon Adjustments (Alloy Phase):	0.56	-0.0005	0.578	0.027	0.224	-0.210	0.215
Chromium Adjustments (Alloy Phase):	0.25	0.0048	0.271	0.315	-0.067	0.062	-0.231
Silicon Adjustments (Slag Phase):	0.57	0.0000	0.647	0.005	0.130	-0.176	0.235
Chromium Adjustments (Slag Phase):	0.31	-0.1709	0.460	0.036	0.188	-0.345	0.085

* SSE : Sum of Square Error

The reasonably high autocorrelation that exists for the adjustments is surprising given, that the daily data reconciliation's were done independently. Furthermore, it can be seen from the table that the error sequence, as determined by the Lagrange Multiplier method, always led to similar or higher R^2 values than the GRG method. This would be the case where a systematic bias contributes significantly to the adjustment, while the random component is relatively small in comparison. Histograms confirmed the non-zero mean (implying bias) and non-normality of the adjustments for both algorithms. This is depicted in Figure 5.35 and 5.36 for the silicon error / adjustment in the slag (S) and alloy phases (A) respectively based on the Lagrange method.

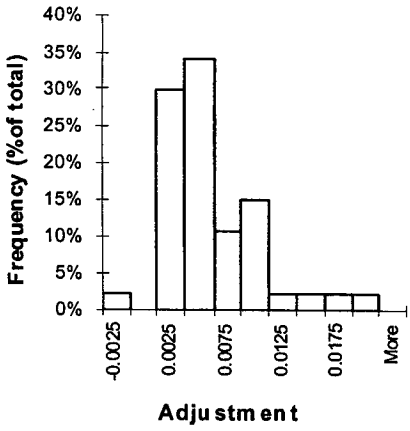

Figure 5.35: Error histogram for Si (S)

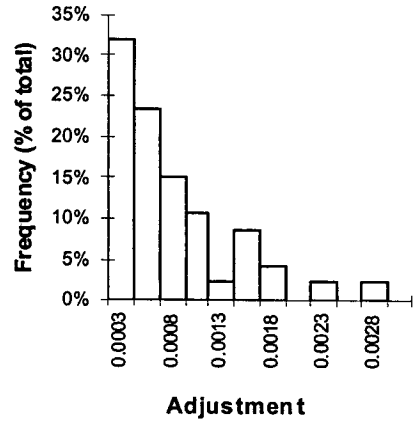

Figure 5.36: Error histogram for Si (A)

The implications of these observations can be summarised as follows;

- While the adjustments to silicon (as silica) in the slag were both positive and negative, the mean provided the bias with which the silicon (silica) assay in the slag has to be adjusted. The distribution of errors show a bell-curve structure, skewed towards smaller adjustments, but with a significant tail region towards larger positive adjustments.
- The adjustments of the silicon assay of the alloy shows a strong non-normal trend (more of an exponential distribution), with all adjustments (in the case of the Lagrange multiplier method) being positive and most of the adjustments being close to zero. However, referring to the silicon fraction for the alloy in figure 5.31, it appears that the GRG method gives a much more normal (equal positive and negative adjustments) distribution of adjustments.
- The GRG method distributed the errors more randomly around the measured values, but still made measurement bias identification possible (as shown for figure 5.30, where the inherent bias was significant. The degree of predictability of the errors, was in general much poorer. However, this in itself show that the allocation of adjustments were more random in nature.
- As one is able to predict the adjustments, it becomes possible to improve the recipe mixes of the feed to obtain a specific product, lending itself therefore to a degree of feed forward control.

5.11 Reconciliation of the materials streams of plasma arc furnace

Only a selected number of components (of which information are available for all streams) are reconciled. For the purpose of presenting a sample of the reconciled results, only the raw data and the reconciled data of the total alloy weights and slag weights are presented. Appendix D shows a typical spreadsheet setup for reconciliation.

5.11.1 Reconciliation of the plasma arc chromite smelting furnace data

The data were reconciled according to the principles described in paragraph 5.5. The elements that were reconciled were: Cr, Fe, O, C, Al, Ca, Si, and Mg. The elements were reconciled for the product streams alloy, slag, dust and off-gas, and the feed consisting of 2 anthracite types, fine, medium and coarse chromite, limestone, quartz, electrode consumption and recycled spills. The reconciliations were all performed using the Generalised Reduced Gradient (GRG) error minimisation routine. The results for the alloy and the slag are presented in Figures 5.37 and 5.38 respectively.

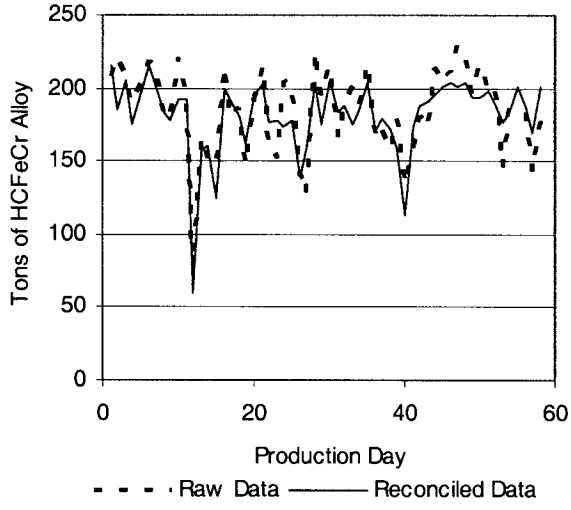

Figure 5.37: Reconciled versus reported tonnages of HCFeCr alloy tapped

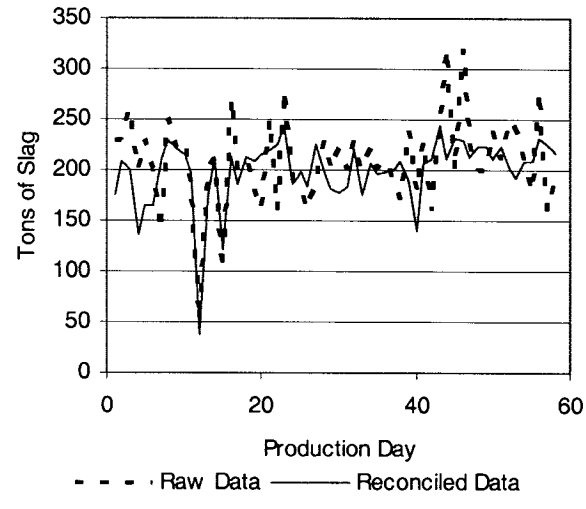

Figure 5.38: Reconciled versus reported tonnages of chromite-based slag tapped

It is clear that the relative daily adjustments in the amounts of alloy tapped versus the amounts of slag tapped are much more for the slag than for the alloy. This corresponds to the fact that the alloy is measured with a much larger degree of certainty than the slag - the alloy, which is tapped into sand moulds, is weighed on a daily basis, while the slag mass is determined by gauging how many slag ladles are filled. The accuracy for determining the slag mass is no better than about 25%, taking into account that the density may vary, the accuracy may vary from operator to operator, and the ladle is slightly tapered towards its bottom. Some crusts of crystallised slag of earlier slag taps may also stick to the ladle interior. The alloy on the other

hand, also picks up some of the mould fines. A constant pick-up % was assumed. The relative % adjustments for the HCFeCr alloy and the slag are shown in Figures 5.39 and 5.40 respectively. The relatively larger adjustments for the slag and the larger spread in slag adjustments are apparent when Figures 5.39 and 5.40 are compared.

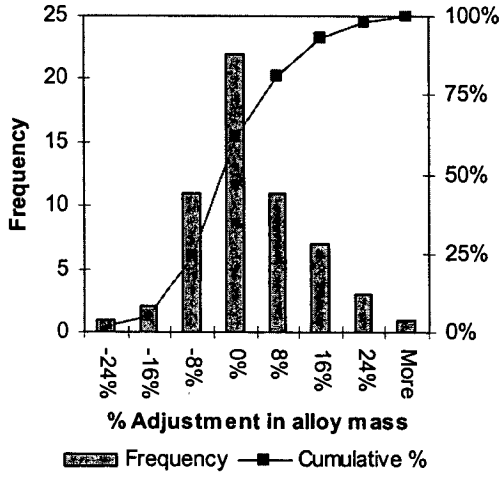

Figure 5.39: Distribution of reconciliation adjustments for HCFeCr alloy mass

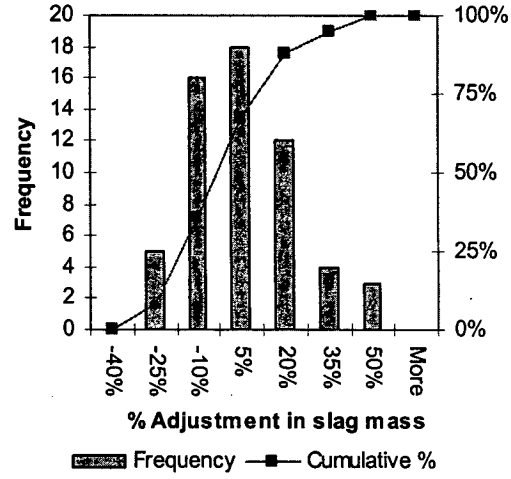

Figure 5.40: Distribution of reconciliation adjustments for HCFeCr slag mass

Similar times series plots and histograms could be drawn for each component fed into or produced by the furnace. Note that the adjustments are always subtracted from the measurement, that is, a positive non-zero mean for the distributions would imply that the reconciled values are normally smaller than the corresponding measured value. In all cases it was found that the GRG-method produced a much more normal, i.e. Gaussian-like distribution, than the Lagrange-multiplier method.

5.11.2 Reconciliation of the plasma arc ilmenite smelting furnace data

As for HCFeCr, the ilmenite smelter data were reconciled according to the principles described in paragraph 5.5. The elements that were reconciled were: Ti, Fe, O, C, Al, Mn, Si, and Mg. The elements were reconciled for the product streams alloy, slag, dust and off-gas, and the feed consisting of anthracite and ilmenite. The reconciliations were all performed using the Generalised Reduced Gradient (GRG) error minimisation routine.

Contrary to the ferrochrome production case, the reconciliation for ilmenite smelting could be compared on a tap-for tap basis, as both the metal and the slag are weighed after each tap (However, the reconciliations were still performed on a daily basis). As before, some crusts

may be recycled in the ladles. A 12.5% bias was noted for the reported slag weight and an 8% bias on the metal weight (the reported values being more than the long-term reconciled values). The results for the hot metal and the high titania slag are presented in Figures 5.41 and 5.42 respectively (bias included). More adjustment of the metal weight is noted in this case, than for the slag weight.

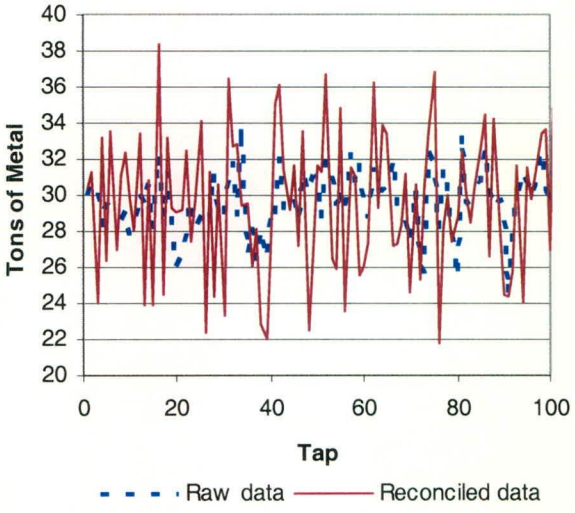

Figure 5.41: Reconciled versus reported tonnages of pig iron metal tapped

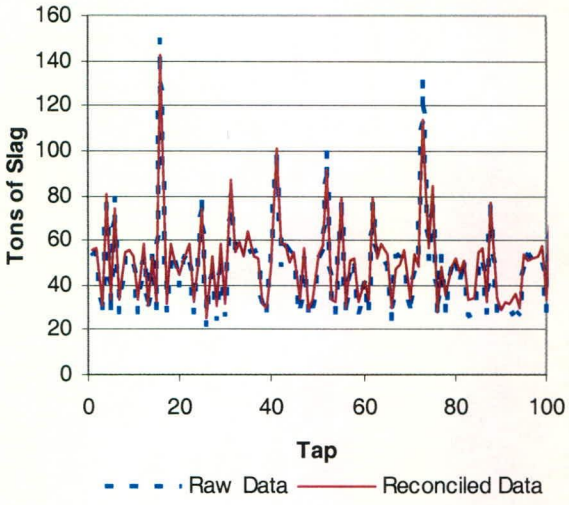

Figure 5.42: Reconciled versus reported tonnages of high titania slag tapped

The histograms depicting the distributions of the adjustments as a percentage of the raw data values are shown for pig iron and slag in Figures 5.43 and 5.44 respectively.

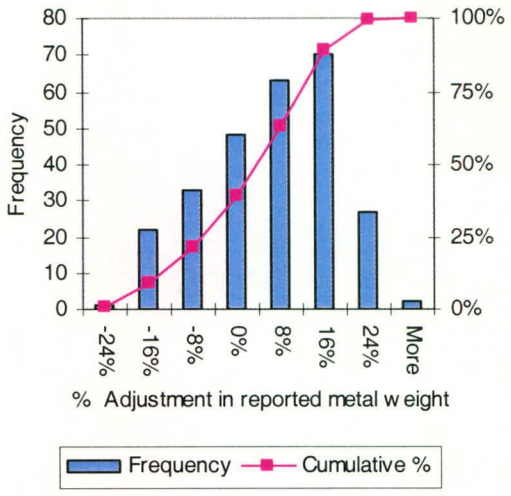

Figure 5.43: Distribution of reconciliation adjustments for pig iron mass

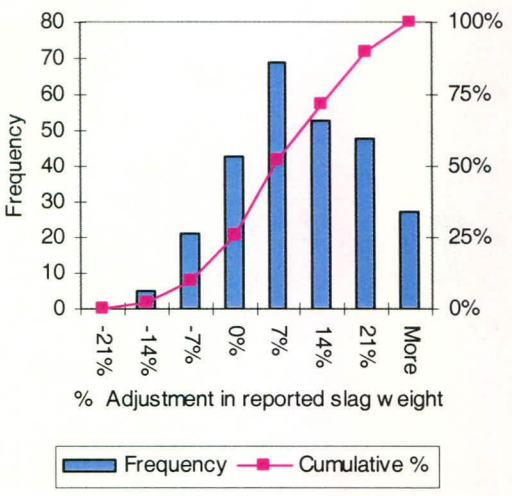

Figure 5.44: Distribution of reconciliation adjustments for high titania slag mass

Comparing the shape of the two histograms show a significant skewness in the adjustment distribution of the pig iron, both mean values significantly positive, showing the effect of bias. The reported values were therefore consistently higher than the reconciled values.

5.12 Tap-to-tap inventory and the furnace heel

The heel is the industry term for the residual amount of a specific melt phase (alloy, matte or slag) that remains after tapping. The quantity of the remaining heel has to be estimated, as the heel of one tap becomes part of the feed to the subsequent tap (although this aspect is normally forgotten by most people - operating staff and metallurgists alike) . Estimation of the heel is based on the amounts of alloy and slag produced, the physical design of the furnace and the amount tapped from the furnace. Therefore, calculation of the heel incorporates the mass balance, design and operational aspects. To estimate the minimum heel, the design of the furnace is required to identify the location of the tap holes and to calculate the inventories of the material between the tap holes, or the taphole and the furnace bottom. The region below the metal (lower) taphole and the furnace bottom is normally a spherical sector. The formulas to calculate the volume of sectors of spheres are given in many engineering handbooks, such as by Perry and Green (1984). The minimum heel defines the minimum residual over an extended production period. The net amount between what was produced (based on reconciled feeds minus reconciled amounts of gas and dust produced) and what was tapped (based on reconciled tapped amounts) can therefore not be less than the residual as determined by furnace design. In the case of the slag, which is always tapped prior to the alloy or metal phase, the minimum heel is zero (all the slag tapped), although in practice some small heel will always remain.

For a furnace for which the bottom is approximately a spherical sector, the volume of the sector could be estimated by (Perry and Green, 1984):

$$V_{\text{Spherical Sector}} = \tfrac{1}{6}\pi h\left(3r^2 + h^2\right) \qquad (5.80)$$

Where h is the depth (height) of the spherical sector and r is the radius of the circular base of the segment. The total metal heel is therefore the spherical sector plus the cylindrical portion below the alloy taphole. Ideally the use of periodic ultrasound measurements to calibrate estimated heel material balances is required. Even so, the determination of the metal-slag interface level is extremely difficult and uncertain.

5.12.1 The role of melt inventories in ferrochrome production

For the example of ferrochrome production, with an alloy pool with a density of 7055 $kg.m^{-3}$, a 4.8 m radius, a spherical sector depth of 0.74 m and a cylindrical portion with a depth of

0.325 m, the minimum heel is about 356 metric ton of alloy. This is a significant amount if it is considered that the average amount of metal tapped is about 50 metric ton of alloy. The alloy heel is therefore typically about 7 times the amount of tapped.

To obtain the reconciled feeds and products on a tap-to-tap basis, the daily adjustments were distributed over all taps for a day. The total reconciled amount fed plus the heel from the previous tap minus the reconciled amounts of gas and dust produced, were used to estimate the new inventory before tapping of the subsequent tap. As the initial inventory after tapping will influence all subsequent taps, the initial inventory was varied to minimize the maximum (minimax principle) inventory, while still allowing for a positive heel, i.e. constraining the optimisation so that the minimum heel at any given stage after tapping is a small positive number in the case of the slag, while the minimum heel should equal 356 tons, in the case of the alloy. Figures 5.45 and 5.46 shows how little of the available inventories were tapped for the HCFeCr slag and alloy respectively.

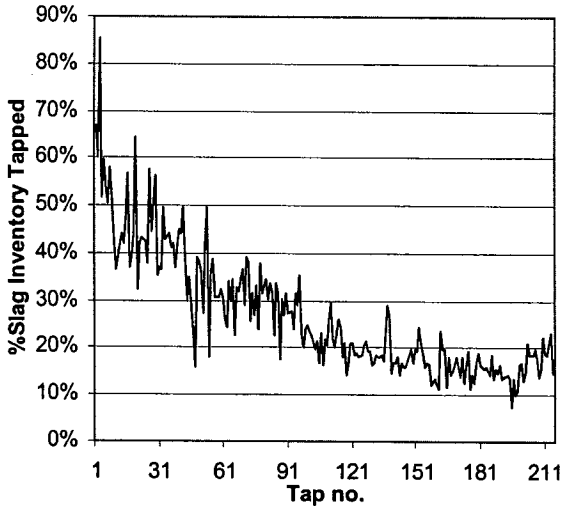

Figure 5.45: Estimated percentage of the HCFeCr slag inventory tapped

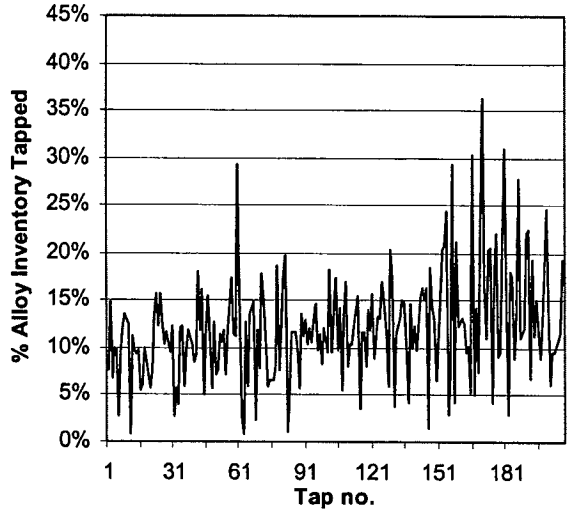

Figure 5.46: Estimated percentage of the HCFeCr alloy inventory tapped

For the HCFeCr production it is quite clear that much of the material remains in the furnace. Figures 5.47 and 5.48 show clearly show that 80% of the time less than 70% of the available slag was tapped, while in the case of the alloy, 80% of the time less than 15% of the available alloy was tapped.

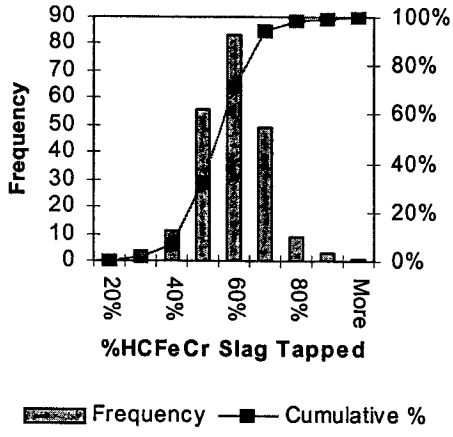

Figure 5.47: Histogram of % slag tapped

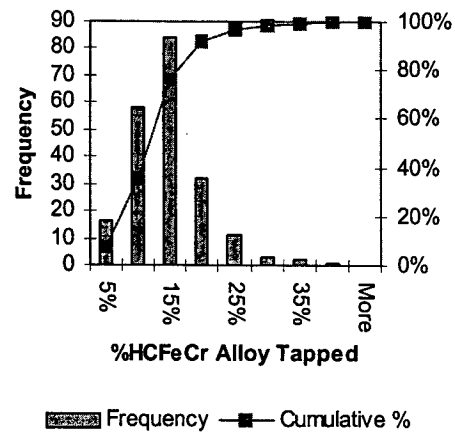

Figure 5.48: Histogram of % alloy tapped

The graphs clearly point out the significant buffer that remains within the furnace, significantly increasing the furnace time constant and stabilisation time. This seriously impedes the furnace controllability that can be achieved with short term feed changes (for example a feed change from one tap to the next) - any feed recipe change therefore has to maintained throughout several taps. It also indicates that the alloy and slag heels are the largest contributors on a mass basis to the metallurgical outcomes of subsequent taps. This is clearly demonstrated by the observation that the metal residence time, based on iron (calculated by inventory mass divided by the average tap-to-tap mass feed rate of iron) is about 63 hours. This time is much longer than any shift and much longer than the average tap-to-tap duration between metal taps (6.5 hours on average) and implies that material that entered the metal phase 9-10 tap cycles previously may still reside within ill-mixed zones within the furnace. The recycling of these large inventories clearly implies that any thermochemical equilibrium predictions cannot only rely on the reported feed composition and masses from the feed bins only.

5.12.2 The role of melt inventories in high titania slag production

Similar trends to the chromite smelting furnace were found for the ilmenite smelting furnace, as shown in Figures 5.49 and 5.50 for the percentage of slag and iron inventories tapped respectively. However, due the fact that there was a larger uncertainty due the unavailability of the furnace design, less certainty could be attached to the % metal tapped, % slag tapped are similar to the chromite smelting furnace, due to the slag being totally drained from time to time. However, as the power rating of the ferrochrome and ilmenite smelting furnaces are the same, and the furnaces are normally designed based on power per unit bath surface area,

assuming similar basic designs with regard to metal bath geometry would lead to similar volumetric heels below the metal tapline.

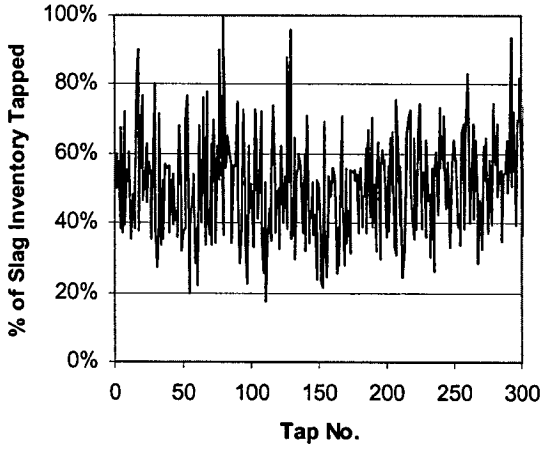

Figure 5.49: Estimated percentage of the high titania slag inventory tapped

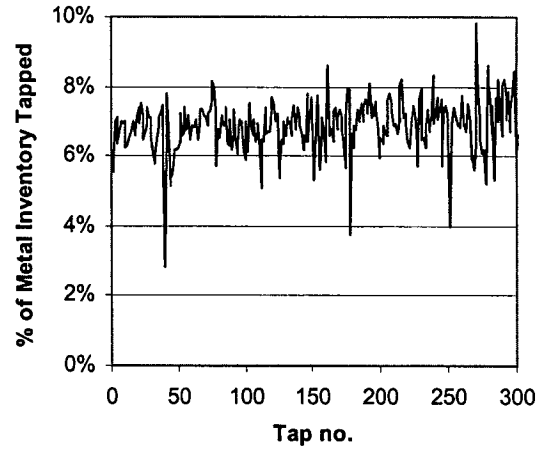

Figure 5.50: Estimated percentage of the metal inventory tapped

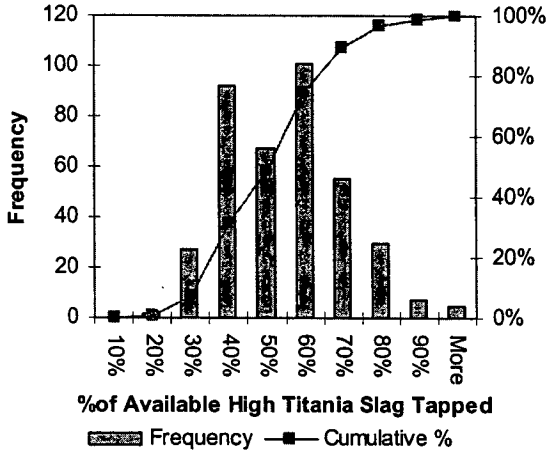

Figure 5.49: Histogram of the percentage of the high titania slag inventory tapped

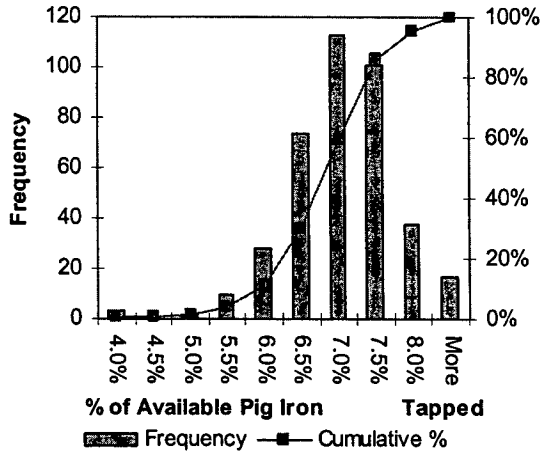

Figure 5.50: Histogram of the percentage of the metal inventory tapped

It is apparent that, while $^{2}/_{3}$ of the available slag is typically tapped, less than 10% of the pig iron is tapped (subject to the assumption of similar volumetric heels below the metal taphole found in ferrochrome production). The expected dynamic impact is therefore similar to chromite smelting, and the same conclusion could be drawn.

5.13 The role of data reconciliation in amplifying the deterministic component in stochastic time series.

It was shown in paragraph 5.2. that time series had a deterministic component and random component. It became apparent that, as the random component increases relative to the deterministic component, so the modelability, or the quality of the data-based model degrades. In paragraph 5.3 it was claimed that data reconciliation is, in principle, a low pass filtering technique which extracts the underlying trend from data. Some measurements from ferrochrome production will be used as an example to demonstrate the effect of data reconciliation on dynamic modelability. It became apparent from the FFT power spectra of carbon in ferrochrome, that it had high-powered spikes right through the frequency spectrum. The trend component has a relatively low power in comparison to the higher frequency components. The FFT spectra of reported carbon content of the daily produced HCFeCr alloy is presented together the spectrum of the corresponding reconciled values, in Figures 5.51 and 5.52 respectively.

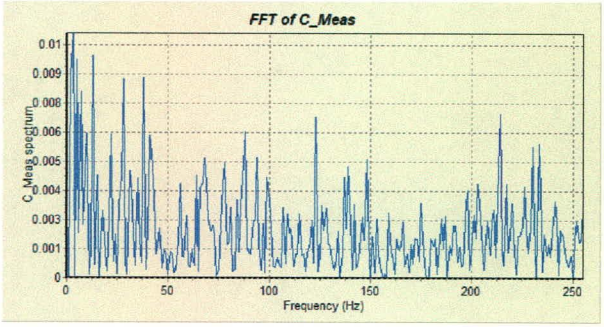

Figure 5.51: FFT spectrum of carbon reported in the daily produced HCFeCr alloy

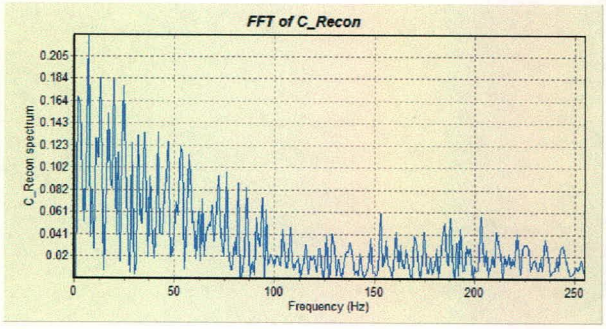

Figure 5.52: FFT spectrum of the carbon in the daily reconciled HCFeCr alloy

It is clear that the first 50 frequency components are significantly amplified relatively to the high frequency components after reconciliation. For instance, comparing the ratio of the maximum peaks in the 0-50 and 200-250 ranges before reconciliation gives 0.01/0.007 = 1.43, while the ratio for the maximum peaks in the same ranges after reconciliation is 0.225/0.051 = 4.41. The power of the low frequency components was therefore significantly increased relatively to the high frequency components.

Another way of demonstrating the degree of deterministic behaviour relative to random behaviour in chaotic time series is through inspection of the state-space diagrams. A chaotic series is a data sequence with a continuous frequency spectrum, and which is sensitive to the initial conditions. It is bounded in magnitude and comprises a broad band of frequencies

which manifest in noise like a continuous frequency spectrum. Due to the characteristic sensitivity in the initial condition, long term, multi-step prediction is not possible for a chaotic series. This happens because, irrespective how closely defined the initial conditions are, the series and the predictor trajectories may increasingly diverge with time and eventually become uncorrelated. Inspection of the FFT spectra of the timeseries associated with pyrometallurgical operations clearly show chaotic behaviour. Kanjilal (1995) mentions that a state-space diagram is a plot, for any given dynamic variable $\{x(k+1), x(k), x(k-1), \ldots, x(k_0)\}$ of $x(k)$ versus $x(k-i)$ for $i \geq 1$ in two dimensions. Higher dimensional spaces may also be used, but visualisation becomes more difficult in 3-D space, due to the convoluted nature of the plot. A process with periodicity generates at least one closed contour in a state-space diagram. These closed contours are called Limit Cycles, which have some interesting characteristics:

- If the sequence $\{x(k+1), x(k), x(k-1), \ldots, x(k_0)\}$ is strictly periodic, a repeating closed contour will be generated in the state space diagram.
- If the sequence is perfectly sinusoidal, the closed contour will be elliptical in shape. If the sequence is periodic but contains more than one sinusoidal component, the closed contour will be repeating, but will deviate from the elliptical shape.
- Real life, chaotic processes with periodicity are very seldom strictly periodic, and therefore have a trend component (a fundamental deterministic component). Such processes will normally generate closely packed closed contours which seem to migrate in a certain direction. To detrend the data one may impose high-pass filtering (differencing) to remove the trend component. In furnace data one would expect the trend to be driven by (and towards) thermochemical equilibrium. Differencing the data (measured or reconciled) would therefore remove the equilibrium component and only leave the dynamic components. Differencing is therefore used to simplify the diagram and centre the limit cycles around an absolute stationary zero-point.
- Processes with periodicity are normally bounded. Any tendency of unboundedness of a sequence is explicitly revealed in the state-space diagram, which would show gradually growing contours.
- The state space diagram of a chaotic process shows a large number of closed contours with no apparent order of arrangement. The contours will be non-intersecting in 3-or higher dimensional spaces.

The state-space diagram is a very simple and concise representation and it may be possible to show the characteristic pattern or abnormality in a periodic or quasi-periodic process through state-space diagrams. While analysis of chaotic processes are more difficult to distinguish on these diagrams, it remains worthwhile as another tool for the analysis of dynamic and stochastic processes. Carbon in HCFeCr alloy will be evaluated in this way. Figures 5.53 and 5.54 show the state-space diagrams (attractors) for C at any given time step and the subsequent time step, for the reported and reconciled values respectively.

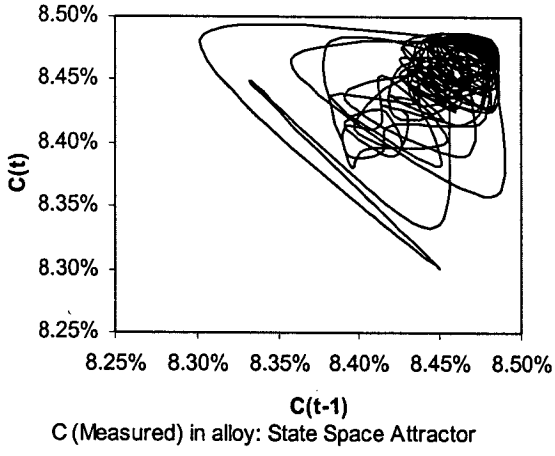

Figure 5.53: State-space diagram of carbon reported in the HCFeCr alloy

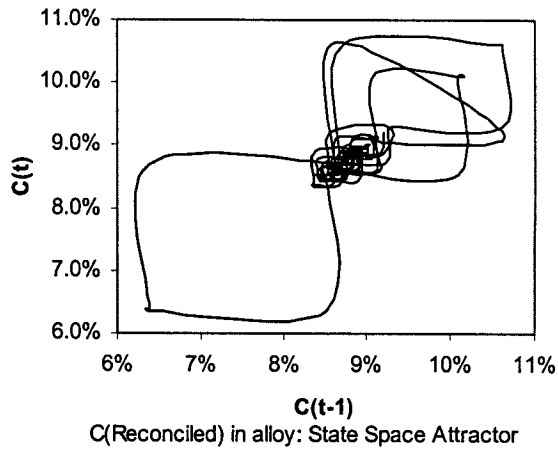

Figure 5.54: State-space diagram of carbon in the reconciled HCFeCr alloy

The difference in the diagrams is obvious. The reconciled attractor is much more well-behaved, with clear limit cycles showing the periodicity, and with a degree of symmetry. The unreconciled carbon state-space attractor shows more randomness in the attractor shape. Both seem to grow along the diagram diagonal, indicating non-stationary behaviour. There is therefore an underlying trend, which could be removed using differencing. When the data of the unreconciled and the reconciled carbon are differenced (subjected to high pass filtering), the attractors have a zero-anchor point to which the attractors periodically return, as is apparent in Figures 5.55 and 5.56.

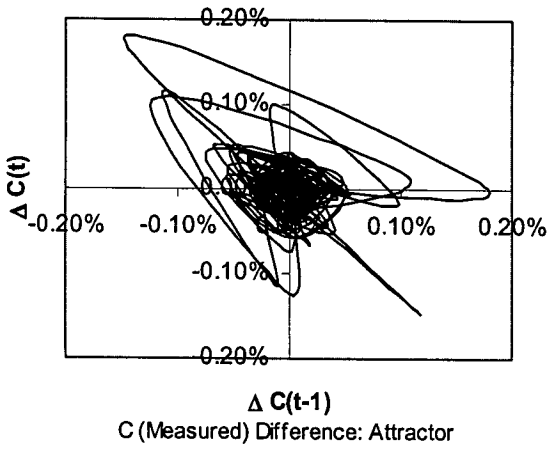

Figure 5.55: State-space diagram of differenced carbon reported in the HCFeCr alloy

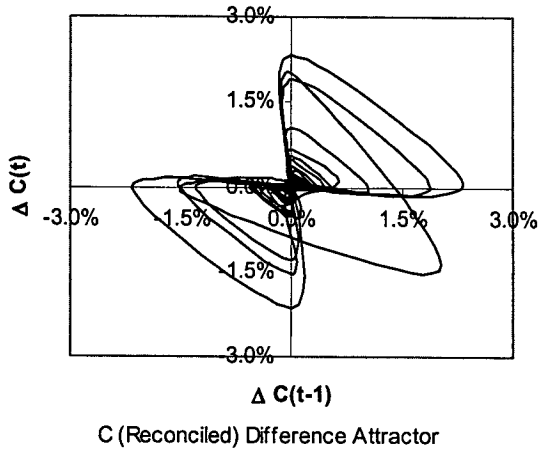

Figure 5.56: State-space diagram of the differenced carbon in the reconciled HCFeCr alloy

A few properties of the data before and after reconciliation could be inferred from the state space diagrams presented above:

- Data reconciliation improved the limit cycle behaviour and trajectory
- The data sequence is non-stationary
- The contours and the process from which it derives are bounded
- The time series is a chaotic series

It therefore is apparent, both from the FFT power spectra and the state-space analysis, that data reconciliation improves the dynamic behaviour and modelability of the data. The data become much more "well-behaved" after data reconciliation. Data reconciliation is therefore valuable, not only in the sense of making the data conform to material balances, but also to improve the overall dynamic behaviour.

At this point it has been shown how to characterise the technology (chapter 2), the process thermochemistry (chapter 3), the spatially distributive nature of the data (chapter 4), and how to prepare the data for modelling using data reconciliation. However, the way that the equilibrium thermodynamics is represented, does not lend itself to good online presentation, neither for integration into systems models as presented in paragraph 5.2. A way must therefore be found to estimate equilibrium in a rapid and reliable way that does not require on-line iterations to find the minimum of nonlinear functions. Artificial neural networks have been suggested as means towards achieving this goal.

5.14 Nonlinear modelling using artificial neural networks

Artificial neural networks (ANN's) offer some of the most versatile ways of modelling nonlinear processes of a diverse nature (Kanjilal, 1995). An ANN attempts to mimic the functioning of the brain in a crude but simplistic manner. The non-linear relationship between the input(s) and the output(s) is modelled using basic building blocs called neurons or nodes. These nodes are interconnected and are often arranged in multiple layers. Each internodal link or interconnection is weighted. At each node, the weighted inputs are added together with an external bias which is known as the threshold, and the result is passed through a nonlinear (activation) function, which determines the output from the node. A typical nodal input-output structure is presented in Figure 5.57 (Demuth and Beale, 2002).

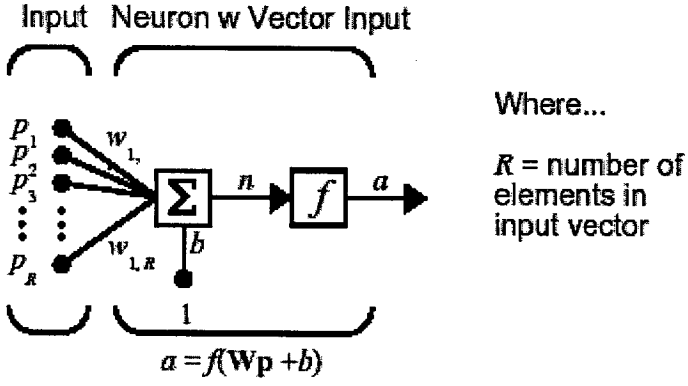

Figure 5.57: Nodal input-output structure (Demuth and Beale, 2002)

Where p_i to p_n are the nodal inputs, b the nodal bias, $w_{1,R}$ the connection weights, n the weighed sum input vector and the bias, and a is the nonlinear transformed nodal output, through the transformation function f. The weights associated with the internodal links are estimated iteratively by a non-linear optimization method using known sets of input and output data, which is referred to as training the ANN. The main characteristic features are the network architecture, the nonlinearity associated with the nodes and the training method used. The ANN designs are not unique and there may be rules of thumb associated with the specification of the network structure.

5.14.1 Strengths and limitations of ANN's

Before using ANN's both the strengths and limitations involved should be understood. ANN's have the following strengths as a modelling approach:

- The information is distributed over a range of nodes, which provides a greater flexibility than one finds in symbolic processing, where information is held in one fixed location.
- ANN's have the ability to learn. If an error or a novel situation occurs that produces inaccurate system results, an error-correction training technique could be used to correct it by adjusting the strengths of the signals emitted by the nodes until the output error disappears. At that point the system has effectively "learned" how to handle the new input. If this situation is encountered in the future, the network will model it properly.
- ANN's allow extensive knowledge indexing. Knowledge indexing is the ability to store large amounts of information and access it easily. Neural networks provide inherent knowledge indexing. They can easily recall, for example, diverse amounts of information associated with a chemical name, a process or a set of process conditions. The network stores/retains knowledge in two forms: (a) the connections between nodes, and (b) the weight factors of these connections. Because it has so many interconnections, the network can index and house large amounts of information corresponding to the interrelations between variables.
- ANN's are better suited for processing noisy, incomplete or inconsistent data. No certain node within a network is directly responsible for associating a certain input with a certain output. Instead, each node encodes a microfeature of the input-output pattern. The concept of microfeature implies that each node affects the input-output patter only slightly, thus minimising the effects of noisy or incomplete data in any given node. Only when all the nodes are assembled together into a single coordinated network, do these microfeatures map the macroscopic input-output pattern.
- ANN's mimic human learning processes. Most human learning and problem solving occurs by trial and error. Neural networks function in the same way. ANN's can be trained by iteratively adjusting the strength of the connections between the nodes. After numerous iterative adjustments, the network can properly predict cause-and-effect relationships.
- ANN's can determine the essentials of input-output relationships automatically (Automated abstraction). A domain expert (an expert in a particular problem-solving domain to develop the knowledge base that expert systems require) is not required. Through training with direct and sometimes imprecise numerical data, the network can automatically determine cause-and-effect relations and develop its own knowledge base.
- ANN's have the potential for online use. ANN's may take a long time to train, but once trained, they can calculate results from a given input very quickly. Since a trained neural

network takes less than a second to calculate results, it has the potential to be used online in a control system (Baughman and Liu, 1995).

Despite having many advantages, ANN's are not the panacea to all modelling problems. Significant limitations exist which should always be considered:

- They may have long training times. The training time of a neural network is a function of the size of the network (number of layers, and nodes in these layers), the amount of training data used, the training algorithm used as well as the number of iterations (epochs) used for the training. In complex systems covering a broad range of operating conditions this training time can be in the order of days. Due to the non-linear optimisation algorithms used in training neural networks, they may often get trapped in "local minima". For this reason neural networks often have to be trained and retrained until an optimal performance is obtained. More recent and advanced training algorithms minimise the probability of the error minimisation being trapped in local minima.
- Large amounts of training data over a large range are required. If too little input-output data exist on a problem or process, the use of neural networks should be reconsidered as they are much dependent on redundancy in the data. Consequently, neural networks are best suited for problems with a large amount of data. Furthermore, a situation may develop where a large database is available, but all the training data are very similar, causing the same problems as in having small training data sets. Thus, a broad-based data set or experimental design is essential because while neural networks are very good at interpolation, they are not suited for extrapolation beyond the domain in which they were trained. Many training algorithms are also very memory intensive, which can become a problem when working with large amounts of training data.
- There is no guarantee of optimal results. Most training techniques are capable of "tuning" the network, but they do not guarantee that the network will operate properly. The training may "bias" the network, making it accurate in some operating regions, but inaccurate in others.
- 100% reliability can never be guaranteed. This applies to all computational applications, but it is particularly true for neural networks with limited training data.
- A good set of input variables is required. Selection of input variables that give the proper input-output mapping is often difficult. It is not always obvious which input variables or forms of these variables (e.g., log, inverse, etc.) obtain the best results. Some trial and error in selecting input variables is often required (Baughman and Liu, 1995).

5.14.2 Neural network modelling applications of process metallurgical systems

Neural networks have become an established tool in the ensemble of artificial intelligent techniques in the past 2 decades. ANNs have also changed from being a research tool to being commercialised and used in industry in a whole range of applications, such as fault diagnosis, process control and non-parametric process modelling.

Jämsä-Jounela (2001) reviewed various model based control approaches and their application in the mineral and metal processing industries, and identifies a number of cases where artificial intelligent systems were used to improve process diagnoses and control. Van der Walt *et al.* (1993) were amongst the earliest researchers to investigate the application of ANNs in the process metallurgical field. Peng *et al.* (1995) used a fuzzy-ANN decision model to model the operation of an electric slag cleaning furnace for cobalt extraction from waste slags. The inputs and outputs only used material flow rates/masses and the electrical power input.

Reuter *et al.* (1997) show how the use of dimensionless feed numbers may be used to characterise the feeds to metallurgical reactors. In their approach, each feedstream to a furnace has various attributes which incorporated into a single dimensionless feed number. These discrete feed numbers are then used to establish optimal reactor operating regimes as a function of the feed material. Neural nets are used in this case to determine these optimal operating regimes.

Fontaine and Germain (2001) studied "model-based" ANNs where fundamental models with a known structure but ill defined parameters are used in conjunction with ANNs. In general they found that the hybrid approach performed better than a purely black box approach using neural networks only. A similar hybrid strategy was applied by Reuter *et al.* (1992a) to develop a generalised kinetic rate equation, where the ill-defined parameters of the rate equation were indirectly estimated using an ANN. This approach was also applied to simulate metallurgical processes (Reuter and Bernhard, 1994). Furthermore it was shown by Reuter *et al.* (1992a) that ANNs may be used to model simple non-ideal slag-metal equilibria to within the experimental error of the data. The modelling of equilibria for the purpose of modelling equilibria useful for industrial processes is developed further in this thesis.

Reuter and Sudhölter (1996) and Sudhölter *et al* (1996) used ANNs for the ecological-economical optimisation of metallurgical flowsheets. Reuter *et al.* (1995) also showed that ANNs may be used to find optimum setpoints for ferroalloy furnaces. A case study is presented for ferrosilicon production, where an optimum on a non-linear surface map could be identified where ferroalloy recovery would be a maximum as a function of electrode tip to bath resistance and metal oxide-to-reductant ratio.

Reuter and Moolman (1999) also investigated the use of thermodynamics to validate the predictions of neural networks and transfer function models, but stopped short of using the thermodynamic equilibria explicitly in the dynamic prediction models. They used a recurrent ANN to model the system dynamics of the MnO content of a slag from a ferromanganese plant. The prediction accuracy of MnO in the slag, one tap ahead into the future, was of the order of $R^2 = 0.56$ for both the recurrent neural network as well as the ARX model. Eksteen and Reuter (2000) also demonstrated how feedforward-backpropagation ANNs and ARX models could be used for prediction during ilmenite smelting. Again, the neural network did not outperform the ARX model, as the autoregressive properties of the dataset totally overshadowed all other physico-chemical properties of the system.

Hussain and Kershenbaum (2000) implemented an inverse-model-based control strategy using ANNs on a partially simulated exothermic reactor, probe to thermal runaway (instability). The implementation involved the control of the reactor temperature in the face of setpoint changes and load disturbances despite the existence of significant plant/model mismatch. They found however, that the model was still sensitive to the plant/model mismatch and that the accuracy of the inverse model required further attention.

Rico-Martinez *et al.* (2000) discuss inherent shortcomings of neural networks used as discrete-time models in system identification, time series processing and prediction. They mention that trajectories of non-linear ordinary differential equations can, under reasonable assumptions, be integrated uniquely backward in time. On the other hand, discrete-time neural network mappings derived from the time series , can give rise to multiple trajectories in time and are therefore non-invertible. They therefore conclude that this fundamental difference could lead to model predictions that are not only slightly quantitatively different, but qualitatively inconsistent with the continuous time series. It is also one of the important

reasons why neural networks, where they are used in this thesis, are not used to predict the system dynamics, but instead only to perform static non-linear mappings.

5.14.3 Neural network fundamentals

5.14.3.1 ANN Architecture

A typical feedforward neural network with interconnected nodes is shown in Figure 5.58. The network has an input layer, two (normally one to three) hidden layers, and an output layer. We can view a neural network as a "black box" into which we send a specific input to each node in the input layer. The network processes this information through the interconnections between nodes, but the entire processing step is hidden from the observer. Finally the network provides output(s) from the nodes in the output layer. The purpose of each layer is as follows:

- *Input Layer* – receives information from an external source, and passes this information to the network for processing.
- *Hidden Layer* – receives information from the input layer, and "quietly" does all of the information processing. The entire processing step is hidden from view.
- *Output Layer* – receives processed information from the network, and sends the results out to an external receptor.

When the input layer receives information from an external source, it becomes "activated" and emits signals to its neighbours. The neighbours receive excitation from the input layer, and in turn emit an output to their neighbours. Depending on the strength of the interconnections, these signals can excite or inhibit the nodes. What results is a pattern of activation that eventually manifests itself in the output layer. The network retains information through:

- The magnitudes of the signals passing through the network.
- The connections between nodes and their neighbours.

Because the network retains numerical information, it can function as a multivariable-computing tool (Baughman and Liu, 1995).

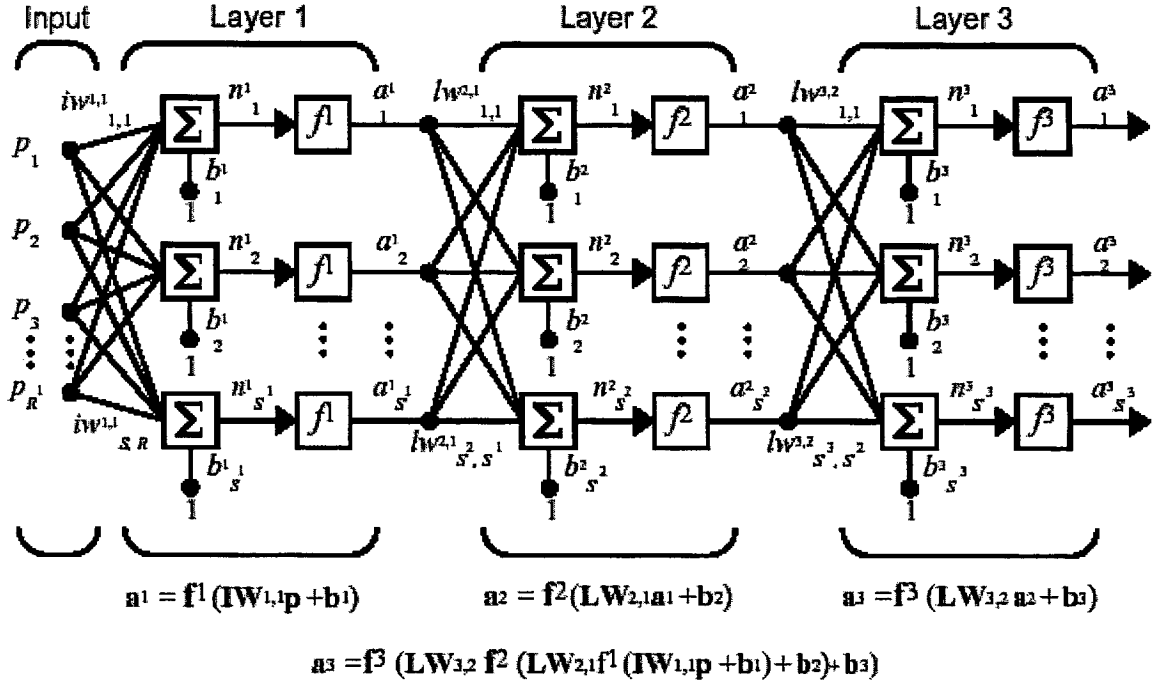

Figure 5.58: Feedforward neural network with interconnections (after Demuth and Beale, 2002)

5.14.3.2 ANN Computation

The inputs to the j^{th} node are represented as an input vector, **p**, with components p_i(i=1 to n). The node manipulates these inputs, or activities, to give the output, a_j, which can then form the part of the input to other nodes (Baughman and Liu, 1995).

Obviously the component values of input **p** have an effect on the output values, however, some additional factors also affect the output a_j. One is the weight factor, w_{ij}, for the i^{th} input, p_i, corresponding to the j^{th} node. Every input is multiplied by its corresponding weight factor, and the node uses this weighted input to perform further calculations. Consider node six for example. The first input into the node is p_1. Multiplying this input by the corresponding weight factor gives $w_{16}p_1$. Weight factors can have either an inhibitory or an excitatory effect. If w_{ij} is adjusted in such that $w_{ij}p_i$ is positive (and preferably large), the node is excited. If $w_{ij}p_i$ is negative, it inhibits the node. If $w_{ij}p_i$ is very small in magnitude relative to other signals, the input signal p_i will have no or little effect (Baughman and Liu, 1995).

The next factor governing the output from a node is the internal threshold or bias. The internal threshold for the j^{th} node, denoted b_j, controls activation of that node. The node calculates all its $w_{ij}p_i$'s, sums the terms together, and then calculates the total activation, n_j, by subtracting the internal threshold value:

$$n_j = \sum_{i=1}^{S}(w_{ij}p_i) - b_j \tag{5.81}$$

If b_j is large and positive, the node has a high internal threshold, which inhibits node firing. Conversely, if b_j is zero (or negative, in some cases), the node has a low internal threshold, which excites node firing. Some, but not all, nodes have an internal threshold. If no internal threshold is specified, b_j can assumed to be zero (Baughman and Liu, 1995).

The final factor governing a node's output is the transfer function. Once the node calculates the dot product of vector $\mathbf{w}_j = [w_{1j}, w_{2j},\ldots,w_{nj}]^T$ with vector $\mathbf{p}$, and subtracts the threshold b_j, it passes this result to a transfer function, $f(\cdot)$. Thus, the complete node calculation is:

$$f_j(\mathbf{w}_j \cdot \mathbf{p} - b_j) = f\left(\sum_{i=1}^{S}(w_{ij}p_i) - b_j\right) \tag{5.82}$$

This calculation is therefore a function of the difference between the weighted total input and the internal threshold. Functions that are generally used as transfer functions include the sigmoid transfer function, Gaussian transfer function and the hyperbolic tangent transfer function. All of the networks developed in this research make use of either the hyperbolic tangent transfer function (Eq. 5.83) or the tansigmoidal function (Eq. 5.84), which typically produces well-behaved networks (Baughman and Liu, 1995). This derives from the fact that the function is continuous over its whole range, it is bounded in its output, and it is fully differentiable over its whole range.

$$a_j = f_j(n) = \tanh(n) = \frac{e^n - e^{-n}}{e^n + e^{-n}} \tag{5.83}$$

$$a_j = \text{tansig}(n) = \frac{2}{1+e^{-2n}} - 1 \tag{5.84}$$

The calculations presented above reflect the feedforward part of the network. However, as the weight matrix is randomly distributed initially, a process is required to iteratively adjust the weights so that the network output corresponds to the required output (for the given inputs) within an acceptable error tolerance. This process is referred to as training, of which the backpropagation algorithm is one of the most frequently used.

5.14.3.3 ANN Training using error gradient backpropagation

A number of aspects regarding ANN training will be covered in this paragraph. Firstly, the mathematical basis for training will be discussed. Secondly, it will be shown how to identify and prevent overtraining and overfitting of the data.

There are many different approaches to training neural networks. Most of these approaches fall into one of two groups, namely supervised and unsupervised learning. In supervised learning an external teacher controls the learning and incorporates global information. During unsupervised learning no external teacher is used and the neural network relies upon both internal control and local information. Frequently, the network develops its own models without additional input information (Baughman and Liu, 1995).

The primary training method used throughout this thesis is through Error Correction Learning, which is a form of supervised learning, where the weights are adjusted in proportion to the output error vector. This method is applied to feedforward neural networks through a technique known as backpropagation (Baughman and Liu, 1995).

Many backpropagation algorithms exist, and can be categorised into those that use Newton's method (or a modified version of Newton's method), those that use the gradient descent method and finally those that use combinations of the two. The choice between which to use is often a trade off between memory usage and speed. Only two algorithms are used in this study, namely the Boyden, Fletcher, Goldfarb and Shanno (BFGS) algorithm, and the Levenberg-Marquardt (LM) algorithm (Demuth and Beale, 2002). Of the two the LM algorithm will have the fastest convergence, this advantage is especially noticeable if very accurate training is required. The LM algorithm does, however, use large amounts of memory. If the memory needed by the LM algorithm becomes too large, the BFGS algorithm can be used. This algorithm is only slightly slower than the LM algorithm, but it consumes far less memory.

The BFGS algorithm is referred to as a quasi-Newton method. It is based on Newton's method, of which the basic step is

$$n_{k+1} = n_k - \mathbf{A}_k^{-1} g_k \tag{5.85}$$

where A_k is the Hessian matrix (second derivative) of the performance index at the current values of the weights and biases. When working with non-linear functions it is important to be able to discern between local and global minima. Determination of convexity or concavity helps determine whether a local optimal solution is also the global optimal solution (Edgar and Himmelblau, 1989). Testing for concavity or convexity is done using the second derivative, for a vector, this is known as the Hessian matrix. However, it is complex and expensive to compute the Hessian matrix for feedforward neural networks. The advantage of the quasi-Newton method is that it does not require calculation of the Hessian matrix. This method updates an approximate Hessian matrix at each iteration of the algorithm. The update is computed as a function of the gradient (Demuth and Beale, 2000).

Like the quasi-Newton method, the LM algorithm was designed to approach second-order training speed without having to compute the Hessian matrix. When the performance function has the form of a sum of squares (as is typical in training feedforward networks), then the Hessian matrix can be approximated as

$$\mathbf{A} = \mathbf{J}^{\mathrm{T}}\mathbf{J} \tag{5.86}$$

and the gradient can be computed as

$$\mathbf{g} = \mathbf{J}^{\mathrm{T}}\mathbf{e} \tag{5.87}$$

where **J** is the Jacobian matrix that contains first derivatives of the network errors with respect to the weights and biases, and **e** is a vector of network errors. The Jacobian matrix can be computed through a standard backpropagation technique that is much less complex than computing the Hessian matrix. The LM algorithm uses the approximation to the Hessian matrix in the following Newton-like update:

$$n_{k+1} = n_k - \left[\mathbf{J}^{\mathrm{T}}\mathbf{J} + \psi \cdot \mathbf{I}\right]^{-1}\mathbf{J}^{\mathrm{T}}\mathbf{e} \tag{5.88}$$

When the scalar ψ is zero, this is just Newton's method, using the approximate Hessian matrix. When ψ is large, this becomes gradient descent with a small step size. Newton's method is faster and more accurate near an error minimum, so the aim is to shift towards Newton's method as quickly as possible. Thus, ψ is decreased after each successful step (reduction in performance function) and it is increased only when a tentative step would

increase the performance function. In this way the performance function will always be reduced at each iteration of the algorithm (Demuth and Beale, 2000).

One of the problems that occurs during neural network training is called overfitting. The error on the training set is driven to a very small value, but when new data (unseen data) is presented to the network the error is large. The network has memorised the training examples, but it has not learned to generalise to new situations. A number of methods can be used to prevent overfitting during training, of which automated regularisation and early stopping are two examples.

Automated regularisation is the preferred method to avoid overfitting, but it is only available for use in Matlab® along with the LM algorithm. One such method of regularisation is the Bayesian framework of MacKay (MacKay, 1992). In this framework, the weights and biases of the network are assumed to be random variables with specified distributions. The regularisation parameters are related to the unknown variances associated with these distributions. These parameters can be estimated using statistical techniques. One feature of this algorithm is that it provides a measure of how many network parameters (weights and biases) are being effectively used by the network. This effective number of parameters should remain approximately the same, no matter how large the total number of parameters in the network becomes. The Bayesian approach automatically embodies "Occam's razor," penalising overflexible and overcomplex models (MacKay, 1992).

In the "early stopping" technique the available data are divided into three subsets. The first subset is used as the training set, which is used for computing the gradient and updating the network weights and biases. The second subset is the validation set. The error on the validation set is monitored during the process. The validation error will normally decrease during the initial phase of training, as does the training set error. However, when the network begins to overfit the data, the error on the validation set will typically begin to rise. When the validation error increases for a specific number of iterations, the training is stopped, and the weights and biases at the minimum of the validation error are returned. The third subset is the test set. The test set error is not used during the training, but it is used to compare different models. It is also useful to plot the test error during the training process. If the error in the test set reaches a minimum at a significantly different iteration number than the validation set error, this may indicate a poor division of the data set (Demuth and Beale, 2000).

5.15 Intelligent mapping of the thermochemical equilibrium database using artificial neural networks

Thermochemical simulation software packages, as discussed in Chapter 3, are ideal for design and process development. Unfortunately, neither the software, nor the format of the results lend themselves to direct on-line prediction. A way to overcome this challenge is to use an alternative mapping function which maps process inputs to predicted equilibrium outputs, as predetermined by, say, FactSage®. A convenient and powerful way to perform this mapping is through the use of non-parametric models such as standard feedforward back propagation neural networks as discussed in the paragraph above. The metallurgical thermodynamics can therefore be reliably predicted within the boundaries of the trained data generated by FactSage®. As FactSage® predicts the amount of each phase (for example for chromite smelting the phases would be lime, periclase, spinels, mullite, pyroxene, and corundum solid solutions, molten slag and molten alloy and alloy carbide precipitates), the data have to be reworked to relate them to the form industry normally would measure it. For instance, where oxidic solid solutions precipitate, the actual slag analysis will reflect the overall analysis of the combined molten and entrained solid components. On the other hand, FactSage will predict the composition of the liquid and solid phases separately. The overall composition has therefore to be reconstituted from the FactSage predictions. Similarly one has to recalculate the actual alloy phase from the liquid alloy and the alloy solid solution and intermetallic precipitates. Therefore, as industrial slags and alloys are analysed based on bulk material chemistry, the assay of a specific element, say carbon in the ferrochrome alloy, has to be recalculated from the carbon in the liquid alloy and the carbon as distributed amongst all the solid (carbide) phases.

From a control perspective the actual composition of the separate solid phases is not so important. However, it is important to calculate the fraction of the reconstituted slag that is solids, as it significantly influence the furnace behaviour through influencing the melt rheology, and therefore such phenomena such as metal entrainment in slag, slag foaming, and melt phase tapability and mixing. For the purpose of viscosity estimation one would also require the composition and temperature of the liquid-only slag component of the slag / alloy, and the total fraction of solids associated with the bulk phase. For this purpose, the correlations discussed in Chapter 4 (equations 4.8 to 4.19) may be used to calculate the

viscosity of the liquid-only slag phase or alloy phase, while the Einstein-Roscoe (4.20 to 4.21) equations may be used to estimate the observed bulk viscosity, once the relative amounts of liquid and total solids are known. *A-priori* knowledge of the viscosity, even within an order of magnitude would allow production staff to gauge if they could expect problems with tapping, foaming or significant entrainment.

Equilibrium data, as calculated by thermochemical simulation software, therefore require reworking before they could be used for neural network training. The neural network becomes an "artificial intelligent" predictor of the thermodynamics in a way that is readily accessible to the production staff, i.e. the data are presented in the same way they are measured in industry. It should be stressed that only the thermodynamic equilibrium predictions are modelled using a neural network, not the plant data. The neural network does this by presenting the outcomes in ways that are directly useful for process interpretation.

The preparation of the thermochemical databases and the neural network prediction performance will be discussed for the three furnace types in turn. The objective is to provide a summary of the ANN architectures used, the way the data were presented for training, and the evaluation of unseen inputs to determine the networks' performance.

A few important points need to be emphasised:

- The datasets for ANN training can be made as large as required, as the data used are generated data and not plant data.
- The size of the designed data set is only constrained by the amount of time available for ANN development, computer RAM and processing power. Very large datasets, especially with many input and output variables and complex interrelationships, may force the supervisor to select less memory intensive training routines. This constraint may be very real in the cases studied below.
- The data can be "designed" to cover all possible ratios of variables within the operating range, even seldom recorded data.
- As testing data, the actual (reconciled where the reconciliation was performed) feeds may be used, as the training data set was a synthetically constructed data set, not corresponding to any of the actual feeds. This leaves all the available industry feed cases as evaluation cases.

- The furnace inventory may significantly change the mass ratios of the feed elements relative to each other.
- All of the ANN's were trained using Matlab 5.3. which included the Neural Network Toolbox. The following network properties had to be specified in the Matlab routines:
    - Training algorithm
    - Transfer function
    - Network architecture
    - Performance function
    - Number of epochs
    - Weight / bias learning function
    - Validation epoch limit (where applicable)

5.15.1 ANN development and evaluation for the thermochemical equilibria of Ni-Cu matte converting

5.15.1.1 ANN development and training

The variables chosen for the thermochemical simulation were presented in 3.3.4.2 in Chapter 3. The thermochemical equilibrium data base was developed using a 3^N factorial experimental design method to vary all the variables within a low, medium and high value within its operating range. In so doing, the whole operating variable space is covered with the minimum number of simulations. An input-equilibrium output database was therefore available for ANN development.

Only 35 458 out of the total of 367 500 simulations that were done for the second stage were used to train and test this network. The amount of data required to accurately train the network over the entire range was minimised as follows:

A constant silica addition to the bath was used. Once the data have been generated the effect of silica was found to be negligible (silica additions were always at a level above saturation). The silica was thus kept constant at 5 g/100g matte, the value closest to the average found from the pilot plant data. This decreased the data set from 367 500 to 122 500 rows.

By removing simulations done under extremely unlikely, or even impossible feed combinations. An example of an unlikely feed combination would be feeding a large amount of coal to the furnace, in combination with no oxygen. An impossible feed combination would

be feeding any amount of nitrogen to the furnace, in combination with no oxygen. It must be stressed that although many simulations were removed in this manner (from 122 500 down to 35 458), the range over which the network was trained was still substantially greater with respect to all the variables (input and output) than the largest ranges encountered for these variables in the plant data.

Reducing the amount of data required to train the network effectively made it possible to use the preferred, but memory intensive, BR algorithm. Of these simulations 70% were used for training and the remaining 30% for testing. Once again no validation set was required.

The database developed for the second stage of the process uses the liquid matte inventory (remaining after completion of stage 1) in the furnace as a basis. This means that predictions for this stage can be made from any point during the stage, provided the mass and composition of the matte inventory at that point are known.

During the pilot plant campaign the matte heel mass was obtained from the dip done at the beginning of each second stage. Unfortunately the nature of the process makes it impossible to obtain accurate dip measurements at intermediate points in the stage. In order to calculate the mass of the matte heel in the furnace at intermediate points, it was assumed that the mass of copper in the matte phase remained constant throughout the second stage blow. In other words it was assumed that no copper reported to the slag phase. This assumption is consistent with the trend shown in Figures 3.6 and 3.8, where the copper content in the slag is shown to be relatively constant for matte concentrations of copper between 10 and 65 mass %. Although this assumption is not entirely accurate, it was the only way to estimate the mass of the matte heel in the furnace at intermediate points during the second stage blow. Conventional mass balance techniques could not be used on the pilot plant data, as the slag was not sampled at the same frequency as the matte. However, for the proposed industrial installation, the slag sampling frequency will be the same as that for the matte. This will allow the matte mass to be calculated accurately throughout the duration of the stage, provided the mass and composition of the matte heel at the beginning of the stage are known.

For the slag equilibrium model a total of 65 499 simulations were used to train, test and validate the network. Validation was required when training this network, as the BFGS algorithm was used. The BR algorithm could not be used due to the large amount of memory

required by this algorithm when working with such a large data set. As before the data set was decreased from the total of 367 500 by firstly setting the value for the nitrogen feed constant. The nitrogen feed was found to have a negligible effect on the slag composition and the bath temperature. The silica could not be kept constant as it has a large effect on the bulk slag chemistry (although not as much on the fully liquid part). Eliminating unlikely feed combinations decreased the data set further, by removing simulations done under extremely unlikely, or impossible feed combinations. Of these simulations, 70% were used for training, 20% for testing and the remaining 10% for validation.

Predictions using this model can only be done from the beginning of the stage, where there is no slag heel in the furnace. Predictions cannot be done from another intermediate point in the stage, as the furnace would then contain a slag inventory that is unaccounted for by the model. This would affect both the mass and energy balance for the furnace resulting in inaccurate composition, and temperature predictions.

Before any networks were trained the input and output training data were scaled to be between –1.0 and 1.0. This was done using the minimum and maximum values for each variable within the data sets. The network properties for the equilibrium neural networks as well as their respective inputs and outputs are summarised in the Tables 5.3, 5.4 and 5.5.

Table 5.3: Network architecture characteristics

	Fe & S Second Stage	Slag Second Stage
Input nodes	8	8
Output nodes	2	7
Hidden layers	1	1
Nodes in hidden layer	45	40
Transfer function	Hyperbolic tangent	Hyperbolic tangent
Epochs	200	600
Net training function	Bayesian regulation backpropagation	BFGS
Performance function	Mean squared error	Mean squared error
Weight/bias learning function	Gradient descent with momentum	Gradient descent with momentum

Table 5.4: ANN Equilibrium Outputs

	Matte Second Stage	Slag Second Stage
Iron	X	X
Sulphur	X	X
Nickel	X	X
Oxygen	X	X
Nitrogen	X	
Carbon	X	X
Silica		X
Bath Temperature	X	
Heat loss from furnace		X

Table 5.5: ANN Equilibrium Outputs

Matte Second Stage	Slag Second Stage
Fe	FeO
S	Fe_2O_3
	NiO
	Cu_2O
	SiO_2
	Bath Temp (°C)
	% Solids

5.15.1.2 ANN evaluation and testing

A tabulated summary of the relative statistics of the neural network model can be seen in Table 5.6. All of the following results were obtained by evaluating the model on unseen data.

Table 5.6: Performance statistics of the neural network prediction of FactSage equilibrium data

	Number of Observations	MSE	R^2(%)
Iron	8101	8.95E-0.4	99.91
Sulphur	8101	8.95E-0.4	99.67

The neural network models the FactSage ® generated data very well, with high R^2 values. It should be kept in mind that the modelled data were generated and therefore contained no noise. The R^2 value suggests quite good correlation and consistency. One may therefore

conclude that the ANN predicts the equilibrium data sufficiently well. Similar results were obtained for the slag, which are presented elsewhere (Georgalli, 2002). It was already shown (paragraph 3.3.4.2.) that this specific system runs relatively close to equilibrium – equilibrium predictions are therefore expected to make a significant contribution to the final process model.

5.15.2 ANN development and evaluation for the thermochemical equilibria of reductive chromite smelting

5.15.2.1 ANN development and training

The ANN modelling approach was similar in all ways to the method used for the Ni-Cu matte, with the exception of using different suite of chemical elements as feeds. As before, a database was set up using a 3^N factorial design procedure using the elements that were reconciled for, being: Cr, Fe, O, C, Ca, Al, Si, and Mg. The ranges for associated oxygen derived from the reconciled ranges. There are however, a few major differences. In the case of the Ausmelt furnace, the furnace is monitored every 5-10 minutes during the batch blowing process, while in the chromite smelting process, the furnace is only monitored during tapping (that is about once in 6 hours per melt phase). In contrast to the Ausmelt where all the matte was present as the inception of the 2^{nd} stage blow, the chromite smelting in the DC plasma arc furnace is fed continuously with all feed materials. Moreover, a highly fluctuating non-zero inventory is present, which has to be taken into account at all times, as the heel also constitutes a (major) part of the feed to the next tap. The highly fluctuating heel increases the ratio of the relative ranges of the elements to each other quite significantly, that is to say much more than the relative element ratios found in the solid feeds to the furnace.

It was of importance to be able to predict the equilibrium composition of the HCFeCr alloy, and to be able to predict the chemistry of the purely liquid portion of the slag and the % solids in slag and alloy. Furthermore the liquidus temperature of the alloy is predicted, due to its importance in influencing alloy mixing as shown in Chapter 4. Naturally, the bulk slag chemistry with respect to Cr and Fe in the slag cannot be well predicted at all with equilibrium predictions, as the main form that those elements exist in the slag are as entrained droplets, even though they are reported as part of the bulk slag analysis. As before, improbable combinations were screened out to reduce the size of the overall dataset. Four different networks were therefore set up:

- ANN1: A network modelling the equilibrium mass of the elements (C, Cr, Fe, Si) as well as the % solids (volume %) in the alloy.
- ANN2: A network modelling the equilibrium mass of the elements (Mg, Fe, Si, Ca, Al, Cr, O) as well as the total mass of solids and liquid that constitute the slag.
- ANN3: A network that predicts the equilibrium mass % of chemical species (MgO, FeO, SiO_2, CaO, Al_2O_3, Fe_2O_3, CrO, Cr_2O_3) as well as the mass % solids in the slag.
- ANN4: A network predicting the liquidus temperature (in °C) of the alloy.

A summary of the characteristics of the basic ANN architectures used is presented in Table 5.7.

Table 5.7: ANN architectures for chromite smelting equilibria

	ANN 1	ANN 2	ANN 3	ANN 4
Input Nodes	8	8	8	4
Output Nodes	5	9	9	1
Hidden Layers	1	1	1	1
# Nodes in Hidden Layer	40	70	70	10
Bias Value	1	1	1	1
Transfer Function	Tansig	Tansig	Tansig	Tansig
Inputs	C_{feed}, O_{feed}, Fe_{feed}, Al_{feed}, Mg_{feed}, Ca_{feed}, Si_{feed}, Temperature	C_{feed}, O_{feed}, Fe_{feed}, Al_{feed}, Mg_{feed}, Ca_{feed}, Si_{feed}, Temperature	C_{feed}, O_{feed}, Fe_{feed}, Al_{feed}, Mg_{feed}, Ca_{feed}, Si_{feed}, Temperature	Cr_{alloy}, Fe_{alloy}, Si_{alloy}, C_{alloy}
Outputs	C_{alloy}, Cr_{alloy}, Fe_{alloy}, Si_{alloy}, Vol% Solids	Mg_{slag}, Si_{slag}, Ca_{slag}, Al_{slag}, Cr_{slag}, O_{slag}, Mass $solids_{slag}$, Mass $Liquid_{slag}$	MgO, FeO, SiO_2, CaO, Al_2O_3, Fe_2O_3, CrO, Cr_2O_3, Mass % Solids	Alloy Liquidus Temperature
Train Cases	45875	45875	45875	80
Test Cases	13106	13106	13106	20
Net training function	BFGS	BFGS	BFGS	LM

Performance function	Mean squared error	Mean squared error	Mean squared error	Mean squared error
Weight / Bias learning function	Gradient descent with momentum	Gradient descent with momentum	Gradient descent with momentum	Gradient descent with momentum
Overfitting Prevention	Early Stopping	Early Stopping	Early Stopping	Automated Regularisation

5.15.2.2 ANN evaluation and testing

A tabulated summary of the relative statistics of the neural network model can be seen in Table 5.8. All of the following results were obtained by evaluating the model on unseen data.

Table 5.8: Performance statistics of the neural network prediction of FactSage equilibrium data

Output Variable	R^2 (%)	Output Variable	R^2 (%)
Cr_{alloy}	99.7	Mass $solids_{slag}$	91.6
C_{alloy}	99.3	Mass $Liquid_{slag}$	95.5
Si_{alloy}	99.0	%MgO	98.6
Vol% Solids in Alloy	95.9	%FeO	94.8
Alloy Liquidus Temp	99.7	$\%SiO_2$	98.1
Mg_{slag}	99.8	%CaO	96.3
Si_{slag}	98.7	$\%Al_2O_3$	95.7
Ca_{slag}	98.0	$\%Fe_2O_3$	96.7
Al_{slag}	98.4	%CrO	98.1
Cr_{slag}	98.1	$\%Cr_2O_3$	94.8
O_{slag}	98.4	Mass% Solids in slag	90.4

As for the case of matte converting presented in the preceding paragraph, the network performs very well in representing the very complex thermochemical equilibria. It is apparent that the worst prediction, at an R^2 of 90.4% is for the mass % solids in the slag. This value is not measured on the plant, but it is useful to estimate the "observed" slag viscosity. As the viscosity estimations are not required to be precise (it is only required to know if the slag is sufficiently fluid or not), some error in the % solids in a specific melt phase could be

tolerated. Again, it is was proved that the network could represent the complex thermochemical equilibria of reductive chromite smelting exceptionally well.

5.15.3 ANN development and evaluation for the thermochemical equilibria of reductive ilmenite smelting

5.15.3.1 ANN development and training

Finally, the ANN modelling approach was also applied to map the predictions derived from reductive ilmenite smelting. An equilibrium database for ilmenite smelting was again generated using a 3^N Factorial design procedure using the elements that were reconciled for, which are: Ti, Fe, O, C, Mn, Al, Si, and Mg. The ranges for associated oxygen were derived from the reconciled ranges. As for chromite smelting, a highly fluctuating non-zero inventory is present, which has to be taken into account at all times, as the heel also constitutes a large part of the feed to the next tap. It was of importance to be able to predict the equilibrium composition of the main components of the pig iron, and to be able to predict the chemistry of the purely liquid portion of the slag and the % solids in slag and alloy. Improbable combinations were again screened out to reduce the size of the overall dataset. Five different networks were therefore set up:

- ANN1: A network modelling the equilibrium mass% of some of the alloy elements (C, Mn, Fe) as well as the mass of the alloy.
- ANN2: A network modelling the equilibrium mass% of the elements (Fe, Ti, O) in the slag, as well as the total mass of the slag.
- ANN3: A network that predicts the equilibrium mass ratio of Ti^{3+} to Ti^{4+} and the mass % solids in the slag.
- ANN4: A network predicting the liquidus temperature (in °C) of the slag.
- ANN5: A network predicting the equilibrium mass % of the contaminant Mg, Mn, Si and Al in the slag.

A summary of the characteristics of the basic ANN architectures used is presented in Table 5.9.

Table 5.9: ANN architectures for ilmenite smelting equilibria

	ANN 1	ANN 2	ANN 3	ANN 4	ANN 5
Input Nodes	5	4	4	7	8
Output Nodes	4	4	2	1	1
Hidden Layers	1	1	1	1	1
# Nodes in Hidden Layer	20	30	20	10	30
Bias Value	1	1	1	1	1
Transfer Function	Tansig	Tansig	Tansig	Tansig	Tansig
Inputs	Temp., Fe_{feed}, Mn_{feed}, O_{feed}, C_{feed}	Temp., C_{feed}, O_{feed}, Fe_{feed}	Temp., C_{feed}, O_{feed}, Fe_{feed}	FeO_{slag}, TiO_{2slag}, SiO_{2slag}, MnO_{slag}, Al_2O_{3slag}, MgO_{slag}, Ti_2O_{3slag}	Temp., Fe_{feed}, Mn_{feed}, O_{feed}, C_{feed}, Si_{feed}, Mg_{feed}, Al_{feed}
Outputs	Alloy Mass, Fe_{alloy}, C_{alloy}, Mn_{alloy},	Slag Mass Ti_{slag}, Fe_{slag}, O_{slag}	%Solids in slag, Ti-ratio	Slag Liquidus Temp.	Mg_{slag}, Mn_{slag}, Si_{slag}, Al_{slag}
Train Cases	2188	2187	2187	300	7654
Test Cases	937	938	938	73	2185
Net training function	BFGS	BFGS	BFGS	BFGS	BFGS
Performance function	Mean squared error	Mean squared error	Mean squared error	Mean squared error	Mean squared error
Weight / Bias learning function	Gradient descent with momentum	Gradient descent with momentum	Gradient descent with momentum	Gradient descent with momentum	Gradient descent with momentum
Overfitting Prevention	Early Stopping	Early Stopping	Early Stopping	Early Stopping	Early Stopping

5.15.3.2 ANN evaluation and testing

A summary of the relative statistics of the neural network model can be seen in Table 5.10. All of the following results were obtained by evaluating the model on unseen data.

Table 5.10: Performance statistics of the neural network prediction of FactSage equilibrium data

Output Variable	R^2 (%)	Output Variable	R^2 (%)
Mn_{alloy}	98.9	%Solids in Slag	96.1
C_{alloy}	99.3	Ti^{3+} / Ti^{4+} $Ratio_{slag}$	93.7
Mass of Alloy	98.7	Liquidus Temperature of Slag	99.4
Fe_{slag}	99.7	Mg_{slag}	99.9
Ti_{slag}	97.1	Mn_{slag}	91.8
O_{slag}	99.3	Si_{slag}	99.1
Mass of slag	99.7	Al_{slag}	92.5

As for matte converting and chromite smelting, the ANN predictions of the FactSage generated equilibria are very accurate. Slightly lower prediction accuracies are noted for the predictions of contaminants such as Mn and Al in the slag, and the Ti^{3+} / Ti^{4+} ratio.

5.15.4 Applications of ANN's using ill defined plant variables

While the neural networks were used above to represent thermodynamics, and therefore fundamental, well-defined equilibria, they may also fulfil a role to predict the influence of less well-defined variables on measured outputs. This was demonstrated by Eksteen and Reuter (2000) to predict the influence of the % Volatiles in anthracite and the median anthracite particle size on the Ti concentration of the pig ion. The 3-D figure depicting this relationship is shown in Figure 5.59.

For this prediction, a backpropagation neural network has been trained on the available input data (320 training sets and 80 test sets) and pruned until 15 input process parameters were identified as the minimum number of significant process variables to be able to explain more than 90% of the variation of the %Ti time series (R^2>90%). An optimum number of 8 primary and no secondary hidden nodes were found after less than 500 epochs, both sets of nodes employing the hyperbolic tangent nodal function. All network weights were randomised to values between –0.9 and 0.9.

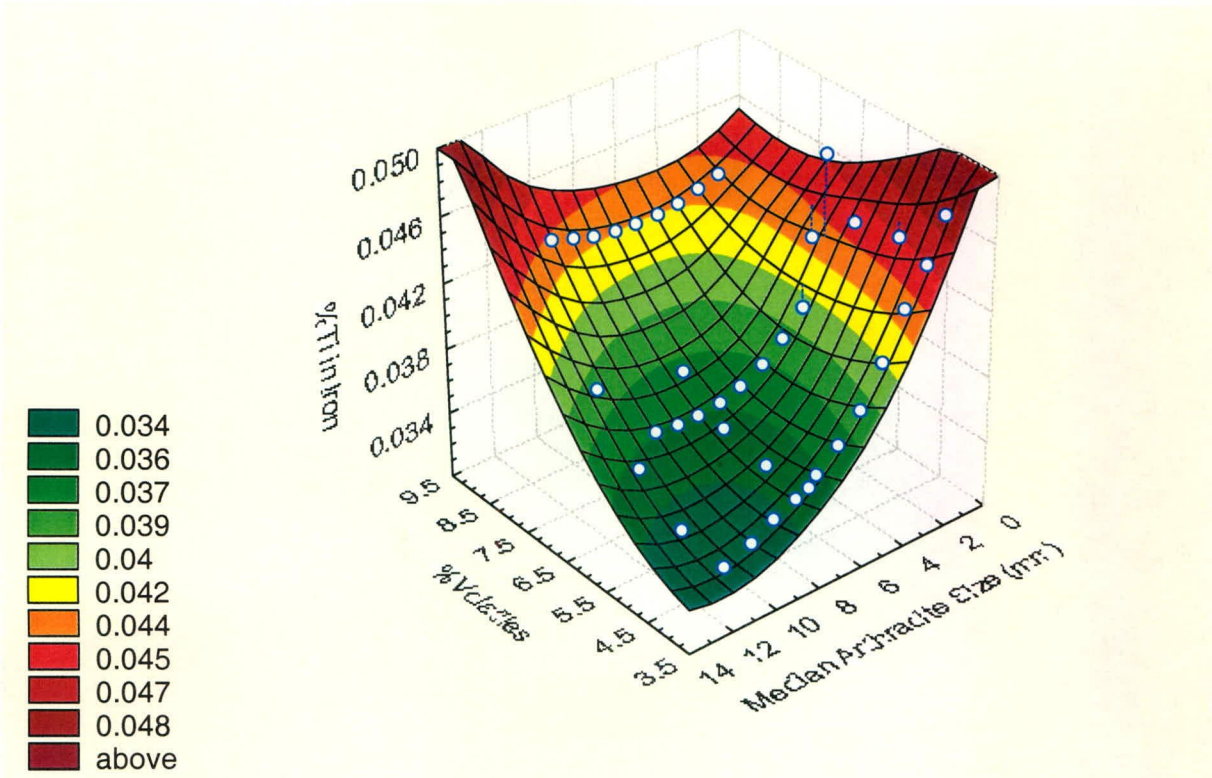

Figure 5.59: Surface plot of the neural network predicted % Ti in pig iron as a function of the %Volatiles in anthracite, and the median anthracite particle size, with all other variables held constant at their average values.

Figure 5.59 illustrates that the %Ti in the alloy is strongly influenced by factors related to coal reactivity. The neural network predictions of the points on the figure were made by keeping all the other variables at their average values, while the % volatiles and coal particle size was varied between their typical operating limits. Variables that tend to influence the rate phenomena, such as particle size, amount of volatiles, and sulphur concentration (which lowers the slag-metal interfacial tension), featured more pertinently as exogenous model variables.

Neural networks therefore still can play a significant part in relating ill-defined variables to each other. In this form, neural networks are not used in the model predictive control systems, but instead to provide information for good metallurgical decision-making. This is for instance useful to relate the coal / anthracite properties to metallurgically important variables, so that anthracite with optimal properties may be sourced, while taking into account financial constraints.

5.16 Key conclusions of the chapter

This chapter provided the theoretical foundation for the processing and empirical modelling of plant and generated metallurgical data, and showed how these techniques could be used to improve the understanding of the process and how to implement them to develop useful models.

It was shown that data reconciliation was not only a useful, but also a necessary step, in preparing the metallurgical data for further use in dynamic models. It was shown that the variances obtained in Chapter 4 could be used constructively to weigh the adjustments made through data reconciliation. In the reconciliation process, gross errors can also be identified, and the biases associated with measurements can be detected. Moreover, it was shown that the data reconciliation adjustments could be dynamically predicted using a simple time series model. It was also shown that data reconciliation proved to be an effective low-pass filter, to amplify the underlying signal in relation to the noise and high frequency components. It was shown that the series were in general non-stationary and that stationarity may be induced on the raw or reconciled data through a process of differencing, whereby the data obtain an integrated noise structure. It was shown that the dynamic state-space attractor of the reconciled data behaves far better than the state-space attractor of the raw data, and even more so when high-pass filtering is further applied to the reconciled data.

The reconciled data were used to determine the quantity of the melt phases produced versus the quantity actually tapped. This was used to estimate the dynamic inventory of the melt furnaces in the furnaces. It became apparent that only a fraction of the available melt inventories were tapped in the case of transferred plasma arc furnaces. It was therefore clear that very large heels were recycled from one tap to the following, consequently leading to large metallurgical "memories", or inertia to metallurgical change. For the two furnaces studied, the metal heel remaining after tapping were very large - around 90% of the inventory before tapping. In contrast to this, the slag heels were much smaller, with about half of the slag typically remaining after tapping. These melt residuals constitutes a major part of the feed to the subsequent tap and should therefore be taken into account as additional feed during equilibrium calculations.

Finally it was shown that artificial neural networks, as part of the suite of artificial intelligence techniques, are very useful to map the complex thermochemical equilibria found

in pyrometallurgical systems. Once trained, these networks therefore replace the role of thermodynamic prediction and simulation software. Furthermore, these trained ANNs do not require any subsequent parameter estimation and therefore they are not handicapped by minimisation routines which may not converge, or which may not reach a global minimum. Furthermore, they can be made to present the equilibrium information in the most useful form for use in further models, and on the plant. It was also shown that the neural networks could be used in guidance role to select, for instance, the reductant with optimal metallurgical properties. In this regard it does not function as a mapping function as described above, but as a complex non-linear function to relate ill-defined variables. At this point four useful pieces of information exist to aid further modelling:

- Reconciled furnace data
- Dynamic furnace inventories
- Fourier power spectra indicating periodicity
- Trained neural networks representing the chemical equilibrium conditions to be expected for the feeds (which include the melt heels).

Using the above information, system models based on transfer functions (of the Equilib-ARMAX type) may be developed to dynamically predict pyrometallurgical outcomes for the purpose of model-based control of furnaces within a practical time horizon. The development of these final dynamic system models for control, and the estimation of the model parameters, are the focus of the following chapter.

5.17 Nomenclature of Chapter 5

$\hat{b}_j$ = estimated bias

a = interfacial area for mass transfer

a_j = amplitude of a periodic series

C = consentration (%)

C^{∞} = equilibrium concentration (%)

$e(k)$ = model error

$E\{\cdot\}$ = expectation function

$f(\cdot)$ = transfer function

f_k , g_k , s_k , m_k d_k = concentrations of a component in the feed, gas, slag, metal and flue dust

g = gradient

$\mathbf{J}$ = Jacobian matrix

K = proprotional gain

k, i, j = counter or index

k_L = liquid phase mass transfer coefficient

L = Lagrangian

M = mass (kg)

N = number of measurements in time series

n_j = total nodal activation

$P(\cdot)$ = probability density function

Q_j = mass flow rate ($kg.s^{-1}$)

$R(\cdot)$ = autocovariance function

$r(\tau)$ = sample autocorrelation function

r, h = radius and height of spherical sector

r_k = mass balance residual

t = time (s)

T = total time associated with time series

$u(k)$ = exogenous input

V = covariance matrix

$V_{spherical\ sector}$ = volume of a spherical sector

w_{ij} = connection weight in neural network

x = general time series variable

$x_\omega(\tau)$ = discrete Fourier transform

$\bar{x}$ = sample or time series average

$y(k)$ = output

z^{-1} = Z-transform (discrete time back-shift operator)

Δt = time between two measurements (s)

Greek Symbols

δ_{ij} = Kronecker delta function

$\Gamma(f)$ = power spectrum function

ψ = scalar acceleration term

σ = population standard deviation

τ = shift in measurement time or index

τ_D , τ_I == derivative and integral time constants, respectively.

6 DYNAMIC SYSTEMS MODELS AND THEIR IMPLEMENTATION IN FURNACE CONTROL

"Everything should be made as simple as possible, but not simpler"
(Albert Einstein)

6.1 Introduction

The technological analysis of the high temperature process, presented in Chapter 2, has shown how difficult it is to model open bath pyrometallurgical processes. This difficulty stems not only from the inherent complexity due to the multiphase-multicomponent-multireaction nature of the system, but also due to the inherent uncertainty in measurements, uncertain boundary conditions, the distributed nature of properties within the system, and the difficulty to obtain reliable data from the process, and even sometimes at laboratory scale. It was shown that very often the position where the measurement is made within the reactor system, as well as the way the products (dust, slag, alloy) are tapped or accumulated, influence the data derived from the system. Keeping all these uncertainties in mind, a way must be found to derive the simplest models that still provide the required degree of accuracy. This required degree of accuracy cannot be claimed to be more than the inherent accuracy associated with the measurements if the models are partially based on plant data. Even a complex distributed parameter fundamental model (such as CFD) cannot be proven to be truly more accurate if the measurements made to validate the model have uncertainties of the same order as the spatial variance within the system, and if the patterns in the measurements are random.

Chapter 3 has shown how the chemical equilibrium, to which a dynamic system will tend, could be calculated. Chapter 4 has shown how variance associated with the spatial distributions of the melt chemistry could be determined, as these variances often contribute most to the overall sample variance. Chapter 5 has shown how the data could be reconciled, filtered and preprocessed, how the inventories may be estimated and how thermodynamic equilibrium may be estimated using neural networks. All these steps were shown to be necessary to incorporate the main fundamental driving forces, as well as the process data. It is only at this point that semi-empirical dynamic process models can be derived.

This chapter will make use of the Equilib-ARMAX model (Eksteen *et al.*, 2002a; Eksteen *et al.*, 2003, 2004b) of which the basic relationship to differential equations has been presented in section 5.2.3. The Equilib-ARMAX model will have the following general form:

$$\hat{y}(k) = \sum_{i=0}^{l} \alpha_i \cdot \tilde{y}_\infty(k-i) + \sum_{i=1}^{m} a_i \cdot y(k-i) + \sum_{i=1}^{n} \sum_{j=1}^{r} b_{ij} \cdot u_j(k-i-d) + \sum_{i=1}^{p} c_i \cdot e(k-i) \tag{6.1}$$

Except for the thermochemical equilibrium variable, all the symbols have already been defined in Chapter 5. The variable $\tilde{y}_\infty(k\text{-}i)$ reflects the predicted equilibrium value for the concentration of the species (y), based on the neural networks trained on FactSage® generated data. The equilibrium prediction is based on the feed input and is therefore a non-linear transformation of the inputs to the equilibrium output in a predefined way. However, the equilibrium prediction stands in a linear relationship with the other model variables, and the model is linear with respect to the regressible parameters. It is also important to note that $\tilde{y}_\infty(k\text{-}i)$ is not a normal exogenous model-input, as it is not a delayed variable, but it predicts the future equilibrium that is associated with the estimated future actual concentration, $\hat{y}(k)$. Predicted past equilibria can also be included $\tilde{y}_\infty(k\text{-}i)$ for $i > 0$. This is quite sensible for systems having large inventory recycling and poor mixing of the species being modelled as the equilibria of historic perturbations may only take effect after more than one tap.

The autoregressive variables are associated with the second term in the equation, while the exogenous and moving average components are associated with the 3rd and 4th terms respectively. Even though the delay in the exogenous variables may be 0, they are all historic variables, that is variables associated the time instants k-1 to k-n and not k itself.

The model errors are derived by first estimating the model parameters in its Equilib-ARX form, and then re-estimating the error parameters once the error time series is known for past model output variables. As only past model errors are used, which are all available, parameters estimation based on historic data is no problem.

6.2 Model Variance, Accuracy and Simplicity

In the dynamic modelling of open bath furnaces, two important variances can be associated with a data time series:

- Dynamic variance over the whole time series of process data, determined by process and chemical driving forces.
- Inherent variance associated with each data point (due to spatial effects, uncertainty in measurements etc.)

The dynamic variance can be modelled using empirical/fundamental models. The quality of the model would determine how well the dynamic variance could be explained, should the measurements contain insignificant uncertainty. One model can be said to be better than another based (among other factors) on how much of the dynamic variance it can explain. On the other hand, the quality of the data is very dependent on the second type (inherent) of variance.

It should be clear that, for a specific measured process variable, it is the ratio of the two variances that would determine how well that variable could be modelled. Therefore a variable which has a large random spatial (inherent) variance, and a similar dynamic variance cannot be modelled with a high degree of accuracy. On the other hand, a variable with a very large dynamic range, and a relatively smaller inherent variance could be modelled with a relatively higher degree of accuracy.

In Chapter 4 it was shown that some process variables such as the silicon in HCFeCr alloy may vary with a relative standard deviation of 39.9% (See Table 4.1 for PAF) associated with the spatial distribution of Si in the melt. If 95% confidence could be claimed for the standard deviation, the error would be twice the standard deviation[1]. The standard error would therefore be ±80% relative to the expected value. For Si at an average value of 1% the Si may therefore vary in a single tap from 0.2% to 1.8%. Even if a model could predict the dynamic process variance with 100% certainty, the variance in the data required to validate the model cause such scatter that the model would not be able predict the data better than within a range with an R^2 between 0.42 and 0.68 (if the process data for the %Si varies between 0.1 and

[1] Standard errors for standard deviations at different confidence levels are:

67%: Error = s; 95%: Error = $2s$; 99%: Error = $3s$, where s = relative sample standard deviation.

2.8%, based on the same number of data points and a relative normal standard deviation of 39.9%).

If this same test is applied to carbon in HCFeCr, using surrogate data, which has a relative standard deviation of 3% (inherent) with carbon with and dynamic average of 8.8% C and a dynamic standard deviation of 0.5% C, the carbon could be predicted with an R^2 varying between 0.73 and 0.84. It is therefore apparent that each element has its own upper limit of predictability, if the process model is inherently perfect.

Akaike (1974) developed an criterion, named the Akaike Information Criterion (*AIC*), to aid in the selection of optimal models, based on two components:

- A measure of the best model fit
- A penalty measure for the number of model variables

The criterion could be stated as follows. When an empirical model with q adjustable parameters is fitted to the process data, the *AIC* of the set S_q is defined as:

$$AIC(S_q) = \ln(\hat{\sigma}_e^2) + q \cdot \gamma \tag{6.2}$$

where $\gamma = 2$ and $\hat{\sigma}_e^2$ is the variance of the residual or the model fitting error. Ideally, the model with the minimum *AIC* is selected. It is anticipated that the parameter estimation is based on maximization of the information entropy, as is the case for a maximum likelihood estimator. For regression of linear-in-the-parameter models, the *AIC* simplifies to:

$$AIC(S_q) = N \cdot \ln\left[\frac{1}{N}\sum_{k=1}^{N} e^2(k)\right] + 2 \cdot q \tag{6.3}$$

where N is the number of data inputs, and e is the estimation error: $e(k) = y(k) - \hat{y}(k)$, $\hat{y}(k)$ being the model estimate of the measured value $y(k)$ based on a model with q parameters. Therefore various candidate models of different possible regressor variables are considered and estimated and the model with the lowest *AIC* is selected. The *AIC* may further be used with stepwise regression / parameter estimation. Unfortunately, the *AIC* tend to overestimate the model error and it is suggested (Kanjilal, 1995) that γ is increased to 5 to penalize overparametrisation more stringently. While many other model order selection criteria exists, all have a certain degree of inherent subjectiveness, with no criterion which can be said to be best (Kanjilal, 1995).

6.3 Parameter estimation of transfer function models

Parameter estimation concerns the determination of the numerical values of the parameters of the process model which best describe the dynamics of the process. This has to be contrasted to system identification which is the process of model structure selection, collection of relevant information, parameter estimation and model validation. Parameter estimation is therefore a component of system identification.

The least squares (LS) technique is one of the most basic, powerful, and often used techniques to estimate parameters. The quality of the estimates are shown to depend on the nature of the noise, and the richness of the information contained in the data (which therefore depends on the inherent variance and the dynamic process variance respectively).

A constraint of LS method is the requirement that the noise needs to be uncorrelated with the measurement of the dependent variable. However, there are other estimation methods which do not have this restriction – Kanjilal (1995) discusses 3 such methods, namely the Instrumental Variable method, the Maximum Likelihood method and the Koopmans-Levin method which is implemented using single value decomposition. The instrumental variable method avoids the requirement that the noise be uncorrelated with the data, through the introduction of auxiliary variables called instrumental variables. The maximum likelihood method applies non-linear optimisation of the statistical information in the data so that parameter estimates are produced with most of the desired properties. However, it is computationally intensive. Finally, the Koopmans-Levin method can handle noise associated with both the dependent and independent variables, and can produce estimates similar to approximate likelihood estimators. In this thesis only the LS technique will be used, but the constraints should be noted and also that other techniques may provide more reliable estimates of the parameters.

6.3.1 Least squares method

Consider a model of the following form:

$$y(k)+a_1y(k-1)+\ldots+a_ny(k-n)=b_0+b_1u(k-1)+\ldots+b_mu(k-m)+e(k) \qquad (6.4)$$

the model in (6.4) may also be given as a concise vector expression:

$$y(k)=\mathbf{h}^{\mathrm{T}}(k)\boldsymbol{\theta}+e(k) \qquad (6.5)$$

where **h**, the data vector and **θ**, the parameter vector, are given by:

$\mathbf{h}(k) = [-y(k\text{-}1)\ \ -y(k\text{-}2) \ldots -y(k\text{-}N)\ \ u(k\text{-}1)\ \ u(k\text{-}2) \ldots u(k\text{-}N)]^T$

$\boldsymbol{\theta} = [a_1\ \ a_2 \ldots a_N\ \ b_1\ \ b_2 \ldots b_N]^T$

If the measurements are available over the time (k-m+1) to k in the form:

$$\begin{aligned} y(k-1) &= \mathbf{h}^T(k-1)\boldsymbol{\theta} + e(k-1) \\ y(k-2) &= \mathbf{h}^T(k-2)\boldsymbol{\theta} + e(k-2) \\ &\vdots \\ y(k-m+1) &= \mathbf{h}^T(k-m+1)\boldsymbol{\theta} + e(k-m+1) \end{aligned} \tag{6.6}$$

which is in concise matrix form:

$$\mathbf{y} = \mathbf{H}\boldsymbol{\theta} + \mathbf{e} \tag{6.7}$$

Given m sets of observations **y**(k) and **H**(k), the objective is to estimate n parameters of **θ** in Eq. 6.7. The least squares estimation is based on the minimisation of the scalar cost function,

$$\begin{aligned} J(\theta) &= \frac{1}{2}\sum_{i=0}^{N-1}\left\{y(k-i) - \mathbf{h}^T(k-i)\boldsymbol{\theta}\right\}^2 \\ &= \frac{1}{2}\mathbf{e}^T\mathbf{e} \\ &= [\mathbf{y} - \mathbf{H}\boldsymbol{\theta}]^T[\mathbf{y} - \mathbf{H}\boldsymbol{\theta}] \end{aligned} \tag{6.8}$$

The minimisation of $J(\theta)$ with respect to θ is given by:

$$\frac{\partial J(\theta)}{\partial \theta} = [\mathbf{y} - \mathbf{H}\boldsymbol{\theta}]^T[-\mathbf{H}] = 0 \tag{6.9}$$

and furthermore

$$\frac{\partial^2 J(\theta)}{\partial \theta^2} = \mathbf{H}^T\mathbf{H} \geq 0 \tag{6.10}$$

as the matrix $\mathbf{H}^T\mathbf{H}$ is positive semi-definite, the function $J(\theta)$ therefore has a minimum given by Eq. 6.9. Therefore the least squares estimate of the parameter vector, $\hat{\boldsymbol{\theta}}$, can be obtained by:

$$\mathbf{H}^T\mathbf{H}\hat{\boldsymbol{\theta}} = \mathbf{H}^T\mathbf{y} \tag{6.11}$$

$$\hat{\boldsymbol{\theta}} = [\mathbf{H}^T\mathbf{H}]^{-1}\mathbf{H}^T\mathbf{y} \tag{6.12}$$

Various efficient numerical algorithms exist to evaluate the matrix inverse $\left[\mathbf{H}^T\mathbf{H}\right]^{-1}$ rapidly and accurately, such as the Cholesky factorisation, QR decomposition and Singular Value Decomposition, all which are dealt with in most textbooks on numerical linear algebraic techniques.

Equation 6.11 is called the normal equation. The LS estimation is a linear transformation of **y** and therefore the LS estimator is called a linear estimator. The LS estimator requires that the number of measurements, *m*, be greater than the number of parameters, *n*. If the rank(**H**) < n, the parameters will not be meaningful. The quality of the LS estimate depends on:

- The richness of information contained in **H**(k), and
- the statistical properties of the noise sequence {e(k)};
- the uniformity of the data.

It is desirable that the data are rich in information so that a complete representation of the process dynamics is available to the estimator through the data. Furthermore the data should be balanced to the desired extent, implying that there should be enough data over the whole range. Therefore one does not want all the data to be in a small cluster with a few "outliers"; instead one would prefer a significant number of data points close to the minimum and maximum of a data range, as well as the population mean. Lack of information in the LS estimation shows in the rank deficiency of **H**, which may stem from one of the following reasons (Kanjilal, 1995):

- Multicolinearity exists between the different regressors.
- The data are too steady (not enough dynamic variance).
- Some independent variables are nearly orthogonal to the dependant variable **y**.

If the data are rich, the information matrix $\mathbf{H}^T\mathbf{H}$ will be non-singular.

Furthermore the columns of **H** should be balanced, which may be ensured through normalisation of the individual columns. As the LS estimates can be seriously affected by outliers (abnormally large or small observations), they should be eliminated in advance.

6.3.2 Recursive least squares (RLS)

In industry new data become available sequentially and sequential execution of the LS algorithm is preferable. At any given instant, given the parameter estimates (based on past

data) and the new set of observations, the recursive least squares method produces updated LS estimates of the parameters.

Consider again equation 6.12, only introducing the index k to signify the least square estimate being based on the available data up to time k:

$$\hat{\boldsymbol{\theta}}(k) = \left[\mathbf{H}(k)^{\mathrm{T}}\mathbf{H}(k)\right]^{-1}\mathbf{H}(k)^{\mathrm{T}}\mathbf{y}(k) \tag{6.13}$$

Then, at instant (k+1), with an additional dataset available, the objective is to determine the updated parameters $\hat{\boldsymbol{\theta}}(k+1)$. Following Eq. 6.6, at time (k+1), the process is given by:

$$\begin{bmatrix} \mathbf{y}(k) \\ y(k+1) \end{bmatrix} = \begin{bmatrix} \mathbf{H}(k) \\ \mathbf{h}^{\mathrm{T}}(k+1) \end{bmatrix}\boldsymbol{\theta}(k+1) + \begin{bmatrix} \mathbf{e}(k) \\ e(k+1) \end{bmatrix} \tag{6.14}$$

where h(k+1) = [-$y(k)$ -$y(k$-1) … -$y(k$-N) u(k) u(k-1) ... u(k-N)]$^{\mathrm{T}}$

Similar to Eq. 6.12, the LS estimate is given by:

$$\hat{\boldsymbol{\theta}}(k+1) = \left[\begin{pmatrix} \mathbf{H}(k) \\ \mathbf{h}^{\mathrm{T}}(k+1) \end{pmatrix}^{\mathrm{T}}\begin{pmatrix} \mathbf{H}(k) \\ \mathbf{h}^{\mathrm{T}}(k+1) \end{pmatrix}\right]^{-1}\begin{bmatrix} \mathbf{H}(k) \\ \mathbf{h}^{\mathrm{T}}(k+1) \end{bmatrix}^{T}\begin{bmatrix} \mathbf{y}(k) \\ y(k+1) \end{bmatrix} \tag{6.15}$$

Equation 6.15 can be simplified (Kanjilal, 1995) so that the RLS estimation law may be formulated as follows (full derivation given by Kanjilal(1995)):

$$\hat{\boldsymbol{\theta}}(k+1) = \hat{\boldsymbol{\theta}}(k) + \mathbf{k}(k+1)\left(y(k+1) - \mathbf{h}^{\mathrm{T}}(k+1)\hat{\boldsymbol{\theta}}(k)\right) \tag{6.16}$$

$$\mathbf{k}(k+1) = \mathbf{P}(k)\mathbf{h}(k+1)\left(1 + \mathbf{h}^{\mathrm{T}}(k+1)\mathbf{P}(k)\mathbf{h}(k+1)\right)^{-1} \tag{6.17}$$

$$\mathbf{P}(k+1) = \left[\mathbf{I} - \mathbf{k}(k+1)\mathbf{h}^{\mathrm{T}}(k+1)\right]\mathbf{P}(k) \tag{6.18}$$

where $\mathbf{k}$ is the Kalman filter estimator gain and $\mathbf{P}$ is covariance of the parameter estimation error, thus:

$$\mathbf{P}(k) = \left[\mathbf{H}(k)^{\mathrm{T}}\mathbf{H}(k)\right]^{-1} \tag{6.19}$$

and :

$$\mathbf{k}(k+1) = \left[\mathbf{H}^{\mathrm{T}}\mathbf{H} + \mathbf{h}\mathbf{h}^{\mathrm{T}}\right]^{-1}\mathbf{h} \tag{6.20}$$

The Kalman filter estimator $\mathbf{k}(k+1)$ can therefore be estimated at time instant k itself, as $\mathbf{h}(k+1)$ consists of terms available at time k. Therefore, at time k+1, as soon as the new

measurement $y(k+1)$ is available, $\hat{\theta}(k+1)$ can be produced. This is then followed by updating $\mathbf{P}(k+1)$ and $\mathbf{k}(k+2)$.

With the LS and RLS techniques, the parameters of transfer function models such as the ARMAX equations may be estimated.

6.4 Temperature and the energy balance

Temperature plays an important role in all predictions and is required in all the thermodynamic submodels. An independent way is therefore required to estimate the melt temperature. Continuous on-line temperature measurement would be the preferred method, if possible. Alternatively it would be required to be estimated using dynamic models. While process temperature is simple to measure accurately and reliably at low temperatures, it is far more difficult to achieve reliable accurate temperature measurement at temperatures associated with smelting and converting (1200 °C to 1900°C for the various operations studied in this thesis). The presence of both alloy (or matte) and slag, makes continuous direct temperature measurement by thermocouple impossible, as no ceramic or metallic sheath exists that could protect the thermocouple sufficiently over an extended period of time. Infrared techniques (Fourie, 2001) are making headway in the measurement of temperature in pneumatic injection furnaces of the Ausmelt type. However, due to the presence of partially molten / softened dust, the sensor surfaces have to be cleaned as a matter of routine. Despite much progress in sensor development, positive feedback from industry regarding successful installations is lacking. Temperature measurement of the off-gas is also dynamically inaccurate, due to the thermal inertia associated with the ceramic thermocouple sheath and the sheath fouling due to dust encrustations.

Although one may estimate the temperature of the melt through imbedded thermocouples in the refractory layer, using the thermal conductivity of the refractory and the estimated convective heat transfer coefficient of the slag / metal (refer to section 2.4.9), the thermal lag is very significant, and the unknown degree of fluid flow and the variable thickness all contribute uncertainty in the estimated absolute temperature.

Finally the use of optical / infrared techniques in the transferred arc furnace is complicated due to the presence of the high intensity electrical arc, itself having a temperature very different from the melts.

Each furnace therefore has to be dealt with separately, due the particular conditions related to each furnace.

6.4.1 The Ausmelt pilot plant furnace

Temperature measurement is the simplest for the Ausmelt furnace, as the melts are well mixed (Chapter 4), and no electrical arc exists that complicates the use optical measurement devices. Furthermore, it was shown (Fourie, 2000) that the pilot furnace freeboard region, the slag and the matte temperatures are similar within experimental error. During the pilot plant trials, the temperature was measured using a disposable dip thermocouple, but it was foreseen that the industrial furnace would use optical temperature sensors. Bath temperature measurements were therefore available as required.

6.4.2 The DC transferred arc ferrochrome alloy production furnace

The smelter producing HCFeCr had the least data available regarding actual process temperature. As explained above, the direct measurement of temperature within industrial transferred arc furnaces is virtually impossible with current technologies. However, the smelter did not even measure melt temperatures during tapping as a matter of routine. It was therefore an objective to also use the dedicated sampling campaign, discussed in Chapter 4, to measure the temperature profile during tapping, and to determine the basic descriptive statistics for each tap. Unfortunately the operating conditions leading to the tap were only available during the second of the two sampling campaigns. Furthermore only a small number of taps were sampled. The small number of data points for melt (alloy) temperature limits the complexity of the empirical that could be derived. As the temperature was not measured for a large number of consecutive taps, it was impossible to establish if an autoregressive component truly exists, and the one had therefore to rely only on exogenous inputs. For the alloy (of which the yield, composition and tapability are the most important), the temperature was thought to be the most strongly dependent on the net MWhr per reconciled ton of alloy. This relationship was evaluated and the results are presented in Figure 6.1.

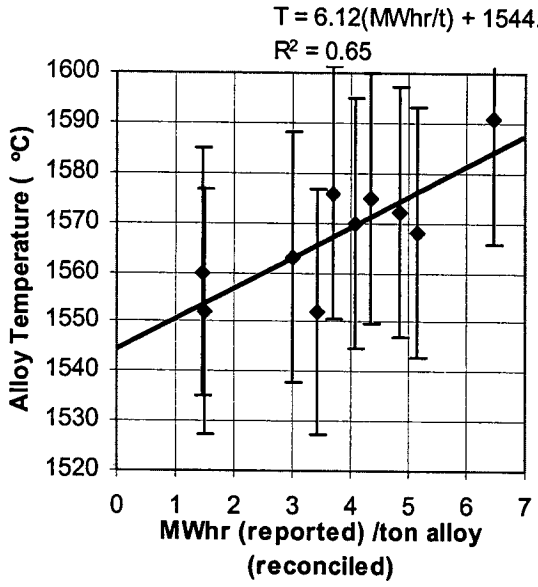

Figure 6.1: Tapped alloy temperature versus "net" specific energy input based on reconciled alloy mass and reported MWhr preceding the tap

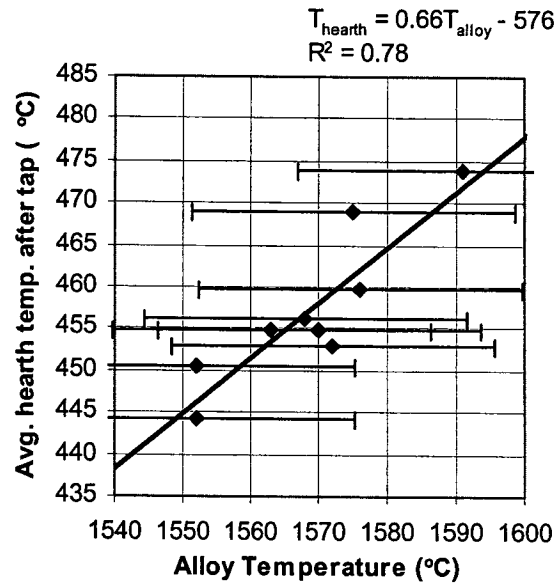

Figure 6.2: Average hearth refractory temperatures versus alloy temperature of the tap preceding the hearth temperature measurement

Figure 6.1. shows clearly that an reasonably strong relationship exists between energy input per reconciled alloy mass and alloy temperature. It is accepted that should the temperature measurement of the preceding alloy tap be consistently available, this temperature could be used as an additional autoregressive input. It is believed that it would definitely contribute much to the model accuracy as so much of the alloy remains in the furnace after each tap. The error bars with regard to the alloy temperature derive from knowledge of the statistical properties of the alloy tap temperature profile. A relative temperature standard deviation of 1.5% was used, based on the average standard deviation observed for the alloy taps. It is clear that the linear estimate falls well within the observed deviation of each data point.

Figure 6.2 shows that the hearth refractory temperatures follow the alloy temperature relatively linearly. The problem is however, that the hearth temperatures cannot be used to estimate the temperature of the subsequent tap. They are only an indication of temperatures of alloy taps that already have occurred. The thermal inertia of the refractory, which dampens and retards the thermal dynamics, therefore prevents the refractory temperature from being used in a predictive mode. No significant relationship was found for refractory temperature and the tap temperature following it. In the absence of more data points, the empirical relationship:

$$T_{alloy}\,(°C) = 6.12\,E_{specific}\,(MWhr/t) + 1544.7 \qquad (6.21)$$

will be used to estimate the alloy temperature for equilibrium purposes. It is quite obvious that the relationship is only moderately accurate, and will therefore impact on all predictions using it as an input variable.

6.4.3 The DC transferred arc high titania slag production furnace

The DC transferred arc furnace used for ilmenite production had the most temperature measurements available for a proper dynamic study. Fundamentally, one would consider the temperatures of preceding taps, the average power input, and some indication of the state of reduction of the slag during previous taps - the Fe:Ti ratio in the slag was used in this case. The greater the ratio of Fe to Ti, the poorer is the slag reduction and the more reactive it will be towards further carbon addition which, due to its endothermic reaction, will remove heat from the bath. A simple second order ARX model was derived of the form:

$$T(k+1) = 0.360 \cdot T(k) + 0.129 \cdot T(k-1) + 0.211 \cdot x_{Pwr}(k) - 135.3 \cdot x_{FeTi\_ratio}(k) + 911 \qquad (6.22)$$

This gave a minimum *AIC* of -2932 when all the variables were scaled between their maximum and minimum. The prediction performance of the ARX model is shown in the scatter diagram in Figure 6.3. While the prediction performance does not appear to be very good, it is apparent that this is close to what could be achieved even with a perfect model. This claim can be made, when the data are compared with a generated surrogate dataset, which has the same statistical properties as the measured data, with noise introduced with the inherent relative standard deviation in temperature of 0.96% superimposed on the surrogate data predictor. The surrogate data have the same average, standard deviation and other statistical properties of the original data time series and therefore reflect the same range and central tendency as the original measured data. Several recalculations based on random number generation gave a range of R^2 for the surrogate data (assuming a perfect model but with measurement noise) of between 0.40 and 0.54. The prediction performance therefore falls within the range, and further modelling effort to improve the model would not be sensible given that the average standard deviation in temperature (inherent deviation) during a single tap is 15°C, while the overall deviation over the total dynamic / time series range is 16 °C. An average tap temperature over the whole time series of 1746 °C is noted.

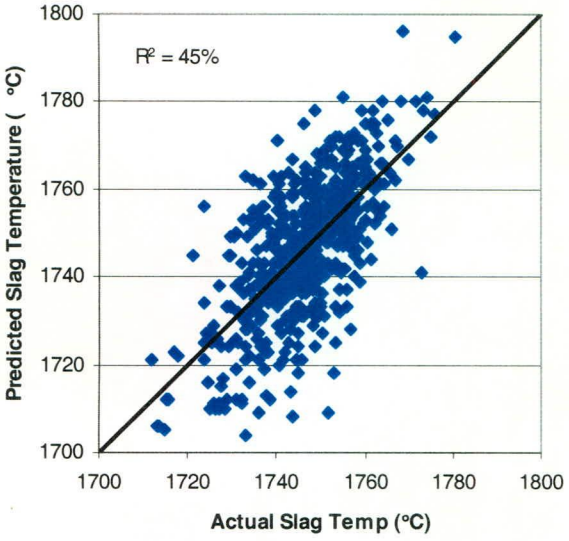

Figure 6.3: Predicted slag temperature (using ARX Eq. 6.22) versus actual measured temperature

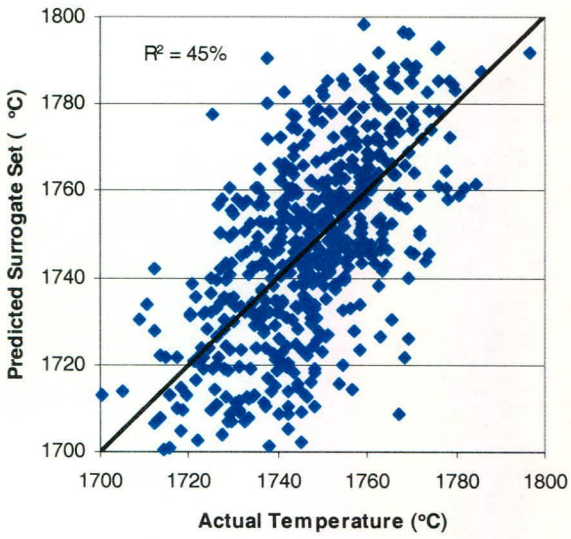

Figure 6.4: Predicted slag temperature for a perfect model based on a surrogate data set with measurement noise superimposed on it (relative standard deviation of 0.096% based on average tap temperature – from mixedness studies)

If each variable of equation 6.22 is scaled between its minimum and maximum (a linear transformation which does not change the regression), the contribution of each coefficient and therefore the sensitivity of the dependent variable with regard to each of the independent variables may be determined. The parameters based on scaled variables are shown as a bar-graph in Figure 6.5. Furthermore, Figure 6.6. shows the performance of the predicted (using equation 6.22) versus the measured time series of slag temperatures.

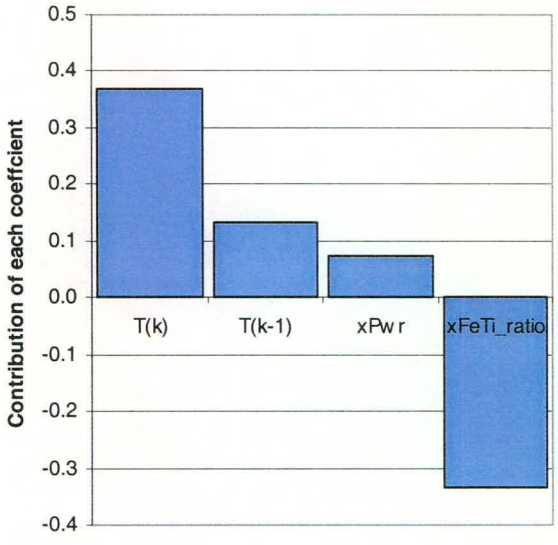

Figure 6.5: Contribution of each coefficient of Eq. 6.22, based on linearly scaled variables.

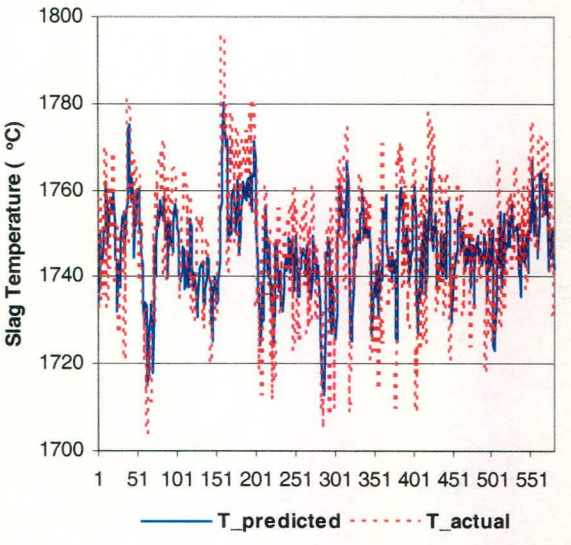

Figure 6.6: Predicted slag temperature versus actual measured temperature in time series format.

It is apparent from the scaled variables that the variables with the most significant influence are the temperature of the previous tap, and the Fe:Ti ratio of the foregoing tap. This is reasonable when one considers that both of these variables are associated with the total slag inventory. Between two taps only a fraction of slag is additionally produced and only a fraction is removed by tapping. The contribution of the power input to the foregoing tap is significant, but as the power is scaled to the feed input according to the guidelines proposed in Chapter 2 (refer to Figure 2.34) and the feed is relatively small compared to the total melt inventory, the contribution of the power coefficient is also smaller.

While other variables were included, they did not improve the model accuracy significantly, but lead only to an increase in model complexity, as also shown by an increasing *AIC*. They were therefore discarded.

Using the temperature measurements or predictions above, one may predict the corresponding equilibrium concentrations and / or use temperature as an exogenous variable in the prediction models.

6.5 Dynamic prediction of the Fe and S in Ni-Cu matte during the 2nd stage blow conversion

Much of this work has been published earlier by the Georgalli and the author (Georgalli *et al.*, 2002b, Eksteen *et al.*, 2002 a, Georgalli *et al.*, 2001a and 2001b). An Equilibrium-ARX model structure was used in all cases. Initial research (Georgalli *et al.*, 2001 a and b) leads to development of the models to predict the actual mass (not concentration which could be back-calculated) of the matte elements. Although not as useful as models that directly predict the mass % of Fe and S, they were the first models developed that demonstrated of the Equilib-ARX kind. The models for the masses of Fe and S in the matte at an future instant with a time horizon about double the sample-turnaround-time, are presented in equations 6.23 and 6.24 respectively.

$$\hat{Fe}(k+1) = 0.1223 \cdot \tilde{Fe}_{\infty}(k+1) + 0.3350 \cdot Fe(k) - 0.0226 \cdot M_{total}(k) + 3.792 \qquad (6.23)$$

$$\hat{S}(k+1) = 0.3827 \cdot \tilde{S}_{\infty}(k+1) + 0.3996 \cdot S(k) - 0.0946 \cdot M_{total}(k) + 13.644 \qquad (6.24)$$

The variables for Fe and S are all in the units of mass, as well as the total matte residual mass, M_{total}. The total matte residual mass was estimated using the observation made in Chapter 3,

that the copper mass remains nearly constant while Fe and Ni remain in the matte to be oxidised. Prediction accuracies of the masses were quite accurate as is reflected by the R^2 in Table 6.1. Significant improvement occurred when the ARX model was used in combination with the equilibrium, versus the equilibrium prediction only.

Table 6.1: Prediction accuracy of Equilib- ARX models based on masses

Component predicted	R^2 (Equilibrium model only)	R^2 (Equilib-ARX model)
Mass $Fe\ (k+1)$	0.76	0.97
Mass $S\ (k+1)$	0.75	0.90

In both models a significant constant is noted. This constant would include all biases inherent to the data, as the Ausmelt furnace data were not reconciled.

If the models are inspected, it will be noted that the presence of the lance-to-matte interface distance is conspicuously absent from the equations. The lance to matte-slag interface distance was originally considered to have a large effect on the state of mixedness of the system. It is also the only variable available that is independent of the thermochemistry of the system, and is thus very valuable in terms of control. Once the total mass of matte in the bath is known, the theoretical level of the matte in the bath can be calculated. The distance from the lance tip to the hearth of the furnace is measured continuously and from these values the distance from the lance tip to the matte-slag interface can be calculated. It must be noted that this calculated height is based on the assumption that there is a clearly defined, horizontal interface between the matte and the slag. Obviously this will never be the case during injection into the bath. It is also assumed that the lance tip is not burned at all, which is not always the case. Due to the fact that the matte mass is only known at the previous time step, the calculated matte height also refers to the value at the end of the previous time step (beginning of the current step). As stage two blow progresses, the matte in the bath decreases, and therefore so does the matte height, which means that the error in the calculated distance will increase as the current time step progresses. Despite all of the above discrepancies and assumptions, it was originally thought that the distance used would still infer the actual effect of the distance between the lance and the matte-slag interface.

It was found that the lance to matte-slag interface distance displayed very little effect on the models. This, combined with the fact that the 95% confidence limits for the lance to matte-slag interface distance variable parameter covered a range from –2.0 to 4.6 for the iron model,

and –2.5 to 2.3 for the sulphur model, lead to the decision that this variable would be excluded from the model, as there is minimal correlation between it and the output variable. This result is very unexpected and seems to indicate that the lance to matte-slag interface distance has minimal effect on the mixing in the furnace. The only way that it is felt this could be true is if the bath is so well mixed that the mixing in the furnace is already almost ideal. This supports the similar conclusion drawn when comparing the actual and predicted equilibrium concentrations of iron and sulphur in the bath. Removing this variable had basically no effect on the model performance, and resulted in a very slight improvement in performance. Although this variable was found to have very little effect on the pilot plant furnace, it may not be so in the industrial installation and it is thought that its effect must be further investigated once actual plant data becomes available. One of the key problems may derive from the small dynamic range of the matte-to-lance distances which was comparatively similar to the uncertainties associated with the measurement.

Furthermore, the Equilib-ARX type models to dynamically predict the Fe and S mass % concentrations in the matte, for any given time step between two dynamic states, Δt, is presented in equations 6.25 and 6.26 respectively. As expected, the parameter of the first autoregressive term takes on the highest value, but the equilibrium value contributes significantly in both cases. It was already shown (see paragraph 3.3.4.2) that, for the converter, the concentrations approximate equilibrium rather closely.

$$\%\hat{Fe}(k+1) = 0.33 \cdot \%\tilde{Fe}_{\infty}(k+1) + 0.594 \cdot \%Fe(k) - 0.271 \cdot \%S(k) - 0.121 \cdot \Delta t + 7.091 \quad (6.25)$$

$$\%\hat{S}(k+1) = 0.136 \cdot \%\tilde{S}_{\infty}(k+1) + 0.654 \cdot \%S(k) - 0.171 \cdot \%Cu(k) - 0.0506 \cdot \Delta t + 8.280 \quad (6.26)$$

Again, the accuracy of the models is significant, if one considers the industrial nature of the measurement environment. The R^2, which is based only on model predictions of unseen data, is contrasted to the situation for equilibrium only in Table 6.2. One should remember that an additional 9 variables were used for the equilibrium predictions, all of them nonlinearly linked to the equilibrium predictions. It is also through manipulation of these variables that control is possible – none of the other variables in the ARX equation are manipulable variables. The copper is required in the sulphur prediction due to its strong affinity for sulphur. As before, the effect of the estimated lance-to-matte distance was negligible.

Table 6.2: Model prediction accuracy of matte concentrations of Fe and S

Component predicted	R^2 (Equilibrium model only)	R^2 (Equilib-ARX model)
$\%Fe\ (k+1)$	0.68	0.86
$\%S\ (k+1)$	0.60	0.82

The result for a few 2nd stage blows for Fe and S are also illustrated in Figures 6.7 and 6.8 respectively.

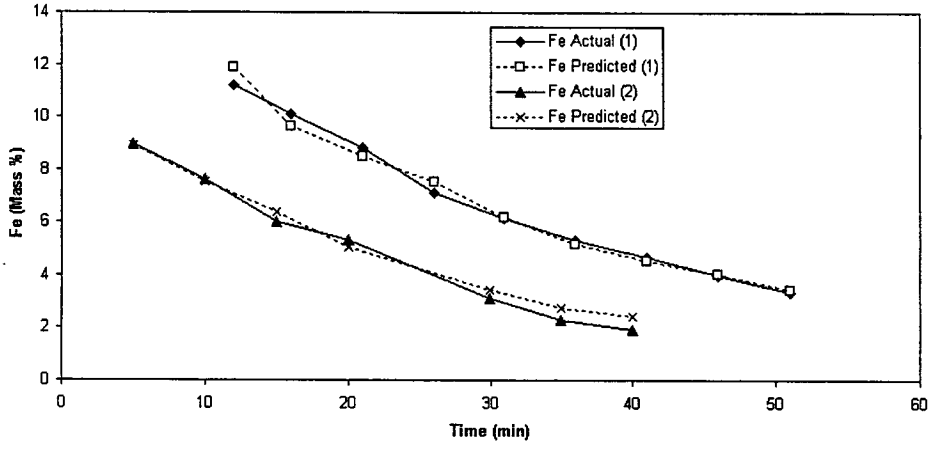

Figure 6.7: Dynamic prediction of the %Fe in matte during 2nd stage blows in an Ausmelt furnace.

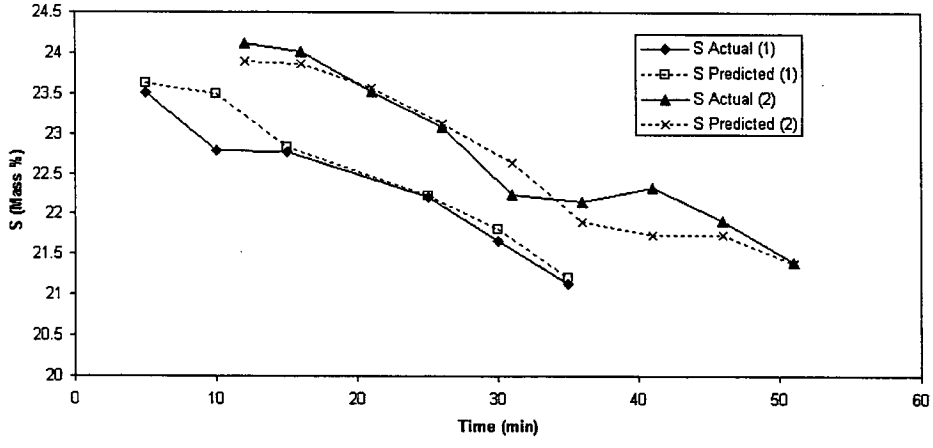

Figure 6.8: Dynamic prediction of the %S in matte during 2nd stage blows in an Ausmelt furnace.

It is clear that the dynamic behaviour of Fe and S are very well predicted using the Equilib-ARX model.

The role of a wide dynamic range is again quite visible. The % Fe varies from 12% to 2% (10% range, or 500% relative to the minimum value) and the sulphur varies from 24 to 21% (3% range, or 14% relative to the minimum value). The smaller dynamic range for sulphur is also reflected in the lower accuracy of the sulphur model predictions.

6.6 Dynamic prediction of the Si and C in HCFeCr alloy production and the levels of Cr in the slag.

The situation for Si and C in HCFeCr alloy and Cr in the associated slag is quite different to for the previous situation of the matte converter using a lance based injection. The poor mixing of Si in the alloy has already been noted in Chapter 4. This would therefore require the dynamic ranges to be much larger. It was also noted in the introduction that with a surrogate data set the best model accuracies that even a perfect model can obtain would lie within a R^2 range of 0.42 and 0.68 for %Si and 0.73 and 0.84 for the %C in HCFeCr alloy. These are therefore the ranges that should be aimed for with regard to the development of predictive models.

As before, the Equilib-ARMAX approach was used, in this case employing the full ARMAX structure (in comparison to the Equilib-ARX structure used above). Furthermore, a few other notable differences exist:

- Data were only available at the time to the tap, and therefore not in-between taps as for the Ausmelt converter.
- The data were furthermore reconciled on a daily basis, and the reconciliations adjustments distributed according to the feed flowrate.

The time series predictions of the equilibrium model, and Equilib-ARX model are displayed for both the %C and the %Si in HCFeCr, in comparison to the reconciled data, in Figures 6.9 and 6.10 respectively.

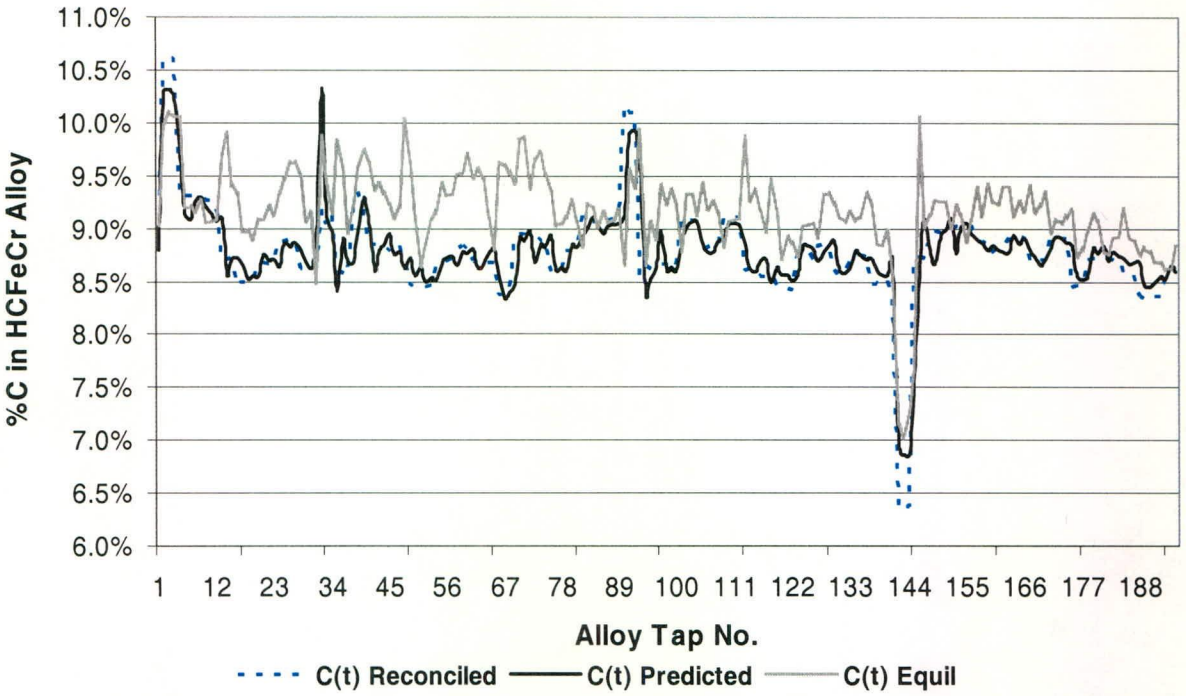

Figure 6.9: Comparison of the predicted, the equilibrium and the reconciled data time series for C in HCFeCr

In the case of carbon in HCFeCr, it is seen that significant deviation from the equilibrium occurs, but that the overall prediction of the Equilib ARMAX combination is quite accurate for a system with a prediction horizon of 6.5 hours. It is clear that the Equilib-ARMAX approach improved significantly on equilibrium prediction only. The equilibrium model took into account the role of heel recycling. The predictions were always for the following tap, based on a set of setpoints for the reagents, and the estimated inventory, as well as the time series history of each variable and the historic model error time series (historic values of the difference between the model prediction and the actual reconciled values).

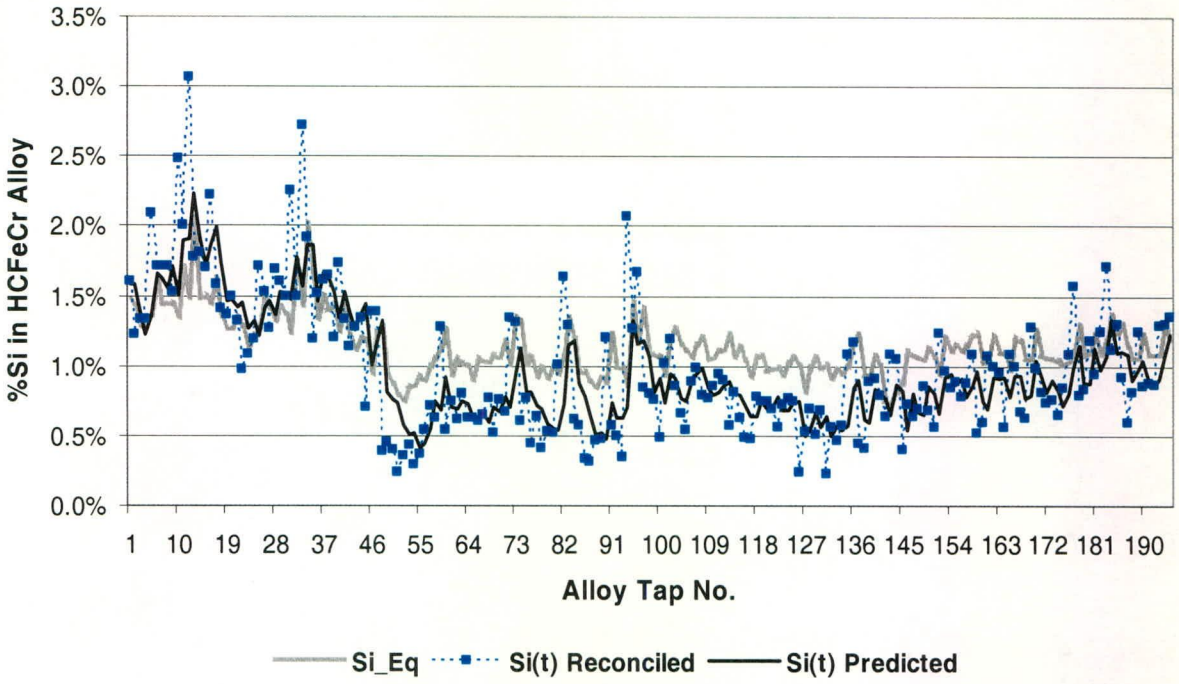

Figure 6.10: Comparison of the predicted, the equilibrium and the reconciled data time series for Si in HCFeCr

The modelling of the silicon in the metal was similar to that of carbon, although it is apparent that the equilibrium prediction of silicon is much closer to the reconciled data, than that observed for carbon. It is furthermore apparent that the Equilib-ARMAX model performs better than Equilibrium only. The performance of both models, as quantified by the R^2, is presented in Table 6.3. In both cases the data fall within the range of surrogate datasets with similar data distributions and noise (R^2 = 0.73 to 0. 84 for %C, and 0.42 to 0.68 for %Si).

Table 6.3: Model prediction accuracy of alloy concentrations of C and Si in HCFeCr

Element	R^2 Equilibrium Model Only	R^2 Equilib-ARMAX Hybrid Model
%C	34%	75%
%Si	42%	54%

Figures 6.11 and 6.12 show the contribution of the various coefficients to the Equilib-ARMAX model. It is clear from the graphs that the historical values of both the %C and the %Si play significant roles, as well as past model errors and predicted and past equilibrium values. The full Equilib-ARMAX model structure is therefore required to model this system. Table 6.4 lists the variables used for the above models to predict the %C and Si respectively:

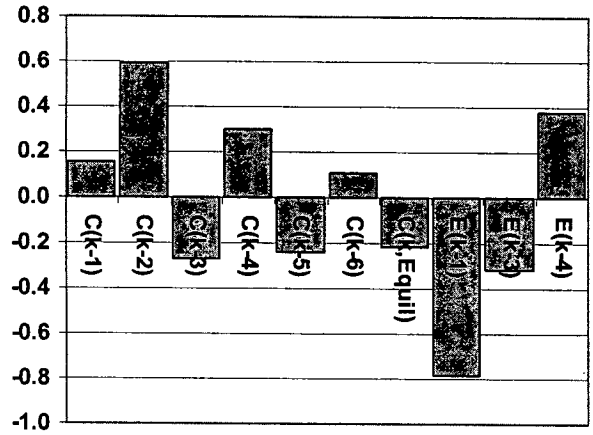

Figure 6.11: Contribution of each coefficient to the associated variable for the dynamic model to predict the %C in HCFeCr.

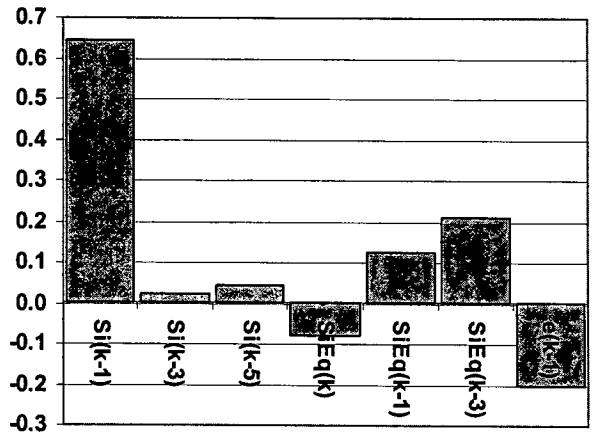

Figure 6.12: Contribution of each coefficient to the associated variable for the dynamic model to predict the %Si in HCFeCr.

Table 6.4: Model variables required to predict the alloy concentrations of C and Si in HCFeCr

Model variables required to predict the %C(k)	Model variables required to predict the %Si(k)
C(k-1), C(k-2), C(k-3), C(k-4), C(k-5), C(k-6), C(k, Equil), e(k-1), e(k-3), e(k-4)	Si(k-1), Si(k-3), Si(k-5), Si(k, Equil), Si(k-1, Equil), Si(k-3, Equil), e(k-1)

6.7 Dynamic prediction of the FeO, TiO_2 and Ti_2O_3 in high titania slag and C in the associated pig iron.

While this system should show similarities to the ferrochrome system discussed above, a few notable differences are noted. Both pilot plant and industrial high titania slags have been proven to deviate very far from the estimated equilibrium conditions (Geldenhuis *et al.*, 1999). It is yet unknown why the system is so out-of-equilibrium despite being well mixed and fluid. Geldenhuis *et al.* (1999) have shown that the TiO_2-Ti_2O_3 and the FeO-Fe as well as the C-CO redox couples are all out of equilibrium based on oxygen potential measurements of the slag. One would therefore not expect good correlation between the equilibrium and measured amounts. The Equilib-ARMAX approach will still be applied, in this case to the %FeO in high titania slag. As the relationship between FeO and Ti_2O_3 and total TiO_2 is known with good accuracy (refer to paragraph 5.7.2), it is of critical importance to be able to predict the %FeO with good accuracy as the overall crystallisation behaviour is critically dependent on the ratio relationship of FeO to TiO_2 and Ti_2O_3. To predict the %FeO in the slag, the anthracite and ilmenite fed to the furnace were normalized relative to the maximum

recorded value. The equilibrium value was predicted, as before using the Neural Network equivalent of the FactSage outputs.

FeO proved to be very predictable (R^2 of 0.77). The prediction accuracy of the Equilib-ARMAX model is apparent in Figure 6.13.

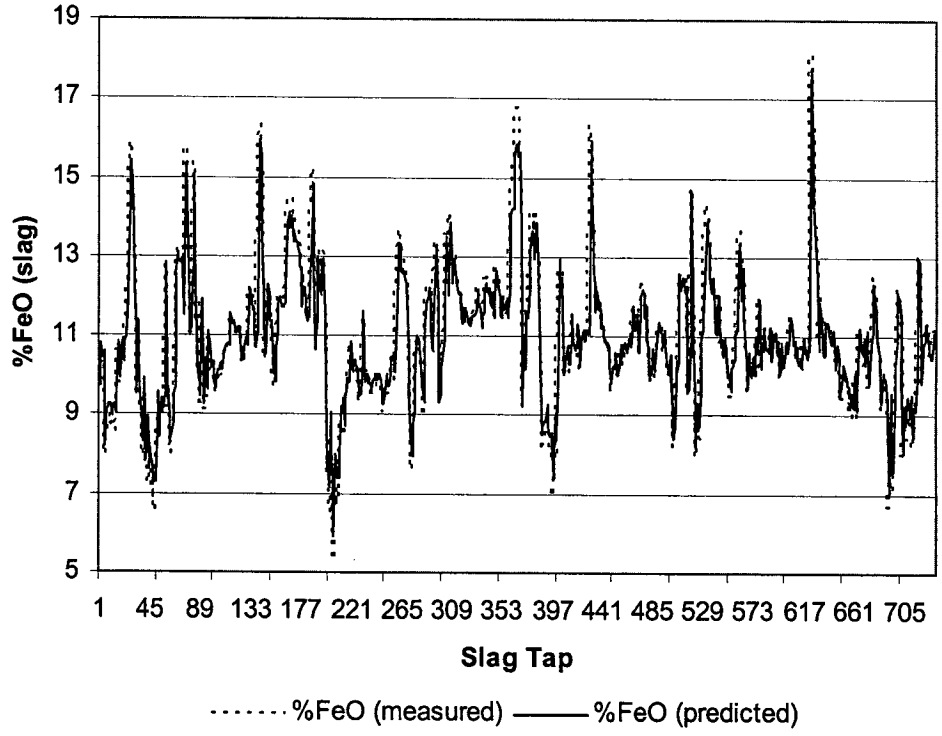

Figure 6.13: Time series of predicted %FeO versus actual %FeO in the slag, one tap into the future

The variables and the associated estimated parameters of the Equilib-ARMAX model with output as presented in Figure 6.13, are presented in Table 6.5. The sensitivity of the model prediction to changes of one standard deviation from the average is shown for each variable. It is clear that the sensitivity does not necessarily follow the pattern of the contribution of the coefficients, as the normal spread of each variable differs. The table shows that the effect of the %FeO of the preceding tap is overriding, as is typical for these systems with large recycled inventories. The contributions of the anthracite and ilmenite fed (based on setpoints) to the tap (k) to be predicted follows the autoregressive variable in significance, each contributing approximately $^1/_5$ and a $^1/_7$ to the overall variance in the predicted tap, if varied within their normal operating range (1 standard deviation). These feed inputs also influence the equilibrium value (nonlinearly). The contribution of the equilibrium value is significant , but relatively small as the system is so far from equilibrium. It is important to note that the variables that may be actively manipulated to change the outcome of the future tap are the anthracite and ilmenite fed (both as explicit variables in the model as well as implicitly

through the equilibrium), and the power supplied to the furnace, which influence the temperature (Eq. 6.22) and therefore also the equilibrium. It is therefore clear that all the variables that can be manipulated in practice could be used to change the %FeO (and therefore the ratio of TiO_2 and Ti_2O_3 and the overall amount of Ti in the slag) in the future slag tap. As the turnaround time for an analysis is 20 minutes, while the average slag tap-to-tap duration is three hours, it provides enough time to adjust the manipulated variables to achieve the target FeO level for the next tap.

Table 6.5: Model variables for the Equilib-ARMAX model for %FeO prediction*.

Model Variable	Parameter Value	Model Sensitivity to variable change within one standard deviation (relative to largest sensitivity)	Variable Type
Intercept	0.0000	0	Constant
%FeO (k-1)	0.9236	100%	Autoregressive
%FeO (k-2)	0.0621	-11%	Autoregressive
Anthracite Fed_{Scaled} (k)	2.5318	19%	Exogenous
Anthracite Fed_{Scaled} (k-1)	-1.0966	4%	Exogenous
Ilmenite Fed_{Scaled} (k)	-1.2451	-14%	Exogenous
Ilmenite Fed_{Scaled} (k-1)	0.2860	-4%	Exogenous
Ilmenite Fed_{Scaled} (k-2)	-0.4033	-4%	Exogenous
Ilmenite Fed_{Scaled} (k-6)	0.5619	4%	Exogenous
Equilibrium (k)	0.0191	8%	Equilibrium
Error (k-1)	0.8573	1%	Moving Average

*Note : The actual sensitivity of the first autoregressive component (%FeO (k-1)) is 15%, which has been scaled to 100% to improve the sensitivity resolution of all the variables.

Similarly to the above approach used to predict the %FeO in this high titania slag, one may model the %C in the pig iron, which is the major component determining the liquidus temperature and precipitation behaviour of the pig iron (refer to Appendix A). All the independent variables were scaled relative to their maximum before the parameters were estimated. As for the %FeO prediction, the full Equilib-ARMAX structure was used. The Equilib ARMAX model with 14 variables were used to model the %C tap-to-tap time series with an R^2 of 0.80.

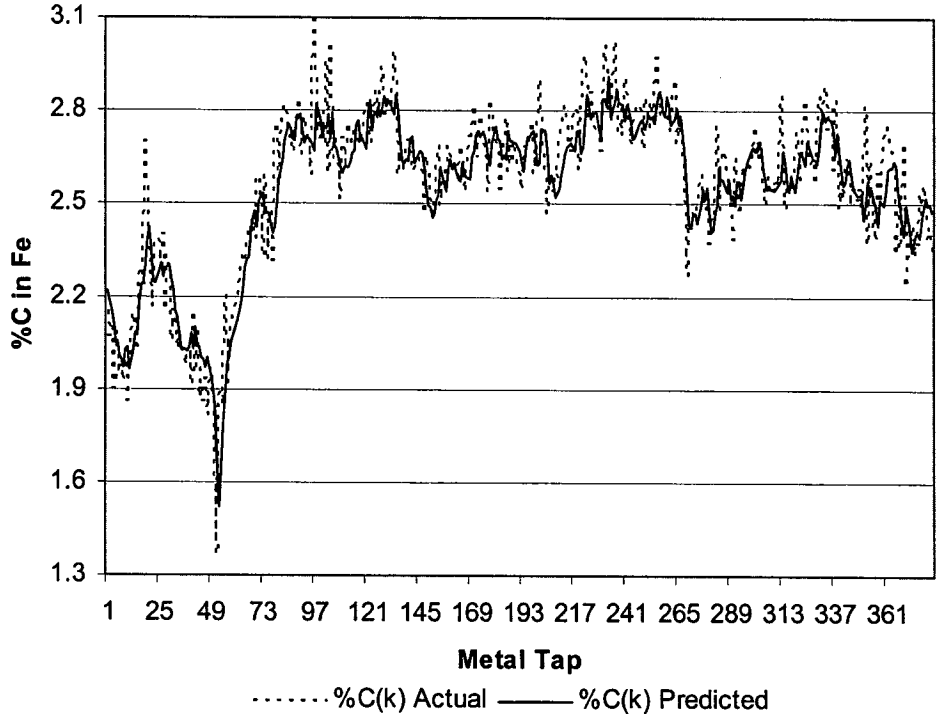

Figure 6.14: Time series of predicted %C versus actual %C in the pig iron, one tap into the future

Table 6.6 presents the influence of the most significant model variables on the model outcome for the prediction of the %C in the pig iron. As in previous cases the first autoregressor contributes the most to the model predictions (both in coefficient and in model sensitivity), followed by the 2nd autoregressor. The model is noted to have a high autoregressive model order, with 4 autoregressors contributing. The anthracite fed and the ilmenite fed to the predicted tap (therefore the setpoints of these variables) contribute the most. As before, they also influence the equilibrium, although the equilibrium also takes into account inventory recycling. The anthracite and ilmenite fed are again the only two directly manipulable variables, although temperature influence the equation outcome via the equilibrium prediction. The model has a third order with regard to both exogenous variables. Finally, the model is second order with respect to the moving average component, where past model

errors are used to "tune" the future predictions. The "recycling of errors" contribute significantly in adjusting the model outcome. Overall the model predicts the %C very well.

Table 6.6: Model variables for the Equilib-ARMAX model for %C prediction*.

Model Variable	Parameter Value	Model Sensitivity to variable change within one standard deviation (relative to largest sensitivity)	Variable Type
Intercept	0.0000	0	Constant
%C (k-1)	2.251	100%	Autoregressive
%C (k-2)	1.985	88%	Autoregressive
%C (k-3)	-0.583	-26%	Autoregressive
%C (k-4)	-0.602	-27%	Autoregressive
$\%FeO_{slag}$ (k-1)	0.067	4%	Exogenous
Anthracite Fed_{Scaled} (k)	0.254	14%	Exogenous
Anthracite Fed_{Scaled} (k-1)	0.227	12%	Exogenous
Anthracite Fed_{Scaled} (k-2)	-0.195	10%	Exogenous
Ilmenite Fed_{Scaled} (k)	-0.271	-16%	Exogenous
Ilmenite Fed_{Scaled} (k-1)	-0.225	-13%	Exogenous
Ilmenite Fed_{Scaled} (k-2)	0.140	-8%	Exogenous
Equilibrium (k)	0.039	2%	Equilibrium
Error (k-1)	0.376	22%	Moving Average
Error (k-2)	0.500	29%	Moving Average

*Note : The actual sensitivity of the first autoregressive component (%FeO (k-1)) is 15%, which has been scaled to 100% to improve the sensitivity resolution of all the variables.

6.8 Prediction alloy viscosity and tappability

The prediction of alloy and slag viscosities remains important to estimate if the smelter operation may expect tapping problems or not. On the smelter plant the viscosities are not measured as a matter of routine. However, it is seldom necessary to know the actual viscosity with high accuracy, only to know if the slag is fluid, viscous (but still tappable), or untappable due to being partially crystallised. To perform this estimation, the viscosities of ferrochrome

alloy will be predicted, as a typical example, using the models discussed in Chapter 4 (paragraph 4.2.5), based on the melt chemistry, the % solids and the operating temperature.

As the absolute value of the viscosity is not of so much importance to production, but more the fluidity class, the viscosity estimates were classified. To estimate the alloy viscosity, the alloy composition and the estimated (Eq. 6.21) operating temperature were used as inputs to the FactSage® simulator, which calculated the equilibrium the composition and amounts of the alloy melt and solid phases, thereby allowing one to calculate the expected % solids in the melt. The information of the alloy liquidus, based on the chemistry of the liquid part of the two-phase alloy only, and the pure component physical properties were used in conjunction with Hirai's Equations (Eq. 4.9-4.11) to estimate the viscosity of the liquid part of the alloy. The effects of the solids were taken into account through the application of the Einstein-Roscoe Equation (Eq. 4.13), with $R = 2.6$ and $n = 2.5$. The viscosities were classified relative to the average liquid-only viscosity, which did not vary significantly within the operating range. If no solid particles were present the liquid was always very fluid. However, the effect of the solids was pronounced. The viscosity classes were categorised according to a logarithmic scale as presented in Table 6.7, to classify the fluidity based on order-of-magnitude:

Table 6.7: Relative viscosity categories for ferrochrome alloy

Viscosity relative to liquid-only viscosity	Fluidity class	Implications
$\eta_R = 1$	Highly Fluid	None
$1<\eta_R<10$	Viscous	Less fluidity, imperfect mixing
$10<\eta_R<100$	Highly Viscous	Poor mixing*
$\eta_R>100$	Tapping Problems Anticipated	Very sticky alloy, which may not be tappable, depending on alloy height above taphole, very poor mixing*

* See Figure 4.18

Based on the above categorisation, the estimated viscosities were classified and a Pareto (sorted) histogram was subsequently developed to observe the frequency of occurrence of the different categories. The histogram is shown in Figure 6.15. The alloy was found to be very fluid for most of the taps, but viscous melts were observed relatively frequently (about one

quarter of the total occurrences). Highly viscous melts and melts where tapping problems were expected to occur, occur far less frequently (3.5% and 2.5% of the total occurrences, respectively), as one would expect for a producing furnace. Unfortunately, no qualitative data were available to determine if tapping problems were actually experienced or not. As two-phase melts start to behave as Bingham plastics (requiring a critical yield stress to flow) at 8-10% solids, and the "Very viscous class" always contains more than 20 mass% solids, one may even experience some tapping problems with this class, depending on the melt level inside the furnace. The tapability of a furnace melt would not only depend on the fluid's viscosity but also on the liquid head inside the furnace (taking into account that is also a slag layer on top of the alloy layer).

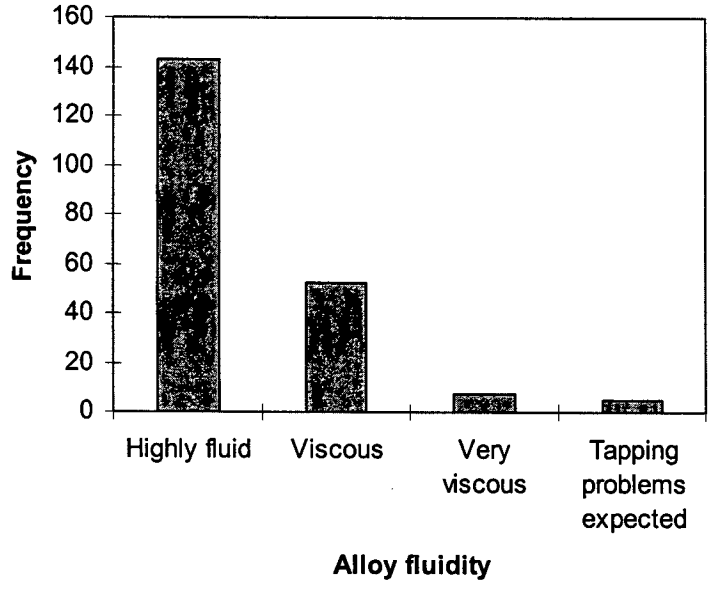

Figure 6.15: Sorted histogram of the occurrence frequency of fluidity classes associated with HCFeCr alloy

One could therefore predict alloy viscosities with a time horizon of 6 hours in advance, by predicting the alloy chemistry and temperature first and estimating the viscosity subsequently. This would allow one to control the furnace in an operating region which would result in highly fluid alloys, with improved tapability and improved alloy homogeneity.

For siliceous slags, such as chromite-based slags, the slag viscosity of the liquid-only part of the slag could be estimated through the correlations developed by Urbain (Equations 4.8 to 4.12). The bulk slag composition and the operating temperature (or estimated tap temperature) can be used as inputs to FactSage® to calculate the composition and quantities of the respective phases. Again, the % solids is incorporated to estimate the observed viscosity via

the Einstein-Roscoe equation (Eq.4.21). The procedure of viscosity categorisation is the same as above.

6.9 Integrating dynamic process models in model predictive control

It has been demonstrated, that the composition, and quantities of the alloys, slags and mattes may be calculated with a reasonable degree of accuracy within a practical time horizon. The obtainable accuracy was limited to the inherent uncertainty associated with the data. Furthermore, it was shown that tapping problems may be anticipated in advance though proper viscosity modelling and classification.

The question therefore arises how these dynamic predictive models may be used to control the furnaces or, alternatively, to suggest good setpoints for operation. It is not the purpose of this thesis to develop the controllers for the various scenarios, but a brief introduction will be given as to how control may be implemented.

Once a reliable predictive control model has been developed, one may incorporate the process model into a model predictive control architecture. Model predictive control (MPC) is a generalised approach to multiple input multiple output (MIMO) control, where the process model is used to predict future outputs over a time period longer than the longest measurement time delay. Model predictive control is defined as a control scheme in which the controller repeatedly determines or optimises the manipulated variable profile, that optimises an open loop performance on a time interval extending from the current time plus a prediction horizon. Feedback is incorporated by using process measurements, as soon as they become available, to update the optimisation problem for the next time step. The receding horizon technique is commonly used as a natural computationally feasible feedback law. The method has proved to have desirable stability properties for non-linear systems. As a consequence of its structure (Figure 6.16), an MPC is a feedforward controller for known process changes and a feedback controller for unknown process changes (Hunt *et al.*, 1992). Thus, MPC can reject measured disturbances more rapidly than conventional controllers, by anticipating their impact on the process.

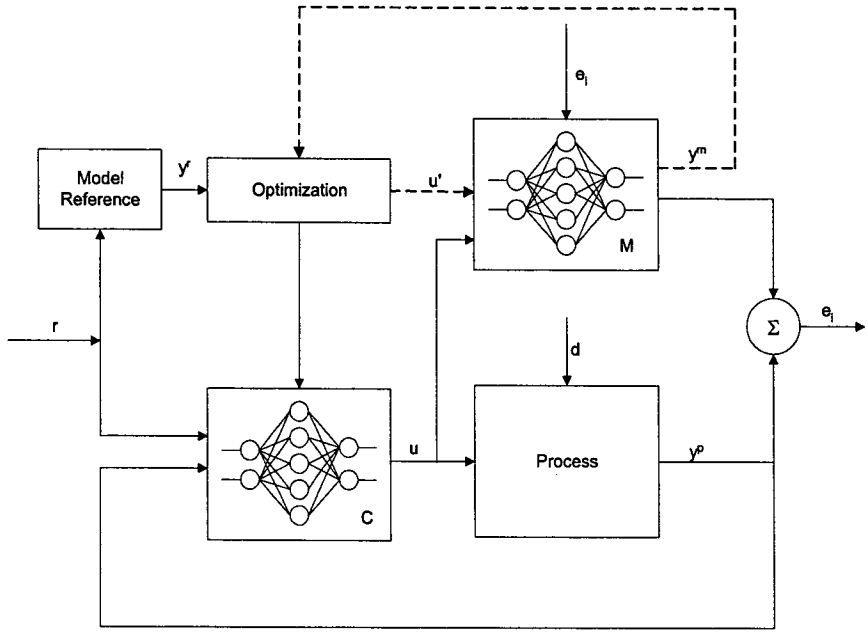

Figure 6.16: Model predictive control structure using neural networks (Hunt *et al.*, 1992).

Setpoint changes are achieved efficiently through their ability to predict an optimal sequence of manipulated input values to be implemented. The feedback element of MPC compensates for the effects of unmeasured disturbances on the process outputs and deviations between model outputs and those measured (process / model mismatch). The prediction horizon allows the MPC controller to take control action at the current time in response to forecast error, even though the error at current time is zero. Also the MPC may be given information about future constraints and future inputs such as planned setpoint changes of forecasts of loads or disturbances.

Implementing MPC with a neural network / NARMAX approach, involves utilising a neural network / NARMAX model to provide predictions of future plant response over the specified horizon. The predictions supplied to the neural network are passed to a numerical optimisation routine such as quadratic programming which attempts to minimise a specified performance criterion in the calculation of a suitable control signal. The control signal may be chosen so as to minimise a quadratic performance criterion, e.g.:

$$J = \sum_{j=N_1}^{N_2}\left[y^r(t+j) - y^m(t+j)\right]^2 + \sum_{j=1}^{N_2}\lambda_j \cdot \left[u'(t+j-1) - u'(t+j-2)\right]^2 \qquad (6.27)$$

subject to the constraints of the dynamic model. The constants N_1 and N_2 define the horizons over which the tracking error and control increments are considered. The values of λ are the control weights. The remaining parameters are illustrated in Figure 6.16.

Another alternative is to train a further neural network to mimic the action of the optimisation routine. The controller network is consequently trained to produce the same control output for a given plant output (Hunt *et al.*, 1992).

The multi-step strategy of MPC has proven performance in controlling processes in unstable operating regimes. However, the MPC approach remains sensitive to modelling errors in these unstable regions. A disadvantage of the MPC approach lies in that the execution of the optimisation algorithm is computationally intensive, especially where linearization of non-linear systems is not applicable. Also, the solution of the optimisation problem - therefore the controller behaviour - depends on a number of tuning parameters, such as weighting coefficients in the objective function, the convergence criterion, and the scaling of variables (Psichogios and Ungar, 1991).

6.10 Nomenclature of Chapter 6

AIC = Akaike information criterion

q = no. of adjustable parameters in an empirical model

h, H = data vector and matrix respectively

e = error matrix

$e(k)$ = model error

g = gradient

J = Jacobian matrix

k, i, j = counter or index

L = Lagrangian

M = mass (kg)

N = number of measurements in time series

t = time (s)

T = temperature (°C)

x_{Pwr} = Power input (Mwatt)

x_{FeTi_ratio} = Fe to Ti ratio

R^2 = coefficient of determination

$u(k)$ = exogenous input

V = covariance matrix

x = general time series variable

$\bar{x}$ = sample or time series average

$y(k)$ = output

Δt = time between two measurements (s)

Greek Symbols

γ = Akaike penalty parameter

θ = parameter vector

$\hat{\sigma}_e^2$ = variance of the residuals

7 A SUMMARY OF THE MODELLING APPROACH

"Why, a four year old child could understand this..."

" ... Someone, bring me a four year old child..."

(Groucho Marx in Fogler, 1995)

7.1 Introduction

It is the objective of this chapter to provide a very brief overview of the major steps in the model development in the form of block diagrams and give a brief discussion as to what information the modeller can obtain from the parameters of the developed Equilib-ARMAX model. As such, it is hoped that the readers will have a conceptual "road map" to aid them in developing their own models according to this approach. Three major stages can be identified, namely data acquisition, model development, and model implementation.

7.2 Obtaining the furnace information

The data used for the models are not isolated from the measurement technique, nor from the sensor reliability, nor from sensor position. These should be characterised and, where possible, the dead time should be estimated between the moment an event occurs and the moment it is registered by a sensor. A good basic knowledge of the technology should also be sought and expert operator observations / interpretations should be logged to annotate the database, as explained in Chapter 2.

One can control only what one can measure (or infer through soft sensors), which implies that if the metallurgical data are available only on a tap to tap basis, the model will be able to predict only to a tap-to-tap time interval, and not on a minute by minute basis.

Finally, once the tap-to-tap events have been logged, together with the operating setpoints, as well as the lead times (dead times before instrument registration), the variance associated with each important variable should be determined through a dedicated sampling campaign. The overall variance associated with each variable is not only the variance associated with material heterogeneity, but also due to sampling, sample preparation and analysis:

$$s^2_{Total} = s^2_{Heterogeneity} + s^2_{Sampling} + s^2_{Samle\ preparation} + s^2_{Analysis} \qquad (7.1)$$

Biases may also enter any of the above steps as well as during the final data logging (if entered manually).

7.3 Development of the Equilib-ARMAX Model

The basic modelling philosophy used in this thesis is shown diagrammatically in Figure 7.1:

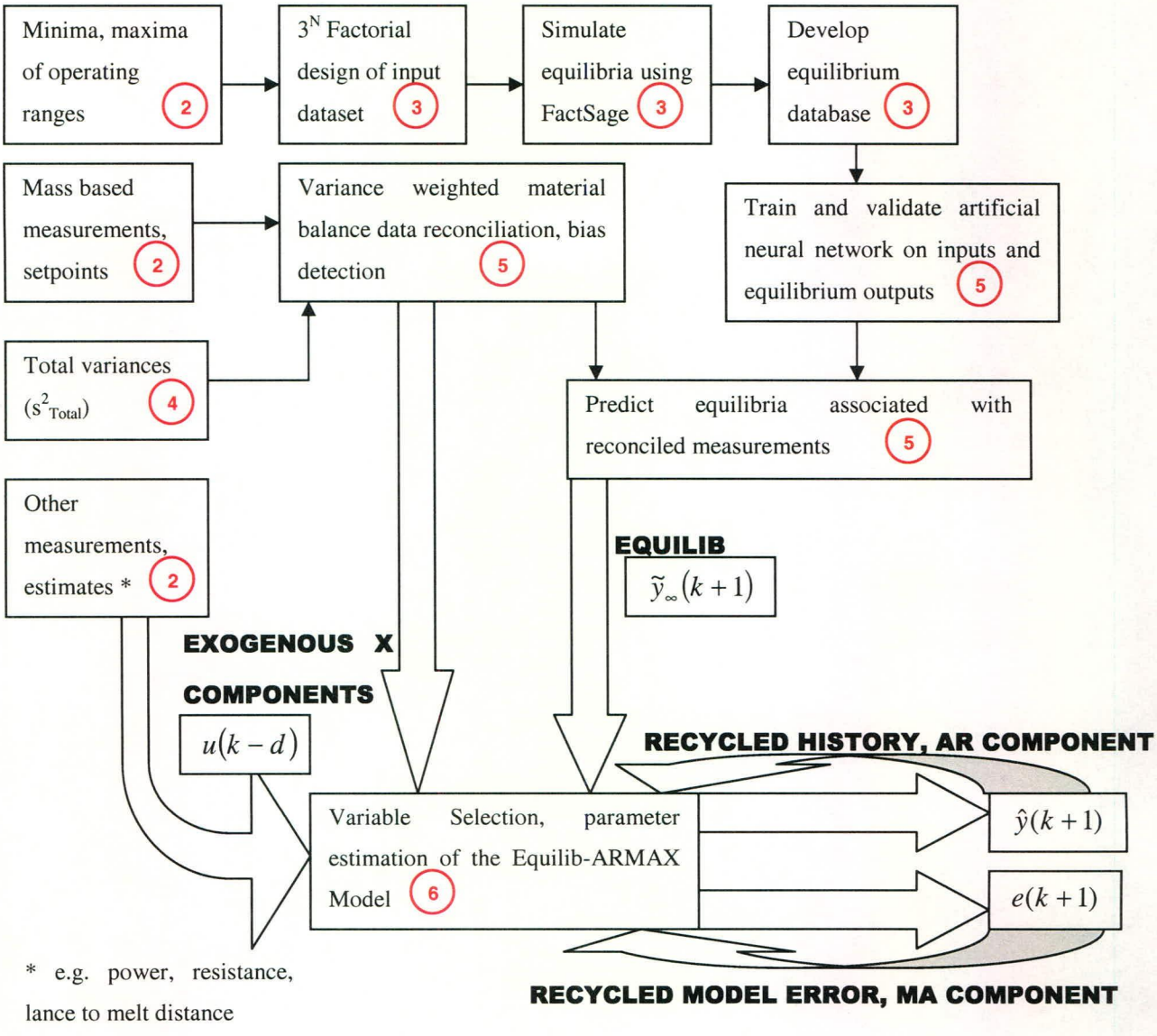

Figure 7.1: Basic modelling approach to obtain the Equilib-ARMAX model

The recycled history and recycled errors in Figure 7.1 refer to $y(k)\ldots y(k\text{-}m)$ and $e(k)\ldots e(k\text{-}p)$ respectively. The relevant chapter numbers of this thesis are shown in red circles. A more detailed flow chart is provided in Chapter 8.

7.4 Implementing the model

The model can be implemented in either as an off-line model to aid metallurgical decision making, or as an on-line to for decision support, or when used in conjunction with a controller for closed loop control or as a setpoint advisor. Recursive parameter estimation (refer to Chapter 6) may be desirable; however, statistical techniques should preferably be used to decide when re-estimation is required.

7.5 Information from the model coefficients

As shown in section 5.2.3, the model coefficients are convolutions of, among other factors, the system inventory and tap-to-tap time (or the time between consecutive samples). Stability in the model coefficients can therefore be improved though inventory stabilisation and fixing the sampling interval.

Furthermore the model coefficients themselves provide a comparison of the relative contribution (and importance) of the variables contributing to the Equilib-Model. A shift in the size of the coefficients from, say a decrease in the equilibrium coefficient, to increasing either the moving average (system dynamic) component, or the exogenous or moving average (stochastic) components, reflects an underlying shift in the overall system dynamics: a shift away from equilibrium towards greater uncertainty (stochastic) or a greater role of inventory (historic system states) or external driving forces (e.g. arc resistance). However, the interpretation is system-dependent. While the relative values of the coefficients have very little meaning to an operator or shift foreman, they provide useful information to the plant metallurgist to categorize furnace operating regimes. However, because of the convoluted nature of the coefficients it is not a simple matter to identify the specific variable in the model which is contributing to the change.

8 CONCLUSIONS

"An idea that is not dangerous is unworthy of being called an idea at all."
(Oscar Wilde, "The Critic as Artist", 1890)

8.1 Modelling and control of pyrometallurgical reactors for sustainable materials production

The thesis introduced furnace control as a necessary step to achieve sustainable processing of primary and recycled materials, where a metal cannot be recovered by physical means only, but pyrometallurgical processing of the raw materials and wastes is required. While the thesis focussed on primary smelting and conversion operations in bath type furnaces, the resulting modelling approach is applicable to all bath type furnaces, irrespective the source of the feed material. If the outcomes of furnaces can be predicted with an acceptable level of accuracy for a given suite of operation setpoints and disturbances, remedial action may be taken in time to prevent unwanted operating scenarios. This leads to smaller wastage of energy and raw materials, less reworking of off-specification products, and larger compliance with the goals of sustainable processing.

The nature of pyrometallurgical operations was shown to be such that neither purely fundamental models nor totally empirical models could model these systems with sufficient accuracy, flexibility, simplicity and robustness. A hybrid approach was therefore described in this thesis, of which the core conclusions will be summarised in the following paragraphs. The thesis used data from various sources: industry data, pilot plant data, laboratory data, physical (cold) modelling information, literature data and generated information using simulation software. The characteristics of the various data sources were briefly presented in Chapter 1.

8.2 Conclusions regarding data sources - knowing and understanding the technology

It was shown that an in-depth knowledge of the production technology is required, which includes the most important metallurgical process phenomena and known kinetic / rate information as described in Chapter 2. Moreover, it was shown that the data are influenced by the method of measurement, data availability, data integrity, data type and data accuracy. A proper technological analysis of the explicit systems aids one in qualitatively identifying the key process variables that determine the outcomes of the process. Chapter 2 explained the main metallurgical phenomena and compared the characteristics of the various bath type furnaces studied in this thesis.

From the technological analysis, the following conclusions could be drawn:

- The Ausmelt furnace is a well-mixed converter type reactor which implements submerged lance injection technology to convert or upgrade base-metal mattes through oxidation. The reactions are exothermic, and the furnace is operated in a two-stage batch process. The key phenomena depend on the matte chemistry, the amounts of oxidant and reductant added, and the lance-to-matte distance. The data derived form a pilot plant, which made continuous tap-to-tap measurements impossible, as the furnace was operated in a batch mode within a scheduled campaign. Instead, the focus was on dynamic matte chemistry prediction during the converting process. Information regarding the off-gas was found not to be trustworthy, and the dust was not sampled. From an analysis of the kinetics of similar processes it was found that the kinetics of the reactions are very rapid and that process dynamic and inventory effects overshadowed any kinetic effects.
- The DC plasma arc furnace used for both reductive chromite smelting and reductive ilmenite smelting was shown to be based on complex phenomena, much of which remain ill-understood – especially with regard to the interaction of the DC-plasma arc with the furnace bath. The characteristics of the plasma arc were qualitatively explained, and supported with quantitative relationships where available. It was shown that electrical arcs have extremely small arc time constants and that the second-by-second arc dynamics would have little influence on the overall metallurgical dynamics. Arc stirring of the molten bath was discussed and it was shown that earlier simulations implied that the molten baths are well stirred, based mostly on CFD

studies looking into the state of thermal mixedness. The current associated with the arc was shown to have the largest effect on dimple formation and electromagnetic arc stirring. The metallurgical impacts of thermal inertia were shown to be significant, which arises from the relatively small arc attachment zone relatively to the bulk of the melt. Finally it was shown that it was possible, with enough information from furnace refractory suppliers, to gauge the thickness of the internal slag freeze lining, which may contribute significantly to the overall furnace inventory.

- The kinetics associated with reductive smelting were found to be overshadowed by the overall process dynamics.
- Many operational differences between the ilmenite and chromite smelting furnaces influenced the way the data were subsequently treated:
- The ilmenite smelting furnace had accurate data on the quantities of slag and alloy produced on a tap-to-tap basis, and the temperatures were known for the slag and alloy melts, for all the taps. The actual inventories were unknown and required estimation. The dust was captured in bag-house filters, which influenced the chemistry of the dust by the time the dust was removed for analysis, as post-oxidation occurred, lowering the amount of entrained char.
- The quantities of the products of the chromite smelting furnace were known with far less accuracy, as the quantities of slag were judged by eye, and the alloy was weighed only daily. Moreover, the temperature was not measured on a routine basis for every tap. However, the dust analysis was more reliable than for ilmenite smelting, as it was quenched in a venturi scrubber, thereby retaining the reduced components and entrained reductant.
- In both cases the oxidation state of the feed materials and the slag were not determined on a regular basis.
- The slag chemistry of the chromite smelting slag could be manipulated through the ratio of acid oxides to basic oxides, thereby changing the liquidus temperature and the activity of the reducible oxides at constant oxygen partial pressure. This degree of freedom was not possible for ilmenite smelting.
- Feedback from operating staff showed that both ilmenite smelting as well as chromite smelting were ill-understood, and the qualitative heuristics used to control the metallurgy were insufficient for stable control.
- Both systems were viewed as very sensitive to the phase equilibria.

8.3 Chemical and Phase equilibria

The chemical and phase equilibrium evaluations performed in Chapter 3 and Appendix A revealed the thermochemical complexities of modelling these reactors - even if only the main components in the furnace are taken into account. It became clear that poor knowledge of the oxidation states of the feed materials and the slags could cause significant errors in estimating the chemical and phase equilibria. Knowledge of the chemical and phase equilibria made it possible to simplify the modelling effort sometimes, for example that the copper concentration in the converter slag remained relatively constant in the operating range studied, and that the silica addition is not expected to have much influence on the matte chemistry, as it was always introduced in excess of that required to flux the metal oxides. Knowledge of the phase equilibria made it possible to predict the amounts of solids formed when the melts were at sub-liquidus temperatures, and therefore the effect on melt viscosity. It was shown that the simulation software used, namely FactSage ®, could predict the non-ideal solution chemistry sufficiently well, as proved using equilibrium data from literature. Knowledge of the phase and chemical equilibria allow modelling of the most critical non-linearities associated with smelting and converting. It was furthermore shown that reprocessing of the equilibrium data is required to present it in a format that is useful for process monitoring and control. Bulk material properties have to be recalculated from the distribution within the constituent phases.

8.4 Uncertainty, heterogeneity and mixing

Chapter 4 showed that quantifying spatial heterogeneity, or mixedness, is required before one can commence with the development of predictive process models. If the distributed nature of melts is not taken into account it may result in gross errors when process data are used to develop semi-empirical models, or it may lead to rejecting fundamental models when they are validated against unrepresentative sample compositions. Once the variances are determined, the data could be reconciled (filtered) within these variances. The variances also established the maximum accuracy within which a model's prediction accuracy may be verified.

It was found that industrial open arc furnaces are not so well mixed as was predicted by some CFD models. The main components showing significant variances in the alloys are the solute components, in particular silicon and sulphur. It was found that the degree of subcooling of the alloy melt relative to the liquidus had the largest identifiable impact on alloy mixedness. In general it was found that alloy mixedness in the submerged arc furnace was significantly

better than for the alloy produced in an open arc furnace. In general the smelting slags always had better mixedness than their corresponding alloys, for the solute species. On the other hand, precipitated or entrained compounds showed a very large variation throughout the volume of the furnace melt. It was found that the slag mixedness of the submerged and open arc furnaces are comparable. Despite the relatively poor mixing of the solute components, the melts were found to be thermally well mixed, which corresponds with CFD predictions. The discrepancy between thermal and compositional homogeneity was explained through the orders of magnitude difference between the thermal and mass diffusivity.

The poor mixedness in DC plasma arc furnaces was also shown on laboratory scale using a specially designed DC plasma arc furnace. The spatial variances observed were of a similar magnitude to those observed industrially.

8.5 Data filtering and pre-processing

The uncertainty in data due to sampling errors, analysis errors, poor melt mixedness and biases that may occur due measurement instrument fouling, implies that the data have to be filtered and pre-processed before it could be used to develop semi-empirical models. Two types of filtering techniques were investigated:

- low pass filtering which used variance weighted data reconciliation
- high pass filtering using error integration by differencing

The two techniques may be used in series to extract the low frequency and high frequency components respectively from the raw data. The improvement in the dynamic data characteristics have been shown, based on diagnostic tools such as the Fast Fourier Transform Power Spectrum and Histogram analysis.

It was found that biases did exist in the data, and that the reconciliation adjustments in the data may sometimes be dynamically predicted in cases where a data series was significantly biased.

The inventories were estimated, and it was apparent that recycling the untapped melt inventory in the furnace made a very large difference in the dynamic behaviour, as it dampened disturbances associated with the feed to the furnaces. The recycled untapped material became part of the feed to the subsequent tap and therefore it was included in the thermodynamic equilibrium modelling as additional feed material.

Furthermore it was shown that artificial intelligent techniques such as Artificial Neural Networks are ideal to map thermochemical and phase equilibria data. The known non-linearities are therefore embedded into the neural network, which serves as an explicit mapping function of inputs to equilibrium outputs without the need for on-line Gibb's free energy minimisation. The latter requires non-linear multivariable optimisation which may either not converge or freeze during the equilibrium search. The off-line generation of an equilibrium database, using FactSage® based on an input dataset generated by 3^N Factorial design therefore prove to be extremely useful to develop trained multilayer perceptron neural networks. Moreover, the equilibrium outputs may be transformed into a format most convenient for final implementation. The neural network therefore become the convenient representation of the equilibrium outcomes, and constitutes the time-infinity endpoint, for a given set of material and thermal inputs.

8.6 Systems modelling and control

Using a combination of filtered or reconciled and generated thermochemical data, it was shown that dynamic systems models could be developed with a high prediction accuracy or, in the case of poorer predictions, it was shown that the prediction was still within the range of a perfect model with the same inherent uncertainty superimposed upon it. The dynamic furnace models can therefore be used to predict the metallurgy of future taps, based on historic information, equilibrium predictions and the feed and power setpoints of the future taps. The dynamic models used in this thesis were always linear in the adjustable parameters, making recurrent on-line parameter estimation simple and rapid. It was shown that the temperature associated with future taps could be predicted with acceptable accuracy, that is, within the inherent uncertainty of the data.

In the case of the matte conversion in the Ausmelt furnace it was shown that models of the Equilib-ARMAX structure can be used to predict the Fe and S concentrations in the matte phase with a very high accuracy and with a time horizon which is practical, taking into account the available sample analyses turn-around times. A simple first-order Equilib-ARX model sufficed for accurate prediction. Despite the cold-model indications that the lance-to-matte distance would have a large influence, too much uncertainty in the estimation of this variable made the model insensitive to its influence.

The melt chemistries of both DC plasma arc furnaces discussed in this thesis could be predicted within their inherent uncertainties, making use of the Equilib-ARMAX structure. Higher order Equilib-ARMAX model structures were required for the modelling of both the reductive chromite smelting and the reductive ilmenite smelting. In all cases it was found that the first autoregressive variable had the most impact on the prediction of a future tap, which corresponded with the effect of recycling large inventories.

It also was shown that slag viscosities can be predicted (within "fluidity" categories) based on predicted slag chemistry and temperature. It is therefore to determine, based on given setpoints, if the smelter will encounter problems with tapping, metal entrainment, or slag foaming.

Finally its was shown that these dynamic Equilib-ARMAX models may be implemented in a feedforward model based control architecture to adjust manipulated variables based on the deviation (model predicted) from the required setpoint. Alternatively, it may be used to suggest the optimal operating conditions through an operator guidance system, or more simply, the model is simple enough to be used in Excel on a manager's desk. The hybrid approach to furnace modelling is therefore both feasible and has an acceptable accuracy for process control.

8.7 A flow chart for the dynamic system modelling of bath type furnaces

Based on the results and conclusions from this thesis, a generic flow chart for the development of Equilib-ARMAX models for bath type furnaces has been developed to aid process modellers of bath type furnaces. This flow chart is presented in Figure 8.1. The flow chart captures all the main elements presented in this thesis.

It was shown that each component in this flow chart adds value to the final model. It is important to realise that all the steps are required to develop a meaningful furnace model. Doing data reconciliation without a proper campaign to determine the variances and biases, leads to erroneous adjustments. Neglecting the melt heel estimation leads to ignoring the largest component in the feed material for the following tap. Thermochemical analysis without data reconciliation leads to fitting models to data with no material balance closure. Thermochemical modelling without the inclusion of dynamic systems modelling leads to exclusion of the dynamic history of the furnace which, in turn, lead to poorly performing models.

It is foreseen that this modelling approach could be extended to all bath type furnaces with a reasonable level of mixing in the melt phases (therefore reverberatory or flash furnaces will probably not be modelled well with this approach).

8.8 Criticism and recommendations

The modelling approach assumed that the distributed component assays of melts could be represented by single reconciled values. Fluid and material flows are therefore not modelled explicitly. Fluid mixedness (which is based on fluid flow) is only incorporated through the process of weighting the reconciliation adjustments. Much value may be added to the modelling approach if multiple off-line CFD predictions are made and neural networks are again used as mapping functions to map operating conditions to CFD predictions of the flow velocities, temperatures, and pressures. If these additions are made, it is foreseen that the modelling approach may be extended to perform the predictive modelling (for control) of a much greater number of furnace types. In all cases the cost-benefit principle of model development remains: one has to compare the effort expended to the marginal increase in model accuracy (if additional process understanding is not a primary requirement), taking into account the practical uncertainties associated with data from high temperature operations.

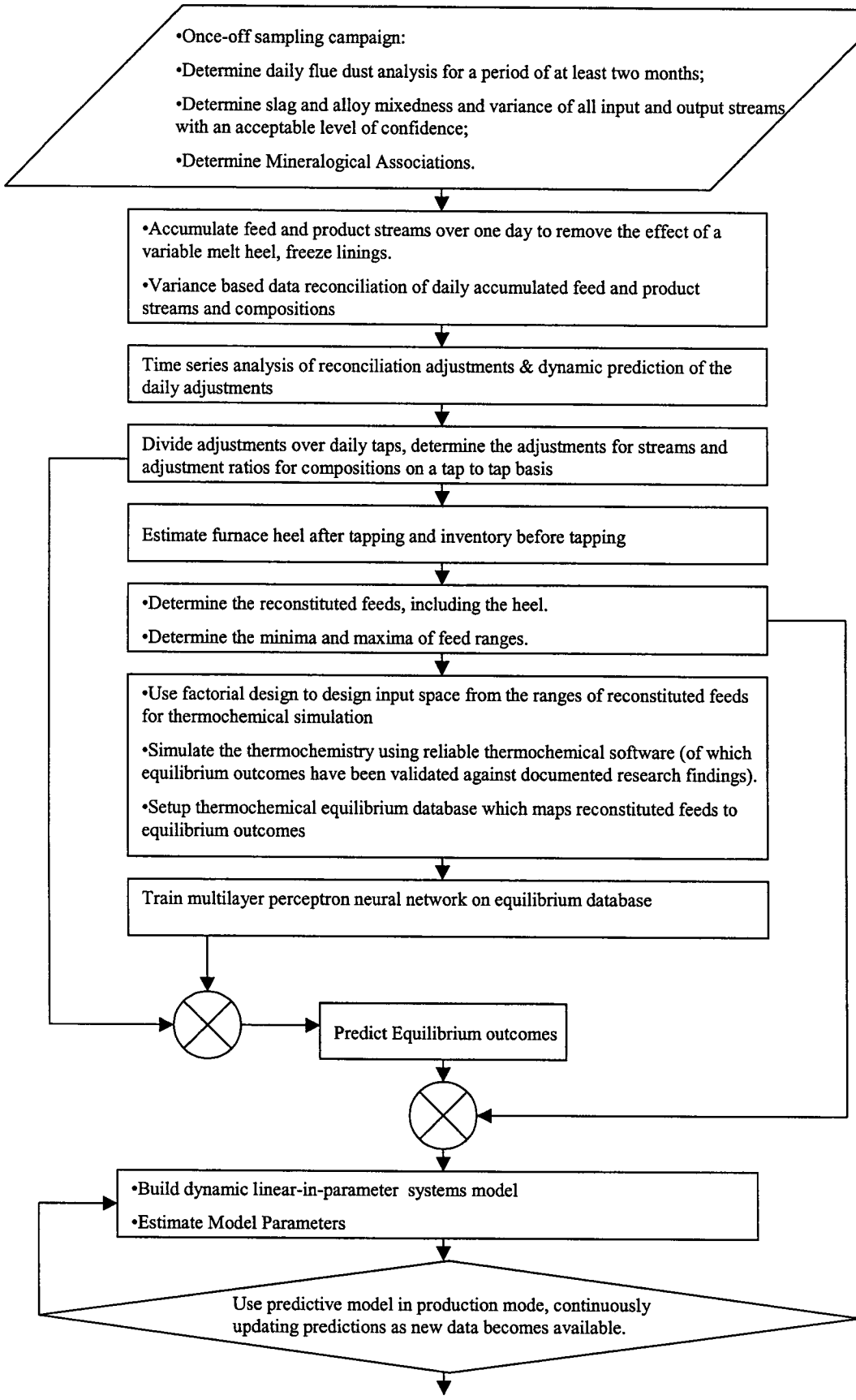

Figure 8.1: A flow chart for the development of generic dynamic semi-empirical models for bath type furnaces

8.9 Postscript

It is clear from the conclusions above that this suggested approach does not permit the forcing of dynamic process data into thermodynamic and/or kinetic metallurgical models at all costs by fitting with parameters. More often than not, these parameters are distributed and are therefore not really suitable for inclusion in classical kinetic and thermodynamic modelling approaches.

This classical modelling approach usually leads to erroneous results due to not incorporating process dynamics, leading to models that often have little or no practical value and do not lead to true furnace optimization and control. Rather consideration of the distributed nature of the system is required, and methods should be applied to extract useful information from the data. Conversely, if simulation becomes very difficult due to poor parameterization, empirical methods should complement semi-empirical models to ensure good predictive control in hybrid architectures.

A new kind of engineering graduate are therefore required to emerge from schools in extractive metallurgy: one who understands the dynamic interactions and the distributed nature of important metallurgical variables in the overall cycle of primary and secondary resource processing. Moreover, the extractive metallurgist of the future should be able to take a multi-disciplinary approach towards the challenges that a larger globally integrated; cost-cutting, minerals, metals and materials industry would pose. This thesis shows clearly that to control the resource cycle and therefore achieve sustainability, good metallurgical process models are required. Good dynamic models of the furnaces make this control ideal possible: more precisely, models that capture the true dynamics (in space and time) of pyrometallurgical reactors are indispensable for proper control and sustainable process metallurgy practice.

9 REFERENCES

The references are first listed alphabetically according to the surnames of authors, and subsequently according to the date of publication.

- Abdul-el-zeet, Z.H., Roberts, P.D., Becerra, V.M., "Enhancing Model Predictive Control using Dynamic Data Reconciliation", American Institute of Chemical Engineers Journal, 48 (2), pp. 324-333, 2002
- Adendorff, K.T., De Villiers, J.P.R., Kruger, G.J., "Crystal Structures of $Ca_5Cr_3O_{12}$ and $Ca_5Cr_2SiO_{12}$, the Chromium Analogs of Silicocarnotite", Journal of the American Ceramic Society, 75 (6), pp. 1416-1422, 1992
- Aguiar, H.C., Filho, R.M., "Neural Network and Hybrid Model: a Discussion about Different Modelling Techniques to Predict Pulping Degree with Industrial Data", Chemical Engineering Science, 56, pp. 565-570, 2001
- Akaike, H., "A new look at Statistical Model Identification", IEEE Transactions in Automatic Control, AC-19, pp. 716-723, 1994
- Akyüzlü and Eric, R.H., "Slag-metal Equilibrium in the Smelting of High Carbon Ferrochromium", Journal of the South African Institute for Mining and Metallurgy, 92 (4), pp. 101-110, 1992
- Amand, T., Heyen, G., Kalitventzeff, B., "Plant Monitoring and Fault Detection Synergy between Data Reconciliation and Principle Component Analysis", Computers and Chemical Engineering, 25, pp. 501-507, 2001
- Anderson, D.K., "Development of a Metallurgical Database and Neural Network Equilibrium Predictor for Nickel-Copper Matte Conversion in an Ausmelt Furnace", Final Year Project Report, University of Stellenbosch, Stellenbosch, 2000
- Andersson, J.-O., Helander, T., Höglund, Shi, P., Sundman, B., "Thermo-Calc and DICTRA: Computational Tools for Materials Science", Calphad, 26(2), pp. 273-312, 2002
- Asaki, Z., "Kinetics of Sulfide Smelting in the Mitsubishi Process", 3rd International Sulfide Smelting Congress, eds. Stephens, R.L., and Sohn, H.Y., (Warrendale PA: The Minerals Metals and Materials Society, 2002), pp. 41-48, 2002
- Bale, C.W., Chartrand, P., Degterov, S.A., Eriksson, G., Hack, K., Ben Mahfoud, R., Melançon, J., Pelton, A.D., Petersen, S, "FactSage Thermochemical Software and Databases", Calphad, 26(2), pp. 189-228, 2002

- Banerjee, S.K., Irons, G.A., "Physical Modelling of Thermal Stratification, Bottom Build-up and Mixing in Submerged Arc Electric Smelting", Canadian Metallurgical Quarterly, 31 (1), pp. 31-40, 1992
- Barcza, N.A., Curr, T.R., Jones, R.T., "Metallurgy of Open-bath Plasma Processes", Pure and Applied Chemistry (IUPAC), 62 (9), pp. 1761-1772, 1990
- Barcza, N.A., Curr, T.R., Winship, W.D., Heanly C.P., "The Production of Ferrochromium in a Transferred Arc Plasma Furnace", Proceedings of the 39th Electric Arc Furnace Conference, Houstonm Iron and Steel Society of the AIME, pp. 243-260, 1981
- Barcza, N.A., Jochens, P.R., Howat, D.D., "The Mechanism and Kinetics of Reduction of Transvaal Chromite Ores", Electric Furnace Conference Proceedings, pp.88-93, 1971
- Baughman, D.R., Liu, Y.A., "Neural Networks in Bioprocessing and Chemical Engineering", Volume 1, Academic Press, 488 p, 1995
- Bayer, W.H., "Handbook of Tables for Probability and Statistics", 2nd Edition, CRC Press, New York, 1968
- Bazin, C., Hodouin, D., "Importance of Covariance in Mass Balancing of Particle Size Distribution Data", Minerals Engineering, 14(8), pp. 851-860, 2001
- Bazin, C., Tremblay, S.R., Tremblay, "Reconciliation of flow, pressure and temperature measurements for a gas solids reactor", Control and Optimisation in Minerals, Metals and Materials Processing, 38th Annual Conference of Metallurgists of CIM, Quebec, 1999
- Bessinger, D., Du Plooy, H., Pistorius, P.C., Visser, C., "Characterisation of some High Titania Slags", Proceedings of the Heavy Mineral '97 Symposium, Symposium Series S17, ed. Robinson, R.E., South African Institute of Mining and Metallurgy, Johannesburg, pp. 151-156, 1997
- Blander, M., Pelton, A.D., Geochimica et Cosmochimica Acta, 51, pp. 85-95, 1987.
- Bodington, C.E., "Planning, Scheduling and Control Integration in the Process Industries", McGraw-Hill, London, 1995
- Bonekamp, I.H., Groeneveld, J.H., and Reuter, M.A., 1999, "Quantification of the Dynamics of the Flash Smelter", Proceedings of Copper 99-Cobre 99 International Conference, Volume VI-Smelting, Technology Development, Process Modelling and Fundamentals, pp. 361-375, 1999
- Booysen, L.M., Nelson, L.R., Swamy, K.N., Visser, M., "Development of an Operator Guidance System for Intermediate Carbon Charge Chromium Production", SAIMM

Colloquium on Modelling and Control of Mineral and Metal Processing Operations, 25 May 2000, Mintek, South Africa, 2000

- Borowiec, K., Rosenquist, T., "Phase Relations and Oxidation Studies in the System Fe-Fe_2O_3-TiO_2 at 700-1100 °C", Scandinavian Journal of Metallurgy, 10, pp. 217-224, 1981
- Bouchard, D., Bale, C., "Simultaneous Optimization of Thermochemical Data for Liquid Iron Alloys Containing C, N, Ti, Si, Mn, S, and P", Metallurgical and Materials Transactions B, 16B, June, pp. 467-484, 1995
- Bowman, B., "Convective Heat Transfer and Power Balance in High Current Free Burning Arcs", Elektrowaerme International, 30 (B2), pp. 87-93, 1972
- Bowman, B., "Effects of Furnace Arcs of Submerging by Slag", Ironmaking and Steelmaking, 17(2), pp. 123-129, 1990
- Bowman, B., Jordan, G.R., Fitzgerald, "The Physics of High Current Arcs", Jounral of the Iron and Steel Institute, June, pp. 798-805, 1969
- Brauer, G., Littke, W., Melting Point and Thermal Dissociation of Titanium Dioxide", Journal of Inorganic and Nuclear Chemistry, 16 (1-2), pp. 67-76, 1960
- Browne, T.E., Journal of the Electrochemical Society, 102 (1), January, pp. 28-37, 1955
- Burns, V.M., Burns, R.G., "Mineralogy of Chromium", Geochimica et Cosmochimica Acta, 39, pp. 903-910, 1975
- Cafferey G., Warnica, D., Molloy, N., and Lee, M., "Temperature Homogenisation in an Electric Arc Furnace Steel Bath", International Conference on CFD in Mineral and Metal Processing and Power Generation, CSIRO, pp. 87-99, 1997
- Chen, J., Bandoni, A., Romagnoli, J.A., "Outlier Detection in Process Plant Data", Computers and Chemical Engineering, 22 (4/5), pp. 641-646, 1998b
- Chen, J., Romagnoli, J.A., "A Strategy for Simulateous Dynamic Data Reconcilliation and Outlier Detection", Computers and Chemical Engineering, 22 (4/5), pp. 559-562, 1998a
- Coley, K.S., Terry, B.S., Grieveson, P., "Simultaneous Reduction and Carburization of Ilmenite", Metallurgical and Material Transactions B, Volume 26B, June, pp. 485-494, 1995
- Conradie, A.v.E., Aldrich, C., "Neurocontrol of a Ball Mill Grinding Circuit Using Evolutionary Reinforcement Learning", Minerals Engineering, 14 (10), pp. 1277-1294, 2001
- Crowe C.M., "The Maximum Power Test for Gross Errors in Original Constraints in Data Reconcilliation", The Canadian Journal of Chemical Engineering, 70, pp. 1030-1036, 1987

- Crowe, C.M., "Recursive Identification of Gross Errors in Linear Data Reconciliation", American Institute of Chemical Engineers Journal, 34 (4), pp. 541-550, 1988
- Curr, T.R., "A Review of Ferrochrome Smelting Technologies", International Chrome Development Association: Spring Meeting, Cape Town South Africa, 1996
- Curr, T.R., "The High Current DC Arc in Extractive Metallurgy", Colloqium on Plasma in Metallurgical Processes, 22 May '98, Mintek, Randburg, South African Institute of Mining and Metallurgy, 1998
- Curr, T.R. and Barcza, N.A., 1982, The Production and Treatment of Ferrochrome, South African Patent no. 827404, South Africa
- Curr, T.R., Barcza, N.A., Maske, K.U., and Mooney, J.F., "The Design and Operation of Transferred Arc Plasma Systems for Pyrometallurgical Operations" Proceedings of ISPC-6, Montreal, pp. 175-180, 1983
- Curr, T.R., Maske, K.U., and Nicol, K.C., "The Attainment of High Power Densities in Transferred Arc Plasma Smelting Processes", Proceedings of ISPC-7, Eindhoven, pp. 1186-1195, 1985
- Curr, T.R., Wedepohl, A., Eric, R.H., "Dissolution of a Transvaal Chromite in Liquid Silicate Slags under Neutral Conditions between 1545 and 1660 °C", pp. 298-304, 1988
- Cutting, G.W., "Estimation of Interlocking Mass Balances on Complex Mineral Beneficiation Plants", International Journal of Mineral Processing, 3, 207-218, 1976
- Dabak, T., Yucel, O, Powder Technology, 52, pp. 193-206, 1987
- Danckwerts, P.V., Chemical Engineering Science, 8, pp. 93, 1958
- Davies, R.H., Castle, J.F., Gabb, P.J., Siraa, M.A.S., Gisby, J.A., Weddick, A.J., "Thermochemical Modelling of Smelting Operations", Proceedings of Copper 99-Cobre 99 International Conference, Volume VI-Smelting, Technology Development, Process Modelling and Fundamentals, pp. 309-321, 1999
- Davies, R.H., Dinsdale, A.T., Gisby, J.A., Robinson, J.A., Martin, S.M., "MTData – Thermodynamic and Phase Equilibrium Software from the National Physical Laboratory", Calphad, 26(2), pp.229-271, 2002
- De Jongh, D., Moolman, D.W., Van Olst, M., "Current Trends in Automation in Process Control using Computational Intelligence Techniques", Proceedings of the Heavy Mineral '99 Symposium, Symposium Series S23, ed. Stimson, R.G., South African Institute of Mining and Metallurgy, Johannesburg, pp.55-58, 1999
- De Villiers, J.P.R., Mathias, J., Muan, A., "Phase Relations in the System $CaO-Cr_xO-SiO_2$ in Air and Solid-Solution Relations along the Ca_2SiO_4 –$Ca_3(CrO_4)_2$ join", Transactions of

the Institution of Mining and Metallurgy (Section C: Mineral Processing and Ectractive Metallurgy), pp. C55-C62, 1987

- De Villiers, J.P.R., Muan, A., "Liquidus-Solidus Phase Relations in the System CrO-Cr_2O_3-SiO_2-CaO", Journal of the American Ceramic Society, 75 (6), pp. 1333-1341, 1992
- Degterov, S., Pelton, A.D., "A Thermodynamic Database for Copper Smelting and Converting", Metallurgical and Materials Transactions B, 30B, August, pp. 661-669, 1999
- Degterov, S., Pelton, A.D., "Critical Evaluation and Optimization of the Thermodynamic Properties of Phase Diagrams of the CrO-Cr_2O_3, CrO-Cr_2O_3-Al_2O_3, CrO-Cr_2O_3-CaO System", Journal of Phase Equilibria, 17 (6), pp. 476-487, 1996
- Degterov, S., Pelton, A.D., "Critical Evaluation and Optimization of the Thermodynamic Properties of Phase Diagrams of the CrO-Cr_2O_3-SiO_2-CaO System", Metallurgical and Materials Transactions B, 28B, April, pp. 235-242, 1997
- Demir, O.D. and Eric, H.R., "Reduction of Chromite in Liquid Fe-Cr-Si-C Alloys", Metallurgical and Materials Transactions, 25B, pp. 549-559, 1994
- Demuth, H., Beale, M., "Neural Network Toolbox User's Guide", The Mathworks, Inc., Natick, 2000
- Denton, G.M., Schoukens, A.F.S., "The Production of High Titania Slag from Ilmenite", South African Patent No. 935072, July, 20 pages, 1993
- Desrosiers, R., Cordua, T., Pedersen, S.T., "Total Laboratory Automation for Iron / Steel, Ore and Slag Samples at QIT-Fer et Titane", Proceedings of the Heavy Mineral '99 Symposium, Symposium Series S23, ed. Stimson, R.G., South African Institute of Mining and Metallurgy, Johannesburg, pp.45-54, 1999
- Ding, Y.L., Warner, N.A., "Smelting Reduction of Carbon-Chromite Composite Pellets – Part 1, Reduction and Kinetics" Transactions of the Institution of Mining and Metallurgy, Section C, 106, pp. C55-C63, 1997
- Ding, Y.L., Warner, N.A., "Smelting Reduction of Carbon-Chromite Composite Pellets – Part 2, Dissolution Kinetics and Mechanism" Transactions of the Institution of Mining and Metallurgy, Section C, 106, pp. C64-C71, 1997
- Downing, J.H., "Smelting Chrome Ore", Geochimica et Cosmologica Acta, 39: 853-856, 1975
- Du Sichen, J., Bygdén, Seetharaman, S., "A Model for the Estimation of Viscosities of Complex Metallic and Ionic Melts", Metallurgical Transactions and Materials B, 25B, August, pp. 519-525, 1994

- Dunlevey, J.N., "Leucoxene", Proceedings of the Heavy Mineral '99 Symposium, Symposium Series S23, ed. Stimson, R.G., South African Institute of Mining and Metallurgy, Johannesburg, pp.59-62, 1999
- Edgar, T.F. and Himmeblau, D.M., "Optimization of Chemical Processes", McGraw-Hill, Singapore, 1989
- Einstein, "Investigation on the Theory of Brownian Movement", Dover Publications, New York, 1956
- Eksteen, J.J., "Dynamic Prediction of Melt Chemistry in Bath Smelting and Converting Furnaces", South African Institute of Mining and Metallurgy Colloqium on: Pyrometallurgy: Current Issues and Future Trends, 22-23 August 2001, Mintek, Randburg, 2001
- Eksteen, J.J., & Reuter, M.A., " The On-line Prediction of Transient Phenomena in the Slag Phase during Ilmenite Smelting, based on Fundamental Slag Chemistry and System Identification Techniques", Proceeding of the XXI IMPC, Rome, 23-28 July 2000, C(3), pp. 55 - 64, 2000
- Eksteen, J.J. and Reuter, M.A., "A Generic Approach to the Development of Semi-empirical Predictive Models for Bath Type Furnaces", Proceedings of the XXII International Mineral Processing Congress, 28 Sep. - 3 Oct., Cape Town, South Africa, Accepted for publication, 2003
- Eksteen, J.J., Georgalli, G.A. and Reuter, M.A., "Online Prediction of the Actual Melt Chemistry in an Ausmelt Converter Using a Thermodynamic- System Identification Hybrid Modelling Technique", Third International Sulphide Smelting Symposium, ed. R.L. Stephens and H.Y. Sohn (Warrendale PA: The Minerals Metals and Materials Society), pp. 457-468, 2002a
- Eksteen, J.J., Frank, S.J., Reuter, M.A., "Dynamic Structures in Variance based Data Reconciliation Adjustments for a Chromite Smelting Furnace", Minerals Engineering, 15 (11), pp. 931-943, 2002b.
- Eksteen, J.J., Frank, S.J., Reuter, M.A., "Distributed Compositional and Temperature Nature of Melts in Submerged and Open Arc Furnaces in High Carbon Ferrochrome Production", 10th International Ferroalloy Congress (INFACON X), Cape Town, February, Accepted for Publication, 2004a
- Eksteen, J.J., Frank, S.J., Reuter, M.A., "Towards Predictive Control of Ferroalloy Furnaces: Combining Thermochemistry, Inventory Modelling and Systems Engineering",

10th International Ferroalloy Congress (INFACON X), Cape Town, February, Accepted for Publication, 2004b

- El-Shahat, R.M., White, J., "Phase-Equilibrium Relationships in Spinel Silicate Systems, I: The Systems $MgAl_2O_4$-$MgCr_2O_4$-Ca_2SiO_4 and $MgFe_2O_4$-$MgCr_2O_4$-Ca_2SiO_4", Transactions of the British Ceramic Society, June, pp.313-330, 1964
- El-Shahat, R.M., White, J., "Phase-Equilibrium Relationships in Spinel Silicate Systems, II The Pseudo-systems $MgAl_2O_4$-$MgCr_2O_4$-$CaMgSiO_4$, $MgFe_2O_4$-$MgCr_2O_4$-$CaMgSiO_4$, $MgAl_2O_4$-$MgFe_2O_4$-$CaMgSiO_4$, and $MgAl_2O_4$-$MgFe_2O_4$- $MgCr_2O_4$-$CaMgSiO_4$", Transactions of the British Ceramic Society, June, pp.309-330, 1966
- El-Shahat, R.M., White, J., "Phase-Equilibrium Relationships in Spinel Silicate Systems, II The Ternary System $MgAl_2O_4$-$MgFe_2O_4$-Ca_2SiO_4, the Quaternary System $MgAl_2O_4$-$MgFe_2O_4$-$MgCr_2O_4$-Ca_2SiO_4, and the Pseudo-ternary System $MgAl_2O_4$-$MgCr_2O_4$-$Ca_3MgSi_2O_8$", Transactions of the British Ceramic Society, September, pp. 497-518, 1966
- Eriksson, G, Pelton, A.D., "Critical Evaluation and Optimization of the Thermodynamic Properties and Phase Diagrams of the MnO-TiO_2, MgO-TiO_2, FeO-TiO_2, Ti_2O_3-TiO_2, Na_2O-TiO_2 and K_2O-TiO_2 Systems", Metallurgical and Material Transactions B, 24B, October, pp. 795-805, 1993
- Eriksson, G., Chemica Scripta, 8, pp. 100-103, 1975
- Eschenbach, R.C., Barcza, N.A., Reid, K.J. "Plasma Torches and Plasma Torch Furnaces", in Plasma Technology in Metallurgical Processing, Ed. J. Feinman, Iron and Steel Society of the AIME, Warrendale, pp. 27-48, 1987
- Fauchais, P., Boulos, M., Pfender, E., "Physical and Thermodynamic Properties of Thermal Plasmas", in Plasma Technology in Metallurgical Processing, Ed. J. Feinman, Iron and Steel Society of the AIME, Warrendale, pp. 11-26, 1987
- Floyd, J.M., "Submerged Bath Smelting Applied to the Non-Ferrous Metal Industry", Proceedings of the Paul E. Queneau Symposium on the Extractive Metallurgy of Copper, Cobalt and Nickel, Volume I: Fundamental Aspects, Eds. Reddy, R.G., and Weizenbach, R.N., pp.473-487, 1993
- Font, J., M. Hino, and K. Itagaki, "Minor Elements Distribution between Iron-Silicate Base Slag and Ni_3S_2-Fe_S Matte under High Partial Pressures of SO_2" Materials Transactions, 39(8), pp. 834-840, 1998a
- Font, J.M., M. Hino, and K. Itagaki, "Phase Equilibrium and Minor Element Distribution between Iron-Silicate Base Slag and Nickel-Copper-Iron Matte at 1573 K under High Partial Pressures of SO_2". Materials Transactions, 40(1), pp. 20-26, 1999

- Font, J.M., Roghani, G., Hino, M., Itagaki, K., "Solubility of Copper or Nickel in Iron Silicate Base Slag Equilibrated with Cu_2S-FeS or Ni_3S_2-FeS Matte under High Partial Pressures of SO_2", Metallurgical Review of the MMIJ, 15 (1), pp. 75-86, 1998c
- Font, J.M., Takeda, Y., Itagaki, K., "Phase Equilibrium between Iron Silicate Based Slag and Nickel-Iron Matte at 1573 K under High Partial Pressures of SO_2", Materials Transactions, JIM, 39 (6), pp. 652-657, 1998b
- Fontaine, J.L., Germain, A., "Model-based Neural Networks", Computers and Chemical Engineering, 25, pp. 1045-1054, 2001
- Fourie, A., Workshop on the ACP Converter Project, Personal Communication, Hatch-Africa, Johannesburg, 2001
- Galgali, R.K., Ray, H.S., Chakrabarti, A.K., "A Study on Carbothermic Reduction of Ilmenite Ore in a Plasma Reactor", Metallurgical and Materials Transactions B, 29B, December, pp. 1175-1180, 1998
- Geldenhuis, J.M.A., Pistorius, P.C., "The use of Commercial Oxygen Probes during the Production of High Titania Slags", Journal of the South African Institute of Mining and Metallurgy, January, pp. 41-47, 1999
- Georgalli, G.A., "Dynamic Predictive Modelling of the Iron and Sulphur Compositions in an Ausmelt Converter", M.Sc. Thesis, University of Stellenbosch, 2002
- Georgalli, G.A., Eksteen, J.J. and Reuter, M.A., "An Integrated Thermochemical-Systems Approach to the Prediction of Matte Composition Dynamics in an Ausmelt Nickel-Copper Matte Converter", Minerals Engineering, 15(11), pp. 909-917, 2002
- Georgalli, G.A., Eksteen, J.J., Hara, K.T., McKenzie, N. (2001a). Characterisation of an Ausmelt Nickel-Copper Converter using Semi-Fundamental Models, SAIMM Proceedings of the Copper, Cobalt, Nickel and Zinc Recovery Conference, July 18-21, Victoria Falls, Zimbabwe, pp. 21-31, 2001a
- Georgalli, G.A., Eksteen, J.J., Anderson, D.K. "Prediction of the Dynamic Behaviour of Iron and Sulphur during Nickel-Copper Matte Conversion using Semi-Empirical Models", Proceedings of the 10th IFAC Symposium on Automation in Mining, Mineral and Metal Processing, September 4-6, Tokyo, Japan, pp. 241-246, 2001b
- Glasser, F.P., Osborn, E.F., "Phase Equilibrium Studies in the System CaO-Cr_2O_3-SiO_2", Journal of the American Ceramic Society, 41 (9), pp. 358-367, 1958
- Glen, H.W., (Ed.), "Measurement, control and optimisation in mineral processing", Mintek Special Publication Series, SP5, 1994

- Grau, A.E., "Liquidus Temperatures in the TiO_2 - Rich Side of the FeO-TiO_2 System", Canadian Metallurgical Quarterly, 18, pp. 313-321, 1979
- Greskovich C., Stubican, V.S., "Divalent Chromium in Magnesium-Chromium Spinels", Journal of Physical Chemistry of Solids, 27, pp. 1379-1384, 1966
- Grey, I.E., Li, C., Reid, A.F., "A Thermodynamic Study of Iron in Reduced Rutile", Journal of Solid State Chemistry", 11, pp. 120-127, 1974b
- Grey, I.E., Merrit, R.R., "Stability Regions in the Pseudobrookite Solid Solution $Fe_yTi_{3-y}O_5$", Journal of Solid State Chemistry, 37, pp. 284-293, 1981
- Grey, I.E., Merrit, R.R., "Stability Regions in the Pseudobrookite Solid Solution FeyTi3-yO5", Journal of Solid State Chemistry, 37, pp. 284-293, 1981
- Grey, I.E., Reid, A.F., Jones, D.G., "Reaction Sequences in the Reduction of Ilmenite, Part IV: Interpretation in terms of the Fe-Ti-O and Fe-Ti-Mn-O Phase Diagram", Transactions of the Institution of Mining and Metallurgy C, 83, pp. C105-C111, 1974a
- Grey, I.E., Ward, J., "an X-Ray and Mössbauer Study of the $FeTi_2O_5$-Ti_3O_5 System, Journal of Solid State Chemistry", 7, pp. 300-307, 1973
- Grund, S.C., Reuter, M.A., Janssen, R.A.G., Nolte, A., "Optimization of a Tin-Lead Smelting Furnace with the aid of Statistical Modelling Techniques" , EPD Congress 1999, Mishra, B. (Ed.), TMS, pp. 851-864, 1999
- Gudenau, H.W., Wu, K., Nys, S., Rosenbaum, H., "Formation and Effects of Slag Foaming in Smelting Rduction", Steel Research, 63 (12), December, pp. 521-525, 1992
- Gunnewick, L.H. and Tullis, S., "Prediction of Heat and Fluid Flow in the Slag Phase of and Electric Arc Furnace", Proceedings of the International Symposium on Computational Fluid Mechanics and Heat/Mass Transfer Modelling in the Metallurgical Industry, eds. Argyropoulos, S.A., Mucciardi, F., August 24-29, Montreal, Quebec, CIM, pp. 250-264, 1996
- Gupta, S.K., Rajakumar, V., Grieveson, P., "Phase Relationships in the System Fe-Fe_2O_3-TiO_2", Canadian Metallurgical Quarterly, 28 (4), pp. 331-335, 1989
- Gupta, S.K., Rajakumar, V., Grieveson, P., "The Influence of Weathering on the Reduction of Ilmenite with Carbon", Metallurgical and Materials Transactions B, 20B, October, pp. 735-745, 1989
- Gy, P.M., "Sampling of Particulate Materials: Theory and Practice", Elsevier, Amsterdam, 1979
- Handfield, G., Charette, G.G., "Titanium Bearing Ore and Blast Furnace Slag Viscosity", Journal of Metals, September, pp. 37-40, 1972

- Handfield, G., Charette, G.G., "Viscosity and Structure of Industrial High Titania Slags", Canadian Metallurgical Quarterly, 10 (3), pp. 235-243, 1971
- Hanson, B., Jones, J.H., " The Systematics of Cr^{3+} and Cr^{2+} partitioning between Olivine and Liquid in the Presence of Spinel", American Mineralogist, 83, pp. 669-684, 1998
- Happel, J., "Viscosity of Suspensions of Uniform Speres", Journal of Applied Physics, 28 (11), pp. 1288-1292, 1957
- Harnby, N., Edwards, M.F., Nienow, A.W., "Mixing in the process industries", Butterworths, London, 1985
- Hauksdottir, A.S., Gestsson, A., Vesteinsson, A., "Current Control of a Three Phase Submerged Arc Ferrosilicon Furnace", Control Engineering Practice, 10, pp. 457-463, 2002
- Hayes, P.C., Okongwu, D.A., Toguri, J.M., "Some Observations of the Reactions between Molten Oxides and Solid Carbon", Canadian Metallurgical Quarterly, 34 (1), pp. 27-36, 1995
- Healy, G.W., "Activities in Liquid Cr-Fe-C System above 1600 °C", Proceedings of the Reinhardt-Schumann International Symposium on Innovative Technology and Reactor Design in Extractive Metallurgy, eds. Gaskell, D.R., Hager, J.P., Hoffmann, J.E., Mackey, P.J., Metallurgical Society, pp. 667-679, 1986
- Hines, A., L., Chung, T-W, "Prediction of Liquid Metal Viscosities Using the Adjustable Hard Sphere Radial Distribution Curve", Metallurgical and Materials Transactions B, 27B, February, pp. 29-34, 1996
- Hino, M., Higuchi, K-I, Nagasaka, T., Ban-Ya, S., "Phase Equilibria and Thermodynamics of $FeO{\cdot}CrO\text{-}MgO{\cdot}Cr_2O_3\text{-}MgO{\cdot}Al_2O_3$ Spinel Structure Solid Solution Saturated with (Cr,Al)2O3, ISIJ International, Vol. 35 (7), pp. 851-858, 1995
- Hino, M., Higuchi, K-I, Nagasaka, T., Ban-Ya, S., "Thermodynamic estimation of the Reduction Behaviour of Iron-Chromium Ore with Carbon", Metallurgical and Materials Transactions B, 29B, April, pp. 351-361, 1998
- Hirai, M., ISIJ International, 33 (2), pp. 251-258, 1993
- Hodouin, D. and Everell, M.D., "A Hierarchical Procedure for the Adjustment and Material Balancing of Mineral Processes Data", International Journal of Mineral Processing, 7, 91-116, 1980
- Hodouin, D., Berton, A., "An Algorithm for Fault Detection and Isolation using Mass Balance Constraints", Proceedings of the XXI IMPC Rome, A3, pp. 59-65, 2000

- Hodouin, D., Jämsä-Jounela, S-L., Carvalho, M.T., Bergh, L., "State of the Art and Challenges in Mineral Processing Control", Control Engineering Practice, 9, pp. 995-1005, 2001
- Hodouin, D., Kasongo, T., Kouame, E., Everell, M.D., " BILMAT: An Algorithm for Material Balancing Mineral Processing Circuits", CIM Bulletin 74 (83) pp. 123-131, 1981
- Hodouin, D., Mirabedini, A., Makni, S., Bazin, C., "Reconcilliation of Mineral Processing Data Containing Correlated Measurement Errors", International Journal of Mineral Processing, 54, pp. 201-215, 1998
- Holzheid, A., H. Palme, and S. Chakraborty, "The Activities of NiO, CoO and FeO in Silicate Melts", Chemical Geology, 139, pp. 21-38, 1997
- Holzheid, A., O'Neill, H.St.C., "The Cr-Cr_2O_3 Buffer and Free Energy of Formation of Cr_2O_3 from High Temperature Electrochemical Measurements", Geochimica et Cosmochimica Acta, 59 (3), pp. 475-479, 1995
- Howat, D.D., "Chromium in South Africa", Journal of the South African Institute of Mining and Metallurgy, 86(2), pp. 37-50, 1986
- Hunt, K.J., Sbarbaro, D., Zbikowski, R., Gawthrop, P.J., "Neural Networks for Control Systems - A Survey", Automatica, 28 (6), pp. 1083-1112, 1992.
- Incropera, F.P., Dewitt, D.P., "Fundamentals of Heat and Mass Transfer", 5th Ed., John Wiley and Sons, New York, 2002
- Ip, S.W., Toguri, J.M., "Surface and Interfacial Tension of the Ni-Fe-S, Ni-Cu-S, and Fayalite Slag Systems", Metallurgical and Materials Transactions B, 24B, August, pp. 657-668, 1993
- Iwamasa, P.K., Fruehan, R.J., "Separation of Metal Droplets from Slag", ISIJ International, 36 (11), pp. 1319-1327, 1996
- Jacob, K.T., Behera, C.K., "Spinel-Corrundum Equilibria and Activities in the System MgO-Al_2O_3-Cr_2O_3 at 1473 K", Metallurgical and Materials Transactions B, 31B, pp. 1323-1332, 2000
- Jacob, K.T., Iyengar, G.N.K., "Thermodynamics and Phase Equilibria Involving the Spinel Solid Solution $Fe_xMg_{1-x}Cr_2O_4$", Metallurgical and Materials Transactions B, 30B, pp. 865-871, 1999
- Jacob, K.T., Petric, A., Kale, G.M., Iyengar, G.N.K., "Phase Relations between Al_2O_3-Cr_2O_3 and $FeAl_2O_4$ – $FeCr_2O_4$ Solid Solutions at 1823 K", Ceramics International, 13, pp. 123-129, 1987

- Jahanshahi, S, Wright, S., "Redox Equilibria in Al_2O_3-CaO-FeO_x-SiO_2 and Al_2O_3-CaO-FeO_x-MgO-SiO_2 Slags", ISIJ International, 33 (1), pp. 195-203, 1993
- Jämsä-Jounela, S-L., "Currrent Status and Future Trends in the Automation of Mineral and Metal Processing", Control Engineering Practice, 9, pp. 1021-1035, 2001
- Ji, F-Z., Sichen, D., Seetharaman, "Experimental Studies of Viscosities in CaO-Fe_nO-SiO_2 Slags", Metallurgical and Materials Transactions B, 28B, October, pp. 827-834, 1997
- Ji, F-Z., Sichen, D., Seetharaman, "Experimental Studies of Viscosities in Fe_nO-MgO-SiO_2 and Fe_nO-MnO-SiO_2 Slags", Ironmaking and Steelmaking, 25 (4), pp. 309-316, 1998
- Jiang, Q., Bagajewicz, M.J., "On a Strategy of Serial Identification with Collective Compensation for Multiple Gross Error Estimation in Linear Steady-State Reconcilliation", Industrial and Engineering Chemistry Research, 38, pp. 2119-2128, 1999
- Jiang, R., Fruehan, R.J., "Slag Foaming in Bath Smelting", Metallurgical and Materials Transactions B, 22B (4), August, pp. 481-489, 1991
- Jinescu, V.V., International Chemical Engineer, 14, pp. 397-420, 1974
- Jones, R.T., La Grange, T.G., Assis, G., "Influence of DC-Arc Furnace Geometry on a Cobalt from Slag Process", Nickel-Cobalt 97, 36th Annual Conference of Metallurgists, Sudbury, August (Also Mintek Paper No. 8389), 1997
- Jones, R.T., Reynolds, Q.G., Alport, M.J., "DC Arc Photography and Modelling", Minerals Engineering, 15 (11), pp., 2002
- Jönsson, B., Sundman, B., "Thermochemical Applications of Thermo-Calc", High Temperature Science, 26, pp. 263-273, 1990
- Jonsson, S., "Assessment of the Fe-Ti-C System, Calculation of the Fe-Ti-N System, and Prediction of the Solubility Limit of Ti(C, N) in Liquid Fe", Metallurgical and Materials Transactions B, 29B, April, pp. 371-384, 1998
- Kaiser, A., Sommer, B., Woermann, E., "The System CaO-"$CaCr_2O_4$"-$CaAl_2O_4$ in Air and under Reducing Conditions", Journal of the American Ceramic Society, 75 (6), pp.1463 – 1471, 1992
- Kanjilal, P.P., Adaptive Prediction and Predictive Control, IEE Control Engineering Series 52, London, Peter Peregrinus Ltd., 1995
- Keith, M.L., "Phase Equilibria in the System MgO-Cr_2O_3-SiO_2", Journal of the American Ceramic Society", 37 (10), pp. 491-496, 1954

- Kim, H.G., Sohn, H.Y., "Effects of CaO, Al_2O_3, and MgO Additions on the Copper Solubility, Ferric / Ferrous Ratio, and Minor Element Behavior of Iron Silicate Slags", Metallurgical and Materials Transactions B, 29B, June, pp. 583-590, 1998
- Kim, S., Lee, M., Park, S., Lee, S., Park, C.H., "A Neural Linearizing Control Scheme for Nonlinear Chemical Process", Computers and Chemical Engineering, 21(2), pp. 187-200, 1997
- Kondratiev, A., Jak, E., "Review of Experimental Data and Modelling of Viscosities of Fully Liquid Slags in the Al_2O_3-CaO-"FeO"-SiO_2 System", Metallurgical Transactions and Materials B, 32B, December, pp. 1015-1025, 2001a
- Kondratiev, A., Jak, E., "Modelling of Viscosities of the Partly Crystallised Slags in the Al_2O_3-CaO-"FeO"-SiO_2 System", Metallurgical and Materials Transactions B, 32B, December, pp. 1027-1032, 2001b
- Kondratiev, A., Jak, E., Hayes, P.C., "Predicting Slag Viscosities in Metallurgical Systems", Journal of Metals, 54 (11), pp. 41-45, 2002
- Kongoli, F., Dessureault, Y., Pelton, A. D., "Thermodynamic Modelling of Liquid Fe-Ni-Cu-Co-S Mattes", Metallurgical and Materials Transactions B, 29B, pp. 591 – 601, 1998
- Kongoli, F., Pelton, A. D., "Model Prediction of Thermodynamic Properties of - Co-Fe-Ni-S Mattes", Metallurgical and Materials Transactions B, 30B, pp. 443-451, 1999
- Königsberger, E., Eriksson, G., "A New Optimization Routine for Chemsage", Calphad, 19 (2), pp. 207-214, 1995
- Kovács, T., Trägårdh, Fuchs, L., "Fourier Spectrum to Recover Deterministic and Stochastic Bahavior in Stirred Tanks", American Institute of Chemical Engineers Journal, 47 (10), pp. 2167-2176, 2001
- Kucharski, M., Stubina, N.M., Toguri, J.M., "Viscosity Measurements of Molten Fe-O-SiO_2, Fe-O-CaO-SiO_2, and Fe-O-MgO-SiO_2 Slags", Canadian Metallurgical Quarterly, 28 (1), pp. 7-11, 1989
- Kyllo, A.K., Richards, "A Mathematical Model of the Nickel Converter: Part I: Model Development and Verification", Metallurgical Transactions B, 22B, April, pp. 153-161, 1991
- Kyllo, A.K., Richards, G.G., "A Kinetic Model of the Pierce Smith Converter: Part I: Model Formulation and Validation", Metallurgical Transactions B, 29B, February 1998, pp. 239-249, 1998a

- Kyllo, A.K., Richards, G.G., "A Kinetic Model of the Pierce Smith Converter: Part II: Model Application and Discussion", Metallurgical Transactions B, 29B, February 1998, pp. 251-259, 1998b
- Kyllo, A.K., Richards, G.G., Marcuson, S.W. "A Mathematical Model of the Nickel Converter: Part II: Application and Analysis of Converter Operation", Metallurgical Transactions B, 23B, October, pp. 573-582, 1992
- Larrain, J.M., and Lee, S., "Thermodynamic Properties of Copper-Nickel-Sulphur Melts", Canadian Metallurgical Quarterly, 19, pp. 183-190, 1980
- Larsen, H.L., Gu, L., and Bakken, J.A., "A Numerical Model for the AC Arc in the Silicon Melting Furnace", INFACON 7, eds., Tuset, Tveit, and Page, Trondheim, Norway, pp. 517-527, 1995
- Latham, D.J., IEEE Transactions on Plasma Science, PS-14 (3), June, 200-227, 1956
- Levenspiel, O., "Chemical Reaction Engineering", 3rd Edition, John Wiley and Sons, New York, 1999
- Lin, Z., Guthrie, R.I.L.; "Model for Slag Foaming for In-bath Smelting Process", Iron & Steelmaker (I&SM), 22 (5), May, pp. 67-73, 1995
- Lynch, D.C., Bullard, D.E., "Phase Equilibria in the Titanium-Oxygen System", Metallurgical and Material Transactions B, Volume 28B, June, pp. 447-453, 1997
- Ma, N., Warner, N.A., "Smelting Reduction of Ilmenite by Carbon in Molten Pig Iron", Canadian Metallurgical Quarterly, 38 (3), pp. 165-173, 1999
- Ma, T., Sarvinis, J., Voerman, N., Wasmund, B., Sanchez, J., Trifilio, O., "Recent Developments in DC Furnace Design", Hatch International (Inc) Homepage, 9 pages, http://www.hatch.ca/ExpertAreas/nonferrous/Projects/furnace.html, down-loaded 30/09/1999
- MacChesney, J.B., Muan, A., "Phase Equilibrium at Liquidus Temperatures in the System Iron Oxide – Titanium Oxide at Low Oxygen Pressures", American Mineralogist, 46, pp. 572-582, 1961
- Maecker, H., "Discharge and Plasma Physics", Haydon, University of New England, Armidal, Australia, 1961
- Maeda, M., Sano, N., Mastushita, Y., "Chromium Recovery from Chromium Containing Slags", Conservation and Recycling, 4(3), pp. 137-144, 1981
- Mah, R.S., Stanley, G.M., Downing, D.M., "Reconcilliation and Rectification of Process Flow and Inventory Data", Industrial and Engineering Chemistry : Process Design and Development, 15 (1), pp. 175-183, 1976

- Maperman, M., Danyushevsky, L.V., Taylor, W.R., Jablonski, W., "Direct Oxygen Measurement of Cr-rich Spinel: Implications for Spinel Stoichiometry", American Mineralogist, 81, pp. 1186-1194, 1996
- Marston, H.F., and Knight, D., "Determination of Divalent and Hexavalent Chrmoium in Slags", Analyst, 102, pp. 745-751, 1977
- Min, D.J., Han, J.W., Chung, W.S., "A Study of the Reduction Rate of FeO in Slag by Solid Carbon", Metallurgical and Materials Transactions B, 30B, pp. 215-221, 1999
- Mirtič, B., Fajgelj, A., Lutar, K., Schara, M., Kaučič, V., "Determination of Chromium Oxidation States in Part of the System $CaO\text{-}3CaO\cdot Cr_2O_3$ in Air", Journal of the American Ceramic Society, 75 (8), 2184-2188, 1992
- Mogensen, P., Thörnblom, J., "Electrical and Mechanical Technology of Plasma Generation and Control", in Plasma Technology in Metallurgical Processing, Ed. J. Feinman, Iron and Steel Society of the AIME, Warrendale, pp. 65-76, 1987
- Mounsey, E.N., Li, H., Floyd, J.W., "The design of the Ausmelt Technology Smelter at Zhong Tiao Shan's Houma Smelter, People's Republic of China", Proceedings of Copper 99-Cobre 99 International Confeence, Volume V – Smelting Operations and Advances, eds. George, D.B., Chen, W.J., Mackey, P.J., Weddick, A.J., (Warrendale PA: The Minerals Metals and Materials Society), pp. 357-369, 1999
- Mounsey, E.N., Piret, N.L., "A Review of Ausmelt Technology for Lead Smelting" , Proceedings of the Lead-Zinc 2000 Conference, eds. Dutrizac, J.E., Gonzalez, J.A., Henke, D.M., James, S.E., and Siegmund, A.H.-J., (Warrendale PA: The Minerals Metals and Materials Society, 2002), pp. 149-169, 2000
- Muan, A., "Phase Relations in Chromium Oxide-Containing Systems at Elevated Temperatures", Geochimica et Cosmochimica Acta, 39, pp. 791-802, 1974
- Muan, A., "Slag-Metal Equilibria involving Chromium as a Component", Mintek 50, pp. 897-904, 1992
- Muan, A., Somiya, S., "Phase Equilibrium Studies in the System $Fe_xO\text{-}Al_2O_3\text{-}Cr_2O_3$", Journal of the American Ceramic Society, 42 (12), pp. 603-613, 1959.
- Musić, S., Popović, S., Ristić, M., "Chemical and Structural Properties of the System $Fe_2O_3\text{-}Cr_2O_3$", Journal of Materials Science, 28, pp. 632-638, 1993
- Nagata, S., Nishikawa, M., Oldshue, J.Y., Yamamoto, "Mixing: Principles and Applications" Kodansha Scientific Books, 1975

- Narasimhan, S., Mah, R.S.H., "Generalized Likelihood Ratio Method for Gross Error Identification", American Institute of Chemical Engineers Journal, 33 (9), pp. 1514-1521, 1987
- Navrotsky, A., "Thermochemistry of Chromium Compounds, Especially Oxides at High Temperature", Geochimica et Cosmochimica Acta, 39, pp. 819-832, 1975
- Nell, J., "An Overview of the Phase Chemistry involved in the Production of High Titania Slag from Ilmenite Feedstock", Proceedings of the Heavy Mineral '99 Symposium, Symposium Series S23, ed. Stimson, R.G., South African Institute of Mining and Metallurgy, Johannesburg, pp.137-145, 1999
- Nell, J., De Villiers, J.P.R., " T-P_{O_2} Topological Analysis of Phase Relations in the System CaO-CrO-Cr_2O_3-SiO_2", Journal of the American Ceramic Society, 76 (9), pp. 2193-2200, 1993
- Nelson, L.R., Personal discussion, 4 February 2004
- Ogawa, Y., Huin, D., Gaye, H., Tokumitsu, N., "Physical Model of Slag Foaming", ISIJ International, 33(1), pp. 224-232, 1993
- Ohta, H., Suitto, H., "Activities of SiO_2 and Al_2O_3 and activity coefficients of Fe_tO and MnO in CaO-SiO_2-Al_2O_3-MgO Slags", Metallurgical and Materials Transactions B, 29B, February, pp. 119-129, 1998
- Ozturk, B., Fruehan, R.J., "Effect of Temperature on Slag Foaming", Metallurgical Transactions B, 26B, October, pp. 1086-1088, 1995
- Pan, X. Livneh, B.Z., "Neural Networks to Predict and Control Pyrometallugical Processes", Proceedings of the Heavy Mineral '97 Symposium, Symposium Series S17, ed. Robinson, R.E., South African Institute of Mining and Metallurgy, Johannesburg, pp.231-236, 1997
- Pan, Y., Sung, S.W., Lee, J.H., "Data-based Construction of Feedback-corrected Nonlinear Prediction Model Using Feedback Neural Networks", Control Engineering Practice, 9, pp. 859-867, 2001
- Paramguru, R.K., Galgali, R.K., Ray, H.S., "Influence of Slag Foam Characteristics on the Reduction of FeO-Containing Slag by Solid Carbon", Metallurgical and Materials Transactions B, 28B, October, pp. 805-810, 1997
- Pei, W. and Wijk, O., "Chromite ore smelting reduction by a carbon saturated iron melt", Scandinavian Journal of Metallurgy, 23, 216-223, 1994

- Pei, W., "Study on some Phenomena during the Smelting Reduction of Chromite Ore", Licentiate Thesis, Department of Process Metallurgy, Royal Institute of Technology, Stockholm, 1991
- Pei, W., Wijk, O., "Mechanism of Reduction of Chromium Oxide Dissolved in the CaO-SiO_2-Al_2O_3-MgO Slag by Solid Carbon", Scandinavian Journal of Metallurgy, 22, pp. 30-37, 1993
- Pelton, A.D., "The Polynomial Representation of Thermodynamic Properties in Dilute Solutions", Metallurgical and Materials Transactions B, 28B, October, pp. 869-876, 1997a
- Pelton, A.D., "Solution Models" in Advanced Physical Chemistry for Process Metallurgy, eds. Sano, N., Lu, W., Riboud, P.V., Maeda, M., Academic Press, London, pp. 87-119, 1997b
- Pelton, A.D., Blander M., "Thermodynamic Analysis of Ordered Liquid Solutions using the Quasichemical Approach – Application to Silicate Slags", Metallurgical and Materials Transactions B, 17B, 805-815, 1997
- Pelton, A.D., Blander M., Proceedings of the AIME Symposium on Molten Salts and Slags, AIME, Warrendale, PA, pp. 281—294, 1984
- Pelton, A.D., Degterov, S.A., Eriksson, G., Robelin, C., Dessureault, Y., "The Modified Quasichemical Model I. – Binary Solutions", Metallurgical and Materials Transactions B, 31B, August 2000, pp. 651-659, 2000
- Peng, X., Mei, C., Zhou, J., Tang, Y., "A Fuzzy Neural Network Decision Model on the Operation Process of Electric Furnace for Slag Cleaning and its Application", Transactions of NFsoc, 5 (3), September, pp.21-24, 1995
- Perry, R.H., Green, D.W., "Chemical Engineers' Handbook, 6^{th} Edition, McGraw-Hill, New York, 1984
- Pesl, J, "Phase Equilibria and Thermodynamics in the Fe-Ti-O-X System at 1500°C and 1600°C", Proceedings of Minerals & Materials '96, Vol. 1, SAIMM, 31 July – 2 August, Somerset-West, South Afrcia, pp.59-66, 1996
- Pesl, J., "Thermodynamics and phase equilibria in the Fe-Ti-O system at 1500 °C and 1600 °C and metal-slag equilibria pertinent to ilmenite smelting", Ph.D. Thesis, University of the Witwatersrand, Johannesburg, 1997
- Pesl, J., Eric, R.H., "Metal-Slag Equilibrium Pertinent to the Smelting Reduction of Ilmenite: Significance for Industrial Processes", Proceedings of the Heavy Mineral '97

Symposium, Symposium Series S17, ed. Robinson, R.E., South African Institute of Mining and Metallurgy, Johannesburg, pp. 143-150, 1997

- Pesl, J and Eric RH, "High Temperature Phase Relations and Thermodynamics in the Iron-Titanium-Oxygen System", Metallurgical and Materials Trnsactions B, 30B, pp. 695-705, 1999
- Pfender, E., Boulos, M., Fauchais, P., "Methods and Principles of Plasma Generation", in Plasma Technology in Metallurgical Processing, Ed. J. Feinman, Iron and Steel Society of the AIME, Warrendale, pp. 27-48, 1987
- Pieters, T., "Refractory Freeze Lining Concepts and Designs in AC Submerged Arc and DC Plasma Arc Furnaces in the Ferroalloy Industry", Pyrometallurgy: Current Issues and Future Trends, 22-23 August, Mintek, Randburg, 2001
- Pistorius, P.C., "Limits on Energy and Reductant Inputs in the Control of Ilmenite Smelters", Proceedings of the Heavy Mineral '99 Symposium, Symposium Series S23, ed. Stimson, R.G., South African Institute of Mining and Metallurgy, Johannesburg, pp.183-193, 1999
- Pomfret, R.J., Grieveson, P., "The Kinetics of Slag-Metal Interactions", Canadian Metallurgical Quarterly, 22 (3), pp. 287-299, 1983
- Pretorius, E.B., Snellgrove, R., Muan, A., "Oxidation State of Chromium in CaO-Al_2O_3-CrO_x-SiO_2 Melts under Strongly Reducing Conditions at 1500 °C", Journal of the American Cermaic Society, 75 (6), 1378-1381, 1992
- Psichogios, D.C. and L.H. Ungar, "Direct and Indirect Model Based Control Using Artificial Neural Networks", Industrial and Engineering Chemistry Research, 30, p. 2564-2573, 1991
- Qian, F., Farouk, B., and Mutharasan, R., "Modelling of Fluid Flow and Heat Transfer in the Plasma Region of the DC Electric Arc Furnace", Metallurgical and Material Transactions B, 26B, pp. 1057-1067, 1995
- Ragot, J., Maquin, D., Adrot, O., "LMI Approach for Data Reconciliation, Control and Optimisation in Minerals, Metals and Materials Processing", 38th Annual Conference of Metallurgists of CIM, Quebec, 1999
- Ramakrishnan, S., Nuon, B., Journal of Physics D: Applied Physics, Vol. 13, pp. 1845-1853, 1980
- Ramakrishnan, S., Stokes, Lowke, J.J., "An Approximate Model for High Current, Free Burning Arcs", Journal of Physics D: Applied Physics, Vol. 11, pp. 2267-2280, 1978

- Rankin, W.J., Biswas, A.K., "Oxidation States of Chromium in Slag and Chromium Distribution in Slag-Metal Systems at 1600 °C", Institution of Mining and Metallurgy, Section C, March, pp. C60-C70, 1978
- Rankin, W.J., Biswas, A.K., "The Behaviour of Chromium in Reduced Slag-Metal Systems", Arch. Eisenhüttenwes. 50 (1), pp. 7-11, 1979
- Reddy, R.G. and G.W. Healy, "Distribution of Cobalt Between Liquid Copper and Copper Silicate Slag at 1523 K", Metallurgical and Materials Transactions B, 12B, pp. 509-516, 1981a
- Reddy, R.G. and G.W. Healy, "The Solubility of Cobalt in Cu_2O-CoO-SiO_2 Slags in Equilibrium with Liquid Cu-Co Alloys", Canadian Metallurgical Quarterly, 20(2), pp. 135-143, 1981b
- Reuter, M.A. and Grund, S.C., "The use of Data Reconciliation as a Soft Sensor in various Hybrid Modelling and Control Architectures for Pyrometallurgical Furnaces", Proceedings Extraction & Processing Division EPD Congress, (ed. P.R. Taylor), Warrendale, PA, 2001 TMS Annual Meeting, New Orleans, Louisana, USA: 629 – 642, 2001
- Reuter, M.A., "Hybrid Neural Net Modelling in Metallurgy", Second International Symposium on Metallurgical Processes for the Early Twenty-First Century, ed. Sohn, H.Y., TMS, Warrendale, pp. 907 - 927, 1994a
- Reuter, M.A., Bernhard, D., "Simulation and Identification of Metallurgical Kinetic Processes using a Generalised Kinetic Rate Equation and Trained Neural Nets", Minerals Engineering,Vol. 7, No.1, pp. 1-19, 1994b
- Reuter, M.A., Eksteen, J.J., Van Schaik, A., "Pyrometallurgical Reactors – Closers of the Recycling Materials Cycle", Proceedings of the Yazawa International Symposium on Metallurgical Materials Processing: Principles and Technologies, eds. F. Kongoli, K. Itagaki, and H.Y.Sohn, TMS, March 3-7, San Diego, California, USA, pp. 1005-1017, 2003
- Reuter, M.A., Moolman, D.W., "Feedforward Quality Control Methodology for Reactors based on Thermodynamics and System Identification Techniques", Erzmetall, 52(2), October, pp. 472-483, 1999
- Reuter, M.A., Pretorius, C., Rennie, M.S., Klopper, K., Barker, I.J., "Intelligent Control of Submerged Arc Furnaces", Proceedings of Infacon 7, Trondheim, 12-13 June, 1/2, pp. 317 – 325, 1995

- Reuter, M.A., Sudhölter, S., "Use of Simmulated Annealing and Neural Nets for the Eco-Techno-Economic Synthesis of Mineral and Metallurgical Flowsheets", Minerals Engineering, 9 (3), pp. 283-299, 1996
- Reuter, M.A., Van der Walt, T.J., Van Deventer, J.S.J., "A Generalised Neural Net Kinetic Rate Equation", Chemical Engineering Science, 48(7), pp. 1281 - 1297, 1993
- Reuter, M.A., Van der Walt, T.J., Van Deventer, J.S.J., "Modelling of Equilibrium Processes in Pyrometallurgy using Neural Nets", Metallurgical Transactions B, 23B, pp. 643 - 650, 1992b
- Reuter, M.A., West, C., Fourie, A., Moolman, D.W., Aldrich, C., "The use of Dimensionless Numbers to Characterise the Feed to Metallurgical Reactors", Minerals Engineering, 10(1), pp. 69 - 80, 1997
- Reuter, M.A., Yang, Y., "Modelling and Control of the Resource Cycle", Report: TA.GV.2001.15, Department of Applied Earth Sciences, Delft University of Technology, 2001
- Reynolds, Q., "Thermal Radiation Modelling of DC Smelting Furnace Freeboards, Minerals Engineering, 15(11), pp., 2002
- Reznik, I.D., "Regularities of Cobalt and Nickel Distribution Between Smelting Products", The Paul E. Queneau International Symposium on Extractive Metallurgy of Copper, Nickel and Cobalt, The Minerals, Metals and Materials Society, Warrendale, pp. 169-183, 1993
- Riboud, P.V., Muan, A., "Effect of Cr_2O_3 on Melting Relations of Iron Oxide at Low Oxygen Pressures", Transactions of the Metallurgical Society of the AIME, 230, February, pp. 88-90, 1964
- Riboud, P.V., Roux, Y., Lucas, D., Gaye, H., Fachber. Hüttenprax., Metallweiterverarb., 19, 859-869, 1987.
- Richards, R.G., White, J., "Phase Relationships of Iron-Oxide Containing Spinels", Transactions of the British Cramic Society, 53, pp. 422-453, 1954
- Richardson, F.D., "Physical Chemistry of Melts in Metallurgy, Volume 2", Academic Press, London, pp. 420 - 425, 1974
- Rico-Martinez, R., Adomaitis, R.A., Kevrekidis, I.G., "Noninvertibility of Neural Networks", Computers and Chemical Engineering, 24, pp. 2417-2433, 2000
- Robertson, D.G.C. Lee, J.H., Rawlings, J.B., "A Moving-Horizon-Based Approach Least Squares Estimation", American Institute of Chemical Engineers Journal, 42 (8), pp. 2209-2222, 1996

- Robertson, D.G.C., Kang, S., "Model Studies of Heat Transfer and Fluid Flow in Slag Cleaing Furnaces", Proceedings of the International Symposium on Fluid Flow Phenomena in Metals Processing, TMS Annual Meeting, San Diego, 28 Feb – 4 Mar, 1999
- Roeder, P.L., Glasser, F.P., Osborn, E.F., "The System Al_2O_3-Cr_2O_3-SiO_2", Journal of the American Ceramic Society, 51 (10), pp. 585-594, 1968
- Roghani, G., Takeda, Y., Itagaki, K., "Phase Equilibrium and Minor Element Distribution between FeO_x-SiO_2-MgO- Based Slag and Cu_2S-FeS Matte at 1573 K under High Partial Pressures of SO_2", Metallurgical and Materials Transactions B, 31B, August, pp. 705-712, 2000
- Roozendaal, A., Philander, C., De Meijer, R.J., "Mineralogy of Heavy Mineral Placers along the West Coast of South Africa", Proceedings of the Heavy Mineral '99 Symposium, Symposium Series S23, ed. Stimson, R.G., South African Institute of Mining and Metallurgy, Johannesburg, pp.63-66, 1999
- Roscoe, R., Brittish Journal of Applid Physics, 3, pp. 267-269, 1952
- Salama, A.I.A., "Sampling Schemes for Mass Balance of Flowsheets with Multi-Component Streams", International Journal of Mineral Processing, 55, pp. 219-229, 1999
- Sano, N., Lu, W., Riboud, P.V., Maeda, M., "Advanced Physical Chemistry for Process Metallurgy", Academic Press, London, pp. 5 - 117, 1997
- Sarma, B., Cramb, A.W., Fruehan, R.J., "Reduction of FeO in Smelting Slags by Solid Carbon: Experimental Results", Metallurgical and Materials Transactions B, 27B, October, pp. 717-730, 1996
- Sarvinis, J., Voermann, N., "Developents in Furnace Design and Refractory Cooling", Developments in Non-Ferrous Metallurgy Workshop, South African Institute of Mining and Metallurgy, 23 August, 2000
- Schoneville, R.H., Toguri, M.T., "Oxidation of Copper Matte by Gas Injection", Proceedings of Copper 99-Cobre 99 International Conference, Volume VI-Smelting, Technology Development, Process Modelling and Fundamentals, pp. 493-507, 1999
- Schwessinger, W.T., Muna, A., "Spinel-Silicate Equilibria in the System MgO-FeO-Fe_2O_3-Al_2O_3-Cr_2O_3-SiO_2", Journal of the American Ceramic Society, 75 (6), pp1390-1398, 1992
- Seborg, D.E., Edgar, T.F., Mellichamp, D.A., "Process Dynamics and Control", John Wiley and Sons, New York, 1989

- Seetharaman, S., Sichen, D., "Viscosities of High Temperature Systems – A Modelling Approach", ISIJ International, 37 (2), pp. 109-118, 1997
- Serth, R.W., and Heenan, W.A., "Gross Error Detection and Data Reconcilliation in Steam-Metering Systems", American Institute of Chemical Engineers Journal, 32 (5), pp. 733-742, 1986
- Sevinc, N., "Thermodynamic Study of the FeO-Fe_2O_3-TiO_2 system at 1500 °C", Transactions of the Institution of Mining and Metallurgy, Section C, 98, September-December, pp. C185-C189, 1989
- Sheikshab B.M., Kurimoto, H., Sano, M., "Effect of Slag Foaming on the Reduction of Iron Oxide in Molten Slag by Graphite", ISIJ International, 32 (10), pp. 1084-1090, 1992
- Sheng, Y.Y., Irons, G.A., "Mathematical Modelling of Fluid Flow and Heat Transfer in Electric Smelting", Canadian Metallurgical Quarterly, 37(3/4), pp. 265 – 273, 1998
- Sheng, Y.Y., Irons, G.A., Tisdale, D.G., "Transport Phenomena in Electric Smelting of Nickel Matte, Part I. Electric Potential Distribution", Metallurgical and Materials Transactions B, 29B, February, pp. 77-83, 1998
- Sheng, Y.Y., Irons, G.A., Tisdale, D.G., "Transport Phenomena in Electric Smelting of Nickel Matte, Part I. Mathematical Modelling", Metallurgical Transactions B, 29B, February, pp. 85-94, 1998
- Shi, F.N., Napier-Munn, T.J., "International Journal of Mineral Processing, 47, pp. 103-123, 1996
- Shridhar, E., Lahiri, A.K., "Steady State Model for Current and Temperature Distribution in An Electric Smelting Furnace", Steel Research, 65(10), 433-437, 1994
- Shridhar, S., "Estimation Models for Molten Slag and Alloy Viscosities", Journal of Metals, 54 (11), pp. 46-50, 2002
- Shridhar, S., Toguri, J.M., Simeonov, S., "Copper Losses and Thermodynamic Considerations in Copper Smelting", Metallurgical and Materials Transactions B, 28B, April, pp.191-200, 1997
- Sichen, D., Bygden, J., Seetharaman, S., "A Model for the Estimation of Viscosities of Complex Metallic and Ionic Melts", Metallurgical Transactions B, 25B, August, pp. 519-525, 1994
- Sigworth, G.K., Canadian Metallurgical Quaterly, 35, pp. 101-122, 1996
- Simeonov, S.R., Sridhar, R., Toguri, J.M., "Sulphide Capacities of Fayalite-Base Slags", Metallurgical and Materials Transactions B, 26B, 325-334, 1994

- Simons, B, Woermann, E., "Iron Titanium Oxides in Equilibrium with Metallic Iron", Contributions to Mineralogy and Petrology, 66, pp. 81-89, 1978
- Singh, S.R., Mittal, N.K., Sen, P.K., "A Novel Data Reconcilliation and Gross Error Detection Tool for the Mineral Processing Industry", Minerals Engineering, 14 (7), pp. 809-814, 2001
- Smith, H.L., Denton, G.M., Barcza, N.A., "Ferrochromium Production", South African Patent no. 960877, South Africa, 1996
- Smithells, "Smithells Metals Reference Book", Butterworth-Heineman, Londen, 1976
- Soderstrom, T.A., Himmelblau, D.M., Edgar, T.F., "A Mixed Integer Approach for Simultaneous Data Reconciliation and Identification of Measurement Bias", Control Engineering Practice, 9, pp. 869-876, 2001
- Sofra, J, "Design of Ausmelt Furnace Based on Deliverable Mixing Power", Personal Communication, Ausmelt®, Pyrometallurgy 2002, 11/03/2002, Cape Town, 2002
- Sommerville, I.D., Bell, H.B., "The Behaviour of Titania in Metallurgical Slags", Canadian Metallurgical Quarterly, 21 (2), pp. 145-155, 1982
- Soykan, O., Eric, R.H., King, R.P., "Kinetics of the Reduction of Bushveld Complex Chromite Ore at 1416 °C", Metallurgical and Materials Transactions B, 22B, December, pp. 801-810, 1991
- Stadler, S.A.C., Eksteen, J.J., Aldrich, C., "An Experimental Investigation of Slag Foaming of High Fe_xO Slags", Proceedings of the 22nd International Mineral Processing Congress, Cape Town, 28 September – 3 October, pp. 1416-1425, 2003
- Steiler, J-M, "Iron-making Reactions", in Advanced Physical Chemistry for Process Metallurgy, eds. Sano, N., Lu, W., Riboud, P.V., Maeda, M., Academic Press, London, pp. 253-280, 1997
- Stenkvist, S.E., Bowman, B., "High Power, Graphite-Cathode DC Arc Plasma – Properties and Pratical Applications for Steelmaking and Ferroalloys Processing", in Plasma Technology in Metallurgical Processing, ed. J. Feinman, Iron and Steel Society of the AIME, Warrendale, pp. 103-110, 1987
- Stephanopoulos, G., Han, C., "Intelligent systems in process engineering : A review", Computers and Chemical Engineering, 1996, 20(6/7), pp.743-791
- Stine, H.A., Watson, V.R., "Numerical Calculations for the Characteristics of a Gas Flowing Axially Through a Constricted Arc", NASA, TN., D-4042, 1967
- Stubican, V.S., Greskovich, C., "Trivalent and Divalent Chromium Ions in Spinels", Geochimica et Cosmochimica Acta, 39, pp. 875-991, 1975

- Sudhölter, S., Reuter, M.A., Krüger, J., "Eco-techno-economic Synthesis of Process Routes for the Production of Zinc using Combinatorial Optimisation", Metallurgical and Materials Transactions B, 27B, June, pp. 655-674, 1996
- Szekely, J., "The Mathematical Modelling Revolution in Extractive Metallurgy", Metallurgical and Materials Transactions B, 19B, pp. 525-540, 1988
- Szekely, J., Evans, J.W., Brimacombe, J.K., "The Mathematical Modelling and Physical Modelling of Primary Metals Processing Operations", John Wiley and Sons, New York, 1988
- Szekely, J., McKelliget, J., and Choudhary, M., "Heat Transfer, Fluid Flow, and Bath Circulation in Electric Arc Furnaces and DC Plasma Furnaces", Iron and Steelmaking, 10 (4), pp. 169-179, 1983
- Szekely, J., Themelis, N.J., "Rate Phenomena in Process Metallurgy", Wiley-Interscience, New York, 1971
- Tan, P., Neuschütz, D., "A Thermodynamic Model of Nickel Smelting and Direct High-Grade Nickel Matte Smelting Processes: Part I. Model Development and Validation", Metallurgical and Materials Transactions B, 32B, April, pp. 341-351, 2001a
- Tan, P., Neuschütz, D., "A Thermodynamic Model of Nickel Smelting and Direct High-Grade Nickel Matte Smelting Processes: Part II. Distribution Behaviour of Ni, Cu, Co, Fe, As, Sb, and Bi", Metallurgical and Materials Transactions B, 32B, April, pp. 353-361, 2001b
- Tan, P., Zhang, C., "Thermodynamic Analysis of Copper Smelting Process", Proceedings of the Symposium on Processing of Metals and Advanced Materials: Modelling, Design and Properties, ed. Li, B.Q., The Minerals, Metals and Materials Society, Warrendale, pp. 109-120, 1998b
- Tan, P., Zhang, C., "Thermodynamic Analysis of Nickel Smelting Process", Proceedings of the Symposium on Processing of Metals and Advanced Materials: Modelling, Design and Properties, Ed. Li, B.Q., The Minerals, Metals and Materials Society, Warrendale, pp. 101-108, 1998a
- Tan, P., Zhang, C., Zeng, D., Li, Z., "Viscosity of High Magnesium Content FeO-Fe3O4-SiO2-CaO-MgO Slags at Nickel Flash Smelting Conditions", EPD Congress, Ed. Mishra, B., The Minerals, Metals and Materials Society, Warrendale, pp. 333-340, 1999
- Taniuchi, K., "Arc-plasma reduction of some refractory metal oxides", High Temperature Materials and Processes, 11 (1-4), January, pp. 369-413, 1993

- Taylor, J.R., Dinsdale, A.T., "A Thermodynamic Assessment of the Cr-Fe-O System", Z. Metallkd., 84 (5), pp.335-345, 1993
- Taylor, P.R., Pirzada, S.A., Manrique, M., "Thermodynamic Predictions for Material Processing in a Plasma Reactor Using Solid Oxide Feed Materials", Metallurgical and Materials Transactions B, Volume 25B, October, pp. 713-720, 1994
- Thomas, B.G., Brimacombe, J.K., "Process Modelling", in Advanced Physical Chemistry for Process Metallurgy, eds. Sano, N., Lu, W., Riboud, P.V., Maeda, M., Academic Press, London, pp. 253-280, 1997
- Toker, N.Y., Darken, L.S., Muan, A. "Phase relationships and thermodynamics of the system Fe-Cr-O in the temperature range of 1600°C to 1825°C under strongly reducing conditions", Metallurgical and Materials Transactions, 22B, pp. 689-703, 1991
- Tong, H., Crowe, C.M., "Detection of Gross Errors in Data Reconciliation by Principal Component Analysis", American Institute of Chemical Engineers Journal, 41 (7), pp. 1712-1722, 1995
- Tsai, H-T, T., Muan, A., "Activity-Composition Relations in Refractory Oxide Solutions at High Temperatures: The System Cr_2O_3-Al_2O_3", Journal of the American Ceramic Society, 75 (6), 1412-1415, 1992
- Turkdogan, E.T., "Physicochemical properties of slags and glasses", The Metals Society, London, 1983
- Tuset, J.K., "Constitution and Melting Properties of Hoigh Titanium Slags", Tidsskr.Kjemi., Bergv., Metallurgi, 28 (11), pp. 232-240, 1968
- Ulmer, G.C., "Chromite Spinels", in High Temperature Oxides, Vol. 1, Academic Press, New York, pp. 251-314, 1970
- Ulmer, G.C., White, W.B., "Existence of Chromous Ion in the Spinel Solid Solution Series $FeCr_2O_4$·$MgCr_2O_4$", Journal of the American Ceramic Society, 49 (1), pp. 50-51, 1966
- Urbain, G., Boiret, M., "Viscosities of Liquid Silicates", Iron and Steelmaking, 17 (4), pp. 255-260, 1990
- Urbain, G., Steel Research, 58, pp. 111-116, 1987
- Urquhart, R.C., Rennie, M.S., Rabey, C.C., "The Smelting of Copper-Nickel Concentrates is an Electric Furnace", Copper Smelting and Converting, pp.274-295, 1976
- Ushio, M., Sezekely, J., Chang, "Mathematical Modelling of the Flow Field and Heat Transfer in a High Current Arc Discharge", Ironmaking and Steelmaking, 8 (6), pp. 279-286, 1981

- Uslu, E., and Eric, R.H., "The Reduction of Chromite in Liquid Iron-Chromium-Carbon Alloys", Journal of the South African Institute of Mining and Metallurgy, 91 (11), pp. 397-409, 1991
- Utigard, T., "An Analysis of Slag Stratification in Nickel Laterite Smelting Furnaces due to Composition and Temperature Gradients", Metallurgical and Materials Transactions B, 25B, August, pp. 491-496, 1994
- Utigard, T., Sanchez, G., Manriquez, A., Luraschi, A., Diaz, C., Cordero, D., Almenras, E., "Reduction Kinetics of Liquid Iron Oxide-Containing Slags by Carbon Monoxide", Metallurgical and Materials Transactions B, 28B, October, pp. 821-826, 1997
- Van der Walt, T.J., Van Deventer, J.S.J., Barnard, E., "The Dynamic Modelling of Ill-defined Processing Operations using Connectionist Networks", Chemical Engineering Science, 48 (7), pp.1945-1958, 1993
- Verein Deutscher Eisenhuttenleute, "Slag Atlas", 2nd Edition, Verlag Stahleisen, Dusseldorf, 1995
- Vernon, P.N. and Burks, S.F., "The Application of Ausmelt Technology to Base Metal Smelting, Now and in the Future", Journal of the South African Institute of Mining and Metallurgy, May/June, pp. 89-98, 1997
- Voermann, N., Ham, F., Merry, J., Veenstra, R., Hutchinson, K., "Furnace Cooling Design for Modern, High Intensity Pyrometallurgical Processes", Proceedings of Copper 99-Cobre 99 International Confeence, Volume V – Smelting Operations and Advances, Eds. George, D.B., Chen, W.J., Mackey, P.J., Weddick, A.J., (Warrendale PA: The Minerals Metals and Materials Society), pp. 573-582, 1999
- Vostryakov A. A., Vatolin, N.A., Esin, O.A., "Viscosity and Electric Resistance of Molten Chromium Alloys", Physics of Metals and Physical Metallurgy (Translated from Russian), 16 (5), 1963
- Wahlbeck, P.G, Gilles, P.W., "Reinvestigation of the Phase Diagram for the System Titanium-Oxygen", Journal of the American Ceramic Society, 49 (4), pp. 180-183, 1966
- Warczok, A., Utigard, T. A., "Fayalite Slag Reduction by Solid Graphite", Canadian Metallurgical Quarterly, 37 (1), pp. 27-39, 1998
- Watson V.R., Pegot, E.B., "Numerical Calculations for the Characteristics of a Gas Flowing Axially Through a Constricted Arc", NASA, TN., D-4042, 1967
- Wedepohl, A., Barcza, N.A., "The Dig-Out of a Ferrochromium Furnace", Special Publication of the Geological Society of South Africa, 7, pp. 351-363, 1983

- Wethmar, J.C.M., Howat, D.D., Jochens, P.R., "Phase Equilibria in the Cr-Fe-Si-C System in the Composition Range Representative of High Carbon Ferrochromium Alloys Produced in South Africa", Metal Science, 9, pp. 291-296, 1975
- White, W.B., Roy, R., "The System Chromium-Oxygen at High Oxygen Pressures", Geochimica et Cosmochimica Acta, 39, pp. 803-817, 1975
- Wicks, J., 2000, "Smelter and Converter Practice at the Waterval Smelter: Process, Challenges and Innovations", Developments in Non-Ferrous Pyrometallurgy Workshop, Cape Town, South African Institute of Mining and Metallurgy, 23 August, 2000
- Wiegel, R.L., "Improving the Plant Metallurgical Balance, Canadian Metallurgical Quarterly, 11(2), pp. 413-424, 1972
- Willis, G.M., "Thermodynamics of Nickel Solubility in Iron Silicate Slags", Canadian Metallurgical Quarterly, 20 (2), pp. 153-161, 1981
- Wills, B.A., "Complex Circuit Mass Balancing – A Simple Practical, Sensitivity Analysis Method", International Journal of Mineral Processing, 16, 245-262, 1986
- Wills, B.A., "Mineral Processing Technology", 6th Edition, Butterworth-Heinemann, Oxford, pp. 84-90, 1997
- Wright, S., Zhang, L., Sun, S., Jahanshahi, S., "Viscosity of a CaO-MgO-Al_2O_3-SiO_2 Melt Containing Spinel Particles at 1646 K", Metallurgical and Materials Transactions B, 31B, February, pp. 97-109, 2000
- Xiao, Y. and Holappa, L., "Determination of activities in slags containing chromium oxides", ISIJ International, 33(1), pp. 66-74, 1993
- Xiao, Y. and Holappa, L., "Thermodynamic properties of chromium bearing slags and minerals, A review", Laboratory of Metallurgy Report TKK-V-B118, Helsinki University of Technology, Espoo, Finland, 1996
- Xiao, Y., "Thermodynamic Study of CrO_x Containing Slags", D.Tech dissertation, Helsinki University of Technology, Espoo, Finland, 1993
- Yamashita, Y., Komori, H., Suzuki, M., "Running Multiple Neural Networks for Process Trend Interpretation", Journal of Chemical Engineering of Japan, 32 (4), pp. 552-556, 1999
- Yang, L., Belton, G.R., "Iron Redox Equilibria in CaO-Al_2O_3-SiO_2 and MgO-CaO-Al_2O_3 Slags", Metallurgical and Materials Transactions B, 29B, August, pp. 837-845, 1998
- Yang, Y., "Modelling and Control of Metallurgical Reactors", Ed. Reuter, M.A., and Yang,Y., Delft University of Technology, Delft, 2000

- Zhang, L., Jahanshahi, S., "Review and Modelling of Viscosity of Silicate Melts: Part I, Viscosity of Binary and Ternary Silicates Containing CaO, MgO, and MnO", Metallurgical and Materials Transactions B, 29B, February, pp. 177-186, 1998a
- Zhang, L., Jahanshahi, S., "Review and Modelling of Viscosity of Silicate Melts: Part II, Viscosity of Melts Containing Iron Oxide in the CaO-MgO-MnO-FeO-F_2O_3-SiO_2 System", Metallurgical and Materials Transactions B, 29B, February, pp. 187 - 195, 1998b
- Zhang, L., Jahanshahi, S., Sun, S., Chen, C., Bourke, B., Wright, S., Somerville, M., "CSIRO's Multiphase Reaction Models and Their Application", Journal of Metals, 54(11), pp. 51- 56, 2002
- Zhang, L., Jahanshahi, S., Sun, S., Lim, M., Bourke, S., Wright, S., Somerville, M., "Development and Applications of Models for Pyrometallurgical Processes", Materials Forum, 25, pp.136-153, 2001
- Zhang, P., Rong, G., Wang, Y., "A new method of Redundancy Analysis in Data Reconciliation and its Application", Computers and Chemical Engineering, 25, 941-949, 2001
- Zhang, P.X., Zhang, Q., Wu, L., Sui, Z., "Optimisation of Compositions of MgO-B_2O_3-SiO_2 Slags Using Artificial Neural Networks and Genetic Algorithms", Z. Metallkd, 87(1), pp. 76-78, 1996
- Zhang, Y., Fruehan, R.J., "Effect of Bubble Size and Chemical Reactions on Slag Foaming", Metallurgical and Materials Transactions B, Vol. 26B, August, pp. 803-812, 1995
- Zhang, Y., Fruehan, R.J., "Effect of Carbonaceous Particles on Slag Foaming", Metallurgical and Materials Transactions B, 26B, August, pp. 813-819, 1995

10 APPENDIX A: BACKGROUND TO THERMOCHEMICAL AND PHASE EQUILIBRIUM MODELLING

10.1 Introduction

The purpose of this appendix is to provide the reader with a review of the background required to:

- Validate simulated predictions
- Review the literature to establish which melt, mineral and crystalline alloy phases are required to be included in the modelling
- Provide a sound basis of the equilibrium relationships published in literature. This serves as a reality "check" to evaluate if FactSage® predicts the same trends.
- Understand the formulation of the quasichemical and other solution models used in FactSage®.

The thermochemistry pertaining to the three systems (matte converting, chromite smelting and ilmenite smelting) will be presented in turn, after which the physical and mathematical background to the solution models will be presented.

10.2 Thermodynamics of nickel-copper matte converting

The characteristics of the converting process have been discussed in Chapters 2 and 3. The major element deportation and the relevant phase equilibria will be discussed in this section.

10.2.1 Metal distribution between slag and matte

The metals that are studied will be constrained to Ni, Cu, Fe and Co (the only minor element discussed).

10.2.1.1 Distribution behaviour of nickel

Font *et al.* (1998c) determined the solubility of nickel in an iron-silicate base slag equilibrated with Ni_3S_2-FeS matte at 1573 K and under SO_2 partial pressures of 0.1, 0.5 and 1 atm. As can be seen in Figure 10.1, it was found that the nickel content in the slag increased slightly in the region of matte grade up to about 38% nickel, and remarkably above this grade with increasing matte grade. It is also obvious from Figure 10.1 that the nickel solubility in the slag is also dependent on the partial pressure of SO_2 and increases with increasing partial pressure of SO_2 at a specific matte grade. Font *et al.* (1999) also investigated the nickel content in the slag with respect to the mass % nickel and copper in the matte. As shown in Figure 10.2, the

nickel content in the slag was found to increase slightly in the region of matte grade up to about 48 % (Cu+Ni) and markedly above this grade with increasing matte grade. This relationship is similar to that found by Font *et al.* when using a Ni_3S_2-FeS matte under the same conditions, but with higher solubility of nickel in all the matte ranges.

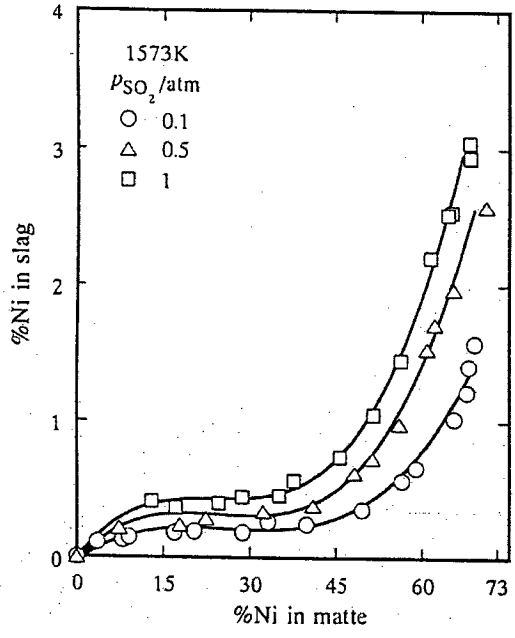

Figure 10.1: Nickel solubility in the slag versus Ni-grade in the matte under SO_2 partial pressures of 0.1, 0.5 and 1 atm at 1573K (Font *et al.*, 1998c).

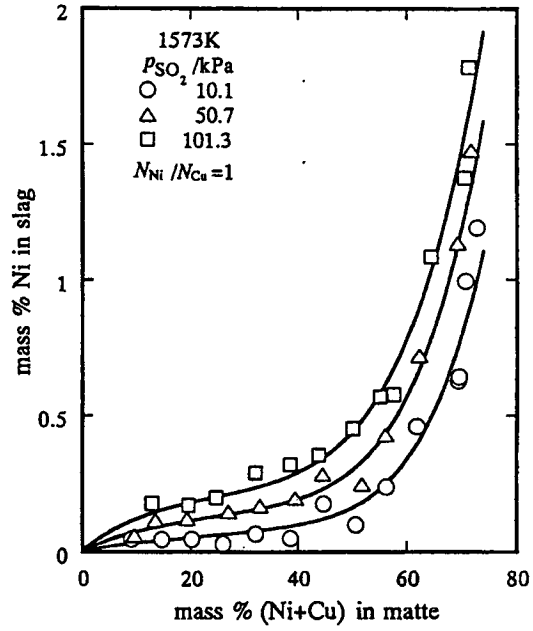

Figure 10.2: Solubility of nickel in slag against nickel and copper content in matte under pSO_2 of 0.1, 0.5 and 1 atm at 1573K (Font *et al.*, 1999).

The graphs shown in Figures 10.1 and 10.2 are as one would anticipate, as the order of thermodynamic stability, based on the reaction $\underline{MS}$+ $1\frac{1}{2}O_2$ (g) = [MO] + SO_2 (g), is Cu_2S > Ni_3S_2 > Co_3S_2> FeS. Therefore, oxidation of Fe, Co and part of the S proceeds before oxidation of the major part of Ni and Cu (and the associated S) commences. The slag has a capacity to dissolve Ni in both its sulphide and oxide form, where the Figures 10.1 and 10.2 depict the total nickel in the slag. A breakdown of the oxidic and sulphide components as dissolved in slag is given in Figure 10.3. It was found that the oxidic part increases sharply with matte grade while the sulphidic part represents a maximum at a matte grade of about 8% Ni and then decreases with increasing matte grade. Consequently the sulphide part is prevailing only in low matte grade region less than about 25 and 13 % Ni for pSO_2 of 0.1 and 1 atm, respectively. The activities of NiO in CaO-MgO-SiO_2-Al_2O_3 slags have been studied by Holzheid *et al.* (1997). They found that the activity coefficient of NiO in slag is nearly temperature independent for the temperature range 1300 °C to 1600 °C, if pure liquid NiO is the reference state. The activity coefficient was found to be independent of oxygen fugacity. Neither was the activity coefficient of NiO influenced much by changes in the FeO, MgO and

CaO concentrations. Similar results were obtained for CoO and FeO in the melt. The experimental precision (relative to the expected value) for the activity coefficient determination was typically 20% for NiO and CoO and 13% for FeO.

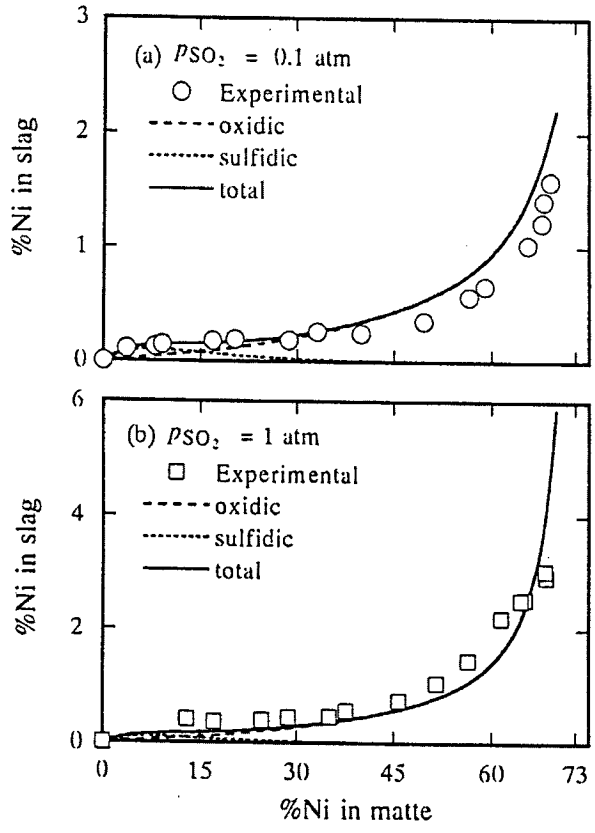

Figure 10.3: Oxidic and sulphidic dissolutions of nickel in slag along with the total nickel content in the slag against matte grade at 1573 K for pSO_2 of 0.1, 0.5 and 1 atm at 1573K (Font *et al.*, 1998c).

10.2.1.2 Distribution behaviour of copper

Font *et al.* (1998c) determined the solubility of copper in an iron-silicate base slag equilibrated with Cu_2S-FeS matte at 1573 K and under SO_2 partial pressures of 0.1, 0.5 and 1 atm. As shown in Figure 10.4, the solubility of copper in the slag increases with increasing matte grade in its low concentration range. However, the copper level in the slag remains very small and nearly constant over a very wide range from 10-65% Cu in the matte, within the experimental error of the measurements. At matte grades higher than 65% Cu (not found for the Ni-Cu matte in this scenario), the Cu-losses to the slag increases significantly. The solubility of copper in the slag also appears to be independent of the partial pressure of SO_2.

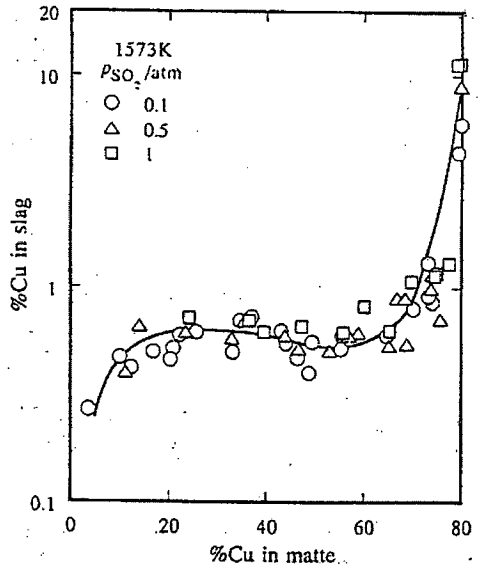

Figure 10.4: Solubility of copper in slag against copper content in matte under pSO_2 of 0.1, 0.5 and 1 atm at 1573K (Font *et al.*, 1998c).

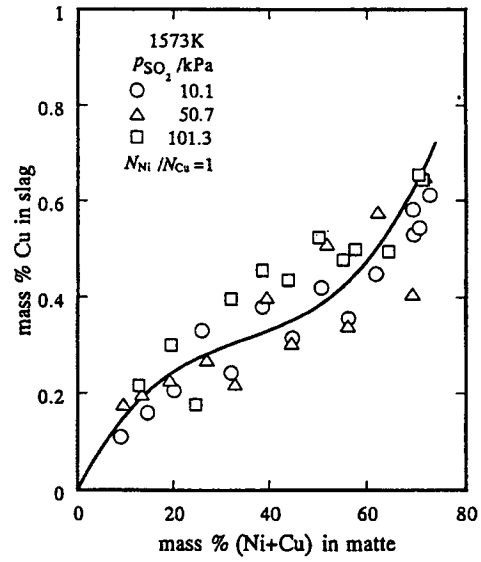

Figure 10.5: Solubility of copper in slag against nickel and copper content in matte under pSO_2 of 0.1, 0.5 and 1 atm at 1573K (Font *et al.*, 1999).

Similar to the study done for Ni, Font *et al.* (1999) also investigated the copper content in the slag with respect to the combined mass % nickel and copper in the matte. As shown in Figure 10.5, the copper content in the slag was found to increase markedly in the low matte grade up to about 20 % (Ni+Cu), slightly in the region between 10-50 % and then abruptly after 50 %. This relationship is similar to that found by Font *et al.* (1998c) when using a Cu_2S-FeS matte under the same conditions, but with higher solubility of copper in all the matte range.

If one compares Figure 10.6 with Figure 10.3, it is apparent that Cu and Ni differs much in their behaviour and distribution between sulphidic and oxidic species dissolved in the slag. It is noted that the sulphidic Cu content of the slag is considerably higher in the regions of low matte grade, while oxidic Cu prevails in the region of high matte grade.

One important aspect of copper is its tendency not to oxidize significantly over a very wide concentration range in the matte. It may therefore be used as a "tie component" in the mass balance sense to estimate matte inventories during a Ni-Cu matte blow as the initial matte mass and initial copper concentration are known, and it is known that the mass of copper remains nearly constant throughout the duration of the blow.

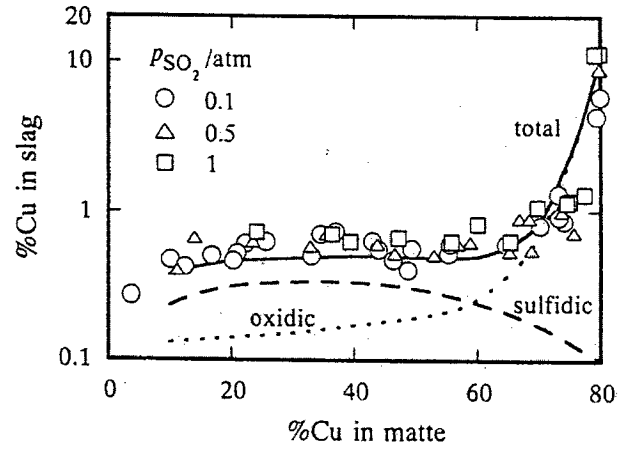

Figure 10.6: Oxidic and sulphidic dissolutions of copper in slag along with the total copper content in the slag against matte grade at 1573 K for pSO_2 of 0.1, 0.5 and 1 atm at 1573K (Font *et al.*, 1998c).

10.2.1.3 Distribution behaviour of iron

Metal recovery depends on the mass of iron transported to slag, the thermodynamic environment in which the transport is made, and the extent to which the slag, once formed, is left in contact with the matte. Grimsey (1993) determined a relationship for metal recovery in terms of the mass fraction of total iron partitioned to the slag at any stage as well as a parameter representing the chemical or thermodynamic environment in which the partition is made. As would be expected, the iron grade of the slag does not change to any significant extent with changes in the copper grade of the matte. This was clearly shown by Roghani *et al.* (2000), as depicted in Figure 10.7.

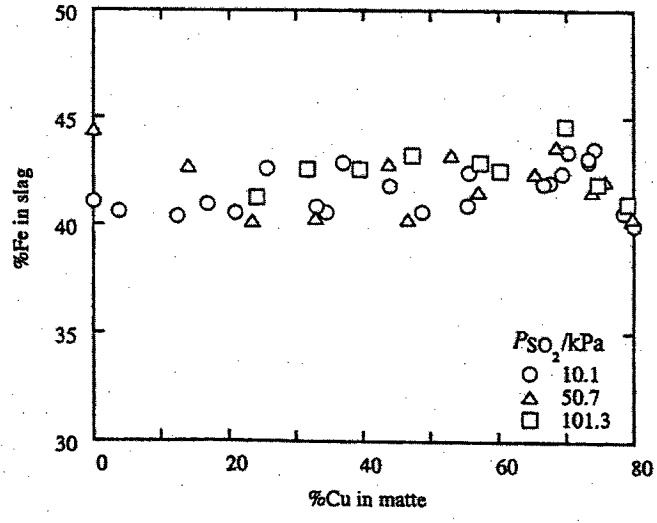

Figure 10.7: Iron content of the slag versus copper content in the matte under pSO_2 of 0.1, 0.5 and 1 atm at 1573K (Roghani *et al.*, 2000)

10.2.1.4 Distribution behaviour of cobalt and other minor elements

Reddy and Healy (1981a) studied the solubility of cobalt in Cu_2O-SiO_2 slag equilibrated with copper-cobalt alloys. This was done for conditions of varying amounts of cobalt in the alloy, at a temperature of 1573 K. Over the entire cobalt feed concentration range of between 2 and 10 % it was found that approximately 99 % of the cobalt added reported to the slag phase.

Reddy and Healy (1981b) also investigated the distribution of cobalt between liquid Cu-Co alloys and Cu_2O-CoO-SiO_2 slags. This was done for conditions of varying amounts of cobalt in the alloy, change in composition of slag, different metal to oxide ratios and in the temperature range of 1473 to 1573 K. It was found that the solubility of cobalt in the slag increased with:

- Decreasing temperature.
- Increasing the Cu_2O/SiO_2 ratio.
- Increasing the amount of Co in the alloy
- Increasing the metal to oxide ratio

Reznik (1993) investigated the regularities of cobalt distribution between slag and matte and between slag and metallic alloy. He found that the distribution of cobalt has a direct proportionality with its content in slag against that of matte, as well as its content in slag against iron monoxide content in the slag.

In a nickel matte smelting stage, the behaviour of minor elements has important implications for the downstream refining and purification processes, the environmental pollution control requirements along the entire metal processing path and the economy of the operation. Font *et al.* (1998a) investigated the distribution ratios between the iron-silicate slag and the Ni_3S_2-FeS matte of copper, silver, cobalt, arsenic, antimony and bismuth. These are shown in Figure 10.8.

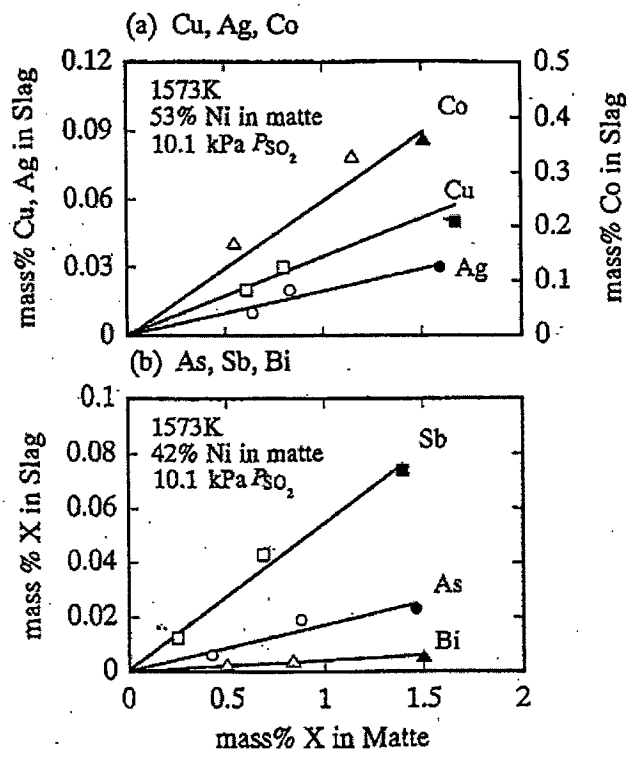

Figure 10.8: Relationship between impurity content in slag and matte phases for matte grade 42 mass % Ni (a) and 53 mass % Ni (b) under 10.1 kPa pSO_2 at 1573K (Font *et al.*, 1998a).

10.2.2 Phase equilibria pertaining to the Ni-Cu mattes

While much research have been done regarding the activities of components in mattes, only the binary phase equilibria pertaining to Ni-Cu-Fe-Co-S mattes have been studied well, while much less data are available for ternary and higher order systems. Due to this reason, it was decided it model the phase equilibria using FactSage® developed by the Centre for Research in Computational Thermochemistry and GTT Technologies (Bale *et al.*, 2002). Degterov and Pelton (1999) and Kongoli and Pelton (1999) have shown that the software could be used to reliably simulate Ni-Cu-Co-Fe-S matte systems. Figure 10.9 presents the quasi-ternary (ratio of sulphur to iron is fixed) phase diagram for FeS_2-Ni-Cu, as calculated by FactSage. It is apparent that alloy formation commences as soon as the FeS_2 concentration is reduced below 22%. This concentration level was found to remain constant irrespective of temperature, as indicated by the coinciding isotherms. The alloy is molten in the copper-rich area of the diagram, but crystallised to a faced-centred cubic (fcc) structure in the nickel-rich part of the system. This corresponds with industrial observations. The isotherms for molten alloy to fcc transition are, as expected, composition dependent; i.e. the fcc melting point isotherms shift significantly with composition. Some bornite precipitation is also noted in the Ni-poor region of the matte, but is normally not noted in the industrial system as this composition region is

too far from the operating line (could be thought of as a near-vertical line from the middle of the triangle towards the Ni-Cu binary. The isotherms are selected to be close to the operating temperatures of the system.

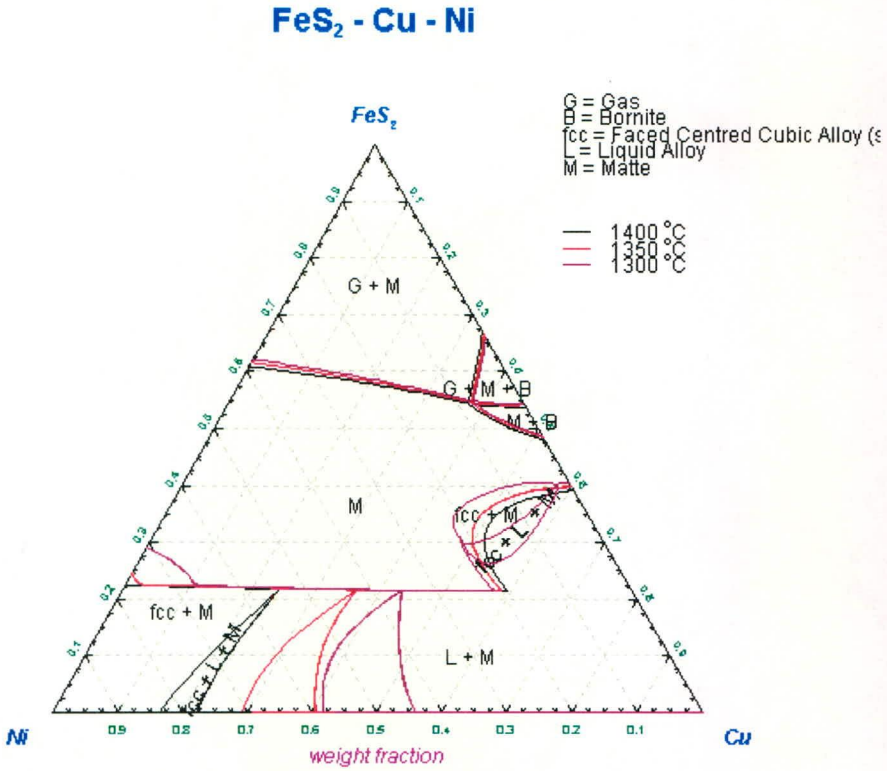

Figure 10.9: Predicted phase equilibria for the FeS_2-Ni-Cu quasi-ternary

Figure 10.10 shows the predicted isotherms for the phase boundaries for the Ni-Cu-S system. The alloy formation is again apparent in the low sulphur region, while solid alloy precipitation occurs in the Ni-rich region and chalcocite precipitation in the copper rich area. Precipitation of Ni_3S_2 or Ni_3S_4, depending on temperature, occurs in the copper-lean-sulphur-rich zone.

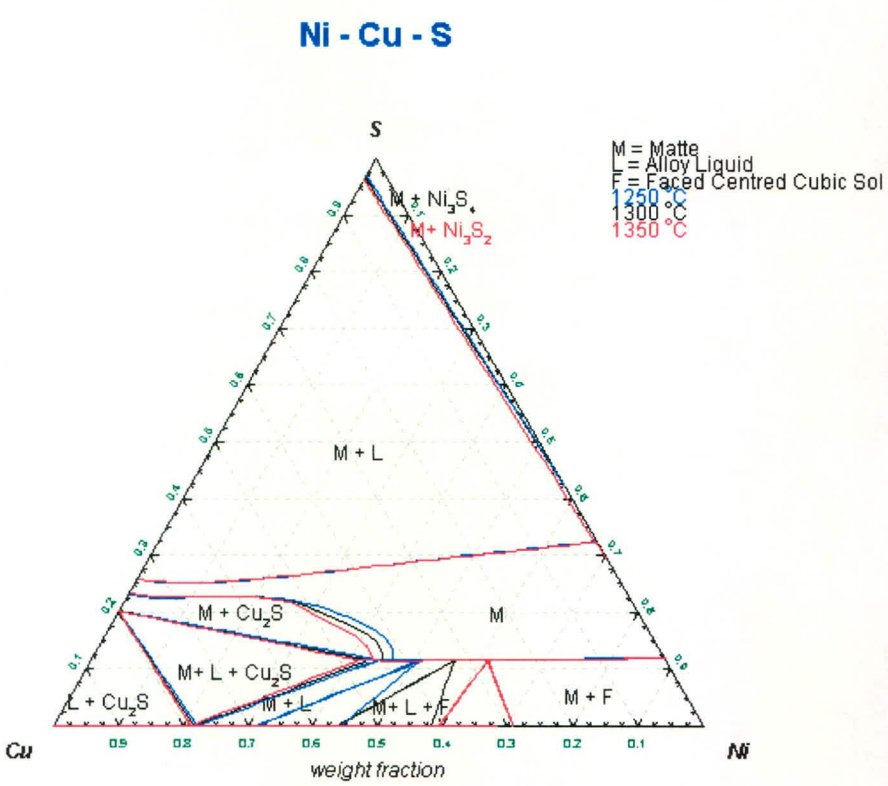

Figure 10.10: Predicted phase equilibria for the Ni-Cu-S ternary

It is apparent from the matte phase equilibria that an alloy-matte emulsion will form during the blowing of the matte. Moreover, solid alloy or sulphide precipitation may occur at certain Ni:Cu ratios, which may influence the rheological behaviour (see Chapter 4) of the melt.

10.2.3 Phase equilibria pertaining to FeO-Fe_2O_3-SiO_2 slags

The slag system that typically applies to matte converting is the FeO-Fe_2O_3-SiO_2 slag system, in cases where silica sand is used as flux (as opposed to the lime ferrite slags which one finds in many modern converting operations which use lime as flux). This system has been well studied by a number of researchers (Muan and Osborne, 1960; Muan, 1955). The phase diagram as published (Slag Atlas, 1995) is presented in Figure 10.11 with the oxygen isobars indicated. The good correspondence of the phase diagram as calculated by FactSage is also presented in Figure 10.12, together with the two-phase tie-lines.

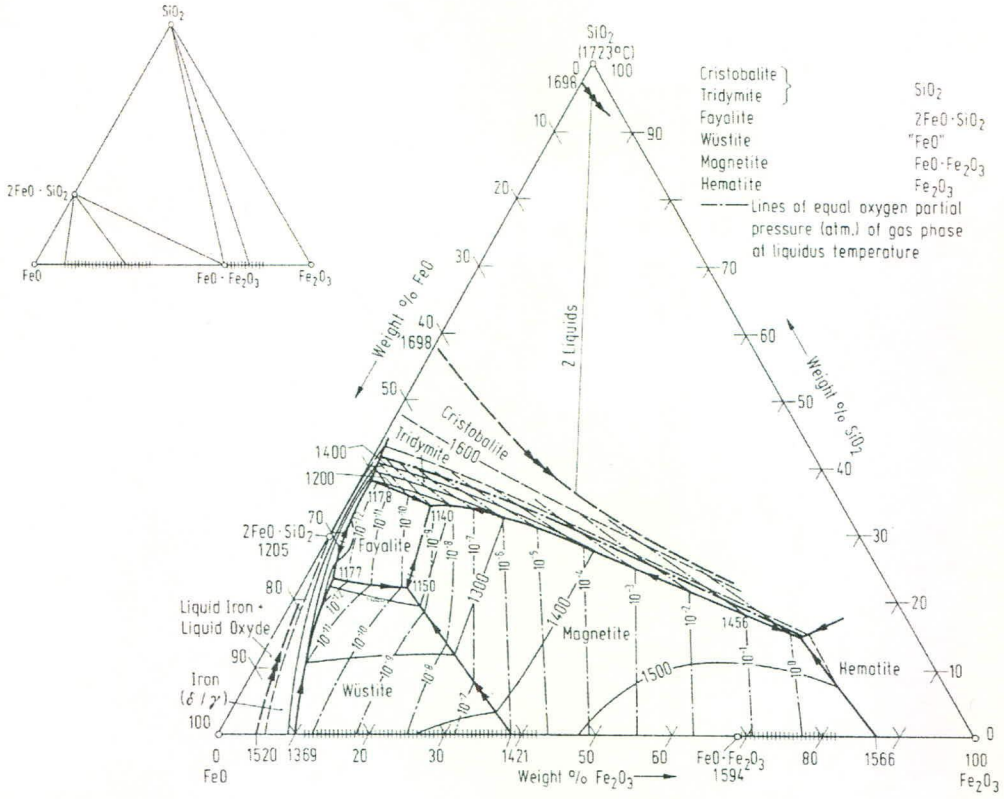

Figure 10.11: Measured phase equilibria for the FeO-Fe_2O_3-SiO_2 ternary

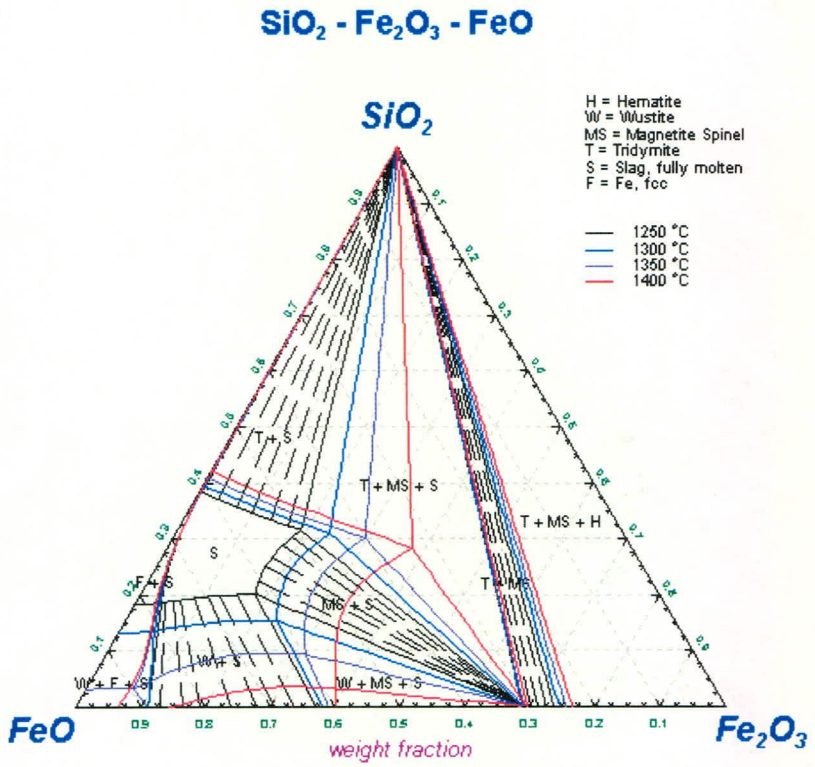

Figure 10.12: Predicted phase equilibria for the FeO-Fe_2O_3-SiO_2 ternary

Under the oxidising conditions found in a converter, the main precipitated phases are tridymite (cristobalite at temperatures above 1500 °C) and magnetite spinel. No new phase

fields appear at higher temperatures. The size of the liquid region of the slag is highly sensitive to increases in temperature, as could be seen from the rapid increase in the molten slag phase field as temperature increases with 50 °C increments (3% variation in the operating temperature). The high density of magnetite (s.g. of 5.1) relative to the slag (s.g. of about 3.2-3.8) implies that the magnetite would tend to settle through the slag and even through the matte region, depending on matte composition, where the density may vary between 4.0 and 5.1 based on the research by Kucharski *et al.* (1994). Banerjee and Irons (1992) studied stratification and bottom build-up due to these density variations and flow patterns in a matte smelting furnace.

10.2.4 Verifying the predicted FactSage® equilibrium outcomes

Before any data were produced, the reliability of the FactSage equilibrium outcomes needed to be ascertained. This was done by first reviewing all the publications involving the study of FactSage, and secondly simulating experimental data from chosen publications relevant to copper-nickel sulphide smelting and converting, and comparing the simulated results with the experimental data.

Anderson (2000) performed simulations using FactSage on published data investigating the phase equilibrium between iron-silicate base slag saturated with silica and Ni_3S_2-FeS matte at 1573 K, under the partial pressures of SO_2 controlled at 10.1, 50.7 and 101.3 kPa (Font *et al.*, 1998b). Since this system is quite similar to the desired system for the database, it is felt that this will give a reasonable idea of the reliability of FactSage for slag-gas-matte component distributions. Similar feed data were fed into FactSage, varying the amount of nickel in the feed, and hence also the matte grade (mass % Ni in matte). These data sets were drawn off and graphs plotted in the same format as those in the publication, so as to compare the two. The exact feed data, however, was not known, hence in a few of the graphs the same trends occur but the values are slightly different. These graphs can be seen in the following figures.

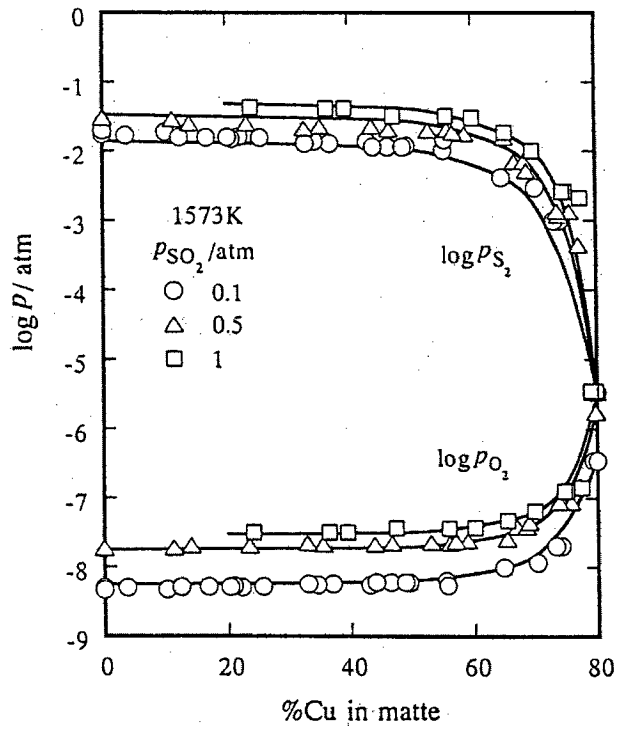

Figure 10.13: Experimental determined relationship between oxygen or sulphur partial pressure and nickel content in matte under pSO_2 of 10.1, 50.7 and 101.3 kPa at 1573 K

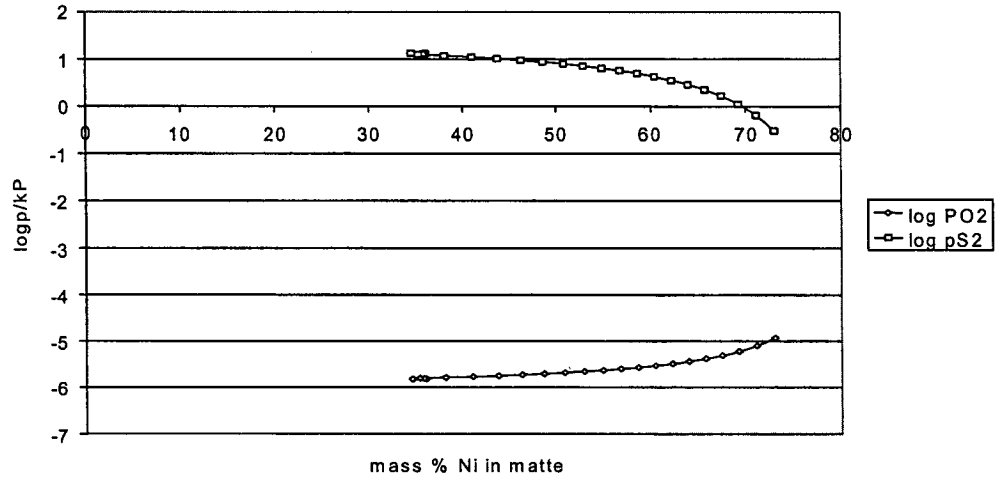

Figure 10.14: Simulated - relation between oxygen or sulphur partial pressure and nickel content in matte under p_{SO2} of 101.3 kPa at 1573 K.

Despite the uncertainty about the precise feed composition, the measured equilibrium corresponds remarkably well with the predicted equilibrium values. A similar observation could be made when one compares Figure 10.15 with Figure 10.4.

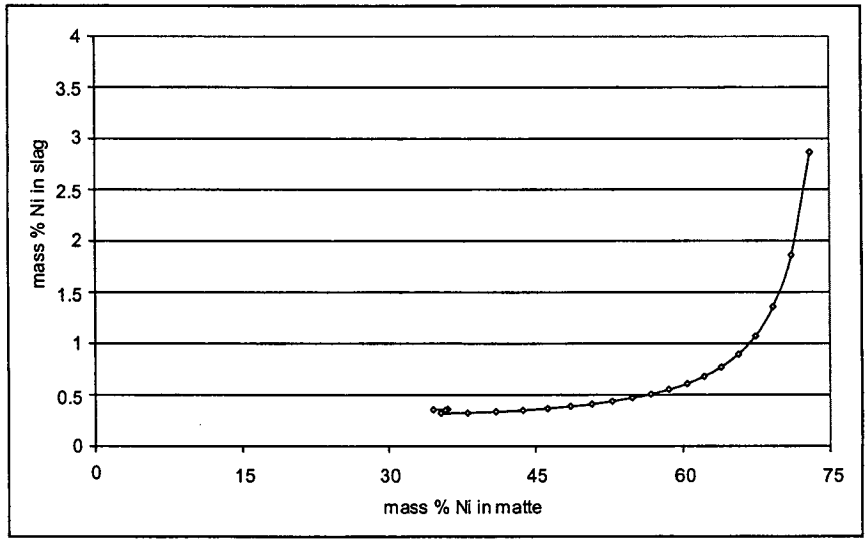

Figure 10.15: Predicted equilibrium distribution between Ni in the matte and Ni in the slag.

These figures demonstrate that FactSage gives reliable equilibrium predictions for matte smelting and converting equilibria.

10.3 Thermodynamics of chromite smelting to produce HCFeCr alloy.

The basic reactions of chromite smelting were presented in Chapter 3. This section provides motivations from the literature to support the phase selection for the modelling of the carbothermic reduction of chromite to HCFeCr.

10.3.1 A review of chrome behaviour in its minerals and the slags

Only the literature pertaining to the thermochemistry associated with HCFeCr manufacture will be dealt with in this section. Much has been published with regard to chromium containing slags in stainless steel manufacture, which will not be reviewed here.

Keith (1954) was one of the earliest researchers who investigated the MgO-Cr_2O_3-SiO_2 system and found no ternary compounds precipitated at the liquidus temperatures. An extensive two-liquid region was noted , while the stability fields of periclase, picrochromite and chromic oxide extend across most of the ternary diagram. The paper is targeted more towards improved refractory development than the equivalent slag system.

Richards and White (1954) subsequently studied the partitioning of Al and Cr between sesquioxide (corundum structure) and spinels solid solutions. It was shown that Cr_2O_3 which forms a continuous series of solid solutions with Fe_xO and raises the dissociation temperature

of the sesquioxide, Al_2O_3, which forms two partial solid solutions has little effect on the dissociation temperature up to the limiting composition in the Al_2O_3 rich solid solution series. Due to this reason it was found that Cr_2O_3 concentrates preferentially in the sesquioxide during the transformation while Al_2O_3 remains evenly distributed between the two phases.

Glasser and Osborn (1958) performed phase equilibrium studies on the CaO-Cr_2O_3-SiO_2 system in all regions except the high-lime part of the ternary. They found that in the high lime region Cr would oxidise to higher oxidation states in an air environment. A liquid miscibility gap was noted for the largest part of the system where the lime contents were less than 45 mass%.

Muan and Sōmiya (1959) studied the Fe_xO-Al_2O_3-Cr_2O_3 system in air and at 1 atmosphere O_2. At temperatures below 1318 °C only sesquioxides with a hexagonal corundum structure were found to be present as equilibrium phases. Between 1318 and 1410 °C in air the monoclinic Fe_2O_3-Al_2O_3 phase with some Cr_2O_3 in solid solution was found in the phase assemblages of certain mixtures. At temperatures above 1380 °C in air, a complex spinel solid solution is one of the phases present at the appropriate composition areas in the system.

Roeder *et al.* (1968) studied the phase equilibria Al_2O_3-Cr_2O_3-SiO_2 system and found that the liquidus diagram is dominated by a large two-liquid region overlying the primary phase field of the corundum solid solution (M_2O_3). Other noted features were the narrow field of mullite solid solution, a very small cristobalite field and a ternary eutectic at 1580 °C. The eutectic liquid (6 Al_2O_3-Cr_2O_3-93SiO_2) was noted to co-exist with a mullite solid solution (61Al_2O_3-10Cr_2O_3-29SiO_2), a corundum solid solution (19Al_2O_3-81Cr_2O_3) and cristobalite (SiO_2). Phase relations and tie-lines for the isothermal planes at 1800 °C, 1700 °C and 1575 °C are presented.

Greskovich and Stubican (1966) investigated divalent chromium in magnesium chromium spinels. A spinel structure of the type $(Mg_{8-x}Cr_x^{2+})Cr_{16}^{3+}O_{32}$ was identified as a new solid solution compound stable in slightly reducing environments in the temperature range 1800 °C -2000 °C.

El-Shahat and White (1966a and 1966b) made an experimental study of the phase equilibrium relationships in spinel-silicate systems and studied the following pseudo-systems:

$MgAl_2O_4$-$MgCr_2O_4$-$CaMgSiO_4$

$MgFe_2O_4$-$MgCr_2O_4$-$CaMgSiO_4$

$MgAl_2O_4$-$MgFe_2O_4$-$CaMgSiO_4$

$MgAl_2O_4$-$MgCr_2O_4$- $MgFe_2O_4$-$CaMgSiO_4$

$MgAl_2O_4$- $MgFe_2O_4$-Ca_2SiO_4

$MgAl_2O_4$-$MgCr_2O_4$- $MgFe_2O_4$-Ca_2SiO_4

$MgAl_2O_4$-$MgCr_2O_4$- $Ca_3MgSi_2O_8$

They found that in all the systems, due to the incongruent melting of $CaMgSiO_4$, a primary crystallisation field of periclase (MgO) occurs. In general it was found that, as the Cr_2O_3 content of the spinel increases, the initial melting temperature of the spinel increases while the solubility of the spinel decreases in the liquid phase.

Ulmer (1970) gives an in-depth discussion of the physico-chemical and geochemical properties of chromite spinels and the solid state solutions of chromium oxides, as well as the slag resistance of chrome containing refractories. The solid state reduction kinetics of chromite, as applicable to submerged arc production of HCFeCr is also discussed.

Muan (1974) studied the phase relationships of chromium oxide containing systems at elevated temperatures. He found that the most dominant feature of the liquidus surface of Cr_2O_3 containing silicate systems are the large liquid miscibility gaps and the dominance of the chromite spinel stability field. He found that the system oxygen partial pressure significantly influences the oxidation state of Fe-Cr oxides. At low oxygen partial pressures Cr^{2+} was found to be prevalent, while Cr^{6+} occurred at high oxygen partial pressure.

Burns and Burns (1975) studied the mineralogy of natural chromium minerals and identified 7 mineral forms that belong to the CaO-MgO-Fe_xO- Al_2O_3-Cr_xO-SiO_2 chemistry group.

Navrotsky (1975) looked into the thermochemistry of oxidic chromium compounds at high temperature. The phase relationships for chromium as it distributes itself in corundum type minerals, spinel solid solutions, garnets, pyroxenes and in shear phases such as the Magnelli-type oxides (also found for ilmenite).

Rankin and Biswas (1977) evaluated the oxidation states of chromium in slag and chromium distribution in slag-metal systems at 1600 °C. They found that the chromium in the reduced slags was predominantly present as CrO. The best average composition of the chromous oxides was $CrO_{1.07}$ which could be viewed as an equivalent mixture of 86% Cr^{2+} and 14% Cr^{3+}. They report that CrO followed Henry's law in the composition range studied. In oxidized slags the saturation form of chromium was found to be an impure form of chromite. Apparent equilibrium constants were calculated for Cr-FeO and Cr-SiO_2 equilibria.

The behaviour of chromium in reduced slag systems was further studied by Rankin and Biswas (1979) and it was established that the Cr content of reduced slags in equilibrium with Fe-Cr-Si alloys decreases with increasing basicity and increasing Si-content of the alloy at constant temperature, as well as with decreasing temperature at constant slag and alloy composition.

Jacob *et al.* (1987) studied the phase relations between Al_2O_3-Cr_2O_3 and $FeAl_2O_4$-$FeCr_2O_4$ solid solutions at 1550 °C. The activities of $FeAl_2O_4$ and $FeCr_2O_4$ in the spinel solid solution were determined through combining the tie-line data with literature values for the activities of Al_2O_3 and Cr_2O_3 in the corundum phase. Activities and GFE of mixing for the spinel solid solution were also obtained from a model based on the cation distribution between non-equivalent crystallographic sites on the oxide lattice.

Toker *et al.* (1991) studied the equilibrium phase relationships of Cr-O systems in the temperature range 1500 °C to 1825 °C. They were able to determine the GFE of formation of Cr_2O_3, Cr_3O_4 and CrO.

Schwessinger and Muan (1992) investigated the distribution of Mg, Fe, Al, and Cr among olivine, orthopyroxene, spinel and a liquid in the system CaO-MgO-Fe_xO- Al_2O_3-Cr_xO-SiO_2 between 1309 and 1471 °C. Distribution coefficients were calculated for the crystals from experimental data. Chromium was found to strongly partition into spinel relative to coexisting liquid olivine and orthopyroxene. Al is enriched in the liquid and spinel relative to the olivine and pyroxene. It was found that the Al/Cr ratio in the spinel increases with decreasing activity of SiO_2 in the melts.

De Villiers and Muan (1992), researched the liquidus-solidus phase relationships of the CaO-CrO-Cr_2O_3-SiO_2 system in equilibrium with metallic chromium in the oxygen partial pressure range of 10^{-10} to 10^{-13} atmospheres. They found that two ternary phases occur in equilibrium with metallic chromium, being the garnet $Ca_3Cr_2Si_3O_{12}$ (uvarovite), and $CaCrSi_4O_{10}$ of the gillespite type structure, where all the Cr is prevalent in the 2+ state. The lowest solidus and liquidus temperatures in the system under these reducing conditions were found to be significantly lower than those for the same system in air. A calcium chromite phase of the approximate composition $Ca_{0.4}Cr_{0.6}Cr_2O_4$ is stable up to the liquidus temperature of the system. It was found that considerable solid solution of the chromium oxide in lime and the various crystalline calcium silicates (pseudowollastonite, rankinite, di- and tri- calcium silicate) occurs, presumably through partial substitution of Cr^{2+} for Ca^{2+}.

Tsai and Muan (1992) studied the activity composition relationships of the Al_2O_3-Cr_2O_3 system at temperatures of 1500 and 1600 °C and found that both species showed considerable positive deviation from ideality (more so for Cr_2O_3 than for Al_2O_3).

The solubility and activity-composition relationships of chromium oxides in melts of the systems CaO-Cr_xO-SiO_2 , and CaO-Al_2O_3-Cr_xO-SiO_2 slags at 1500 °C have been studied by Pretorius *et al.* (1992) in the oxygen pressure range of $10^{-9.56}$ to $10^{-12.5}$ atm. They noted an increase in the concentration of divalent chromium ions as the oxygen partial pressure and the slag basicity decreased which was associated with a dramatic increase in the solubility of chromium oxide in the melt. The activity coefficient of CrO was found to increase with increasing melt basicity and decreasing oxygen partial pressure. The activity-composition relationships of CrO was found to behave similarly to that of other transition metal oxides such as FeO and NiO. An increase in the Al_2O_3 content of the melt led to an increase in the CrO activity coefficient.

The slag-metal equilibrium in the smelting of high-carbon ferrochromium was studied by Akyüzlü and Eric (1992) under atmospheres of pure CO gas and Ar gas at 1600°C. The slag had the typical composition of HCFeCr production slags and consisted of the CaO-MgO-Al_2O_3-CrO-Cr_2O_3-FeO-Fe_2O_3-SiO_2 system. The equilibrium distributions of Cr, C, and Si between the slag and metal phases were determined for a range of compositions of condensed and gas phases. It was shown that Si transfer from the slag to the metal increased with increasing temperatures, decreasing CO partial pressure, decreasing carbon content of the

metal, increasing chromium-to-iron ratio of the metal, increasing silica content of the slag, and decreasing lime-to-alumina ratio of the slag. It was also shown that a decrease in the iron content and an increase in the slag basicity decrease the chromium content of the slag. Most of the Cr in the slag was found to be in the divalent state under the reducing conditions used in the research, which corresponds to the work done by earlier researchers, as mentioned above. The Cr^{2+} capacities of the slags were calculated and it was found to decrease with increasing basicity.

Taylor and Dinsdale (1993) critically assessed the thermodynamics of the Cr-Fe-O system to derive solution models for the system. Both the alloy as well as the slag could be modelled using the two-sublattice ionic liquid model. The models were regressed to contribute to the MTData ® database developed by the National Physical Laboratory.

Xiao (1993) and Xiao and Holappa (1993) reviewed the thermodynamic behaviour of Cr_xO in $CaO\text{-}SiO_2\text{-}Cr_xO$ slags at 1600°C. The partitioning of Cr between its 2+ and 3+ oxidation states were also investigated as a function of temperature and slag composition. It was found that when the temperature was raised from 1500 °C to 1600 °C, the fraction of Cr^{2+} of the total chrome increased, while the overall activity of chromium decreased. The effect of slag basicity was found to be highly significant. It was found that higher slag basicities favoured Cr in its 3+ oxidation state, while the overall activity of Cr increased in the slag. Partial substitution of CaO by MgO led to a slight decrease in the activities of Cr^{2+} and Cr^{3+}. Increasing the Al_2O_3 content from 0 to 10 mol% (about 15 mass %) led to smaller fraction of Cr^{2+} and a higher overall Cr activity at a molar basicity ratio (CaO/SiO_2) of 1.0. Further increases to 20 mol% (30 mass%) did not lead to any significant change. Xiao (1993) indicated that CrO and Cr_2O_3 show a positive deviation from ideal solution behaviour in the $CaO\text{-}SiO_2\text{-}Cr_xO$ quasi ternary system. This would imply that it would be easier to reduce Cr from its oxide in the slag, than it would have been if the chrome behaved ideally. Conversely Cr would also tend to precipitate in one of its many possible mineral forms (such as the Cr spinel) to lower its own activity in the slag.

Pei and Wijk (1994) also performed an experimental study of Cr_xO activities in the $CaO\text{-}MgO_{saturated}\text{-}Al_2O_3\text{-}CrO\text{-}Cr_2O_3\text{-}SiO_2$ system. Their work corroborates the work done by Xiao (1993) with similar results being obtained. They also found that the ratio of divalent chromium in proportion to the total chromium content in the slag was increased by decreasing

basicity, increasing temperature and decreasing oxygen partial pressure. As for Xiao (1993), the CrO showed a large positive deviation from ideality which increased with increasing basicity.

The Al_2O_3-CrO-Cr_2O_3-SiO_2 system has also been critically evaluated by Degterov and Pelton (1996), who critically assessed all thermodynamic and phase diagram data for all phases in the mentioned system and its sub-systems, with oxygen partial pressures ranging from in equilibrium with metallic Cr to equilibrium with air. The modified quasichemical model has been used for the slag phase to be implemented in FactSage ®. The ω_{ij} and η_{ij} parameters were determined for the different binaries and the ternary system as a function of composition.

Degterov and Pelton (1997) also performed a critical evaluation and optimisation of the CaO-CrO-Cr_2O_3-SiO_2 system. As for the previous system stated above, the slag phase was modelled using the modified quasichemical solution model. As before, the ω_{ij} and η_{ij} parameters were determined (either constants or simple polynomial functions of composition). These parameters therefore make out part of the FactSage database.

The systematics of partitioning of Cr^{3+} and Cr^{2+} between liquid slag, olivine and spinel has been determined by Hanson and Jones (1998) over a wide range of redox conditions and melt compositions. The presence of Fe^{3+} was found to suppress the presence of Cr^{2+}. The partitioning is expressed as a function of temperature and oxygen fugacity. The emphasis of the paper is however, geochemical in nature.

It is clear from the amount of research reported that the CaO-MgO-Al_2O_3-CrO-Cr_2O_3-FeO-Fe_2O_3-SiO_2 system has an extremely complex thermochemistry. The extreme multi-component nature of the system makes the system complex to model and difficult to represent as a phase diagram. However, as the equilibrium chromium content in slags associated with HCFeCr production in plasma arc furnaces are very small, and the FeO content is insignificant (from a phase equilibrium point of view), it was decided to only investigate the phase diagram of the CaO-MgO-Al_2O_3- SiO_2 system, as presented in the Slag Atlas (Verein Deutscher Eisenhüttenleute, 1995). Figure 10.16 and Figure 10.17 show the phase equilibria for this system at 25 % and 30 % Al_2O_3.

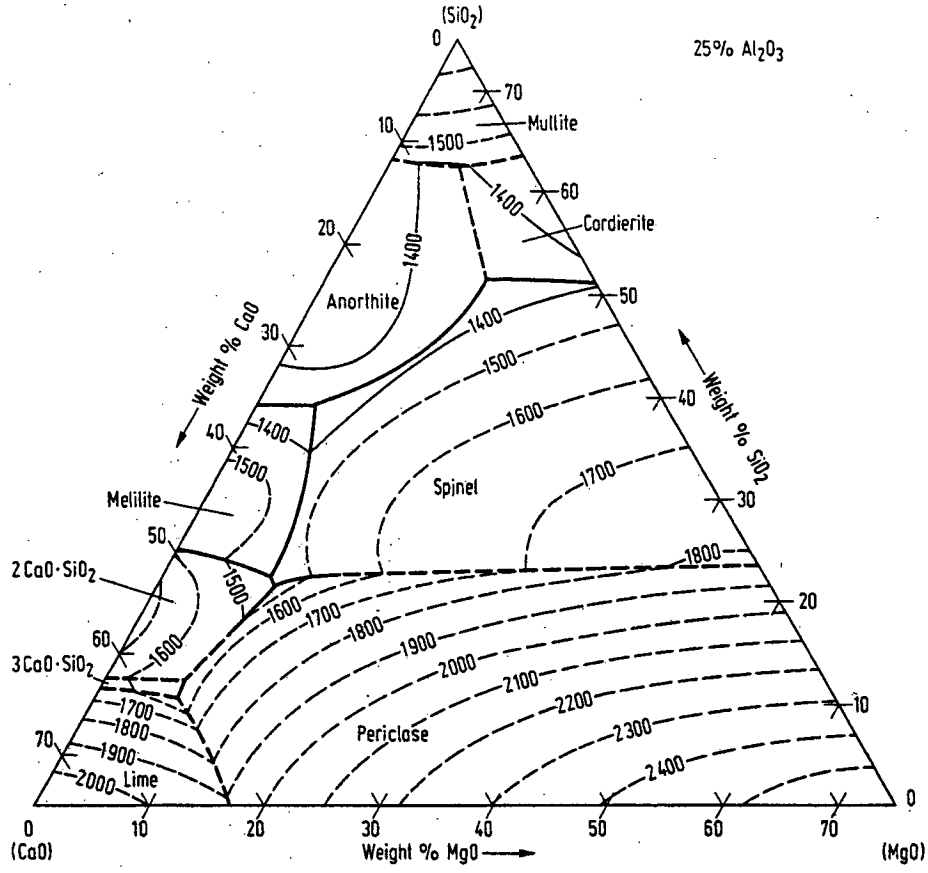

Figure 10.16: The phase relations of the CaO-MgO-Al_2O_3- SiO_2 system with 25% Al_2O_3.

The Periclase (Monoxide in FactSage) and spinel phase fields are predominant. The liquid region at 1600 °C is fairly small and decreases with increases in the amount of alumina present. Increases in the alumina concentration in the bulk slag leads to an increase of the spinel phase field at the cost of the other phase fields. Low liquidus temperatures are associated with low basicities (more acid slags) with the %silica greater than 40%. However, as low basicities favours lower Cr (overall) activities and activity coefficients, larger amounts of Cr remain dissolved in the slag due to the higher chromous capacity of the slag. Furthermore, larger amounts of Si would be reduced to the metal at low basicities and the slag would have a lower ionic conductivity due to the higher degree of polymerisation. The best slag composition from a melting point perspective is therefore not the best from an Cr-recovery and operating perspective.

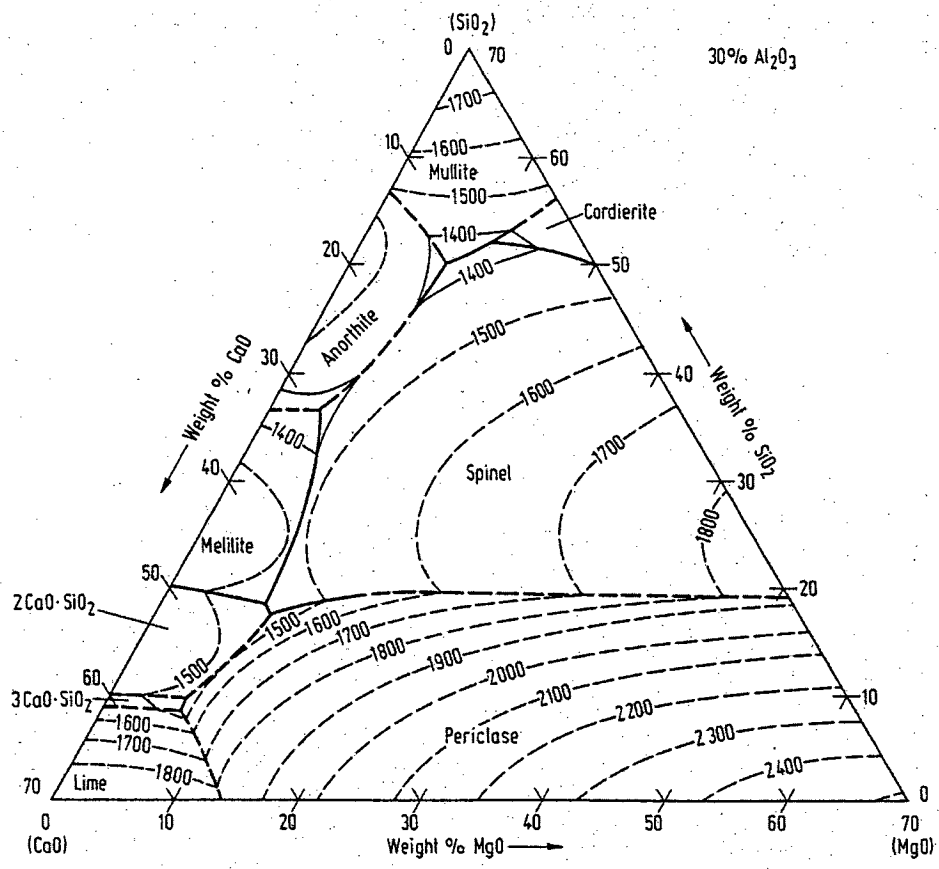

Figure 10.17: The phase relations of the CaO-MgO-Al_2O_3- SiO_2 system with 30% Al_2O_3.

It was shown that FactSage could reliably predict the phase equilibria of the CaO-Al_2O_3-CrO-Cr_2O_3-SiO_2 system. The effects of MgO replacement of CaO in the slag on Cr activity was found to be minimal by Xiao (1993) – which is important as the MgO-Al_2O_3-CrO-Cr_2O_3-SiO_2 system has not been critically evaluated, although the interactions of MgO with all other (non-chrome oxides) have been assessed. The expected prediction error in Cr distribution between slag and alloy is therefore expected not to be significantly influenced by this parameter. FactSage ® was also used to develop the quasi-ternary of the Mg-Spinel ($MgAl_2O_4$) and lime and silica. The use of Mg-spinel is supported by the observation that the Mg to Al ratio does not vary significantly in the chromite spinels. Figure 10.18 gives the phase equilibrium as predicted by FactSage ® of Mg-spinel for a situation where SiO_2 gangue intergrowths exist and lime is used as flux.

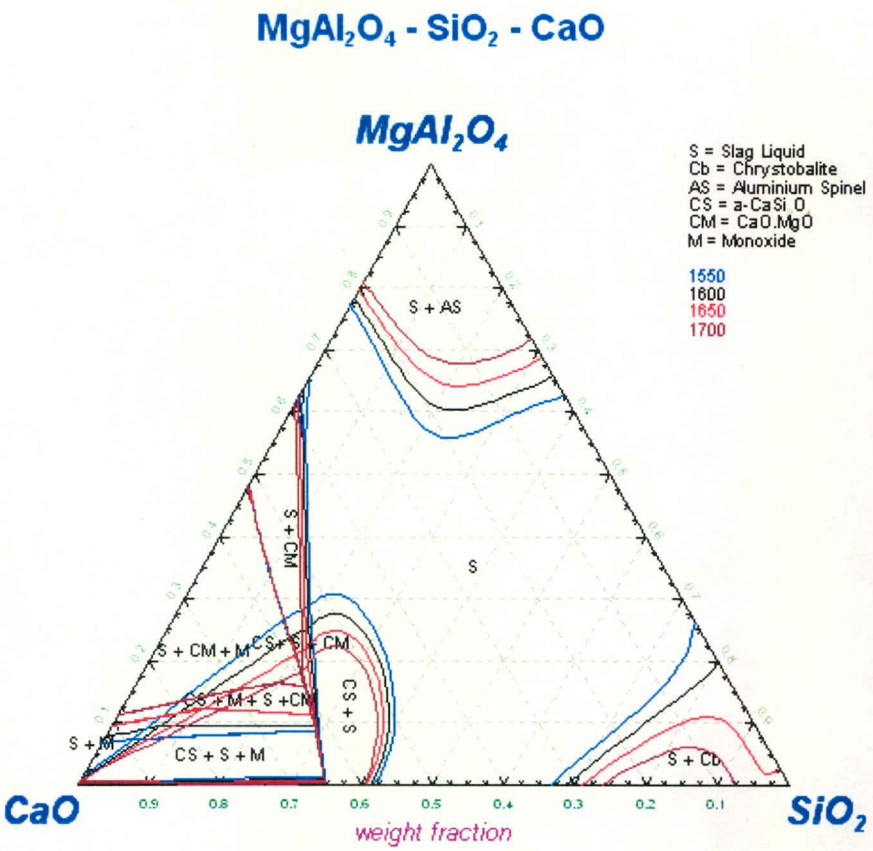

Figure 10.18: Quasi-ternary of Mg-Al-spinel with lime and silica.

10.3.2 Thermochemistry of High Carbon Ferrochrome alloys

Much less research has been done regarding high carbon ferrochrome alloys than for the associated slags. Most of the early research was published by Russian researchers, and then only in the Russian language. Fortunately, Wethmar *et al.* (1975) reviewed the work by the Russian and other authors and complemented it with additional phase equilibrium determinations of their own. The research work by Griffen *et al.* (1962) on the C-Fe-Cr system is incorporated in their work. Furthermore, their research focussed on the Fe-Cr-C-Si system for HCFeCr as produced in South Africa, with Cr in the region 50-65%, 0-10%Si, 4-8% C with the remainder being iron. They found that the $(Cr, Fe)_7C_3$ is the primary precipitated phase over the entire range of alloys investigated and that its stability range expanded with an increase in carbon content and chromium-to-iron ratio. Two pseudo binary eutectics were identified. These Eutectic reactions resulted in the formation of $(Cr, Fe)_7C_3$ and either a α (FCC) or a γ (BCC) solid solution of iron and chromium, together with a eutectic reaction, which results in a γ -iron-chromium solid solution and $(Cr,Fe)_{23}C_6$. A

peritectic reaction was found between the liquid alloy and $(Cr, Fe)_7C_3$ that yields $(Cr,Fe)_{23}C_6$ and a peritectoid reaction where $(Cr, Fe)_7C_3$ and α -iron-chromium solid solution react to form $(Cr,Fe)_{23}C_6$. Phases that contain silicon were also identified. At all carbon levels, the metallic (α and γ) solid solutions may contain silicon, if silicon is present in the bulk alloy. The liquidus temperature is found to increase with increasing carbon content and increasing ratios of Cr to Fe. At 8% carbon it was found that increasing the silicon content led to reduced liquidus temperatures. For example, at 53% Cr and 8 % C (typical of HCFeCr from the plasma arc furnace), the following liquidus temperature pattern is noted for increasing amounts of Si:

Mass % Si	0.5%	2.5%	3.0%	5%
Alloy Liquidus (°C)	1605	1590	1575	1560

The research by Akyüzlü and Eric (1992) also found the same predominant phases to precipitate based on XRD analysis of their samples. For experiments performed at 1600 °C, they found that the alloy melt was very often unsaturated with respect to the $(Cr, Fe)_7C_3$, which is as expected, as their melts contained varied amounts of silicon, which reduces the liquidus below 1600 °C as shown above.

Healy (1986) modelled the activities of liquid Fe-Cr-C alloys above 1600 °C up to carbon saturation based on the data of Griffen *et al.* (1962) using a simplification of the unified interaction parameter formalism with linear and quadratic terms for the concentrations, but failed to take into account the effect of the $\ln \gamma_{Fe,Solvent}$.

The system was also modelled with FactSage, with an additional SGTE alloy database by GTT technologies. In general, the results of Wethmar *et al.* (1975) are well reproduced, with the exception of a bias of about 25-30 °C (FactSage predicts slightly lower temperatures than measured by Wethmar *et al.* (1975)). The phase diagram simulation results are presented in Figures 10.19 – 10.21 below.

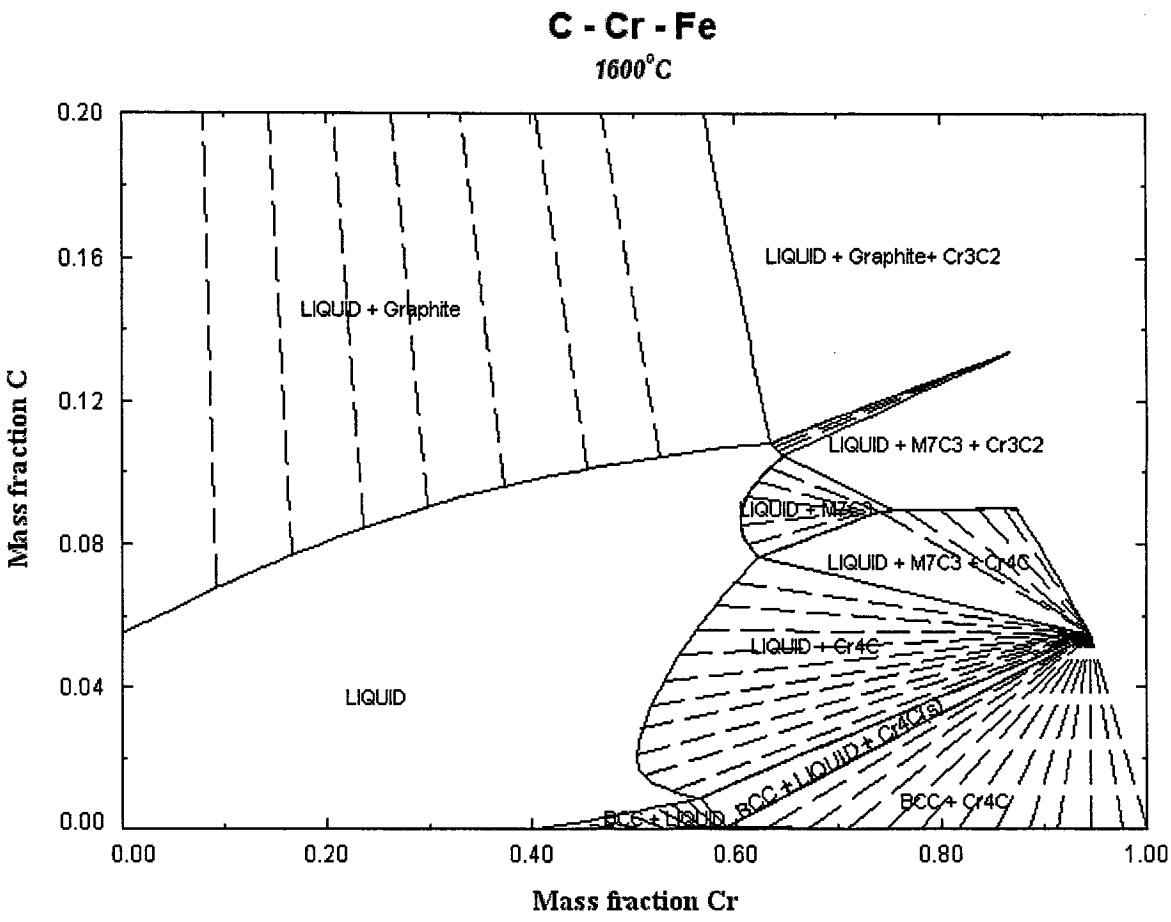

Figure 10.19: Phase stability fields of the C-Fe-Cr system at 1600°C as generated by FactSage ®.

A 1600 °C, in the absence of silicon, the $(Cr, Fe)_7C_3$ phase does precipitate before the Cr in the alloy exceeds 62%, and it remains localised in the region from 7-9% C. Lower chrome alloys (50-60%) lead to the graphite precipitation when the carbon exceeds 9%. In the chromium-rich-carbon-rich domain, Cr_3C_2 starts to precipitate, while in the chromium-rich-carbon-poor domain, BCC alloy solid solution and Cr_4C predominates (Although, in reality a true Cr_4C phase is not observed but instead the $Cr_{23}C_6$ phase. The effect of various C-Si pairings are shown in Figures 10.20 and 10.21. These pairings were derived from a relationships found for HCFeCr alloys from plant data – similar to the results by Akyüzlü and Eric (1992), the Si decreased with increased level of C.

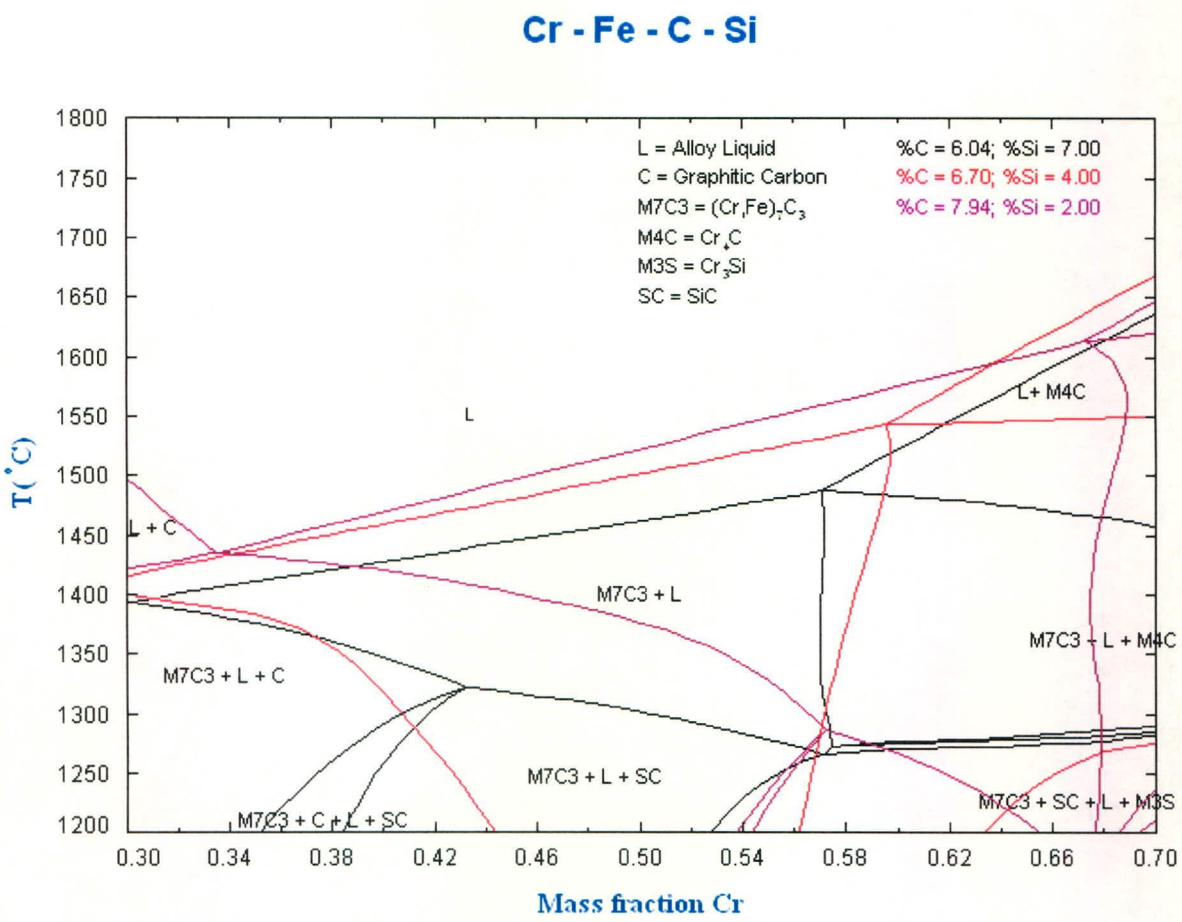

Figure 10.20: Phase diagram for various Si-C (medium C range) pairings for Cr in the range 30-70 mass %.

Figure 10.20 show the phase diagram as it would be applicable to submerged arc HCFeCr production, which is associated with lower basicity slags, lower concentration of C in the alloy and higher amounts of Si. It is readily apparent that in the range 42-58% Cr, the (Cr, $Fe)_7C_3$ phase predominates (the chromium concentration range associated with South African Ferrochrome production) and the liquidus increases as the amount of Si decreases (C increases). For the high carbon cases, an increase is noticeable for the graphitic carbon phase field, which either precipitates as pure C or co-precipitates with (Cr, $Fe)_7C_3$, which is the most expected scenario for HCFeCr produced in South Africa. Very low Si levels lead to a steep liquidus in the Cr-poor region as shown in Figure 10.22 which depicts graphite saturation.

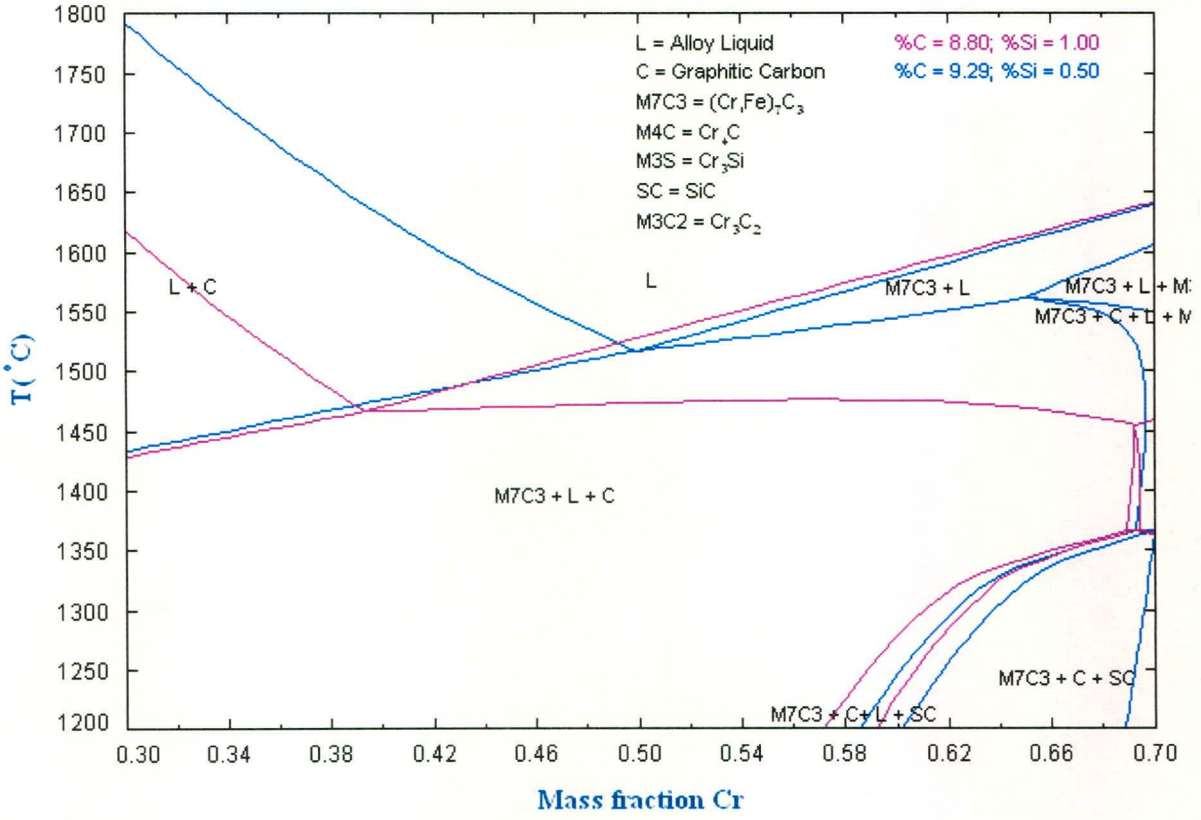

Figure 10.21: Phase diagram for various Si-C (high C range) pairings for Cr in the range 30-70 mass %.

The phase diagram of the HCFeCr system as determined by Wethmar *et al.* (1975) is presented in Figure 10.22 for carbon contents at 4, 5, 6, 7, and 8 %. The predominant phases identified were the same as shown in the Figrues 10.19 to 10.21. This phase diagram was used in Chapter 4 to determine the degrees of superheat relative to the liquidus (refer to Figure 4.17).

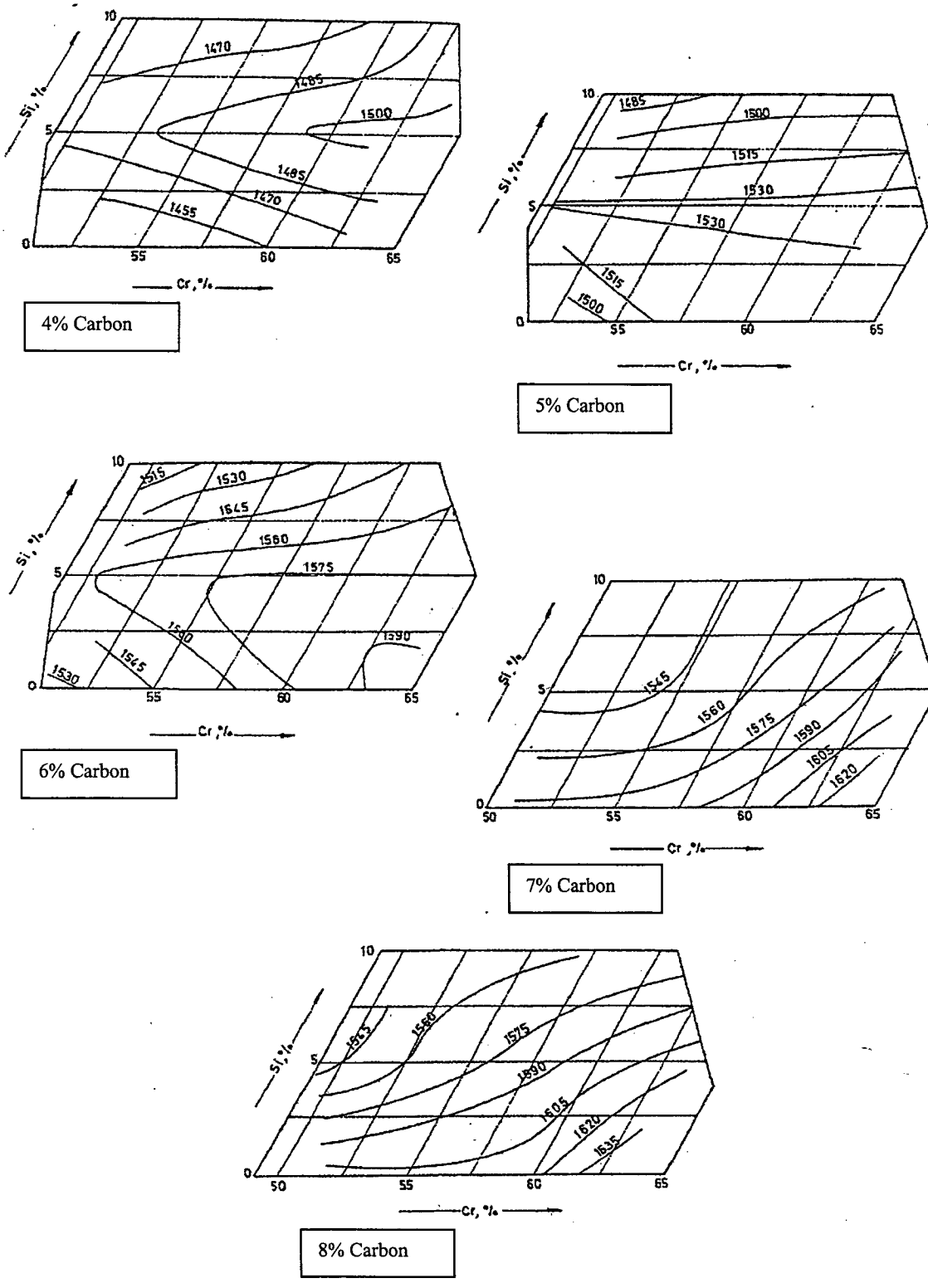

Figure 10.22: Phase diagrams of HCFeCr for C at 4, 5, 6, 7 and 8%.

10.3.3 Slag-metal equilibria in HCFeCr production

To serve as basis for the further analysis of HCFeCr slag-metal equilibria, some of the results of Akyüzlü and Eric (1992) are given for purposes of comparison. Figure 10.23 presents the effect of basicity on the remaining (equilibrium) %Cr in the slag. At 1600 °C in a CO environment (typical to the gas environment found in a DC plasma arc furnace), the Cr behaviour shows two distinct behavioural zones:

- A region where the Equilibrium %Cr in the slag reduces very rapidly (from 0.65% to 0.2%) with a small incremental increase in basicity from 0.80 to 0.82.
- A region where the equilibrium % Cr remains nearly constant (from 0.20 to 0.18) over a wide range of basicity (0.82 to 1.55).

It is noted that at lower temperatures the rate of change from the one region is more gradual. Equivalent equilibrium Cr levels are obtained at much lower basicities.

The relationship between C and Si in the alloy is presented in Figure 10.24. The non-linear, concave upwards trend is apparent. It is also clear that as the Cr:Fe ratio decrease, the slope of the Si:C curve decreases. It is also clear that the equilibrium levels of Cr in the slag is an order of magnitude smaller than the %Cr reported in industrial slags (0.2-0.6% Cr versus 6%).

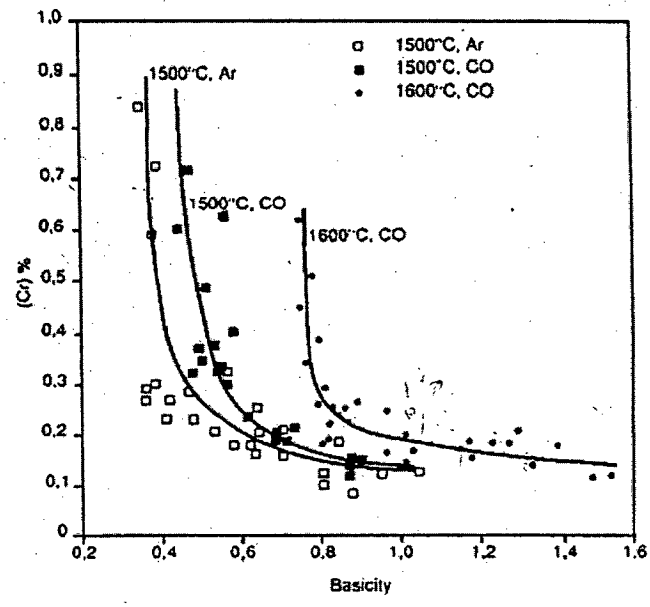

Figure 10.23: The effect of basicity of the equilibrium chromium content of slags.

The effect of MgO to CaO ratio is to increase the silicon that partitions preferentially to the slag, although the effect of MgO replacement of CaO is very small, as is shown in Figure 10.25.

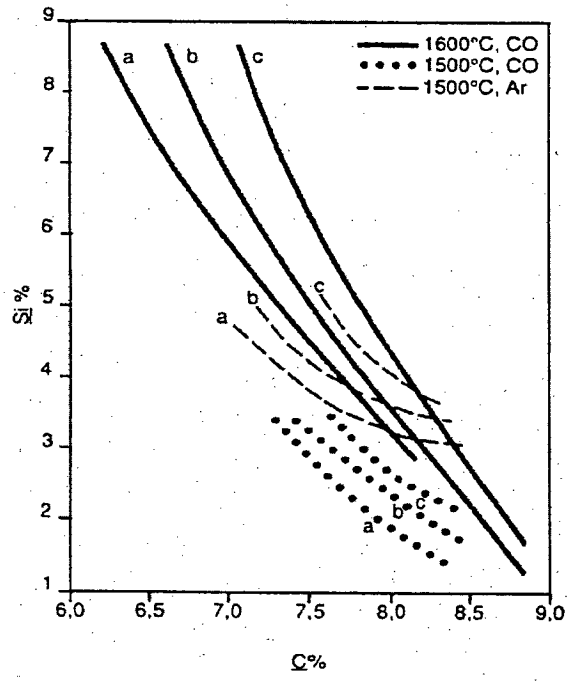

Figure 10.24: The relationship between %Si and %C dissolved in the alloy. Cr:Fe ratios are a:1.1; b:1.3; c:1.7

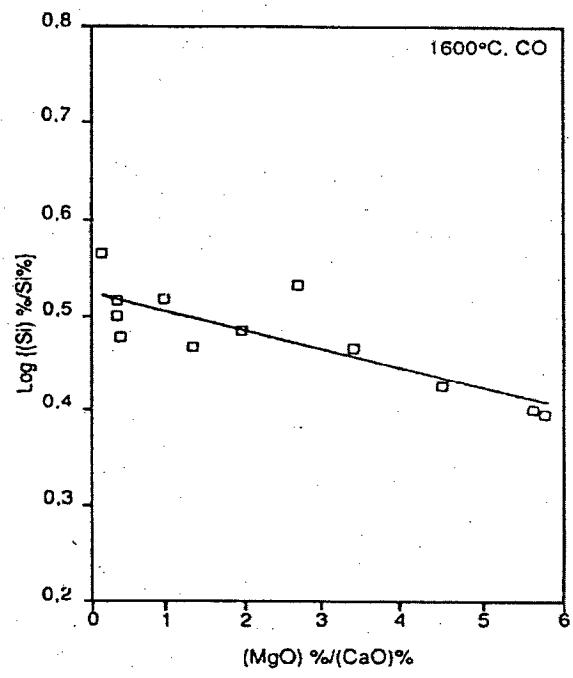

Figure 10.25: The relationship between the distribution coefficient of %Si and MgO:CaO ratio, at 25% Al_2O_3 and 39.3 % SiO_2.

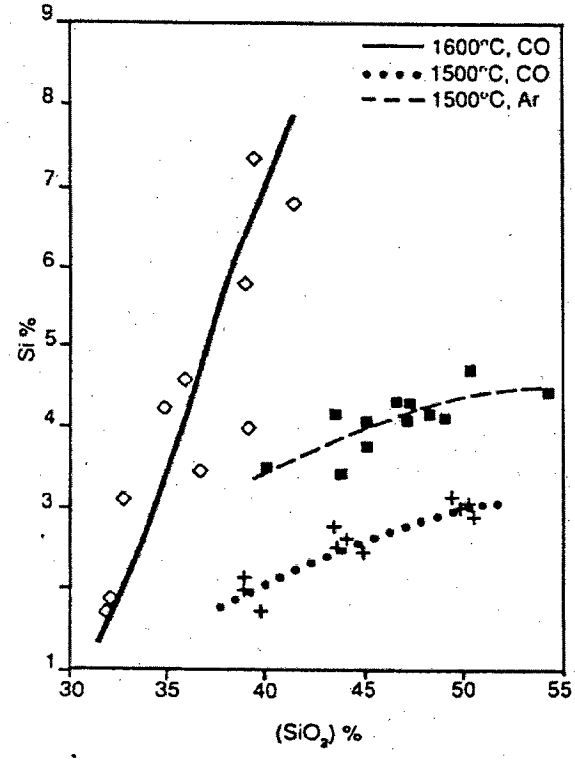

Figure 10.26: The effect of silica content of the slag phase on silicon content of the metal phase at a metal phase Cr:Fe ratio of 1.3

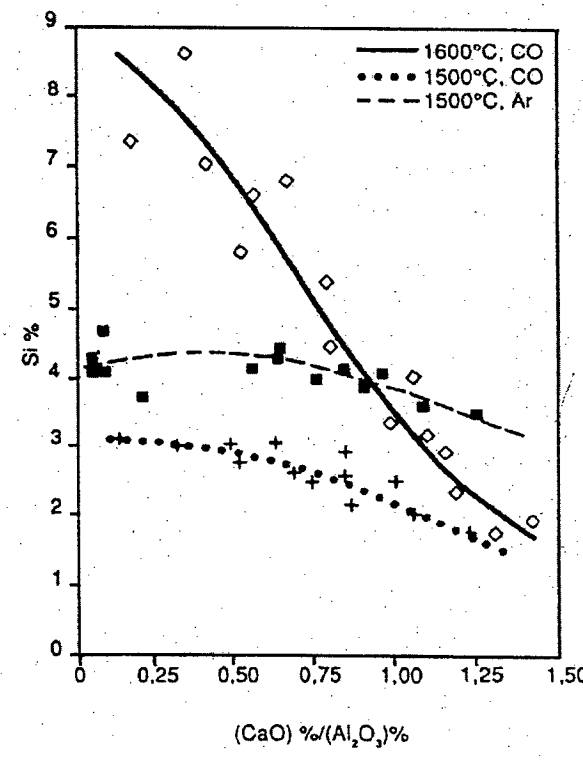

Figure 10.27: The effect of lime to alumina ratio of the slag on the silicon content of the metal at a metal phase Cr:Fe ratio of 1.3

It is clear from Figure 10.26 that the Si content of the alloy is highly sensitive to the amount of Si in the slag. At 1600 °C, an increase of silica in the slag from 30% SiO_2 to 40% SiO_2 (33% relative increase), causes the silicon in the alloy to increase from 1% Si to 7.5% Si. (650% relative increase). The effect is less pronounced at lower temperatures. As lime complexes Si as silicates in the slag, it lowers the SiO_2 activity. The shape of the curves and the decreasing trend of %Si in the metal versus $CaO:Al_2O_3$ ratio in Figure 10.27 is therefore to be expected – more so due to the suppression of Si activity than due to the effect of CaO or Al_2O_3.

10.4 Thermodynamics of ilmenite smelting to produce high titania slag and pig iron.

From the analyses of the ilmenite and the slag presented in the Chapter 3, it is apparent that the major feed components belong to the TiO_2-Fe_2O_3-FeO ternary for the mineral feedstock and TiO_2-Ti_2O_3-FeO for the slag. The discussion of the whole Ti-Fe-O system is therefore important, as a number of mineral types may crystallise from the melt. Ilmenite may also convert to a number of various Fe-Ti oxides when preheated or pre-reduced, as very often happens when feed pretreatment systems are installed, for example to make use of the hot CO gas from the smelting process.

Lynch and Bullard (1997) reviewed the phase equilibria of the Ti-O system for temperatures below 1100 °C. They critically assessed the GFE of formation for a range of Magnelli oxides (sub-oxides of TiO_2) from Ti_4O_7 to $Ti_{50}O_{99}$. The GFE data were used to develop phase predominance diagrams of the subsolidus Magnelli oxides as a function of oxygen partial pressure and temperature.

Waldner and Eriksson (1999) critically reviews the Ti-O system from the pure metal up to rutile composition. The optimization of the system solution parameters was performed with ChemSage ®, and is accessible through the FactSage ® software. Sublattice models were used to model all solid solutions.

The TiO_2-Ti_2O_3 system is of specific relevance as it is not believed that Ti is reduced below its trivalent state in high titania slags (Pesl, 1997). The region between TiO_2 and Ti_2O_3 also contains Ti_3O_5. A number of researchers investigated the melting points of Ti-O oxides in

TiO_2-Ti_2O_3 system, but disagreement about the measured melting points and the type of transition is apparent, as shown in Table 10.1:

Table 10.1: Melting points and transitions of Ti-oxides determined by different researchers

Melting Point (°C) Ti_2O_3	Melting Point (°C) TiO_2	Melting Point (°C) Ti_3O_5	Comment	Reference
1842	1870	1700	Ti_3O_5 Melts incongruently	Brauer, Littke (1960)
		1774	Ti_3O_5 Melts incongruently	Wahlbeck, Gilles (1966)
1847		1832	Ti_3O_5 Melts congruently	Tuset (1968)
1842	1857	1718	Ti_3O_5 Melts congruently	Eriksson, Pelton (1993)

The conclusions of Eriksson and Pelton is accepted in this thesis, as the parameters within the FactSage ® database is as determined by them. The modified quasichemical model parameters ω and η have been derived for the TiO_2-Ti_2O_3 system by Eriksson and Pelton (1993) as a function of composition for use in the FactSage ® database.

The subsolidus (the region of interest for the ilmenite mineral group) equilibrium has a number of solid solutions. Grey *et al.* (1974a) constructed a partial phase diagram at 1200 °C and identified a number of solid solution series, being:

- a M_3O_4 series with a spinel structure between Fe_3O_4 (magnetite) and Fe_2TiO_4 (ulvospinel / Ti-spinel)
- a M_2O_3 series with a hexagonal structure between Fe_2O_3 (hematite) and $FeTiO_3$ (ilmenite)
- a M_3O_5 series, with an orthorhombic structure between Fe_2TiO_5 (ferric pseudobrookite) and $FeTi_2O_5$ (ferrous pseudobrookite).

Grey and Merrit (1981) found that the miscibility gap between $FeTi_2O_5$ and Ti_3O_5 closes at 1346 °C (± 8°C). Grey and Ward (1973) also established a phase predominance diagram in terms of oxygen partial pressure and the ratio Fe : (Fe+Ti) at 1400 °C for the compositions

between $FeTi_2O_5$ and Ti_3O_5 where the phase regions may be identified. Two regions were identified in the M_3O_5 system:

- Fe_2TiO_5 - $FeTi_2O_5$ with Fe^{3+}, Fe^{2+} and Ti^{4+};
- And $FeTi_2O_5$ - Ti_3O_5 with Fe^{2+}, Ti^{4+}, Ti^{3+} as Fe^{3+} will be completely reduced by Ti^{3+}. In equilibrium with metallic iron, Ti^{4+} will always be partially reduced to Ti^{3+}.

It was also shown by Simons (1978) that the Ti-rich end-members in equilibrium with iron are stoichiometric at 1000 °C, but at 1300 °C ilmenite contains 2 mol% Ti_2O_3 and $FeTi_2O_5$ 17 mol% Ti_3O_5. It was also shown by Borowiecs and Rosenquist (1981) that for the M_3O_5 binary a complete solid solution exists above 1346 °C. It was found that at lower temperatures the solid solution decomposes into two M_3O_5 series, as well as iron, rutile and Magnelli phases. Furthermore, the $FeTi_2O_5$ phase decomposes further below 1140 °C. At temperatures lower than 1066 °C metallic iron becomes a stable phase when the Ti_3O_5 phase is more than 50 mol%. This happens as the Ti^{3+} reduces the Fe^{2+} ion to metallic iron according to:

$$2\ Ti^{3+} + Fe^{2+} = 2\ Ti^{4+} + Fe^{0} \qquad (3.49)$$

On the other hand Fe^{2+} is stabilised in M_3O_5 solid solutions at higher temperatures even in the presence of Ti^{3+}. The M_2O_3 binary was also studied by Borowiecs and Rosenquist (1981) and it was found that ilmenite and hematite shows complete solid solution above 780 °C, up to the liquidus. However, should the Ti_2O_3 content exceed 50 mol %, metallic iron is again stabilised according to equation 3.49 above. It was shown that at lower temperatures the reaction proceeds to the point when rutile Magnelli phase or ilmenite co-exist with iron. At higher temperatures the stabilisation of the divalent iron again takes place as explained earlier. The maximum solubility of FeO in Magnelli phases in contact with iron was measured by Grey *et al.* (1974). The solubility was found to be very low (0.8% to 1.2% was incorporated as divalent iron into the lattice).

MacChesney and Muan (1961) studied the phase diagram of the FeO-TiO_2 system at iron saturation. At high Ti levels significant concentrations of trivalent Ti were present leading to the formation of Ti-spinels such as ulvospinel which melts congruently at 1395 °C, rhombohedral ilmenite which melts congruently at 1400 °C and ferrous pseudobrookite ($FeTi_2O_5$), which melts at 1494 °C.

The liquidus temperatures of the TiO_2-rich side of the FeO-TiO_2 system was further investigated by Grau (1979). He specifically investigated the region between 52.4 wt % TiO_2 and 80 wt% TiO_2. Contrary to MacChesney and Muan's research , Grau finds that melts $FeTi_2O_5$ incongruently at 1475 °C. Furthermore no eutectic was detected between $FeTi_2O_5$ - TiO_2 , but instead between $FeTiO_3$ and $FeTi_2O_5$. As the results from MacChesney and Muan (1961) differed so much from other authors (Grau, 1979; Eriksson and Pelton, 1993) due to their experimental setup, the results from Grau are the preferred choice (Pesl, 1997).

The FeO-TiO_2 system was also critically assessed by Eriksson and Pelton (1993). They also argue that both $FeTiO_3$ and $FeTi_2O_5$ melt incongruently (decomposes by peritectic reaction) at 1377 °C and 1455 °C respectively. In the composition range of ulvospinel, they obtained similar results to MacChesney and Muan (1961), and reason that the disagreement in phase equilibria at higher TiO_2 is caused due to the presence of trivalent Ti in the slag. The modified quasichemical model parameters ω and η (Appendix A) have been derived for the FeO-TiO_2 system as a function of composition for use in the FactSage ® database.

The phase relationships in the system TiO_2-Fe_2O_3-Fe was studied by Gupta *et al.* (1989) at 700 °C and 900°C. A new phase according to XRD measurements was identified namely $Fe_2Ti_2O_7$. Furthermore, results showed that magnetite-(spinel) rutile was not found to be stable phase at 700 °C, nor in equilibration studies performed using Western Australian mineral sands.

Sevinç (1989) studied the TiO_2-Fe_2O_3-FeO system at 1500 °C. He determined the phase boundaries and projected the oxygen partial pressure isobars onto the ternary. The activity of the TiO_2 component has been determined by Gibbs-Duhem integration of the ternary. This system is of importance when the feed is preheated or prereduced in the solid state.

Pesl and Eriç (1999) studied the high temperature relationships of the TiO_2-Ti_2O_3-FeO system at 1500 and 1600 °C at a number of oxygen partial pressures. Oxygen isobars were projected onto the isotherms of the ternary system. The problem with this system is, however, that the Ti_2O_3-FeO binary cannot exist by itself at high temperature without forming TiO_2 and metallic iron as well. However, their data proved useful when incorporated with that of the previous mentioned researchers for further optimisation using the modified quasichemical and cell models (Fourie *et al.*, 2003). It was established by Pesl and Eriç (1999) that, while a

regular solution model may be used for the TiO_2- FeO binary, the full ternary cannot be adequately modelled using regular solution behaviour only. They therefore investigated the use of a sub-regular model which allows for ternary interactions (the regular solution model only allows for binary interactions). They found that all sub-regular solution model parameters have negative values, except for the ternary interaction parameter, which confirmed that there is a prevailing attraction force between the corresponding oxides or cations respectively. While the interaction between TiO_2-FeO is fairly symmetric and small, the Ti_2O_3-FeO interaction is large and asymmetric. Attraction between TiO_2-Ti_2O_3 is shown to moderate and also asymmetric.

The phase diagrams of the TiO_2-Fe_2O_3- $FeTiO_3$ and TiO_2-Ti_2O_3-$FeTiO_3$ systems have been developed by FactSage, as presented in Figures 10.28 and 10.29 respectively. $FeTiO_3$ has been chosen for both the systems instead of FeO, to provide a better resolution of the phase diagram in the region of interest and as the ilmenite mineral approaches stoichiometric ilmenite. In so doing the slag region becomes much more expanded.

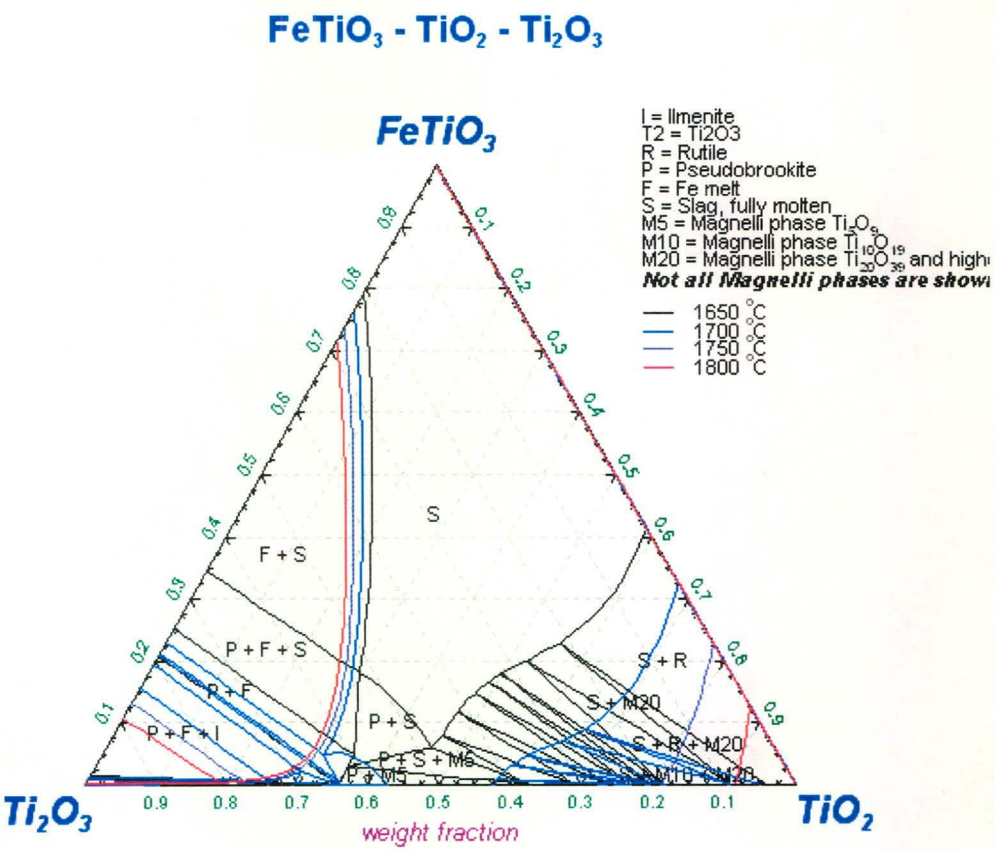

Figure 10.28: Representation of a number of phase boundary isotherms for the high titania slag system.

If the only the ternary components slag and the ilmenite mentioned in the introductory paragraph are projected onto the phase diagrams, their compositions (recalculated for the equivalent $FeTiO_3$ and normalised) gives the following mineral and slag composition:

Ilmenite: 54.3% $FeTiO_3$, 27.0% Fe_2O_3, 18.8% TiO_2

Slag: 25.8% $FeTiO_3$, 32.2% Ti_2O_3, 42% TiO_2

For this specific slag system it is noted that the slag is in the fully molten range at 1650 °C. However, the presence of titanium oxycarbide particles (not taken into account here) may still lead to an increase in the observed viscosity of the slag.

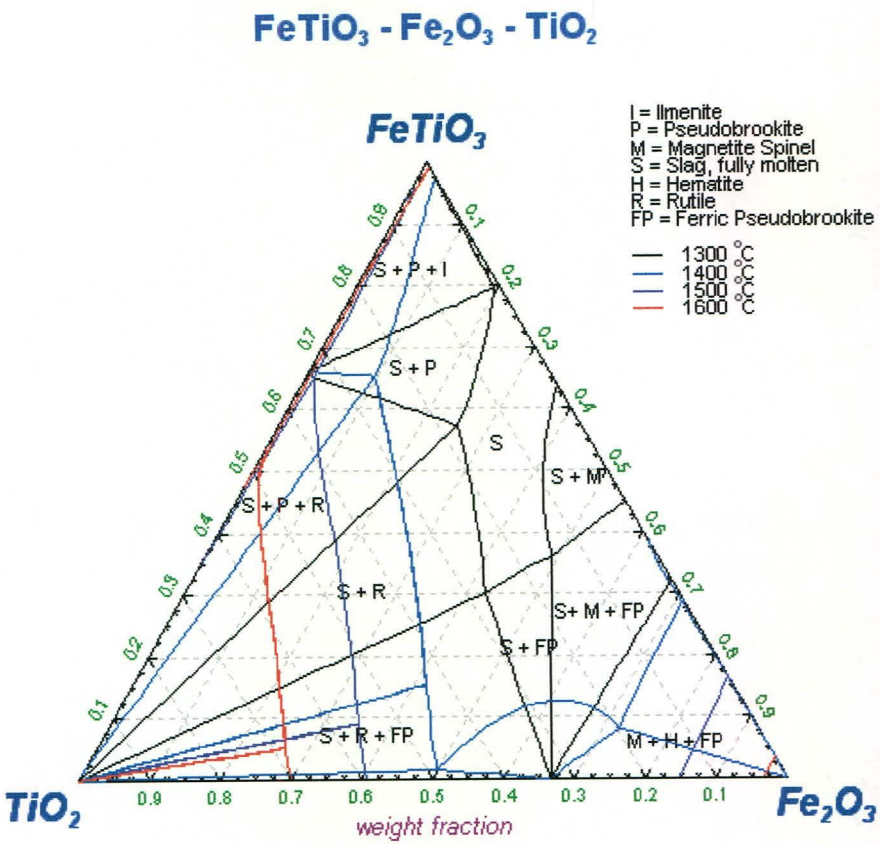

Figure 10.29: Representation of a number of phase boundary isotherms for the mineral system.

10.4.1 Phase relations for the pig-iron metal

Experimental and theoretical investigations to characterise the phase relationships and interactions between dilute alloy components in iron abound in literature, and are derived mostly from research in the field of steel production. The phase diagram for the system is predominantly influenced by its two major constituents, Fe and C.

The Fe-C phase diagram has been well researched and can be found in many metallurgical textbooks (Smithells, 1976). The system is also well predicted by FactSage as depicted in Figure 10.30. Predictions of the system fall within the experimental error of the phase diagram determination.

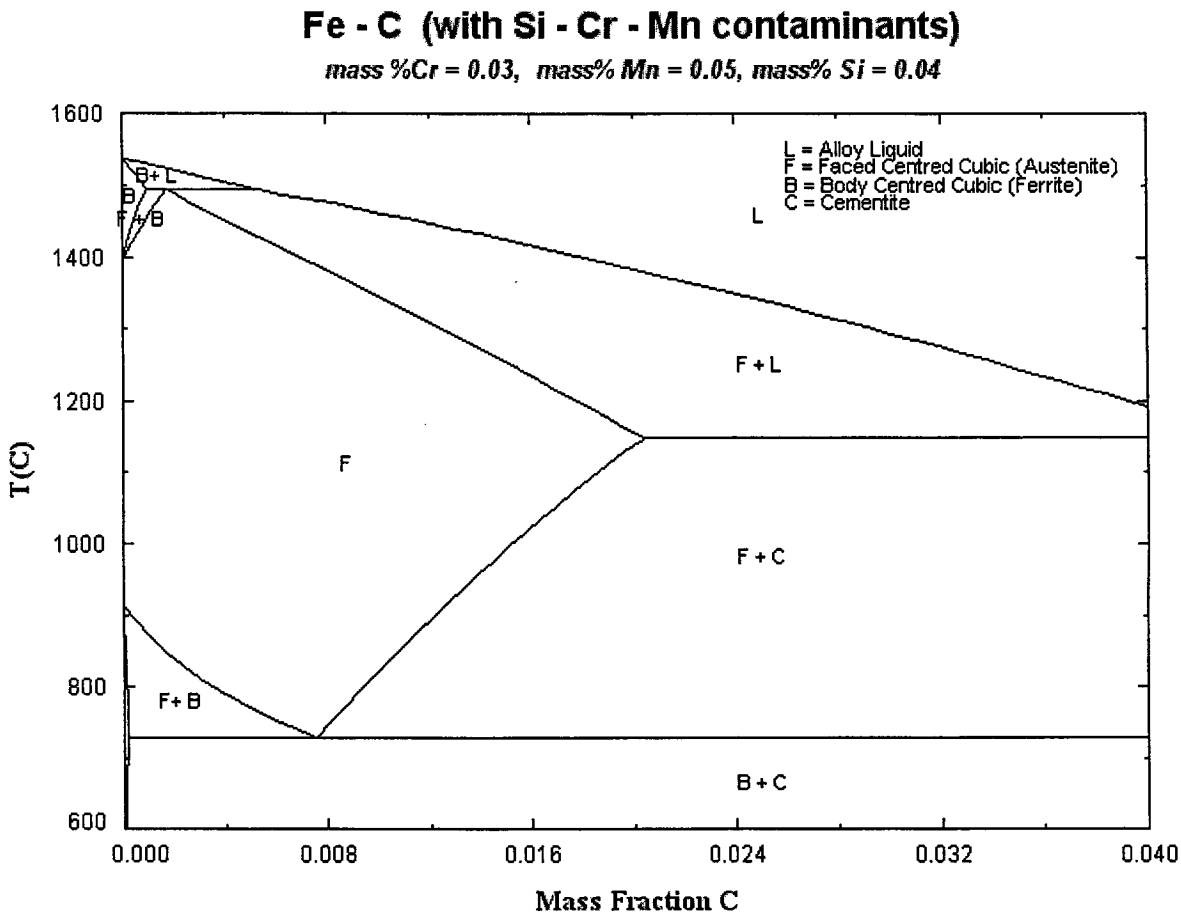

Figure 10.30: Fe-C binary phase diagram with Cr, Mn and Si contaminants.

In the range of operation, (2.4-2.8 %C) the primary phase to precipitate is austenite (fcc), while the liquidus temperature reduces from 1348 °C to 1314 °C over the range. The solidus temperature coinciding with eutectic is at 1150 °C.

The activity coefficients of the different elements in hot metal can be described according to the Unified Interaction Parameter Formalism, which takes on the general form of equation 10.1, for solute i interacting with other components j and k, and where the activity coefficient is expressed relative to the Henrian infinitely dilute weight % standard state.

$$\log(\dot{\gamma}_i) = \ln \gamma_{solvent} + \sum_j e_i^j (\%j) + \sum_j \sum_k q_i^{j,k} (\%j)(\%k) \qquad (10.1)$$

Where e_i^j are the first order interaction parameters, and $q_i^{j,k}$ are the second order interaction parameters. Most metallurgical textbooks have values for the interaction parameters at various temperatures (Steiler, 1997). The activities of silicon, phosphorous and sulphur are strongly

increased by the presence of carbon, while the activity of most metals are reduced, especially reactive metals which are strong carbide formers such as Ti and Cr (Steiler, 1997).

Bouchard and Bale (1995), both researchers with CRCT, critically evaluated liquid iron alloys containing C, N, Ti, Si, Mn, S and P and performed simultaneous optimisation of the thermochemical data available and found the optimal parameters for the Unified Interaction Parameter Formalism first proposed by Pelton and Bale (1986, 1990). These parameters are stored within the FactSage ® database. The experimental measured thermochemical data was found to be well modelled and reproduced using the Unified Interaction Parameter Formalism, based on the optimised parameter set. Furthermore, Jonsson (1998) evaluated the Fe-Ti-C-N system and its subsystems, and determined the solubility of Ti(C,N) in liquid iron. Ti(C,N) solid solution was shown to have a very low solubility in iron, and to give rise to a steep rise in the metal liquidus temperature. The formation of Ti(C,N) precipitates in molten iron was found to be a distinct possibility, due to the very strong affinity of Ti for C and N.

10.5 Thermochemical solution modelling

The basis of the thermodynamic calculations used in this research is the principle on Gibbs Free Energy (GFE) Minimisation. In principle, the GFE minimiser finds the relative amounts of the different phase assemblages that minimises the total system Gibbs Free Energy:

$$G_{system} = \sum_{i=1}^{N} n_i G_i^o + RT \sum_{gas}^{N} n_i \ln f_i + RT \sum_{Solution1}^{N} n_i \ln a_i + RT \sum_{Solution2}^{N} n_i \ln a_i + \ldots \qquad (10.2)$$

Where a_i are the component activities for components $i = 1$ to N as calculated by the solution models, n_i are the moles of the various components, G_i° are the pure component GFE of formation, G_{system} is the overall system GFE, and f_i are the fugacities of the gaseous components. The quasi-chemical model will first be discussed for a generalised binary system A-B and then will be expanded to a general ternary A-B-C system.

10.5.1 Basic Quasi-chemical Formalism

In a binary system with components A and B, the A and B particles are considered to mix substitutionally on a quasi-lattice. The relative amounts of the three types of nearest neighbour pairs ($A-A$, $B-B$ and $A-B$) are determined by the energy change associated with the formation of two $A-B$ pairs from a $A-A$ and a $B-B$ pair:

$$[A-A]+[B-B]=2\,[A-B] \qquad (10.3)$$

If this energy change is zero, then the solution is an ideal mixture. As the energy change becomes more negative, the formation of $A-B$ pairs is favoured. The result is then that the enthalpy of mixing tends to form a negative peak at the composition $X_A = X_B = ½$, while the entropy of mixing has the shape of a letter m (Figure 10.31). This suggests that the maximum ordering of any binary system $A-B$ occur at 0.5 mole fraction. Therefore the basic quasi-chemical theory cannot be used for silicate melts where the minimum enthalpies and entropies of mixing are not at a mole fraction of 0.5. Pelton *et al.* (1997) modified the basic theory in order to provide an expression for the entropy and enthalpy of a highly ordered system with minima in entropy and enthalpy at any desired composition. As a further modification, the energy change for reaction (Eq. 10.3) was expressed as a function of composition with adjustable coefficients.

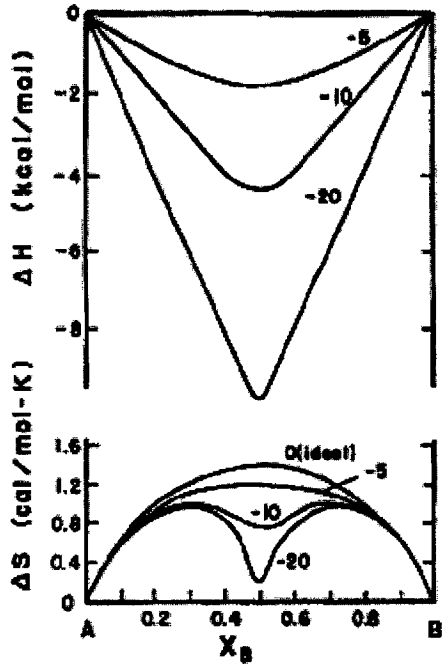

Figure 10.31: Enthalpy and entropy of mixing of a binary system for different degrees of ordering about XA = XB = ½. Curves are calculated from the modified quasichemical theory at T = 1000 °C with z = 2 for the constant values of ω (kcal) and with η = 0. (Pelton, 1984)

In the following sections, the general modified quasi-chemical theory will first be developed for binary systems and then extended to ternary systems.

10.6 The modified binary quasi chemical theory

As in the basic quasi-chemical theory, a binary system with components A and B are considered where the A and B particles mix substitutionally on a quasi-lattice with a constant co-ordination number z. The three types of nearest neighbour pairs ($A-A$, $B-B$ and $A-B$) have "pair bond energies" ε_{ij}. The total number of such pairs per mole of solution is $N^0 z/2$ where N^0 is Avogadro's number. The formation of two $A-B$ pairs from a $A-A$ and $B-B$ pair according to reaction (10.3) is considered. The enthalpy change for this reaction is then:

$$\left(2\varepsilon_{AB} - \varepsilon_{AA} - \varepsilon_{BB}\right)$$

A molar enthalpy change ω is defined by multiplying by $N^0 z/2$:

$$\omega = \frac{N^{\circ} z}{2}\left(2\varepsilon_{AB} - \varepsilon_{AA} - \varepsilon_{BB}\right) \tag{10.4}$$

A molar non-configurational entropy change η, can also be defined:

$$\eta = \frac{N^{\circ} z}{2}\left(2\sigma_{AB} - \sigma_{AA} - \sigma_{BB}\right) \tag{10.5}$$

where σ_{ij} is the "pair bond non-configurational entropy".

Let n_A and n_B be the number of moles of A and B particles. Then, for one mole of solution, $(n_A + n_B) = 1$. the mole fractions of A and B are defined as $X_A = n_A/(n_A + n_B) = 1 - X_B$. Now let n_{AA}, n_{BB} and n_{AB} be the number of moles of each type of pair in solution. The fraction of $i-j$ pairs are defined as:

$$X_{ij} = n_{ij}/\left(n_{AA} + n_{BB} + n_{AB}\right) \tag{10.6}$$

from the mass balance it follows that:

$$zn_A = 2n_{AA} + n_{AB} \tag{10.7}$$

$$zn_B = 2n_{BB} + n_{AB} \tag{10.8}$$

and that

$$2X_A = 2X_{AA} + X_{AB} \tag{10.9}$$

$$2X_B = 2X_{BB} + X_{AB} \tag{10.10}$$

When components A and B are mixed, $A-B$ pairs are formed at the expense of $A-A$ and $B-B$ pairs. The enthalpy of mixing, ΔH, is given in the model by the summation of the pair bond energies:

$$\Delta H = (X_{AB}/2)\omega \tag{10.11}$$

The non-configurational excess entropy of the solution is then given by:

$$\Delta S^{nonconfig} = (X_{AB}/2)\eta \tag{10.12}$$

The approximate configurational entropy of mixing as proposed by Guggenheim (1935), is:

$$\Delta S^{config} = -R(X_A \ln X_A + X_B \ln X_B) - \frac{Rz}{2}\left(X_{AA} \ln \frac{X_{AA}}{X_A^2} + X_{BB} \ln \frac{X_{BB}}{X_B^2} + X_{AB} \ln \frac{X_{AB}}{2X_A X_B} \right) \tag{10.13}$$

Therefore, the total molar excess entropy (configurational plus non-configurational entropy) of the solution is given from equations 10.12 and 10.13 as:

$$\Delta S^E = -\frac{Rz}{2}\left(X_{AA} \ln \frac{X_{AA}}{X_A^2} + X_{BB} \ln \frac{X_{BB}}{X_B^2} + X_{AB} \ln \frac{X_{AB}}{2X_A X_B} \right) + (X_{AB}/2)\eta \tag{10.14}$$

The equilibrium concentrations are given by minimizing the Gibbs energy at constant composition:

$$d(\Delta H - T\Delta S)/dX_{AB} = 0 \tag{10.15}$$

This gives:

$$\frac{X_{AB}^2}{X_{AA}X_{BB}} = 4e^{-2(\omega-\eta T)/zRT} \tag{10.16}$$

Equation resembles an equilibrium constant for reaction (10.3) and therefore the model is called "quasi chemical".

Substitute equations (10.9) and (10.10) into equation (10.16):

$$X_{AB}/2 = 2X_A X_B/(1+\xi) \tag{10.17}$$

where

$$\xi = \left[1 + 4X_A X_B\left(e^{2(\omega-\eta T)/zRT} - 1\right)\right]^{1/2} \tag{10.18}$$

For a given value of $(\omega - \eta T)$ at a given composition X_A, equations (10.17) and (10.18) give X_{AB} and equations (10.9) and (10.10) then give X_{AA} and X_{BB}. Substituting these values into equations (10.11) and (10.12) gives ΔH and S^E.

In the case when, $\omega = 0$ and $\eta = 0$ it follows that $\Delta H = 0$ and $S^E = 0$ and the solution is ideal. When ω and η are very small, $S^E \approx 0$ and $X_{AB} \approx 2X_A X_B$. Then equation (10.15) becomes: $\Delta H = X_A X_B\ \omega$. In this case the solution is regular. As $(\omega - \eta T)$ is made progressively more negative, ΔH assumes a negative peaked form as in Figure 10.31, and ΔS assumes the "m-shaped" form of Figure 10.31. The configurational ΔS as calculated by equation (10.13) assumes large negative values around $X_A = X_B = ½$ for large negative values of $(\omega - \eta T)$. This is clearly incorrect since when $(\omega - \eta T) = -\infty$, perfect ordering will result at the composition $X_A = X_B = ½$ with all A particles having only B particles as nearest neighbours and vice-versa. Therefore, the configurational ΔS should be zero at this composition. The fact that the calculated configurational ΔS is not zero is a result of the approximate nature of the entropy equation (10.13). If the preceding equations are solved for $(\omega - \eta T) = -\infty$, we obtain for the configurational entropy of mixing at $X_A = X_B = ½$:

$$\Delta S = R\left(\frac{z}{2} - 1\right)\ln\frac{1}{2} \tag{10.19}$$

This will only be equal to zero when z = 2.

For highly ordered systems, the model therefore gives the correct entropy expression only when z = 2. If one was to consider a one-dimensional "necklace" of n_A particles of type A and n_B particles of type B with n_{AA}, n_{BB} and n_{AB} being the numbers of $A-A$, $B-B$ and $A-B$ pairs. Now place the n_A particles of type A in a ring and choose at random $(n_A - n_{AA})$ of the n_A spaces between them. This choice can be made in $\Omega_A = n_A!/(n_{AA}!(n_A - n_{AA})!)$ ways. We now place one particle of type B in each of these chosen spaces. This leaves $n_B - (n_A - n_{AA}) = n_{BB}$

particles of type B. These are all placed into the $(n_A - n_{AA})$ chosen spaces with no restriction on the number in each space. This can be done in $\Omega_B = n_B!/(n_{BB}!(n_B - n_{BB})!)$ ways since $(n_A - n_{AA}) = (n_B - n_{BB})$.

The entropy is then given by:

$$\Delta S = -k_B \ln \Omega_A \Omega_B \tag{10.20}$$

where k_B is Boltzmann's constant.

Solving for one mole of particles gives an expression for ΔS identical to that of equation (10.13) with z = 2.

Hence, the model as presented is exact in one-dimension (z = 2). Thus, for highly ordered systems, the correct entropy is only approached by the model when z = 2. For solutions that are only slightly ordered ($S^E \approx 0$), it may be argued that the approximate three-dimensional expression is superior to the exact one-dimensional expression and so a larger value of z should be used.

10.6.1 Fixing the composition of maximum ordering

The next modification to the model concerns the composition of maximum ordering. As presented above, the model always gives maximum ordering at $X_A = X_B = ½$. In order to make the model general, we must be able to choose the composition of maximum ordering to correspond to that which is observed. For instance in the binary system MgO – SiO_2, this composition is observed near $X_{MgO} = {}^2/_3$, $X_{SiO_2} = {}^1/_3$.

The simplest means of accomplishing this is to replace the mole fractions X_A and X_B in the preceding equations by equivalent fractions, Y_A and Y_B defined by :

$$Y_A = \frac{aX_A}{aX_A + bX_B} \tag{10.21}$$

$$Y_B = \frac{bX_B}{aX_A + bX_B} \tag{10.22}$$

Where a and b are numbers chosen so that $Y_A = Y_B = ½$ at the composition of maximum ordering. For example, in the MgO – SiO_2 system, by choosing a and b such that $a/(a + b) = ⅓$ (for example, by choosing $a = 1$, $b = 2$) we obtain $Y_A = Y_B = ½$ when $X_A = ⅔$ and $X_B = ⅓$. Formally, in the model, we let the coordination numbers of A and B particles be (az) and (bz) respectively. Equations (10.7) to (10.10) then become:

$$zan_A = 2n_{AA} + n_{AB} \tag{10.23}$$

$$zbn_B = 2n_{BB} + n_{AB} \tag{10.24}$$

$$2Y_A = 2X_{AA} + X_{AB} \tag{10.25}$$

$$2Y_B = 2X_{BB} + X_{AB} \tag{10.26}$$

The molar enthalpy of mixing and molar excess entropy (per mole of components A and B) become:

$$\Delta H = (b_A X_A + b_B X_B)(X_{AB}/2)\omega \tag{10.27}$$

$$\Delta S^E = -\frac{Rz}{2}(b_1 X_1 + b_2 X_2)\left(X_{11} \ln \frac{X_{11}}{X_1^2} + X_{22} \ln \frac{X_{22}}{X_2^2} + X_{12} \ln \frac{X_{12}}{2X_1 X_2} \right) + (b_1 X_1 + b_2 X_2)(X_{12}/2)\eta \tag{10.28}$$

In the ideal entropy term however, we do not replace X_A and X_B by Y_A and Y_B, but we retain the expression:

$$\Delta S^{ideal} = -R(X_A \ln X_A + X_B \ln X_B) \tag{10.29}$$

In order that when $(\omega - T\eta) = 0$ the equations reduce to the ideal solution equations. In order to choose the composition of maximum ordering, it is only the ratio $a/(a + b)$ which must be fixed. For example, the choice $a = 2$, $b = 4$ or the choice $a = 1$, $b = 2$ will both give $Y_A = Y_B = ½$ at $X_A \approx {}^2/_3$. As before, however, we may apply the additional condition that $\Delta S = 0$ when $\omega = -\infty$ at the composition of maximum ordering ($Y_1 = Y_2 = ½$). This condition is satisfied when:

$$b_2 z = -\left[\ln(r) + \left(\frac{1-r}{r} \right) \ln(1-r) \right] \Big/ \ln 2 \tag{10.30}$$

$$b_1 = b_2 r/(1-r) \tag{10.31}$$

Where $r = a/(a + b)$ is the ratio required to fix the composition of maximum ordering.

10.6.2 Composition dependence of ω and η

The final modification to the quasichemical model concerns the composition dependence of ω and η. Constant values may be sufficient to represent the main features of the curves of ΔH and ΔS for ordered systems, but for a quantitative representation of the thermodynamic properties of real systems it is necessary to introduce an empirical composition dependence. Pelton and Blander (1997) chose simple polynomial expansions in the equivalent fraction Y_B:

$$\eta = \eta_0 + \eta_1 Y_B + \eta_2 Y_B^2 + \eta_3 Y_B^3 + \ldots \tag{10.32}$$

$$\omega = \omega_0 + \omega_1 Y_B + \omega_2 Y_B^2 + \omega_3 Y_B^3 + \ldots \tag{10.33}$$

where the temperature- and composition-independent coefficients ω_I and η_I are chosen empirically to give the best representation of the available experimental data for a system

When (ω - ηT) is small, then the excess configurational entropy is also small and $X_{AB} \approx 2X_AX_B$. (For simplicity, let $a = b = 1$ so that $X_A = Y_A$ and $X_B = Y_B$). In this case:

$$\Delta H \approx X_A X_B \left(\omega_0 + \omega_1 X_B + \omega_2 X_B^2 + \ldots\right) \tag{10.34}$$

$$S^E \approx X_A X_B \left(\eta_0 + \eta_1 X_B + \eta_2 X_B^2 + \ldots\right) \tag{10.35}$$

These equations are identical to the enthalpy of mixing and the excess entropy expressed as polynomial expansions in the mole fractions of the components.

Therefore, as the solution approaches ideality, the present model approaches the simple and common representation of excess properties by polynomial expansions and the coefficients ω_i and η_i become numerically equal to the coefficients of these expansions.

10.6.3 Partial molar properties

Expressions for the partial molar Gibbs energies of the components are obtained by differentiation:

$$\Delta G_A = RT\ln a_A = RT\ln X_A + \frac{az}{2}RT\ln\frac{X_{AA}}{Y_A^2} - a\left(\frac{X_{AB}}{2}\right)Y_B\frac{\partial(\omega-\eta T)}{\partial Y_B} \tag{10.36}$$

$$\Delta G_B = RT\ln a_B = RT\ln X_B + \frac{bz}{2}RT\ln\frac{X_{BB}}{Y_B^2} - b\left(\frac{X_{BB}}{2}\right)Y_A\frac{\partial(\omega-\eta T)}{\partial Y_B} \tag{10.37}$$

Where a_A and a_B are the activities of the components.

10.7 The modified quasichemical theory for ternary solutions

The modified quasichemical equations may be extended to multicomponent systems in a straightforward manner. Consider a ternary solution with mole fractions X_A, X_B, X_C. Equivalent fractions Y_A, Y_B, Y_C may be defined as:

$$Y_A = \frac{aX_A}{aX_A + bX_B + cX_C} \tag{10.38}$$

$$Y_B = \frac{bX_B}{aX_A + bX_B + cX_C} \tag{10.39}$$

$$Y_C = \frac{cX_C}{aX_A + bX_B + cX_C} \tag{10.40}$$

For the various nearest-neighbour pairs $i-j$ we defined pair mole fractions X_{ij} as before. Mass balance considerations then give, by extension of equations (10.25) and (10.26):

$$2Y_A = 2X_{AA} + X_{AB} + X_{CA} \tag{10.41}$$

$$2Y_B = 2X_{BB} + X_{AB} + X_{BC} \tag{10.42}$$

$$2Y_C = 2X_{CC} + X_{CA} + X_{BC} \tag{10.43}$$

The functions ω_{AB}, ω_{BC}, ω_{CA} and η_{AB}, η_{BC}, η_{CA} are the molar enthalpy and non-configurational entropy changes for the three pair exchange reactions as in equation (10.3).

The ternary enthalpy of mixing and excess entropy is then given by:

$$\Delta H = \left(aX_A + bX_B + cX_C\right)\left(X_{AB}\omega_{AB} + X_{BC}\omega_{BC} + X_{CA}\omega_{CA}\right)/2 \tag{10.44}$$

$$\Delta S^E = -\frac{Rz}{2}\left(aX_A + bX_B + cX_C\right)\cdot$$
$$\left(X_{AA}\ln\frac{X_{AA}}{Y_A^2} + X_{BB}\ln\frac{X_{BB}}{Y_B^2} + X_{CC}\ln\frac{X_{CC}}{Y_C^2} + X_{AB}\ln\frac{X_{AB}}{2Y_AY_B} + X_{BC}\ln\frac{X_{BC}}{2Y_BY_C} + X_{CA}\ln\frac{X_{CA}}{2Y_CY_A}\right.$$
$$\left. + \left(aX_A + bX_B + cX_C\right)\left(X_{AB}\eta_{AB} + X_{BC}\eta_{BC} + X_{CA}\eta_{CA}\right)/2 \right. \qquad (10.45)$$

By minimising the total Gibbs energy at constant composition, three equations similar to equation (10.16) are generated:

$$\frac{X_{ij}^2}{X_{ii}X_{jj}} = 4e^{-2\left(\omega_{ij}-\eta_{ij}T\right)/zRT} \qquad (10.46)$$

The functions ω_{ij} and η_{ij} are the polynomial expansions in the three binary subsystems which can be obtained by analysis of the measured binary data. In order to be able to estimate the thermodynamic properties of the ternary from the binary data, it is necessary to approximate ω_{ij} and η_{ij} in the ternary system from their values in the binaries. Two methods which suggest themselves are illustrated in Figure 10.32. In the "symmetric approximation", ω_{ij} and η_{ij} are assumed to be constant along lines of constant molar ration Y_i/Y_j, while in the asymmetric approximation" ω_{AB} and ω_{CA} (and η_{AB} and η_{CA}) are constant at constant Y_A, while ω_{CA} (and η_{CA}) are constant at constant Y_B/Y_C.

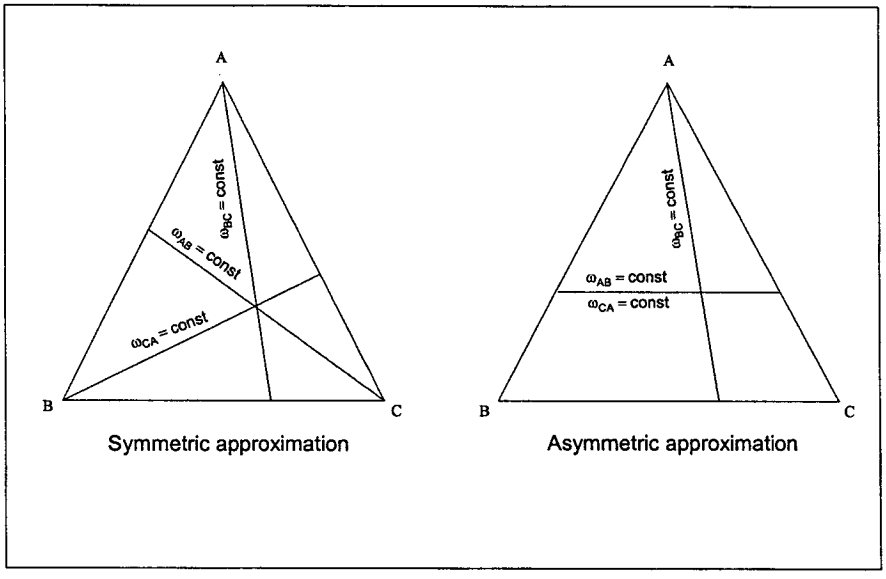

Figure 10.32: Two methods to approximate ω_{ij} and η_{ij} in the ternary system from their values in the binaries

With values of ω_{ij} and η_{ij} in the ternary obtained by one of these approximation techniques, the three equations (10.46) can be solved simultaneously with equations (10.41) through (10.43) to give the six bond fractions X_{ij} which can then be substituted into equations (10.44) and (10.45) to give ΔH and S^E. The calculation is similar to a simultaneous complex chemical equilibrium calculation and can be solved by similar computer algorithms.

The properties of ternary phases may be approximated from the assessed parameters of the binary subsystems in this manner. If experimental ternary data are available, then the approximations may be refined by the addition of "ternary terms" to the Gibbs energy expression such as $\phi_{ijk} X^i_A X^j_B X^k_C$ where *i, j, k* are all positive non-zero integers and where ϕ_{ijk} are adjustable ternary parameters. Ideally the model should be good enough so that such ternary terms should be small, or not necessary at all.

Extension of the equations of this section to systems with more than 3 components is straightforward. The solution of the resultant set of equations for the "complex quasichemical equilibria" can be solved by computer algorithms, such as those which are used in the FactSage ® software.

10.8 Partial molar properties

Expressions for ternary partial molar properties of the components may be obtained by differentiation. In the symmetric approximation:

$$\Delta G_A = RT \ln a_A$$
$$= RT \ln X_A + \frac{az}{2} RT \ln \frac{X_{AA}}{X_A^2} - a\left(\frac{X_{AB}}{2}\right) \frac{Y_B}{(Y_A + Y_B)^2} \frac{\partial(\omega_{AB} - \eta_{AB} T)}{\partial[Y_B/(Y_A + Y_B)]} \qquad (10.47)$$

and similarly for ΔG_B and ΔG_C.

In the asymmetric approximation equation (10.47) becomes:

$$\Delta G_A = RT \ln a_A$$
$$= RT \ln X_A + \frac{az}{2} RT \ln \frac{X_{AA}}{Y_A^2} + \frac{a(1 - Y_A)}{2} \left(X_{AB} \frac{\partial(\omega_{AB} - \eta_{AB} T)}{\partial Y_A} + X_{CA} \frac{\partial(\omega_{CA} - \eta_{CA} T)}{\partial Y_A} \right) \qquad (10.48)$$

$$\Delta G_B = RT \ln a_B$$

$$= RT \ln X_B + \frac{bz}{2} RT \ln \frac{X_{BB}}{Y_B^2} + \frac{bY_A}{2} \left(X_{AB} \frac{\partial(\omega_{AB} - \eta_{AB}T)}{\partial Y_A} + X_{CA} \frac{\partial(\omega_{CA} - \eta_{CA}T)}{\partial Y_A} \right)$$

$$= b \frac{X_{BC}}{2} \frac{Y_C}{(Y_B + Y_C)^2} \frac{\partial(\omega_{BC} - \eta_{BC}T)}{\partial[Y_C/(Y_B + Y_C)]}$$

(10.49)

And similarly for ΔG_C.

Equations 10.1 through to 10.39 therefore forms the basis of the FactSage software. The databases of FactSage therefore stores all therefore the pure component data such as $G°$, $H°$, $S°$, Cp, and the solution interaction parameters, ω_{ij} and η_{ij} and their polynomial expansions. It furthermore uses equation 3.1 and a powerful Solgasmix solver engine to determine the equilibrium outcomes.

10.9 Nomenclature of Appendix A

a_i = component activities for components i = 1 to N

n_i = moles of the various components (mole)

$G°$ = pure component Gibbs Free Energy (GFE) of formation (J.mole^{-1})

G_{system} = overall system GFE (J)

H = enthalpy (J)

S = entropy (J.K^{-1})

f_i = fugacities of the gaseous components (atm)

T = system temperature (K)

$N°$ = Avogadro's Number

R = ideal gas constant (J.mole^{-1}K^{-1})

X, Y = mole fraction

z = coordination number between components in solution

k_B = Boltzman constant

e_i^j = first order interaction parameter of the unified interaction parameter formalism

$q_i^{j,k}$ = second order parameter of the unified interaction parameter formalism

Greek Symbols

ΔH = Enthalpy change

ΔS = Entropy change

$\dot{\gamma}$ = activity coefficient relative to the mass % infinite dilute standard state

ε_{ij} = pair bond energy of the modified quasichemical model ($J.mole^{-1}$)

ξ = extent of reaction, or extent of association in case of modified quasichemical model

η_{ij} = non configurational entropy of the modified quasichemical model ($J.mole^{-1}K^{-1}$)

σ_{ij} = pair bond non-configurational entropy of modified quasichemical model ($J.mole^{-1}K^{-1}$)

ω_{ij} = molar enthalpy of component association of modified quasichemical model ($J.mole^{-1}$)

11 APPENDIX B: LABORATORY STUDIES

11.1 Laboratory Arc Furnace Tests

A laboratory size plasma arc furnace was designed by the author and built in-house. Figure 11.1 is a photo of the laboratory furnace set-up.

Feeding of the premixed feed (ore, fluxes and reductant) is performed using a vibratory feeder shown on the right hand side in Figure 11.1. The arc was monitored through a sight glass with a welding glass type light filter. The operating voltage was measured with a multimeter connected to the copper bus bar and the aluminium anode plate. The roof, cathode, anode plates and side walls are water cooled using a baffled jacket type cooler. The crucibles were manufactured from impervious graphite or magnesite. The crucible itself should be electrically conductive, or a connection allowing the current to flow from the melt to the anode is required. The crucible fits into a solid graphite cylinder using an unthreaded male-female connection. The solid graphite cylinder is threaded at the bottom so that it could be screwed into the aluminium anode plate. The roof is lightweight and removable. Removing the roof is also the only way to access and remove the crucible using steel tongs. The off gas was cooled in a horizontal double tube cooler, after which it passes though a knock-out chamber to capture most of the flue dust. The height of the graphite cathode (connected to the copper bus bar) relative to the melt or crucible bottom, was controlled using a rack-and-pinion mechanism which was driven by a geared-down electrical motor. The arc current (DC) and power was regulated using a plasma cutting torch power supply, which could provide a near constant direct current while the voltage was allowed to vary according to arc length.

Figure 11.1: Laboratory plasma arc furnace

Figure 11.2 shows the typical crucibles used – the graphite crucible in the background and a magnesite crucible with a steel anode connection in the foreground.

While the graphite itself may partake in the reactions, its reactivity is extremely low compared to the coal or anthracite added. Moreover, slag corrosion is not as significant as with a refractory container, which also would influence the slag chemistry. Unfortunately is extremely difficult to simulate exact conditions in an industrial furnace such as freeze line behaviour.

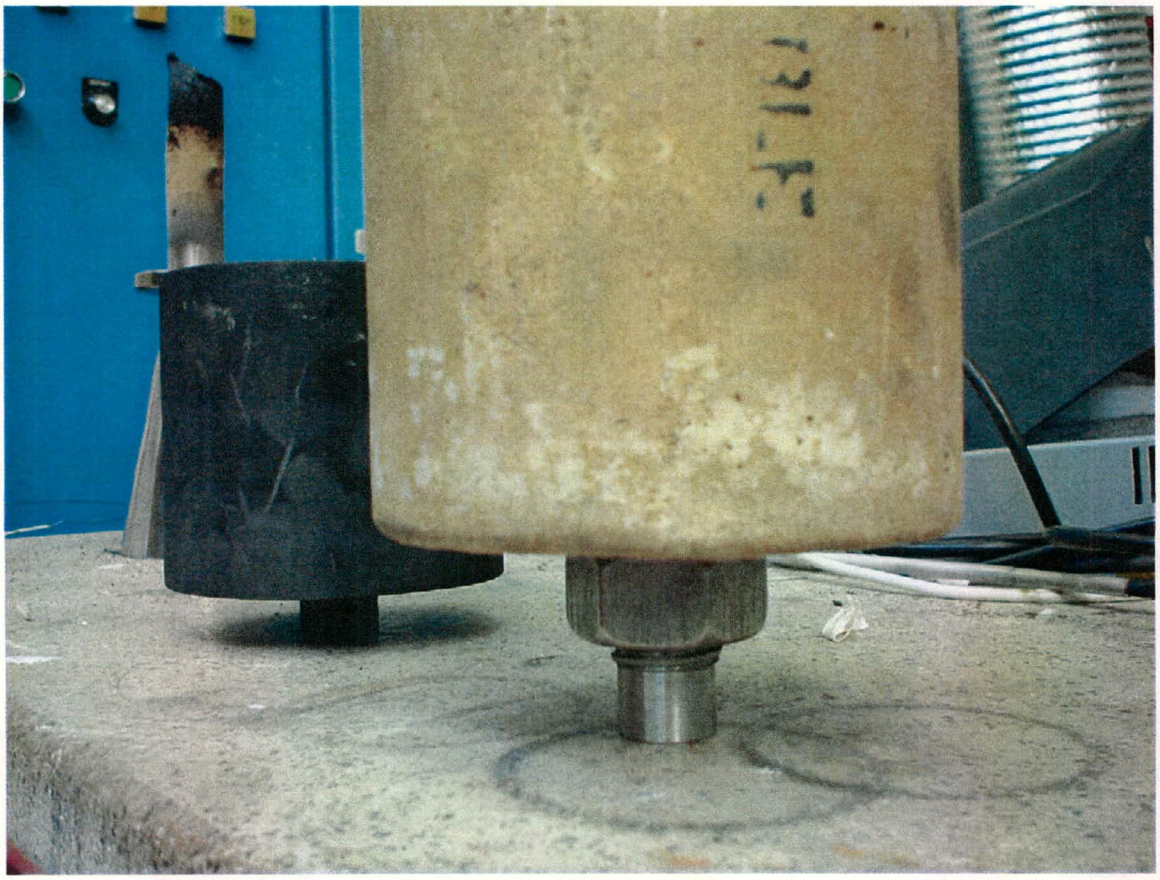

Figure 11.2: Magnesite and graphite crucibles used in the laboratory plasma arc furnace

Arc length was gauged by determining the height difference between the position at which the electrode was just touching the melt and higher position. As only the difference mattered, an arbitrary baseline could be used. A 1.0 m ruler was used to determine the height of the copper bus bar at the point of incipient electrode submergence in the melt and subsequent measurements when the arc was drawn. The arc was typically initiated through short circuiting through a thin layer of metal powder in crucible. The crucible is pre-filled with enough iron metal powder to cover the bottom of the crucible. The intense heating of the short circuit ionises the surrounding gas and initiates the arc, as described in more detail in section Chapter 2.

Once a stable arc was obtained, the material was gradually fed into the molten iron bath, using the vibratory feeder. Severe foaming made stable operation (maintenance of stable electrical characteristics) very difficult. Secondary arcing to the crucible side-walls (in the case of the graphite crucible) was sometimes noted when the arc was drawn out too long. The rapid movement of the arc between the melt and the crucible sometimes caused severe oscillation in the operating voltage which made exact arc power determination extremely difficult. The maxima an minima in the voltage were noted and the minimum was recorded as the voltage

associated with the arc length to the bath surface. It was aimed to establish if the arc length had an influence on the mixing in the furnace. To do this the arc had to be characterised. The arc characteristics as a function of arc length are presented in Figure 11.3.

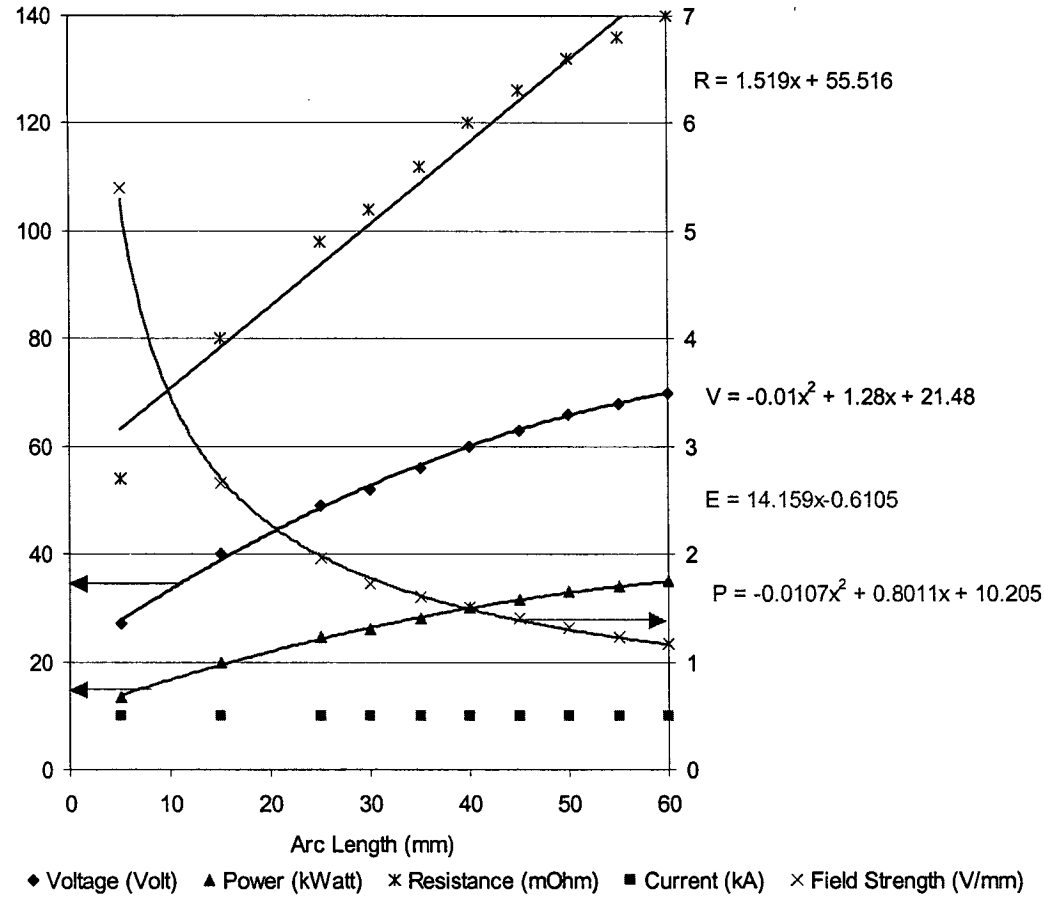

Figure 11.3: Arc characteristics of the laboratory arc furnace

A non-zero value for resistance is apparent at zero arc length. This could be ascribed to the resistance associated with the molten bath (most of the resistance) and other electrical conductors (little resistance) excluding the plasma. The "best fit" value for the bath was therefore 55.5 mOhm this would vary according to bath chemistry. The maximum realised power dissipation was determined as 35 kW, of which 10.2 kW can be associated with non-arc heating, therefore, I^2R_{melt} heating.

Due to the size of the crucible, and the extreme difficulty of withdrawing samples while the melt is still molten, the plasma was switched off and the crucible was removed 5 minutes after the last material was fed, and allowed to air cool. Quenching in water or another liquid would result in shattering of the crucible and dangerous situations. Unfortunately, due to the fact that rapid quenching was impossible, the air cooling may have led to additional segregation, causing a higher degree of spatial variance within the crucible than would have been present

when all the material was molten. The crucibles were subsequently cut axially into two halves. Sample materials were drilled our of the solidified slag and metal layers and subsequently analysed using a SEM equipped with EDS. All elements with atomic mass greater than that of carbon could be analysed this way.

9 Trials were performed on ilmenite smelting, using the same raw materials and ratios as found industrially. Figures 11.4 and 11.7 show the histograms for Fe (as a combination of FeO and entrained Fe) and SiO_2 in the slag phase respectively.

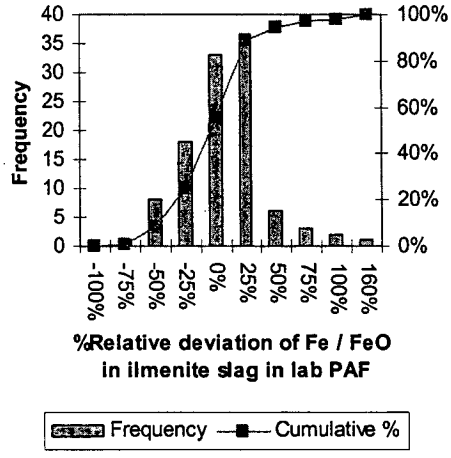

Figure 11.4: Distribution of iron in slag.

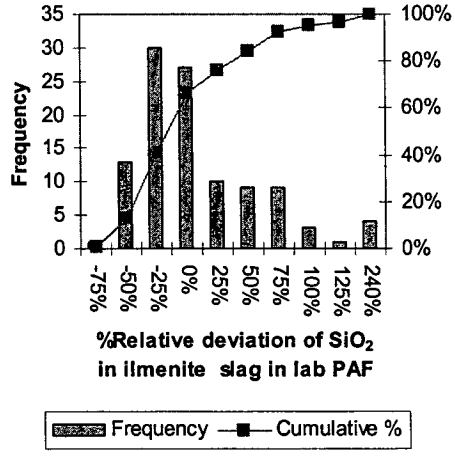

Figure 11.5: Distribution of silica in slag.

Figures 11.4 and 11.5 both show a very large spread in composition relative to the average composition of the melt in the crucible. This increased variance was expected for the laboratory furnace for reasons as discussed above. The non-normal distributions may be attributed to the few (9) runs performed. Normally 8 samples were drilled at random positions across the cross section of the solidified melt. The pig iron metal was analysed similarly and the distributions of the relative deviations of S and Si from the average bulk chemistry are depicted in the histograms in Figures 11.6 and 11.7 respectively.

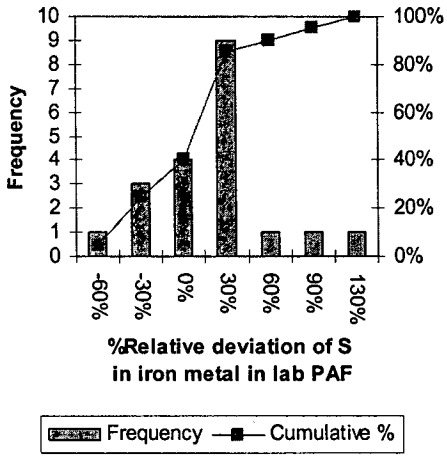

Figure 11.6: Distribution of iron in the slag.

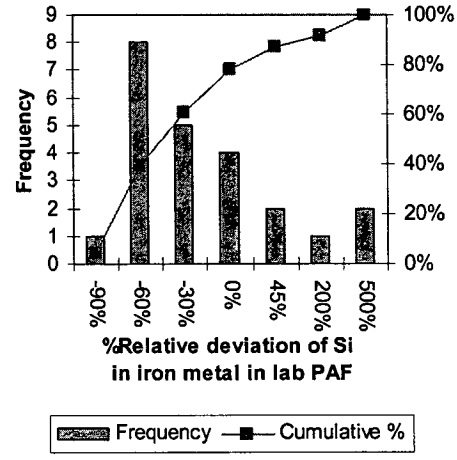

Figure 11.7: Distribution of silica in slag.

These two contaminants show the highest variance, as found in the industrial furnaces. However, the spreads for both elements are larger than found in industry. A summary of the relative standard deviations is given in Table 11.1.

Table 11.1: Mean relative deviations from bulk chemistry for ilmenite smelting in a laboratory PAF.

Component	Fe	Ti	Mn	Si	S
$\%s_{rel}$ (metal)	4%	75%	28%	86%	32%
$\%s_{rel}$ (slag)	24%	16%	15%	42%	49%

12 APPENDIX C: VISCOSITY ESTIMATION OF SLAGS

This appendix briefly discussed two methods of estimating slag viscosity, mentioned in Chapter 4, namely Urbain's model (Urbain, 1987) and Riboud's model (Riboud et al., 1981). The models predict the activation energy and pre-exponential factors for viscous flow for the Weymann-Frenkel viscosity expression (Equation 4.8).

12.1 Estimation methods for fully liquid slag viscosities according to Urbain's model (Urbain, 1987)

Urbain identifies three types of oxides to be used in the model: Glass formers, modifiers and amphoterics. The "mole fraction" of these three types are calculated as follows:

"Glass formers" $= x_G = x_{SiO_2} + x_{P_2O_5}$

"Modifiers" $= x_M = x_{CaO} + x_{MgO} + x_{MnO} + x_{FeO} + x_{Na_2O} + x_{K_2O} + 3x_{CaF_2} + 1.5x_{FeO_{1.5}} + 2x_{TiO_2} + 2x_{ZrO_2}$

"Amphoterics" $= x_A = x_{Al_2O_3} + x_{B_2O_3}$ (12.1)

"Normalised" values are obtained for x_G , x_M , x_A and are written as x_G^* , x_M^* , x_A^*. These normalised values are obtained by the mole fractions x_G , x_M , x_A, by the term $(1+ x_{CaF_2} + 0.5x_{FeO_{1.5}} + x_{TiO_2} + x_{ZrO_2})$. Urbain proposed that the parameter E_η is influenced both by the ratio $\alpha_{Urbain} = x_M^* / (x_M^* + x_A^*)$ and by x_G^*. The parameter can be expressed in the form of equation 12.2 where E_1, E_2, and E_3 which could be obtained from equation 12.3. E_1, E_2, and E_3 can be calculated from the equations listed in Table 12.1.

Table 11.1 : E-parameters for Urbain's model for viscosity $\alpha = \alpha_{Urbain}$

$E_0 = 13.8 + 39.9355\alpha - 44.049\alpha^2$
$E_1 = 30.481 - 117.1505\alpha + 139.9978\alpha^2$
$E_2 = -40.9429 + 234.0486\alpha - 300.04\alpha^2$
$E_3 = 60.7619 - 153.9276\alpha + 211.1616\alpha^2$

$$E_\eta = E_0 + E_1 x_G^* + E_2 (x_G^*)^2 + E_3 (x_G^*)^3 \quad (12.2)$$

$$E_i = a_i + b_i \alpha + c_i \alpha^2 \quad (12.3)$$

$$-\ln(A_\eta) = 0.2693 E_\eta + 11.6725 \quad (12.4)$$

The expression was further modified (Urbain, 1987) to calculate the separate E_η values for the different individual modifiers CaO, MgO and MnO. The global E_η value for a slag containing all three oxides can be derived from equation 12.5.

$$E_\eta = \frac{x_{CaO}E_{CaO} + x_{MgO}E_{MgO} + x_{MnO}E_{MnO}}{x_{CaO} + x_{MgO} + x_{MnO}} \tag{12.5}$$

12.2 Estimation methods for fully liquid slag viscosities according to Riboud's model (Riboud *et al.*, 1987)

Riboud *et al.* (1981) used a similar approach to Urbain, also using the WF-model as basis, while the parameters of Eq. 4.8 were based on 5 groupings, based on the ability to break or form polymeric chains in the molten slag:

- "SiO_2" = $SiO_2 + P_2O_5 + TiO_2 + ZrO_2$
- "CaO"= $CaO + MgO + FeO + BO_{1.5}$
- $Al_2O_3 = Al_2O_3$
- $CaF_2 = CaF_2$
- $Na_2O = Na_2O + K_2O$ (12.6)

Based on these groupings the following empirical equations were develop to calculate A_η and E_η:

$$\ln(A_\eta) = -19.81 + 1.73x_{"CaO"} + 5.82x_{CaF_2} + 7.02x_{"Na_2O"} - 35.76x_{Al_2O_3} \tag{12.7}$$

$$E_\eta = 31.140 - 238.996x_{"CaO"} - 46.356x_{CaF_2} - 39.159x_{"Na_2O"} + 68.833x_{Al_2O_3} \tag{12.8}$$

Other models, based on the thermodynamic heat and free energy of mixing have also been developed (Sridhar, 2002) as well as models based on the relative amounts of bridging, non-bridging and terminal O bonds existing in slags (Zhang and Jahanshahi, 1998a and 1998b), but will not be discussed here, as the above two models are most commonly used for industrial slags.

13 APPENDIX D: DATA RECONCILIATION

13.1 Data Accumulation

Raw data were accumulated from a data historian on the smelter plant. To obtain tap-to-tap data, the 5 minutely data had to be averaged over the period, or time integrated to obtain cumulative totals. Practical difficulties occur due to when a "Production day" starts and ends, which is not the same as a normal weekday. For example, for the ferrochrome smelter, the start of a new production day would be at 05:00 in the morning. This has implications with regard to linking the raw materials analyses to the correct production run. For instance, the raw materials may be analysed daily, but the transition of one raw material batch to another may happen at any given time during the production day. Other problems arise due to the actual production occurring during one production day, but the alloy weights of the last tap of the day only being logged on the following production day. This would occur very frequently, as the end of a production day often occurred in-between two taps. The amounts of raw materials being fed in the time preceding the tap would then be used to allocate the tap to the "correct" production day.

During tap-to-tap periods, the raw materials and energy input may fluctuate wildly, although the averages are more consistent. For example, very little of a specific raw material may have been fed at the start of a new production run, but the average recipe is still maintained due to dumping most of the material closer to the following tap event. These variations in raw material feeding in-between two taps were not included in this thesis, but it is acknowledged that the variations will significant impact on the metallurgy of the products and wastes.

Representative sampling remains to be a significant problem for the dust and gas streams. It is extremely difficult to sample directly from the raw gas stream leaving the furnace, and one has to resolve to sampling from either heaps, accretions or slurry stream from a venturi scrubber, or of the venturi scrubber filter cake, all of which lead to unsatisfactory and inaccurate sampling. Large bias ranges and relative standard deviations were consequently allocated to the quantity and analyses of the dust stream.

Finally errors also creep into the system where manual inputs are required, such as updating the laboratory information system with the latest assays, as well as the recorded weights of alloy produced and the inventories of the slag ladles tapped.

13.1.1 Preparation for Reconciliation

The analyses are based on either elemental analyses using spark-OES instruments, LECO analysers, or an ICP, or the analyses were reported as oxides, based on XRF analyses. The mineralogy of the feed is taken into account, but in a stationary proportion type of way. For example, it is known that the "ilmenite" that is smelted is not necessarily stoichiometric ilmenite, but may include leucoxene, ulvospinel or pseudobrookite. A long term average is therefore used to gauge the Fe^{3+}:Fe^{2+} and Ti^{4+}:Ti^{3+} ratios. Once determined through wet analyses or XRD characterisation, these ratios remain fixed, even though the ratio of total Fe to total Ti in the feed may vary. The chrome minerals are treated in a similar way.

With regard to the slags and alloys, it was decided to establish if any particular relationships exists which could be used to estimate generally unmeasured quantities. It was shown in Chapter 5 how this was done to relate the concentration Ti^{3+} in high titania slags to the %FeO in the slag. Similarly it was shown for Ferrochrome that a good relationship exists between the %Si and %C in the alloy. Similarly the relative proportions of Cr as Cr metal, Cr^{2+} and Cr^{3+} in slag has to be estimated based on thermodynamic knowledge of the system, microscopy studies and wet analysis. The estimation of the oxidation states is a crucial step in the whole process as it determines the ratio of oxidising to reducing agents and the overall oxygen partial pressure of the system. The oxygen associated with the feeds and products of the system leads to a very constrained oxygen balance, i.e. there is very little room for adjustment, as stoichiometric constraints also have to be satisfied.

13.1.2 Reconciliation

The reconciliations were done within spreadsheets, using the advanced "Solver" facility, from Frontline Systems Incorporated, which allowed the goal-seeking of very large multi-variable non-linear and integer optimisation problems. For example, the reconciliation of the ferrochrome smelter data led to:

- 9 Feed Streams and 4 Product Streams,
- Reconciled for totals flows and 9 elements, therefore 9 mass balances
- Non-negative constraints on all variables

- Forcing the adjusted variable to lie within 3 relative standard deviations
- Stoichiometric constraints, especially for oxygen
- Allowing for a small tolerance on the total streams

The solver first searches the solution space for all possible solutions satisfying the constraints, and subsequently searches for the specific group of adjusted variables that minimises the objective function (sum of squares of the relative adjustments).

13.1.3 Bias Determination

The biases were determined based on a maximum likelihood criterion. In this case, the adjustments were first determined without bias over the whole campaign time, and then statistically characterised to obtain the most likely adjustment. In non-biased cases the most likely adjustment would be zero, assuming a normal distribution of random errors. If the most likely absolute adjustment is significantly greater than zero, using statistical levels of significance, the bias is viewed as a true bias. To ensure that only significant variations from zero are classified as biases, threshold adjustment values are determined for each adjusted variable, which the adjustment must exceed before being classified as a real bias. It also helps in the analyses to determine from operating staff if they know of any biased measurements, or any situation where they apply "fudge factors" to interpret the measured data. Once the biases were established they were treated as constant over the whole period. Again, there may be error in this assumption.

13.1.4 Reconciliation Spreadsheet Example

An example of a part of the spreadsheet, in this case for ferrochrome, is given in Figure 12.1. The measured value listed per element gives the mass fraction of the element in the stream in which row the measurement is listed. The data in green blocks make up part of the mass balance constraints. It is clear that biases occurred only for some streams and some elements. The "objective" column for each element is determined by the square relative standard deviation weighed, bias-included, relative adjustment. The squares of these weighed adjustments are then totalled per element for all streams, and then totalled for all elements, as well as the total stream balance. The overall objective (to be minimised) is given in the yellow-shaded cell in the column furthest to the left.

Figure 13.1: Example of a portion of a spreadsheet used to reconcile the streams and elements for a ferrochrome smelter.

1	Tap interval		MACRO	Ctrl Z										
	Flow Rate					Cr					Fe			
Feed	Measured	σ	Bias	Adjusted	objective	Measured	σ	Bias	Adjusted	objective	Measured	σ	Bias	
Anthracite	100.803	1.016124			10452.775						0.003519	7.74E-09		0.
Selsum	16.831	0.028328		10.901	1241.2035						0.004958	1.54E-08		0.
Screenings	297.364	2.210634		341.521	882.01833	0.272597	4.64E-05		0.490	1021.6838	0.184772	2.13E-05		0.
WC-2mm	85.683	0.734158		46.415	2100.3254	0.254654	4.05E-05		0.283	19.301099	0.17828	1.99E-05		0.
Open Cast - 8mm	20.375	0.041514		18.183	115.73904	0.253419	4.01E-05		0.263	2.2477694	0.176472	1.95E-05		0.
Spills	20.3745	0.041512		18.941	49.493676	0.26023	4.23E-05		0.271	2.9179253	0.179842	2.02E-05		0.
Quartz	8.352	0.006976		8.078	10.80133									
Limestone	63.861	0.407823		39.218	1489.0303						0.004027	1.01E-08		0.
Electrode	0	0.000225		0.006	0.1373458									
Product	613.644													
Metal	208.665	27.21318	-10.433	339.485	733.18807	0.538889	4.31E-05		0.554	5.4358279	0.362078	3.25E-05		0.
Slag	230	132.25	-52.302	33.311	157.63813	0.062682	1.22E-05	0.007	0.064	2.5841415	0.056345	8.56E-06	0.004	0.
Off Gas	209.70535	109.9408	25.164642	104.764	153.96948									
Dust	2.121764	0.011255		3.446	155.87429	0.080658	1.63E-05		0.074	2.3642951	0.086878	1.89E-05		0.
	650.492													
Ojective	25945.833		in	481.006	17542.194					1056.5349				
			out	481.006										
Constraint#1	0.000													
	0.000													

Constraint#2: Anthracite	
Selsum	
Screenings	167.49125
WC-2mm	13.117998
Open Cast-8mm	4.7806348
Spills	5.1395443
Quartz	
Limestone	
Electrode	
Metal	188.13875
Slag	2.1340729
Off-gas	
Dust	0.2565998
	0.0000

Constraint#3: Anthracite	0.988	0.9879162
Selsum	0.977	0.9772576
Screenings	1.000	1
WC-2mm	0.994	0.9943366
Open Cast-8mm	0.995	0.9946183
Spills	0.996	0.9963212
Quartz	1.000	1
Limestone	0.994	0.993754
Electrode	1	1
Metal	0.997	0.9970983
Slag	1.004	1.0035436
Off gas	1.000	1
Dust	0.992	0.9915911